This microfiche was produced according to ANSI/AIIM Standards and meets the quality specifications contained therein. A poor blowback image is the result of the characteristics of the original document.

Studying Turbulence Using Numerical Simulation Databases - VI

Proceedings of the 1996 Summer Program

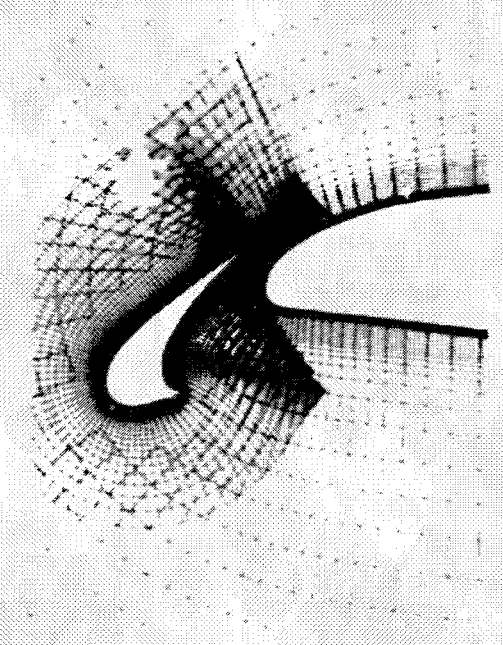

Center for Turbulence Research

December 1996

Ames Research Center

Stanford University

Studying Turbulence Using Numerical Simulation Databases - VI

Proceedings of the 1996 Summer Program

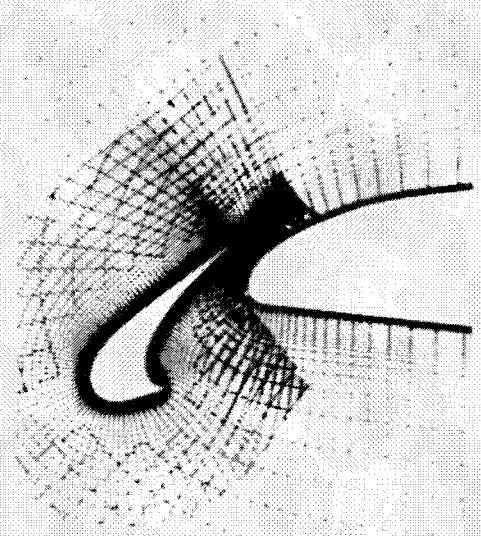

Center for Turbulence Research

December 1996

Ames Research Center

Stanford University

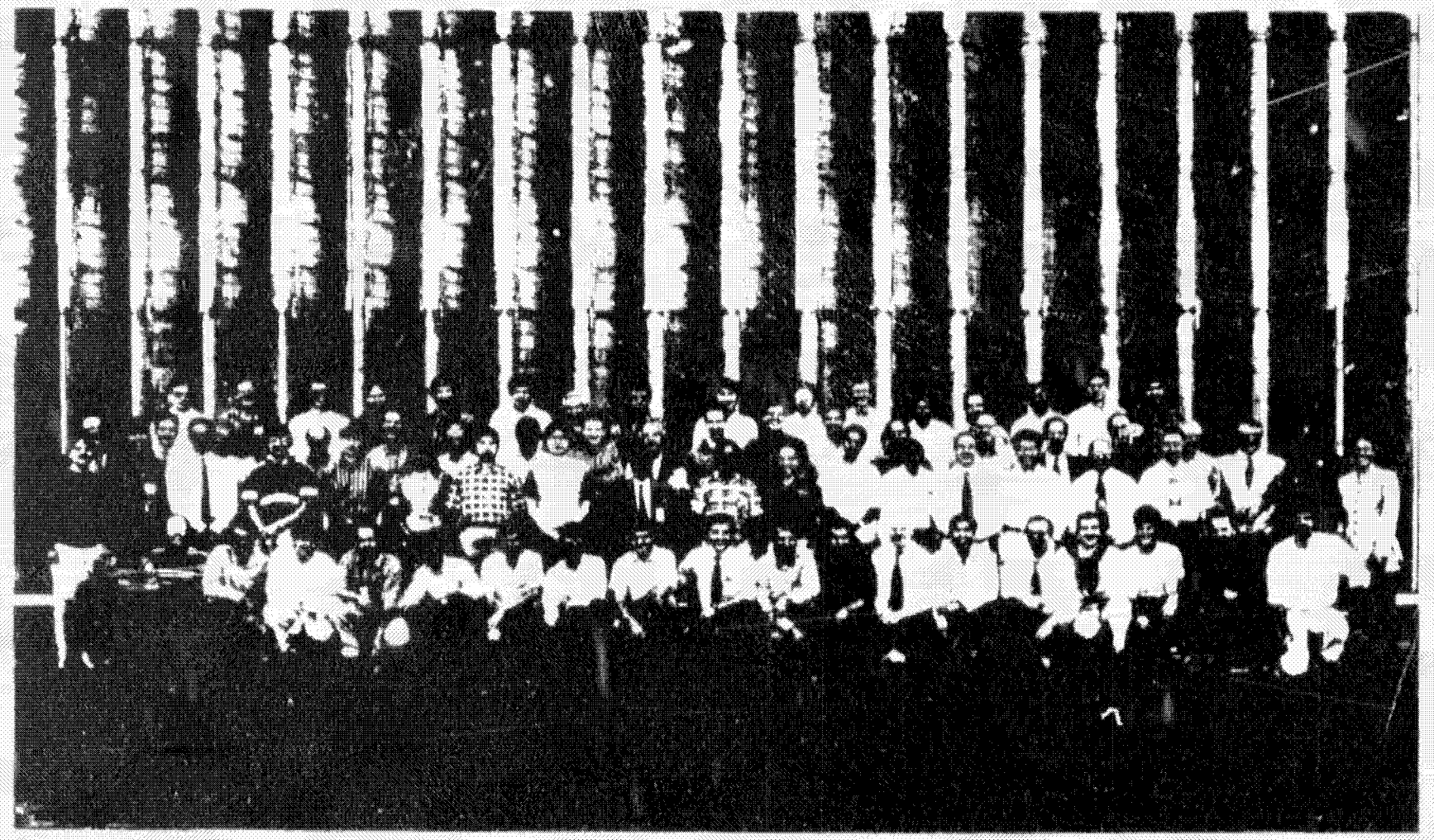

CONTENTS

REPORT DOCUMENTATION PAGE

Form Approved
OMB No. 0704-0188

1. AGENCY USE ONLY (Leave blank)	2. REPORT DATE	3. REPORT TYPE AND DATES COVERED
	December 1996	Technical Proceedings

4. TITLE AND SUBTITLE
Studying Turbulence Using Numerical Simulation Databases - VI
Proceedings of the 1996 Summer Program

5. FUNDING NUMBERS

6. AUTHOR(S)

7. PERFORMING ORGANIZATION NAME(S) AND ADDRESS(ES)
Center for Turbulence Research
Bldg. 500
Stanford, CA 94305-3030

8. PERFORMING ORGANIZATION REPORT NUMBER

9. SPONSORING / MONITORING AGENCY NAME(S) AND ADDRESS(ES)
NASA Ames Research Center
Moffett Field, CA 94035-1000

10. SPONSORING / MONITORING AGENCY REPORT NUMBER

11. SUPPLEMENTARY NOTES

12a. DISTRIBUTION / AVAILABILITY STATEMENT

12b. DISTRIBUTION CODE

13. ABSTRACT (Maximum 200 words)

Proceedings of the 1996 Summer Program of the Center for Turbulence Research held

14. SUBJECT TERMS large eddy simulation, turbulence modeling, Reynolds averaged modeling, combustion, control, structures, hydroacoustics,

15. NUMBER OF PAGES 456

16. PRICE CODE

17. SECURITY CLASSIFICATION OF REPORT	18. SECURITY CLASSIFICATION OF THIS PAGE	19. SECURITY CLASSIFICATION OF ABSTRACT	20. LIMITATION OF ABSTRACT
unclassified	unclassified	unclassified	

Preface

The Sixth Summer Program of the Center for Turbulence Research was held during the four-week period June 24 to July 19, 1996. There were thirty-seven participants from the U. S. and nine other countries and twenty-six local Stanford, NASA-Ames, and CTR staff who devoted virtually all of their time to the program. As in the previous summer programs, the participants used the archived direct numerical simulation databases to test turbulence models and study turbulence physics. In addition, several calculations of complex flows and new simulations were performed during the Program.

A hallmark of the 1996 Summer Program was a very large turbulence modeling and application group. The so-called Reynolds averaged modeling, RANS, is an important industrial tool for prediction of turbulent flows. New modeling ideas recently put forward at CTR and a special focus on a specific application were the catalysts that brought together this group of turbulence modelers and computational fluid dynamicists.

As in the past Summer Programs, the combustion community was well represented. Of particular interest were promising findings in the application of the large eddy simulation technique, LES, to turbulent reacting flows. The LES group contributed the largest number of papers to this volume. New subgrid scale models were tested and several important issues in application of LES were addressed. The LES group also included two representatives from aerospace and automobile industries which recently have shown interest in using this tool for simulation of complex flows encountered in power systems. The control, structures, and hydroacoustics group included such fundamental studies as control strategies for laminar/turbulent transition and detection of organized structures in separated flows. It also included a group from David Taylor Laboratory who evaluated models of space/time characteristics of wall pressure fluctuations in separated flows.

As part of the Summer Program three review tutorials were given on ***Large eddy simulation*** (Parviz Moin), ***DNS of premixed combustion*** (Thierry Poinsot and Denis Veynante), and ***Turbulence/shock wave interaction*** (Krishnan Mahesh); and one seminar entitled ***Controlling complex systems with MEMS*** was presented by James McMichael. A number of colleagues from universities, government agencies, and industry attended the final presentations of the participants on July 19. They provided valuable input on the work accomplished and participated in the discussions.

There are twenty-eight papers in this volume grouped in the above four areas. Each group is preceded with an overview by the CTR coordinator of the group. Early reporting of thirteen of the projects occurred at the Forty Ninth Meeting of the Division of Fluid Dynamics of the American Physical Society in Syracuse, New York, November 24-26, 1996.

The success of an intensive program such as this results from the efforts of many professionals. We are grateful to several administrative staff members of NASA Ames for going beyond the call of duty to facilitate this Summer Program. It is also

a pleasure to acknowledge the diligent efforts of Debra Spinks in the organization of the Program and compilation of this report. Her efforts in the planning and operation of this and other CTR Summer Programs have been invaluable.

Parviz Moin
William C. Reynolds
Nagi N. Mansour

The turbulence modeling group

This introduction will highlight notable aspects of the reports from the turbulence modeling group. Five visitors participated in this group: Fue-Sang Lien, from the University of Manchester Institute of Science and Technology (UMIST); Gianluca Iaccarino, from the Centro Italiano Ricerche Aerospaziali (CIRA); Dominique Laurence, from the Electricité de France (EDF); Deji Demuren, from Old Dominion University; Vittorio Michelassi, from the University of Florence; and Blair Perot, a private consultant. The NASA and CTR hosts were Sacha Parniex, Mike Rogers, Parviz Moin, Nagi Mansour and Paul Durbin. The projects involved exploring new modeling approaches, variants on existing models, *a priori* testing of models with DNS data, and computation of complex flows. Turbulent flow in high-lift aerodynamics was a special subtopic for this summer program: Iaccarino and Lien's contributions address that application.

Blair Perot's report proposes 'a new approach to turbulence modeling'. He asks whether predictions comparable to those obtained by second-moment closure can be obtained from a simpler closure, if only the mean flow is required. The mathematical origin of this question comes from applying the Helmholtz decomposition of vector fields to the RANS equations. The mean flow equation contains a Reynolds-stress force: $F_i = -\partial_j \overline{u_i u_j}$. This is a vector field, to which the Helmholtz decomposition into curl and divergence-free components applies: $\mathbf{F} = \nabla\phi + \nabla \times \boldsymbol{\psi}$. What are the physical meaning of the scalar and vector potentials ϕ and $\boldsymbol{\psi}$? Can one develop a closure model for ϕ and $\boldsymbol{\psi}$? Will it contain as much 'physics' as SMC? Read Blair's contribution for a status report on these questions.

Gianluca Iaccarino and Fue-Sang Lien worked on 'modeling with application to high-lift aerodynamics'. Phenomena that arise in high-lift flows include trailing edge separation at high angles of attack, 3-dimensional separations, impinging wakes, gap jets, and other element-element interactions. So this application challenges the abilities of turbulence models and turbulence modelers.

Iaccarino and Lien worked primarily with the $k-\varepsilon-v^2$ model. Iaccarino computed flows around two and three-element airfoils. He found that the basic model did a good job of capturing many of the pertinent features of these flows. A good deal of his time was spent on numerical issues; after some disappointment with his explicit, compressible code, he decided to work with our version of INS-2D (RS_INS) that has the model implemented. His are the first multi-block and chimera-grid computations with this model.

Lien implemented the $k-\varepsilon-v^2$ model into his finite-volume, pressure-correction, incompressible code. His article explores several variations on the basic model: the first is a non-linear constitutive equation that is developed with the aid of DNS data; second is a 'code friendly' variation that is proposed in the interest of numerical schemes that solve the equations in an uncoupled form; finally, he investigates transitional properties of the model, introducing a Reynolds number dependent coefficient. The non-linear constitutive relation allows for normal stress anisotropies

that are not accommodated by the usual Boussinesq relation. The natural boundary conditions for the $k-\varepsilon$ and $\overline{v^2}-f$-equations are imposed explicitly on k and $\overline{v^2}$ and determine ε and f implicitly, so it is natural to solve these as coupled pairs of equations. However, some CFD codes are written to solve equations one at a time, or use fully explicit methods. It is for these types of codes that the 'code friendly' variant — primarily in the $\overline{v^2}$ boundary condition — is proposed in Lien's contribution. Lien computed flow around a single element airfoil and around a three-dimensional, inclined prolate spheroid. The flow round the spheroid contains a three-dimensional separation line.

Dominique Laurence, Deji Demuren and Vittorio Michelassi worked on 'modeling dissipation and turbulence transport'.

Michelassi's article compares the original $k-\varepsilon-v^2$ model to a variant that offers some apparent improvements to the analytical formulation. He found that the predictions of the two forms are very similar, which suggests that the modifications are viable. In his RANS computations Michelassi focuses on flow over a backstep, looking at how the model affects reattachment and recirculation. Various shortcomings are discussed.

Laurence and Parneix's article describes an innovative method for studying turbulence modeling by using a DNS database. Commonly, *a priori* tests of turbulence models consist of plugging DNS data into algebraic formulas used in the models. Such tests are of little value: the formulas in question are closures for a set of differential equations, they are not algebraic models. Their mathematical and predictive value can only be assessed by solving the differential equations. Is there any way to use DNS data that will test the properties of the differential equations? Laurence and Parneix's idea is to solve a subset of the model equations, using the entire DNS fields for the other variables. This permits an assessment of the model in its proper mathematical context. For example: if the convection velocity U and production rate $\overline{u_i u_j}\partial_j U_i$ are right, do the differential equations predict k and ε correctly? This technique uses the DNS fields more comprehensively than have previous *a priori* model tests: see this article for more on this intriguing development.

Demuren evaluated pressure-diffusion and pressure-strain terms in turbulent mixing layers and wakes using DNS data. His article discusses comparisons between Lumley's formula relating pressure-diffusion to third moments of velocity and Mike Roger's DNS data. However, these third moments are not variables in second-moment closures, so it is usual to invoke a gradient diffusion assumption to relate third and second moments. Demuren shows that Lumley's formula is often quite good, but that the gradient diffusion assumption often fails. The velocity-pressure gradient correlations were split into slow and rapid parts, in the usual manner. Their relative roles are investigated in Demuren's article, with some interesting results.

NEXT
DOCUMENT

Non-linear k-ε-v^2 modeling with application to high-lift

By F. S. Lien[1] AND P. A. Durbin[2]

The $k-\varepsilon-\overline{v^2}$ model has been investigated to quantify its predictive performance on two high-lift configurations: 2D flow over a single-element aerofoil, involving closed-type separation: 3D flow over a prolate spheroid, involving open-type separation. A 'code-friendly' modification has been proposed which enhances the numerical stability, in particular, for explicit and uncoupled flow solvers. As a result of introducing Reynolds-number dependence into a coefficient of the ε-equation, the skin-friction distribution for the by-pass transitional flow over a flat plate is better predicted. In order to improve deficiencies arising from the Boussinesq approximation, a non-linear stress-strain constitutive relation was adopted, in which the only one free constant is calibrated on the basis of DNS data, and the Reynolds-stress anisotropy near the wall is fairly well represented.

1. Introduction

Eddy-viscosity models based on the linear Boussinesq relations are known to be afflicted by numerous weaknesses, including an inability to capture normal stress anisotropy, insufficient sensitivity to secondary strains, seriously excessive generation of turbulence at impingement zones, and a violation of realizability at large rates of strain. Notwithstanding these defects, eddy-viscosity models remain popular, and their use in complex flows is widespread due, principally, to their formalistic simplicity, numerical robustness, and computational economy. Second-moment closure, on the other hand, accounts for several of the key features of turbulence that are misrepresented by linear eddy-viscosity models, but is considerably more complex and can suffer from poor numerical stability due to the lack of dominance of second-order fragments in the set of terms representing diffusion. As a result, the CPU requirements for second-moment closure models can be high, especially in 3D flows.

A potential alternative to second-moment closure, but one which retains advantageous elements of the linear eddy-viscosity framework, is to use a constitutive relation that equates the Reynolds-stresses to a non-linear expansion in powers of the mean rate of strain and rate of rotation tensors. This may be cast in the form of a sum of terms, each pre-multiplied by an apparent viscosity—hence the term 'non-linear eddy-viscosity models'. Examples include the models of Speziale (1987), Shih *et al.* (1993), Durbin (1995a), Craft *et al.* (1995) and Lien *et al.* (1996). The

1 University of Manchester Institute of Science and Technology, UK

2 Stanford University

main differences between the above modeling strategies can be summarized in the following table:

Authors(s)	Model form	Order in the stress-strain relationship	Number of turbulence transport equations
Speziale (1987)	High-Re	quadratic	2, $k-\varepsilon$
Shih *et al.* (1993)	High-Re	quadratic	2, $k-\varepsilon$
Durbin (1995a)	Low-Re	quadratic	3, $k-\varepsilon-\overline{v^2}$
Craft *et al.* (1995)	Low-Re	cubic	3, $k-\varepsilon-A_2$
Lien *et al.* (1996)	Low-Re	cubic	2, $k-\varepsilon$

The A_2 value the second Reynolds-stress invariant in Craft *et al.*'s $k-\varepsilon-A_2$ model is obtained by solving a related transport equation as follows:

$$\partial_t A_2 + U\cdot\nabla A_2 = -2\frac{A_2}{k}(d_k + P_k - \varepsilon)$$

$$+2\frac{a_{ij}}{k}(d_{ij} + P_{ij} + \phi_{ij} - \varepsilon_{ij}), \tag{1}$$

with fragments consistent with second-moment closure. In order to be free from topological constraints, the unit vector in the wall-reflection term is replaced by the length-scale gradient. The expansion of (1) in 3D curvilinear coordinate systems is tedious and prone to error. Also, a major drawback of this model is the high level of sensitivity to the near-wall grid parameters, including resolution, distribution, and aspect ratio.

The $\overline{v^2}$-equation in Durbin's $k-\varepsilon-\overline{v^2}$ model, to be addressed in Section 2, was simplified from second-moment closure on the basis of the IP pressure-strain model in conjunction with elliptic relaxation. This approach is algorithmically simple, applicable to the low-Re region, and naturally mimics the kinematic blocking effect on the turbulence of a solid wall.

Another important feature which distinguishes Durbin's model from most others is the expression of eddy-viscosity ν_t, which plays an important role in determining the correct level of shear stress. In Craft *et al.*'s model,

$$\nu_t = 0.734\frac{r_\eta[1-\exp\{-0.145\exp(1.3\eta^{5/6})\}]}{1+1.8\eta}\frac{\sqrt{\tilde{\epsilon}/\epsilon}\{1-0.8\exp(-\hat{R}_t/30)\}}{1+0.6A_2+0.2A_2^{3.5}}(kT) \tag{2}$$

where

$$r_\eta = 1+\left[1-\exp(-\frac{A_2^3}{0.125})\right]\left[1+4\sqrt{\exp(-\hat{R}_t/20)}\right],\ \eta = \max(\hat{S},\hat{\Omega})r_\eta, \tag{3}$$

and $\hat{S}$ and $\hat{\Omega}$ are strain and vorticity invariants. While in Durbin's model,

$$\nu_t = 0.19\frac{\overline{v^2}}{k}(kT). \tag{4}$$

One distinct difference between Eqs. (2) and (4) is that the latter does not require any damping function: a result of using $\overline{v^2}$ as the velocity scale in the direction of the wall. The former, on the other hand, sensitizes ν_t to $\hat{S}$, $\hat{\Omega}$, $\hat{R}_t$ (i.e., Reynolds number) and A_2, with the functional dependency being carefully calibrated on a range of flows, including straining flow, channel flow, impinging jet, and transitional flow. However when this model was tested for turbomachinery flows at (and near) off-design conditions, the size of the leading-edge separation bubble was overestimated, and in some cases no converged solution could be obtained. This is due to η (strain and vorticity) and A_2 being too large along the curved shear layer . As a result of both parameters appearing in the denominator of ν_t expression, the level of shear stress was significantly under-predicted (Chen, 1996).

In the present work, the $k-\varepsilon-\overline{v^2}$ model of Durbin (1995b) is applied to high-lift configurations, both 2D and 3D. In the course of this study, numerical instability arising from the boundary condition at wall was encountered, due to our use of a solution algorithm that uncouples the $\overline{v^2}$ and f-equations. A 'code-friendly' modification is introduced, which not only circumvents this numerical difficulty, but also gives better predictions for transitional flows. This variant is then combined with the non-linear stress-strain constitutive equation with the aim of improving the near-wall behavior of normal-stress anisotropy.

2. $k-\varepsilon-\overline{v^2}$ model

The turbulence model uses the standard $k-\varepsilon$ equations:

$$\partial_t k + U\cdot\nabla k = P_k - \varepsilon + [(\nu + \frac{\nu_t}{\sigma_k})\nabla k], \tag{5}$$

$$\partial_t \varepsilon + U\cdot\nabla \varepsilon = \frac{C_{\varepsilon 1}P_k - C_{\varepsilon 2}\varepsilon}{T} + [(\nu + \frac{\nu_t}{\sigma_\varepsilon})\nabla \varepsilon]. \tag{6}$$

On no-slip boundaries, $y \to 0$,

$$k = 0,\ \epsilon \to 2\nu\frac{k}{y^2}. \tag{7}$$

The $\overline{v^2}$ transport equation is

$$\partial_t \overline{v^2} + U\cdot\nabla \overline{v^2} = kf - n\overline{v^2}\frac{\varepsilon}{k} + \nabla\cdot[(\nu+\nu_t)\nabla\overline{v^2}], \tag{8}$$

where kf represents redistribution of turbulence energy from the streamwise component. Non-locality is represented by solving an elliptic relaxation equation for f:

$$L^2\nabla^2 f - f = \frac{1}{T}\left[(C_1 - n)\frac{\overline{v^2}}{k} - (C_1 - 1) - \frac{2}{3}\right] - C_2\frac{P_k}{k}, \tag{9}$$

where

$$T = \max\left[\frac{k}{\varepsilon}, 6(\frac{\nu}{\varepsilon})^{1/2}\right],\ L = C_L\max\left[\frac{k^{3/2}}{\varepsilon}, C_\eta(\frac{\nu^3}{\varepsilon})^{1/4}\right]. \tag{10}$$

The Boussinesq approximation is used for the stress-strain relation:

$$a_{ij} = \frac{\overline{u_i u_j}}{k} - \frac{2}{3}\delta_{ij} = -\frac{\nu_t}{k} S_{ij}, \tag{11}$$

where the eddy viscosity is given by

$$\nu_t = C_\mu \overline{v^2} T. \tag{12}$$

The constants of the model are:

$$C_\mu = 0.19,\ \sigma_k = 1,\ \sigma_\epsilon = 1.3,$$

$$C_{\epsilon 1} = 1.55,\ C_{\epsilon 2} = 1.9$$

$$C_1 = 1.4,\ C_2 = 0.3,\ C_L = 0.3,\ C_\eta = 70. \tag{13}$$

As $y \to 0$ — y being the minimum distance to walls — and $k \to (1/2\nu)\epsilon y^2$, Eq. (8) becomes:

$$\nu \partial_y^2 \overline{v^2} - 2n\nu \frac{\overline{v^2}}{y^2} = kf. \tag{14}$$

The viscous and kinematic conditions at the wall show that $\overline{v^2}$ should be $O(y^4)$ as $y \to 0$. In the original $k - \epsilon - \overline{v^2}$ model, $n = 1$, yielding the boundary condition for f

$$f(0) \to -\frac{(24 - 4n)\nu^2 \overline{v^2}}{\epsilon(0) y^4}\Big|_{n=1} = -\frac{20\nu^2 \overline{v^2}}{\epsilon(0) y^4}. \tag{15}$$

on no-slip walls.

2.1 Code-friendly modification

Equation (15) works fairly well for coupled, implicit solvers [e.g. INS2D code of Rogers & Kwak (1990)]. However, for explicit and uncoupled schemes, numerical instability arising from y^4 in the denominator of Eq. (15) sometimes occurs. Therefore, a code-friendly modification is made here by setting $n = 6$, which allows $f(0) = 0$ to be imposed as the boundary condition. In addition, $C_{\epsilon 1}$ and $C_{\epsilon 2}$ are replaced by

$$C_{\epsilon 1} = 1.55 + \exp(-A_\epsilon R_y^2)\big|_{A_\epsilon = 0.00285},\ C_{\epsilon 2} = 1.92, \tag{16}$$

where $R_y = y\sqrt{k}/\nu$, and the other model constants are:

$$C_\mu = 0.19,\ \sigma_k = 1,\ \sigma_\epsilon = 1.5,$$

$$C_1 = 1.4,\ C_2 = 0.3,\ C_L = 0.17\ C_\eta = 70. \tag{17}$$

2.1.1 Fully-developed channel flow

The model constants, in particular $A_\epsilon = 0.00285$ and $C_L = 0.17$, were first calibrated with the channel-flow DNS data of Kim *et al.* (1987) and then optimized

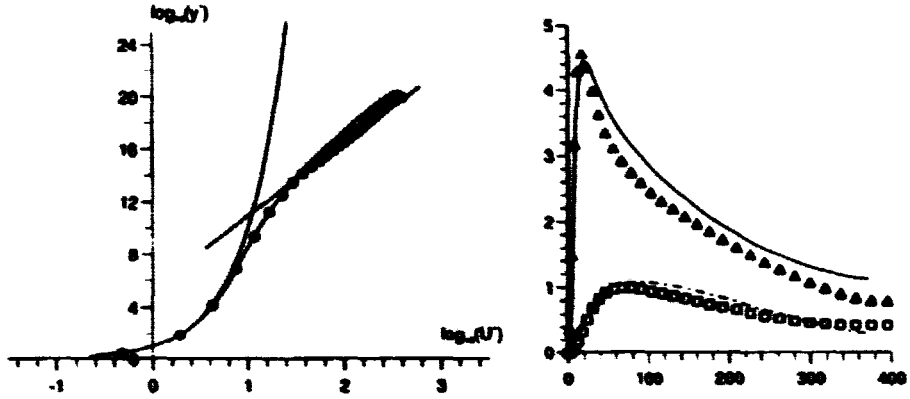

FIGURE 1. Channel flow: (Left) mean velocity; (Right) k and $\overline{v^2}$. DNS: • velocity; Δ k; $\square$ $\overline{v^2}$.

on the basis of 2D/3D separated flows to be presented later. As seen in Fig. 1, both the mean-velocity and turbulence profiles, the latter including k and $\overline{v^2}$, agree reasonably well with the data.

2.1.2 By-pass transitional flow over a flat plate

The second case examined here is the flow over a flat plate with free-stream turbulence intensity $T_u = 3\%$ and dissipation length scale $\ell_\varepsilon^\infty = 10$ mm. The experimental study was conducted at Rolls Royce Aeroengines in Derby, UK. The skin-friction distributions, obtained with the original and code-friendly $k-\varepsilon-\overline{v^2}$ variants and Launder-Sharma model (1974), are shown in Fig. 2(L). As seen, introducing the R_y-dependency in $C_{\varepsilon 1}$ for the code-friendly variant improves transition predictions. Although the resulting onset of transition is slightly earlier than that returned by the Launder-Sharma model, the length of transition is better represented. As the flow becomes fully turbulent, the velocity profiles obtained with both $k-\varepsilon-\overline{v^2}$ variants are almost identical as demonstrated in Fig. 2(R).

2.2 Non-linear constitutive relation

A general constitutive relation of the type proposed by Pope (1975) can be written as:

$$a_{ij} = \frac{\overline{u_i u_j}}{k} - \frac{2}{3}\delta_{ij} = \sum_{\lambda=1}^{10} G^\lambda(S_{ij}, \Omega_{ij}, \overline{v^2}/k, T) T_{ij}^\lambda. \tag{18}$$

where $T_{ij}^1 = S_{ij}$, $T_{ij}^2 = S_{ik}\Omega_{kj} - \Omega_{ik}S_{kj}$, $T_{ij}^3 = S_{ik}S_{kj} - \frac{1}{3}\delta_{ij}S_{lk}S_{kl}\cdots$. Truncating at the third term for simplicity gives rise to

$$a_{ij} = -\frac{\nu_t}{k}S_{ij} + G^2(S_{ik}\Omega_{kj} - \Omega_{ik}S_{kj}) + G^3(S_{ik}S_{kj} - \frac{1}{3}\delta_{ij}S_{lk}S_{kl}). \tag{19}$$

where

$$S_{ij} = \frac{\partial U_i}{\partial x_j} + \frac{\partial U_j}{\partial x_i}, \quad \Omega_{ij} = \frac{\partial U_i}{\partial x_j} - \frac{\partial U_j}{\partial x_i}. \tag{20}$$

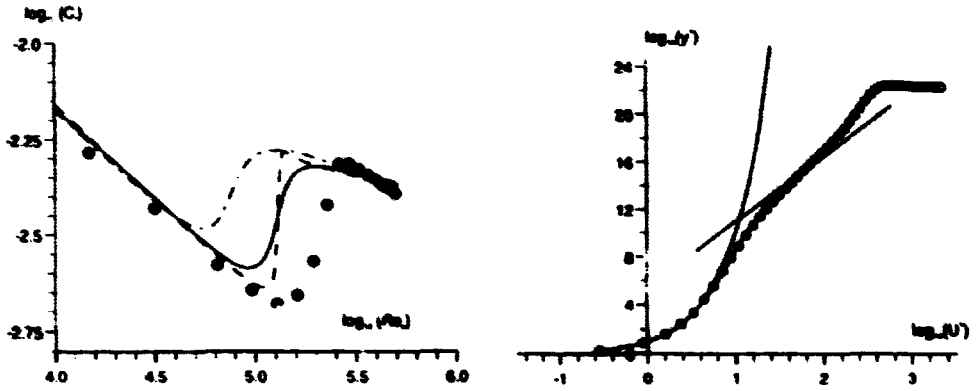

FIGURE 2. Flat plate: (Left) skin friction; (Right) mean-velocity profile. • expt.; ---- $k-\varepsilon$; —·— o original $k-\varepsilon-\overline{v^2}$; —— modified $k-\varepsilon-\overline{v^2}$

Two constrains for parallel flow will be imposed:

$$a_{22} = a_{\overline{v^2}}, \quad a_{11} = \alpha a_{22} = \alpha a_{\overline{v^2}}, \tag{21}$$

where $a_{\overline{v^2}} = \frac{\overline{v^2}}{k} - \frac{2}{3}$. These yield

$$G^2 = \frac{1}{4}\frac{(1-\alpha)a_{\overline{v^2}}}{S^2}T^2, \quad G^3 = \frac{3}{2}\frac{(1+\alpha)a_{\overline{v^2}}}{S^2}T^2, \tag{22}$$

where $S = \frac{k}{\varepsilon}|\frac{\partial U}{\partial y}|$ or $(= \frac{k}{\varepsilon}\sqrt{S_{ij}S_{ij}/2}$, in general) and T is defined in Eq. (6). The remaining unknown, α, can be evaluated from DNS data of channel flow (Kim *et al.*, 1987), boundary-layer flow (Spalart, 1988) and flow over a backward-facing step (Le *et al.*, 1993). As seen in Fig. 3,

$$\alpha = -1 - \frac{6S}{15+10S} \tag{23}$$

fits DNS data reasonably well. The algebraic model was initially used by Durbin (1995a) as an *a postiori* formula for evaluating $\overline{u_i u_j}$. In order to apply Eq. (19) to mean flow prediction while preventing computational intractability, the coefficients G^2 and G^3 are modified as:

$$G^2 = \frac{1}{4}\frac{(1-\alpha)a_{\overline{v^2}}}{S^2+1}T^2, \quad G^3 = \frac{3}{2}\frac{(1+\alpha)a_{\overline{v^2}}}{S^2+1}T^2. \tag{24}$$

3. Numerical method

All flows have been computed with the STREAM general geometry, block-structured, finite-volume code (Lien & Leschziner, 1994a). Advection is approximated by a TVD scheme with the UMIST limiter (Lien & Leschziner, 1994b). To avoid checkerboard oscillations within the co-located storage arrangement, the "Rhih and Chow" interpolation method (1983) is used. The solution is effected by an iterative pressure-correction SIMPLE algorithm, applicable to both subsonic and transonic conditions (Lien & Leschziner, 1993).

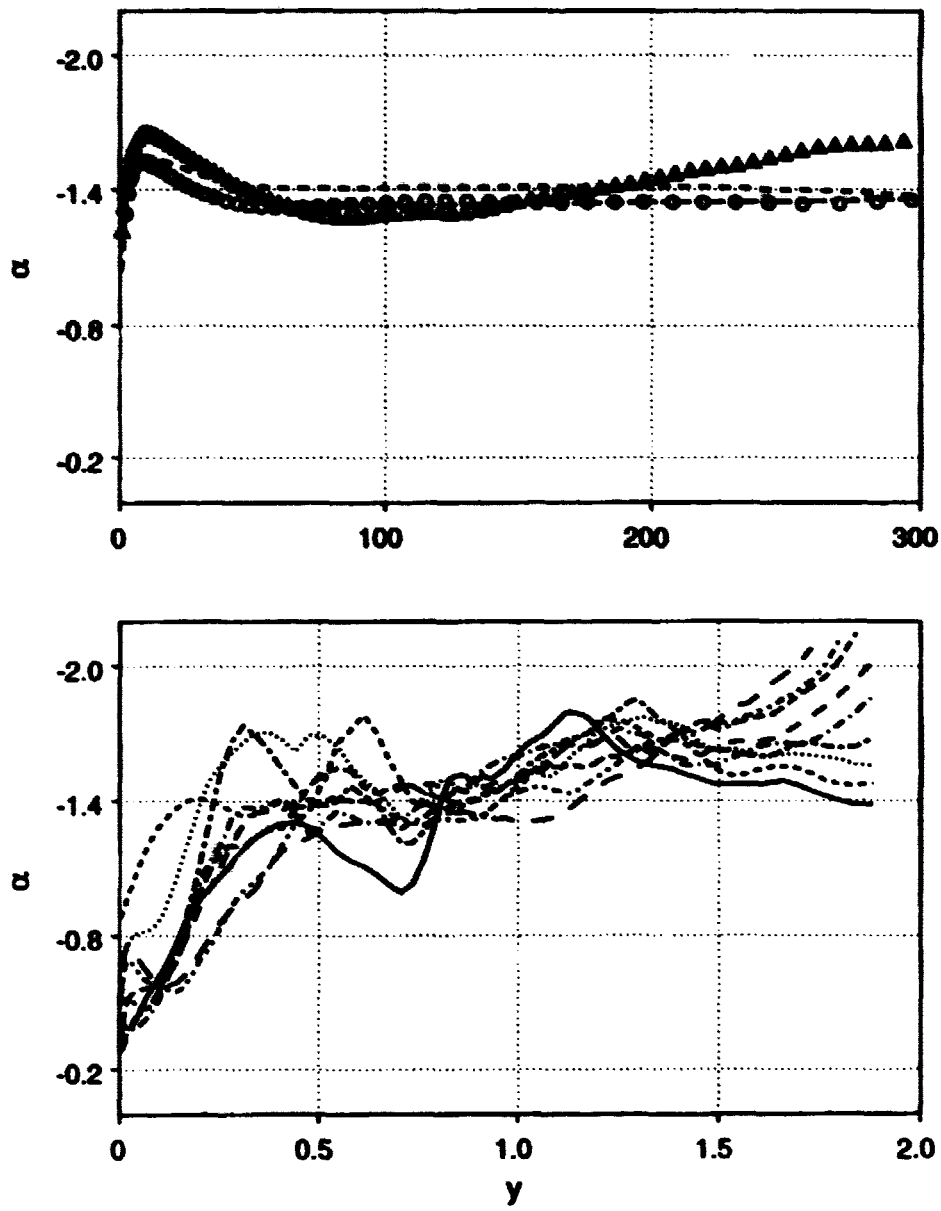

FIGURE 3. Correlation of α in the non-linear constitutive equation with DNS data. Top: DNS channel: $R_\tau = 395$, $\triangle$; formula, ---- . DNS boundary layer: $R_\theta = 1410$ o ; formula, —·— . Bottom: Backstep DNS: $x = 1$, —— ; $x = 2$, ---- ; $x = 3$, ····· ; $x = 4$, —·— ; $x = 5$, —·— ; $x = 6$, — — ; $x = 7$, —·—·— ; $x = 8$, —···— ; $x = 9$, — —.

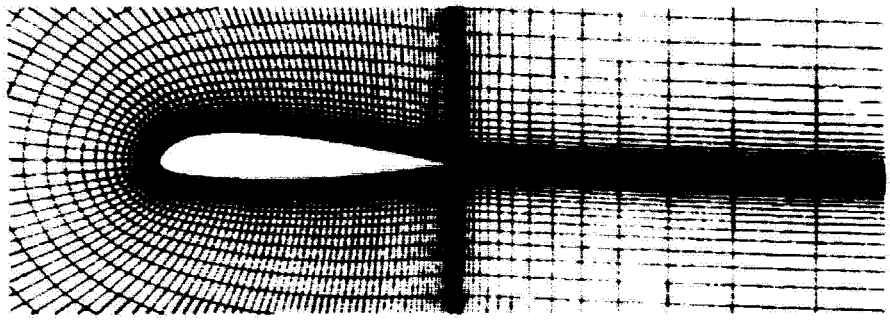

FIGURE 4. A-aerofoil: geometry and partial grid

4. Results and discussion

4.1 Aerospatiale A-aerofoil

Computations for the A-aerofoil have been performed at 13.3° incidence, with transition on the suction side prescribed at 12% of chord. The geometry and a partial view of the grid are given in Fig. 4. The Reynolds number, based on free-stream velocity and chord length, is 2.1×10^6. Solutions have been obtained on a grid containing 177×65 lines, extending to 10 chords into the free stream.

In total, four turbulence-model variants have been applied to this case [comparisons to second-moment closure can be found in Lien & Leschziner (1995)]:

(1) the low-Re $k-\varepsilon$ model of Lien & Leschziner (1993);
(2) the original $k-\varepsilon-\overline{v^2}$ model of Durbin (1995b);
(3) the code-friendly variant;
(4) the above variant combined with the non-linear stress-strain relation.

The skin-friction and wall-pressure distributions obtained with three linear eddy-viscosity models, one $k-\varepsilon$ and two $k-\varepsilon-\overline{v^2}$, are compared in Fig. 5. These, as well as the associated profiles of streamwise velocity and shear stress on the suction side in Figs. 6-7, clearly demonstrate the superiority of $k-\varepsilon-\overline{v^2}$ variants relative to the conventional $k-\varepsilon$ model.

Attention is turned next to comparisons between linear and non-linear $k-\varepsilon-\overline{v^2}$ models in Figs. 8–10 for profiles of streamwise velocity and Reynolds normal-stresses. It is found from these figures that the Reynolds-stress anisotropy is fairly well predicted by the non-linear model at x/c=0.5, which is consistent with the constraints in Eq. (21) imposed on the constitutive equation. As the flow approaches the trailing edge, streamline curvature arising from secondary strain becomes important and the omission of its production term ($\sim \frac{\partial v}{\partial x}$) in the $\overline{v^2}$-equation is no longer valid, resulting in large discrepancies between predictions and data at x/c=0.9.

4.2 DLR prolate spheroid

The shape of this body and a partial view of the numerical grid surrounding it are shown in Fig. 11. The Reynolds number, based on the chord, is 6.5×10^6.

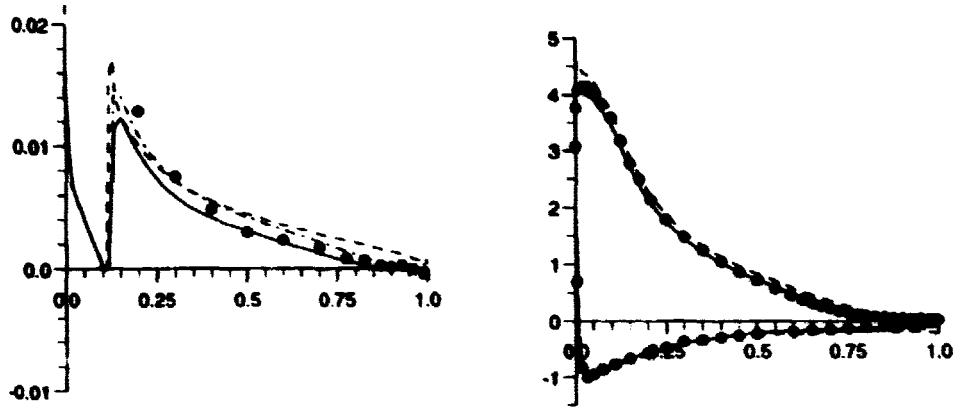

FIGURE 5. A-aerofoil: (Left) skin friction; (Right) pressure coefficient. • expt.; ---- $k-\varepsilon$; —— original $k-\varepsilon-\overline{v^2}$; — — modified $k-\varepsilon-\overline{v^2}$

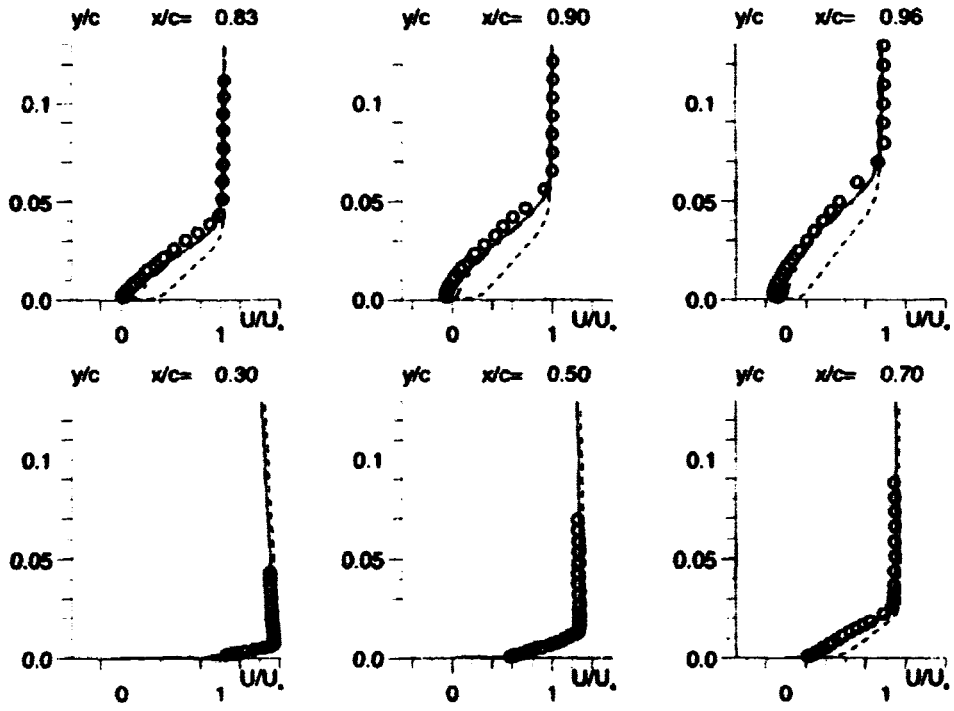

FIGURE 6. A-aerofoil: profiles of streamwise velocity. o expt.; ---- $k-\varepsilon$; —— original $k-\varepsilon-\overline{v^2}$; — — modified $k-\varepsilon-\overline{v^2}$

Computations have been performed at 30° incidence in which transition is free. The solution domain, containing $65 \times 65 \times 65$ lines, extends 10 chords into the outer

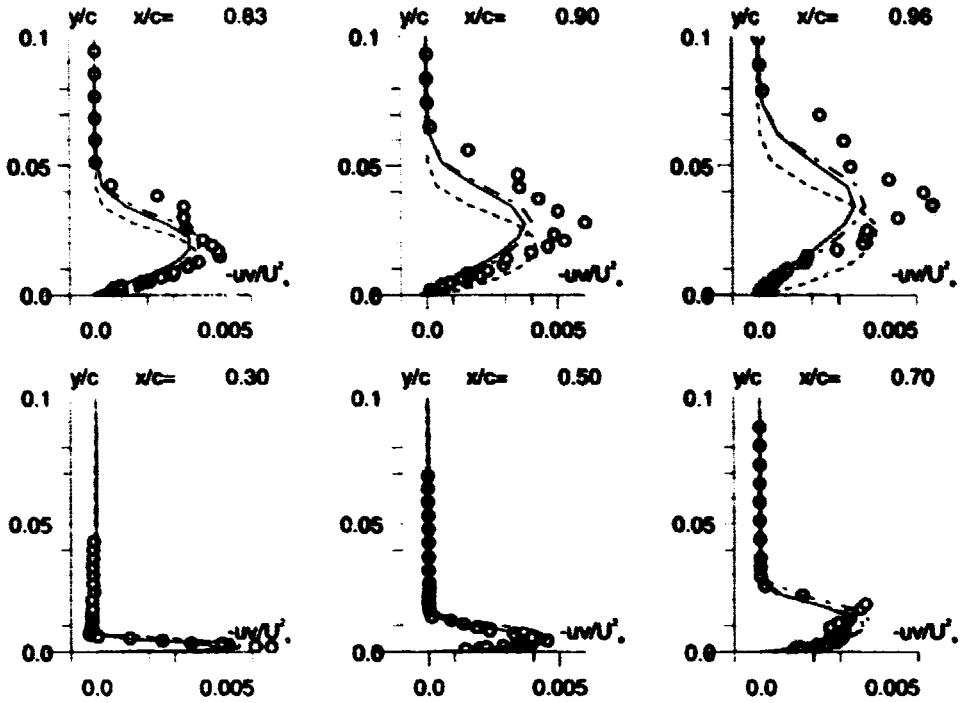

FIGURE 7. A-aerofoil: profiles of shear stress. o expt.; ---- $k-\varepsilon$; —— original $k-\varepsilon-\overline{v^2}$; — — — modified $k-\varepsilon-\overline{v^2}$

stream.

Numerical solutions have been obtained with two models [comparisons with second-moment closure can be found in Lien & Leschziner (1995b)]:

(1) the low-Re $k-\epsilon$ model of Lien & Leschziner (1993);

(2) the code-friendly $k-\varepsilon-\overline{v^2}$ variant in conjunction with Launder and Kato's modification in the turbulence production P_k (1993).

A well-known defect of any conventional, linear eddy-viscosity model is that it predicts excessive levels of turbulence energy in impingement regions, due to the fact that the irrotational strains appearing in the turbulence-energy equation ($\sim S_{ij}S_{ij}$) act to generate turbulence irrespective of their sign. The rationale behind Launder & Kato's proposal is to partially replace the strain by the vorticity, i.e.

$$P_k = 0.5\nu_t \mathcal{S}_{ij}\Omega_{ij}. \tag{25}$$

A similar idea, based on 'realizability' constraints on the turbulence time scale, has been suggested recently by Durbin (1996), in which a upper bound to k/ε proportion to $\sqrt{2/S_{ij}S_{ij}}$ was introduced. As a result, the rate of turbulence-energy generation in the vicinity of stagnation regions becomes *linear*, which is similar to that returned by most of the non-linear eddy-viscosity models mentioned in Section

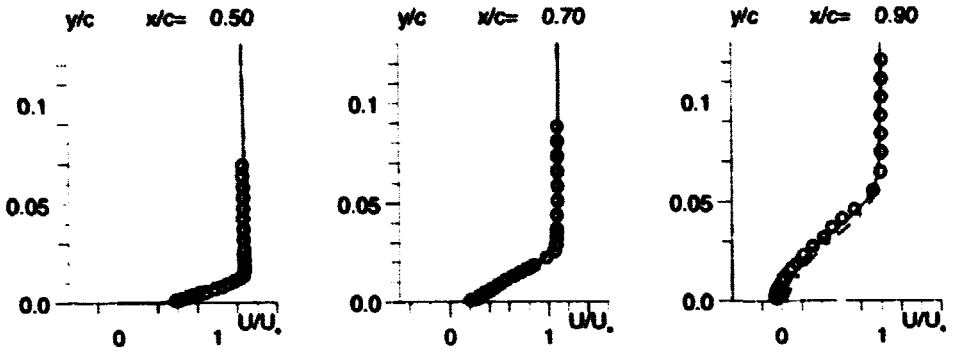

FIGURE 8. A-aerofoil: profiles of streamwise velocity. o expt.; — · — linear $k-\varepsilon-\overline{v^2}$; —— non-linear $k-\varepsilon-\overline{v^2}$

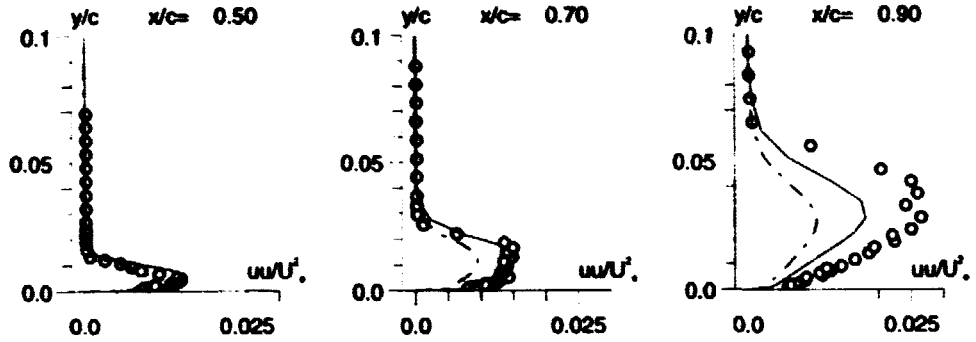

FIGURE 9. A-aerofoil: profiles of streamwise normal stress. o expt.; — · — linear $k-\varepsilon-\overline{v^2}$; —— non-linear $k-\varepsilon-\overline{v^2}$

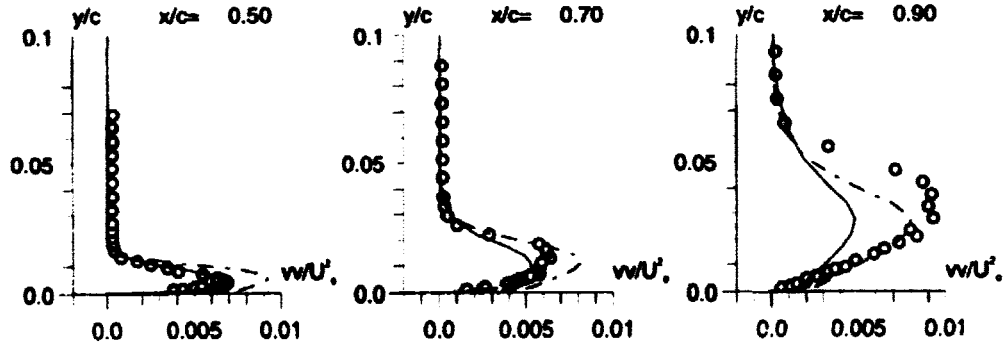

FIGURE 10. A-aerofoil: profiles of transverse normal stress. o expt.; — · — linear $k-\varepsilon-\overline{v^2}$; —— non-linear $k-\varepsilon-\overline{v^2}$

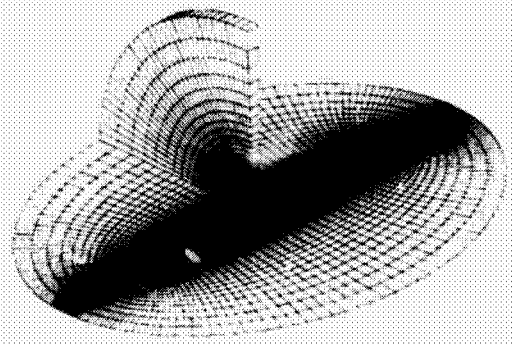

FIGURE 11. Prolate spheroid: geometry and partial grid

1; those models use

$$C_\mu \sim \frac{a}{1 + s\sqrt{0.5 S_{ij} S_{ij}}}. \tag{26}$$

Azimuthal variations of skin-friction magnitude and direction at four streamwise locations are shown in Figs. 12 and 13, and the circumferential distributions of wall pressure are given in Fig. 14. As seen at $x/2a = 0.223$, the $k - \varepsilon - \overline{v^2}$ model in conjunction with Launder & Kato's modification returns a transition-like behavior in the boundary layer close to the windward side. Although the model is unable on fundamental grounds to predict any aspect of *natural* transition, the predicted transitional phenomenon is mainly due to a strong suppression of turbulence energy at the impingement regions, in which the flow becomes 'laminar', combined with the fact that the free-stream turbulence diffuses into the boundary layer and ultimately triggers transition. It is clear from Fig. 14 that the extent of pressure plateau regions, signifying the azimuthal extent of separation zone, at $x/2a > 0.564$ are under-estimated by both models. This observation is consistent with the azimuthal distributions of skin-friction direction γ shown in Fig. 13; $\gamma = 0$ denotes either the separation or the reattachment point. The performance of $k - \varepsilon - \overline{v^2}$ model is slightly better than that of $k - \varepsilon$ in terms of the extent of the separation zone. Some of the discrepancies between predictions and experiment might be due to the grid density adopted here; in particular, close to the rear end of the spheroid it is too coarse and a grid-refinement test is required.

5. Conclusions

A computational study has been undertaken to investigate the predictive capabilities of $k - \varepsilon - \overline{v^2}$ variants when applied to high-lift configurations, including 2D aerofoil and 3D prolate spheroid. Both the linear and non-linear stress-strain constitutive relations are examined. The outcome of the present study may be summarized as follows:

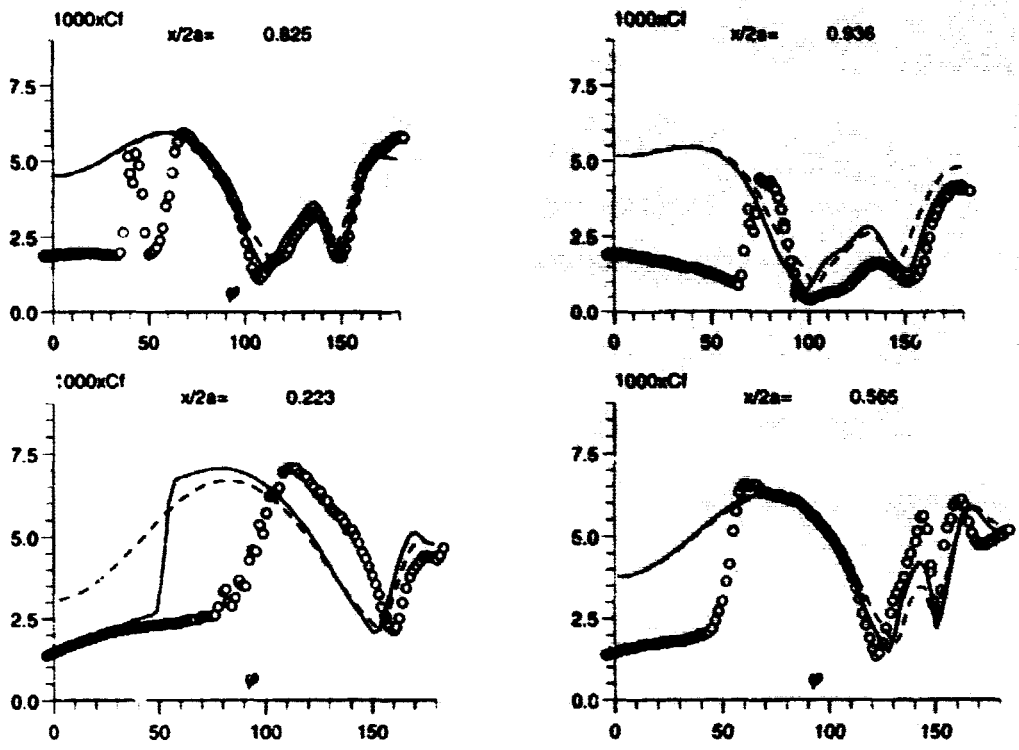

FIGURE 12. Prolate spheroid: skin-friction magnitude. ○ expt.; ---- $k-\epsilon$; —— modified $k-\epsilon-\overline{v^2}$;

(1) The $k-\epsilon-\overline{v^2}$ model and its variants, whether linear or non-linear, return superior predictions relative to the conventional $k-\epsilon$ model.

(2) This superiority can be attributed to the use of $\overline{v^2}$ as the velocity scale in the eddy-viscosity expression without resorting to an *ad hoc* damping function.

(3) The $\overline{v^2}$ is obtained from a simplified form of Reynolds-stress transport equation, governing the turbulence intensity normal to streamlines, the pressure-strain term of which is represented mathematically by an elliptic relaxation model.

(4) A code-friendly modification is proposed here, including the assurance of the near-wall behavior $\overline{v^2} \to O(y^4)$ as $y \to 0$, the introduction of R_y-dependency in $C_{\epsilon 1}$, and the use of $f = 0$ as the boundary condition on no-slip boundaries. As a result, the numerical stability, in particular, for the uncoupled solution procedure used herein is greatly enhanced.

(5) The introduction of R_y in $C_{\epsilon 1}$ yields improved results for the transitional flow. However, it requires the minimum distance to walls, which can be difficult to apply to complex geometries.

(6) Following a similar idea suggested by Durbin & Laurence (1996), a first attempt

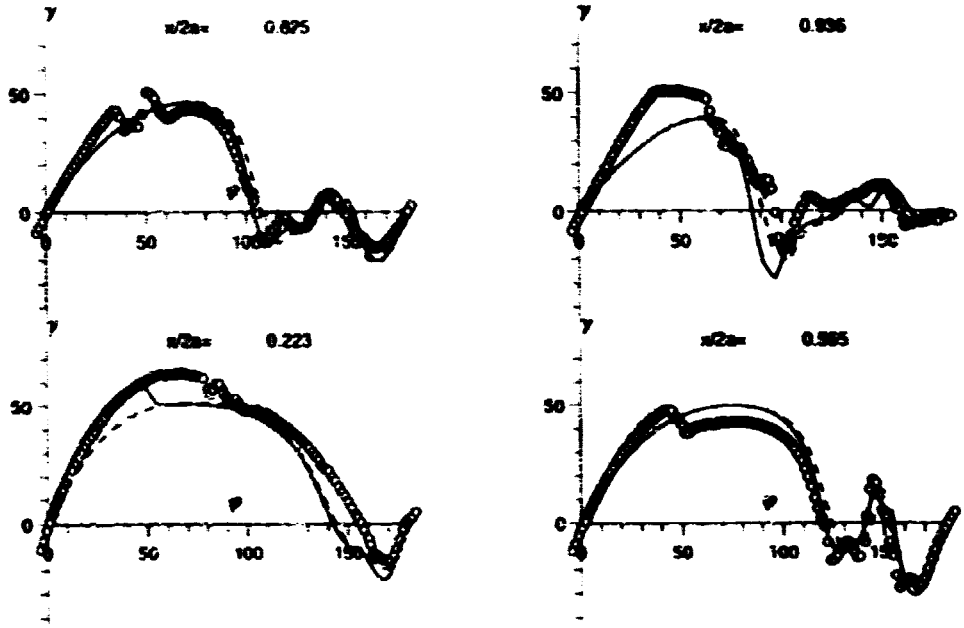

FIGURE 13. Prolate spheroid: skin-friction direction. o expt.; ---- $k-\epsilon$; —— modified $k-\epsilon-\overline{v^2}$.

has been made by adopting

$$C_{\epsilon 1} = 1.44(1 + 0.0333\sqrt{k/\overline{v^2}}),\ C_{\epsilon 2} = 1.85,\ C_L = 0.188.$$

and preliminary results for flows over a flat plate and the A-aerofoil, described in Sections 2.1.1-2.1.2, are given in Figs. 15-17. As seen, the use of $\sqrt{k/\overline{v^2}}$ returns very similar mean velocity profiles for the A-aerofoil case. However, the onset of transition for the flat-plate case is too early and the length of transition is too long.

(7) In order to improve the performance of $k-\epsilon-\overline{v^2}$ model for both transitional and fully turbulent flows, in particular, in complex geometries, instead of adopting R_y and $\sqrt{k/\overline{v^2}}$, there is a need to devise a new parameter, depending on the local Reynolds number and avoiding the use of the minimum distance to walls.

(8) The level of normal stress anisotropy returned by the non-linear model is fairly well represented at the mid-chord of A-aerofoil, where the curvature effect is unimportant. Close to the trailing edge, however, both $\overline{u^2}$, $\overline{v^2}$ and, consequently, k and its production P_k are under-predicted. Since $P_k = \nu_t(\frac{\partial U_i}{\partial x_j} + \frac{\partial U_j}{\partial x_i})\frac{\partial U_i}{\partial x_j} + \cdots$ and the mean-velocity profile and, hence, its gradient at $x/c = 0.9$ are in good agreement with the data, this indicates that ν_t is too low, which is consistent with the under-estimation of $\overline{v^2}$ at the same location.

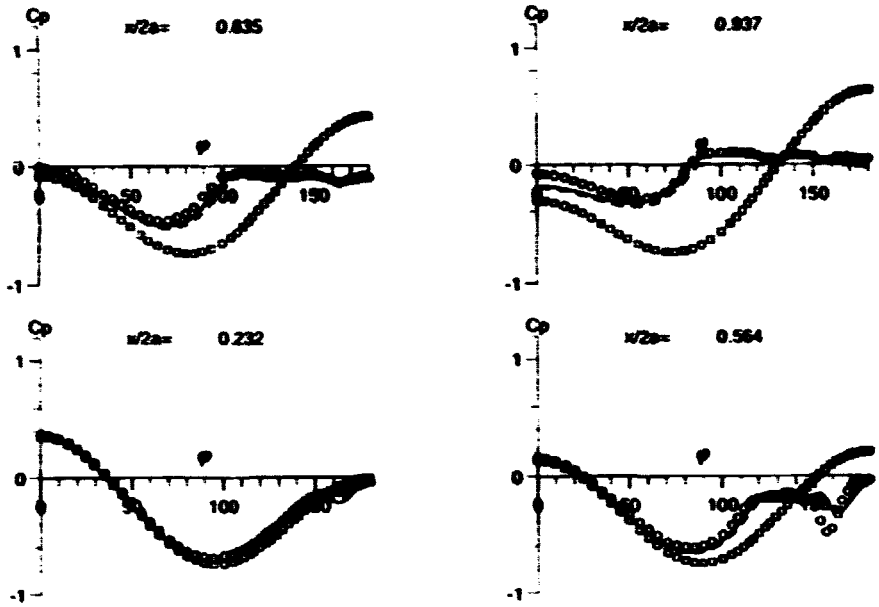

FIGURE 14. Prolate spheroid: pressure coefficient. o expt.; □ inviscid solution; ---- $k-\epsilon$; —— modified $k-\epsilon-\overline{v^2}$;

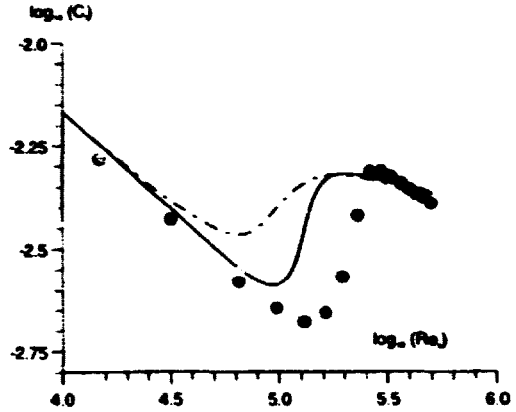

FIGURE 15. Flat plate: skin friction. • expt.; —— based on R_y; — — based on $\sqrt{k/\overline{v^2}}$

(9) For open 3D separation, the size of separation zone, reflected by the azimuthal extent of pressure plateau, is slightly under-predicted by the $k-\varepsilon-\overline{v^2}$ model, which might be partially attributed to the grid density adopted here being insufficient.

(10) To ensure a wide range of applicability of the non-linear model, the free coefficients

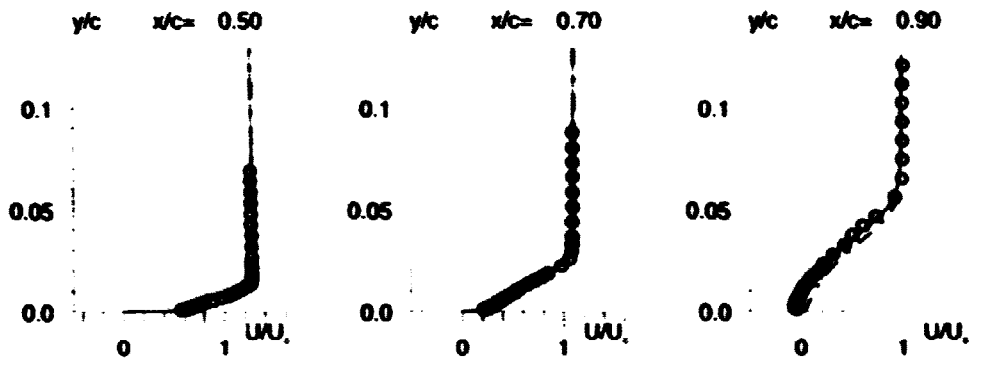

FIGURE 16. A-aerofoil: profiles of streamwise velocity. o expt.: —— based on R_y; — · — based on $\sqrt{k/\tilde{v}^2}$

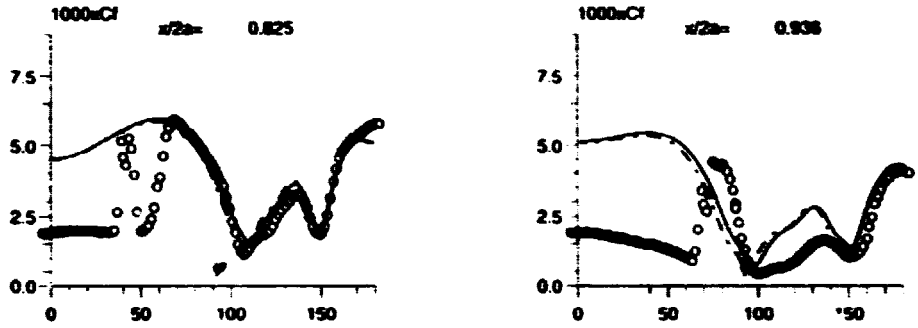

FIGURE 17. Prolate spheroid: skin-friction magnitude. o expt.: —— based on R_y; — · — based on $\sqrt{k/\tilde{v}^2}$

and their associated functionals need to be more carefully optimized by reference to different types of flow, featuring separation, impingement, swirl, rotation, and transition.

Acknowledgments

The first author would like to express his gratitude to CTR, UMIST and the Royal Academy of Engineering in the UK for their financial support.

REFERENCES

CHEN, W. L. 1996 *Turbulence Modeling for highly-loaded cascade blade*. Ph.D Thesis, University of Manchester Institute of Science and Technology, UK.

CRAFT, T. J., LAUNDER, B. E. & SUGA, K. 1995 A non-linear eddy viscosity model including sensitivity to stress anisotropy. *Proc. 10th Symp. on Turbulent Shear Flows.* **2**, 23.19-23.24.

DURBIN, P. A. 1995a Constitutive equation for the $k-\varepsilon-\overline{v^2}$ model. *Proc. 6th Int. Symp. on Computational Fluid Dynamics.* **1**, 258-262.

DURBIN, P. A. 1995b Separated flow computations with the $k-\varepsilon-\overline{v^2}$ model. *AIAA J.* **33**, 659-664.

DURBIN, P. A. 1996 On the $k-\epsilon$ stagnation point anomaly. *Int. J. Heat and Fluid Flow.* **17**, 89-90.

DURBIN, P. A. & LAURENCE, D. 1996 Non-local effects in single point closure. *Advances in Turbulence Research*, Seoul, Korea, May 17, 1996, 109-120.

LAUNDER, B. E. & SHARMA, B. I. 1974 Application of energy-dissipation model of turbulence to the calculation of flow near a spinning disc. *Letters in Heat and Mass Transfer.* **1**, 131-138.

LAUNDER, B. E. & KATO, M. 1993 Modeling flow-induced oscillations in turbulent flow around a square cylinder. *ASME FED.* **157**, 189-199.

LE, H., MOIN, P. & KIM, J. 1993 Direction numerical simulations of turbulent flow over a backward-facing step. *Proc. 9th Symp. on Turbulent Shear Flows.* **2**, 13.2.1-13.2.5.

LIEN, F. S. AND LESCHZINER, M. A. 1993 A pressure-velocity solution strategy for compressible flow and its application to shock/boundary-layer interaction using second-moment turbulence closure. *ASME J. Fluids Engineering.* **115**, 717-725.

LIEN, F. S. AND LESCHZINER, M. A. 1994a A general non-orthogonal collocated finite volume algorithm for turbulent flow at all speeds incorporating second-moment closure, Part 1: Computational implementation, Part 2: Application. *Comput. Methods Appl. Mech. Eng.* **114**, 123-167.

LIEN, F. S. AND LESCHZINER, M. A. 1994b Upstream monotonic interpolation for scalar transport with application to complex turbulent flows. *Int. J. Numer. Methods Fluids.* **19**, 527-548.

LIEN, F. S. & LESCHZINER, M. A. 1995a Modeling 2D separation from a high-lift aerofoil with a non-linear eddy-viscosity model and second-moment closure. *Aeronautical J.* **99**, 125-144.

LIEN, F.S. & LESCHZINER, M.A. 1995b Computational modeling of multiple vortical separation from streamlined body at high incidence. *Proc. 10th Symp. on Turbulent Shear Flows.* **1**, 4.19-4.24.

LIEN, F. S., CHEN, W. L. & LESCHZINER, M. A. 1996 Low-Reynolds-number eddy-viscosity modeling based on non-linear stress-strain/vorticity relations. *Engineering Turbulence Modeling and Experiments.* **3**, W. Rodi & G Bergeles (ed.) 91-101.

KIM, J., MOIN, P. & MOSER, R. D. 1987 Turbulence statistics in fully-developed channel flow at low Reynolds number. *J. Fluid Mech.* **177**, 133-166.

POPE, S. B. 1975 A more general effective-viscosity hypothesis. *J. Fluid Mech.* **72**, 33-340.

RHIE, C. M. & CHOW, W. L. 1983 Numerical study of the turbulent flow past an airfoil with trailing edge separation. *AIAA J.* **21**, 1525-1532.

ROGERS, S. E. & KWAK, D. 1990 Upwind differencing scheme for the time-accurate incompressible Navier-Stokes equations. *AIAA J.* **28**, 253-262.

SPEZIALE, C. G. 1987 On non-linear $K-l$ and $k-\varepsilon$ models of turbulence. *J. Fluid Mech.* **178**, 459-475.

SPALART, P. R. 1988 Direction simulation of a turbulent boundary layer up to $R_\theta = 1410$. *J. Fluid Mech.* **187**, 61-98.

NEXT
DOCUMENT

Application of the k-ε-v^2 model to multi-component airfoils

By G. Iaccarino[1] AND P. A. Durbin[2]

Flow computations around two-element and three-element configurations are presented and compared to detailed experimental measurements. The $k-\varepsilon-\overline{v^2}$ model has been applied and the ability of the model to capture streamline curvature effects, wake-boundary layer confluence, and laminar/turbulent transition is discussed. The numerical results are compared to experimental datasets that include mean quantities (velocity and pressure coefficient) and turbulent quantities (Reynolds normal and shear stresses).

1. Introduction

An accurate prediction of turbulent flow over a wing is still a challenging problem. Even a two-dimensional computation over a multi-element airfoil close to the maximum lift is an unsolved problem due to the complex geometry producing complicated viscous flow.

Within the aircraft industry the design of high-lift devices is an important topic which can have a major influence on the overall economy and safety of the aircraft. Therefore, development and improvements of numerical tools capable of handling separated viscous flows are of great interest. Computational methods for the design of high-lift systems are, traditionally, based on the viscous-inviscid interaction approach with integral methods for boundary layers and wakes.

Today, due to developments in computer technology and improvements in numerical algorithms, there is a renewed interest in the possibility of obtaining Reynolds averaged Navier-Stokes solutions for high-lift flows. The main open topics in this field of application are grid generation and turbulence modeling. The first one has been addressed and partially solved with the introduction of the *zonal* methods. By this way, the computational domain is divided into zones and the mesh and solutions are computed independently; the matching conditions between different regions provide boundary conditions for the zones. In particular, multiple-zones meshes can be either patched (pointwise continuous) or *chimera* (overlapping) grids. The use of unstructured grids is another interesting answer to this problem and is still under development for viscous applications.

1 CIRA, Centro Italiano Ricerche Aerospaziali, Italy
2 Stanford University

The other crucial point is the handling of the turbulence for such a complicated flow situation. There is no shortage of numerical methods to take into account turbulent fluctuations when solving Reynolds Averaged Navier-Stokes (RANS) equations based either on algebraic or differential equations. It is only the effectiveness of the models that is at issue.

2. Numerical model

2.1 RANS flow solver

The numerical method is based on an extended version of the incompressible Navier-Stokes two-dimensional (INS2D) code of Rogers and Kwak (Rogers, 1991). The incompressible, Reynolds Averaged Navier Stokes equations are solved by an artificial compressibility method. The basic technique is based on cell-vertex finite differences over structured meshes. The spatial discretization scheme is a third-order upwind biased for convective contributions and second-order centered for diffusive terms. The time integration is implicit and the equations are solved in a coupled way. The implicit matrices are inverted by ADI line relaxations.

2.2 Turbulence modeling

The turbulence model is based in part on the standard $k-\varepsilon$ equations:

$$\partial_t k + U\cdot\nabla k = P_k - \varepsilon + \nabla\cdot[(\nu + \frac{\nu_t}{\sigma_k})\nabla k], \tag{1}$$

$$\partial_t \varepsilon + U\cdot\nabla \varepsilon = \frac{C_{\varepsilon 1}P_k - C_{\varepsilon 2}\varepsilon}{T} + \nabla\cdot[(\nu + \frac{\nu_t}{\sigma_\varepsilon})\nabla \varepsilon]. \tag{2}$$

Another transport equation is introduced to model near-wall effects and the anisotropy of the Reynolds stresses. This reads as

$$\partial_t \overline{v^2} + U\cdot\nabla \overline{v^2} = kf - \overline{v^2}\frac{\epsilon}{k} + \nabla\cdot[(\nu + \nu_t)\nabla \overline{v^2}], \tag{3}$$

where $\overline{v^2}$ can be regarded as the turbulent intensity normal to streamlines and kf, the production of $\overline{v^2}$, accounts for the redistribution of turbulence intensity from the streamwise component. By using this equation 'wall-echo' effects are automatically taken into account. The production of $\overline{v^2}$ is modeled by means of an elliptic relaxation equation for f (Durbin, 1991)

$$L^2\nabla^2 f - f = \frac{1}{T}(C_1 - 1)\left[\frac{\overline{v^2}}{k} - \frac{2}{3}\right] - C_2\frac{P_k}{k}. \tag{4}$$

In the previous equations time and length scales are computed as

$$T = \max\left[\frac{k}{\varepsilon}, 6(\frac{\nu}{\varepsilon})^{1/2}\right],\ L = C_L\max\left[\frac{k^{3/2}}{\varepsilon}, C_\eta(\frac{\nu^3}{\varepsilon})^{1/4}\right]. \tag{5}$$

The treatment of the wall boundary conditions for the turbulent quantities is based on the asymptotic behavior of k and $\overline{v^2}$. As $y \to 0$

$$k = 0, \; k \to y^2 \frac{\epsilon}{2\nu}, \tag{6}$$

$$\overline{v^2} = 0, \; \overline{v^2} \to -y^4 \epsilon \frac{f}{20\nu^2}. \tag{7}$$

The eddy viscosity is given by

$$\nu_t = C_\mu \overline{v^2} T. \tag{8}$$

The constants of the model are:

$$C_\mu = 0.19, \; \sigma_k = 1, \; \sigma_\epsilon = 1.3,$$

$$C_{\epsilon 1} = 1.55, \; C_{\epsilon 2} = 1.9$$

$$C_1 = 1.4, \; C_2 = 0.3, \; C_L = 0.3, \; C_\eta = 70. \tag{9}$$

The space discretization of Eqs. (1) to (4) is the same used for the mean flow and the time integration is based on the same implicit procedure. The equations are solved as a coupled two-by-two block tridiagonal system (the mean flow is solved as a coupled three-by-three system).

3. Two-component configuration

3.1 Experimental test conditions

The experimental test was conducted in the 7x10" wind tunnel at NASA Ames Research Center, Moffett Field, California (Adair, 1989). The airfoil/flap configuration includes a NACA 4412 main airfoil section equipped with a NACA 4415 flap airfoil section. The geometric location of the flap was specified by the flap gap (FG), the flap overlap (FO), and the flap deflection (δ_f). In this work, we are using $FG = 0.035c$, $FO = 0.028c$ and $\delta_f = 21.8°$, where c is the chord length of the main airfoil. The angle of attack was set to $\alpha = 8.2°$ and flow conditions were specified as Mach number $M = 0.09$ and Reynolds number $Re = 1.8 \times 10^6$. Two-dimensionality of the measurements was ensured by using fences, and the transition to turbulence was enforced by using trips at the main airfoil leading edge and at the suction side of the flap close to the flap pressure minimum.

3.2 Numerical test conditions

A two-dimensional model is used for the computations; it represents the midspan section of the experimental set-up. The airfoil configuration was characterized by the value of FG, FO, and δ_f indicated previously. The presence of the wind-tunnel walls was taken into account because of the large blocking effects, as was recommended by the experimental investigators (Adair, 1989); for simplicity, slip boundary conditions were imposed on the wind-tunnel walls. The inlet and outlet sections were set at 5 chords upwind and 15 chords downwind respectively to minimize their effects on the computed flow field. The angle of attack and the Reynolds

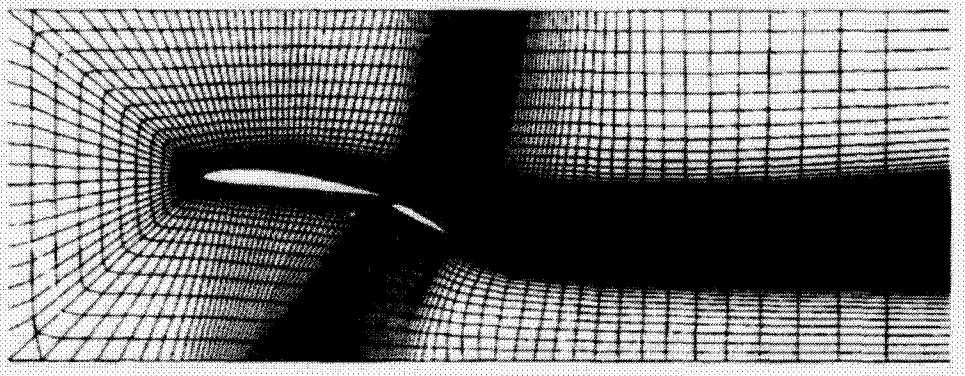

FIGURE 1. View of the computational grid.

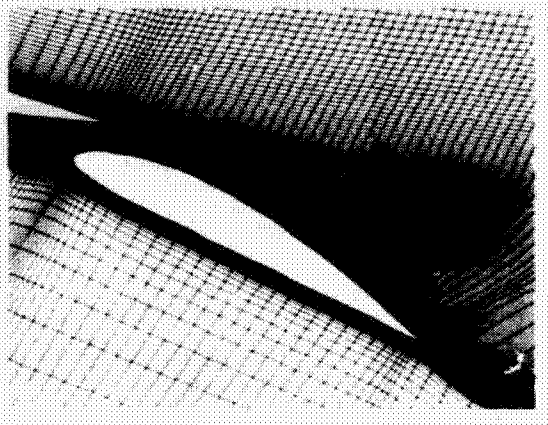

FIGURE 2. Close-up of the grid around the flap.

number were the same as the experiments, while the flow was assumed to be incompressible. Transition trips were not accounted for: the flow is considered to have a very low turbulence intensity at the wind tunnel inlet, and the model is allowed to undergo its natural, bypass transition.

The computational grid was generated by FFA (Sweden Research Center) under the auspices of the GARTEUR Action Group AG 25. A general view of mesh is reported in Fig. 1, while a close-up of the grid around the flap is given in Fig. 2. Due to the complexity of the geometry the computational grid was generated via a multiblock approach; seven zones were created allowing very good resolution of the mesh close to the airfoils (a C-type grid); about 100.000 total grid points were used. The square trailing edges of both airfoils were also retained (see Fig. 2) even though the resolution in the streamwise direction is quite limited.

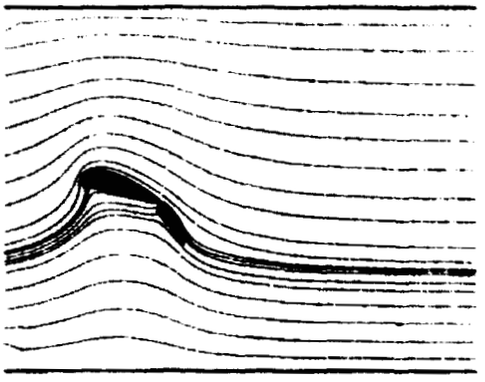

FIGURE 3. Computed streamlines.

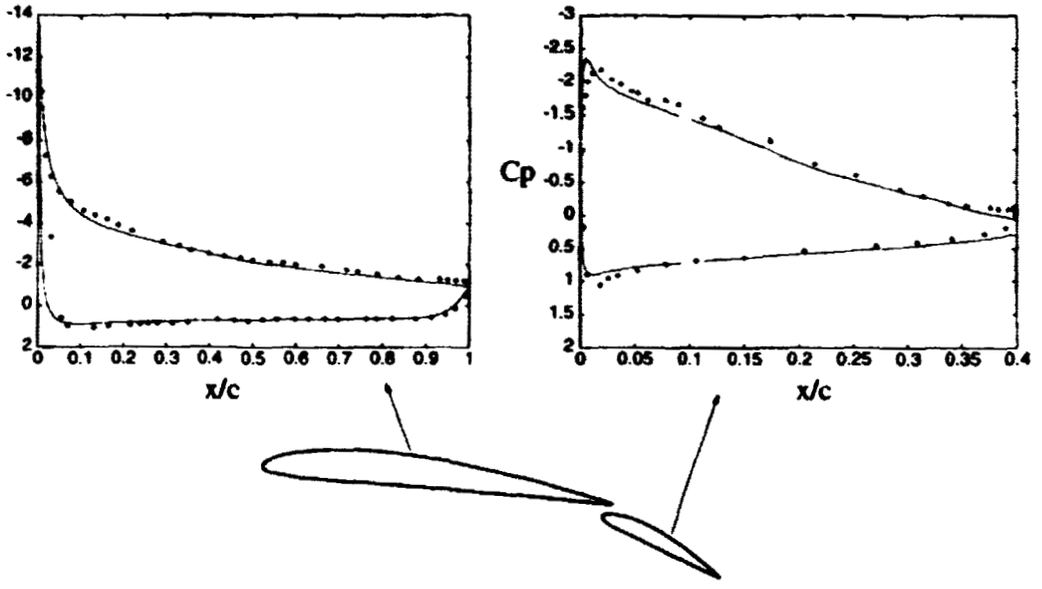

FIGURE 4. Pressure distributions on the airfoil surface. ——— : computed results; ◊: measured data.

3.3 Results

The characterization of the flow field is reported in Fig. 3 by means of the streamlines. Only a portion of the flow domain is shown. The blocking effect of the wind tunnel walls and the large curvature of the wake downstream of the flap are evident. A little separation bubble is also present at the flap trailing edge, in accord with the experimental findings.

3.3.1 Mean flow: pressure

The comparison between computed and measured pressure coefficient is reported

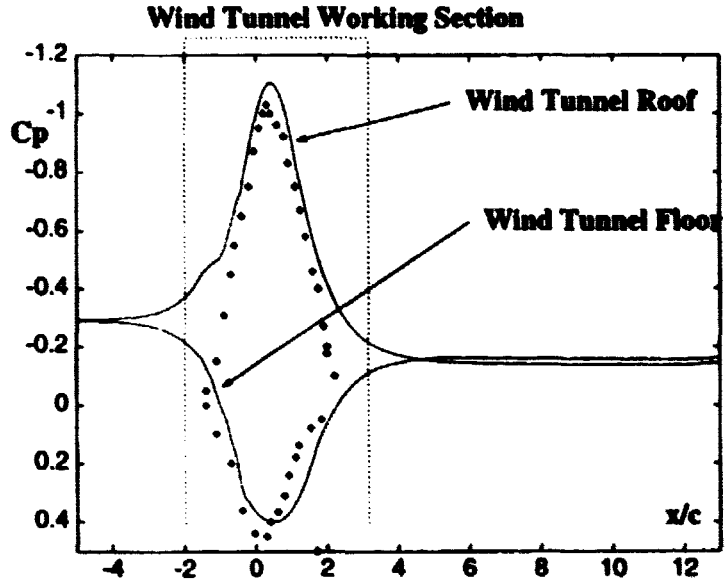

FIGURE 5. Pressure distributions on the wind tunnel walls. ——— : computed results; ◊: measured data.

in Fig. 4. These results can be compared to those published by Rogers *et al.* (1993).

The agreement is quite satisfactory for both the main airfoil and the flap. The suction peak is very well captured on the main airfoil although the stagnation point is completely misplaced. This is probably due to three-dimensional effects in the experimental test as can be seen from Fig. 3 of (Adair, 1987). Another reasonable explanation for this discrepancy is a difference between the geometric location of the airfoil/flap configuration in the experimental and numerical models. It is worth noting that the numerical results of Rogers (1993) show this same discrepancy in the location of the stagnation point. We point out that the geometry definition of the airfoil/flap configuration (in terms of FG, FO, and δ_f) is somewhat confusing and this could have led to a different shape of the slot in the numerical and experimental models.

The pressure peak over the flap is overpredicted and, in particular, located upstream with respect to the experimental one. The numerical model fails to capture the correct pressure plateau at the trailing edge of the flap and, therefore, the separation region. In particular, the separation point is well captured (it is located at 7% upstream of the trailing edge) as is shown in Fig. 4, but the maximum height of the recirculation bubble is underpredicted.

In Fig. 5, the pressure distribution over the wind tunnel walls is reported and compared to the experimental findings. On the working section roof, the agreement is satisfactory even though an overprediction of the pressure level is present. On the other hand, at the floor, a shift in the pressure distribution is observed. However, the grid resolution in the region is quite coarse. Note that as the inlet and the

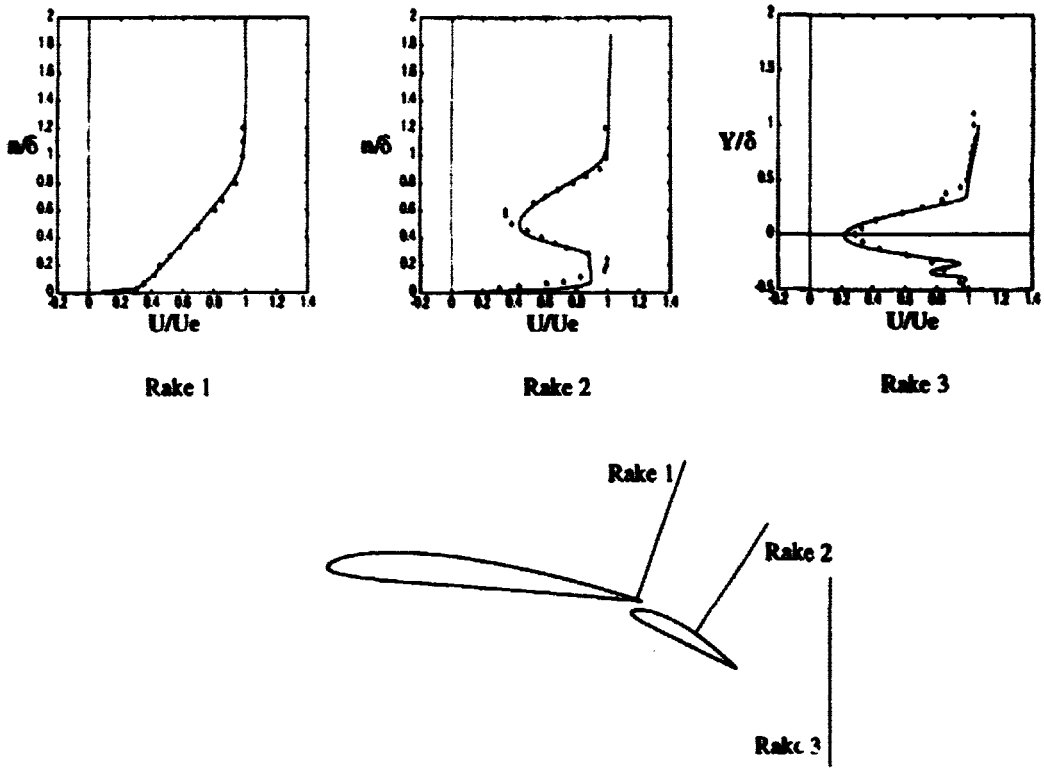

FIGURE 6. Mean velocity profiles: ——— : computed results; ♦: measured data.

outlet are approached the pressure levels become constant. This shows that the computational domain was large enough.

3.3.2 Mean flow: velocity

The mean velocity was measured at three locations using a hot-wire anemometer and a 3-D laser velocimeter. The comparison between computed and experimental x-component velocity is reported in Fig. 6.

The agreement is very encouraging even if there is a difference between computed and measured flap boundary layer thickness. Comparisons with previous results by Rogers (1993) confirm that the main differencies are related to a different gap velocity off the surface of the flap leading edge. It is necessary to point out that in the numerical model no transition trips are mounted on the flap and, therefore, the development of the turbulent boundary layer is not the same as in the experiments.

3.3.3 Turbulence results

The evolution of the turbulent boundary layer on the flap surface can be analyzed from Fig. 7, where the tangential skin friction is reported. The model is capable of capturing the laminar/turbulent transition automatically as it is evident from the skin friction rise in the leading edge region. In the work by Lien *et al.* (1996)

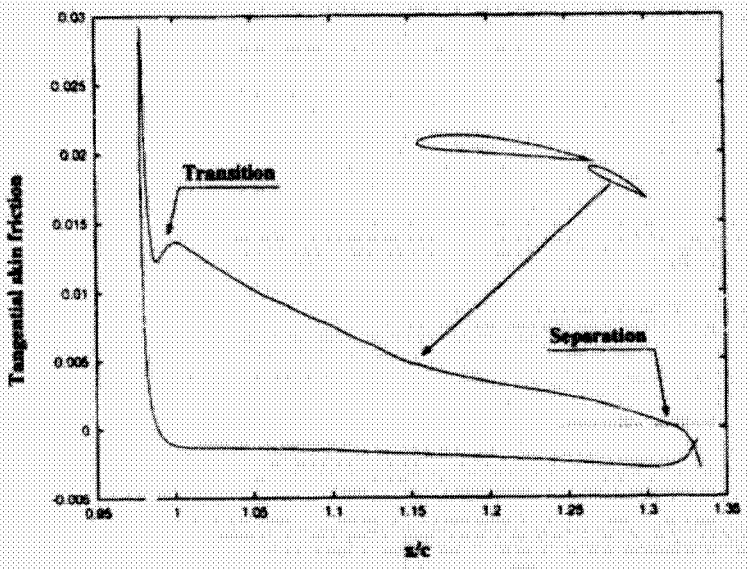

FIGURE 7. Computed tangential skin friction on the flap surface.

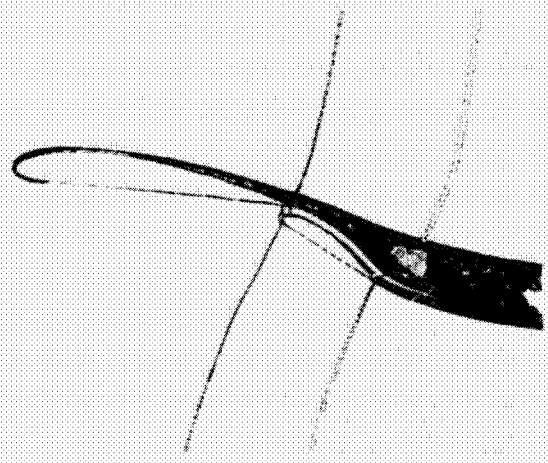

FIGURE 8. Turbulent kinetic energy contours.

the transitional flow in turbomachinery was investigated and the capability of the $k-\varepsilon-\overline{v^2}$ were stressed in detail.

In Fig. 8 the turbulent kinetic energy contours are reported to show the strong interaction between the main airfoil wake and the inviscid jet coming from the slot. It is also clear that on the lower surfaces of the main and flap the boundary layer is laminar and very thin.

FIGURE 9. Three-element airfoil configuration.

4. Three-component configuration

4.1 Experimental test conditions

The three element airfoil configuration of Fig. 9 was investigated in the Farnborough (UK) wind tunnel by I.R. Moir (private communications) in the frame of the AGARD Working Group 14.

The geometric location of the flap and the slat with respect to the main airfoil was prescribed as:

- slat/wing overlap: $SO = -0.01c$

  slat/wing gap: $SG = 0.02c$

  slat deflection: $\delta_s = 25°$

- wing/flap overlap: $FO = 0$

- wing/flap gap: $FG = 0.023c$

  flap deflection: $\delta_f = 20°$

A set of angles of attack were investigated, but relevant measurements correspond to $\alpha = 20°$. The Reynolds number was $Re = 3.52 \times 10^6$ and a trip was mounted over the main airfoil to control transition to turbulence since the wind tunnel turbulence intensity very low.

Experimental data include pressure surface measurements over the airfoil surface at two spanwise locations on the wind tunnel model to outline the absence of three-dimensional effects.

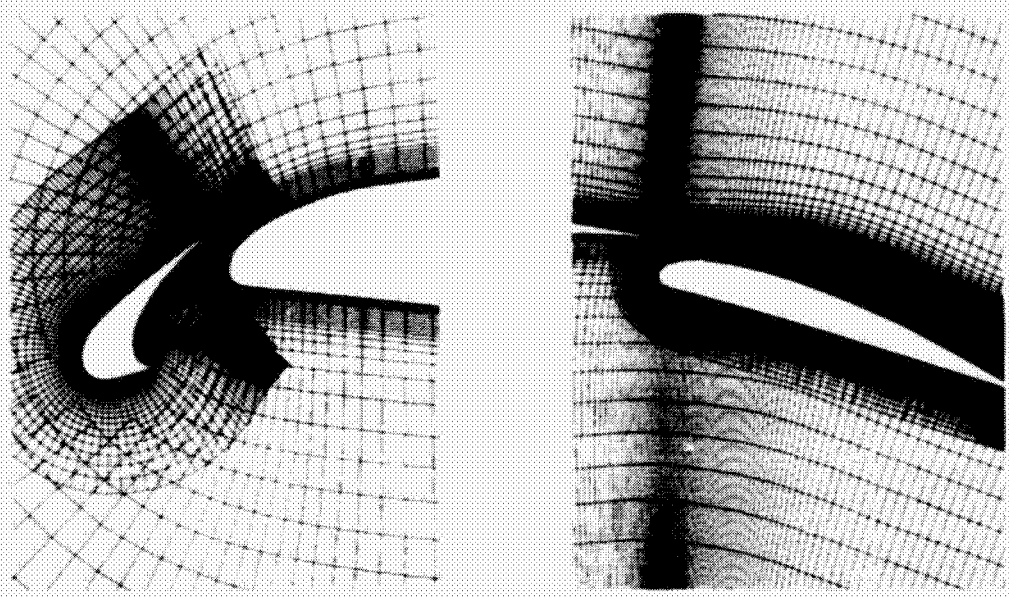

(a) (b)

FIGURE 10. (a) Close up of the computational grids around the slat; (b) Close-up of the computational grids around the flap.

4.2 Numerical test conditions

The airfoil configuration was defined using the gap and overlap definitions of the preceding section. In this case, the presence of wind tunnel walls was not taken into account, but a correction of the angle of attack (as suggested by the experimental investigators) was adopted: in particular an incidence of $\alpha = 20.18°$ was used for the computations. The far field boundaries of the computational domain were set to a distance of ≈ 20 chords from the airfoil. The Reynolds number was the same used in the experiment and the flow was assumed to be incompressible. Laminar to turbulent transitions were not fixed.

The computational grid was generated by Rogers (private communication), using three different overlapping zones. Fig. 10 *(a)* reports the mesh around the slat and the main airfoil leading edge, while Fig. 10 *(b)* reports the grid around the main airfoil trailing edge and the flap.

4.3 Results

The pressure distributions over the surface of the three airfoil elements are reported in Fig 11. Comparison with the experimental findings is very promising: the distributions over the main wing and the flap are in very good agreement.

The C_p distribution over the slat presents an overprediction of the suction peak and this is the main discrepancy between experiments and calculations.

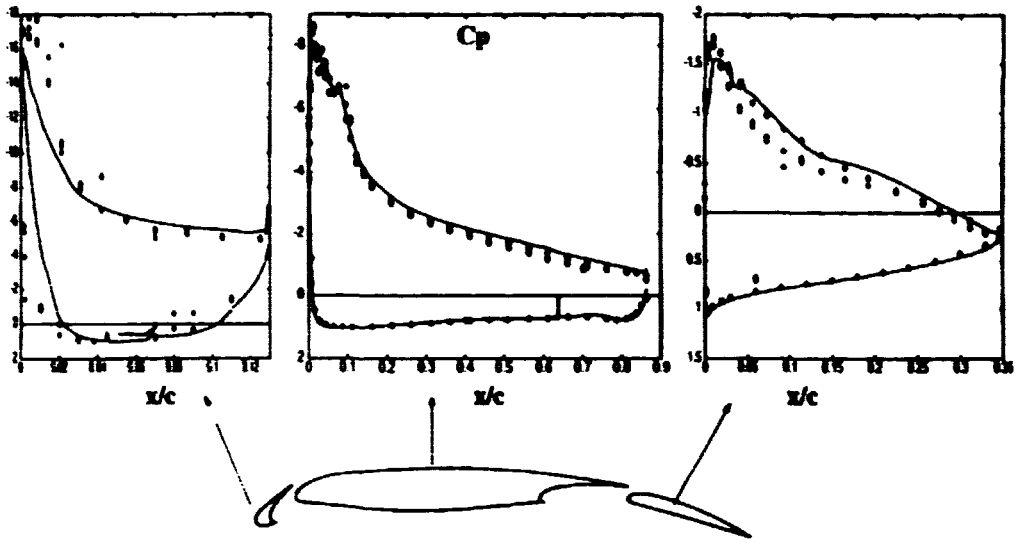

FIGURE 11. Pressure distributions on the airfoil surface. ——: computed results; ♦: measured data.

REFERENCES

ADAIR, D. & HORNE, W. C. 1989 Turbulent separated flow over and downstream of a two-element airfoil. *Experiments in Fluids.* **7**, 531-541.

DURBIN, P. 1991 Near-wall turbulence closure modeling without 'damping functions'. *Theoretical and Computational Fluid Dynamics.* **3**, 1-13.

DURBIN, P. 1995 Separated flow computations with the $k-\varepsilon-\overline{v^2}$ model. *AIAA Journal.* **33**, 659-664.

LARSSON, T. 1994 Separated and high-lift flows over single and multi-element airfoils. *Proceedings of ICAS Conference 1994.* **2505-2518.**

LIEN, F. S., DURBIN, P. 1996 Non-linear $k-\varepsilon-\overline{v^2}$ modeling with application to high-lift. *Proceedings of the Summer Program 1996.* NASA Ames/Stanford Univ.

PAPADAKIS, M., LALL, V. & HOFFMANN K. A. 1994 Performance of Turbulence models for planar flows: a selected review. *AIAA Paper 94-1879.*

ROGERS, S. E., KWAK, D. & KIRIS C. 1991 Numerical solution of the incompressible Navier-Stokes equations for steady-state and time-dependent problems. *AIAA Journal.* **29**, 603-610.

ROGERS, S. E., KWAK, D. & WILTBERGER N. L. 1993 Efficient simulation of incompressible viscous flow over single and multielement airfoils. *Journal of Aircraft.* **30**, 736-743.

ROGERS S. E., MENTER F. R., DURBIN P. A. & MANSOUR N. N. 1994 A comparison of turbulence models in computing multi-element airfoil flows. *AIAA Paper 94-0291*.

NEXT
DOCUMENT

A new approach to turbulence modeling

By B. Perot[1] AND P. Moin[2]

A new approach to Reynolds averaged turbulence modeling is proposed which has a computational cost comparable to two equation models but a predictive capability approaching that of Reynolds stress transport models. This approach isolates the crucial information contained within the Reynolds stress tensor, and solves transport equations only for a set of "reduced" variables. In this work, direct numerical simulation (DNS) data is used to analyze the nature of these newly proposed turbulence quantities and the source terms which appear in their respective transport equations. The physical relevance of these quantities is discussed and some initial modeling results for turbulent channel flow are presented.

1. Introduction

1.1 Background

Two equation turbulence models, such as the k/ϵ model and its variants, are widely used for industrial computations of complex flows. The inadequacies of these models are well known, but they continue to retain favor because they are robust and inexpensive to implement. The primary weakness of standard two equation models is the Boussinesq eddy viscosity hypothesis: this constitutive relationship is often questionable in complex flows. Algebraic Reynolds stress models (or non-linear eddy viscosity models) assume a more complex (nonlinear) constitutive relation for the Reynolds stresses. These models are derived from the equilibrium form of the full Reynolds stress transport equations. While they can significantly improve the model performance under some conditions, they also tend to be less robust and usually require more iterations to converge (Speziale, 1994). The work of Lund & Novikov (1992) on LES subgrid closure suggests that even in their most general form, non-linear eddy viscosity models are fundamentally incapable of completely representing the Reynolds stresses. Industrial interest in using full second moment closures (the Reynolds stress transport equations) is hampered by the fact that these equations are much more expensive to compute, converge slowly, and are susceptible to numerical instability.

In this work, a turbulence model is explored which does not require an assumed constitutive relation for the Reynolds stresses and may be considerably cheaper to compute than standard second moment closures. This approach is made possible by abandoning the Reynolds stresses as the primary turbulence quantity of interest.

1 Aquasions Inc., Canaan NH

2 Center for Turbulence Research

The averaged Navier-Stokes equations only require the divergence of the Reynolds stress tensor, hence the Reynolds stress tensor carries twice as much information as required by the mean flow. Moving to a minimal set of turbulence variables reduces the overall work by roughly half, but introduces a set of new turbulence variables, which at this time are poorly understood. This project attempts to use DNS data to better understand these new turbulence variables and their exact and modeled transport equations.

1.2 Formulation

The averaged Navier-Stokes equations take the following form for incompressible, constant-property, isothermal flow:

$$\nabla \cdot \mathbf{u} = 0 \tag{1a}$$

$$\frac{\partial \mathbf{u}}{\partial t} + \mathbf{u} \cdot \nabla \mathbf{u} = -\nabla p + \nu \nabla \cdot \mathbf{S} - \nabla \cdot \mathbf{R} \tag{1b}$$

where $\mathbf{u}$ is the mean velocity, p is the mean pressure, ν is the kinematic viscosity, $\mathbf{S} = \nabla \mathbf{u} + (\nabla \mathbf{u})^T$ is twice the rate-of-strain tensor, and $\mathbf{R}$ is the Reynolds stress tensor. The evolution of the Reynolds stress tensor is given by:

$$\frac{\partial \mathbf{R}}{\partial t} + \mathbf{u} \cdot \nabla \mathbf{R} = \nu \nabla^2 \mathbf{R} + \mathbf{P} - \boldsymbol{\epsilon} + \boldsymbol{\Pi} - \nabla \cdot \mathbf{T} - [\nabla \mathbf{q} + (\nabla \mathbf{q})^T] \tag{2}$$

where $\mathbf{P}$ is the production term, $\boldsymbol{\epsilon}$ is the (homogeneous) dissipation rate tensor, $\boldsymbol{\Pi}$ is the pressure-strain tensor, $\mathbf{T}$ is the velocity triple-correlation, and $\mathbf{q}$ is the velocity-pressure correlation. The last four source terms on the right-hand side must be modeled in order to close the system. The production term $\mathbf{P}$ is exactly represented in terms of the Reynolds stresses and the mean velocity gradients. This is the standard description of the source terms, but it is by no means unique and there are numerous other arrangements.

Note that turbulence effects in the mean momentum equation can be represented by a body force $\mathbf{f} = \nabla \cdot \mathbf{R}$. One could construct transport equations for this body force (which has been suggested by Wu *et al.*, 1996), but mean momentum would no longer be simply conserved. To guarantee momentum conservation, the body force is decomposed using Helmholtz decomposition, into its solenodal and dilatational parts, $\mathbf{f} = \nabla \phi + \nabla \times \boldsymbol{\psi}$. A constraint (or gauge) must be imposed on $\boldsymbol{\psi}$ to make the decomposition unique. In this work we take $\nabla \cdot \boldsymbol{\psi} = 0$. With this choice of gauge, the relationship between ϕ and $\boldsymbol{\psi}$ and the Reynolds stress tensor is given by,

$$\nabla^2 \phi = \nabla \cdot (\nabla \cdot \mathbf{R}) \tag{3a}$$

$$\nabla^2 \boldsymbol{\psi} = -\nabla \times (\nabla \cdot \mathbf{R}) \tag{3b}$$

Note that the choice of gauge influences the value of $\boldsymbol{\psi}$, but does not affect how $\boldsymbol{\psi}$ influences the mean flow.

Using these relationships, transport equations for ϕ and ψ can be derived from the Reynolds stress transport equations.

$$\frac{\partial \phi}{\partial t} + \mathbf{u} \cdot \nabla \phi = \nu \nabla^2 \phi - 2\nabla \cdot \mathbf{q} - \nabla^{-2} \nabla \cdot \nabla \cdot [\epsilon - \Pi + \nabla \cdot \mathbf{T} - \mathbf{P}] + \nabla^{-2} \mathbf{S}_\phi \quad (4a)$$

$$\frac{\partial \psi}{\partial t} + \mathbf{u} \cdot \nabla \psi = \nu \nabla^2 \psi + \nabla \times \mathbf{q} + \nabla^{-2} \nabla \times \nabla \cdot [\epsilon - \Pi + \nabla \cdot \mathbf{T} - \mathbf{P}] + \nabla^2 \mathbf{S}_\psi \quad (4b)$$

These equations contain extra production-like source terms $\mathbf{S}_\phi$ and $\mathbf{S}_\psi$ which contain mean velocity gradients. Note that the production term is not an explicit function of ϕ and ψ (except under limited circumstances) and, in general, must be modeled. The inverse Laplacian ∇^{-2} that appears in these equations can be thought of as an integral operator.

2. Theoretical analysis

2.1 Turbulent pressure

Taking the divergence of Eq. (1b) (the mean momentum equation) gives the classic Poisson equation for pressure,

$$\nabla^2 p = -\nabla \cdot (\mathbf{u} \cdot \nabla \mathbf{u}) - \nabla \cdot (\nabla \cdot \mathbf{R}) \quad (5)$$

Since this is a linear equation, the pressure can be split conceptually into two terms: one can think of the mean pressure as being a sum of a mean flow pressure due to the first term on the right-hand side,

$$\nabla^2 P_{mean} = -\nabla \cdot (\mathbf{u} \cdot \nabla \mathbf{u}) \quad (6a)$$

and a turbulent pressure due to the second term on the right-hand side,

$$\nabla^2 P_{turb} = -\nabla \cdot (\nabla \cdot \mathbf{R}) \quad (6b)$$

Given the definition of ϕ and assuming that ϕ is zero when there is no turbulence, then it is clear that $\phi = -P_{turb}$. For this reason, ϕ will be referred to as the turbulent pressure. This quantity is added to the mean pressure in the averaged momentum equation, which results in $P_{mean} = p + \phi$ being the effective pressure for the averaged equations. The quantity P_{mean} tends to vary more smoothly than p, which aids the numerical solution of these equations.

For turbulent flows with a single inhomogeneous direction, the turbulent pressure can be directly related to the Reynolds stresses. In this limit Eq. (3a) becomes $\phi_{,22} = R_{22,22}$ where x_2 is the direction of inhomogeneity. This indicates that $\phi = R_{22}$ for these types of flows. Note that R_{22} is positive semi-definite, so ϕ is always greater than or equal to zero in this situation. Positive ϕ is consistent with the picture of turbulence as a collection of random vortices (with lower pressure cores) embedded in the mean flow. It is not clear what the conditions for a negative turbulent pressure would be, if this condition is indeed possible.

2.2 Turbulent vorticity

To understand the role of ψ it is instructive to look again at turbulent flows that have a single inhomogeneous direction. Under this restriction Eq. (3b) becomes $\psi_{i,22} = -\epsilon_{i2k}R_{k2,22}$ where x_2 is the direction of inhomogeneity. If ψ goes to zero when there is no turbulence then $\psi_i = -\epsilon_{i2k}R_{k2}$. (or $\psi_1 = -R_{32}$, $\psi_2 = 0$ and $\psi_3 = R_{12}$). These are the off diagonal, or shear stress components of the Reynolds stress tensor.

For two-dimensional mean flows with two inhomogeneous flow directions, only the third component of ψ is non-zero, and Eq. (3b) becomes

$$\psi_{3,11} + \psi_{3,22} = R_{12,22} - R_{12,11} + (R_{11} - R_{22})_{,12} \tag{7}$$

Since ψ is responsible for vorticity generation, it is appropriate that it be aligned with the vorticity in two-dimensional flows. As a first level of approximation, it is not unreasonable to think of ψ as representing the average vorticity of a collection of random vortices making up the turbulence, and therefore ψ will be referred to as the turbulent vorticity.

For two-dimensional flows with a single inhomogeneous direction $\psi_3 = R_{12}$.

Note how the components of ψ reflect the dimensionality of the problem, while the mathematical expressions for these components reflects the degree of inhomogeneity.

2.3 Relationship with the eddy viscosity hypothesis

The linear eddy viscosity hypothesis for incompressible flows takes the form,

$$\mathbf{R} = -\nu_T(\nabla\mathbf{u} + (\nabla\mathbf{u})^T) + \frac{2}{3}k\mathbf{I} \tag{8}$$

where ν_T is the eddy viscosity, $\mathbf{I}$ is the identity matrix, and k is one half the trace of the Reynolds stress tensor.

Taking the divergence of Eq. (8) and rearranging terms gives,

$$\mathbf{f} = \nabla\cdot\mathbf{R} = \nabla(\frac{2}{3}k - 2\mathbf{u}\cdot\nabla\nu_T) + \nabla\times(\nu_T\nabla\times\mathbf{u}) + 2\mathbf{u}\cdot\nabla(\nabla\nu_T). \tag{9}$$

If the eddy viscosity varies relatively slowly, as is usually the case, then the very last term (involving the second derivative of the eddy viscosity) will be small and can be neglected. Under these circumstances the linear eddy viscosity model is equivalent to the following model,

$$o = \frac{2}{3}k - 2\mathbf{u}\cdot\nabla\nu_T \tag{10a}$$

$$\psi = \nu_T\nabla\times\mathbf{u}. \tag{10b}$$

So to a first approximation the turbulent vorticity, ψ should be roughly equal to the mean vorticity, times a positive eddy viscosity; and the turbulent pressure should be roughly equal to two thirds of the turbulent kinetic energy. These results are entirely consistent with the findings of the previous subsections.

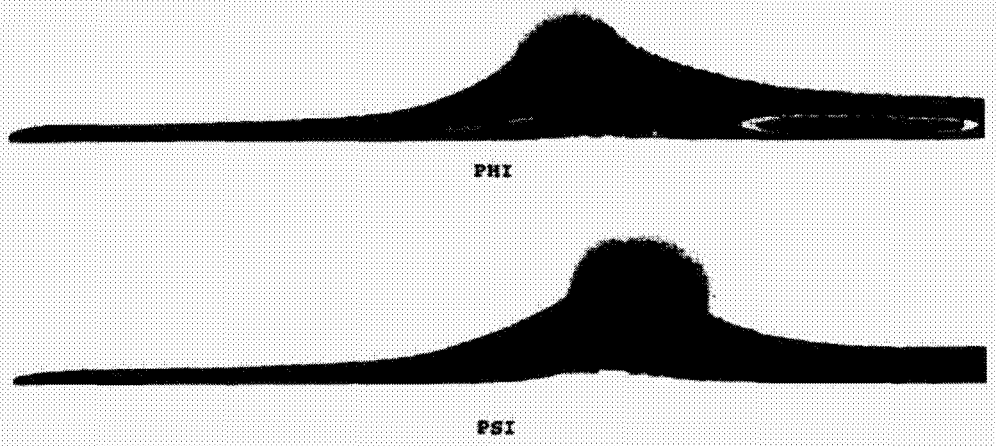

FIGURE 1. Contours of turbulent pressure (ϕ) and negative turbulent vorticity ($-\tilde{\omega}$) for the separating boundary layer of Na & Moin.

3. Computational results

Equations (3a) and (3b), relating the turbulent pressure and turbulent vorticity to the Reynolds stresses, were used to calculate ϕ and $\tilde{\omega}$ from DNS data for two relatively complex two-dimensional turbulent flows: a separating boundary layer (Na & Moin, 1996) and flow over a backward facing step (Le & Moin, 1995). The purpose was to assess the behavior of these turbulence quantities in practical turbulent situations, and to provide a database of these quantities for later comparison with turbulence models.

3.1 Separated boundary layer

The values of ϕ and $-\omega_3$ are shown in Fig. 1. As mentioned previously, for two-dimensional flows only the third component of $\tilde{\omega}$ is nonzero. The flow moves from left to right, separates just before the midpoint of the computational domain, and then reattaches before the exit. The contours are the same for both quantities and range from $-0.0004U_\infty^2$ to $0.01U_\infty^2$, where U_∞ is the inlet free-stream velocity.

Both the turbulent pressure and turbulent vorticity magnitudes increase in the separating shear layer and the reattachment zone. In addition, both quantities become slightly negative in the region just in front (to the left) of the separating shear layer, and show some "elliptic" (long range decay) effects at the top of the separation bubble. There is some speculation at this time that these effects could be numerical, but there is also some reason to believe that they are a legitimate result of the elliptic operators which define these variables. Changes in the far-field boundary condition (from zero value to zero normal gradient) had no visibly perceptible effect on the values of ϕ and ω_3.

The visual observation that ϕ and $-\omega_3$ are roughly proportional is analogous to the observation that $0.3k \approx -R_{12}$ (originally developed by Townsend, 1956, and successfully used in the turbulence model of Bradshaw, Ferriss & Atwell, 1967).

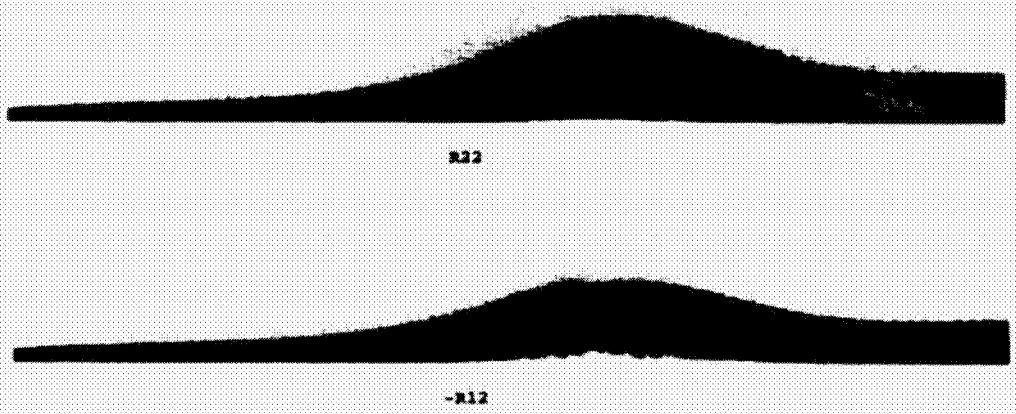

FIGURE 2. Contours of the normal Reynolds stress (R_{22}) and negative turbulent shear stress ($-R_{12}$) for the separating boundary layer of Na & Moin.

It is also consistent with the (first order) notion of turbulence as a collection of embedded vortices, with $-\phi$ representing the average vortex core pressure and ψ representing the average vortex strength.

In the case of a single inhomogeneous direction, $\phi = R_{22}$ and $\psi_3 = R_{12}$. It is instructive therefore to compare the results shown in Fig. 1 with the R_{22} and $-R_{12}$ components of the Reynolds stress tensor, shown in Fig. 2. The magnitudes of the contours in Fig. 2. are the same as Fig. 1. This comparison clearly shows the additional effects that result from inhomogeneity in the streamwise direction. The leading and trailing boundary layers (which have very little streamwise inhomogeneity) are almost identical. However, the magnitudes of the turbulent pressure and turbulent vorticity are enhanced in the separated shear layer due to the streamwise inhomogeneity.

3.2 Backward facing step

Computations of ϕ and $-\psi_3$ for the backward facing step are shown in Fig. 3. The flow is from left to right, and there is an initial (unphysical) transient at the inflow as the inflow boundary condition becomes Navier-Stokes turbulence. The boundary layer leading up to the backstep has moderate levels of the turbulent pressure and turbulent vorticity (which closely agree with the values of R_{22} and $-R_{12}$ in that region). As with the separating boundary layer, the turbulent pressure and turbulent vorticity increase significantly in the separated shear layer and reattachment zone. There is an area of slight positive turbulent pressure and negative turbulent vorticity in the far field (about one step height) above the backstep corner. This may or may not be a numerical artifact, and is discussed in the next section.

3.3 E[illegible]

Identifying the exact nature of the complicity of these new turbulence quantities is important to understanding their overall behavior and how they should be modeled.

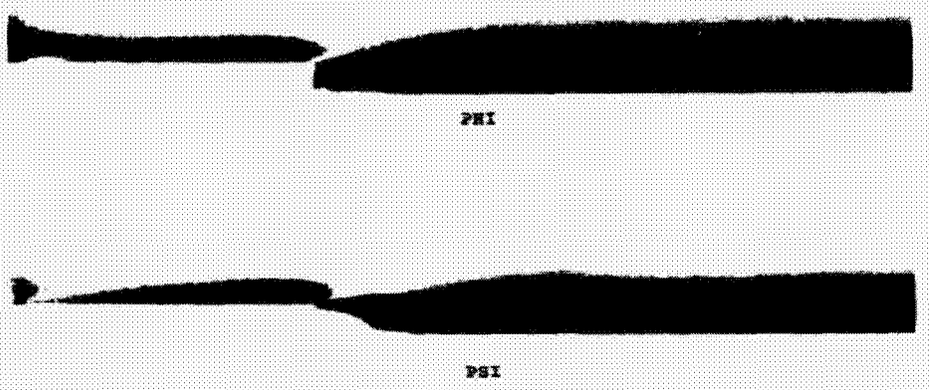

FIGURE 3. Contours of turbulent pressure (ϕ) and negative turbulent vorticity ($-\psi$) for the backward facing step of Le & Moin.

When rewritten, Eqs. (3a) and (3b) become,

$$\phi = \nabla^{-2}\nabla\cdot(\nabla\cdot\mathbf{R}) \tag{11a}$$

$$\psi = -\nabla^{-2}\nabla\times(\nabla\cdot\mathbf{R}) \tag{11b}$$

These are elliptic, but order one, operators on the Reynolds stress tensor. As demonstrated in §2, when there is only a single inhomogeneous direction, these operators simply lead to various Reynolds stress components. Under these conditions they do not produce "action at a distance" or long range effects normally associated with elliptic (Poisson or Helmholtz) operators.

For two and three inhomogeneous directions, it is still not clear whether these operators produce long range effects. There are certainly some situations in which they do not. One example is when the Reynolds stress tensor can be represented in the following form (somewhat reminiscent of the linear eddy viscosity relation) $R_{ij} = s\delta_{ij} + v_{i,j} + v_{j,i}$, where s is some scalar and $\mathbf{v}$ is a vector. If this is the case then, $\phi = s + 2\nabla\cdot\mathbf{v}$ and $\psi = -\nabla\times\mathbf{v}$, and there are no long range ("elliptic") effects.

In fact, the presence of long range effects in ϕ and ψ is somewhat unsettling. It would suggest that these turbulence quantities can exist in regions where there is no Reynolds stress. Since $\nabla\cdot\mathbf{R} = \nabla\phi + \nabla\times\psi$, this would imply that a precise cancellation of these long range effects must occur in regions where the Reynolds stresses are small or negligible. While the results presented in Fig. 1 and Fig. 3 seem to show that long range elliptic effects do indeed take place, they could also be a numerical artifact. The numerical solution of Eqs. (3a) and (3b) requires double differentiation of the DNS data; this produces compact Poisson equation source terms that are only marginally resolved by the mesh. It is our current conjecture that these operators are actually local in nature and only serve to "mix"

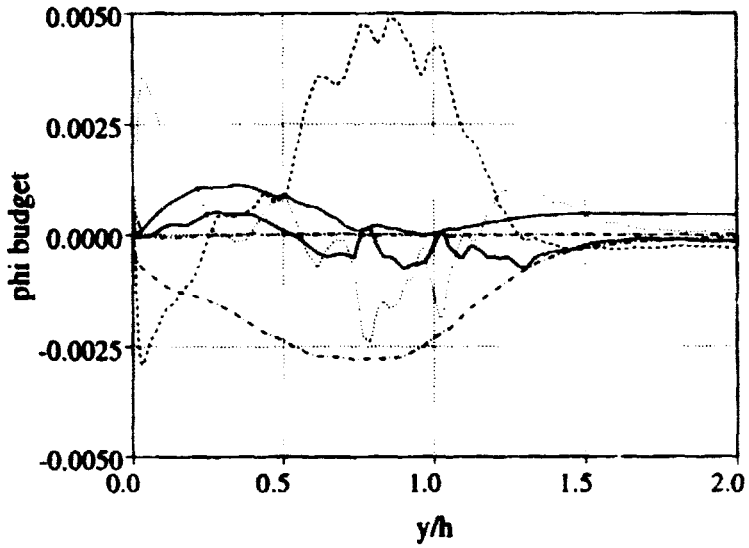

FIGURE 4. Budget of the ϕ transport equation at a station roughly half way through the recirculation bubble of the backward facing step ($x/h = 4.0$). —·— dissipation or diffusion; - - - - velocity pressure-gradient; ····· triple correlation term; —— production (positive) or convection.

various components of the Reynolds stress tensor. It is also conjectured from these computational results that the turbulent pressure is a positive semi-definite quantity.

Note that the ellipticity discussed here is not the same as an ellipticity in the governing evolution equations for these quantities. An elliptic term in the evolution equations is both physical and desirable (see Durbin, 1993). Such a term mimics long range pressure effects known to occur in the exact source terms. The exact evolution equations for ϕ and ψ, described below, have just this elliptic property.

3.4 *Turbulent pressure evolution*

Considerable insight can be obtained about the evolution of the turbulent pressure by considering the case of a single inhomogeneous direction. It has been shown that under these circumstances $\phi = R_{22}$, so the evolution is identical with the Reynolds stress transport equation for the normal Reynolds stress, R_{22}. For the case of turbulent channel flow (Mansour *et al.*, 1988), the R_{22} evolution is dominated by a balance between dissipation and pressure-strain, with somewhat smaller contributions from turbulent transport and viscous diffusion. There is considerable interest in determining if these same trends continue for ϕ evolution in more complex situations, since the ultimate goal is to construct a modeled evolution equation for this quantity.

Figure 4 shows the terms in the exact ϕ evolution equation for flow over a backward facing step, at a station roughly in the middle of the recirculation bubble. These terms were calculated in the same manner as the turbulent pressure. Both

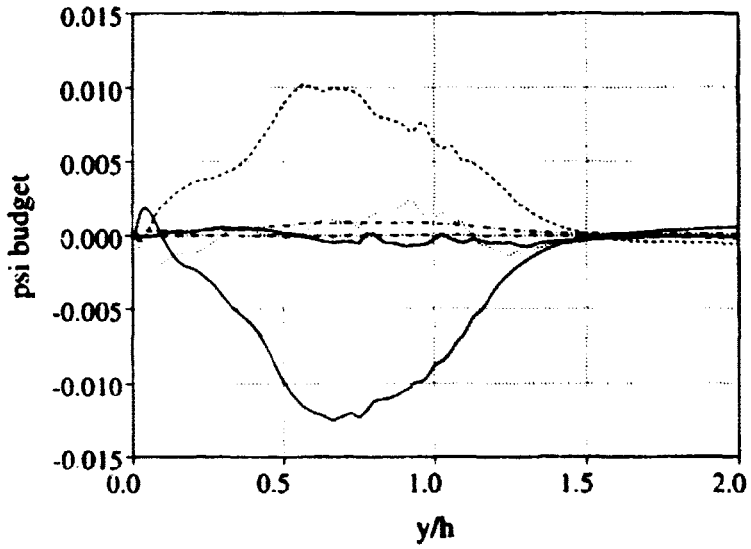

FIGURE 5. Budget of the ψ_3 transport equation at a station roughly half way through the recirculation bubble of the backward facing step: see Fig. 4 for caption.

the detached shear layer and the backward moving boundary layer are visible in the statistics. In the shear layer, the expected dominance of dissipation and pressure-terms (presumably dominated by pressure-strain) is evident. In the recirculating boundary layer, turbulent transport and pressure-terms (probably dominated by pressure transport) are dominant. It is interesting to note that the production term dominates in the middle of the recirculation bubble. The fact that some of these source terms are not exactly zero at roughly two step heights away from the bottom wall is thought to be a numerical artifact similar to those found when calculating ϕ and ψ. Some of the curves have an erratic nature due to the lack of statistical samples. This phenomena is also present in the (unsmoothed) Reynolds stress transport equation budgets presented in Le & Moin, 1993.

3.5 Turbulent vorticity evolution

As with the turbulent pressure, it is useful to consider the case of a single inhomogeneous direction when analyzing the evolution of the turbulent vorticity. Under these circumstances ψ_3 evolves identically to the Reynolds shear stress, R_{12}. In turbulent channel flow, the R_{12} evolution is dominated by a balance between production and pressure-strain, with somewhat smaller contributions from turbulent and pressure transport. This trend continues in the ψ_3 evolution equation, which is shown in Fig. 5., for the backward facing step at a cross section roughly halfway through the recirculization bubble ($x/h = 4.0$). The small value of the dissipation is consistent with the fact that isotropic source terms can be shown not contribute to the evolution of ψ.

4. Modeling

4.1 Formulation

An initial proposal for modeled transport equations for the turbulent pressure and turbulent vorticity are:

$$\frac{\partial \phi}{\partial t} + \mathbf{u}\cdot\nabla\phi = \nabla\cdot(\nu+\nu_T)\nabla\phi - \left(\frac{3}{2}C_\mu\right)\left(\frac{1}{T}\right)\phi - \left(\frac{12\nu}{y^2}\right)\phi + \left(\frac{2}{3}\right)\frac{\boldsymbol{\psi}\cdot\boldsymbol{\psi}}{15\nu+\nu_T} \quad (12a)$$

$$\frac{\partial \boldsymbol{\psi}}{\partial t} + \mathbf{u}\cdot\nabla\boldsymbol{\psi} = \nabla\cdot(\nu+\nu_T)\nabla\boldsymbol{\psi} - \left(\frac{1}{T}\right)\boldsymbol{\psi} - \left(\frac{6\nu}{y^2}\right)\boldsymbol{\psi} + \phi\boldsymbol{\omega} \quad (12b)$$

where, $C_\mu = 0.09$, y is the normal distance to the wall, the time-scale is given by $T = (\nu+\nu_T)/\phi$, and the eddy viscosity is given by $\nu_T = |\boldsymbol{\psi}|/|\boldsymbol{\omega}|$. Dissipation (and some redistribution) is modeled as an exponential decay process (roughly corresponding to Rotta's, low Reynolds number dissipation model). Turbulent and pressure transport are collectively modeled as enhanced diffusive transport. Production and energy redistribution are proportional to the turbulence pressure times the mean vorticity for the turbulent vorticity, and are proportional to the square of the turbulent vorticity magnitude for the turbulent pressure. High Reynolds number constants are determined so that $\phi = \frac{2}{3}k$ at high Reynolds numbers. The low Reynolds number constants (which appear with a ν) are set to obtain exact asymptotic behavior and good agreement with the channel flow simulations of the next section.

Note that both ϕ and $\boldsymbol{\psi}$ have the same units. An extra turbulent scale is currently defined by using the mean flow timescale $|\boldsymbol{\omega}|$ to define the eddy viscosity. The solution of an additional scale transport equation (such as ϵ) would remedy a number of potential problems with the current model. It could eliminate the singularity in the eddy viscosity at zero vorticity, remove any explicit references to the wall normal distance, and allow better decay rates for homogeneous isotropic turbulence. The disadvantage of this approach (which will be tested in the future) is the added computational cost and additional empiricism.

4.2 Channel flow simulations

The model equations (12a and 12b) were solved in conjunction with mean flow equations for fully developed channel flow at Re_τ of 180 and 395. Since there is only one inhomogeneous direction, the turbulent pressure is proportional to the normal Reynolds stress, and ω_1 is proportional to the turbulent shear stress. Comparisons of the model predictions and the DNS data of Kim, Moin, & Moser (1987), are shown in Fig. 6.

When a turbulent channel flow is suddenly perturbed by a spanwise pressure gradient, the flow suddenly becomes three dimensional and the turbulence intensities first drop before increasing due to the increased total shear (Mein *et al.*, 1990). Durbin (1993) modeled this effect by adding a term to the dissipation equation which increases the dissipation in these three-dimensional flows. The same qualitative effect can be obtained by defining the eddy viscosity in the proposed model as $\nu_T = \frac{\boldsymbol{\psi}\cdot\boldsymbol{\omega}}{\boldsymbol{\omega}\cdot\boldsymbol{\omega}}$. In two-dimensional flows this is identical to the previous definition.

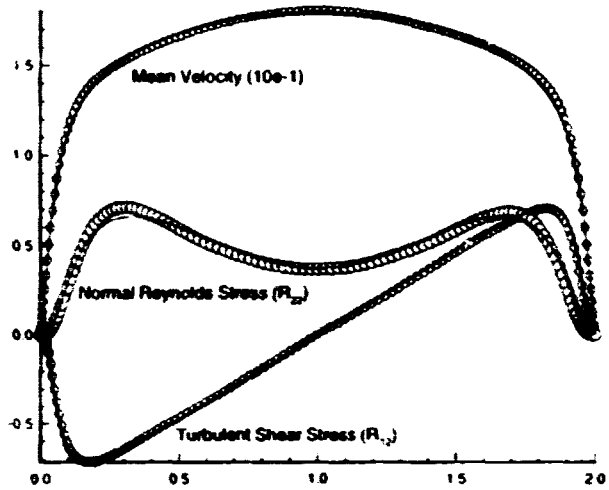

FIGURE 6. Model results (solid lines) and DNS data (circles) for turbulent channel flow. ($Re_\tau = 180$)

However, in three-dimensional flows, the orientation of ψ will lag ω, and the eddy viscosity will drop initially. A smaller eddy viscosity leads to a smaller timescale and increased dissipation. Unfortunately, the magnitude of this effect is severely underestimated in the present model, and a scale equation (and a correction like Durbin's) may be required to model this effect accurately.

5. Conclusions

This work proposes abandoning the Reynolds stresses as primary turbulence quantities in favor of a reduced set of turbulence variables, namely the turbulent pressure o, and the turbulent vorticity ψ. The advantage of moving to these alternative variables is the ability to simulate turbulent flows with the accuracy of a Reynolds stress transport model (i.e. with no assumed constitutive relations), but at a significantly reduced cost and simplified model complexity. As the names imply, these quantities are not simply mathematical constructs formulated to replace the Reynolds stress tensor. They are physically relevant quantities.

At first glance the operators which relate o and ψ to the Reynolds stress tensor suggest the possibility of ellipticity or action at a distance. However, we have shown that under a number of different circumstances this does not happen, and conjecture that it may never happen. The physical relevance of these quantities would be complicated if they were finite when there was no turbulence (Reynolds stresses). A proof to this effect may also prove our second conjecture, that o is a positive definite quantity.

The budgets for the transport equations of these new variables indicated that the extra production terms were not significant, and that these equations could be

modeled analogously to the Reynolds stress transport equations. An initial model was constructed for these equations using basic modeling constructs which showed good results for turbulent channel flow. It is likely, that for this shearing flow, the turbulent timescale is well represented by the mean flow vorticity. However, for more complex situations, it is likely that an additional scale equation (such as an ϵ equation) will be required.

Acknowledgments

The authors would like to thank Paul Durbin for his comments on this work, and particularly for discussions concerning the ellipticity of these variables.

REFERENCES

BRADSHAW, P., FERRISS, D. H. & ATWELL, A. 1967 Calculation of boundary layer development using the turbulent energy equation. *J. Fluid Mech.* **28**, 593-616.

DURBIN, P. A. 1993 Modeling three-dimensional turbulent wall layers. *Phys. Fluids A.* **5**(5), 1231-1238.

KIM, J., MOIN, P. & MOSER, R. D. 1987 Turbulence statistics in fully-developed channel flow at low Reynolds number. *J. Fluid Mech.* **177**, 133-166.

LE, H. & MOIN, P. 1993 Direct numerical simulation of turbulent flow over a backward-facing step. *Report TF-58.* Thermosciences Division, Department of Mechanical Engr., Stanford Univ.

LUND, T.S. & NOVIKOV, E. A. 1992 Parameterization of subgrid-scale stress by the velocity gradient tensor. *Annual Research Briefs - 1992.* Center for Turbulence Research, NASA Ames/Stanford Univ.

MANSOUR, N. N., KIM, J. & MOIN, P. 1988 Reynolds-stress and dissipation rate budgets in a turbulent channel flow. *J. Fluid Mech.* **194**, 15-44.

MOIN, P., SHIH, T.-H., DRIVER, D. & MANSOUR, N. N. 1990 Direct numerical simulation of a three-dimensional turbulent boundary layer. *Phys. Fluids A.* **2**(10), 1846-1853.

NA, Y. & MOIN, P. 1996 Direct numerical simulation of a turbulent separation bubble. *Report TF-.* Thermosciences Division, Department of Mechanical Engr., Stanford Univ.

ROTTA, J. 1951 Statistical theory of inhomogeneous turbulence. Part I., *Zeitschrift fur Physik.* **129**, 257-272.

SPEZIALE, C.G. 1994 A review of Reynolds stress models for turbulent flows., *20th Symposium on Naval Hydrodynamics.* University of California, Santa Barbara.

TOWNSEND, A.A. 1956 *The Structure of Turbulent Shear Flow.* Cambridge University Press, London.

WU, J.-Z., ZHOU, Y. & WU, J.-M. 1996 Reduced stress tensor and dissipation and the transport of Lamb vector. *ICASE report* No. 96-21.

NEXT
DOCUMENT

Second moment closure analysis of the backstep flow database

By S. Parneix, D. Laurence[1] AND P. Durbin[2]

A second moment closure computation (SMC) is compared in detail with the direct numerical simulation (DNS) data of Le and Moin for the backstep flow at $Re = 5,000$ in an attempt to understand why the intensity of the backflow and, consequently, the friction coefficient in the recirculation bubble are severely underestimated. The data show that this recirculation bubble is far from being laminar except in the very near wall layer. A novel 'differential *a priori*' procedure was used, in which the full transport equation for one isolated component of the Reynolds stress tensor was solved using DNS data as input. Conclusions are then different from what would have been deduced by comparing a full simulation to a DNS. One cause of discrepancy was traced back to insufficient transfer of energy to the normal stress by pressure strain, but was not cured. A significant finding, confirmed by the DNS data in the core region of a channel flow, is that the coefficient that controls destruction of dissipation, C_{ϵ_2}, should be decreased by a factor of 2 when production is vanishing. This is also the case in the recirculation bubble, and a new formulation has cured 25% of the backflow discrepancy.

1. Introduction

The flow over a backward-facing step has been probably the most popular separated flow test case of the past 20 years, for which numerous experiments (by Kim, Johnston, Eaton, Vogel, Durst, Driver, etc.) provide data on the effects of geometry, inlet conditions, and Reynolds number. With the improvement of turbulence models and numerical methods, it is now generally possible to recover the reattachment length, but the intensity of the backflow and, as a consequence, the negative peak in skin friction are always underestimated by nearly a factor of 2 when second moment closures (SMC) are used.

The recent DNS database of Le and Moin (1993) at $Re = 5,000$, well corroborated by the experiments of Jovic & Driver (1995) and of Kasagi *et al.* (1995), is analyzed here to understand this severe defect common to all SMC.

2. Full simulation of the backward-facing step

The flow was computed using INS2D, a finite difference code in generalized coordinates written at NASA Ames Research Center. A fine, non-uniform grid of

1 Electricité de France, DER, Lab. Nat. d'Hydraulique, 6 quai Watier, 78400 Chatou, France
2 Stanford University

120 × 120 cells was used to cover the region $x/h = -3$ to 35, $x = 0$ being the location of the sudden expansion and h being the step height. The inlet values for the mean velocities, Reynolds stresses, and dissipation were taken from the DNS database. The elliptic relaxation procedure of Durbin (1993) has been combined with the Speziale, Sarkar, Gatski (SSG) pressure strain model in the 'neutral' formulation as in Laurence *et al.* (1995) (see Appendix).

FIGURE 1. Streamlines (a) Second moment closure, (b) DNS

Figure 1 shows the predicted streamlines compared to the DNS data. The reattachment is correct and a secondary bubble is found. However, the size of this corner bubble is much smaller in the simulation than in the data. In fact, if one looks at the predicted friction coefficient compared to the DNS and experimental data (Fig. 2), the intensity of the main recirculation is underpredicted by a factor 1/2 (the slight improvement shown by a dashed curved is discussed further in section 5). The stagnating flow between the two recirculations at $x/h = 2$ is also missed. Since it is believed that the underestimation of the secondary bubble is a consequence of the underestimation of the primary recirculation, we will concentrate in the following on curing the latter discrepancy. Note that the recovery after reattachment is also too slow – this is a problem in virtually all turbulence transport models.

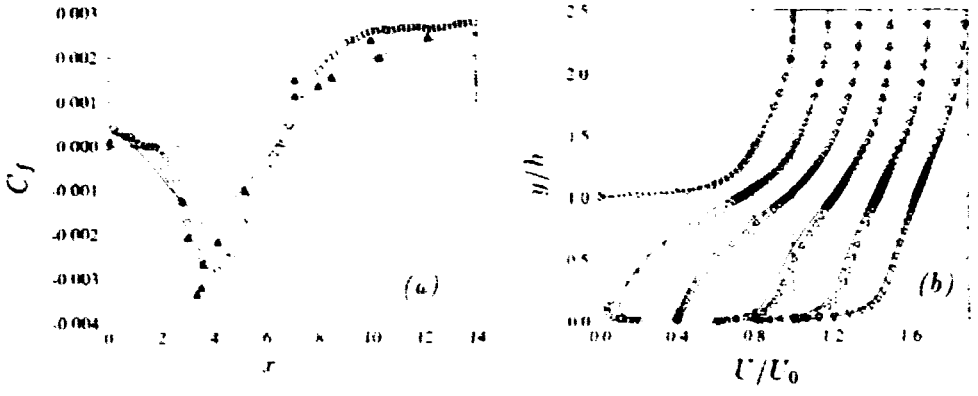

FIGURE 2. (a) Friction coefficient. ○ DNS (Le & Moin), ▲ experiment (Jovic & Driver), —— SMC, ---- modified SMC (cf. section 5). (b) DNS U-profiles at locations $x/h = -3$ (○), 4 (□), 6 (◇), 10 (△), 15 (◁) and 19 (▽), —— : model.

The above observations are believed to reflect what can be expected from any state of the art SMC. In Fig. 2, the mean streamwise velocity U is shown. The center of the recirculation is well predicted, but its intensity is severely underestimated

(see station $x/h = 4$). Since C_f is too weak, this is not due to an overprediction of turbulent mixing in the near wall region, but rather to an underestimation of the entrainment from the shear layer. Since the flow in the upper layer splits at the stagnation point into the recirculation and the downstream flow, this same velocity defect is transported into the recovery region. Le & Moin noted, in good agreement with the Jovic & Driver experiment, that the log profile of the law of the wall was still not recovered at $x/h = 19$; this as a consequence of the low Reynolds number. In the Reynolds-averaged Navier-Stokes (RANS) computation, the recovery at $x/h = 19$ is, however, still slightly underestimated.

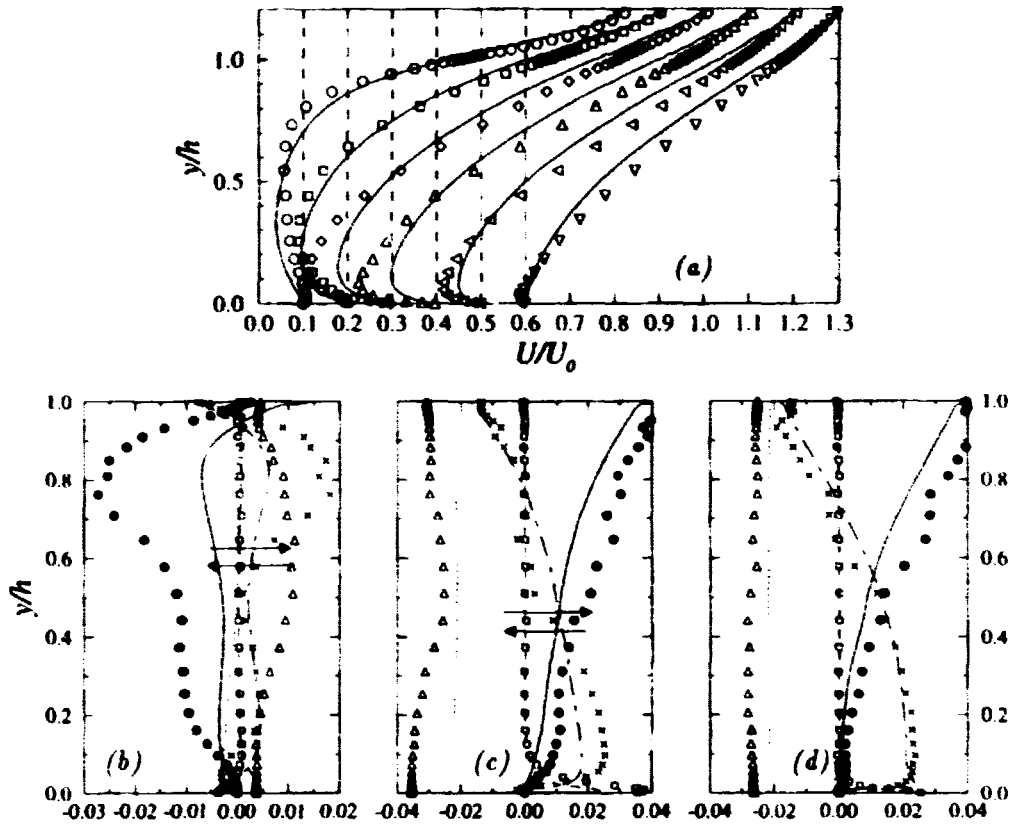

FIGURE 3. (a) Zoom of U in recirculation at locations $x/h = 1$ (○), 2 (□), 3 (◇), 4 (△), 5 (◁) and 6 (▽), ——— : model. (bcd) Budget of U at locations (b) $x/h = 2$ (c) $x/h = 4$ (d) $x/h = 6$, convection (• DNS, ——— SMC) turbulent force (× DNS, — - — SMC), viscous force (□ DNS, - - - - SMC), pressure force (△ DNS, ····· SMC).

Figure 3 focuses on the recirculation and shows the budgets of the U momentum equation. The underestimation of the backflow is most severe at station $x/h = 4$. As expected, the adverse pressure gradient driving the backflow is fairly constant across the whole height and balances the viscous shear stress at the wall; hence, the pressure gradient determines the value of $C_{f_{min}}$. Jovic and Driver (1995) found

that the minimum of C_f follows a 'laminar like' law, $C_{f_{min}} = -0.19 Re_h^{-1/2}$ for Reynolds numbers between 5,000 and 50,000. It is very clear, however, that the recirculation is *not* laminar like, except for the very near wall region below the maximum of the reverse flow.

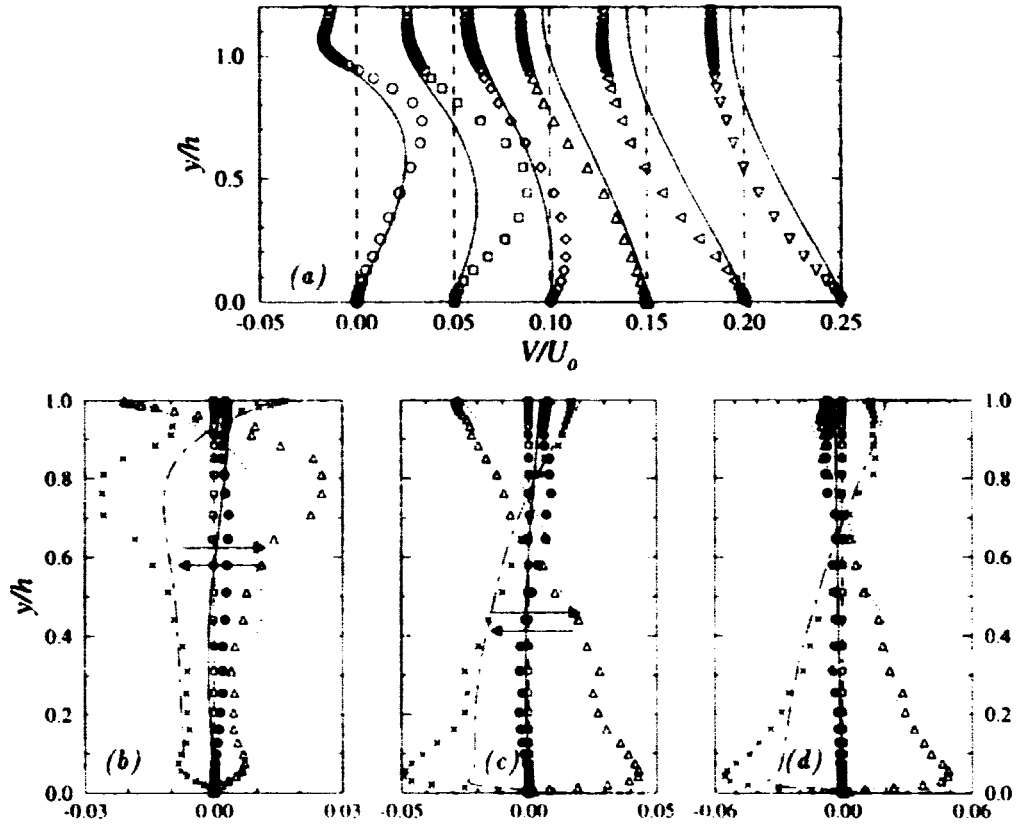

FIGURE 4. (a) Zoom of V in recirculation, legend cf. Fig.3a. (bcd) Budget of V at (b) $x/h = 2$ (c) $x/h = 4$ (d) $x/h = 6$, legend cf. Fig.3bcd.

A possible explanation for the Reynolds number dependence, consistent with the fact that the turbulent Reynolds number remains high in the recirculation bubble, might be as follows. The pressure field is a consequence of the general form of the separated layer (which causes flow expansion and pressure rise). The form of the separated layer is determined by the turbulence. The Reynolds number influence noted by Jovic and Driver (1995) might come from a wider (compared to h) shear layer detaching from the step, causing a stronger adverse pressure gradient at lower values of Re. This view is supported by our observation that RANS computations were more sensitive to model changes in the shear layer than in the recirculating flow. The near-wall, viscous layer of reversed flow results from a balance of the pressure force and the viscous friction, and covers only a few percent of the bubble height—so this cannot lead to 'laminar like' behavior. The turbulent Reynolds

$k^2\varepsilon/\nu$ (i.e., $\approx 10\nu_t/\nu$) in the bubble is in the range 400 - 500 (Fig. 11), similar to its value in the shear layer. Incidently, this makes any low Reynolds 'damping function' ineffective in the main portion of the bubble.

The momentum budget station at $x/h = 2$ shows that entrainment by the turbulent shear stress is underestimated right below the shear layer detaching from the corner. At $x/h = 4$ it was checked that $\overline{uv}$ and VdU/dy are by far the major contributors to the turbulent and convection terms. The shear is weakly opposing the recirculation (a pair of arrows in Figs. 3 and 4 indicates the position of $U = 0$) while advection is driving the recirculation in its upper part. Overall, the model seems only slightly to underestimate this turbulent shear force in the full simulation, even if at this stage the defect is traced to insufficient entrainment at the top part of the recirculation. However, we will see that $\overline{uv}$ itself is in error.

The V component in the shear layer shown in Fig. 4 is severely underestimated. The turbulence force was found to be due almost entirely to $\overline{v^2}$. Again, right near the corner, at $x/h = 2$, the turbulent force is underestimated by about a factor of 2, although not far upstream at $x/h = 0$, the RANS results were in accordance with the DNS data. At $x/h = 4$ and 6 (near reattachment), it is still $\overline{v^2}$ which is driving the flow downward. Advection (inertia or streamline curvature) effects are negligible, showing that a reattaching flow is different from an impinging flow. Fig. 1 shows that the streamlines become smoothly tangent to the wall; some RANS simulations have produced a kink in the streamlines at this reattachment point (Hanjalic, 1996).

3. Differential *a priori* tests

3.1 Reynolds stresses

The Reynolds stresses will now be analyzed from two different sets of computations. The first corresponds to the full simulation and explains the mean velocity budgets shown previously. The second is from a differential *a priori* test and permits an analysis of the true effects of the pressure-strain and transport models. The latter results are obtained by solving the full differential equations of each individual stress $\overline{u_i u_j}$ one by one, while the other stresses and the mean flow are taken directly from the DNS database.

An overall glance at Figs. 5-7 explains why a comparison using only the full simulation may entail erroneous conclusions: the full simulation could lead one to believe that the model has problems in the recirculation bubble, whereas the *a priori* test shows that discrepancies are mainly located in the shear layer.

The $\overline{u^2}$ streamwise fluctuation in the *a priori* test is overestimated in the shear layer, but improved in the recirculation when the correct mean velocity (used in the *a priori* test) enters its production. In both the full and *a priori* simulations, the $\overline{v^2}$ component is seen to be underestimated in the shear layer, and elsewhere at station $x/h = 4$. On the other hand, the shear stress seems to be, on average, correct in the full simulation and overestimated in the *a priori* test. This is because in the former an erroneously small value of $\overline{v^2}$ is entering its production term. The origin of the problem lies in insufficient return to isotropy in the SSG pressure-strain

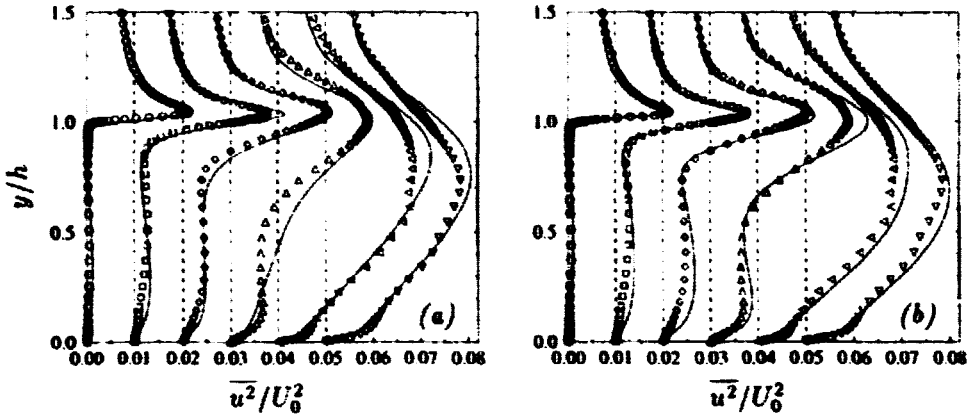

FIGURE 5. $\overline{u^2}$ profiles (a) full computation, (b) *a priori* test, at locations $x/h = 0.1$ (o), 0.5 (□), 1 (◇), 2 (△), 4 (◁) and 6 (▽), ——— : model.

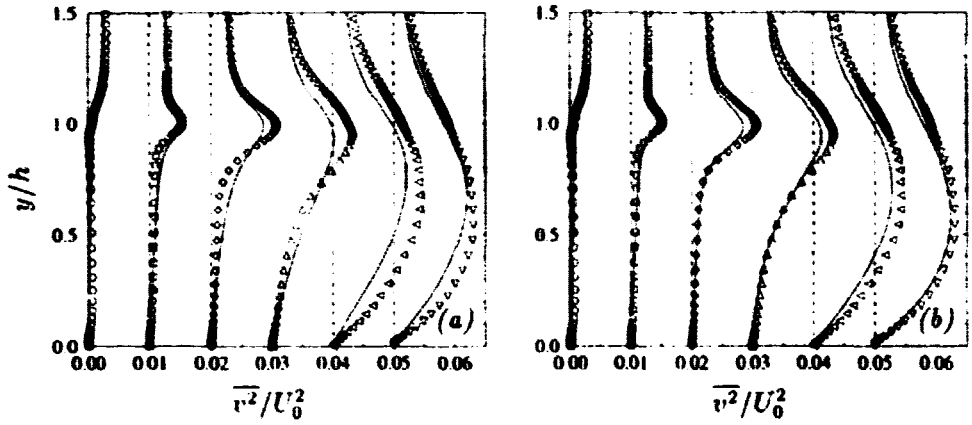

FIGURE 6. $\overline{v^2}$ profiles (a) full computation. (b) *a priori* test, legend cf. Fig.5.

model, which should increase $\overline{v^2}$ and decrease both $\overline{u^2}$ and $\overline{uv}$, but only in the shear layer.

3.2 Budgets

For the analysis of budgets, the DNS data has been processed in the same form as the elliptic relaxation model (see appendix); i.e., some anisotropy effects in the dissipation are lumped with the so-called pressure-strain term.

For the budgets of $\overline{u^2}$ in Fig. 8, the production terms coincide perfectly of course, since the mean velocities and Reynolds stresses other than $\overline{u^2}$, are taken from the DNS. That is the method of this *differential, a priori* test. The model for turbulent transport (Daly-Harlow) performs well, but the pressure gradient-velocity correlation (kf_{12}) is underestimated in the free shear layer.

The budgets of $\overline{v^2}$ (Fig. 9) show here again that in the shear layer the pressure correlation term is underestimated—at $x/h = 2$ by a factor of 2. The pressure term

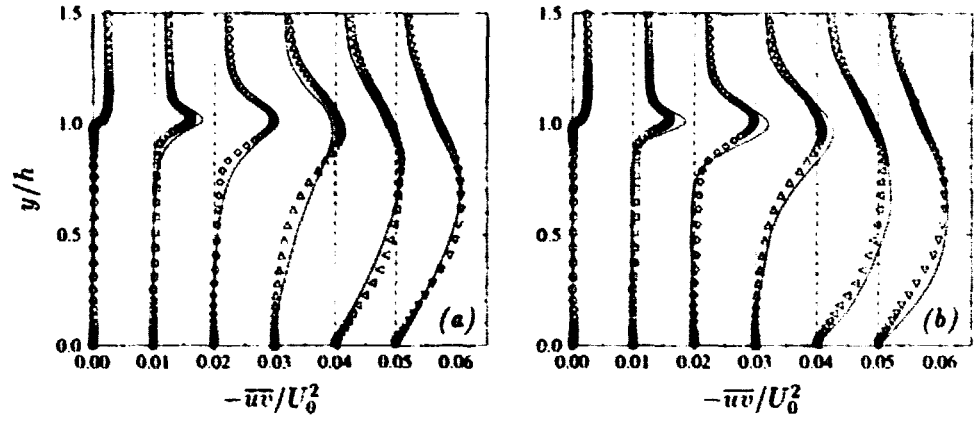

FIGURE 7. $\overline{uv}$ profiles (a) full computation, (b) *a priori* test, legend cf. Fig.5.

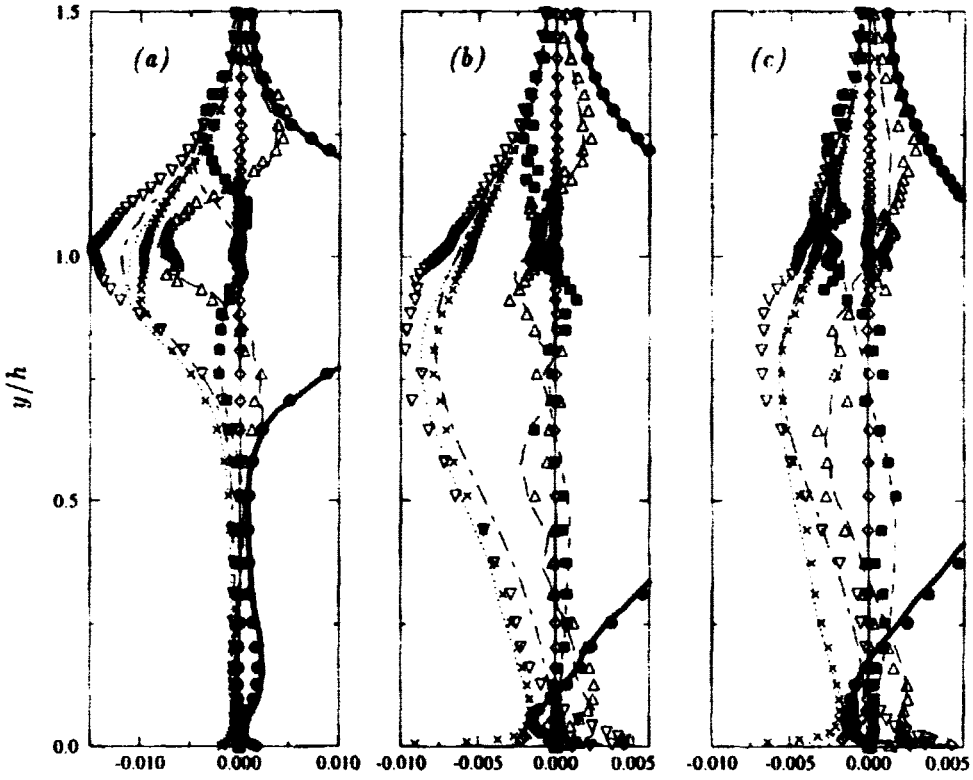

FIGURE 8. *A priori* test: budget of $\overline{u^2}$ at locations (a) $x/h = 2$, (b) $x/h = 4$, (c) $x/h = 6$. production (• DNS, —— SMC), $[-\varepsilon R_{ij}/k]$ (× DNS, ····· SMC), convection (▪ DNS, - - - - SMC), transport (Δ triple correlations DNS, — — — SMC), viscous diffusion (◇ DNS, —— SMC), pressure-deformation + dissipation anisotropy effects ($\nabla[\Pi_{ij}^{vpg} - \varepsilon_{ij} + \varepsilon R_{ij}/k]$ DNS, —·— $[kf_{ij}[$ SMC)

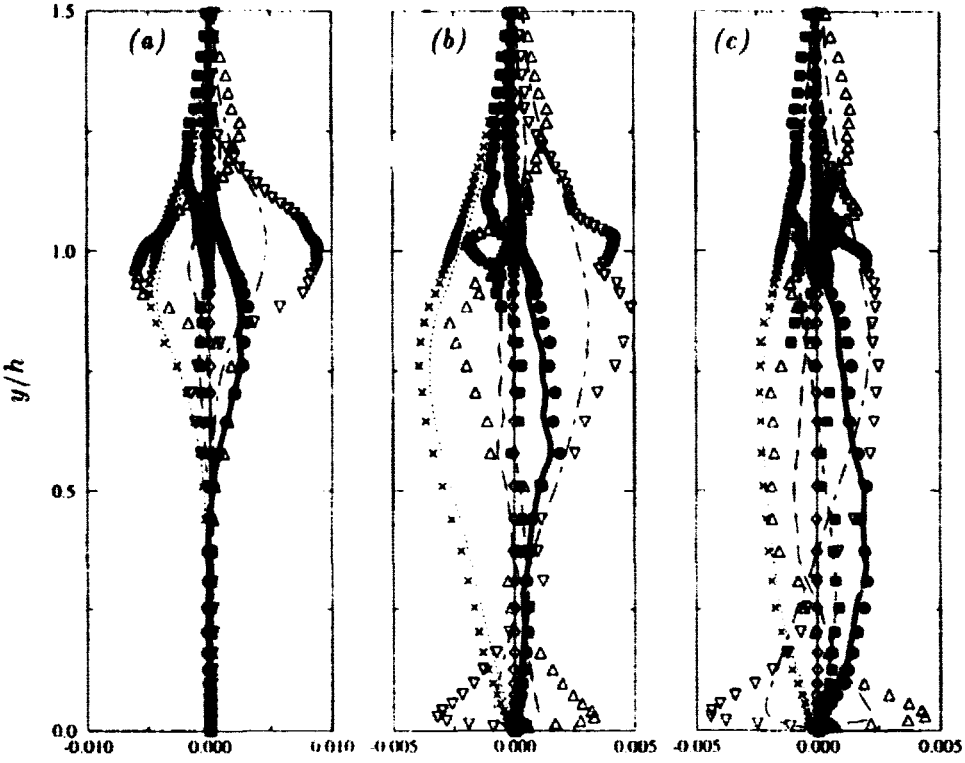

FIGURE 9. *A priori* test: budget of $\overline{v^2}$ at locations (a) $x/h = 2$, (b) $x/h = 4$, (c) $x/h = 6$, legend cf. Fig.8.

includes pressure-transport effects (in the present case countergradient transport effects) which partially balance the turbulent diffusion terms, and which, as a consequence, are also underestimated by the model. Note that the production term is making a significant contribution, and since it is mainly composed of $-\overline{v^2}DV/dy$, underestimations of both $\overline{v^2}$ and V (which is affected by $\overline{v^2}$) self-amplify through this term. Near the wall, turbulent diffusion is generating the wall normal fluctuations, while the wall blocking effect is impeding them; the latter is represented by the elliptic relaxation effect (the homogeneous solution to Eq. 4 of the appendix is actually positive in this area).

The budget of $\overline{uv}$, on the other hand, shows an overestimation of the pressure-correlation, though again this compensates for an underestimation of the turbulent transport. At $x/h = 4$, near the wall, the production term is seen to change sign, but still $\overline{uv}$ remains approximately zero because of the strong transport term. Hence, in the narrow region between the maximum of the backflow and the wall, the mean flow is largely viscous, as seen previously. With increasing Reynolds number, one can expect the ratio of production to transport terms to become larger, and the turbulent shear stress would then decelerate this backflow, leading to a smaller peak in C_f. Because $\overline{uv}$ is countergradient with respect to the velocity gradient,

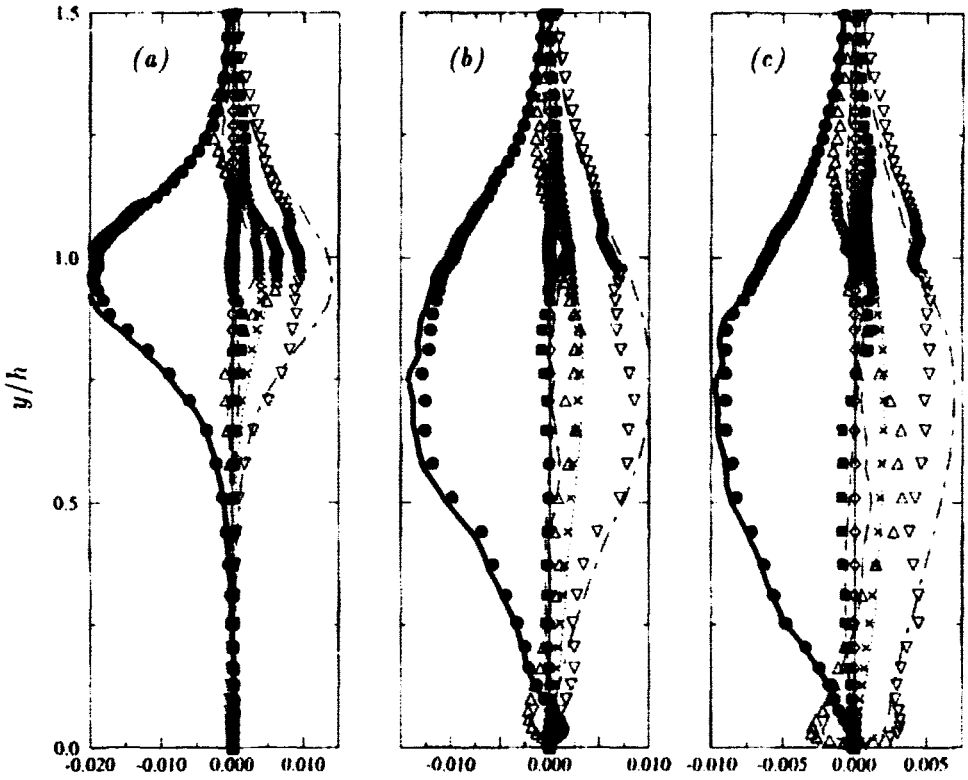

FIGURE 10. *A priori* test: budget of $\overline{uv}$ at locations (a) $x/h = 2$, (b) $x/h = 4$, (c) $x/h = 6$, legend cf. Fig.8.

the production of $\overline{u^2}$ and k becomes negative in this area.

4. Model parameters

Fine tuning of models is often based on functions of the following parameters: anisotropy of the Reynolds stresses, A; turbulent Reynolds number, Re_t; production over dissipation, P/ε (sometimes the non-dimensional rate of strain, Sk/ε is used); and turbulent lengthscale, $k^{3/2}/\varepsilon$. In seeking improvements here, one should look for parameters that exhibit different values from those in simpler shear flows, for which the model should not be changed. The above parameters have been computed from DNS data to see if they are pertinent.

The range of variation of A (Fig. 11) from 0.6 to 0.8 in the recirculation bubble shows no particularity; the Re_t values in the range of 400 to 800 (Fig. 11) is too high to invoke low Reynolds effects; the ratio P/ε (Fig. 12) decreases from 2 to 1.5 in the shear layer, but is seen to be particularly weak in the lower half of the recirculation bubble. This last is a feature that is significantly different from near wall regions of boundary layers and should be considered further. Indeed, even negative production occurs along the wall from the reattachment to $x/h = 4$.

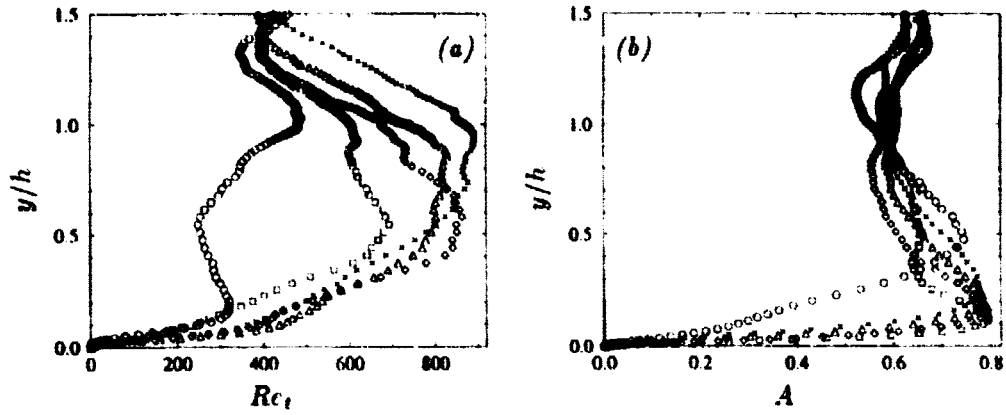

FIGURE 11. DNS profiles (a) Turbulent Reynolds number $Re_t = k^2/(\nu\varepsilon)$, at locations $x/h = 2$ (○), 4 (□), 6 (◇), 8 (△) and 10 (×). (b) Anisotropy $A = 1 - 9/8(A_2 - A_3)$, A_2 and A_3 are the second and third invariants of a_{ij}, legend cf. Fig.11a.

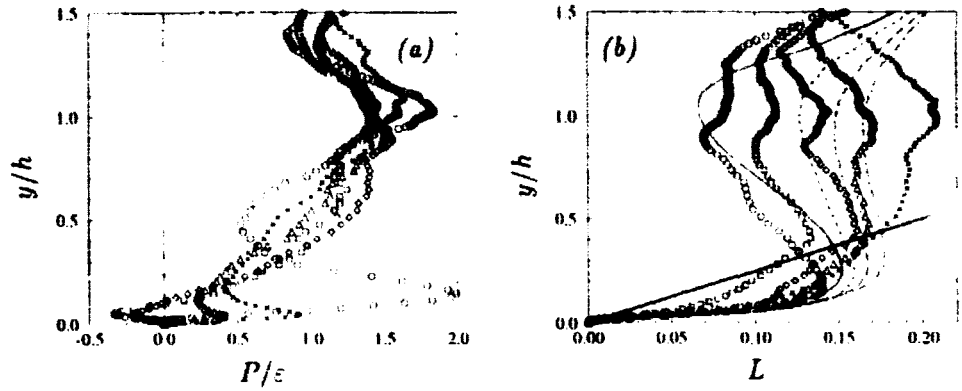

FIGURE 12. DNS profiles (a) Production over dissipation P/ε, legend cf. Fig.11a. (b) Turbulent length scale $L = 0.09^{3/4}k^{3/2}/\varepsilon$, at locations $x/h = 2$ (○ DNS, —— SMC), 4 (□ DNS, ····· SMC), 6 (◇ DNS, - - - - SMC), 8 (△ DNS, — — — SMC) and 10 (× DNS, — - — SMC), κy ——.

The production of dissipation is usually modeled as proportional to that of k, and negative values might lead here to unphysical effects.

5. Modeling dissipation

Several attempts were made to increase the pressure-strain in the shear layer, but all resulted in a (sometimes dramatic) shortening of the reattachment length, without amplifying the strength of the recirculation. Though the previous analysis indicates that this is a route to pursue, the following only reports some success in improving the dissipation equation.

An *a priori* test of the $k - \varepsilon$ equations was carried out by solving the coupled

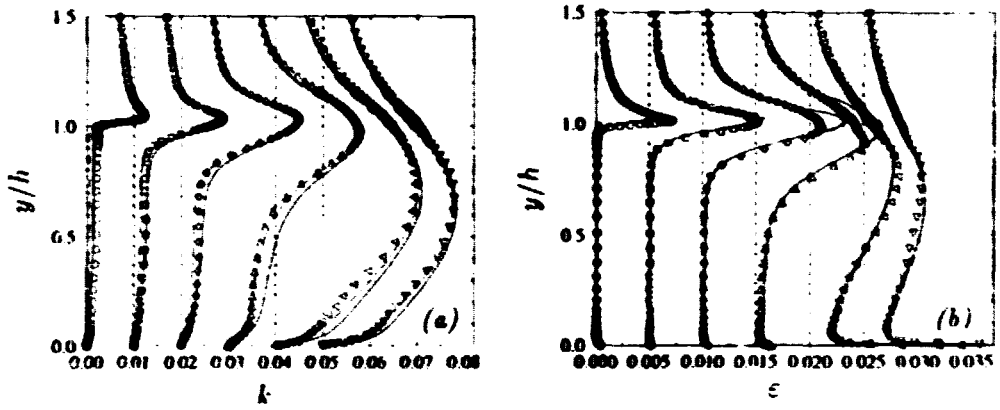

FIGURE 13. *A priori* test: (a) k, (b) ε, at locations $x/h = 0.1$ (○), 0.5 (□), 1 (◇), 2 (△), 4 (◁) and 6 (▽), ——— : model, — · — : modified model (ε equation).

$k-\varepsilon$ system with DNS data for $\overline{v'u'_j}$ and U. Dissipation is, of course, the exact source term for k, but k also has a strong relation to dissipation through the inverse timescale ε/k in front of its source term: this is why the equations were solved as a coupled system.

Figure 13 seems to indicate that k is overestimated and dissipation is correct in the coupled, differential test. In the recirculation bubble the effect of the source term in the ε equation is destruction of ε, since production is low. The 'modification' cited in the figure caption that is detailed below was intended to increase dissipation, but actually it leaves ε unchanged and decreases k, bringing it closer to the DNS. This is because when the source term coefficient in ε equation is decreased, the balance of the dissipation budget is re-established by a decrease of the time-scale, i.e. a decrease of k/ε, that occurs by k decreasing with little change of ε.

Tuning of the dissipation equation has been a popular game for the past two decades, so it needs to be shown that the present modification should not deteriorate predictions in other flows, and what the rationale is behind it.

Various procedures have been developed to enhance dissipation. In near wall flows below $y^+ = 10$, an extra viscous production term is usually included in low Re models. However, it is ineffective here because of the relatively high value of Re_t. Another dissipation enhancement is the 'Yap correction' (Launder 1989), which consists in a positive source term in the dissipation equation that is activated whenever the turbulent lengthscale L is larger than the mixing length κy. Though rather *ad hoc*, this 'Yap correction' has been particularly effective for backstep or sudden expansion flows (Hanjalic 1996), and shows that something peculiar is happening to the dissipation that is still not understood. Indeed Fig. 12 shows that L is overestimated in the recirculation bubble near the wall. Although the Yap correction goes in the right direction, there is no justification for forcing L to be smaller than κy since the DNS data shows it to be considerably larger than this.

Another way to increase the production of ε in the near-wall region is to use the non-dimensionalized parameter P/ε (Durbin 1993). This proved effective for

channel and boundary layer flow, but showed unfortunately high levels of numerical instability in more complex flows. Moreover, this does not suffice in the backflow region since P/ε is fairly small. Durbin and Laurence (1996) recently proposed to replace this unstable term by a ratio of k and $\overline{v^2}$ in the $k-\varepsilon-\overline{v^2}$ model: $C_{\varepsilon_1}(1+a_1\sqrt{k/\overline{v^2}})$ with $a_1 = 1/30$. In this study, we have generalized this idea in the full SMC by introducing the following: $C_{\varepsilon_1}(1+a_1\sqrt{P_{k-\varepsilon}/|P_{SMC}|})$ with $a_1 = 0.035$. $P_{k-\varepsilon} = 0.09kTS_{ij}S_{ji}$ and $P_{SMC} = \overline{u_i u_j}S_{ij}$ are respectively the $k-\varepsilon$ formula for production and the exact Reynolds-stress production. This correction has been found to have similar effects to P/ε in the near-wall region of channel flow, without any numerical instabilities in more complex situations. It does not cure the underestimation of the backflow in the present case; of course, that was not its intent.

Very little data is available concerning the dissipation equation budget aside from the channel flow DNS at CTR. From that data, the following adjustment to destruction of dissipation (which we called 'modified model') was devised: $C_{\varepsilon_2} = 1.83 * f(I_\varepsilon)$ with $I_\varepsilon = (P_\varepsilon + D_\varepsilon)/2D_\varepsilon$. This measures the weight of transport in the budget of ε by using the imbalance of production minus destruction. The function f varies from 1 (for shear flows) to 0.5 when production is zero. In order to preserve numerical stability, we combined this modification with the same adjustment for C_{ε_1} (multiplication by $f(I_\varepsilon)$). The following function f was chosen to avoid non-realistic coefficients: $f(x) = \max(\min(x,1),0.5)$. The result for the backstep as concerns the C_f profile was found to be modest (see Fig. 2), yet it is larger than any results obtained through modifications of the pressure strain model.

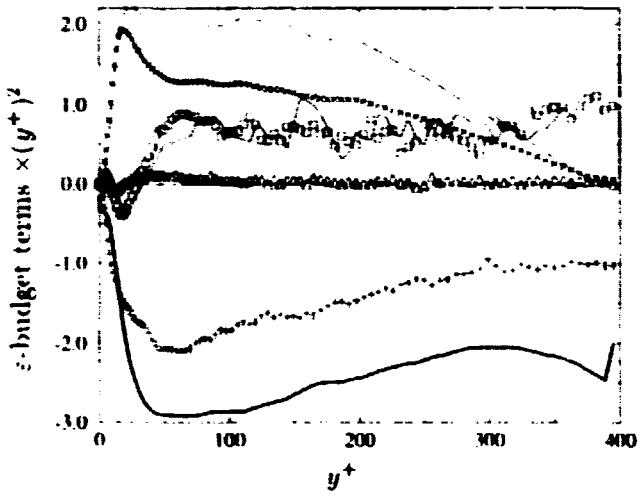

FIGURE 14. Budget of ε for the $Re_\tau = 395$ channel flow, all the terms have been multiplied by $(y^+)^2$. 'rapid part' ($\times$ $[P_1+P_2+P_3]$, – – – modelisation term: $[1.44P_k\varepsilon/k]$) 'slow part' ($+$ $[P_4-\Upsilon]$, —— modelisation term: $[-1.83\varepsilon^2/k]$), transport (□ DNS, —— modelisation term), viscous diffusion ($\triangle$), sum of the modelisation terms (· · · · ·).

The idea of re-adjusting C_{ε_2} actually came from the analysis of channel flow at $Re_\tau = 395$, for which the budgets of dissipation are available (Mansour & Kim, private communication). The near wall region has been analyzed in detail by Rodi & Mansour, but what interests us here is the central part of the channel. It is well known to modelers that dissipation is underestimated in the core region, but with little consequence except that the modeled L is continuously increasing instead of leveling off just outside of the log-layer. Since ε decreases as y^{-1} and the terms in its budget are as y^{-2}, all terms in this budget were multiplied by y^2 to produce Fig. 14.

The dissipation budget, as discussed by Mansour, Kim & Moin 1988, or by Mansour & Moin 1993, comprises a viscous transport term, negligible in the core region, a turbulent transport, very well modeled here by gradient diffusion with $\sigma_\varepsilon = 1.3$, and five source terms. It is known on fundamental grounds that these five terms cannot be clearly grouped into production and destruction terms. For the present, the terms involving gradients of velocity are grouped as $P_1 + P_2 + P_3$ and compared to the 'rapid' part of the model, ε/kP_k, while the remaining 'slow' terms are compared to ε^2/k. The DNS values of k and ε are used in the model terms, hence the jagged appearance of the model transport, due to double differentiation of this DNS data. It would seem from Fig. 14 that both constants C_{ε_1} and C_{ε_2} are severely overestimated; but again, the present split is arguable. It is, however, very clear that near the center of the channel, where the rapid terms go to zero, a value of $C_{\varepsilon_2} = 1.83$ is too large by a factor of 2. On the other hand, the transport is accurately modeled with the standard value $\sigma_\varepsilon = 1.3$.

6. Conclusion

A detailed comparison of a SMC computation with the DNS data for the backstep flow at $Re = 5{,}000$ leads to the following conclusions:

(1) The intensity of the backflow and the friction coefficient in the recirculation bubble are severely underestimated.

(2) The recirculation bubble is far from being pseudo-laminar; an understanding of the problems encountered by SMC should, thus, be of general interest.

(3) The SMC underestimates entrainment out of the recirculating bubble by the detaching shear layer. The mechanism is the following: pressure-strain ϕ_{22} generates normal fluctuations $\overline{v^2}$, which create the transverse mean velocity V; this in turn provides a momentum impulse to the bubble. In the shear layer, ϕ_{22}, $\overline{v^2}$, V are underestimated.

(4) A new *differential a priori* procedure was used, in which the full transport equations are solved one by one.

(5) A modification was proposed to enhance dissipation in, and only in, the recirculation bubble. The new formulation cured 25% of the backflow discrepancy.

(6) The model is supported by a significant finding from the DNS data in the core region of a channel flow: the constant related to destruction of dissipation, C_{ε_2}, should be decreased by a factor of 2 as production vanishes.

REFERENCES

DURBIN, P. 1993 A Reynolds-stress model for near-wall turbulence. *J. Fluid Mech.* **249**, 465-498.

DURBIN, P. A. & LAURENCE, D. 1996 Nonlocal effects in single point closure. *Turbulence Research Associates-96 meeting.* Seoul Korea.

HANJALIC, K. 1996 Some resolved and unresolved issues in modeling non-equilibrium and unsteady turbulent flows. *Engineering Turbulence Modeling and Measurements.* W. Rodi and G. Bergeles Eds., Elsevier Pub. **3**, 3-18.

JOVIC, S. & DRIVER, D. 1995 Reynolds number effect on the skin friction in separated flows behind a backward-facing step. *Experiments in Fluids.* **18.**

KANNICHE, M., LAURENCE, D., & WIZMAN, V. 1995 Combining a second moment closure with elliptic relaxation in rotating turbulent flows. *10th. Symp. on Turbulent Shear Flows, Penn State Pennsylvania.* **20-19.**

KASAGI, N. & MATSUNAGA, A. 1995 Three-dimensional particle-tracking velocimetry measurements of turbulence statistics and energy budget in a backward-facing step flow. *Int. J. Heat and Fluid Flow.* **16**, 477-485.

KO, S. & DURBIN, P. 1994 Separated turbulent flows computed with a near-wall Reynolds stress model. *ASME-FED Summer Meeting.* **196**, 83-92.

LAUNDER, B. E. 1989 Second-moment closure: present ... and future? *Int. J. Heat and Fluid Flow.* **10**, N. 4, 282-300.

LAURENCE, D., DURBIN, P. A. & DEMUREN, A. O. 1995 Modeling near wall effects in second moment closures by elliptic relaxation. *10th. Symp. on Turbulent Shear Flows, Penn State Pennsylvania.* **20-1.**

LE, H., MOIN, P. & KIM, J. 1993 Direct numerical simulation of turbulent flow over a backward-facing step. *Proc. 9th Symp. on Turbulent Shear Flows, Kyoto, Japan.* 13.2.1-13.2.6

MANSOUR, N. N., KIM, J. & MOIN, P. 1988 Reynolds stress and dissipation-rate budgets in a turbulent channel flow. *J. Fluid Mech.* **194**, 15-44.

RODI W. & MANSOUR, N. N. 1993 Low Reynolds number $k-\varepsilon$ modeling with the aid of direct simulation data. *J. Fluid Mech.* **250**, 509-529.

SPEZIALE, C. G., SARKAR, S. & GATSKI, T. B. 1991 Modeling the pressure-strain correlation of turbulence: an invariant dynamical systems approach. *J. Fluid Mech.* **227**, 245-272.

APPENDIX : Elliptic relaxation

The Reynolds stress transport equation is written as:

$$D_t\overline{u_iu_j} = P_{ij} + \varphi_{ij} - \overline{u_iu_j}\frac{\epsilon}{k} + T_{ij} + \nu\nabla^2\overline{u_iu_j} \tag{1}$$

with

$$\begin{aligned} P_{ij} &= -\overline{u_iu_k}\partial_k U_j - \overline{u_ju_k}\partial_k U_i \\ \varphi_{ij} &= -\overline{u_i\partial_j p} - \overline{u_j\partial_i p} - (\epsilon_{ij} - \overline{u_iu_j}\frac{\epsilon}{k}) + \frac{2}{3}\overline{u_k\partial_k p}\delta_{ij} \\ T_{ij} &= -\partial_k(\overline{u_ku_iu_j} + \frac{2}{3}\overline{u_kp}\delta_{ij}) \end{aligned} \tag{2}$$

The term φ_{ij} differs from the usual pressure-strain ϕ_{ij} since it includes a deviatoric dissipation tensor in the form

$$\varphi_{ij} = \phi_{ij} - \left(\epsilon_{ij} - \overline{u_iu_j}\frac{\epsilon}{k}\right) \tag{3}$$

The following *neutral* formulation for the elliptic relaxation is now obtained (Durbin and Laurence 1996):

$$\frac{\varphi_{ij}}{k} - L^2\nabla^2\frac{\varphi_{ij}}{k} = \frac{\varphi^h_{ij}}{k} \tag{4}$$

For homogeneous turbulence φ_{ij} ($\equiv kf_{ij}$) in Eq. 4 reduces to φ^h_{ij}, for which any standard redistribution model ϕ^h_{ij} can be used. The SSG rapid model is

$$\phi^h_{ij_{rapid}} = -C_2\mathrm{dev}(P_{ij}) - C_3\mathrm{dev}(D_{ij}) - C_skS_{ij} \tag{5}$$

The coefficients are:

$$C_2 = \frac{g_4 + g_5}{4};\ C_3 = \frac{g_4 - g_5}{4};$$
$$C_s = \frac{2}{3}g_4 - g_3 + \frac{g_3^*}{2}\sqrt{A_2}$$

The slow term is of the form

$$\phi^h_{ij_{slow}} = -[(C_1 + 1)a_{ij} + C_1'\mathrm{dev}(a_{ik}a_{kj})]\frac{k}{T} \tag{6}$$

$$C_1 + 1 = \frac{1}{2}\left[g_1 + g_1^*\frac{P}{\epsilon}\right],\ C_1' = -\frac{g_2}{4}$$

The dissipation equation is

$$D_t\epsilon = \frac{C_{\epsilon_1}'P - C_{\epsilon_2}\epsilon}{T} + \partial_k\left((\nu + \frac{C_\mu\overline{u_ku_l}T}{\sigma_\epsilon})\partial_l\epsilon\right) \tag{7}$$

The time scale, T, is defined as:

$$T = \sqrt{\frac{k^2}{\epsilon^2} + 36\frac{\nu}{\epsilon}} \tag{8}$$

The length scale L appearing in Eq. 4 also is prevented from going to zero at the wall by using the Kolmogorov scale as a lower bound:

$$L = C_L \sqrt{\frac{k^3}{\varepsilon^2} + C_\eta^2 \frac{\nu^{3/2}}{\varepsilon^{1/2}}} \tag{9}$$

Lastly, the Daly-Harlow expression for the turbulent diffusion is used:

$$T_{ij} = \partial_l \left(C_\mu \overline{u_l u_m} T \partial_m \overline{u_i u_j} \right) \tag{10}$$

The constants used in this report are:

$$C_\mu = 0.2, \sigma_\varepsilon = 1.5, C_L = 0.1, C_\eta = 200.$$

$$C_{\varepsilon_1} = 1.44, C_{\varepsilon_2} = 1.83$$

Also

$$\begin{aligned} &a_{ij} = \mathrm{dev}(\overline{u_i u_j})/k,\ A_2 = a_{ij} a_{ij}, \\ &A_3 = a_{ij} a_{jk} a_{ki},\ A = 1 - 9(A_2 - A_3)/8 \end{aligned} \tag{11}$$

was used in the text.

NEXT
DOCUMENT

On modeling pressure diffusion in non-homogeneous shear flows

By A. O. Demuren,[1] M. M. Rogers,[2] P. Durbin[3] AND S. K. Lele[3]

New models are proposed for the "slow" and "rapid" parts of the pressure diffusive transport based on the examination of DNS databases for plane mixing layers and wakes. The model for the "slow" part is non-local, but requires the distribution of the triple-velocity correlation as a local source. The latter can be computed accurately for the normal component from standard gradient diffusion models, but such models are inadequate for the cross component. More work is required to remedy this situation.

1. Introduction

In higher-order turbulence models 'pressure diffusion' is usually neglected, or at best added to 'turbulent diffusion' (Launder 1984) and the two modeled in aggregate. Pressure diffusion refers to the term $\partial_i \overline{u_j p}$ in the Reynolds stress budget; turbulent diffusion refers to $\partial_k \overline{u_i u_j u_k}$. The latter represents the ensemble averaged effect of random convection and can often be modeled as a diffusion process; the former, however, is harder to explain as diffusion. Turbulent diffusion is usually considered to be the dominant diffusion mechanism, and pressure diffusion is considered to be negligible. However, Lumley (1975a) showed that for homogeneous turbulence the application of symmetry and incompressibility constraints to the exact equation for the "slow" or non-linear part of the pressure diffusion led to the result that its magnitude is 20% that of the triple velocity correlation. In addition, it is of opposite sign, so that if turbulent diffusion could be modeled as a gradient transport, pressure diffusion would represent counter-gradient transport. Demuren *et al.* (1994) examined DNS databases for several shear flows, namely: the mixing layer simulation of Rogers and Moser (1994); the wake simulation of Moser *et al.* (1996); the boundary layer simulation of Spalart (1988); and the backward facing step simulation of Le *et al.* (1993). These confirm for the $\overline{q^2}$-equation that in simple shear regions pressure diffusion is roughly 20-30% of turbulent diffusion, and it appears to be mostly counter-gradient transport, so that it merely reduces the effect of turbulent diffusion, which is mostly gradient transport. Thus, the current practice of absorbing pressure diffusion and turbulent diffusion into a single model term appears reasonable, as far as the main shear regions are concerned. But the DNS data show that near the edges of the shear layers turbulent diffusion decreases

1 Old Dominion University
2 NASA Ames Research Center
3 Stanford University

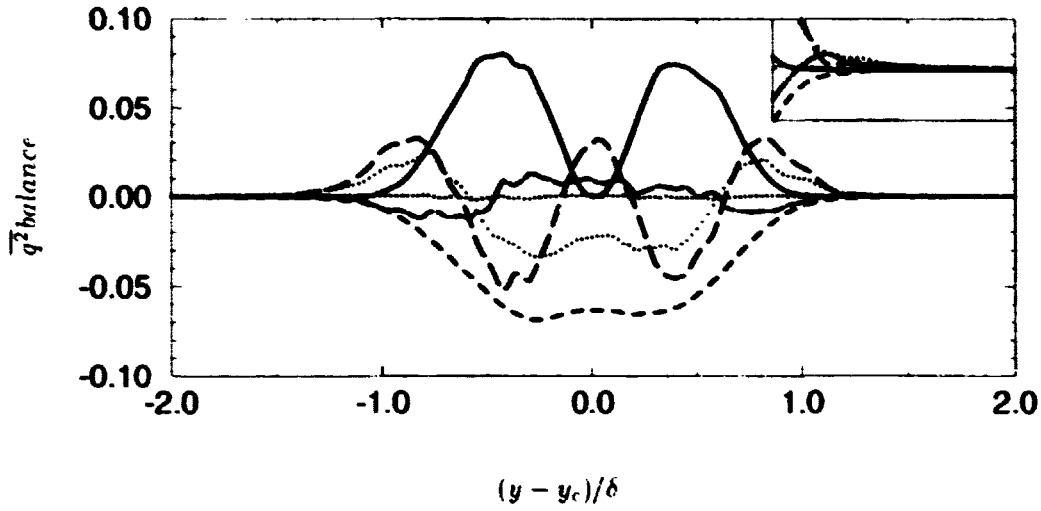

FIGURE 1. Reynolds stress budget of $\overline{q^2}$ from DNS of a plane wake:——— , production;— — — , turbulent diffusion;— · — , velocity-pressure gradient;····· , pressure diffusion;- - - - , viscous dissipation;× , viscous diffusion;+ , temporal drift. (Inset is a blowup of the vertical axis near the edge).

rapidly to zero, while pressure diffusion decreases only very gradually, so the latter then becomes dominant. Thus, the budgets show that near the free stream edge the balance is between pressure transport and mean convection, or temporal drift, rather than between turbulent transport and the latter. Further, where shear layer interactions occur, as near the middle of a wake, pressure diffusion no longer follows counter-gradient transport (see Fig. 1), and Lumley's model becomes inadequate. It in fact becomes additive very close to the center, leading to an overall increase in total transport, in contrast to the effect in the simple shear layers on either side. Both effects cannot be captured by a mere change in model coefficient. Therefore, in order to build a model for total diffusive transport in general shear flows one must look beyond the homogeneous model of Lumley. The pressure diffusion should also be modeled separately. Inhomogeneous effects can be introduced via a non-local model based on the elliptic relaxation concept of Durbin (1991, 1993) as implemented in the previous study of Demuren *et al.* (1994). The local model, required in this formulation, will be based on the "slow" or non-linear part of the pressure diffusion. A splitting of the pressure diffusion into "slow" and "rapid" parts is therefore necessary.

DNS databases for the mixing layer simulation of Rogers and Moser (1994) and the wake simulation of Moser *et al.* (1996) are post-processed to split the velocity-pressure gradient and pressure diffusion terms into "slow" and "rapid" parts. Separate models are then proposed for these terms.

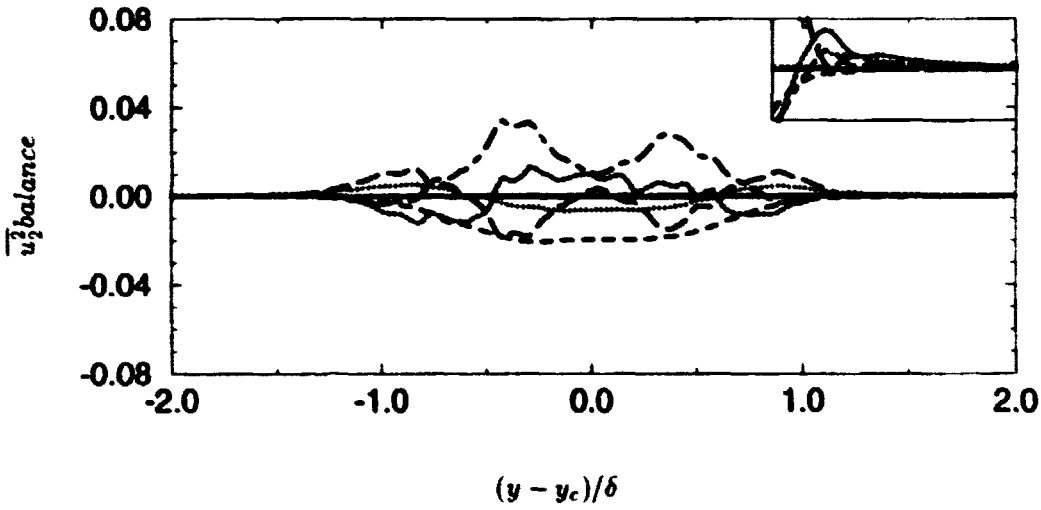

FIGURE 2. Reynolds stress budget of $\overline{u_2^2}$ from the DNS of plane wake. (See Fig. 1 for legend.)

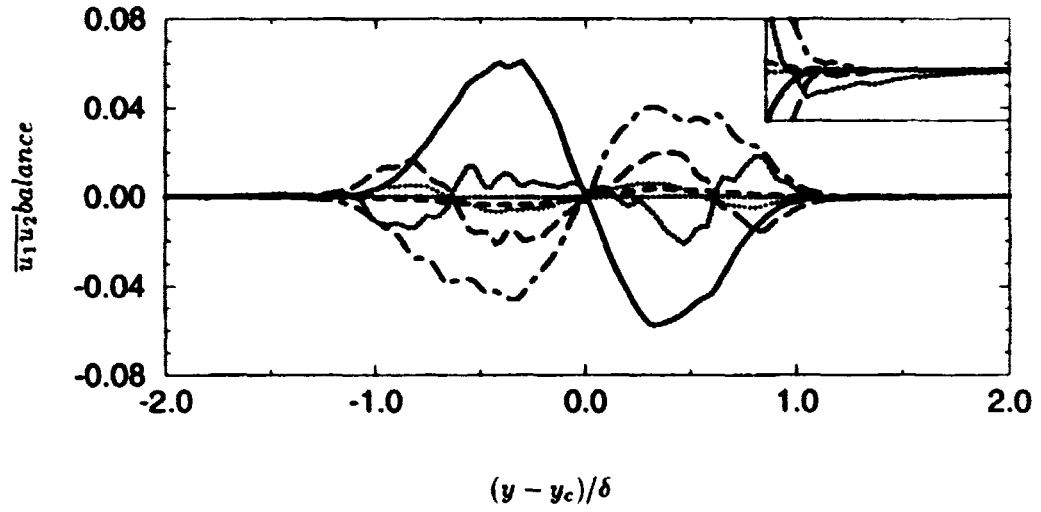

FIGURE 3. Reynolds stress budget of $\overline{u_1u_2}$ from the DNS of plane wake. (See Fig. 1 for legend.)

2. Governing equations

The Reynolds stress equations can be written for time-developing plane shear flows as:

$$D_t\overline{u_iu_j} = -(\overline{u_iu_k}\partial_k U_j + \overline{u_ju_k}\partial_k U_i) - \partial_k\overline{u_iu_ju_k} - (\overline{u_i\partial_j(p/\rho)} + \overline{u_j\partial_i(p/\rho)})$$
$$-2\nu\overline{\partial_k u_i\partial_k u_j} + \nu\nabla^2\overline{u_iu_j} \qquad (1)$$

(D_t represents the total derivative and ∂_k the partial derivative in the x_k coordinate.) Thus, the time-derivative is balanced by the production, turbulent transport, velocity-pressure gradient correlation, dissipation, and viscous diffusion, respectively. For the cases under consideration in this study, only normal (x_2) derivatives of turbulent statistics are non-zero. There is also only one non-zero mean-velocity gradient, $\partial_2 U_1$.

Budgets for the $\overline{u_2^2}$ normal component of the Reynolds stress and the shear stress $\overline{u_1u_2}$, obtained from the DNS database for the plane wake of Moser *et al.* (1996), are presented in Figs. 2 and 3, respectively. (In all these figures, y_c is the center-line, δ is the wake half-width, and δ_m is the mixing layer momentum thickness.) In both cases, turbulent and pressure transports are of comparable magnitude. Therefore, it would be inconsistent to model one and not the other. And, if one tries to model them together, then the comment in the introduction with respect to the $\overline{q^2}$-equation also applies to the $\overline{u_2^2}$-equation. On the other hand, in the $\overline{u_1u_2}$-equation, these terms virtually cancel each other out, except near the edges of the shear layers. Hence, it appears unlikely that a single composite model could reproduce all these features.

The velocity-pressure gradient correlation can be split into a pressure-strain correlation and a pressure diffusive transport as:

$$-(\overline{u_i\partial_j(p/\rho)} + \overline{u_j\partial_i(p/\rho)}) = \overline{(p/\rho)(\partial_j u_i + \partial_i u_j)} - (1/\rho)(\delta_{j2}\partial_2\overline{pu_i} + \delta_{j2}\partial_2\overline{pu_j}) \qquad (2)$$

Further, each of these terms can be split into "slow" and "rapid" parts by splitting the pressure p, used in the correlations, into p_s and p_r, respectively. In the present study, p_s and p_r are obtained from solution of the equations:

$$\nabla^2 p_s = -\partial_q u_p\partial_p u_q + \partial_{22}\overline{u_2^2}$$
$$\nabla^2 p_r = -2\partial_2 U_1\partial_1 u_2 \qquad (3)$$

Figure 4 shows results of the splittings of the velocity-pressure gradient correlations into "slow" and "rapid" parts for the four non-zero components of the Reynolds stresses. We note that for the diagonal components all energy is produced in the streamwise component $\overline{u_1^2}$ and then transferred to the normal $\overline{u_2^2}$ and transverse $\overline{u_3^2}$ components via pressure scrambling. The transfer mechanism appears to be quite different for these components; transfer to the normal component is solely

through the "slow" part, and transfer to the transverse component is through the "rapid" part. It is conjectured that some structural mechanism must be responsible for these, though it could not be identified from the analyzed data. However, these results agree quite well with those for the homogeneous shear flow simulation of Rogers *et al.* (1986). On the other hand, the shear stress results do not agree. Whereas the present results for wakes and mixing layers (not shown) show the velocity-pressure gradient correlation to be mostly in the "rapid" part, the homogeneous shear flow results showed nearly equal distribution between the "slow" and "rapid" parts. Figure 5 shows results of the splittings of the pressure diffusive transport the $\overline{u_2^2}$ and $\overline{u_1 u_2}$ components, all others being zero. In both cases, "slow" and "rapid " parts are comparable, and are mostly of opposite sign. Hence, they are, in general, larger in magnitude than the sum. Further, the "slow" part appears to represent counter-gradient transport, and the "rapid" part gradient transport, i.e., more like turbulent diffusion.

3. Proposed transport models

It is proposed to model the transport terms in the Reynolds stress equations in three parts, namely, turbulent diffusion, "slow" pressure diffusion, and "rapid" pressure diffusion.

3.1 Turbulent diffusion model

Turbulent diffusive transport (TDIFF) is modeled following the proposal of Mellor and Herring (1973), (hereafter denoted MH) as:

$$TDIFF_{\overline{u_i u_j}} = -[\overline{u_i u_j u_k}]_{,k} = c_3[(k^3/\varepsilon)[(\overline{u_j u_k})_{,i} + (\overline{u_k u_i})_{,j} + (\overline{u_i u_j})_{,k}]]_{,k} \quad (4)$$

("$,_k$" represents derivative with respect to x_k.) This model is derived from the isotropization of coefficients in the more complex Hanjalic and Launder(1972) diffusion model. It does preserve the symmetry of the indices in the triple-velocity correlation. It was found by Demuren and Sarkar (1993) to yield the correct anisotropy of the Reynolds stress in the wake region of channel flows, and a variant by Mellor and Yamada (1986) is widely used in geophysical flows. The model will also be used to calculate triple-velocity correlations which are required for the modeling of "slow" pressure diffusion in the next section.

3.2 "Slow" pressure diffusion model

The "slow" part of the pressure transport (SPDIFF) is modeled using a non-local elliptic relaxation approach as:

$$SPDIFF_{\overline{u_i u_j}} = -[\delta_{jk}\overline{p_s u_i} + \delta_{ik}\overline{p_s u_j}]_{,k} = [\delta_{jk} f_i + \delta_{ik} f_j]_{,k} \quad (5)$$

where

$$L^2 \partial_2^2 f_i - f_i = -f_i^L \quad (6)$$

The local source term f^L is given by Lumley's (1975a) model as:

$$f_i^L = \overline{p_s u_i}^L = -0.2\overline{q^2 u_i} \quad (7)$$

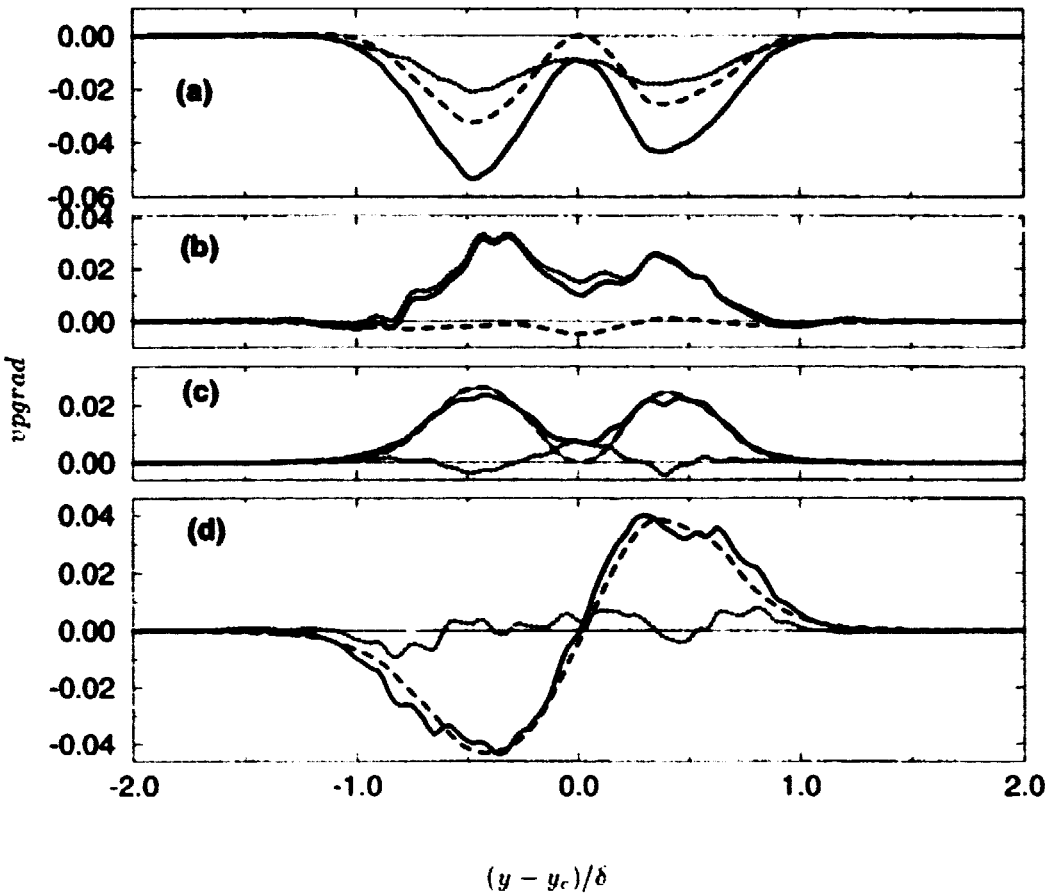

FIGURE 4. Separation of velocity-pressure gradient correlation into "slow" and "rapid" parts, from DNS data for plane wake, (a)$\overline{u_1^2}$, (b)$\overline{u_2^2}$, (c)$\overline{u_3^3}$, (d)$\overline{u_1 u_2}$:——— , total;····· , "slow";- - - - , "rapid".

It is assumed that the same length scale which governs the non-locality in the pressure redistribution would also govern the non-locality in the pressure transport. For the $\overline{u_1 u_2}$ and $\overline{u_2^2}$ equations, respectively, $\overline{q^2 u_1}$ and $\overline{q^2 u_2}$ are obtained from the MH model. This treatment represents a generalization of the previous study by Demuren *et al.* (1994) in which the $k - \varepsilon$ turbulence model was used.

The principal effect of the non-local model is to "elliptically" spread the influence of the local source over the length scale L. Figures 6 and 7 present comparisons of the pressure diffusion, based on the local model, to DNS data for mixing layer. In each case, two model computations are made; one assumes that the triple-velocity correlations are known from DNS, and the other computes them from the MH model. For $\overline{u_2^2}$, shown in Fig. 6, both computations yield similar results, with peaks that are somewhat higher than in the DNS. Hence, full application of the non-local model

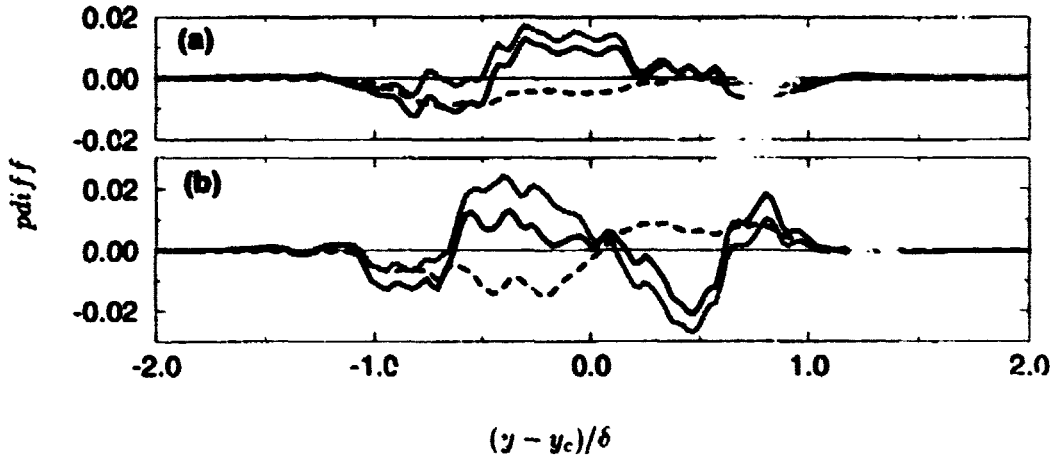

FIGURE 5. Separation of pressure diffusion into slow and rapid parts: DNS data for plane wake, (a)$\overline{u_2^2}$, (b)$\overline{u_1 u_2}$. (See Fig. 4 for legend.)

would produce quite good agreement. For $\overline{u_1 u_2}$, shown in Fig. 7, only the first approach, which assumes a pre-knowledge of the triple-velocity correlation, gives results in agreement with DNS. The MH model grossly underpredicts the $\overline{q^2 u_1}$, and hence its derivative. This appears to be a general flaw of gradient-diffusion models for the triple-velocity correlation. They are usually calibrated to reproduce the normal component of the turbulent diffusion in simple shear flows. They fail to reproduce other components, if these are present, as in the 3D boundary layer study of Schwarz and Bradshaw (1994) or the shearless mixing layer study of Briggs *et al.* (1996). This problem will have to be addressed before a reliable, self-contained model for the pressure diffusion of $\overline{u_i u_2}$ can be produced.

3.° *"Rapid" pressure diffusion model*

The "rapid" part of the pressure transport (RPDIFF) is modeled in terms of the Reynolds stresses and mean velocity gradients. The simplest such model has the form:

$$RPDIFF_{\overline{u_i u_j}} = -[\delta_{jk}\overline{p_r u_i} + \delta_{ik}\overline{p_r u_j}]_{,k} = [\delta_{jk} g_i + \delta_{ik} g_j]_{,k} \tag{8}$$

where

$$g_{i,k} = c_r \overline{u_i u_l} U_{l,k} \tag{9}$$

Equation (8) is similar in form to the "rapid" part of some pressure-strain models. This is consistent with the suggestion of Lumley (1975b) that the traditional separation of velocity-pressure gradient correlation into a pressure-strain correlation and a pressure transport is not unique. Preliminary tests show that c_r should have a value between 0.1 and 0.3. It has been suggested that this part should also be modeled with non-local effects, consistent with the modeling of the slow part

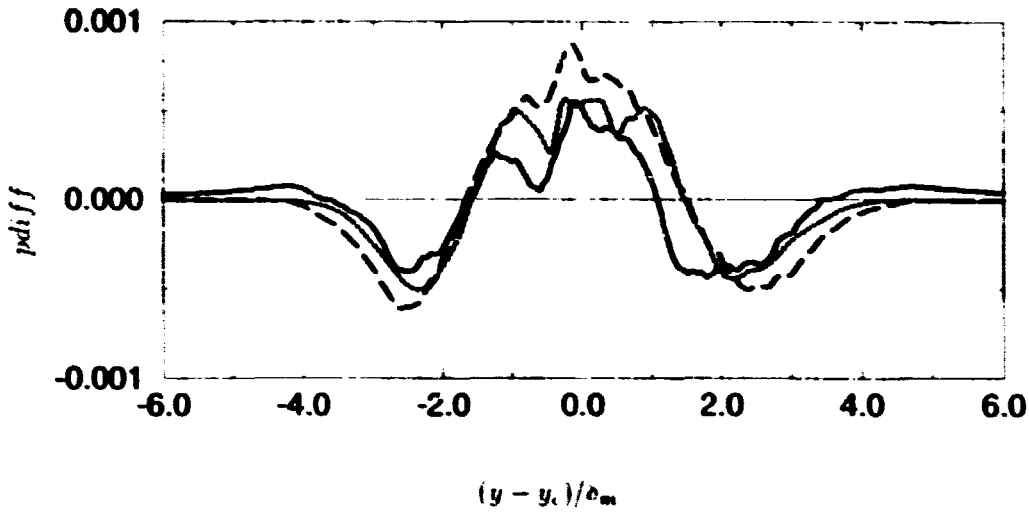

FIGURE 6. Model predictions of pressure diffusion of $\overline{u_2^2}$ in the plane mixing layer: ——, DNS; – – –, model with triple-correlations from DNS; · · · · ·, model with triple-correlations from MH.

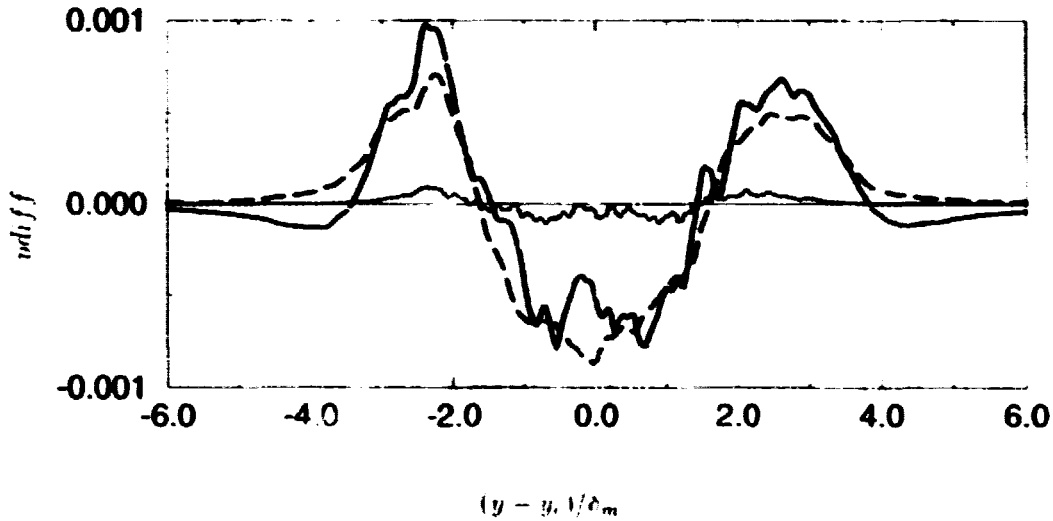

FIGURE 7. Model predictions of pressure diffusion of $\overline{u_1 u_2}$ in the plane mixing layer. (See Fig. 6 for legend.)

and the pressure-strain correlation, but evidence for such behavior could not be discerned from the DNS data. Further testing is desirable.

4. Conclusions

The "slow" and "rapid" parts of the velocity-pressure gradient correlations and the pressure transport have been calculated from DNS databases of plane mixing layers and wakes. These show that, in agreement with homogeneous shear flow simulation, the mechanism for the transfer of energy from the streamwise component of the Reynolds stress to the normal component is via the "slow" part, whereas for the transverse component it is through the "rapid" part. But pressure transport is distributed significantly into both "slow" and "rapid" parts, the former being mostly counter-gradient transport, and the latter closer to gradient transport. Models are proposed for both parts, which show qualitative agreement with DNS data for the normal component of the Reynolds stress but have shortcomings when applied to the Reynolds shear stress. The main flaw is the inability of gradient diffusion models to predict other than the normal component of the triple-velocity correlation for which they have been calibrated. Further development and testing is required.

REFERENCES

BRIGGS, D. A., FERZIGER, J. H., KOSEFF, J. R., & MONISMITH, S. G. 1996 Entrainment in a shear-free turbulent mixing layer. *J. Fluid Mech.* **310,** 215-241.

DEMUREN, A. O., LELE, S., & DURBIN, P. 1994 Role of pressure diffusion in non-homogeneous shear flows. *Proc. CTR Summer Prog.* Center for Turbulence Research, NASA Ames/Stanford Univ.

DEMUREN, A. O., & SARKAR, S. 1993 Perspective: Systematic study of Reynolds stress closure models in computations of plane channel flows. *J. Fluid Engr.* **115,** 5-12.

DURBIN, P. 1991 Near-wall turbulence closure modeling without 'damping functions'. *Theoret. Comput. Fluid Dynamics.* **3,** 1-13.

DURBIN, P. 1993 A Reynolds stress model for near-wall turbulence. *J. Fluid Mech.* **249,** 465-498.

HANJALIC, K., & LAUNDER, B. E. 1972 A Reynolds stress model of turbulence and its applications to thin shear flows. *J. Fluid Mech.* **52,** 609-638.

LE, H., MOIN, P., & KIM, J. 1993 Direct numerical simulation of turbulent flow over a backward-facing step. *Rep. TF-58,* Thermosciences Division, Department of Mechanical Engineering, Stanford University.

LAUNDER, B. E. 1984 Second-moment closure: methodology and practice. In *Turbulence Models and Their Applications,* (Editions Eyrolles, Paris).

LUMLEY, J. L. 1975a Prediction methods for turbulent flows - Introduction. *Lecture Series 76.* von Karman Inst., Rhodes St. Genese, Belgium.

LUMLEY, J. L. 1975b Pressure-strain correlation. *Phys. Fluids.* **18**, 750.

MELLOR, G. L., & HERRING, H. J. 1973 A survey of mean turbulent field closure. *AIAA J.* **11**, 590-599.

MELLOR, G. L., & YAMADA, T. 1986 Development of a turbulence closure model for geophysical fluid problems. *Rev. Geophys. Space Phys.* **20**, 851-875.

MOSER, R. D., ROGERS, M. M., & EWING, D. W. 1996 Self-similarity of time-evolving plane wakes. (Submitted).

ROGERS, M. M.,& MOSER, R. D. 1994 Direct simulation of a self-similar turbulent mixing layer. *Phys. Fluids.* **6**, 903-923.

ROGERS, M. M., MOIN, P., & REYNOLDS, W. C. 1986 The structure and modeling of the hydrodynamic and passive scalar fields in homogeneous turbulent shear flow. *Rep. TF-25*, Thermosciences Division, Department of Mechanical Engineering, Stanford University.

SCHWARZ, W. R., & BRADSHAW, P. 1994 Term-by-term tests of stress-transport turbulence models in a three-dimensional boundary layer. *Phys. Fluids.* **6**, 986-998.

SPALART, P. R. 1988 Direct simulation of a turbulent boundary layer up to R_θ = 1410. *J. Fluid Mech.* **187**, 61-98.

NEXT
DOCUMENT

Prediction of the backflow and recovery regions in the backward facing step at various Reynolds numbers

By V. Michelassi[1], P. A. Durbin[2] AND N. N. Mansour[3]

A four-equation model of turbulence is applied to the numerical simulation of flows with massive separation induced by a sudden expansion. The model constants are a function of the flow parameters, and two different formulations for these functions are tested. The results are compared with experimental data for a high Reynolds-number case and with experimental and DNS data for a low Reynolds-number case. The computations prove that the recovery region downstream of the massive separation is properly modeled only for the high Re case. The problems in this case stem from the gradient diffusion hypothesis, which underestimates the turbulent diffusion.

1. Introduction

The Reynolds Averaged Navier Stokes equations (RANS) equations need a turbulence model for computation of Reynolds stresses that stem from averaging the non linear convective terms. A large family of turbulence models exists in the literature. The models range from simple algebraic expressions for the eddy viscosity to more elaborate formulations which introduce a separate transport equation for each component of the Reynolds Stress tensor. Eddy viscosity models such as the $k-\epsilon$ model still represent a good compromise between accuracy and computational efficiency and will be the subject of this investigation. Moreover, the results of a recent workshop (Rodi *et al.*, 1995) showed that, even though full Reynolds stress models bring more *physics* into the model, the large increment in the computational effort associated with these models is not always followed by a proportional improvement in the quality of the predictions.

Two-equation models of turbulence have been recently tuned with the aid of Direct Numerical Simulation (DNS) data (see *e.g.* Michelassi and Shih, 1991, Rodi *et al.*, 1993). This tuning was mostly done to allow modeling of the near wall region and to reproduce the profiles of the turbulent kinetic energy, k, and of the dissipation rate ϵ in this critical flow region. The tuning was done by using fully developed or turbulent boundary layer flows (Rodi and Mansour, 1990). Most of the so called "low Reynolds number modifications" (LR) to the two-equation models of

1 University of Florence Energetics Department, Italy
2 Stanford University
3 NASA Ames Research Center

turbulence were able to improve the model capability in the flow layer close to the wall. Nevertheless, little or no change at all was found in the core region of the flow since most of the modifications were designed to vanish away from solid boundaries (Zhu and Shih, 1993).

The *LR* models, which allow the integration of the equations in the near wall region, can successfully model a wide range of flows, but often do not allow flows with strong adverse pressure gradients and/or separation to be computed accurately. This seems to be a general problem associated with the two-equation formulation irrespective of the treatment of the near-wall region (Michelassi, 1993). In the backward facing step flow, both an adverse pressure gradient and flow separation are to be modeled, which makes this test case particularly challenging.

Durbin (1995) computed the backward facing step flow at different Reynolds numbers. His computations proved that downstream of the reattachment point the computed velocity profiles tend too slowly to a boundary layer profile for the high Reynolds number case, but not for the low Reynolds number case. A similar failure was encountered by Rodi (1991) with a two-layer model of turbulence. Again, the velocity profiles in the recovery region tend too slowly to a developed profile. Durbin and Rodi use forms of the two-equation $k-\epsilon$ model which, while based on the Boussinesq assumption, have very little in common with the treatment. This indicates that the problems are stemming from the $k-\epsilon$ frame and not from the wall treatment.

This phenomenon is also of great importance in practical flows with engineering relevance such as the flow in turbomachines. In fact, immediately downstream of the trailing edge of a turbine or a compressor blade, two counterrotating vortices interact with the wake in a very similar manner to that found for the backward facing step. The modeling of the wake downstream of the two vortices is of primary importance in turbomachinery flows because of its impact on the stator-rotor interaction. In this case, the computed wake decay, which is similar to the flow recovery region in the backward facing step, seems to be too slow compared to the measurements as indicated by a number of computations for subsonic and transonic turbines (Michelassi *et al.* 1995). These results were shown to be true regardless of the assumption of a fully turbulent or transitional boundary layer along the blade profile. In the turbomachinery flow case, it is not clear if the discrepancies are due to the inherently unsteady nature of the experimental flow field, or to deficiencies in the model as in the backward facing step where the steadiness of the flow is not an issue.

Although the *recovery region problem* with computing the backstep has been often pointed out, very little has been done so far to identify the causes of the slow recovery downstream of the reattachment point. Two-equation models are known to have theoretical limitations which stem mainly from the eddy viscosity assumption. Still, the ability of these simple turbulence models to mimic a flow with massive separation and the wake decay needs to be improved.

With this in mind three different backward facing step data sets are used to compare with the computations and to identify the reasons for the discrepancies

between computations and measurements in the recovery region.

2. The turbulence model

The turbulence model uses the standard $k-\varepsilon$ equations:

$$\partial_t k + U \cdot \nabla k = P_k - \varepsilon + [(\nu + \frac{\nu_t}{\sigma_k})\nabla k]. \tag{1}$$

$$\partial_t \varepsilon + U \cdot \nabla \varepsilon = \frac{C_{\varepsilon 1} P_k - C_{\varepsilon 2}\varepsilon}{T} + [(\nu + \frac{\nu_t}{\sigma_\varepsilon})\nabla \varepsilon]. \tag{2}$$

The model constant $C_{\varepsilon 1}$ is computed as:

$$C_{\varepsilon 1} = 1.3 + \frac{0.25}{(1 + (d/2L)^2)^4}. \tag{3}$$

in which d is the minimum distance from the wall, and L is the turbulence length scale. On no-slip boundaries, $y \to 0$.

$$k = 0,\ \epsilon \to 2\nu \frac{k}{y^2}.$$

Two additional equations are solved. The first transport equation determines the velocity fluctuation normal to the wall, $\overline{v^2}$. The $\overline{v^2}$ transport equation is

$$\partial_t \overline{v^2} + U \cdot \nabla \overline{v^2} = kf - \overline{v^2}\frac{\varepsilon}{k} + \nabla \cdot [(\nu + \nu_t)\nabla \overline{v^2}]. \tag{4}$$

where kf represents redistribution of turbulence energy from the streamwise component. Non-locality is represented by solving an elliptic relaxation equation for f:

$$L^2 \nabla^2 f - f = \frac{C_1 - 1}{T}\left[\frac{\overline{v^2}}{k} - \frac{2}{3}\right] - C_2 \frac{P_k}{k}. \tag{5}$$

in which

$$T = \max\left[\frac{k}{\varepsilon}, 6(\frac{\nu}{\varepsilon})^{1/2}\right],\ L = C_L \max\left[\frac{k^{3/2}}{\varepsilon}, C_\eta (\frac{\nu^3}{\varepsilon})^{1/4}\right]. \tag{6}$$

The Boussinesq approximation is used for the stress-strain relation:

$$a_{ij} = \frac{\overline{u_i u_j}}{k} - \frac{2}{3}\delta_{ij} = -\frac{\nu_t}{k} S_{ij},$$

where the eddy viscosity is given by

$$\nu_t = C_\mu \overline{v^2} T.$$

The constants of the model are:

$$C_\mu = 0.19,\ \sigma_k = 1,\ \sigma_\epsilon = 1.3, C_{\epsilon 1} = 1.55,\ C_{\epsilon 2} = 1.9$$

$$C_1 = 1.4,\ C_2 = 0.3,\ C_L = 0.3,\ C_\eta = 70. \tag{7}$$

The boundary conditions are

$$\overline{v^2} = 0,\ f(0) \to -\frac{20\nu^2\overline{v^2}}{\epsilon(0)y^4}.$$

on no-slip walls.

The original model formulation was modified by Durbin and Laurence (1996) in the expressions for the length and time scales, L and T, and the definition of the model constant $C_{\epsilon 1}$. The length and time scales are now computed to allow a smoother switch from the core-flow values to the near-wall values as follows:

$$L^2 = C_p^2\left(k^3/\epsilon^2 + C_\eta^2\nu^{3/2}/\epsilon^{1/2}\right),\ T^2 = k^2/\epsilon^2 + C_T^2\nu/\epsilon \tag{8}$$

The selected values of the constants are $C_p = 0.2$, $C_\eta = 70$, and $C_T = 6$.

In Eq. (3) the scaling of $C_{\epsilon 1}$ in the near wall region is done by using the wall distance y. The definition of the wall distance can be problematic in complex flows so that Durbin and Laurence (1996) replaced Eq. (3) with another expression based on $\overline{v^2}$ which is suited to feel the proximity of the wall:

$$C_{\epsilon 1} = 1.44\left(1 + 1/30(k/\overline{v^2})^{1/2}\right). \tag{9}$$

This expression, like the one in Eq. (3), is supposed to increase the production of dissipation in the near wall region, where $\overline{v^2}$ goes to zero faster than k. Both the original formulation, hereafter referred as form (1) of the model, and the modified formulation, hereafter referred as form (2), have been applied with the same inlet and boundary conditions.

3. The data sets and the computations

The turbulence model with the two different forms described in the previous section was applied to the computation of three different backward-facing step geometries and different Reynolds numbers.

The first experimental data set considered here is that of Driver and Seegmiller (*DS*) (1985) which allowed testing the model in a high Reynolds-number configuration with a Reynolds number based on the step height of 37.500. Measurements were taken by using laser velocimetry and include mean and instantaneous quantities and triple correlations.

The low Reynolds-number case refers to the measurements by Kasagi and Matsunaga (*KM*) (1995). In this case the flow Reynolds number, based again on the

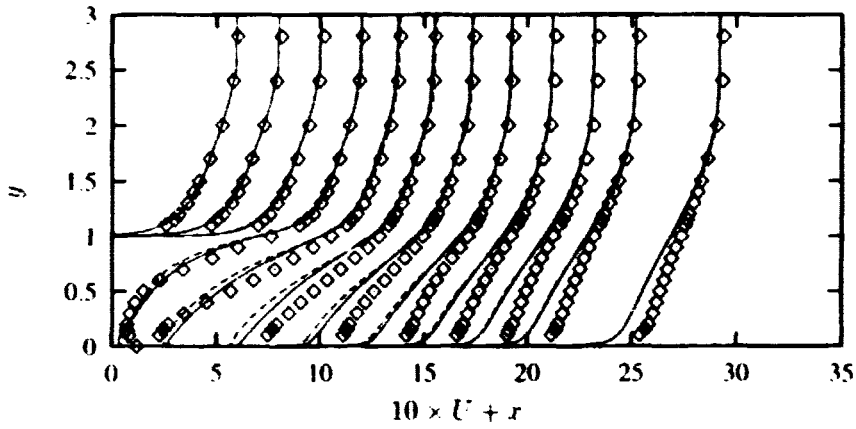

FIGURE 1. *DS* Velocity profiles. ◇ experiments. —— model version (1). – – – model version (2).

step height, is 5540. Measurements were taken by using a particle image velocimetry method (PIV) which allowed measuring instantaneous and average quantities. The measured profiles were also carefully tested to verify mass conservation. A similar Reynolds number (Re = 5100) was achieved by Le and Moin (LM) (1994) which produced a DNS data set for the backward facing step geometry. The large amount of information on the flow field makes this DNS data set very valuable for testing and developing two-equation models of turbulence.

The investigation is carried out on three different data sets to test the model under different Reynolds number conditions. At the present stage of research it is still impossible to perform the DNS of a backward facing step at high Reynolds number, so the use of an experimental data set was compulsory. The two data sets for the low Reynolds number case were selected to verify that model testing done by using a classical experimental data set could be extended to the DNS data for such a flow field.

The computational gr for the three test cases have 120 × 120 grid nodes clustered near solid walls inlet section profiles have been carefully specified as follows. For the *DS* case the inlet profiles have been computed by a boundary layer code until the momentum thickness of 5000 was reached (Durbin, 1995). These profiles were then imposed at the inlet sectior of the computational domain. For the *KM* case the inlet profiles were those of a fully developed channel flow, as indicated by Kasagi and Matsunaga (1995) in their discussion of the flow nature upstream of the separation point. For the test case proposed by Le and Moin, the inlet profiles were those computed by the DNS at the section upstream of the separation point corresponding to the inlet section of the present computational grid. No other grids were used for the calculations since the 120 × 120 grid was already found adequate for this kind of computation by Durbin (1995).

The first set of computations refer to the *DS* case. Fig. 1 compares the measured profiles with those computed by using the two versions of the model. In all the

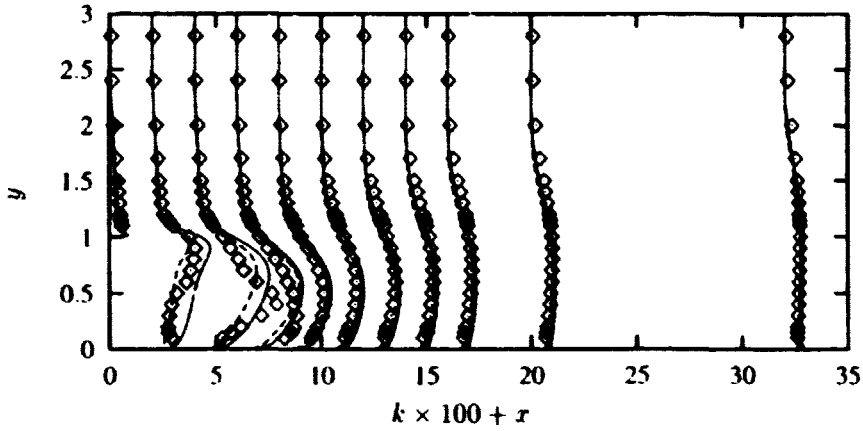

FIGURE 2. *DS* Turbulent kinetic energy profiles. Symbols as in Fig. 1.

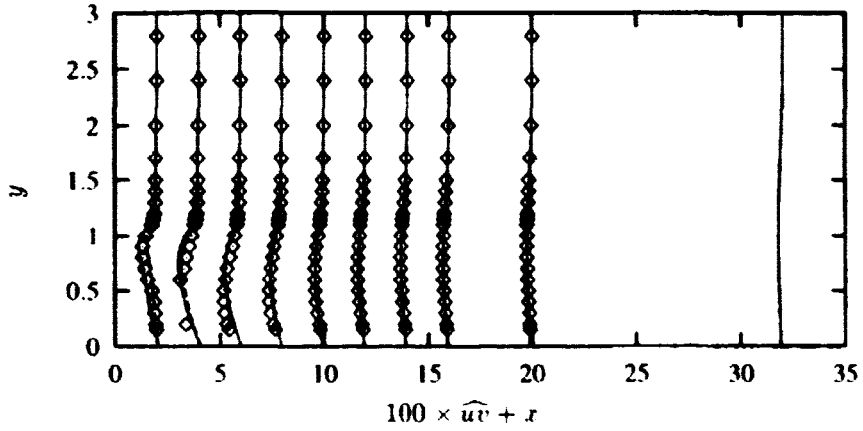

FIGURE 3. *DS* Turbulent shear stress profiles. Symbols as in Fig. 1.

following plots the ordinate $y = 1$ corresponds to the step corner. The reattachment point is not affected by the change in the model, but the different functions adopted for the computation of the length scale L, the time scale T, and the coefficient of the production rate of dissipation $C_{\epsilon 1}$ show some effect in the backflow region. Here version (2) of the model moves the computed profiles closer to experiments. A sensitivity analysis made by changing the coefficients in Eqs. (8,9) proved that the model is sensitive to the value of C_p, which was set equal to 0.2. The model can be seen to predict velocity profiles which are steeper than the measured ones in the backflow region. Moreover, in the recovery region the computations lag behind the experimental boundary layer profile. The agreement is indeed quite good in terms of turbulent kinetic energy (see Fig. 2) and turbulent shear stress (see Fig. 3). Apparently, the models succeed in reproducing the correct level of turbulent kinetic energy and shear stress with the only exception of a narrow region deep inside of the backflow, where the maximum of turbulent kinetic energy and turbulent shear stress are not correctly predicted and somewhat misplaced.

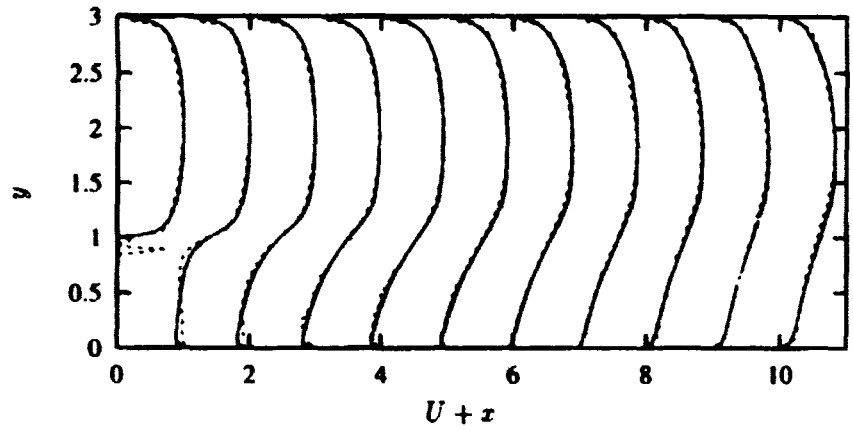

FIGURE 4. *KM* Velocity profiles. ---- experiments, —— model version (1), – – – model version (2).

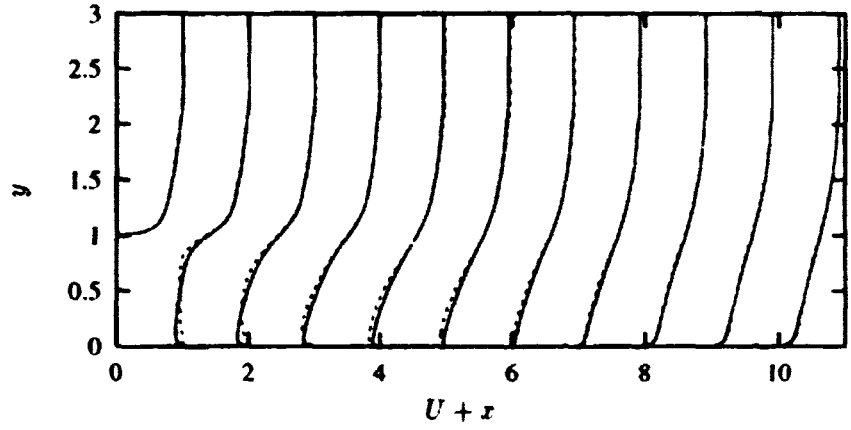

FIGURE 5. *LM* Velocity profiles. Symbols as in Fig. 4.

When moving to the *KM* and *LM* test cases, a more careful analysis is possible due to the large number of measurements. Figure 4 compares the measured and computed velocity profiles in several stations starting from the separation point for the *KM* test case. The agreement is again quite good, and apparently the two versions of the model give almost identical results in this case. The recovery region is well predicted here. Again, the backflow region shows the steep velocity profiles predicted in the high Reynolds number case, while the experiments show a profile which seems to indicate quite a low turbulence level. Figure 5 shows the same velocity profiles for the *LM* test case. In this last computation the recirculation bubble length was underestimated by approximately 4%. The backflow region length was computed in almost perfect agreement with the experiments for the *KM* case. The plots also show that the differences in the computation of the length and time scales in the two versions of the code bring very little change to the computed profiles, which are almost collapsing on each other, in the low *Re* case.

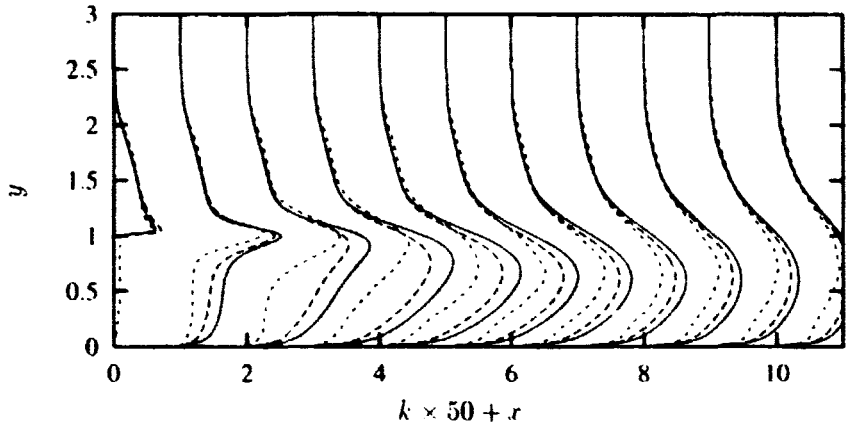

FIGURE 6. *LM* Turbulent kinetic energy profiles. Symbols as in Fig. 4.

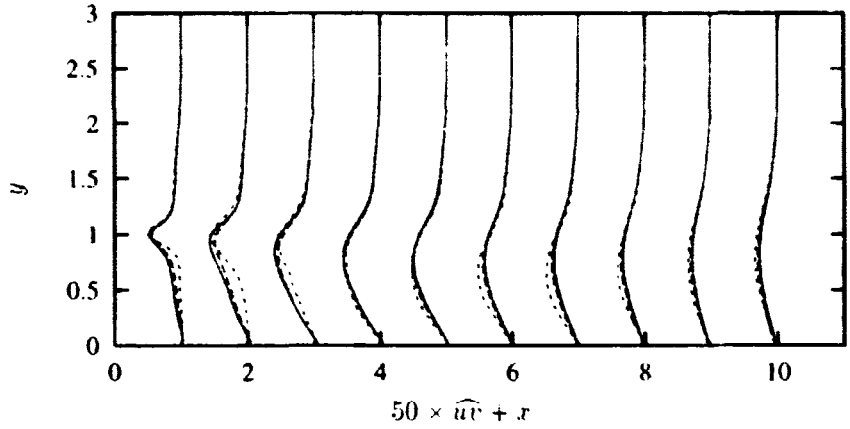

FIGURE 7. *LM* Turbulent shear stress profiles. Symbols as in Fig. 4.

Figures 4 and 5 show that there is very little difference between the *LM* and *KM* data sets. Since the information given by the *KM* and *LM* cases do not show significant differences, only the latter will be described in detail in what follows.

Figure 6 compares the measured and computed turbulent kinetic energy profiles at several stations starting from the separation point. The agreement between computations is generally satisfactory, even though the models overpredict the turbulent kinetic energy in the backflow region. Of the two, version (2) of the model seems to reduce the overprediction. This was also found in the high Reynolds number case. This overprediction spreads in the shear layer as the flow proceeds downstream.

The overprediction of k seems to have an effect in terms of turbulent shear stress also, as shown in Fig. 7. Here the turbulent shear stress is overestimated by both the formulations in the backflow region and underestimated in the recovery region. The change from overestimation to underestimation takes place gradually across the reattachment point and the fit between DNS and computations improves only far downstream.

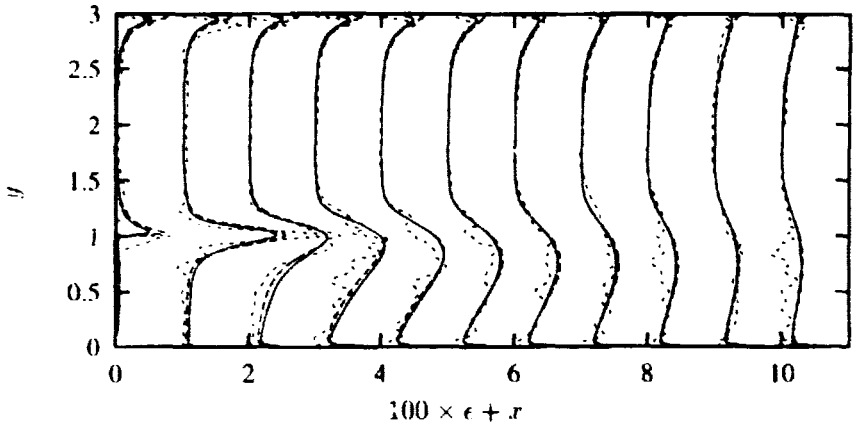

FIGURE 8. *LM* Dissipation rate profiles. Symbols as in Fig. 4.

The *LM* data set also includes the dissipation rate. Figure 8 shows that the computed dissipation rate level is larger than that given by the DNS in the backflow region. The ϵ levels are well predicted in the recovery region.

The skin friction coefficients in Figs. 9 and 10 show that version (2) of the model tends to reduce the recirculation bubble length in the low-Re number case (a similar trend was also found for the *KM* test), whereas the same model seems to increase the backflow region length in the high-Re case. In the *KM* case, also, a reduction of the recirculation bubble length was observed.

4. Discussion and conclusions

The brief description of the computations done in the previous section evidences how the computed overall flow pattern agrees with the high-Re and low-Re cases, although some discrepancies between the computations and the measurements (and DNS) arise in terms of turbulence quantities.

In the recovery region, as already pointed out by several authors, (*e.g.* Durbin, 1995), the computations recover to a boundary layer profile much more slowly than experiments would indicate at high Reynolds numbers. This disagreement fades away for smaller Reynolds numbers, as those typical of the DNS. In the backflow region the computed profiles seem too steep, which would indicate too large a turbulence level.

Version (2) of the model was found to work slightly better than the original version of the model in the backflow region. This can be attributed to the different choice of the length scale formula. In version (1) the model chooses between two different values of the length scale, whereas in version (2) the expression for the length scale allows a smooth switch from the two values. Observe that the same smooth switch is guaranteed for the computation of the time scale. This seems to play a significant role in the improvement of the results where, due to the small local Reynolds number, the expressions for the length and time scale are switching between the two values. In the recovery region the local Reynolds number is larger

and the beneficial effects of the smooth transition between the two values of the time and length scale formulas disappear.

In terms of turbulent shear stress, the backflow region again shows some slight inaccuracies for both the high-Re and low-Re cases. This fits with the shape of the computed velocity profile, which indicates that the mean velocity gradient and the turbulence levels are too high. From the DNS data set it is possible to compute a turbulent viscosity μ_t via the definition of the turbulent shear stress given in the Boussinesq assumption. This sort of computation does not guarantee that the turbulent viscosity is positive, since there is no guarantee that the mean shear and the turbulent shear stress always have opposite sign: in fact Fig. 11 shows that turbulent viscosity computed from the turbulent shear stress by DNS gives negative values.

The turbulent viscosity is small deep inside the backflow region and grows toward the reattachment point. The two versions of the model are found to overestimate the turbulent viscosity in the backflow region. There is very little difference between the computations all through the computational domain. Observe that a large turbulent viscosity would imply a large momentum diffusion, which should decrease the recirculation bubble length. Surprisingly, this is not the case in the computations: the overestimation in μ_t is followed by an excellent agreement between the computed and measured reattachment point. The figure also shows that the disagreement between the computations and the DNS fades away downstream of the reattachment point. But the same figure also shows that in the recovery region the turbulent viscosity is underestimated. The smaller momentum diffusion in the computation could partially explain why the computed velocity profiles tend to the boundary layer profiles too slowly. The discrepancies between DNS and computations are mainly in the backflow region and the shear layer, since above the latter the computations seem to follow the DNS profiles quite well.

The DNS data set also contains all the terms of the transport equation for the turbulent kinetic energy. With these data it was possible to evaluate the accuracy of each term of the modeled transport equation for k. A full comparison of all the terms (*i.e.* convection= C_k, viscous diffusion= Vd, turbulent diffusion= Td, pressure diffusion= Pd, production= P_k, and dissipation= ϵ) showed that the viscous diffusion Vd has nearly no effect. The computed convection of k, C_k, is in very good agreement with both the measurements by KM and the DNS by LM. The dissipation rate, although not in perfect agreement with the data in the backflow region, closely resembles the DNS profiles in the shear layer. So, the terms which need a further check, and that are not often compared with the experiments for models based on the eddy viscosity, are the production rate P_k and both the turbulent and pressure diffusion terms Td and Pd respectively.

Figure 12 compares the DNS production rate versus the profiles obtained by using the two different versions of the model. The agreement between computations and the DNS profiles is good. Observe that the peak in the production rate, which is probably caused by the very high mean shear downstream of the separation point, is well captured. The production rate is somewhat overpredicted in the backflow

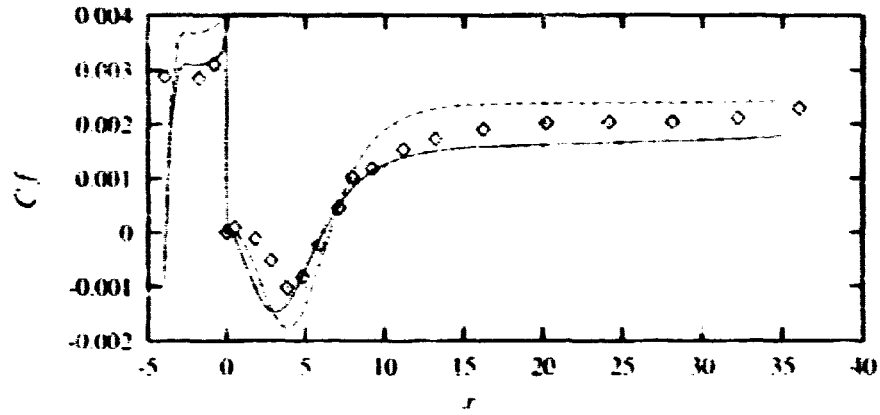

FIGURE 9. *DS* Skin friction coefficient. ◇ experiments. —— model version (1). – – – model version (2).

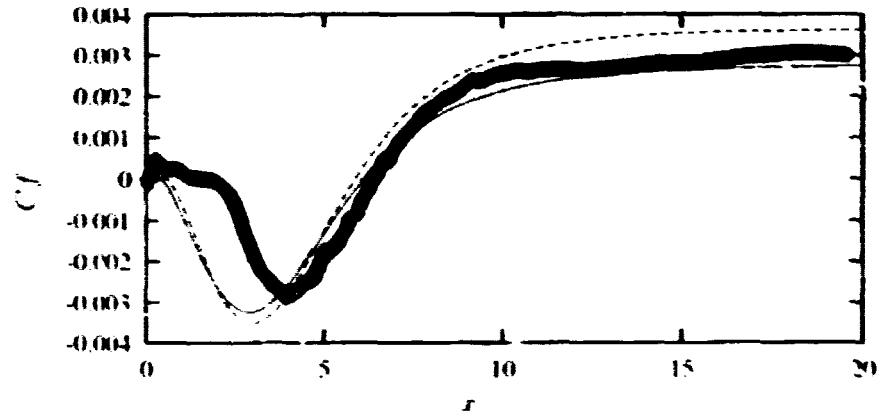

FIGURE 10. *LM* Skin friction coefficient. Symbols as in Fig. 9.

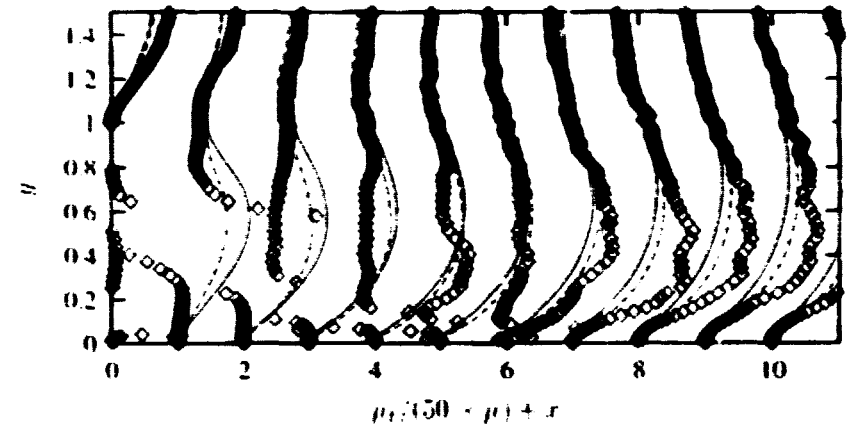

FIGURE 11. *LM* Turbulent viscosity profiles. Symbols as in Fig. 9.

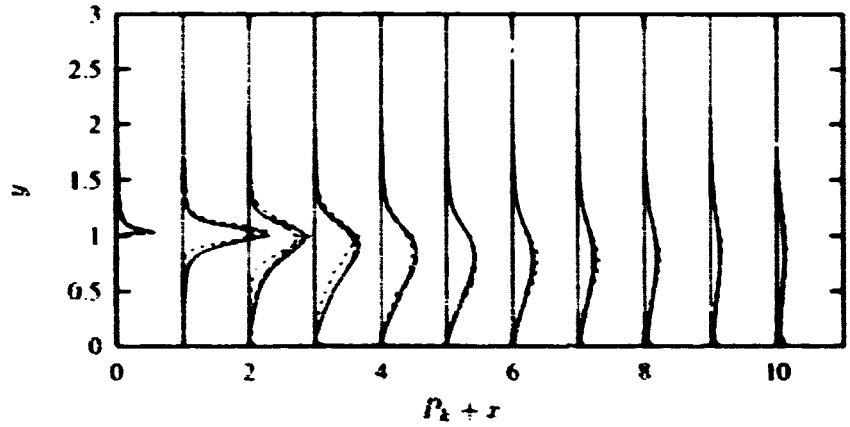

FIGURE 12. *LM* Productic . .ate profiles. ---- experiments, —— model version (1), – – – model version (2).

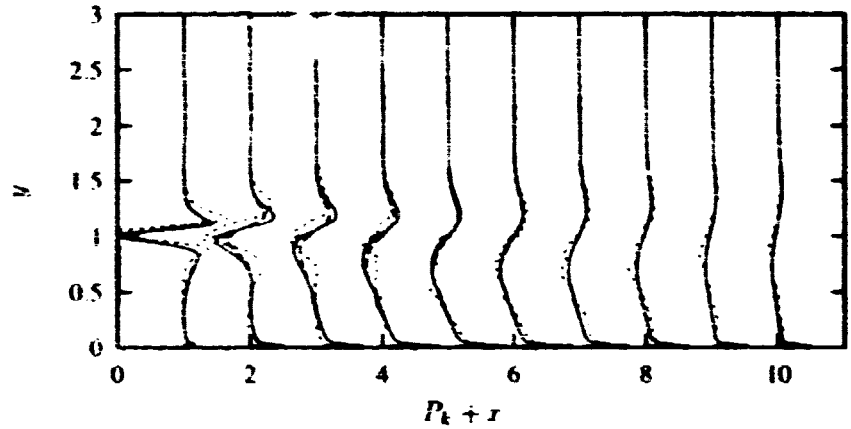

FIGURE 13. *LM* $Td + Pd$ profiles. Symbols as in Fig. 12

region, but this overprediction seems to fade away as the reattachment point is reached. The same agreement was found in the high-Re case.

Before comparing the turbulent and pressure diffusion terms, one should recall that the gradient diffusion hypothesis, done in the $k-\epsilon$ model, does not distinguish between Pd and Td, which are just lumped together. Still, it is possible to compare the sum of Td and Pd from the DNS calculations with the computed turbulent diffusion of turbulent kinetic energy, which should be the sum of the two. Observe that the comparison is done for the diffusive terms (second order derivative of k for the $k-\epsilon$ model and first order derivative of Td and Pd for the DNS data). Figure 13 compares the computed diffusion of k with the sum of the turbulent diffusion and pressure diffusion from the DNS. The agreement between computations and DNS is quite good. The up-down shape of the profile from the DNS is closely reproduced by the calculations. The agreement remains good in the entire computational domain and does not deteriorate when making the same comparison for the KM data set.

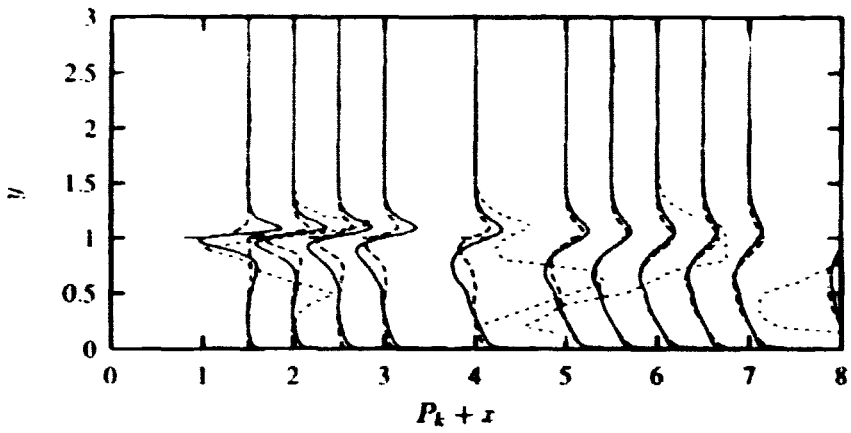

FIGURE 14. *DS Td* profiles. Symbols as in Fig. 12.

When making the same comparison by using the *DS* data base at a higher Reynolds number, some problems arise due to the scatter of the measured data. Figure 14 compares the turbulent diffusion of turbulent kinetic energy for the *DS* case. Although there are not as many data as in the DNS case, the figure clearly suggests that the turbulent diffusion is largely underestimated in the shear layer from the separation point till far downstream. The underestimation is quite severe and clearly limited to the flow region where the mean shear is high. However, the experimental data are probably not accurate enough to differentiate, as in Fig. 14.

Figures 13 and 14 indicate that as long as the Reynolds number is small, the gradient diffusion hypothesis gives the correct estimate of the turbulent plus the pressure diffusion, especially in the high shear layer. The two figures also show that the same closure hypothesis fails when the Reynolds number is large. Apparently at large R_t there is a large scatter of turbulence time and length scales. This scatter is probably not modeled when using a linear eddy viscosity model. The scatter is reduced at smaller Reynolds number, and the turbulence model then agrees much better with the experiments and DNS.

In conclusion, the computations show that the slow recovery downstream of the reattachment point occurs only in high Reynolds number flows and is probably caused by the gradient diffusion hypothesis, which is not able to model the large turbulent diffusion typical of the high shear layer. In the backflow region the computations and the comparison with the experiments and the DNS do not allow identification of any specific deficiency of the model. Still, the plots indicate that in the backflow region the models predict too high a turbulence level and too much velocity gradient, which are interrelated deficiencies.

Acknowledgements

The first author would like to express his gratitude to CTR, and the Energetics Department of the University of Genova, Italy, for their financial support.

REFERENCES

DRIVER, D., & SEEGMILLER, H. L. 1985 Features of Reattaching Turbulent Shear Layer in Divergent Channel Flow. ***AIAA J.*** **23,** 162-171.

DURBIN, P. A. 1995 Separated flow computations with the $k-\varepsilon-\overline{v^2}$ model. ***AIAA J.*** **33,** 659-664.

DURBIN, P. A. & LAURENCE, D. 1996 Non-local effects in single point closure. ***Advances in Turbulence Research,*** Seoul, Korea, May 17. 1996, 109-120.

KASAGI, N., & MATSUNAGA, A. 1995 Three-dimensional particle-tracking velocimetry measurements of turbulence statistics and energy budget in a backward-facing step flow. ***Int. J. Heat and Fluid Flow.*** **16,** 477-485.

LE, H., & MOIN, P. 1994 Direct numerical simulation of turbulent flow over a backward facing step. ***Report TF-58,*** Thermosciences Division, Department of Mechanical Engineering, Stanford University.

MICHELASSI, V. 1993 Adverse pressure gradient flow computation by two-equation turbulence models. ***Engineering Turbulence Modeling and Experiments.*** **2,** W. Rodi & F. Martelli (ed.) 123-132.

MICHELASSI, V., RODI, W.,& GIESS, P.-A. 1997 Experimental and numerical investigation of boundary-layer and wake development in a transonic turbine cascade. ***IGTI Conference,*** Orlando, FL.

MICHELASSI, V., & SHIH, T. H. 1991 Low Reynolds Number Two-Equation Modeling of Turbulent Flows. ***NASA TM-104368.***

MICHELASSI, V., THEODORIDIS, G., & PAPANICOLAOU, E. 1995 A Comparison of Time Marching and Pressure Correction Algorithms for Transonic Turbine blades. ***ASME AD.*** **49,** 115-126.

RODI, W. 1991 Experience with two-layer models combining the $k-\epsilon$ model with a one-equation model near the wall. ***AIAA-91-0216.***

RODI, W., BONNIN, J.-C., & BUCHAL, T. (ED.) 1995 Proceedings of the ERCOFTAC Workshop on data bases and testing of calculation methods for turbulent flows ***University of Karlsruhe, Germany.***

RODI, W., & MANSOUR, N. N. 1990 Low Reynolds number $k-\epsilon$ modeling with the aid of direct simulation data. ***Proceedings of the Summer Program.*** Center for Turbulence Research, NASA Ames/Stanford Univ. 85-106.

RODI, W., MANSOUR, N. N., & MICHELASSI, V. 1993 One-equation near-wall modelling with the aid of direct simulation data. ***ASME Journal of Fluids Engineering.*** **115,** 196-205.

ZHU, J., & SHIH, T. H. 1993 Calculations of Turbulent Separated Flows. ***NASA TM-106154.***

NEXT
DOCUMENT

A-priori testing of sub-grid models for chemically reacting nonpremixed turbulent shear flows

By J. Jiménez[1], A. Liñán[2], M. M. Rogers[3] AND F. J. Higuera[2]

The β-assumed-pdf approximation of (Cook & Riley 1994) is tested as a subgrid model for the LES computation of nonpremixed turbulent reacting flows, in the limit of cold infinitely fast chemistry, for two plane turbulent mixing layers with different degrees of intermittency. Excellent results are obtained for the computation of integrals properties such as product mass fraction, and the model is applied to other quantities such as powers of the temperature and the pdf of the scalar itself. Even in these cases the errors are small enough to be useful in practical applications. The analysis is extended to slightly out of equilibrium problems such as the generation of radicals, and formulated in terms of the pdf of the scalar gradients. It is shown that the conditional gradient distribution is universal in a wide range of cases whose limits are established. Within those limits, engineering approximations to the radical concentration are also possible. It is argued that the experiments in this paper are essentially in the limit of infinite Reynolds number.

1. Introduction

The computation of turbulent reacting flows is an open challenge even after having been the focus of intensive work for several decades. The subject of the present note, nonpremixed flames with fast chemistry, was one of the first to be tackled, and it is somewhat simpler than others, but it still represents a large number of cases of theoretical and practical importance. Recent reviews can be found in (Bilger 1989, Libby & Williams 1994).

Our analysis is subject to several simplifications. The diffusion coefficients of all the species and of heat are assumed to be identical, $\kappa_i = \kappa$ and, although not explicitly needed for most of the theoretical arguments, all of our numerical experiments are done at Schmidt number $Sc = 0.7$. Our flows are incompressible, and we assume that any heat released by the reaction is weak enough for the fluid density to be unchanged, $\rho = 1$. The role of the chemistry is thus passive with respect to the flow, although it is modified by it.

In most cases we assume an irreversible binary reaction

$$\nu_A A + \nu_B B \rightarrow \nu_P P, \tag{1}$$

in a shear flow between two streams, each of which initially contains either pure A or B reactant.

1 Center for Turbulence Research

2 School of Aeronautics, U. Politécnica, Madrid

3 NASA Ames Research Center

Under those circumstances the mass fractions Y_i of the different species can be linearly combined to form a set of conserved scalars which are transported by the flow with the common diffusion coefficient κ. If in addition the Damköhler number, which measures the ratio of the characteristic diffusion and chemical times, is large enough, the reaction occurs in a thin flame that can be treated as a surface, and the problem reduces to the mixing of a single conserved scalar

$$\xi = \frac{Y_{A0} - Y_A + rY_B}{Y_{A0} + rY_{B0}}, \tag{2}$$

called the mixture fraction, which takes values $\xi = 0$ and $\xi = 1$ at the free streams (see Williams 1985). Here Y_{i0} is the mass fraction of the i-th species at the appropriate free stream, and

$$r = \nu_A W_A / \nu_B W_B, \tag{3}$$

where ν_i and W_i are stoichiometric coefficients and molecular weights. The flame is located at the stoichiometric mixture fraction

$$\xi_s = \frac{Y_{A0}}{Y_{A0} + rY_{B0}}, \tag{4}$$

and most quantities of interest can be computed as algebraic functions of ξ, which are continuous but have discontinuous derivatives ξ_s. Thus the mass fraction of the product Y_P is proportional to the triangular function

$$f(\xi) = \xi/\xi_s \quad \text{if} \quad \xi \le \xi_s, \qquad (1-\xi)/(1-\xi_s) \quad \text{otherwise.} \tag{5}$$

In modeling turbulent flows we can usually estimate averaged or locally filtered values of ξ, and we would like to have similarly filtered values of mass fractions or other quantities, but we are prevented from doing so by the nonlinear nature of (5).

It was realized soon that what is needed is an approximation to the probability density function (pdf) of ξ, and that the mean value of any quantity which can be expressed as a function of ξ is (Lin & O'Brien 1974, Bilger 1976)

$$\langle f \rangle = \int f(\xi) p(\xi)\, \mathrm{d}\xi, \tag{6}$$

where $p(\xi)$ is the pdf. Numerous experimental (LaRue & Libby 1974, Anselmet & Antonia 1978, Breidenthal 1981, Mungal & Dimotakis 1984, Koochesfahani & Dimotakis 1986), theoretical or numerical (Eswaran & Pope 1988, Pumir 1994, Holzer & Siggia 1994), and modeling (Kollman & Janicka 1982, Broadwell & Breidenthal 1982) efforts have been undertaken to understand the properties of the pdf of passively mixed scalars.

Of particular interest in this report is the β-pdf model of (Cook & Riley 1994), in which the form of the scalar pdf is modeled as a function of its mean value and standard deviation and, especially, its use as a sub-grid model for large eddy simulations (LES). Large eddy simulation has proven to be a powerful technique for

the computation of complex flows and good results have been obtained in the computation of filtered scalar mean values (Lesieur & Rogallo 1989, Moin *et al.* 1991). We will show below that the subgrid fluctuation intensity can also be estimated with good accuracy. In this report we will assume that exact filtered mean scalar values can be computed by some LES scheme, but we will obtain them by filtering direct numerical simulation fields. The β-pdf model has been tested in this way for isotropic turbulent flow at relatively low Reynolds numbers in (Cook & Riley 1994, Réveillon & Vervisch 1996). We will test it here in the more realistic case of a mixing layer at medium Reynolds numbers (Rogers & Moser 1994).

At issue is the question of large-scale turbulent intermittency, which is the presence of essentially laminar pockets in an otherwise turbulent flow, and whether the same subgrid mixing model can be used in homogeneous turbulence and in the presumed interface between turbulent and laminar regions. A lot of effort has gone into modeling such intermittency effects (Libby 1975, Dopazo 1977, Kollman 1984, Pope 1985, Pope & Correa 1988) but, if it is really a large scale effect, LES should be able to resolve it without resorting to modeling. The main difference between homogeneous flows and the mixing layer is that, while large-scale intermittency is rare in the former, it is prevalent in the latter.

The simulation experiments are described in the next section. The results of applying the β-pdf model to the prediction of different quantities in infinitely fast chemistry are presented in §3. We then extend the model to finite rate chemistry in the flamelet limit, and introduce some results on the joint pdf of the scalar and the scalar gradients, followed by discussion and conclusions.

2. Numerical experiments

The two flow fields used in this report are taken from the simulations in (Rogers & Moser 1994), where they are described in detail. Briefly, they are direct simulations of three-dimensional, temporally growing mixing layers, spatially periodic in the streamwise and spanwise directions, with initial conditions which represent turbulent boundary layers. The flow fields chosen are those in Figs. 18.a and 18.c of that paper, at which time the momentum thickness, θ, of the layers has grown by factors of 2.47 and 2.94 respectively from the initial conditions, and the streamwise integral scale has increased by a factor of about four. The energy spectra have a short power-law range with an exponent close to $-5/3$, and the layers are growing self-similarly. Both layers appear to be slightly beyond the "mixing transition" identified in (Konrad 1976, Breidenthal 1981). The Reynolds numbers based on the instantaneous momentum thickness are 1980 and 2350, and correspond to longitudinal microscale Reynolds numbers $Re_\lambda = 127$ and 214 at the central plane of the layer. Note that both flows are quite intermittent, especially the second one, and that these values would probably change if they were conditioned only to the turbulent fluid. The ratio between vorticity and momentum thickness is about 4.85 in both cases.

The computational boxes are, in both cases, 125×31.25 initial momentum thickness and contain five or six large spanwise structures at the times chosen for our

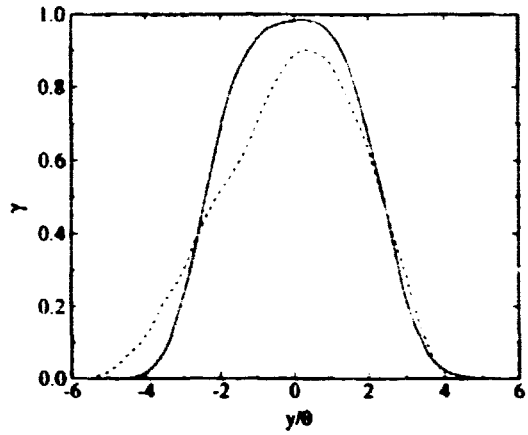

FIGURE 1. Scalar intermittency across the two mixing layers used in the text, defined as the fraction of fluid for which $\xi \in (0.02, 0.98)$. ——— : unforced case. ---- : forced.

experiments. A passive scalar is introduced at the initial condition with a laminar profile of thickness similar to that of the vorticity layer and a range $\xi \in (0, 1)$. Although the original simulations were spectral, using a mesh that was neither uniform nor isotropic, they were spectrally interpolated to physical variables on a uniform isotropic mesh for the purpose of our experiments. This implies some reduction in the resolution, which is dictated by the least resolved direction. Thus while the original computations were carried using $512 \times 180 \times 128$ and $384 \times 96 \times 96$ spectral modes, the interpolated fields contain $512 \times 128 \times 128$ and $384 \times 120 \times 128$ points. The pitch of the interpolated grids is $\Delta x/\theta \approx 0.1$ in both cases, although the original grids are finer by about a factor of two, especially at the central plane and in the transverse, y, direction. All lengths in this report are normalized with the instantaneous momentum thickness of the layers. In terms of the Kolmogorov scale at the center of the layer, $\theta/\eta = 67$ and 72 respectively, and the resolution of our interpolated grid is about 7η in both cases.

It was found in (Rogers & Moser 1994) that the structure of the layer depends during the whole simulation on the initial conditions, corresponding to similar long term effects during the initial development of experimental layers. Different amounts of initial perturbations were introduced in the simulations to mimic this effect. Our two flow fields correspond to two extreme cases in the amount of two-dimensional perturbations applied to the initial conditions. In the first one, which will be referred from now on as the "unforced" case, the initial conditions were synthesized from two turbulent boundary layers without modification. At the time of our experiment, both the vorticity and the scalar field are fairly disorganised with weak spanwise coherent structures, and there is very little fresh fluid at the center of the layer. In contrast, the second case was initialized by amplifying the spanwise-coherent modes of the initial boundary layers by a factor of 20, and the resulting

two-dimensional forcing gives rise to clear spanwise rollers with fresh fluid from one or the other stream present across the layer. This is clear in Fig. 1, which presents the fraction of mixed fluid in both cases, arbitrarily defined as $\xi \in (0.02, 0.98)$. Not only is the mixed fraction higher in the unforced case, but the presence of a few larger structures in the forced one results in insufficient statistics which are not symmetric with respect to the central plane. The statistics for the unforced case are symmetric.

Of the two cases, the forced one is the hardest to compute because of the larger intermittency. Most of the results given below are for this case. The corresponding ones for the unforced case are at least as good, and usually better.

We will generally compare mean quantities, denoted by $\langle\cdot\rangle$, which are averaged over whole $x - z$ planes. Occasionally the averages will be extended to slabs of the mixing layer, in which case the limits of the transverse coordinate y will be given explicitly. In our simulations of LES we define our basic filtering operation as a box filter in physical space. Quantities are averaged over a cubical box of contiguous grid points of side $h = n\Delta x$, and assigned to the center of the box. This operation will be denoted by an overbar. Other filtering kernels have been used by other investigators, and it is not clear which is the best choice to mimic the projection operation implicit in a discrete grid, but our choice seems natural for finite differences or finite volumes codes, and has the advantage of providing a simple definition for subgrid statistics.

Equation (6) extends trivially to filtered quantities, but the pdf has then to be taken to refer only to the interior of the filter box. Thus for a filter of width h we can define a subgrid mean

$$\bar{\xi}(\mathbf{x}) = h^{-3} \int_{h^3} \xi(\mathbf{x} - \mathbf{x}')\, \mathrm{d}^3\mathbf{x}' = \int \xi\, p_h(\xi; \mathbf{x})\, \mathrm{d}\xi, \tag{7}$$

and a variance as

$$\xi_h'^2 = \overline{\xi^2} - \bar{\xi}^2. \tag{8}$$

All quantities are functions of y and, in addition, filtered quantities are also functions of the homogeneous coordinates x and z. To increase the number of data points available for the statistics, filtered quantities are computed at all grid points, even if they are only strictly independent over a coarser grid of pitch h. Plane averages are then computed for these filtered quantities and used to generate filtered profiles, which satisfy

$$\langle \bar{f} \rangle = h^{-1} \int_{-h/2}^{h/2} \langle f \rangle\, \mathrm{d}y = \overline{\langle f \rangle}. \tag{9}$$

Note that we can combine (6) and (9) to generate a "filtered" pdf for ξ,

$$\bar{p}(\xi, y) = h^{-1} \int_{h/2}^{h/2} p(\xi, y - y')\, \mathrm{d}y', \tag{10}$$

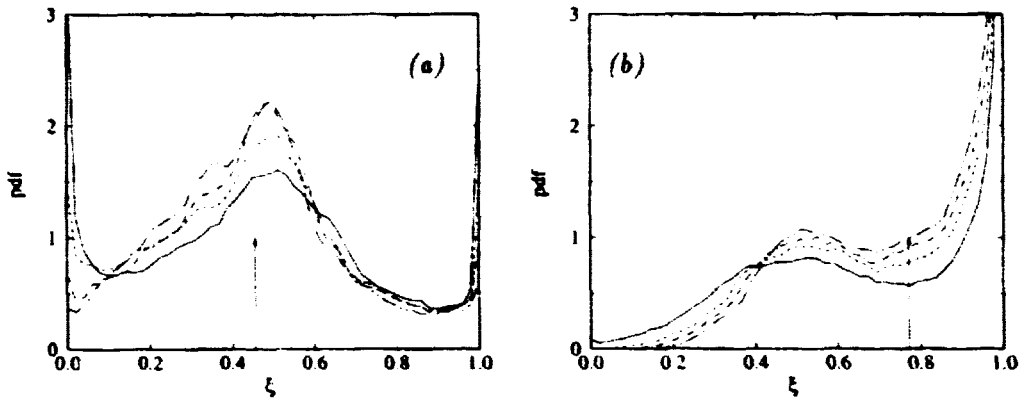

FIGURE 2. Mixture fraction pdfs from LES without subgrid modeling. Forced layer. (a) $y/\theta = 0$. (b) $y/\theta = 3$. ——— : no filter. - - - - : $h/\theta = 0.44$. — · — : 0.66. — · · — : 0.88. Vertical arrows mark the mean value of ξ for each plane.

such that (6) generalizes to

$$\overline{\langle f \rangle} = \int f(\xi)\tilde{p}(\xi)\,\mathrm{d}\xi. \tag{11}$$

The error of any approximation to the mean profiles depends on our success in approximating $\tilde{p}$ from our local models for p_h. In most of our experiments the filter width will be small enough with respect to the width of the layer that we will be able to neglect the difference between laterally filtered and unfilte.ed pdfs.

3. Fast chemistry

3.1 No subgrid model

It should be clear from the discussion in the last section that the aim of any approximation should be to reproduce $\tilde{p}(\xi)$ as closely as possible. In RANS computations, all the available information is the mean value of the mixture fraction over a plane and perhaps some of its statistical moments. Unless some model is applied for the form of the pdf, the implied representation is a delta function $\tilde{p} = \delta(\xi - \langle\xi\rangle)$, and is known to be poor.

In LES we have some hope of avoiding subgrid modeling, since the grid elements are small parts of the flow in which the fluid may be assumed to be mixed and well represented by its mean. Large intermittent unmixed regions are hopefully contained in individual grid elements. In this approximation

$$p_h(\xi) = \delta(\xi - \bar{\xi}), \qquad \overline{f(\xi)} = f(\bar{\xi}). \tag{12}$$

In practice the filtered grid values are treated like real points and used to compile statistics.

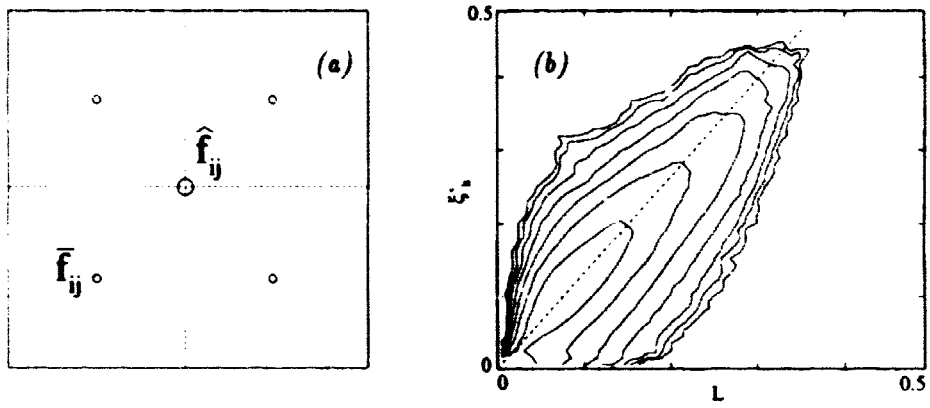

FIGURE 3. (a) Sketch of the two filters for the estimation of the subgrid variance. (b) Joint pdf of the band-passed mixture fraction fluctuation L and its true subgrid value ξ_h'. The dashed line is (15) with spectral slope $-5/3$. Isolines are logarithmically spaced by half an order of magnitude. Forced layer. $y/\theta = (-2, 2)$.

The approximation (12) is tested directly in Fig. 2 for the pdfs of the mixture fraction in two planes of the forced mixing layer. Each figure contains the pdfs resulting from several different filters, compared to the real one. The widths of the filters are of the order of the momentum thickness (30-50 Kolmogorov lengths), and correspond to grids of 10-20 points across the layer (Fig. 1). Even with these relatively coarse grids it is interesting that the approximation of the pdf is already a large improvement over the delta function of the global mean, and that the general shape of the pdf is recovered. Product mass fraction profiles obtained from using these pdfs in (11) have errors of the order of 20%.

Nevertheless there are clear differences between the true and the approximate pdfs. A sizable percentage of the pure fluid that should be associated to the delta functions at $\xi = 0$ and $\xi = 1$ has been aliased as mixed fluid into the central peak. This is especially evident deep into the layer (Fig. 2.a) where the unmixed regions are presumably of small size and are almost completely obliterated by the filter.

3.2 The Beta subgrid model

To improve the approximation in the previous section it was noted in (Cook & Riley 1994) that, if the subgrid variance (8) were known at each grid point, it should be possible to make a reasonable guess as to the form of the subgrid pdf, $p_h(\xi; \bar{\xi}, \xi_h')$, and to obtain a better estimate of the true pdf in terms of the joint pdf of those two subgrid variables

$$\bar{p}(\xi) = \int p(\bar{\xi}, \xi_h') p_h(\xi; \bar{\xi}, \xi_h') \, \mathrm{d}\bar{\xi} \, \mathrm{d}\xi_h'. \tag{13}$$

In the particular model proposed in that paper, the subgrid pdf is represented as a Beta distribution, $p_h \sim \xi^{a-1}(1-\xi)^{b-1}$, and the two exponents a and b are computed at each point from the values of $\bar{\xi}$ and ξ_h'.

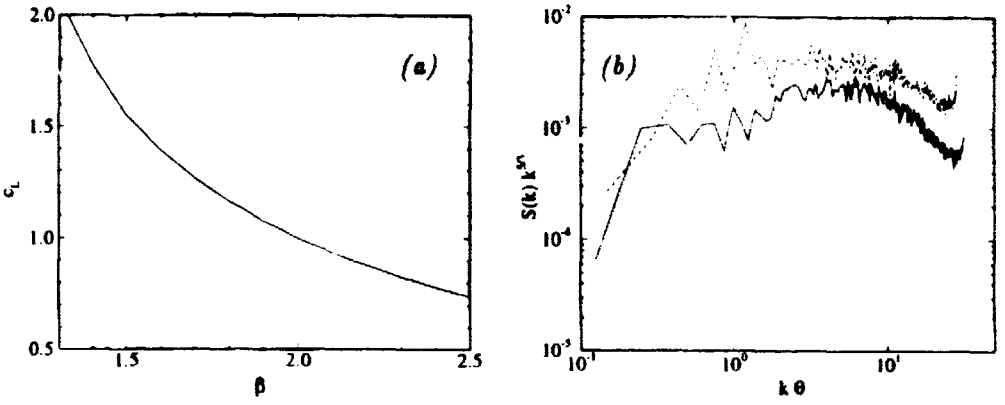

FIGURE 4. (a) Proportionality constant between band-passed and subgrid fluctuations, versus spectral slope. (b) Compensated scalar longitudinal spectra at the central planes (arbitrary units). ——— : unforced layer. ----- : forced. Vertical dotted lines are $kh = \pi$ for the two filters used in Fig. 3.b.

This correction needs the subgrid scalar variance, ξ_h', which is generally not given by the LES equations, but the same paper suggests that it may be obtained by a similarity argument from the behavior of the scalar at scales close to grid filter. Consider in our implementation two filter levels (Fig. 3.a). The first one is the grid filter of width h, which is represented by the dashed squares. The test filter $\bar{\xi}$ is formed by averaging a 2^3 cubic box of contiguous, non-overlapping, grid values. In this implementation

$$\bar{\bar{\xi}} = \bar{\xi}, \tag{14}$$

and we can define the subgrid variance at the test level

$$\xi_{2h}'^2 = \widehat{\xi^2} - \bar{\xi}^2. \tag{15}$$

Neither (15) nor (8) are known, but they can be combined to give a band-passed "Leonard" term which, using (14), can be written as

$$L^2 = \xi_{2h}'^2 - \widehat{\xi_h'^2} = \widehat{\bar{\xi}^2} - \bar{\bar{\xi}}^2. \tag{16}$$

The right-hand side involves only filtered quantities, and can be computed as the standard deviation of $\bar{\xi}$ within the box defining the test filter. The similarity assumption is that

$$\xi_h' = c_L L, \tag{17}$$

and is seen to be reasonable in Fig. 3.b, where it is tested for the central part of the forced layer.

The proportionality constant can be estimated by assuming a form for the scalar spectrum, $S(k) \sim k^{-\beta}$. The subgrid variance is obtained by filtering the spectrum

through the transfer function of the filter, which has the form $F(kh)$. The result is that $\xi_h'^2 \sim h^{\beta-1}$ and, from (17)

$$c_L = (2^{\beta-1} - 1)^{-1/2}. \tag{18}$$

This quantity, which assumes an infinite Reynolds number in that it integrates the spectrum to $k \to \infty$, is plotted as a function of the spectral slope in Fig. 4.a. For the Kolmogorov slope $\beta = 5/3$ it has a value $c_L = 1.305$, which is the one used for the dashed line in Fig. 3.b, and represents the data well. In reality it is known that scalar spectra have slopes which are somewhat lower than 5/3 for Reynolds numbers in the range of our experiments (Sreenivasan 1996). This would imply proportionality constants somewhat higher than our value, but this effect is partly compensated by the presence of a Kolmogorov cutoff in the spectrum, which would lead to a lower value of c_L. Figure 4.b shows our scalar spectra and the position of our filters with respect to them. The fact that both effects compensate at our Reynolds number, and that they should vanish as $Re \to \infty$, suggests that the asymptotic value of c_L is a reasonable approximation for most of the Reynolds numbers of interest in LES.

In the two previous tests of the β-pdf model, the proportionality constant c_L was fitted to the data and found to be smaller than ours. Réveillon and Vervisch (1996) found $c_L = 0.5$ for a filter ratio of two, while Cook and Riley (1994) found $c_L \approx 1$ for $\hat{h}/\overline{h} = 1.8$, which would correspond to $\beta \approx 2.15$ according to (18), and to $c_L \approx 0.9$ for $\hat{h}/\overline{h} = 2$. Both simulations, however, were carried at Reynolds numbers substantially lower than ours. Réveillon and Vervisch worked at $Re_\lambda = 17$, for which there is no inertial range and no self-similar spectrum, and where turbulence is still barely developed. Cook and Riley do not give their Reynolds number, but their filters are only 6 times larger than the Batchelor scale, which would be near the right-most points in the spectra in Fig. 4, and within the dissipative range. Neither experiment can therefore be expected to agree with an inertial range prediction. It is probably a general rule that, if LES models are to behave independently of the type of flow, they should only be used in well-developed turbulence with filters in the inertial range.

The results of applying the β correction to the pdf in the previous section are shown in Fig. 5, where it is seen that error has decreased considerably with respect to Fig. 2 and, especially, that it is now relatively insensitive to the filter width. Note that the good behavior of the model is not only at the level of integral quantities, but at the detailed level of the pdf, implying that it should give good results for the average of *any* function of ξ and not only for the mass fraction (5). This includes the approximation of the pdf at a particular value of ξ, which is useful, for example, in evaluating source terms located at the flame. The figure includes the Beta distributions corresponding to the global averages and (true) standard deviations at each plane, as would be used in RANS.

Although they are not included in the figure, there is no appreciable difference between the LES results obtained using the true value of ξ_h' and those obtained using the estimation (17).

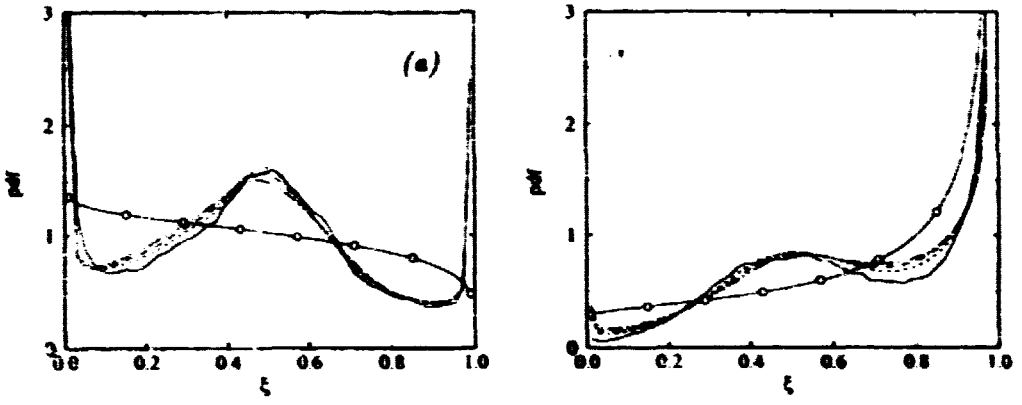

FIGURE 5. Mixture fraction pdf's from LES using the similarity β subgrid model. Forced layer. (a) $y/\theta = 0$. (b) $y/\theta = 3$. ——— : no filter. ---- : $h/\theta = 0.55$. —·— : 0.77. —··— : 0.99. -o- : Beta distributions using the global mean and standard deviation for each plane.

It is curious that, when the RANS pdfs are used to compute the mean value of the mass fraction (5), the result is within a few percent of the actual one, but it is clear from Fig. 5 that this is due to compensating errors and that it cannot be extrapolated to other quantities.

3.3 Mean profiles

The results of using the approximate pdfs of the previous section to compute mean profiles of various quantities are presented in Fig. 6, in which the degree of difficulty increases from top to bottom and from the left to the right. Plots on the left of the page are computed for a stoichiometric mass fraction $\xi_s = 1/2$, for which the flame is roughly in the middle of the mixing layer. There the fluid is relatively well mixed, and the results should be comparable to those obtained in homogeneous turbulence. Those on the left of the page are for $\xi_s = 1/9$, which corresponds to global models of the H_2-O_2 reaction. For this stoichiometry the flame is near the edge of the mixing layer, in the interface between mixed and unmixed fluid, and LES may be expected to have more problems. The first two plots are mass fraction profiles obtained from the relatively smooth function (5). Those in the middle are profiles of Y_p^4, which is proportional to the fourth power of the temperature, and would therefore be a rough model for radiative heat in a flow with a real, hot, flame. This function (see Fig. 7.a) is much sharper than Y_p and is therefore sensitive to the local values of the pdf, in spite of which the errors in the mean profile are still small. The last two plots are the values of the pdf at a given ξ_s and are the most sensitive test of the three. They are also the ones for which the errors are larger, but it is remarkable that the general form of the profile is still captured and that the errors stay, at worse, of the order of 25%.

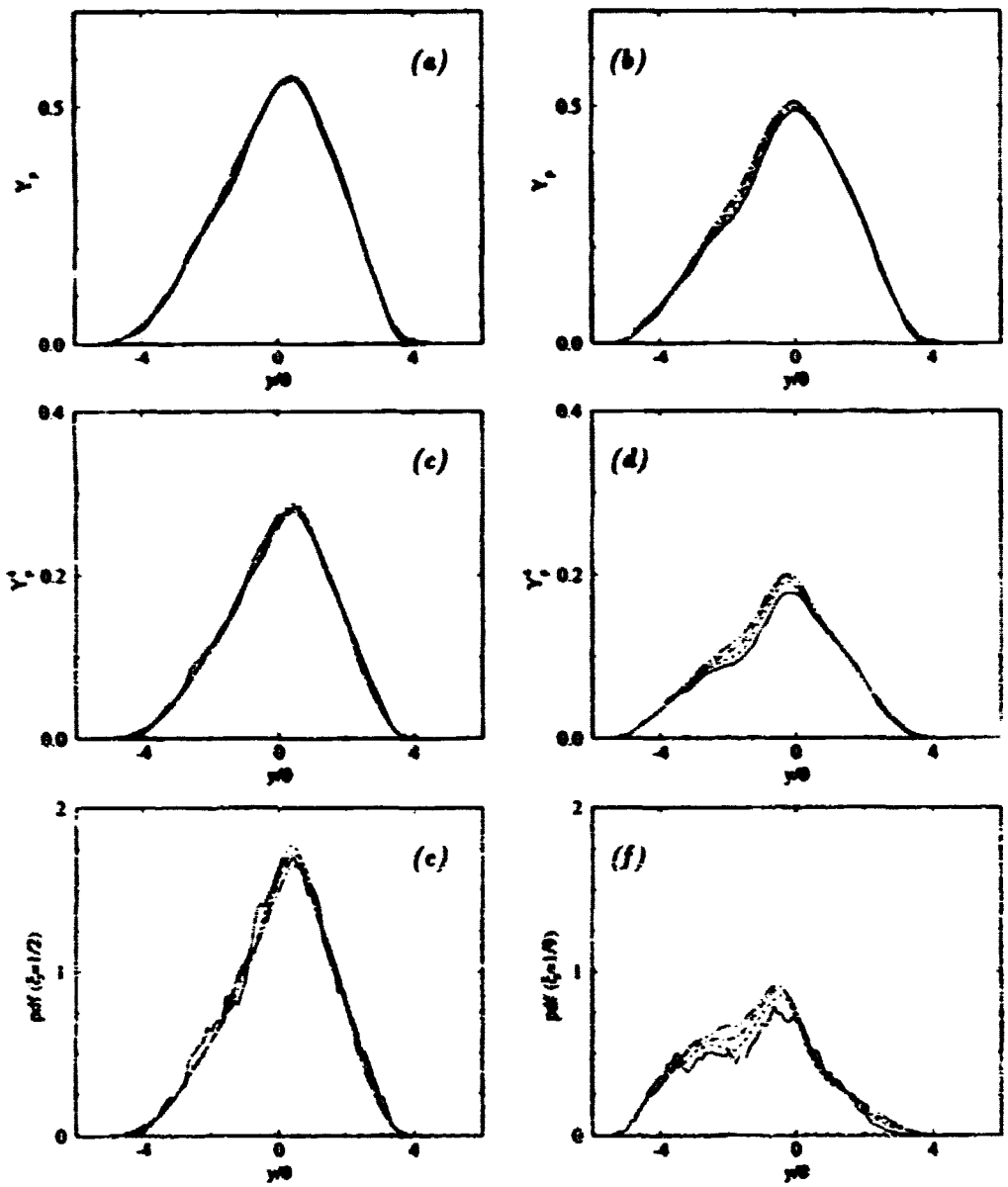

FIGURE 6. Average profiles for different functions in the forced layer. (a)-(b): Product mass fraction Y_p. (c)-(d): "Radiation" source Y_p^4. (e)-(f): Pdf(ξ_s). (a), (c) and (e) are for $\xi_s = 1/2$. The other three are for, $\xi_s = 1/9$.

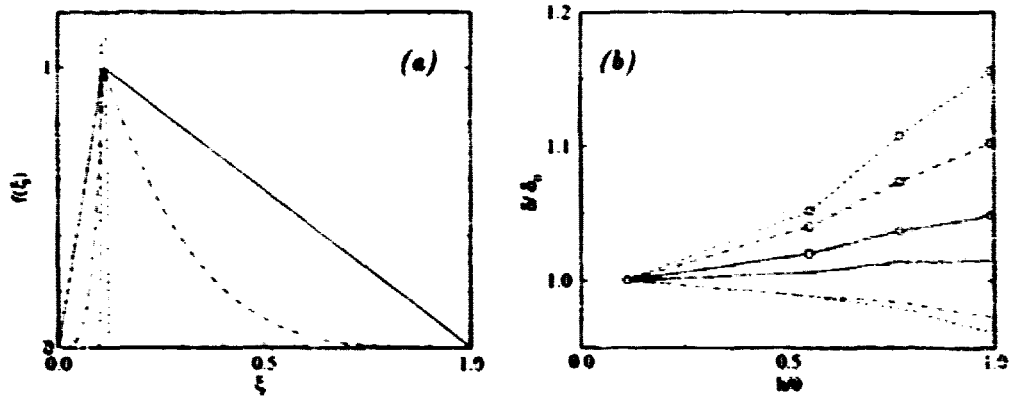

FIGURE 7. (a) The three functions used for the profiles in Fig. 6. $\xi_s = 1/9$. (b) Relative variation of the profile thickness with filter width. Forced layer. Lines with symbols are for $\xi_s = 1/9$. Other lines are for $\xi_s = 1/2$. ——: Y_p. — · —: Y_p^4. - - - -: Delta function with $\Delta\xi = 0.02$.

For any profile which vanishes at $y = \pm\infty$ we can define a "thickness"

$$\delta_f = \int_{-\infty}^{\infty} f(y)\,dy. \tag{19}$$

which is proportional to the total amount of the particular quantity contained in the layer and which can be used to quantify the global error of the approximation. Note that this thickness is unchanged by the filtering, $\delta_{\tilde{f}} = \delta_f$. The results for the different profiles of Fig. 6 are presented in Fig. 7.b, where they have been normalized with their DNS values. The errors for $h/\theta < 1$ vary from better than 5% for the product mass fraction to about 15% for the pdf. They are, as expected, generally larger for flames near the interface than for those at the center of the mixed region.

4. Finite rate effects

If the speed of the chemical reaction is large but not infinite, it is still possible to treat the combustion problem as a perturbation of the Burke Schuman limit that we have used up to now. In this "flamelet" regime the deviations from infinitely fast chemistry are confined to a thin region around the location of the stoichiometric mixture fraction, whose width is a function of the Damköhler number.

Although the reaction zone is typically thin, there are cases in which the non-equilibrium effects are globally important. One such example is the H_2–O_2 reaction, in which an intermediate species is the H radical which, even in small amounts, controls the global exothermic properties. A simplified scheme

$$3\,H_2 + O_2 \rightarrow 2\,H_2O + 2\,H. \tag{20.a}$$

$$2\,H + M \rightarrow H_2 + M. \tag{20.b}$$

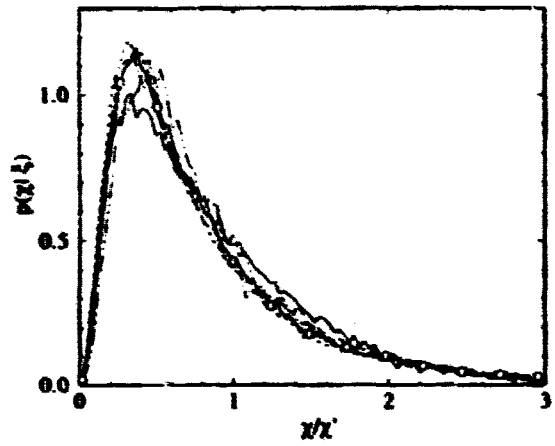

FIGURE 8. Pdfs of the mixture fraction gradients conditioned on the mixture fraction and compiled at different locations across the forced layer. ——— : $\xi = 0.2$. - - - - : 0.5. —·— : 0.8. —··— : 0.2. -o- : 0.5. The first three curves are for $y/\theta \in (-1, 1)$, $\langle\xi\rangle = 0.46$. The last two are for $y/\theta \in (1, 3)$, $\langle\xi\rangle = 0.72$.

was analyzed in (Sánchez *et al.* 1995). The first reaction is very fast and can be described by a conserved mixture fraction ξ and by an infinitely thin flame located at its stoichiometric isolevel ξ_s, while the second one is slower and leads to finite reaction rate corrections. The Damköhler number is defined as $D = (\kappa\chi^2 t_r)^{-1}$, where κ is the diffusion coefficient of the scalars, $\chi = \nabla\xi$ is the mixture fraction gradient at the stoichiometric level, and t_r is a chemical time which is only a weak function of temperature. The combination $\kappa\chi^2$ is usually called the scalar dissipation. In our approximation the only variable is χ, which therefore controls the structure of the flame. Other reactions involving radicals are technologically important. For example, the NO_x production in air is controlled by the temperature and by the concentration of the O radical.

It turns out that both the thickness and the maximum concentration in the radical containing region are proportional to $D^{-1/3}$, so that the total mass of H radical per unit flame area is proportional to

$$m \sim D^{-2/3} \sim \kappa^{2/3}\chi^{4/3}. \tag{21}$$

There is a chemical energy associated to this mass which leads to a lowering of the flame temperature. The dependence on a power of the gradients is common in many other examples of slightly out-of-equilibrium reactions (Williams 1985), although the exponents change from one case to another. Assume in general that $m = \kappa^n\chi^{2n}$. We can estimate the average mass fraction of radical by a procedure similar to that used to derive (6). If S is the area per unit volume we write

$$\langle Y_H\rangle = \int_S m\,\mathrm{d}S, \tag{22}$$

which we wish to transform into a probability integral. Introduce the joint pdf of χ and ξ and define dn as the element of length normal to the flame, located at $\xi = \xi_s$. We can define the volume element both in terms of the geometry and of the pdf

$$dV = dn\,dS = p_2(\chi, \xi)\,d\chi\,d\xi, \tag{23}$$

from where, using that $\chi = d\xi/dn$, it follows that $dS = \chi\, p(\chi, \xi)\,d\chi$, and

$$\langle Y_H \rangle = \int_{\xi=\xi_s} \chi\, m(\chi) p_2(\chi, \xi)\,d\chi = p(\xi_s) \int_0^\infty \chi\, m(\chi) p(\chi|\xi_s)\,d\chi. \tag{24}$$

The new pdf which appears in the second part of this equation is the pdf of gradients *conditioned* to $\xi = \xi_s$. Note that (24) has the same form as (6) for a function

$$f(\xi) = C_\chi \delta(\xi - \xi_s), \qquad C_\chi = \int_0^\infty \chi\, m(\chi) p(\chi|\xi_s)\,d\chi, \tag{25}$$

which is a delta function at the location of the flame, with a prefactor which depends on a moment of the conditional gradient pdf.

Formulas of this type have been known for a long time in the context of nonequilibrium chemistry (Bilger 1976), and the joint pdf of the gradients and of a mixing scalar has been the subject of intensive study. There is general consensus that the *unconditional* gradient pdf is approximately log-normal (Kerstein & Ashurst 1984, Anselmet & Antonia 1985, Eswaran & Pope 1987, Pumir 1994, Holzer & Siggia 1994), a form for which there is incomplete theoretical support (Gurvich & Yaglom 1967, Meyers & O'Brien 1981) but which seems to be only an approximation to the real one. There is less consensus on the conditional pdf and, in particular, on whether the conditional variance of the gradients is correlated to the value of ξ_s or to the local turbulent dissipation ϵ.

We have checked conditional gradient pdfs for our two shear layers and the results are shown in Figs. 8 to 10. It is seen in the first figure that the form of the pdf is fairly independent of both ξ_s and of the location in the flow, when each pdf is referred to its own standard deviation χ'. It also has a general log-normal shape, but is not really log-normal. Note that the figure includes pdfs conditioned on values of ξ_s close to zero, but compiled at locations at which the mean value of ξ is close to one.

Figure 9 presents a two-dimensional map of the conditional $\chi'(\xi)$, as a function of ξ and of the location across the layer. It was found that the map was more uniform if the conditional χ' was normalized with χ'_0, the unconditional standard deviation at the center of the layer, than when the normalization was done with the unconditional χ' at the particular y location. The first choice is used in the figure. It is seen that the dissipation has a central plateau, in which $\chi'/\chi'_0 \approx 1$, but becomes larger near the edges of the layer, and vanishes at $\xi = 0$ and $\xi = 1$. The latter is an obvious property of laminar unmixed fluid and will be discussed below. The decline is, on the other hand, quite local and only happens when ξ is

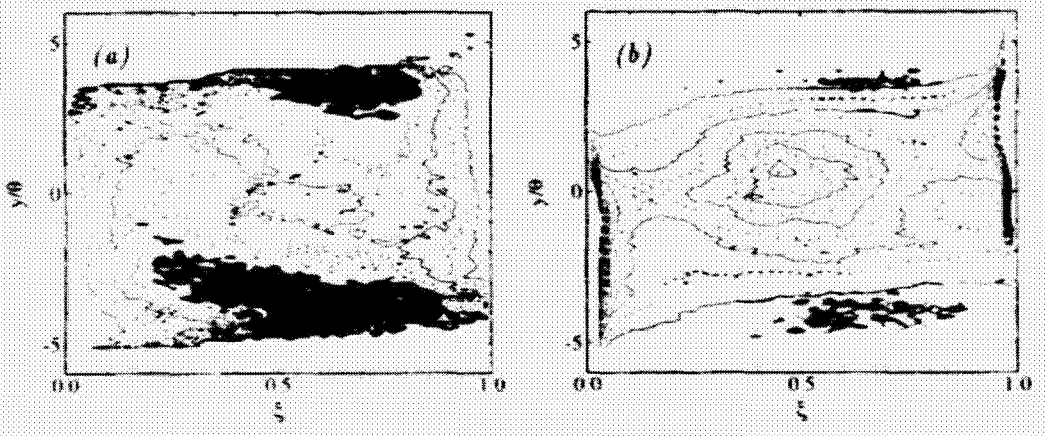

FIGURE 9. (a) Standard deviation of the scalar gradient magnitude as a function of y/θ, conditioned on ξ and normalized with the unconditional χ_0' at the central plane. Isolines are $\chi'/\chi_0' = 0.6(0.2)1.2$, and shaded area is $\chi'/\chi_0' \geq 1.4$. Forced layer. (b) Pdf of ξ for the same flow. Each horizontal section represents the pdf over one plane. Isolines $p(\xi) = 0.1(0.2)2.1$. Isolines alternate line style for clarity, and shaded regions correspond in both figures.

within 10% of the unmixed fluid. It should therefore not be important unless the stoichiometric ξ_s is very close to 0 or 1. The rise near the edges of the layer is real, but it corresponds to combinations of mixture fraction and location which are relatively improbable, as can be seen in Fig. 9.b, in which the areas of high scalar dissipation have been overlaid on a two dimensional map of the mixture fraction pdf. It is clear that they correspond to events whose probability is mostly below 10% and which will not have a large weight in (24).

In Fig. 10 we have presented cross-stream profiles of $\chi'(\xi)/\chi_0'$ for various values of ξ. These are essentially vertical cross-sections of Fig. 9.a, but they have been included to give some quantitative information on the magnitude of the deviations of the scalar dissipation from its unconditional value, and to present data from the unforced layer. As in the previous figure it is seen that the scalar dissipation in the central part of the layer, where the fluid is well mixed, is more or less constant and equal to its unconditioned maximum value, but that the gradients conditioned on mixtures fractions close to the free stream values and all the gradients near the edges of the layer have standard deviations that may differ from the global maximum by almost a factor of two. They also have a characteristic parabolic shape. Most of these high deviations occur at places at which the absolute probability of ξ is small, as seen on the figures on the right hand side of 10, which are conditioned on $p(\xi) > 0.1$, and they will only have a small effect on (24), but the effect is real and begs, at least, for some theoretical explanation.

It is also interesting to note that the general magnitude of the gradients is low. The value of $\chi_0'\theta$ is 1.5 for the unforced case and 2.0 for the forced one, so that the peak of the distributions in Fig. 8 is for gradients of the order of those of the

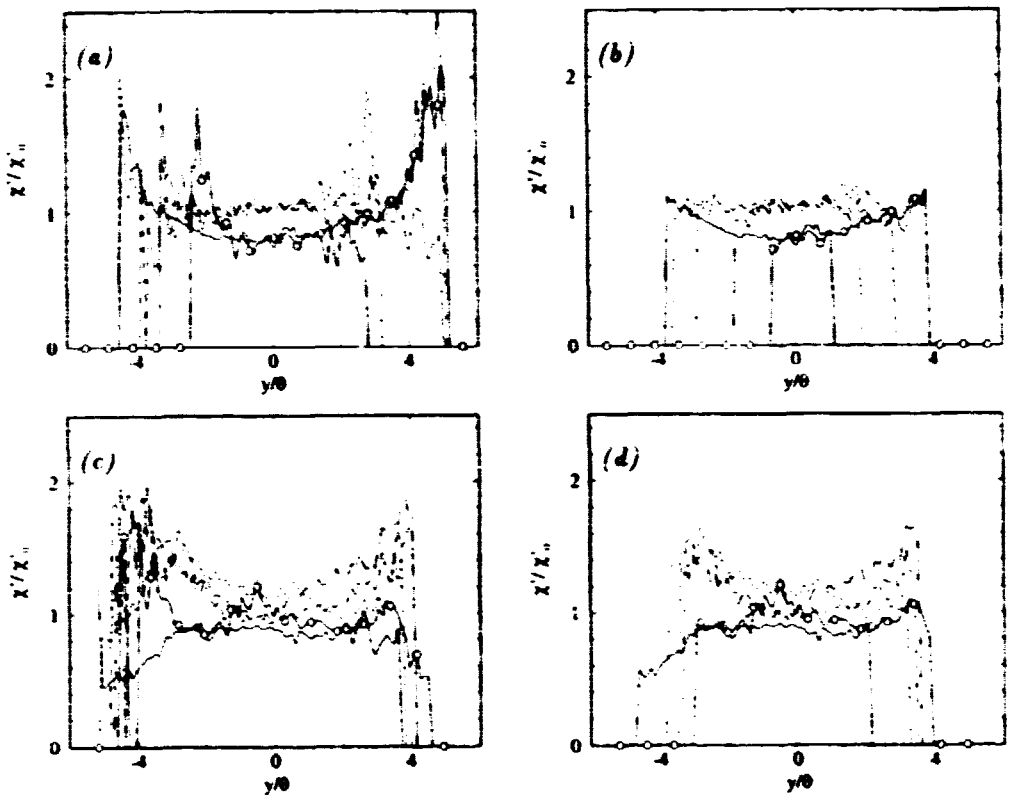

FIGURE 10. Variation of the conditional standard deviation of the gradients across the layer, as a function of ξ. ——— : ξ=0.1. - - - - : 0.3. — — : 0.5. — · — : 0.7. o : 0.9. (a) and (b) are for the unforced layer; (c) and (d) for the forced one. (a) and (c) present full profiles, but (b) and (d) are only for those points in which $p(\xi) > 0.1$.

mean ξ profile. Since high gradients lower the Damköhler number and may lead to extinction of the flame, the probability of local extinction for a given flow can be read from these distributions.

In LES computations it might be harder to estimate the value of χ_0' than that of the subgrid scalar fluctuation. The problem is that while the spectrum of ξ decreases with wavenumber approximately like $S(k) \sim k^{-5/3}$, that for the gradient increases as $k^2 S(k) \sim k^{1/3}$. Thus, while most of the contribution to ξ' comes from the resolved large scales, χ' comes mostly from the unresolved small ones. In terms of the standard LES or modeling equations, ξ'^2 is equivalent to the subgrid energy, while χ'^2 is equivalent to the subgrid dissipation. Conservation equations and closures for the subgrid dissipation have been written among others by Newman, Launder & Lumley (1981) and Elgobashi & Launder (1983).

The "engineering" consequences of the errors due to the gradient pdfs are summarized in Fig. 11. Assume that we are interested in computing the total amount of

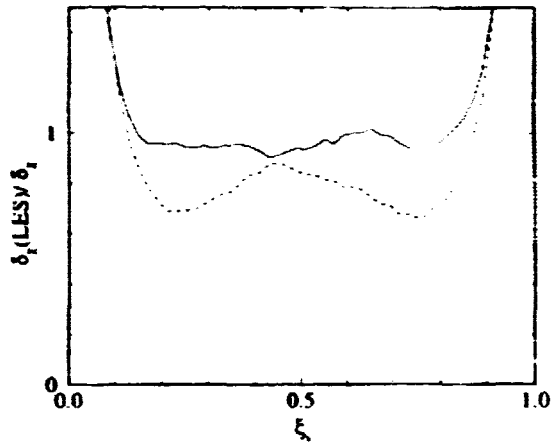

FIGURE 11. Computed scalar dissipation thickness as defined in text, compared to its DNS value. $h/\theta \approx 0.9$. ——— : unforced layer. ---- : forced.

H radical in the example (20), and that we use as a subgrid model for the gradients an average pdf taken from Fig. 8, and a representative unconditional χ_0' estimated for the center of the layer. Using (24) and integrating as in (19), we obtain a "radical" thickness which is the integral across the layer of the $\alpha + 1$ moment of the conditional pdf of the gradients, weighted with the pdf of the stoichiometric mixture fraction. This can be compared with the result of using the true distributions, and gives a global error due to the simplified assumption on the gradients. The result depends on the exponent α, but it is especially simple in the case of $\alpha = 1$ since the $\alpha + 1$ moment is then proportional to the scalar dissipation, and the integral can be obtained directly from the data in Fig. 9. In this case the approximation is equivalent to taking everywhere χ_0' as an approximation to $\chi'(\xi_s)$. This normalized thickness is not very different from the results for $\alpha = 4/3$, and is presented in Fig. 11. It is seen that, because the deviations from a universal distribution are mostly associated with places in which $p(\xi_s)$ is small, the final errors are still reasonable, especially for the unforced case, although they become $O(1)$ when the stoichimetric ratio approaches 0 or 1.

The reason for this failure is clearly that we have not taken into account that gradients have to vanish when the scalar is very near its maximum or minimum value. Simple engineering models should be able to alleviate this problem, but they are beyond the purpose of this paper. It is, however, interesting to estimate the width of the region for which a correction needs to be applied, which either from Fig. 9 or 11 is in this case about $\Delta\xi \approx 0.1$, but which can be related to the Reynolds number of the simulation. It follows from the form of the scalar spectrum that, for $Sc = O(1)$, most of χ' is associated with scales of the order of the Kolmogorov length η, and that the scalar fluctuations at length ℓ are $\Delta\xi_\ell \approx \xi'(\ell/L_c)^{1/3}$, where

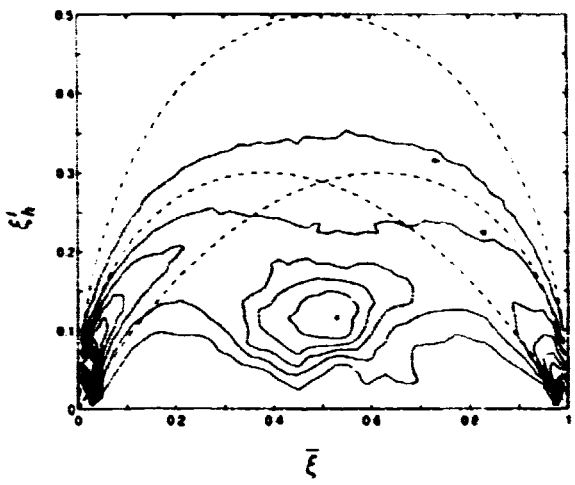

FIGURE 12. Jo[illegible]df for $\bar{\xi}$ and the subgrid fluctuation ξ_h'. Forced layer. $h/\theta = 0.88$. $y/\theta \in (-2,$ [illegible]olines are $p_2(\bar{\xi}, \xi_h') = 1(2)21$. Dashed semicircle is the limit of possible $(\bar{\xi}, \xi_h')$ [illegible]inations. Lower dashed lines are the limits below which the Beta distribution looks like a single broadened spike.

L_ϵ is an integral length. Since $L_\epsilon/\eta \approx Re_\lambda^{3/2}$ (Tennekes & Lumley 1972), it follows that the scalar fluctuations which carry the gradients are of order

$$\Delta\xi \approx \xi' Re_\lambda^{-1/2}, \tag{26}$$

which in our case 0.03. As long as ξ_s and $1 - \xi_s$ remain large with respect to this value, the small eddies should not be affected by the proximity to the level of the unmixed fluid, but if they are of the same order as (26), large gradients become impossible. This suggests that the width of the lateral bands in Fig. 11 should decrease as the Reynolds number increases, but it would be interesting to get experimental confirmation of that estimate.

5. Conclusions

We have shown that relatively simple subgrid models for the pdf of a conserved scalar can be used to obtain useful engineering approximations to global quantities in LES simulations of reacting nonpremixed turbulent shear flows in the fast chemistry limit. This is true even when the flow, in our case two different mixing layers, contains substantial intermittency.

The magnitude of the approximation error varies from less than 5% for the total amount of generated products, to about 15% for the pdf of the scalar itself. When finite reaction rate corrections are introduced in the flamelet limit, the model has to be extended to the pdf of the scalar gradients, conditioned on the value of the scalar. We have shown that those pdfs have an approximately universal form and that they can be expressed in terms of a single parameter, the conditional scalar

dissipation, which varies little except at places in which the probability of finding mixed fluid is low. It is possible in those cases to obtain the global concentration of intermediate products (e.g. radicals) with errors which stay in the 20-30% range, except for reactions with stoichiometric mixture fractions very near those of the free streams. We have argued that the range of stoichiometric ratios for which the approximation fails should decrease with increasing Reynolds numbers. It should be clear, however, that even within this range the integrated quantities such as product concentration or radiation thickness are well predicted (Fig. 7).

The particular approximation used in our experiments is the β model of (Cook & Riley 1994), but it is clear from the lack of correspondence between actual and assumed pdfs that other models might work as well. This also follows from similar observations of Cook & Riley in their paper, and is in contrast with the situation in RANS, in which it is known that good subgrid models have to be used for the assumed pdf if any but the simplest quantities are to be computed accurately (Fig. 5). It is important to understand the reason for this difference, which is essentially contained in Fig. 2, where the scalar pdfs are reasonably well approximated even in the absence of a subgrid model. This means that most of the scalar fluctuations are associated to scales which are resolved by the LES, even for coarse grids like the ones used here. All that is left for the model is to correct situations in which the subgrid fluctuation is strong enough that the use of the average as a representation of the pdf is no longer appropriate.

The situation would still be hopeless if those fluctuations were large enough to allow for a considerable latitude in the choice of subgrid pdfs, but this is fortunately not the case. Consider the $(\tilde{\xi}, \xi_h'')$ plane in Fig. 12. It can be shown that there can be no points above the dashed semicircle, and that pdfs that fall on the semicircle must be formed exclusively by unmixed fluid with $\xi = 0$ and $\xi = 1$. In the same way, pdfs on the horizontal axis are single delta functions of uniform fluid with $\xi = \tilde{\xi}$. Pdfs near that axis are roughly spread deltas, and those near the semicircle, spread bimodals. The border between the two cases varies for different models, but it is always near the two intermediate dashed lines in the figure, which correspond to the β-model. Below those lines, the pdf are bells, and almost any model should be equivalent. Pdfs within the two crescents correspond to spread deltas near one or the other free stream, and are also easy to model. Pdfs in the high-fluctuation central part of the diagram are harder, and are likely to depend on more than two parameters.

We have overlaid on the diagram a typical joint pdf for $\tilde{\xi}$ and ξ_h'', for a relatively wide filter in the intermittent "hard" flow but, even in this case, most of the mass of the distribution is associated with pdfs within the easily modeled part of the diagram. The Beta distributions form a flexible set of pdfs which interpolate smoothly between the different cases, and they provide a simple numerical tool to evaluate the necessary integrals. This explains their practical success, but the reason why the approximation works lies in the small value of the subgrid standard deviations in Fig. 12. Since we have seen in Fig. 3 that these deviations can be estimated from large-scale quantities using an infinite Reynolds assumption on the upper limit of

the spectrum, it is unlikely that much higher values might be found in other flows.

The small values of the fluctuations are also the reason why our relatively crude estimation of ξ'_k works so well. Even large errors in this estimation have relatively small effects on the final results, and some experiments in which the estimated subgrid fluctuations where systematically increased or decreased by 20% did not show any appreciable differences with the results shown here.

The convergence of the gradients also needs some discussion. It appears at first sight that, since the dominant contribution to χ'^2 comes from the high end of the spectrum, the estimates for this quantity would depend of the value of the Batchelor scale, and would diverge at high Reynolds numbers. What is needed in (21), however, is not χ'^2 but the scalar dissipation $\kappa\chi'^2$, and it is easy to see that, for a $k^{-5/3}$ spectrum, this quantity is independent of Reynolds number.

REFERENCES

ANSELMET, F. & ANTONIA, R. A. 1985 Joint statistics between temperature and its dissipation in a turbulent jet. *Phys. Fluids.* **28,** 1048-1054.

BILGER, R. W. 1976 The structure of diffusion flames. *Combust. Sci. Tech.* **13,** 155-170.

BILGER, R. W. 1989 Turbulent diffusion flames. *Ann. Rev. Fluid Mech.* **21,** 101-135.

BREIDENTHAL, R. E. 1981 Structure in chemically mixing layers and wakes using a chemical reaction. *J. Fluid Mech.* **109,** 1-24

BROADWELL, J. E. & BREIDENTHAL,R.E. 1982 A simple model of mixing and chemical reaction in a turbulent shear flow. *J. Fluid Mech.* **125,** 397-410.

COOK, A. W. & RILEY, J. J. 1994 A subgrid model for equilibrium chemistry in turbulent flows. *Phys. Fluids.* **6,** 2868-2870.

DOPAZO, C. 1977 On conditional averages for intermittent turbulent flows. *J. Fluid Mech.* **81,** 433-438.

ELGOBASHI, S. E. & LAUNDER, B. E. 1983 Turbulent time scales and the dissipation rate of temperature variance in the thermal mixing layer. *Phys. Fluids.* **26,** 2415-2419.

ESWARAN, V. & POPE, S. B. 1988 Direct numerical simulations of the turbulent mixing of a passive scalar. *Phys. Fluids.* **31,** 506-520.

GURVICH, A. S. & YAGLOM, A. M. 1967 Breakdown of eddies and probability distributions for small-scale turbulence, boundary layers and turbulence. *Phys. Fluids Suppl.* **10,** S 59-65.

HOLZER, M. & SIGGIA, E. D. 1994 Turbulent mixing of a passive scalar. *Phys. Fluids.* **6,** 1820-1837.

KERSTEIN, A. R. & ASHURST, W. T. 1984 Lognormality of gradients of diffusive scalars in homogeneous, two-dimensional mixing systems. *Phys. Fluids.* **27,** 2819-2827.

KOLLMAN, W. 1984 Prediction of intermittency factors for turbulent shear flows. *AIAA J.* **22,** 486-492.

KOLLMAN, W. & JANICKA, J. 1982 The probability density function of a passive scalar in turbulent shear flows. *Phys. Fluids.* **25,** 1755-1769.

KONRAD, J. H 1976 An experimental investigation of mixing in two-dimensional turbulent shear flows with applications to diffusion-limited chemical reactions. *PhD thesis.* Caltech (CIT-8-PU).

KOOCHESFAHANI, M. M. & DIMOTAKIS, P. E. 1986 Mixing and chemical reactions in a turbulent liquid mixing layer. *J. Fluid Mech.* **170,** 83-112.

LARUE, J C. & LIBBY, P. A. 1974 Temperature fluctuations in the plane turbulent wake. *Phys. Fluids.* **17,** 1956-1967.

LESIEUR, M. & ROGALLO, R. S. 1989 Large-eddy simulation of passive scalar diffusion in isotropic turbulence. *Phys. Fluids.* **A 1,** 718-722.

LIBBY, P. A. 1975 On the prediction of intermittent turbulent flows. *J. Fluid Mech.* **68,** 273-295.

LIBBY, P. A. & WILLIAMS, F. A. (editors) 1994 Turbulent reacting flow. Academic Press.

LIN, C. H. & O'BRIEN, E. E. 1974 Turbulent shear flow mixing and rapid chemical reaction: an analogy. *J. Fluid Mech.* **64,** 195-206.

MEYERS, R. E. & O'BRIEN, E. E. 1981 The joint pdf of a scalar and its gradient at a point in a turbulent fluid. *Combust. Sci. Tech.* **26,** 123-134.

MOIN, P., SQUIRES, K., CABOT, W. & LEE, S. 1991 A dynamic subgrid-scale model for compressible turbulence and scalar transport. *Phys. Fluids.* **3,** 2746-2757.

MUNGAL, M. G. & DIMOTAKIS, P. E. 1984 Mixing and combustion with low heat release in a turbulent shear layer. *J. Fluid Mech.* **148,** 349-382.

NEWMAN, G. R., LAUNDER, B. E. & LUMLEY, J. L. 1981 Modeling the behavior of homogeneous scalar turbulence. *J. Fluid Mech.* **111,** 217-232.

POPE, S. B. 1985 PDF methods for turbulent reacting flows. *Prog. Energy Combust. Sci.* **11,** 119-192.

POPE, S. B. & CORREA, S. M. 1988 Joint pdf calculation of a non-equilibrium turbulent diffusion flame. *21st. Symp. (Int.) Combust.*, 1341-1348. Pittsburg. Combust. Inst.

PUMIR, A. 1994 A numerical study of the mixing of a passive scalar in three dimensions in the presence of a mean gradient. *Phys. Fluids.* **6,** 2118-2132.

RÉVEILLON, J. & VERVISCH, L. 1996 Dynamic large eddy simulation and subgrid pdf for nonpremixed turbulent flame modeling. *Preprint.*

ROGERS, M. M. & MOSER, R. D. 1994 Direct simulation of a self-similar turbulent mixing layer. *Phys. Fluids.* **6,** 903-923.

SÁNCHEZ, A. L., LIÑÁN, A., WILLIAMS, F. A. & BALAKRISHNAN, G. 1995 *Combust. Sci. Tech.* **110**, 277-301.

SREENIVASAN, K. R. 1996 The passive scalar spectrum and the Obukhov-Corrsin constant. *Phys. Fluids.* **6**, 189-196.

TENNEKES, H. & LUMLEY, J. L. 1972 *A first course in turbulence.* MIT Press.

WILLIAMS, F. A. 1985 *Combustion Theory*, 2nd. ed., Benjamin-Cummings. Menlo Park. Ca.

NEXT
DOCUMENT

Turbulent flame propagation in partially premixed flames

By T. Poinsot[1], D. Veynante[2], A. Trouvé[3] AND G. Ruetsch[4]

1. Introduction

Turbulent premixed flame propagation is essential in many practical devices. In the past, fundamental and modeling studies of propagating flames have generally focused on turbulent flame propagation in mixtures of homogeneous composition, i.e. a mixture where the fuel-oxidizer mass ratio, or equivalence ratio, is uniform. This situation corresponds to the ideal case of perfect premixing between fuel and oxidizer. In practical situations, however, deviations from this ideal case occur frequently. In stratified reciprocating engines, fuel injection and large scale flow motions are fine-tuned to create a mean gradient of equivalence ratio in the combustion chamber which provides additional control on combustion performance. In aircraft engines, combustion occurs with fuel and secondary air injected at various locations resulting in a nonuniform equivalence ratio. In both examples, mean values of the equivalence ratio can exhibit strong spatial and temporal variations. These variations in mixture composition are particularly significant in engines that use direct fuel injection into the combustion chamber. In this case, the liquid fuel does not always completely vaporize and mix before combustion occurs, resulting in persistent rich and lean pockets into which the turbulent flame propagates.

From a practical point of view, there are several basic and important issues regarding partially premixed combustion that need to be resolved. Two such issues are how reactant composition inhomogeneities affect the laminar and turbulent flame speeds, and how the burnt gas temperature varies as a function of these inhomogeneities. Knowledge of the flame speed is critical in optimizing combustion performance, and the minimization of pollutant emissions relies heavily on the temperature in the burnt gases. Another application of partially premixed combustion is found in the field of active control of turbulent combustion. One possible technique of active control consists of pulsating the fuel flow rate and thereby modulating the equivalence ratio (Bloxsidge *et al.* 1987). Models of partially premixed combustion would be extremely useful in addressing all these questions related to practical systems. Unfortunately, the lack of a fundamental understanding regarding partially

1 Institut de Mecanique des Fluides de Toulouse and CERFACS, France
2 Laboratoire EM2C, Ecole Centrale Paris, France
3 Institut Francais du Petrole, France
4 Center for Turbulence Research

premixed combustion has resulted in an absence of models which accurately capture the complex nature of these flames.

Previous work on partially premixed combustion has focused primarily on laminar triple flames. Triple flames correspond to an extreme case where fuel and oxidizer are initially totally separated (Veynante *et al.* 1994 and Ruetsch *et al.* 1995). These flames have a nontrivial propagation speed and are believed to be a key element in the stabilization process of jet diffusion flames. Different theories have also been proposed in the literature to describe a turbulent flame propagating in a mixture with variable equivalence ratio (Müller *et al.* 1994), but few validations are available. The objective of the present study is to provide basic information on the effects of partial premixing in turbulent combustion. In the following, we use direct numerical simulations to study laminar and turbulent flame propagation with variable equivalence ratio.

2. Framework for analyzing and modeling partially premixed flames

Perfectly premixed combustion is usually described using a progress variable $c \equiv (Y_F^0 - Y_F)/(Y_F^0 - Y_F^1)$, where Y_F and Y_O are the fuel and oxidizer mass fractions, and the superscripts 0 and 1 refer to the values in the unburnt reactants and burnt products, respectively. Using the assumption of single-step chemistry and unity Lewis numbers, the progress variable provides a complete description of the transition from unburnt to burnt states and is the single relevant quantity used in model development and the postprocessing of simulation results. In partially premixed combustion, a new theoretical framework is required which will allow variable equivalence ratio along with simultaneous premixed and diffusion modes of combustion. This framework must use at least two scalar variables: one variable to describe the species composition, and a second variable to describe the progress of the premixed reaction. We use the mixture fraction Z as a description of the species composition, and a modified form of the progress variable c which accommodates the variable species composition in the fresh reactants.

We assume irreversible single step chemistry and unity Lewis numbers:

$$F + r_s(O + bN_2) \rightarrow P \tag{1}$$

where r_s is the stoichiometric oxidizer-fuel mass ratio and b is the N_2-O mass ratio, where N_2 is a diluent in the fresh reactants. The mixture fraction Z is then defined as:

$$Z \equiv \frac{(Y_F - Y_O/r_s + 1/(r_s(1+b))}{1 + 1/(r_s(1+b))}. \tag{2}$$

For stoichiometric mixtures, Z is equal to $Z_{st} = 1/(r_s(1+b)+1)$.* The fuel

* The equivalence ratio, $\phi \equiv r_s Y_F/Y_O$, is a more familiar quantity to the engineering community. However ϕ and Z are simply related (Müller *et al.* 1994) through $\phi = Z(1 - Z_{st})/Z_{st}/(1 - Z)$. We use Z rather than ϕ for the following reasons: ϕ is a conditional quantity that is only defined in the unburnt reactants whereas Z is not only defined everywhere in the flow but is also conserved through the reaction and Z is a linear combination of the species mass fractions and leads to straightforward expressions when averaging is employed.

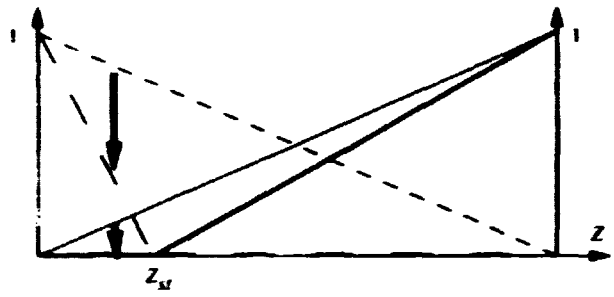

FIGURE 1. Fuel and oxidizer mass fractions as a function of the mixture fraction Z. ——— : Fuel Y_F^0/Y_F^∞ (mixing line) ; ---- : Oxidizer Y_O^0/Y_O^∞ (mixing line) ; ——— . Fuel Y_F^1/Y_F^∞ (fast chemistry line) ; — — — : Oxidizer Y_O^1/Y_O^∞ (fast chemistry line). The arrows indicate the transition from unburnt to burnt states in the case of perfectly premixed combustion, at a given equivalence ratio.

consumption rate, $\dot{\omega}_F$, and the heat release rate, $\dot{\omega}_T$, are written as:

$$\dot{\omega}_F = A\rho^p Y_F^n Y_O^m \exp(-T_a/T) \quad \text{and} \quad \dot{\omega}_T = q\dot{\omega}_F \tag{3}$$

where A, p, n, m are model constants, ρ is the mass density, and q is the heat of reaction per unit mass of fuel. The activation temperature T_a is specified via a Zeldovich number, $\beta \equiv \alpha T_a/T_b(Z_{st})$, where α is the stoichiometric heat release factor, $\alpha \equiv (T_b(Z_{st}) - T_0)/T_b(Z_{st})$. The unburnt gas temperature, T_0, is assumed uniform in the present study, and the adiabatic flame temperature, $T_b(Z_{st})$, is calculated under stoichiometric conditions.

The mixture composition upstream of the flame zone is only a function of Z and may be described by the two mixing lines shown in Fig. 1 and given by

$$\frac{Y_F^0}{Y_F^\infty} = Z \quad \text{and} \quad \frac{Y_O^0}{Y_O^\infty} = 1 - Z \tag{4}$$

where the superscript ∞ denotes the value of the mass fraction in the respective feeding streams, such that $Y_F^\infty = 1$ and $Y_O^\infty = 1/(1+b)$.

If the chemistry is sufficiently fast, the mixture composition downstream of the premixed flame corresponds to the classical Burke-Schumann limit where fuel and oxidizer cannot coexist. This limit is a function of Z alone, and is sketched in Fig. 1 and given by

$$\frac{Y_F^1}{Y_F^\infty} = Max\left(0, \frac{Z - Z_{st}}{1 - Z_{st}}\right) \quad \text{and} \quad \frac{Y_O^1}{Y_O^\infty} = Max\left(0, 1 - \frac{Z}{Z_{st}}\right). \tag{5}$$

Premixed combustion changes the mixture composition from an unburnt state, as described by Eq. (4), to a burnt state, as described by Eq. (5). Under the flamelet assumption, this change occurs in a thin flame zone. Note that in perfectly premixed combustion, the mixture fraction Z is constant and the transition from unburnt to

burnt states occurs on a vertical line in Fig. 1. In partially premixed combustion, the transition may occur with simultaneous variations in Z.

Equations (4) and (5) lead to the following generalized definition of the premixed reaction progress variable:

$$c \equiv \frac{ZY_F^{\infty} - Y_F}{ZY_F^{\infty} - Max\left(0, \frac{Z-Z_{st}}{1-Z_{st}}\right)Y_F^{\infty}}. \tag{6}$$

For lean mixtures, where $Z \leq Z_{st}$ everywhere, we have

$$c = 1 - \frac{Y_F}{ZY_F^{\infty}} \tag{7}$$

and for rich mixtures, with $Z \geq Z_{st}$ everywhere, the following holds:

$$c = \frac{ZY_F^{\infty} - Y_F}{ZY_F^{\infty} - \left(\frac{Z-Z_{st}}{1-Z_{st}}\right)Y_F^{\infty}} = 1 - \frac{Y_O}{(1-Z)Y_O^{\infty}}. \tag{8}$$

If Z is constant, Eq. (6) reduces to the standard definition of c used in perfectly premixed combustion.

For the sake of simplicity, we now limit our discussion to the case of a lean mixture. A balance equation for c may be derived from basic conservation equations for the fuel mass fraction Y_F and for the mixture fraction Z:

$$\frac{\partial c}{\partial t} + u_i \frac{\partial c}{\partial x_i} = \frac{1}{\rho}\frac{\partial}{\partial x_k}\left(\rho D \frac{\partial c}{\partial x_k}\right) - \frac{\dot{\omega}_F}{\rho Z Y_F^{\infty}} + \frac{2D}{Z}\frac{\partial c}{\partial x_i}\frac{\partial Z}{\partial x_i} \tag{9}$$

where u_i is the fluid velocity and D is the mass diffusivity. This equation is similar to the one obtained in perfectly premixed combustion, except for the last term on the right-hand side. The sign of this additional term can be either positive or negative, suggesting flame propagation can either accelerate or decelerate as a result of partial premixing. Following Trouvé and Poinsot (1994), the conservation equation for c may be used to define the displacement speed of iso-c surface contours:

$$s_d(c = c^*) = \frac{1}{|\nabla c|}\left[\frac{\partial c}{\partial t} + u_i \frac{\partial c}{\partial x_i}\right] = \frac{1}{|\nabla c|}\left[\frac{1}{\rho}\nabla \cdot (\rho D \nabla c) - \frac{\dot{\omega}_F}{\rho Z Y_F^{\infty}} + \frac{2D}{Z}\nabla c \cdot \nabla Z\right] \tag{10}$$

where all quantities are evaluated at $c = c^*$. An alternative form of this equation is:

$$s_d = \frac{1}{|\nabla c|}\left[\frac{1}{\rho}\nabla \cdot (\rho D \nabla c) - \frac{\dot{\omega}_F}{\rho Z Y_F^{\infty}}\right] - \frac{2D}{Z}\mathbf{n} \cdot \nabla Z \tag{11}$$

where $\mathbf{n}$ is the local unit vector normal to the iso-c surface, $\mathbf{n} \equiv -\nabla c/|\nabla c|$. Adopting a flamelet point of view, we identify the thin flame surface as an iso-c surface with $c^* = 0.8$. Equation (11) can then be interpreted as an expression for the flame

propagation speed. The terms within brackets on the right-hand side of Eq. (11) show the dependence of the flame propagation speed on the local mixture fraction Z. The last term on the right-hand side shows the dependence of the flame propagation speed on the local Z-gradient normal to the flame. Hence, one basic effect of incomplete reactant mixing is the modification of the local flame speed, $s_L(Z, \boldsymbol{n}\cdot\nabla Z)$.

We now discuss the implications of partial premixing in the framework of flamelet combustion. In the flamelet picture, the mean reaction rate may be written as the product of a mean mass burning rate times the flame surface density:

$$\langle\dot{\omega}_F\rangle = \langle\dot{m}\rangle_S\Sigma \tag{12}$$

where $\dot{m}$ is the local mass burning rate per unit flame surface area, $\dot{m} = \int_n \dot{\omega}_F dn$, and Σ is the mean flame surface-to-volume ratio (the flame surface density). The operator $\langle\rangle_S$ denotes a flame surface average (Pope 1988).

Partial premixing can induce modifications of the mean reaction rate through several mechanisms: a modification of the local flame structure and corresponding modifications to the mean mass burning rate $\langle\dot{m}\rangle_S$, and contributions to the flame wrinkling resulting in a modification to the flame surface density Σ. The effect of partial premixing on flame wrinkling may be analyzed by considering the exact balance equation for Σ (Pope 1988, Candel & Poinsot 1990, Trouvé & Poinsot 1994):

$$\frac{\partial\Sigma}{\partial t} + \nabla\cdot\langle\mathbf{u}\rangle_S\Sigma + \nabla\cdot\langle s_L\mathbf{n}\rangle_S\Sigma = \langle\kappa\rangle_S\,\Sigma = \langle\nabla\cdot\mathbf{u} - \boldsymbol{n}\boldsymbol{n} : \nabla\mathbf{u}\rangle_S\,\Sigma + \langle s_L\nabla\cdot\boldsymbol{n}\rangle_S\,\Sigma \tag{13}$$

where κ is the flame stretch, which is decomposed in Eq. (13) into a production term due to hydrodynamic straining and a production or dissipation term due to flame propagation. The propagation term is the mean product of the local flame propagation speed, s_L, times the local flame surface curvature, $\nabla\cdot\boldsymbol{n}$. Hence, the effect of partial premixing on the local flame speed, $s_L(Z, \boldsymbol{n}\cdot\nabla Z)$, as seen in Eq. (11), can be interpreted as an effect of partial premixing on flame stretch, $\kappa(Z, \boldsymbol{n}\cdot\nabla Z)$, and thereby an effect on Σ. One objective of the present study is to determine the relative weight of effects induced by partial premixing on Σ and $\langle\dot{m}\rangle_S$ relative to the effects of turbulence on these quantities.

3. Numerical configurations and diagnostics

In the present study, one-, two-, and three-dimensional direct numerical simulations are performed with variable density and simple chemistry. The simulations use a modified Padé scheme for spatial differentiation that is sixth-order accurate (Lele 1992), a third-order Runge-Kutta method for temporal differentiation, and boundary conditions specified with the Navier Stokes characteristic boundary condition procedure (Poinsot & Lele 1992). We refer the reader to the Proceedings of the 1990, 1992, and 1994 CTR Summer Programs for further details concerning the system of equations solved and the numerical methods

CONFIGURATION	FLOW	Z distribution (Lean=L Rich=R)
1/ x-inhomogeneous 1D unsteady flame	LAMINAR	
2/ y-inhomogeneous 2D steady flame	LAMINAR	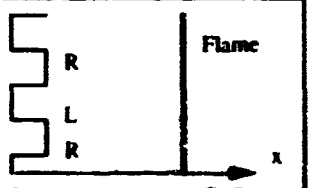
3/ xy-inhomogeneous 2D unsteady flame	LAMINAR	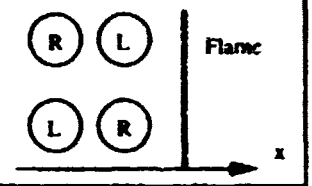
4/ xyz 3D flame	TURBULENT	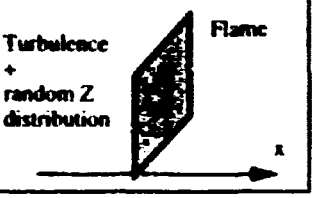

FIGURE 2. Configurations for DNS of partially premixed flames

The numerical configuration corresponds to a premixed flame propagating into a mixture with variable equivalence ratio. The mixture composition upstream of the flame is specified according to the probability density function, an integral length scale of the scalar field, and the relevant directions of inhomogeneity. The probability density function of Z is denoted as $p(Z)$ and can be characterized by its mean and rms values, $\langle Z \rangle$ and Z'. The amplitude of the fluctuations, ΔZ, can be used in place of the rms fluctuation for laminar cases. The characteristic integral length scale of the Z-field is denoted as l_Z. The directions of inhomogeneity in the Z-field are compared to the mean flame front orientation. We choose the direction of mean flame propagation as the x-direction. A numerical configuration is called x-inhomogeneous if gradients of Z exist in the x-direction, the direction normal to the mean flame front. Likewise, a $y-$inhomogeneous configuration corresponds to a case where species gradients exist tangent to the mean flame front. A fully turbulent three-dimensional configuration is called xyz inhomogeneous.

Four different configurations are pursued in this study, as depicted in Fig. 2: Case 1 is a one-dimensional, x-inhomogeneous, unsteady, laminar flame, with a double-peak Z-pdf. Case 2 is a two-dimensional, y-inhomogeneous, steady, laminar flame,

with a double-peak Z-pdf: Case 3 is a two-dimensional, xy-inhomogeneous, unsteady, laminar flame, with a triple-peak Z-pdf; and Case 4 is a three-dimensional, xyz-inhomogeneous, non-stationary, turbulent flame, with a Guassian Z-pdf. These configurations each have a slightly different simple chemistry scheme, as summarized in Table I. Case 4 corresponds to a single step reaction mechanism proposed by Westbrook & Dryer (1981) for C_3H_8-air combustion.

Table I. Parameters for the four simulation configurations.

Case	Dim	b	r_s	Z_{st}	p	n	m	β	α
1	1D	0	1	0.5	1	1	1	8	0.75
2	2D	0	1	0.5	2	1	1	8	0.75
3	2D	0	1	0.5	1	1	1	8	0.75
4	3D	3.29	3.64	0.06	1.75	0.1	1.65	8	0.75

In all cases we characterize the effects of partial premixing by comparing the results to those obtained with perfect premixing in the same configuration. The effects of partial premixing on the local flame structure are characterized by the mass burning rates:

$$r \equiv \frac{\dot{m}}{\dot{m}(Z_{st})} \quad \text{and} \quad r' \equiv \frac{\dot{m}}{\dot{m}(\langle Z \rangle)} \tag{14}$$

where the unprimed quantity uses the stoichiometric homogeneous laminar flame as a reference, whereas the primed quantity uses the homogeneous laminar flame with $Z = \langle Z \rangle$. The global effects of partial premixing are characterized by the total reaction rate ratios:

$$R \equiv \frac{\Omega}{\Omega_0(Z_{st})} \quad \text{and} \quad R' \equiv \frac{\Omega}{\Omega_0(\langle Z \rangle)} \tag{15}$$

where $\Omega \equiv \int_V \langle \dot{\omega}_F \rangle dV$, with Ω_0 corresponding to a homogeneous, planar, laminar flame. These total reaction rate ratios can be rewritten as:

$$R = \frac{\int \langle r \rangle_S \Sigma dV}{\int \Sigma dV} \frac{\langle S_V \rangle}{S_0} \quad \text{and} \quad R' = \frac{\int \langle r' \rangle_S \Sigma dV}{\int \Sigma dV} \frac{\langle S_V \rangle}{S_0} \tag{16}$$

where S_V is the total flame surface area within V, and S_0 is the projected area of the flame on a surface perpendicular to the direction of mean propagation. The first ratio in these expressions for R and R' accounts for modifications of the mean mass burning rate due to partial premixing, and the second ratio accounts for flame surface wrinkling due to turbulence and partial premixing. We write $W \equiv S_V/S_0$ and $\widehat{r'} \equiv \int \langle r' \rangle_S \Sigma dV / \int \Sigma dV$. The effects of partial premixing on flame temperatures are characterized by the following temperature ratios:

$$\theta \equiv \frac{T_{max} - T_0}{T_{max,0}(Z_{st}) - T_0} \quad \text{and} \quad \theta' \equiv \frac{T_{max} - T_0}{T_{max,0}(\langle Z \rangle) - T_0} \tag{17}$$

where $T_{max,0}$ corresponds to the case of a homogeneous, planar, laminar flame.

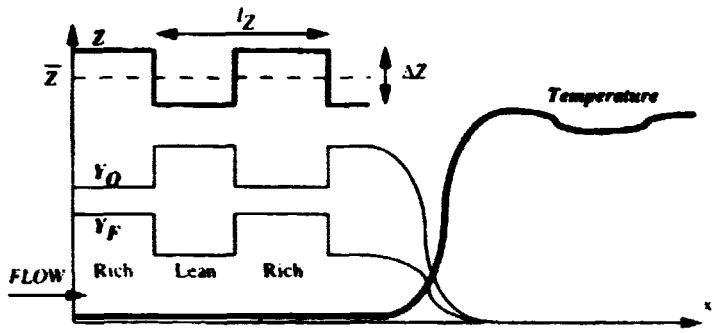

FIGURE 3. Case 1: One-dimensional, x-inhomogeneous, unsteady, laminar flames

4. Case 1: One-dimensional, x-inhomogeneous, unsteady, laminar flames

In this case, the inhomogeneity of reactant species is longitudinal with respect to the flow, and thus the flame response to temporal fluctuations in the mixture composition is studied. The mixture composition is forced at the inlet of the computational domain in order to generate harmonic perturbations in the Z-field upstream of the flame. These perturbations in Z are characterized by their mean value, $\langle Z \rangle$, their amplitude, ΔZ, and their wavelength l_Z (see Fig. 3). This case is well-suited to bring basic information on both flame structure modification and quenching by partial premixing.

In order to study the flammability limits of partially premixed flames, it is important to determine whether the simplified kinetic scheme used in the simulation is capable of reproducing realistic variations of the laminar flame speed, S_L, when variations occur in the mixture composition or equivalence ratio, ϕ. In particular, the lean and rich flammability limits must be correctly predicted. The single-step chemistry model presented in Section 2 does not have this capability unless heat losses are added to the energy equation. The choice of a nonadiabatic flame may be viewed as a simple fix to produce realistic variations $S_L(\phi)$, which is presented in Fig. 4. Following Williams (1985), we use a volumetric heat loss term $\mathcal{L}$ that is linear in $(T - T_0)$ (see also Poinsot *et al.* 1991):

$$\mathcal{L} = \frac{h}{\beta} \tau \rho_0 \frac{S_L(Z_{st})^2}{D_{th}} C_p T_0 \frac{\alpha}{1-\alpha} \tag{18}$$

where h is a model constant, chosen as $h = 0.031$, and $\tau \equiv (T - T_0)/(T_b(Z_{st}) - T_0)$.

As seen in Fig. 4, no abrupt transition to extinction is observed for the adiabatic single-step chemistry model, where very lean and very rich mixtures continue to burn. As a result, flame speeds are unrealistically high in these lean and rich regions. However, a domain of flammability is obtained using nonadiabatic single-step chemistry. This domain compares reasonably well to computations performed with a detailed mechanism proposed by Westbrook & Dryer (1981), for CH_4-air flames. While the prediction of the rich flammability limit is overestimated, the overall level of accuracy is deemed acceptable at the present stage.

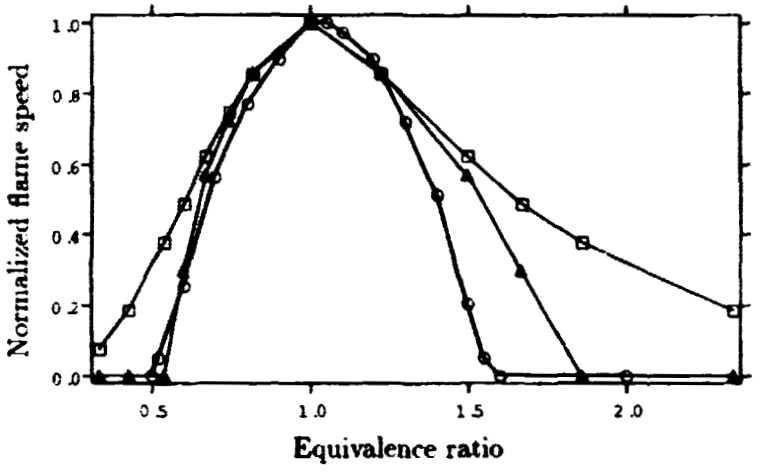

FIGURE 4. Variations of normalized flame speed with equivalence ratio, $s(\phi)$, for a one-dimensional, homogeneous, laminar flame. □ : Adiabatic one-step chemistry; ▪ : Non-adiabatic one-step chemistry; o : Detailed mechanism.

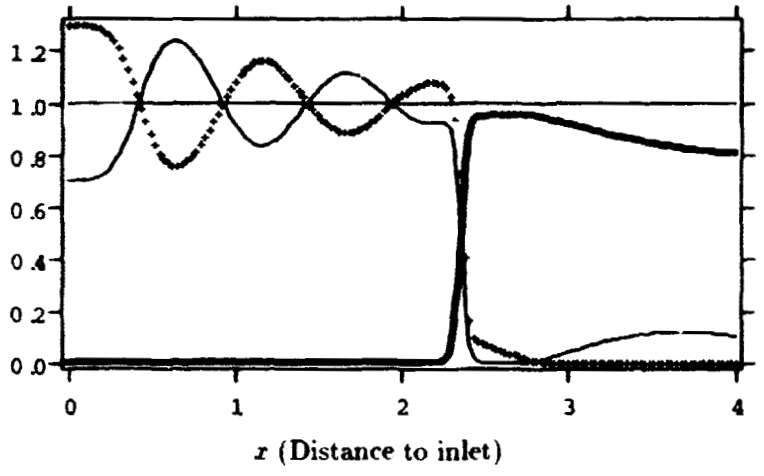

FIGURE 5. Case 1 with $\langle Z \rangle = Z_{st} = 0.5$, $\Delta Z = 0.2$ (at inlet), and $l_Z/\delta_L^0 = 14$, where δ_L^0 is the thermal thickness of the perfectly premixed flame with $Z = \langle Z \rangle$. + : Reduced Y_f ; —— : Reduced Y_O ; —— : Reduced temperature τ.

Figure 5 presents a typical snapshot of Y_F, Y_O, and temperature profiles across the flame zone. Species mass fractions are normalized in this figure by their stoichiometric values. One difficulty in these low Reynolds number simulations is that the perturbations in Z imposed at the inlet are strongly affected by molecular diffusion and are significantly damped before they reach the flame. In this situation, the flame response has the undesirable feature of depending on the flame location inside the computational domain. Nevertheless, we feel that the present simulations

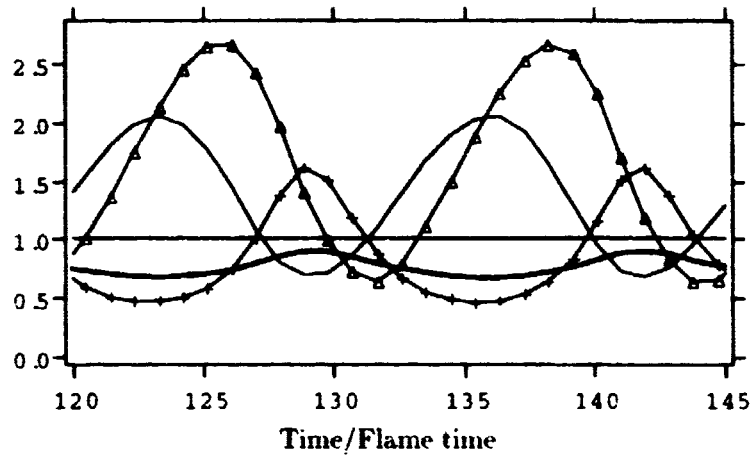

FIGURE 6. Case 1 with $\langle Z \rangle = 0.4$, $\Delta Z = 0.2$ (at inlet), and $l_Z/\delta_L^0 = 11$, where δ_L^0 is the thermal thickness of the perfectly premixed flame with $Z = \langle Z \rangle$. ——— : reduced flame thickness ; ——— : reduced maximum temperature θ' ; + : reduced flame speed r' ; ▵ : flame distance to inlet.

can still be used to describe the basic features of partially premixed flames.

The example presented in Fig. 5 corresponds to a perturbation in Z with alternative fuel rich ($Z \geq Z_{st}$) and fuel lean ($Z \leq Z_{st}$) pockets. The excess fuel and excess oxidizer that are not consumed by the premixed flame will burn in a diffusion flame. The intensity of this post-diffusion flame is rather low and in the case of Fig. 5, some unburnt fuel is found at the outlet of the computational domain. In a similar simulation, but with $\langle Z \rangle = 0.45$, there is no leakage of fuel.

Figure 6 presents typical time variations of the different diagnostics used to characterize the flame response. When the flame meets a pocket with a mixture composition close to stoichiometry, the flame speed and temperature increase, the flame thickness decreases, and the flame moves upstream in the computational domain. The converse is true when a pocket of mixture composition further from stoichiometry reaches the flame. Variations in flame speeds are large, with $0.5 < r' < 1.5$, and show deviations from a sinusoidal evolution: the time required for the flame to cross a given constant-Z pocket increases as Z moves away from stoichiometric conditions. This bias accounts for a reduced overall mean combustion rate compared to the perfectly premixed case, thus $R' < 1$.

Depending on the values of $\langle Z \rangle$, ΔZ, and l_Z, the effect of partial premixing on the mean reaction rate can either be positive, with $R' > 1$, or negative, with $R' < 1$. Figures 7 and 8 show that this effect remains weak, however, except for conditions close to the flammability limit. In Fig. 7, mixtures with $\Delta Z = 0.2$, and $\langle Z \rangle$ below 0.38 are quenched, while they would burn if perfectly premixed ($\Delta Z = 0.0$). Similarly, in Fig. 8 mixtures with $\Delta Z = 0.2$, $\langle Z \rangle = 0.4$, and $l_Z/\delta_L^0 > 14$ are quenched while they would burn if perfectly premixed. Fig. 8 also shows a comparison between the adiabatic and nonadiabatic simulations. Differences are

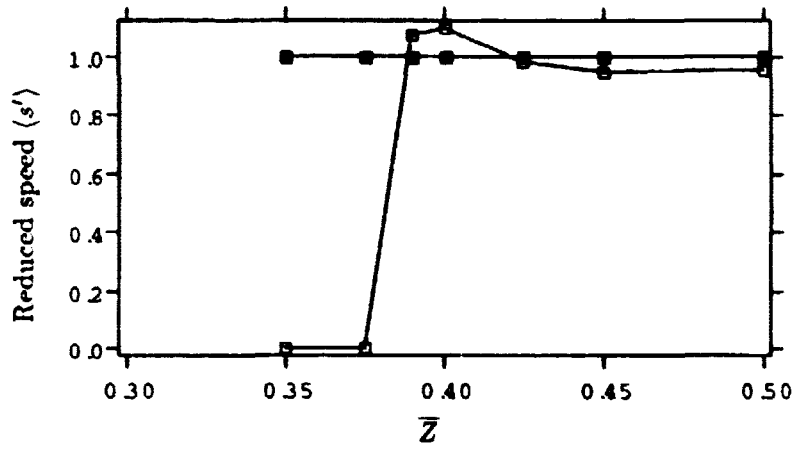

FIGURE 7. Case 1 with variable $\langle Z \rangle$. □ : R' (reduced overall mean combustion rate) in partially premixed flames ($\Delta Z = 0.2$ at inlet) ; ■ : R' in perfectly premixed flames ($\Delta Z = 0.$).

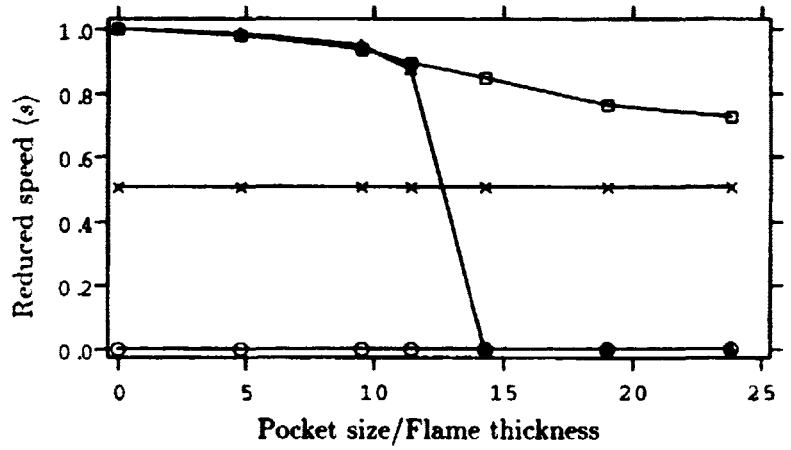

FIGURE 8. Case 1 with variable l_Z, $\langle Z \rangle = 0.4$, and $\Delta Z = 0.2$ (at inlet). □ : R (reduced overall mean combustion rate) in adiabatic flames ; ▲ : R in non-adiabatic flames ; × : asymptotic value S_a for adiabatic flames ; ○ : asymptotic value S_a for non-adiabatic flames.

small until transition to extinction is observed in the non-adiabatic case. In both cases, as l_Z becomes very large, the mean flame speed tends to an asymptotic value S_a given by the following expression:

$$S_a = \frac{2}{\frac{1}{S_L^-} + \frac{1}{S_L^+}} \tag{19}$$

where $S_L^- = S_L(\langle Z \rangle - \Delta Z/2)$ and $S_L^+ = S_L(\langle Z \rangle + \Delta Z/2)$. In Fig. 8, without heat

loss, $S_a/S_L(Z_{st}) = 0.51$; with heat loss, $S_a = 0$.

In summary, partial premixing in the one-dimensional case leads to strong temporal variations of the laminar flame structure, and in particular to strong fluctuations in the instantaneous values of the flame speed S_L and the mass burning rate $\dot{m}$. In the absence of quenching, these variations tend to cancel in the mean, and $\langle S_L \rangle$ and $\langle \dot{m} \rangle$ remain close to the values of S_L and $\dot{m}$ obtained in perfectly premixed systems. However, quenching induced by partial premixing has been observed in the case of strong variations in mixture composition, characterized by large amplitudes of $\Delta Z > 0.2$, or large length scales of $l_Z/\delta_L^0 > 10$.

5. Case 2: Two-dimensional, y-inhomogeneous, steady, laminar flames

In this configuration, inhomogeneities in the reactant species exist in the direction tangent to the flame, allowing the solution to converge to a steady state. This configuration is depicted in Figure 2, where the mixture fraction at the inlet is given by:

$$Z = \langle Z \rangle - \frac{\Delta Z}{2} \cos\left(\frac{2\pi y}{l_Z}\right)$$

For two dimensional flows, the parameter space becomes larger than the one-dimensional flows discussed previously, and we restrict ourselves to varying $\langle Z \rangle$ and ΔZ while maintaining l_Z constant. As these parameters are varied, we expect both the flame structure and propagation speed to change. As a result, the flame can advance or recede out of the computational domain. To avoid this problem, the inlet velocity, which remains uniform, is adjusted to accommodate changes in the flame speed. This procedure has been used in partially premixed combustion (Ruetsch *et al.* 1995 and Ruetsch and Broadwell 1995) and results in a steady-state configuration. This allows a well defined flame speed to be assessed in each run. Note that by defining the flame speed as the inlet velocity required to reach a steady state, we are considering a displacement speed.

As in the one-dimensional case, the mixture fraction is greatly modified from the time it is specified at the inlet to the time it reaches the flame. The range in mixture fraction at the flame surface is affected by several phenomena, including diffusion and the strain induced by the flame. Strain does not directly affect the mixture fraction, but does so implicitly by modifying the mixture fraction gradient in the lateral direction, which alters mass diffusion. The range of mixture fraction on the flame surface for all cases is shown in Fig. 9 as a function of the average mixture fraction. In addition to the reduction in mixture fraction range, the minimum and maximum values are no longer centered around the average value of the mixture fraction. The reason for this asymmetry becomes clear when we examine the structure of the flames when exposed to gradients in the mixture fraction.

5.1 Flame structure

The reaction rates and streamlines for flames subjected to different levels of $\langle Z \rangle$ are displayed in Fig. 10. For $\langle Z \rangle = Z_{ST} = 0.5$, we observe two leading edge flames within the domain. Since $\langle Z \rangle$ is at the stoichiometric value, we expect two equidistant leading edge flames and two equidistant troughs. As we decrease $\langle Z \rangle$ from the

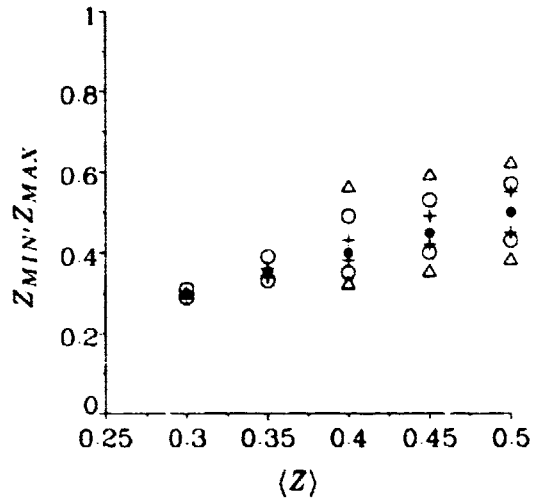

FIGURE 9. Range in mixture fraction on flame surface as a function of $\langle Z \rangle$. The different symbols correspond to different values of ΔZ at the inlet according to the following: • represents the homogeneous case ($\Delta Z = 0$ at inlet), + represents $\Delta Z = 0.2$, ○ represents $\Delta Z = 0.4$, and △ represents $\Delta Z = 0.8$. For the chemical scheme used in this case, $Z_{ST} = 0.5$.

stoichiometric value, this symmetry no longer exists. For the case with $\langle Z \rangle = 0.45$, we still have two stoichiometric points on the flame surface, although they have moved closer together. For the other cases of $\langle Z \rangle = 0.4$ and 0.35, stoichiometric points no longer exist on the flame surface. In these cases, the leading edge is located where the mixture fraction is closest to the stoichiometric value.

The reason for the asymmetric nature of the minimum and maximum values of Z on the flame surface, as observed in Fig. 9, can be easily understood from the flame shapes in Fig. 10. Diffusion of species has a longer time to act before reaching the flame surface the farther the flame is from the inlet. Therefore, the difference in mixture fraction along a horizontal line between the flame's leading edge and inlet is smaller than this difference along a line passing through the flame trough. For the case of $\langle Z \rangle = 0.5$, the maximum and minimum values of Z are both located in the troughs which occur at the same horizontal location, and we have symmetry in minimum and maximum values. As we depart from average stoichiometry, with $\langle Z \rangle < Z_{ST}$, the trough with rich composition moves forward and the lean trough backwards, so that diffusion has less time to act in the rich branch as compared to the lean branch. Therefore, the mixture fraction in the lean branch moves closer to stoichiometry.

Another factor that affects Z on the flame surface concerns the role strain plays on species diffusion. The divergence of streamlines in front of the leading edge reduces the mixture fraction gradient along the flame surface at that location, thus inhibiting diffusion. The opposite occurs in the flame trough, where the gradient in mixture fraction steepens due to the convergence of streamlines, accentuating the

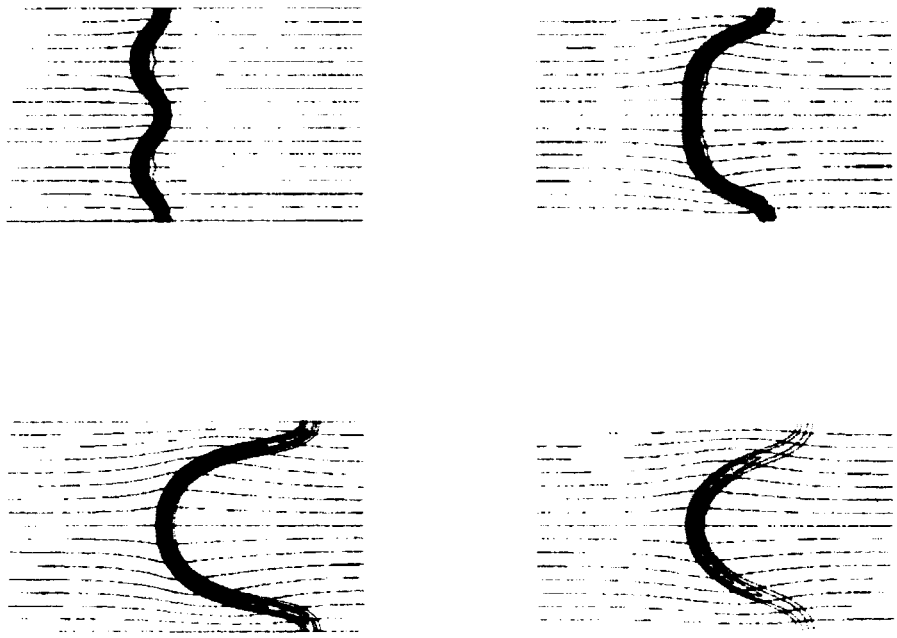

FIGURE 10. Contour plots or streamlines and reaction rates for simulations with $\Delta Z = 0.4$ and: $\langle Z \rangle = 0.5$ top left, $\langle Z \rangle = 0.45$ top right, $\langle Z \rangle = 0.4$ bottom left, and $\langle Z \rangle = 0.35$ bottom right.

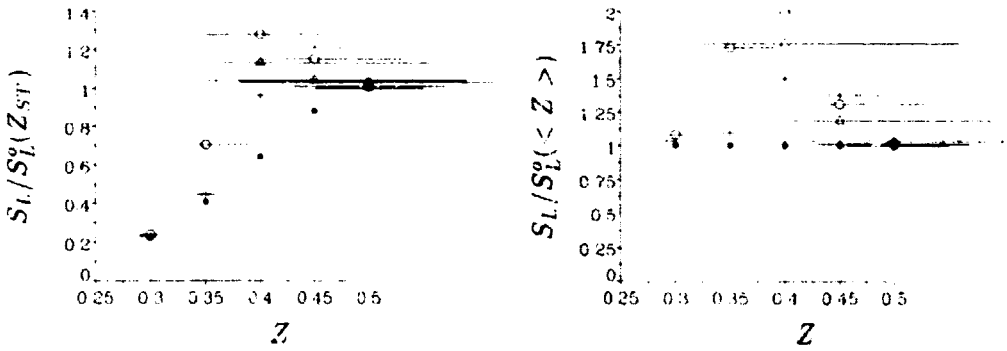

FIGURE 11. Propagation speed as a function of mixture fraction. The speeds are normalized by the homogeneous case at stoichiometric conditions, $S_L^0(Z_{ST})$, on the left, and by the homogeneous case at the average mixture fraction, $S_L^0(\langle Z \rangle)$ on the right. In addition to displaying the average mixture fraction of the run with the symbols, the range of mixture fraction on the flame surface is shown by the lines through each symbol. The legend for the symbols is provided in Fig. 9.

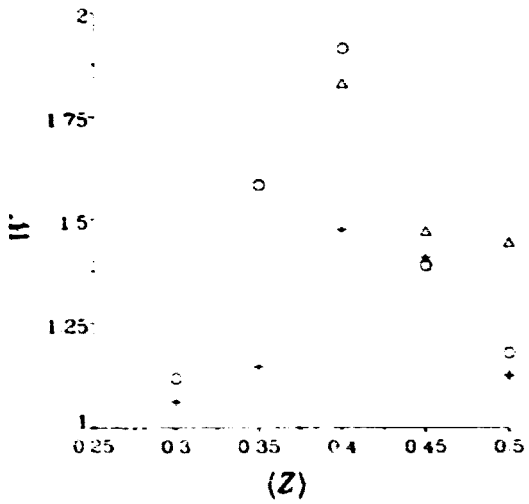

FIGURE 12. Flame wrinkling for the simulations. See Fig. 9 for a description of the symbols.

diffusion process.

As we progress towards lean mixture fractions to the point where stoichiometric conditions do not exist on the flame surface, the flame shape changes to the point where the spatial extent doubles, as the trough corresponding to rich mixture fractions disappears. This, in effect, alters the parameter l_Z without changing the computational domain. This doubling in lateral dimension has an effect on the flame speed as well as the flame shape, as is discussed in the next section.

5.2 Flame speed

When discussing the change in flame speed due to the inhomogeneous medium, it is useful to relate this displacement speed to that of the homogeneous case at both the average and stoichiometric mixture fractions, as shown in Fig. 11. In these figures, both the average mixture fraction at the inlet and the range of mixture fraction on the flame surface are shown by the symbols and lines, respectively. We begin discussion of the flame speed examining what occurs when the average composition is stoichiometric. Independent of the range in mixture fraction at the flame surface, the propagation speed remains that of the homogeneous case. This behavior was previously observed (Ruetsch and Broadwell 1995) when studying confined flames. For this value of l_Z, the lateral divergence of streamlines due to heat release is greatly inhibited by the confinement, and therefore the heat release mechanism responsible for enhanced flame speeds, as in the case of triple flames (Ruetsch and Broadwell 1995), is absent. As we depart from stoichiometry in the mean, the flame shape changes, effectively doubling l_Z, and we quickly move into a regime where streamline divergence is much stronger in front of the leading edge. An increase in flame speed is observed relative to $S_L(\langle Z \rangle)$, and in some cases even relative to $S_L''(Z_{ST})$. It is interesting to note that flames with lean compositions

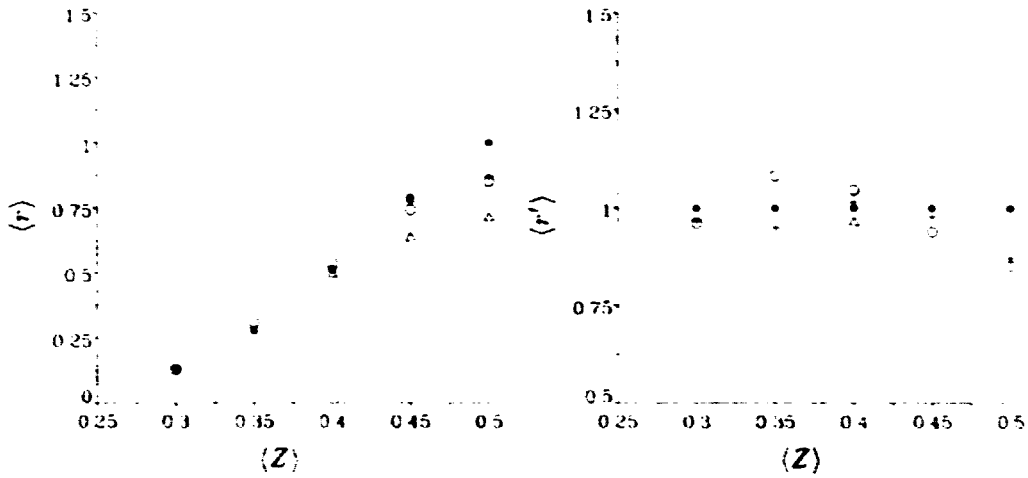

FIGURE 13. Average local reaction rate along flame surface normalized by the homogeneous case at Z_{ST} (left) and $\langle Z \rangle$ (right), as a function of the average mixture fraction.

along the entire length of the flame, designated in Fig. 11 by lines that do not cross $Z = Z_{ST} = 0.5$, can achieve flame speeds greater than the homogeneous stoichiometric case.

As $\langle Z \rangle$ further decreases, the reduction in reaction rate along the flame intensifies, and in spite of the streamline divergence the flame speed drops. As the flame speed drops, and along with it the inlet velocity in order to stabilize the flame in the computational domain, the mixture has a longer time to laterally diffuse as it approaches the flame. It is for this reason that the small range in mixture fraction at the flame surface is observed for very lean mixtures, apparent from Fig. 9, and is why the flame speed collapses to the homogeneous case.

Thus far we have concentrated on variations of flame speed with the average mixture fraction. We now turn our attention to how the fluctuation in mixture fraction about the mean affects the flame speed. As we have already mentioned, at mean stoichiometry the degree of inhomogeneity plays no role in flame speed. As the average mixture becomes lean, the flame speed increases as long as the composition at the leading edge stays near the stoichiometric value. For flames where the composition along the surface is always lean, the greatest speeds in absolute terms occur when the range in mixture fraction is the largest. This feature can be explained if we re-examine the flame structure. The streamline divergence depends on the flame curvature, which itself is determined by the local burning rate hence species composition. Therefore, the greatest range in mixture fraction along the surface would generate the greatest streamline divergence and increase in flame speed. This does not hold when the composition along the flame surface crosses stoichiometric values.

5.3 Fuel consumption

Having discussed the flame structure and propagation, we now turn our attention

to fuel consumption. Due to mass conservation, the global consumption rates given by R and R' are equivalent to the flame speed ratios shown in Fig. 11. There are slight discrepancies between the global reaction rate and flame speed ratios resulting from excess fuel leaving the domain in cases which have stoichiometric values on the flame surface. However, the domain is large enough, with a grid of $N_x = 361$ and $N_y = 121$, that almost all of the fuel is burned in either the premixed or diffusion modes before the flow exists the domain. We therefore use the flame speed ratios in Fig. 11 as R and R' in the following discussion.

For laminar flames we decompose the global burning rate in terms of the flame wrinkling, W, and the average burning rate along the flame surface, $\langle r \rangle_S$ or $\langle r' \rangle_S$, according to the following relations:

$$R = \langle r \rangle_S W; \qquad R' = \langle r' \rangle_S W \tag{20}$$

Th. frame wrinkling is given in Fig. 12, and the mean reaction rates along the flame surface in Fig. 13. It is clear from Figs. 12 and 13 that flame wrinkling is the predominant factor in the global reaction rate modification.

The predominance of flame wrinkling over reaction zone modification is apparent for this steady-state configuration. We must now turn our attention to assessing whether this trend prevails when we consider flows with unsteadiness in both the scalar and flow fields. We address this issue for unsteady scalar fields in the following case, followed by a fully turbulent configuration.

6. Case 3: 2D, *xy*-inhomogeneous, unsteady, laminar flames

Case 3 includes two slightly different configurations, shown in Fig. 14. In Case 3a, the perturbations in Z correspond to an isolated pair of fuel lean and fuel rich pockets, whereas in Case 3b, the perturbations in Z correspond to an infinite array of such pockets. Case 3a provides basic information on the impulse response of a laminar flame subjected both to normal and tangential Z gradients, while Case 3b provides information on the response of a flame to periodic Z forcing. Table II gives the run parameters for the different simulations.

Table II. Simulation parameters for Case 3

Run	Case	$\langle Z \rangle$	ΔZ	$l_Z/\delta_L^0(\langle Z \rangle)$	h	$N_x \times N_y$
A	3a	0.4	0.2	5.0	0.	127 x 127
B	3a	0.35	0.2	3.5	0.	127 x 127
C	3b	0.4	0.2	5.	0.	127 x 127
D	3b	0.35	0.2	3.5	0.	127 x 127
E	3b	0.3	0.2	1.9	0.	127 x 127
F	3a	0.4	0.2	5.0	0.031	127 x 127
G	3a	0.4	0.2	6.2	0.031	127 x 127

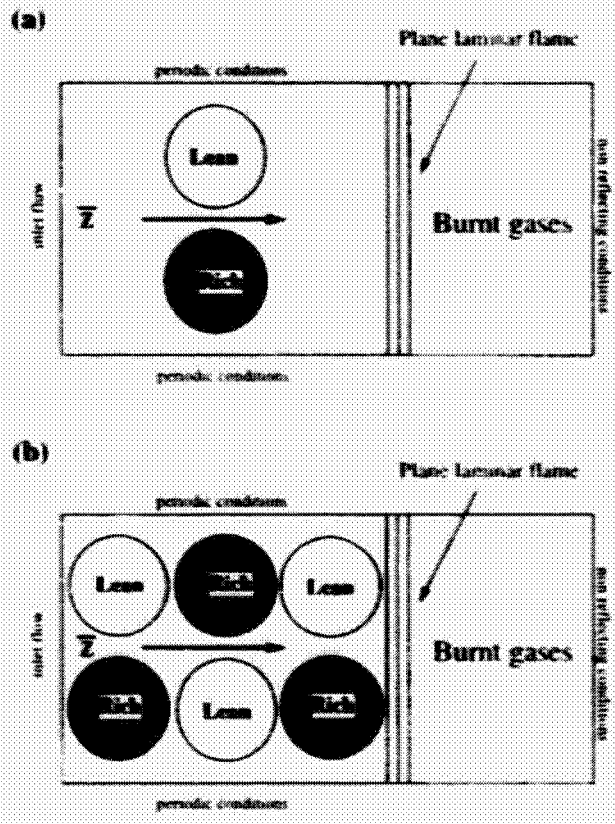

FIGURE 14. Case 3: Two-dimensional, xy inhomogeneous, unsteady, laminar flames. (a) an isolated pair of lean ($Z = \langle Z \rangle - \Delta Z/2$) and rich ($Z = \langle Z \rangle + \Delta Z/2$) pockets, of size l_Z; (b) an infinite array of such pockets.

Figure 15 presents a typical snapshot of isocontours of ω_F, Z, c, and Y_P, as obtained in run A. Note that the generalized reaction progress variable defined in (7) is a good marker of the premixed flame front. Because it is affected by mixing within the burnt gases, Y_P is not a good choice to track the flame front. At the top of the figure, the flame is seen to interact with a fuel lean pocket ($Z = 0.3$), during which it decelerates and is convected downstream. At the bottom of the figure, the flame crosses a fuel rich pocket ($Z = Z_{st} = 0.5$), accelerates, and is convected upstream. These variations in the local flame displacement speed u correspond to strong variations in the local flame structure, as observed in Case 1. They also correspond to flame surface production.

As done in the steady-state situation of Case 2, we now compare the relative weight of the two basic effects of partial premixing as indicated in Eq. (20): the modification of the flame structure through $\langle \dot{\omega} \rangle_S$, and the generation of flame surface due to wrinkling, W. Figure 16 compares the temporal evolution of the relative contributions of these two terms to the global reaction rate from data obtained in

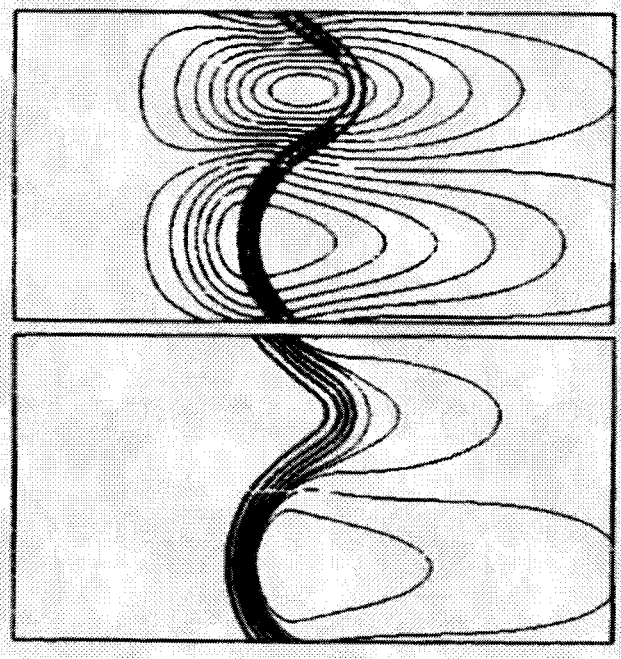

FIGURE 15. Case 3, run A, with $\langle Z \rangle = 0.4$, $\Delta Z = 0.2$, and $l_Z/\delta_L^0 = 5$. Top figure, isocontours of reaction rate ω_F (——) and mixture fraction Z (——). Bottom figure, isocontours of reaction progress variable c (——) and product mass fraction Y_P (——).

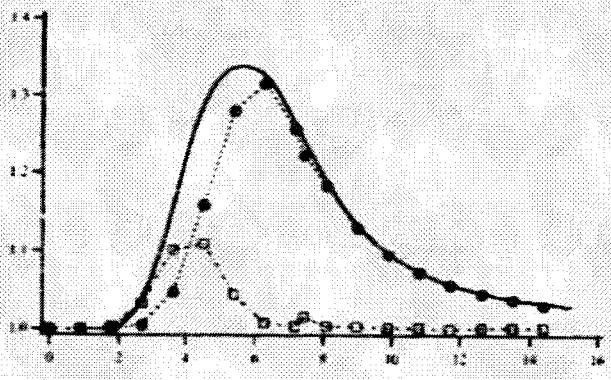

FIGURE 16. Case 3a, run A. Time evolution of the reduced global reaction rate R' (——), the reduced flame surface area W' (●), and the reduced surface-averaged mass burning rate $\langle r' \rangle_S$ (□). Time is made non dimensional by the laminar flame time $\delta_L^0(\langle Z \rangle)/S_L(\langle Z \rangle)$.

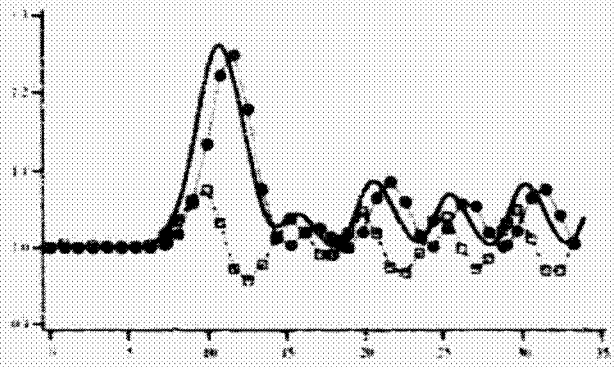

FIGURE 17. Case 3b, run C. Time evolution of the reduced global reaction rate R' (——), the reduced flame surface area W (●), and the reduced surface-averaged mass burning rate $\langle r' \rangle_S$ (□). Time is made nondimensional by the laminar flame time $\delta_L^0(\langle Z \rangle)/S_L(\langle Z \rangle)$.

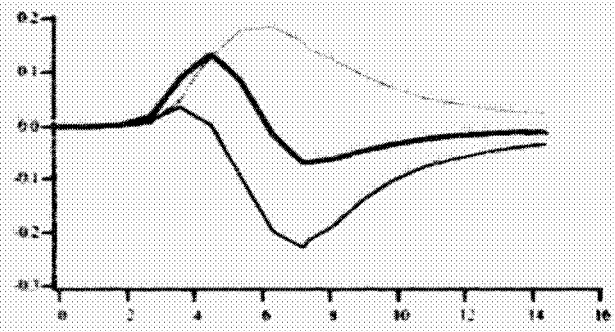

FIGURE 18. Case 3a, run A. Time evolution of the surface-averaged flame stretch $\langle \kappa \rangle_S$ (——), and its two components: the surface averaged strain rate $\langle a_T \rangle_S$ (- - - -) and the surface-averaged propagation term $\langle s \nabla \cdot \mathbf{n} \rangle_S$ (——). Time is made nondimensional by the laminar flame time $\delta_L^0(\langle Z \rangle)/S_L(\langle Z \rangle)$.

run A. Data from run A indicate behavior that is similar to the steady-state situation in Case 2. Partial premixing increases the global reaction rate, $R' > 1$, and the magnitude of the increase is typically 30-40%. The dominant effect of partial premixing is a production of flame surface area, $\langle r' \rangle_S \approx 1$ and $R' \approx W$.

Figure 17 presents similar results for run C. After an initial transient phase, the flame response reaches a limit cycle with periodic time-variations. At the limit cycle, the global reaction rate is increased compared to the perfectly premixed configuration, $R' > 1$; the magnitude of that increase is small, typically 10%; and this increase is related to flame surface production resulting from partial premixing, $R' \approx W$.

As indicated by Eq. (13), the production of flame surface area is measured by flame stretch, and the surface-averaged flame stretch $\langle \kappa \rangle_S$ can be decomposed into

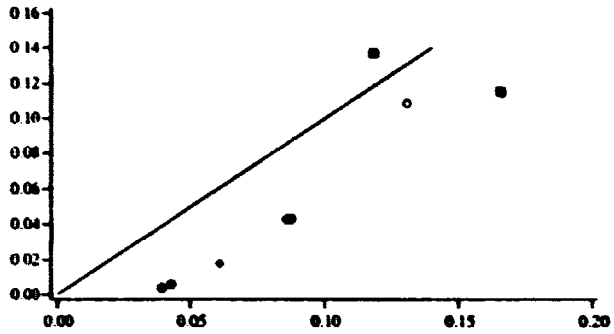

FIGURE 19. Test of Eq. (21): K_a^{PP} vs $(\Delta w/l_Z)(\delta_L^0/S_L(\langle Z\rangle))$. o Case 3a (runs A - B) ; • Case 3b (runs C - E); • Case 3a with heat losses (runs F - G); ◇ A case with a single lean pocket.

a strain rate term, $\langle a_T\rangle_S = \langle \nabla.\boldsymbol{u} - \boldsymbol{nn} : \nabla\boldsymbol{u}\rangle_S$, and a propagation term, $\langle w\nabla.\boldsymbol{n}\rangle_S$. Figure 18 presents the temporal evolution of these two components of flame stretch and shows that partially premixed effects on stretch are not limited to the propagation term. A strong positive contribution of $\langle a_T\rangle_S$ is also observed. This contribution corresponds to a modification of the flow streamlines upstream of the curved flame, as observed in Fig. 10 for the steady configuration of Case 2.

It remains, however, that while the details of the temporal variations of $\langle\kappa\rangle_S$ depend on the effects of both hydrodynamic straining and flame propagation, the basic driving mechanism for flame surface production is the variation of the flame propagation speed w with mixture composition. A simple estimate of the global flame stretch induced by partial premixing may then be expressed as follows:

$$\kappa_{PP} \approx \frac{\Delta w}{l_Z} \tag{21}$$

where Δw is the amplitude of the variations of w measured at the flame location (due to molecular diffusion and unsteady effects, Δw is somewhat smaller than $S_L(\langle Z\rangle + \Delta Z/2) - S_L(\langle Z\rangle - \Delta Z/2)$), and l_Z is the size of the pocket. We use the peak value of $\langle\kappa\rangle_S$ observed in the flame's response to perturbations in Z to estimate the global flame stretch. In nondimensional form, we get the following estimate for a Karlovitz number induced by partial premixing:

$$K_a^{PP} \approx \frac{\Delta w}{l_Z}\frac{\delta_L^0(\langle Z\rangle)}{S_L(\langle Z\rangle)} \tag{22}$$

This relation is tested in Fig. 19 and is found to be satisfactory. Note, however, that the values of this Karlovitz number remain small, $K_a^{PP} \leq 0.2$.

In summary, partial premixing in Case 3 leads to both modification of the flame structure and production of flame surface area. In the absence of quenching, the dominant effect on the mean reaction rate is flame surface wrinkling, $R' \approx W$. It

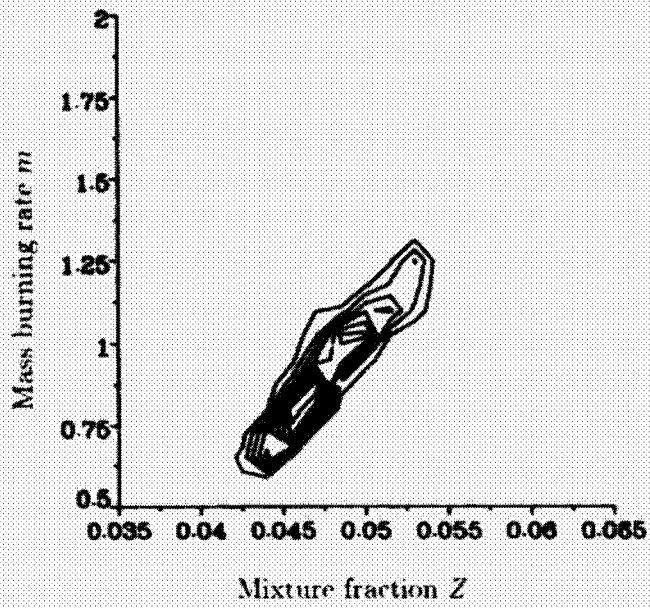

FIGURE 20. Case 4A. Joint probability density function of the reduced mass burning rate, r', and the flame mixture fraction, Z. Time = $4l_t/u'$.

is always positive, $R' > 1$, but the magnitude of that effect as measured by an estimate of the partially premixed Karlovitz number remains small, $K_a^{PP} \leq 0.2$.

Table III. Initial conditions for Case 4 simulations

Case	$\langle\phi\rangle$	$\langle Z\rangle$	ϕ'	Z'	$l_Z/\delta_L^0(Z_{st})$	u'/S_L	$l_t/\delta_L^0(Z_{st})$	Re_t
4A	0.8	0.049	0.3	0.018	2	7.5	2	75
4B	0.8	0.049	0.3	0.018	2	2.5	2	25

7. Case 4: 3D, *zyz*-inhomogeneous, unsteady, turbulent flame

In this case, partial premixing effects are compared to those due to the turbulent motions. The numerical configuration corresponds to a premixed flame propagating into three-dimensional, decaying, isotropic turbulent flow, with variable equivalence ratio. We refer the reader to Trouvé & Poinsot (1994) for more information on the configuration, as well as the initial and boundary conditions. The new feature in the present simulations lies in the initialization of the scalar field in the flow of fresh reactants: Y_F, Y_O, and Y_{N2} are specified according to a model energy spectrum, as proposed by Eswaran & Pope (1988). The initial probability distribution of equivalence ratio is a pdf with two peaks at $\phi = 0.5$ and $\phi = 1.1$. Because of turbulent mixing, this distribution quickly evolves to a Guassian pdf. Two different

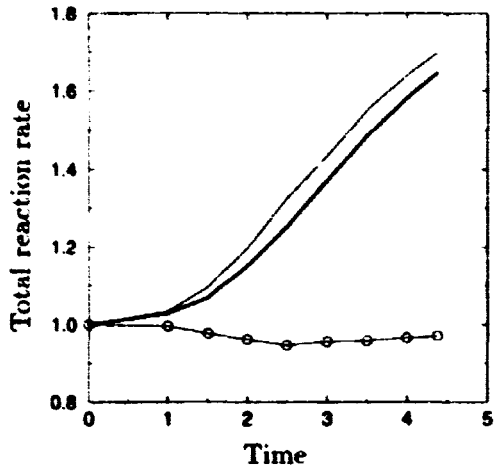

FIGURE 21. Case 4A. Time evolution of the reduced total reaction rate, R' (——), the reduced mean mass burning rate, $\widehat{r'}$ (o), and the reduced total flame surface area, $\langle W \rangle$ (——). Time is made non-dimensional by the initial, turbulent eddy turnover time, l_t/u'.

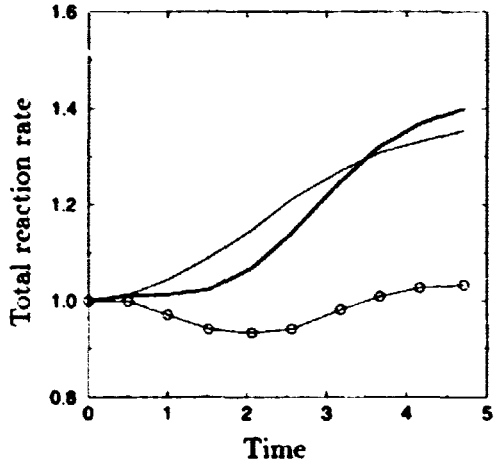

FIGURE 22. Case 4B. Time evolution of the reduced total reaction rate, R' (——), the reduced mean mass burning rate, $\widehat{r'}$ (o), and the reduced total flame surface area, $\langle W \rangle$ (——). Time is made non-dimensional by the initial, turbulent eddy turnover time, l_t/u'.

simulations were performed. The run parameters are given in Table III. In this table l_Z designates the integral length scale of the scalar field, u' the turbulent rms velocity, l_t the integral length scale of the velocity field, and Re_t the turbulent Reynolds number (based on u' and l_t). Cases 4A and 4B correspond to strongly and moderately turbulent flames, respectively. Also, the present simulations use the single step reaction mechanism proposed by Westbrook & Dryer (1981).

In the simulations, partial premixing results in strong spatial variations of the

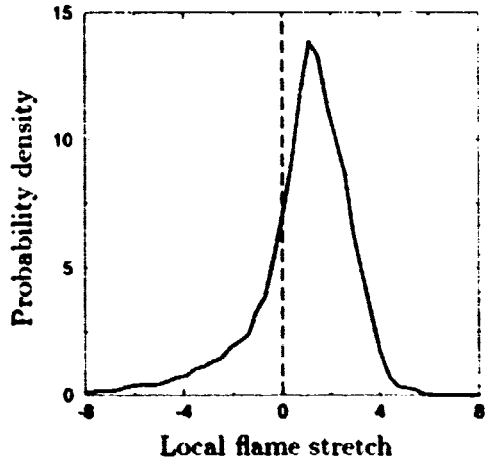

FIGURE 23. Case 4A. Probability density function of flame stretch, κ. Stretch is made non-dimensional by the laminar flame time $\delta_L^0(\langle Z\rangle)/S_L(\langle Z\rangle)$. Time = $4l_t/u'$.

local combustion intensity along the turbulent flame front, consistent with the findings from the previous cases. In Fig. 20, this intensity is quantified by the reduced mass burning rate per unit flame surface area, r', where r' is seen to vary between 0.5 and 1.5. r' is also seen to correlate strongly with the local mixture composition, as measured by the flame mixture fraction. Interestingly, the correlation is approximately linear, so that departures of the mass burning rate $\dot{m}$ from the reference value $\dot{m}(\langle Z\rangle)$ (obtained from a homogeneous, planar, laminar flame) tend to cancel in the mean when averaged over the whole flame. This tendency is confirmed in Figs. 21 and 22, which present the temporal evolution of the two components of the total reaction rate, written for the turbulent case as:

$$R' = \widehat{r'}\langle W\rangle.$$

In Cases 4A and 4B, the mean mass burning rate remains within 10% of unity, so $\widehat{r'} \approx 1$, and the total reaction rate is approximately proportional to the flame surface area, $R' \approx \langle W\rangle$.

There are two mechanisms responsible for the production of flame area in these turbulent simulations: the interaction of the turbulent velocity field with the flame surface, and the partial premixing mechanism described in Cases 2 and 3. Eq. (21) can be used to determine the relative weight of these two mechanisms. The following nondimensional number gives an estimate of the ratio of stretch resulting from partially premixing to stretch due to the turbulent motion:

$$N_T \equiv \frac{\Delta w}{l_Z}\frac{l_t}{u'} = \frac{\Delta w}{S_L(\langle Z\rangle)}\frac{\delta_L^0(\langle Z\rangle)}{l_Z}\frac{l_t}{\delta_L^0(\langle Z\rangle)}\frac{S_L(\langle Z\rangle)}{u'} \tag{23}$$

where the turbulent stretch is estimated using the integral time scale of the turbulence. If $l_t \approx l_Z$, N_T may be further estimated as $(Z'/\langle Z\rangle)(S_L/u')$. Hence, N_T

scales as the inverse of the ratio of a characteristic turbulent flow velocity divided by a laminar flame velocity. N_T is likely to remain small in most practical situations. At the initial time, $N_T \approx 0.03$ in Case 4A; and $N_T \approx 0.1$ in Case 4B.

This last point is illustrated in Fig. 23. Figure 23 presents a typical probability distribution for flame stretch, as obtained in Case 4A. Stretch is normalized in Fig. 23 by a laminar flame time so that stretch values can be directly interpreted as values of the flame Karlovitz number, K_a. The simulation values of K_a range from -8 to 4. These values are quite large and the simulated flame is beyond the domain of possible stretch resulting from partial premixing, ($K_a^{PP} \leq 0.2$). Similar results are obtained in Case 4B.

In summary, partial premixing in the turbulent case leads to strong variations in the local flame mass burning rate, but these variations tend to average out, $\widehat{r'} \approx 1$. Due to the much larger values of turbulent stretch compared to partial premixing induced stretch, the production of flame surface area by partial premixing remains negligible, $N_T < 0.1$.

8. Conclusions

Direct numerical simulations of premixed flames propagating into laminar or turbulent flow, with variable equivalence ratio, are used in this paper to study the effects of partial premixing on the mean reaction rate. The flamelet theory is shown to provide a convenient framework to describe partially premixed flames.

Partial premixing leads to strong variations of the local flamelet structure, and in particular to strong variations of the mass burning rate per unit flame surface area, $\dot{m}$. In the absence of quenching, these variations tend to average out and the effect of partial premixing on the mean flamelet structure remains limited, $\langle \dot{m} \rangle_S \approx \dot{m}_L(\langle Z \rangle)$. Note, however, that quenching induced by partial premixing has been observed in the present simulations, in the case of strong variations in mixture composition, characterized by large amplitudes ($\Delta Z > 0.2$) or large length scales ($l_Z/\delta_L^0 > 10$).

Partial premixing induces flame stretch and, in the absence of quenching this effect, is dominant for laminar flames. It is always positive and will result, in the laminar case, in a partially premixed flame burning faster than the corresponding perfectly premixed flame. The magnitude of the effect of partial premixing on flame surface production is measured by Eq. (22). Typical values of the flame Karlovitz number are below 0.2, and this effect will be negligible in highly turbulent flames. This has been observed in the turbulent flames of this study, where wrinkling effects from partial premixing are small compared to wrinkling created by the fluid motion for the given initial conditions.

REFERENCES

BLOXSIDGE, G., DOWLING, A., HOOPER, N. & LANGHORNE, P. 1987 Active control of reheat buzz. *25th Aerospace Sciences Meeting.*

CANDEL, S. M. & POINSOT, T. 1990 Flame stretch and the balance equation for the flame surface area. *Combust. Sci. Tech.* **70**, 1-15.

ESWARAN, V. & POPE, S. B. 1988 Direct numerical simulations of the turbulent mixing of a passive scalar. *Phys. Fluids.* **31 (3),** 506-520.

HAWORTH, D. C. & POINSOT, T. J. 1992 Numerical simulations of Lewis number effects in turbulent premixed flames. *J. Fluid Mech.* **244,** 405-436.

LELE, S. 1992 Compact finite difference schemes with spectral like resolution. *J. Comput. Phys.* **103,** 16-42.

MÜLLER, C., BREITBACH, H. & PETERS, N. 1994 Partially premixed turbulent flame propagation in jet flames. *25th Symp. (Int.) Comb., The Combustion Institute.*

POINSOT, T., VEYNANTE, D. & CANDEL, S. 1991 Quenching processes and premixed turbulent combustion diagrams. *J. Fluid Mech.* **228,** 561-605.

POINSOT, T. & LELE, S. 1992 Boundary conditions for direct simulations of compressible viscous flows. *J. Comput. Phys.* **101,** 104-129.

POPE, S. 1988 The evolution of surfaces in turbulence. *Int. J. Engr. Sci.* **26,** 445-469.

RUETSCH, G. R., VERVISCH, L. & LIÑÁN, A. 1995 Effects of heat release on triple flames. *Phys. Fluids.* **7,** 1447.

RUETSCH, G. R. & BROADWELL, J. E. 1995 Effects of confinement on partially premixed flames. *Annual Research Briefs 1995.* Center for Turbulence Research, NASA Ames/Stanford University. 323-333.

TROUVÉ, A. & POINSOT, T. 1994 The evolution equation for the flame surface density. *J. Fluid Mech.* **278,** 1-31.

VEYNANTE, D., VERVISCH, L., POINSOT, T., LIÑÁN, A., & RUETSCH, G. R. 1994 Triple flame structure and diffusion flame stabilization. *Proceedings of the 1994 Summer Program.* Center for Turbulence Research, NASA Ames/Stanford University. 55-73.

WESTBROOK, C. & DRYER, F. 1981 Simplified Reaction Mechanism for the Oxidation of Hydrocarbon Fuels in Flames. *Combust. Sci. Tech.* **27,** 31-43.

WILLIAMS, F. A. *Combustion Theory.* Addison-Wessley, NY, 1986.

NEXT
DOCUMENT

A dynamic subgrid-scale model for LES of the G-equation

By A. Bourlioux[1], H. G. Im[2] and J. H. Ferziger[3]

1. Introduction

Turbulent combustion is a difficult subject as it must deal with all of the issues found in both turbulence and combustion. (We consider only premixed flames in this paper, but some of the ideas can be applied to the non-premixed case.) As in many other fields, there are two limiting cases that are easier to deal with than the general case. These are the situations in which the chemical time scale is either much shorter or much longer than the time scale associated with the turbulence. We deal with the former case. In this limit, the flame is thin compared to the turbulence length scales and can be idealized as an infinitely thin sheet. This is commonly called the flamelet regime; it has been the subject of many papers and the basis for many models (see, *e.g.*, Liñán & Williams 1993).

In the flamelet model, the local flame structure is assumed to be identical to the laminar flame structure; thus the flame propagates normal to itself at the laminar flame speed, S_L. This allows the use of simple approximations. For example, one expects the rate of consumption of fuel to be proportional to the area of the flame surface. This idea allowed Damköhler (1940) to propose that the wrinkled flame could be replaced by a smooth one which travels at the turbulent flame speed, S_T, defined by

$$S_T/S_L = A_L/A_p \tag{1}$$

where A_L is the total flame surface area and A_p is the area projected onto the mean direction of propagation. This relation can be expected to be valid when the flame structure is modified only slightly by the turbulence. A measure of the degree of modification is the Karlovitz number, Ka; Eq. (1) should hold when this parameter is not too large.

More recent approaches have attempted to relate the turbulent flame speed to turbulence intensity, u', which, presumably, characterizes the wrinkling of the flame. These result in relationships that typically take the form:

$$S_T/S_L = 1 + C(u'/S_L)^\alpha. \tag{2}$$

For the turbulent flow dominated by an inertial range, Pocheau (1992) derived a linear relation (Eq. (2) with $\alpha = 1$). Earlier work (Clavin & Williams 1979) also

1 CERCA, Université de Montréal
2 Center for Turbulence Research
3 Stanford University

predicted linear behavior in the limit of high turbulence intensity; other authors have produced theories that give different exponents (Yakhot 1988, Kerstein & Ashurst 1992). In §3, we shall use DNS to demonstrate that the linear relation is valid, at least in the limit appropriate to LES; we shall use the database of Trouvé & Poinsot (1994) and the zero heat-release data of Im (1996).

2. Large eddy simulation based on the G-equation

The above ideas can be applied to modeling the small scales of the wrinkling and thus produce the basis for large eddy simulation. It can be shown that a surface that moves at speed S_L normal to itself in a moving fluid can be represented as a level surface of the G-equation (Kerstein *et al.* 1988):

$$\frac{\partial G}{\partial t} + \frac{\partial}{\partial x_j}(u_j G) = S_L|\nabla G|. \tag{3}$$

To perform large-eddy simulation, the G-equation is filtered to produce an equation for $\bar{G}$, a quantity that is smoother than G. This equation contains, of course, terms representing effects of the scales that have been filtered out; these are the subgrid scale terms that must be represented by a model (Im 1995). In a simulation based on the filtered G-equation, the propagating flame is considered a contour of $\bar{G}$, which must propagate at a speed, $\bar{S}$, greater than the laminar flame speed; the increased speed plays the role of a subgrid scale model; alternative approaches to modeling will be discussed later. The filtered G-equation can then be written:

$$\frac{\partial \bar{G}}{\partial t} + \frac{\partial}{\partial x_j}(\bar{u}_j \bar{G}) = \bar{S}|\nabla \bar{G}|, \tag{4}$$

where

$$\bar{S}/S_L = 1 + C(u'/S_L), \tag{5}$$

and u' is the velocity fluctuation characterizing the unresolved scales and C is a constant that can be prescribed or calculated by the dynamic procedure. In an LES, u' must be modeled as well. However, as the present study is an initial investigation of modeling the G-equation, we shall calculate u' directly from the DNS velocity field. Likewise, the filtered velocity field, $\bar{u}$, is obtained directly from the DNS field. For later reference, we note that when the flame stretch and the Karlovitz number are not negligible, a diffusion-like term that represents the effect of stretch (Matalon & Matkowsky 1982) on flame propagation should be included on the RHS of Eq. (3) or (4).

3. A priori test of the flame area scaling law

We now present an *a priori* test of a dynamic subgrid-scale model for the turbulent flame speed; it is based on the model introduced by Bourlioux *et al.* (1996). Combining Eq. (1) and Eq. (5), we obtain the following equation:

$$\bar{S}/S_L = A_L/\bar{A} = 1 + C(u'/S_L). \tag{6}$$

where A_L is the flame area computed in a DNS, $\bar{A}$ is the filtered flame area to be computed in an LES, and S is the flame speed used in the LES. The latter was discussed above and should be selected to guarantee the correct overall burning rate, i.e. $SA = S_L A_L$. Eq. (6) is a useful subgrid-scale model if one can specify the model parameters appropriately. In this section, we first validate the linear relation, Eq. (6), and determine the constant C by using the resolved flame area A_L computed from the DNS results.

3.1 Test procedure

To check the validity of Eq. (6), we process the DNS databases in the following way:

1. Identify a flame surface in the DNS G-field and compute its area A_L by triangulation.
2. Filter the G and u obtained from the DNS database at various filter sizes (2Δ, 4Δ, ... are used, where Δ is the DNS mesh size).
3. For each filter, compute u' as the square root of the subgrid kinetic energy (i.e. the L_2 norm of the difference between the resolved DNS velocity field and the filtered field).
4. Given the filtered G-field, identify the 'filtered flame surface' and compute its area $\bar{A}$.

We then investigate the relationship between the ratio $A_L/\bar{A}$ and u' as a function of filter size.

3.2 Databases

We first consider premixed flames in homogeneous decaying turbulence (Trouvé & Poinsot 1994). In the flame, there is a smooth transition of the reaction progress variable, c, from 0 (fresh mixture) to 1 (burnt gas). We begin by defining a flame surface. Following Trouvé & Poinsot (1994) we choose the level surface with $c = 0.8$ as the flame front and define $G = c - 0.8$. Heat release effects are included in this DNS. Since the viscosity depends strongly on temperature, the turbulence intensity varies significantly across the flame so one must be careful when computing the turbulence intensity u': the value on the unburnt side of the flame should be used. In practice, we obtain u' by taking a 2-D Fourier transform of the velocity field on cross-sections ahead of the flame, averaging over the unburnt side of the domain. Our tests show that the choice of averaging volume is not important as long as it is sufficiently far from the boundary.

The second data set is the result of DNS of the passive G-equation in forced isotropic turbulence (Im 1996). There is no heat release in this simulation. Several simplifications are used in the test procedure:

1. *The G variable* is available from the DNS and can be filtered for *a priori* tests.
2. In the absence of heat release, any contour of G can be considered a flame surface. The average front area can be computed from the volume average of $|\nabla G|$ (Kerstein *et al.* 1988).

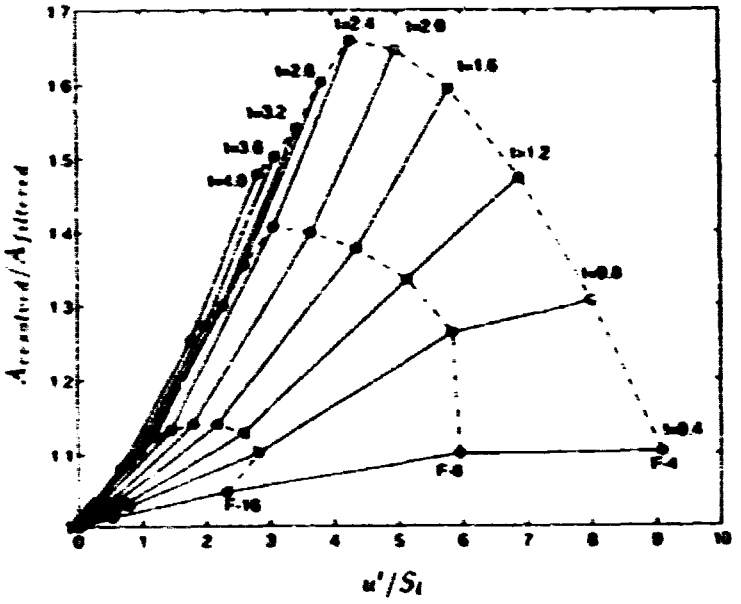

FIGURE 1. Ratio of the resolved DNS flame area to the filtered flame area as a function of the subgrid kinetic energy u'. DNS data by Trouvé & Poinsot (1994).

3. The entire flow field can be used to estimate u' - one does not need to distinguish the 'burnt' and 'unburnt' regions.

3.3 Results of the a priori test

Results of *a priori* tests applied to the database of Trouvé *et al.* (1994) are shown in Fig. 1. The ratio of the DNS flame area A_L to the filtered flame area $\bar{A}$ is plotted vs. the subgrid kinetic intensity u' at various times; the times shown are normalized by the large eddy turnover time. The DNS data were obtained on a 128^3 grid; each circle is a data point; the field was filtered to grids of 64^3, 32^3, 16^3 (F-16 on the figure), 8^3 (F-8) and 4^3 (F-4).

Figure 1 clearly shows that, if Eq. (6) is valid, its coefficient is strongly time dependent. There are two reasons for this. Firstly, the flame is initially planar and a few eddy turnover times are required to reach an 'equilibrium' state. Secondly, the turbulence is not forced; its decay can be seen from the decrease of the turbulence intensity at the coarsest filter size (F-4) with time. Nevertheless, the results do seem to indicate the existence of a universal relationship after the flame is sufficiently wrinkled; the change between times t=2.4 and t=4 is small compared to the change from t=0.4 to t=2.4. Even at large times, a distinction must be made between the behavior at small scales (the 64^3, 32^3, and 16^3 filters) and the large scales. The linear fit (6) appears reasonable for the small scales but not the large ones. This is an argument in favor of LES; modeling may be more universal for the small scales than for the large scales.

In the passive database (Im 1996), the flame front is again initially planar but,

after several turnover times, the flame area levels out. Plots of the inverse of the filtered flame area vs. the turbulent intensity are very similar to those found from the Trouvé/Poinsot database, with linear behavior for small values and quadratic behavior at larger scales.

We next test the dynamic procedure; it is based on the dynamic model for non-reactive flows. The parameter is adjusted using the smallest resolved scales of an LES. We shall not address the question of estimating u' but focus instead on estimating the subgrid flame wrinkling. Given A_1 and $\bar{A}_2$, the flame area at filter sizes Δ_1 and Δ_2, and the corresponding subgrid turbulence intensities, u'_1 and u'_2, we use Eq. (6) to obtain:

$$A_L/A_1 = 1 + Cu'_1.$$

$$A_L/A_2 = 1 + Cu'_2.$$

This system can be solved to produce the resolved flame area A_L and/or the model constant C dynamically. Table 1 gives the results for the flame speed (characterized by $1/A_L$) obtained by applying the procedure described above to Im's data. The DNS field was filtered to 32^3 (F_1) and 16^3 (F_2) grids. The modeled turbulent speed is compared to the exact value obtained from the DNS. The agreement is excellent. There is little wrinkling on the small scales and the enhancement of the flame speed (the difference between turbulent and laminar speeds) is very small. The table also gives the error in the enhancement, which is acceptable. In the next section, we will describe attempts to incorporate this procedure into a dynamic LES.

Time	7.77	8.08	8.37	8.68	8.99	9.31
$\bar{S}_{dyn}$	1.0681	1.0598	1.0825	1.0887	1.1246	1.0706
$\bar{S}_{exact}$	1.0906	1.0633	1.0804	1.0801	1.1069	1.0672
E_1 (turbulent speed)	-0.7%	-0.3%	0.2%	0.8%	1.6 %	0.33 %
E_2 (enhanced speed)	-8%	-6%	3%	11%	16%	5%

Table 1. A priori test of a dynamical model for $\bar{S}$.

4. LES modeling test with spectral method

In this section, the SGS model presented in §2 is tested by applying it to flames in forced three-dimensional incompressible homogeneous isotropic turbulence; the simulations are carried out using a spectral method. Heat release is neglected in this test so the G-field behaves essentially as a passive scalar.

The calculation procedure is as follows. The flow field is fully resolved on a 64^3 grid using a pseudo-spectral method and second-order Runge-Kutta time-stepping (Rogallo 1981). The Reynolds number based on Taylor microscale is about 74. The turbulence is forced at the lowest wavenumber to maintain the kinetic energy constant. At every time step, the flow field is filtered onto a 32^3 grid; the resulting velocity field is then used in solving the filtered G-equation (4).

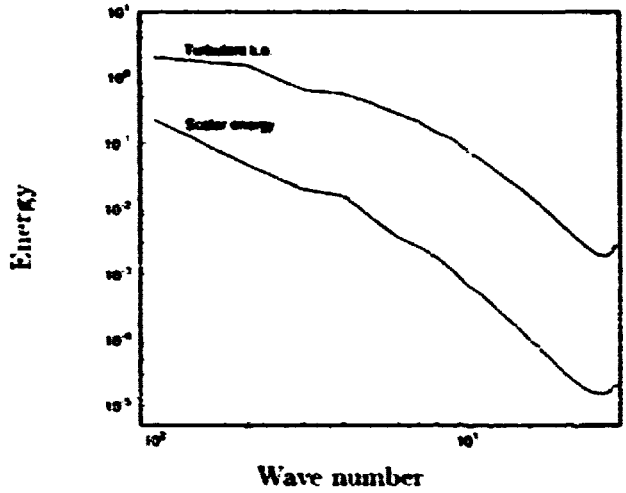

FIGURE 2. Spectra of turbulent kinetic energy and scalar fluctuations in the 64^3 DNS calculation with $u'/S_L = 0.5$.

When the code was run with the model described above, numerical instability resulted. Investigation showed that the instability is due to an increase in the high wavenumber G-field, i.e., to cusp and strong gradient formation. It is necessary to do something to stabilize the calculation; one possibility is to add a second order diffusive term, $\mathcal{D}\nabla^2 G$, to the RHS of Eq. (4). As mentioned earlier, similar terms are used to represent the effects of flame stretch and curvature on the flame speed. In the present DNS, $\mathcal{D}/\nu = 4$ is used where $\nu = 0.015$ is the molecular diffusivity.

Figure 2 shows the spectrum of turbulence kinetic energy and the scalar fluctuations, $\langle g^2 \rangle = \langle (G - \tilde{G})^2 \rangle$ for $u'/S_L = 0.5$ obtained from the DNS. The turbulence was forced to allow attainment of steady state spectra in a few eddy-turnover times. We shall use this DNS field to construct the initial condition for the LES.

Specifically, the following subgrid-scale models are tested:

A. $\tilde{S} = S_L$, i.e. no subgrid-scale model is used.

B. $\tilde{S} = 1.08 S_L$, where the constant 1.08 was obtained from the *a priori* test.

C. $\tilde{S}/S_L = 1 + 0.411(u'/S_L)$, a curve fit obtained from the *a priori* test similar to Fig. 1; u' is computed from the DNS flow field.

D. $\tilde{S}/S_L = 1 + C(u'/S_L)$ with the parameter C computed dynamically by filtering the G-field to 16^3 resolution and assuming that the model $\hat{S}/S_L = 1 + C(u'/S_L)$ applies at that level. The ratio $\hat{\tilde{S}}/\hat{S}$ can be computed as the area of the constant G surface at the appropriate level of filtering.

The predictions produced by all these models are compared with results obtained by filtering the 64^3 DNS G-field. The Markstein diffusivity $\mathcal{D}$ used in all of the above LES was increased to twice the value used in the DNS to achieve stability. This can be interpreted as an extra subgrid-scale scalar transport required to represent the effects of the filtering. A more rigorous treatment of this term is necessary

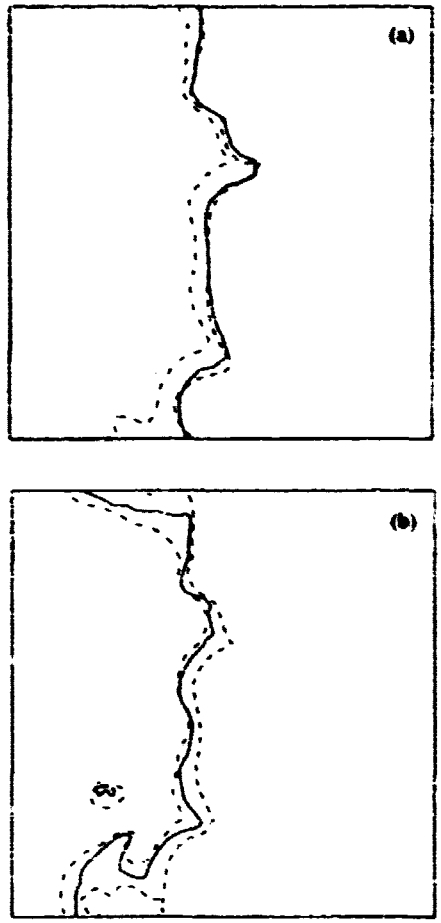

FIGURE 3. The contours of $\tilde{G}$ obtained with various LES models after one eddy-turnover time; (a) $\bar{G} = 1.45$ which is the average value and (b) $\tilde{G} = 1.95$. A single slice in 3-D is shown. In each figure, DNS result: ——— ; model A: - - - - ; model B: ····· ; model D: —·—. Flame propagates from right to left.

in the future; for example, a dynamic computation of $\mathcal{D}$ can be appended to the computation of C.

Figure 3 shows two $\tilde{G}$ contours (1.45, 1.95) after one eddy turnover time for the various LES modeling strategies. Although the four fronts approximately reproduce the smoothed DNS contour, the various models give different average flame locations. It appears that model B overpredicts the turbulent flame speed, while model A underpredicts it, as expected.

The volume-averaged front location predicted by each LES model is compared to the DNS result in Fig. 4. All three LES models (B,C,D) overpredict the average flame speed. However, gradual improvement is obtained as the level of complexity of the model changes from the simple *a priori* procedure to the more sophisticated

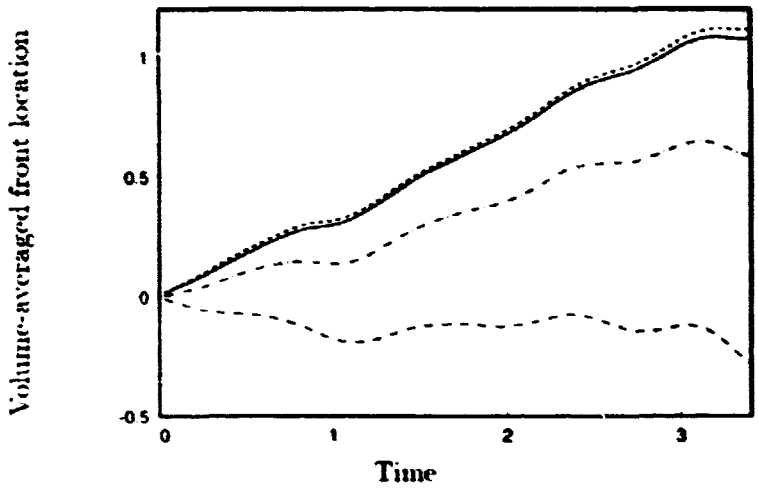

FIGURE 4. The volume-averaged front location according to DNS and various LES models: model A: - - - - ; model B: ——— ; model C: ····· ; model D: — · — .

dynamic model. It is interesting to observe that, although model A underpredicts the flame speed, it gives the best agreement with the DNS.

It should be noted that the models used here are not complete. The supplementary subgrid-scale transport in the LES simulation was imposed by *ad hoc* adjustment of the diffusion coefficient, and was chosen mainly to achieve numerical stability of the spectral method. Improvement might be obtained by introducing a Smagorinsky-type model for the subgrid transport with model constant determined dynamically. This is currently being investigated.

5. Dynamic LES using a high order upwind scheme

The numerical stability issue addressed in §4 is easily understood by examination of Fig. 5 which gives several contours G at $t = 0.25$. The major cause of instability is the formation of cusps, which are present even at this early stage of the computation. Another difficulty is the squeezing together of contours, resulting in high gradients that are difficult to capture numerically. To address those difficulties, we repeated some of the experiments of §5 using a different solver for the G-equation, while retaining the spectral velocity field computation. The G-equation is now solved using a numerical strategy based on level-set technology (Osher & Sethian 1988, Sussman *et al.* 1994; for combustion applications Zhu & Sethian 1992, Klein 1995). For the advection term, we use a higher order upwind code developed by LeVeque (1993). The source term on the right hand side of Eq. (1) is solved with the procedure of Zhu & Sethian (1994). A reinitialization procedure is performed at every time step; the G-function is reinitialized to be the signed distance function with respect to the flame, using the procedure of Sussman *et al.* (1994). This means that only the $G = 0$ contour is considered to be a flame. Figure 6 displays contours obtained with this method: accuracy is maintained even when the flame becomes very distorted and no additional numerical viscosity needs to be added when the

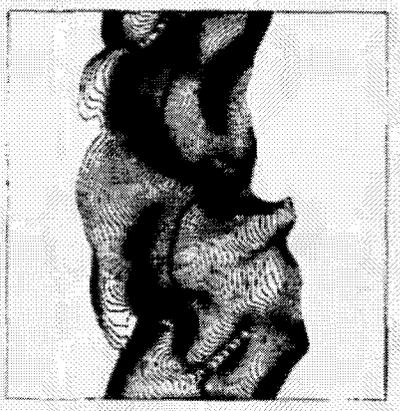

FIGURE 5. Contours of the G function computed with spectral method. Flame propagates from right to left.

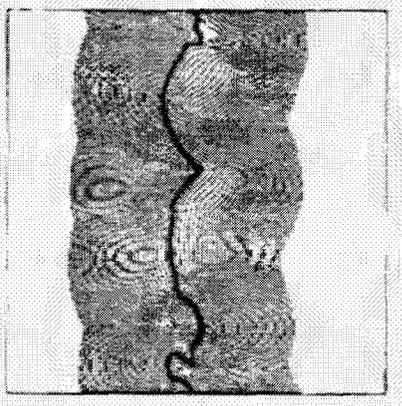

FIGURE 6. Contours of the G function computed with higher order upwind method. Flame propagates from right to left.

mesh is coarsened. This method is roughly equivalent to introducing a viscosity or diffusivity selectively at those points at which the method of the preceding section had trouble, i.e. at cusps and in regions of large gradient of G.

In Fig. 7, we compare the results of a 32^3 computation with this procedure with the fully resolved 64^3 case results. The turbulent flame area is plotted as a function of time for different resolutions. The solid line is the 32^3 LES result, the dot-dash curve is the flame area in the 16^3 G-field obtained by filtering the 32^3 G-field. Using those data and the dynamic procedure of §3.3, the wrinkled flame area is extrapolated to the 64^3 grid (----). This result is compared to the wrinkled flame area computed directly on a 64^3 grid ($\circ$). It is clear that the suggested procedure underestimates the flame wrinkling. To explain the difference, we also show the flame area on a 32^3 grid ($\square$) and a 16^3 grid (∇) obtained by filtering the DNS data. The discrepancy between the LES and DNS results can be traced to two effects:

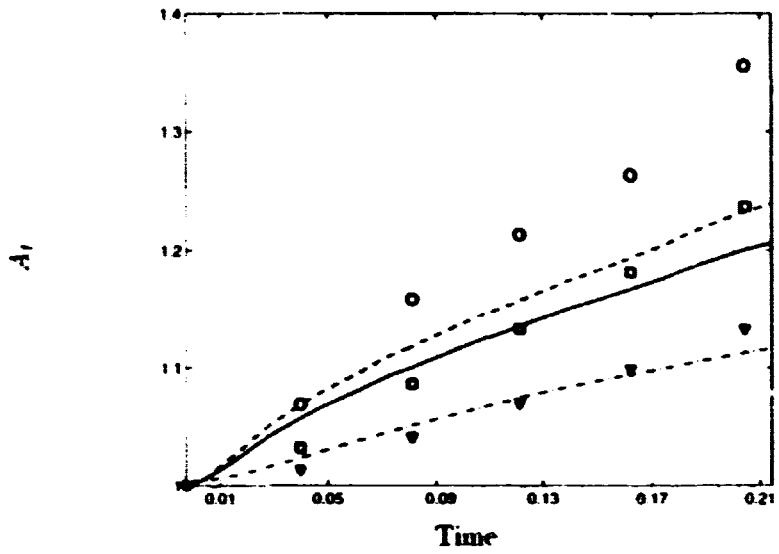

FIGURE 7. Turbulent flame speed as a function of time from various DNS/LES calculations obtained with higher order upwind scheme. DNS results: 64^3, o ; 32^3, □ ; 16^3, ▽ . LES results: 64^3, ---- ; 32^3, —— ; 16^3, — · — .

- Underestimation of the flame area on the 32^3 grid: by comparing the 32^3 LES (——) and 32^3 filtered DNS (o) flame areas, it is clear that the upwind/reinitialization scheme smooths the wrinkled front slightly. This is to be expected from an upwind method - this effect is relatively small and could be controlled with a higher order method or a solution-adaptive integration procedure.
- Poor extrapolation of the subgrid wrinkling: extrapolation from the 32^3 and the 16^3 grids to the 64^3 grid magnifies the error which is relatively small on coarser grids: this is the major source of error.

This error can be better understood by looking at Fig. 8. In the computations, the linear fit (6) was used for dynamic extrapolation—the plot in Fig. 8 indicates that, in the early stages of flame wrinkling, the linear fit is inappropriate: a square root fit would be more suitable. This is consistent with the *a priori* test results reported in §3. Longer computations are being performed to assess whether this effect will disappear as the flame becomes sufficiently wrinkled.

6. Conclusions

Large eddy simulation will be necessary if reacting flows in complex geometries are to be simulated. This paper is a first attempt at evaluating models of subgrid scale effects that could be used in those flows. The laminar flamelet regime is considered in this paper such that the G-equation can be used as the basis for the modeling.

Since the effect of filtering is to smooth a wrinkled flame, a natural model is one in which the smoothed flame has a higher speed than that of the laminar flame. Simple models of this kind were constructed and tested using the *a priori* approach

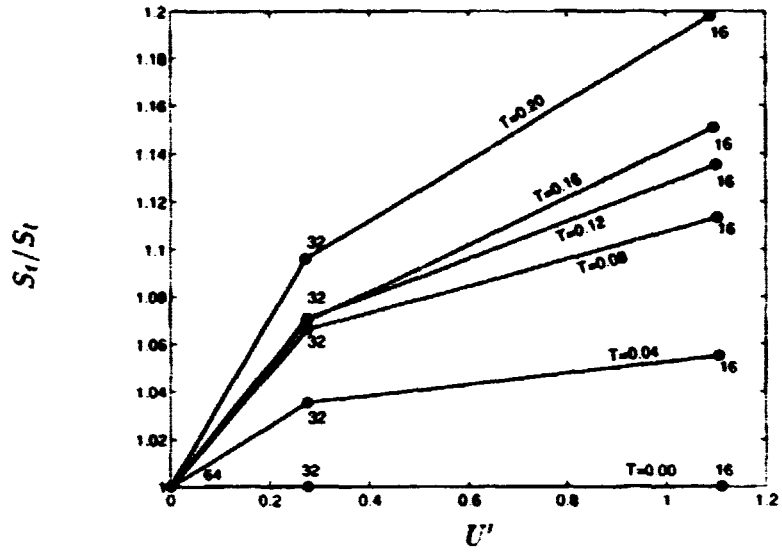

FIGURE 8. Ratio of the resolved DNS flame area to the filtered flame area as a function of the subgrid kinetic energy u' at various filter levels. Results for passive G-field with higher order upwind method.

and large eddy simulations. ***A priori*** tests show that a linear relationship between the flame speed and the subgrid scale turbulent velocity is reasonable.

The models were then tested in two types of LES. In the first, the passive G-equation is solved along with the Navier–Stokes equations using a pseudo-spectral method. This approach is incapable of allowing heat release. Several versions of the model for the G-field were used including ones with a fixed constant and others with the parameter computed dynamically. These computations are numerically unstable, a problem that can be traced to the creation of cusps and high gradient regions. This problem can be eliminated through the addition of a diffusive term to the subgrid scale model. This can be justified in the same way that the Smagorinsky model is justified but, in this paper, the addition of the diffusive term was done in an ***ad hoc*** manner.

In the other type of LES, the G-equation is solved using a high order upwind method and the G-field is reinitialized at each time step. This approach essentially introduces diffusion where required to prevent the formation of cusps and high-gradient regions and requires no explicit diffusive terms.

The results show that the models are reasonable, but it appears that the LES models either overestimate (with a spectral method) or underestimate (with an upwind method) the turbulent flame speed. The reasons for this behavior are under investigation.

REFERENCES

BOURLIOUX, A., KLEIN, R. & MOSER, V. 1996 A dynamic subgrid scale model

for turbulent premixed flames. ***CERCA*** technical report.

CLAVIN, P. & WILLIAMS, F. A. 1979 Theory of premixed-flame propagation in large-scale turbulence. *J. Fluid Mech.* **90,** 589.

DAMKÖHLER, G. 1940 *Z. Elektrochem.* **46**, 601.

IM, H. G. 1995 Study of turbulent premixed flame propagation using a laminar flamelet model. ***Annual Research Briefs-1995***, Center for Turbulence Research, NASA Ames/Stanford Univ.

IM, H. G. 1996 Large eddy simulation of turbulent premixed combustion using the G-equation model. ***In preparation.***

KERSTEIN, A. R. & ASHURST, WM. T. 1992 Propagation rate of growing interfaces in stirred fluids. *Phys. Rev. Lett.* **68,** 934.

KERSTEIN, A. R., ASHURST, WM. T., & WILLIAMS, F. A. 1988 Field equation for interface propagation in an unsteady homogeneous flow field. *Phys. Rev. A.* **37,** 2728.

KLEIN, R. 1995 The level set approach to premixed turbulent combustion in the flamelet regime: theory and numerical implementation. Lecture Notes, ***Euroconference on Premixed Combustion***, Aachen.

LEVEQUE, R. J. 1993 High-resolution conservative algorithms for advection in incompressible flow. *SIAM J. Num. An.* **33,** 627.

LIÑÁN, A. & WILLIAMS, F. A. 1993 ***Fundamental aspects of combustion***, Oxford University Press.

MATALON, M. & MATKOWSKY, B. J. 1982 Flames as gasdynamic discontinuities. *J. Fluid Mech.* **124,** 239.

OSHER, S. & SETHIAN, J. A. 1988 Fronts propagating with curvature-dependent speed: algorithms based on Hamilton-Jacobi formulations. *J. Comp. Phys.* **79,** 12.

POCHEAU, A. 1992 Front propagation in a turbulent medium. *Europhysics Letters.* **20,** 401.

ROGALLO, R. 1981 Numerical experiments in homogeneous turbulence. *NASA TM81315.*

TROUVÉ, A. & POINSOT, T. 1994 The evolution equation for the flame surface density in turbulent premixed combustion. *J. Fluid Mech.* **278,** 1.

SUSSMAN, M., SMEREKA, P. & OSHER, S. 1994 A level set approach for computing solutions to incompressible two-phase flow. *J. Comp. Phys.* **114,** 146.

YAKHOT, V. 1988 Propagation velocity of premixed turbulent flames. *Comb. Sci. Tech.* **60,** 191.

ZHU, J. & SETHIAN, J. A. 1992 Projection methods coupled to level set interface techniques. *J. Comp. Phys.* **102,** 128.

NEXT
DOCUMENT

A new methodology to determine kinetic parameters for one- and two-step chemical models

By T. Mantel[1], F. N. Egolfopoulos[2] & C. T. Bowman[3]

In this paper, a new methodology to determine kinetic parameters for simple chemical models and simple transport properties classically used in DNS of premixed combustion is presented. First, a one-dimensional code is utilized to performed steady unstrained laminar methane-air flame in order to verify intrinsic features of laminar flames such as burning velocity and temperature and concentration profiles. Second, the flame response to steady and unsteady strain in the opposed jet configuration is numerically investigated. It appears that for a well determined set of parameters, one- and two-step mechanisms reproduce the extinction limit of a laminar flame submitted to a steady strain. Computations with the GRI-mech mechanism (177 reactions, 32 species) and multicomponent transport properties are used to validate these simplified models. A sensitivity analysis of the preferential diffusion of heat and reactants when the Lewis number is close to unity indicates that the response of the flame to an oscillating strain is very sensitive to this number. As an application of this methodology, the interaction between a two-dimensional vortex pair and a premixed laminar flame is performed by DNS using the one- and two-step mechanisms. Comparison with the experimental results of Samaniego *et al.* (1994) shows a significant improvement in the description of the interaction when the two-step model is used.

1. Introduction

During the past ten years, direct numerical simulation (DNS) of turbulent reacting flows has been widely utilized to obtain physical understanding and precious information for modeling purposes. The recent articles of Poinsot (1996) and Poinsot *et al.* (1996) can be consulted for a review concerning DNS of turbulent reacting flows. Although any kind of model is needed to solve the Navier-Stokes equations for a non-reacting system, closures have to be provided in order to model transport properties of the different species and chemical reactions as well. These two aspects can rapidly lead to tremendous needs of storage capacity and CPU time even for the combustion of simple hydrocarbons such as methane. As an example, the recent detailed mechanism proposed by the Gas Research Institute (GRI) for methane combustion requires 177 reactions of 32 species. This kind of chemical scheme can only be used in the computations of one-dimensional problems such as the study

1 Renault, Research Division, France
2 University of Southern California, Department of Mechanical Engineering
3 Stanford University

of strained laminar premixed flames (Egolfopoulos 1994a-b). We can, however, cite the two-dimensional numerical study of vortex-premixed laminar flame interactions performed by Hilka *et al.* (1994) using a detailed mechanism (17 species and 55 reactions). Thus, in order to investigate turbulent flames propagating in the combustion regime of existing devices, the chemistry and transport properties have to be drastically simplified. Currently, a one-step irreversible chemical model is used to performed parametric studies of complex flows such as flame-vortex interactions (Poinsot *et al.* 1991), three-dimensional decaying turbulence interacting with a premixed flame (Trouvé & Poinsot 1994), or a diffusion flame (Vervisch 1992). In order to take into account the highly diffusive behavior of some radicals, two-step mechanisms have been used in numerical studies of turbulent diffusion flames (Vervisch 1992) and flame-vortex interactions (Mantel 1994). The difficulty of these simple models is to find realistic transport properties and kinetic parameters which correspond to the studied medium. In the DNS code used by these various authors, the transport properties are modeled using a temperature dependence for the dynamic viscosity and constant Prandtl, Schmidt numbers, and calorific capacity. For the chemical models, the activation energy E_a and frequency factor B for each reaction have to be estimated. Usually, a high activation energy in the range of 30 to 60 kcal/mol is considered. For premixed systems, the kinetic parameter of these simple chemical models are chosen to match the laminar burning velocity S_L alone. An *a priori* global activation energy must be taken high enough to be realistic but low enough to reduce the number of grid points required to resolve the flame (generally the lower limit of the range 30 to 60 kcal/mol). In fact, the asymptotic analysis of Williams (1985) shows that $\delta_f \sim \beta^{-1}$ where δ_f is the thickness of the reaction zone and β the Zel'dovich number defined by $\beta = E_a(T_b - T_u)/R^o T_b^2$. Here R^o and T_b represent respectively the universal gas constant and the temperature of the fresh and burnt gases. Once the activation energy is imposed, the frequency factor is tuned to find the chosen laminar flame velocity. However, since an infinity of couple (B, E_a) exists for a given value of S_L, additional features of the laminar flame have to be verified. Thus, this technique has to be improved in order to predict other intrinsic characteristics of the flame such as concentration of reactants and temperature profiles, especially in the downstream end of the flame where reactions take place.

The motivation of this study is to provide realistic kinetic parameters for one- and two-step mechanisms classically used in DNS of premixed turbulent combustion. To do so, a new methodology allowing the determination of kinetic parameters is proposed. This methodology allows to verify the following quantities: (1) the laminar burning velocity, (2) the temperature and concentration of reactant (and intermediate species for the two-step mechanism) profiles, and (3) the strain rate imposed to the flame in the opposed jet flame configuration leading to extinction.

Points 1 and 2 are performed using the PREMIX code (Kee *et al.* 1994), which has been modified to accept artificial species, constant molecular weight, constant calorific capacities for all the species, and modified heat of formation to predict the adiabatic flame temperature. Point 3 is numerically investigated by studying

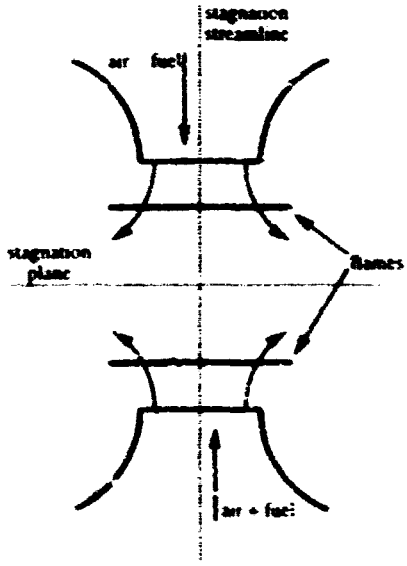

FIGURE 1. Counterflow flame configuration.

the counterflow opposed jet flame configuration (Egolfopoulos 1994). For these 3 points, computations using the GRI-mech 2.1 mechanism (Frenklach *et al.* 1995) are performed and utilized as reference cases for comparison with one- and two-step mechanisms.

In order to validate this methodology on real configurations, the response of a premixed laminar flame to unsteady strain is numerically investigated in two different configurations using one- and two-step chemical models and simple transport properties:

- the opposed jet flame submitted to an oscillating strain rate
- the vortex-premixed laminar flame interaction experimentally studied by Samaniego *et al.* (1996)

In the first unsteady configuration, the effect of thermo-diffusive properties of the mixture is investigated. It appears that this effect seems to have a strong influence on the unsteady behavior of the heat release rate. On this configuration, both one- and two-step models allow a good description of the behavior of the flame. In the case of the vortex-premixed laminar flame interaction, a significant effect of the diffusivity of the intermediate species on the heat release is observed when the two-step mechanism is employed. Comparison with the experimental results of Samaniego *et al.* (1996) shows an improvement in the description of the interaction using the two-step model and simplified transport model.

2. Lean premixed laminar flames submitted to a steady strain

2.1 Presentation of the counterflow flame configuration

To study the ability of one- and two-step models to describe the response of a laminar flame to stretch, the counterflow flame interaction configuration is chosen.

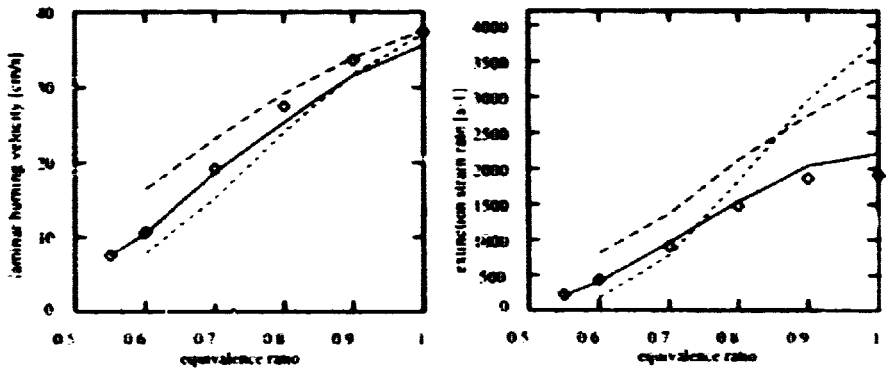

FIGURE 2. Evolution of the laminar burning velocity and extinction strain rate versus the equivalence ratio. ○ : GRI-mech; —— : model; - - - - : E_a = 35kcal/mol; ------ : E_a = 60kcal/mol.

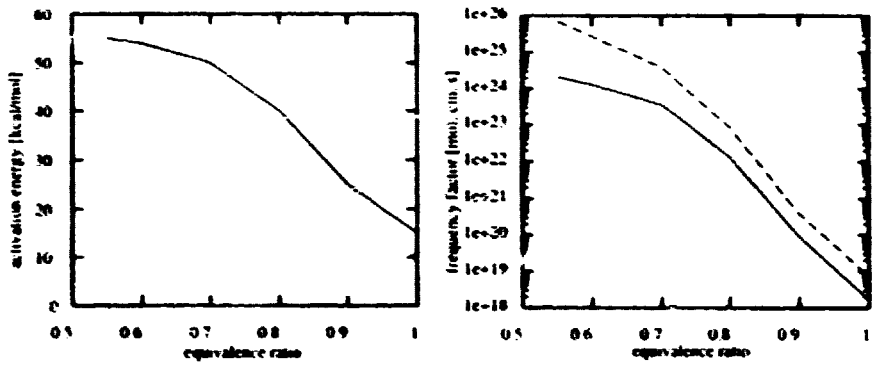

FIGURE 3. Evolution of the activation energy in kacl/mol and frequency factor in cm.mol. s for reaction (1) versus the equivalence ratio. —— : PREMIX code; - - - - : asymptotic analysis

Such a configuration (see Fig. 1) has been widely studied both experimentally (Chung *et al.* 1986, Law *et al.* 1986) and numerically (Egolfopoulos 1994a,b). The main goal of these studies was to determine the extinction and flammability limits of laminar premixed flames. Extinction strain rates and laminar flame velocity have been determined for a wide range of equivalence ratio for various air/fuel mixtures for premixed laminar.

Here, this problem is treated using a code solving the equations of mass, momentum, energy, and species along the stagnation streamline of the counterflow opposed jet flame configuration. Details concerning the equations and boundary conditions are given in Egolfopoulos (1994a).

The conditions of our simulations are those retained by Egolfopoulos (1994). The temperature of the unburnt mixture (methane-air) is 300 K, and the distance separating the nozzles is 0.7 cm.

2.2 A one-step model for the combustion of lean methane-oxygen flames

A new model for the combustion of lean methane-air flame is proposed following the methodology presented in the introduction. The global one-step reaction for lean methane-air combustion is:

$$CH_4 + 2O_2 \rightarrow CO_2 + 2H_2O \tag{1}$$

and the reaction rate for this reaction is expressed by

$$RR = B[CH_4][O_2]^2 \exp(-E_a/R^oT) \tag{2}$$

Computations are performed using the PREMIX code including reaction (1) and multi-component properties. The parameters B and E_a are thus determined for each value of the equivalence ratio ϕ. Figure (2) shows the evolution of S_L and K_{ext} for the global mechanism and for the solution obtained from the GRI-mech mechanism. The values for B and E_a are presented in Table (1) as a function of ϕ varying from 0.55 to 1.

Two additional cases are presented in Fig. (2) by keeping constant kinetic parameters: (i) $E_a = 35$ kcal/mol; $B = 4.1\ 10^{21}$ (ii) $E_a = 60 kcal/mol$; $B = 6\ 10^{24}$. These sets of parameters are determined for $\phi = 1.0$ and are kept constant for the other values of Φ. For these two cases, both S_L and K_{ext} are not correctly predicted. For some values of ϕ, K_{ext} is even over-predicted by a factor of two (see Fig 2).

ϕ	E_a	A
	kcal/mol	cm/(mol s)
0.55	55	$2.1\ 10^{24}$
0.6	54	$1.1\ 10^{24}$
0.7	50	$3.1\ 10^{23}$
0.8	40	$1\ 1\ 10^{22}$
0.9	25	$9.1\ 10^{19}$
1.0	15	$1.1\ 10^{18}$

Table 1. Kinetics parameters for global reaction defined by Eq. (1) used in Fig. (1)

The evolution of B as a function of ϕ obtained in the present study can be compared with the asymptotic analysis of Clavin (1985), who proposes an expression for the laminar burning velocity S_L as a function of B and β:

$$S_L = \frac{\rho_b}{\rho_u}\left[2\Gamma_{n+1} L \epsilon^n \frac{D_{th}(T_b)}{\beta^{n+1}\tau_r}\right]^{1/2} \tag{3}$$

where

$$\Gamma_{n+1} = \int_0^\infty X^n e^{-X} dX \tag{4}$$

$$\frac{1}{\tau_r} = \nu \frac{W}{Y_u} B C_{o,u}^{n_o} C_{f,u}^{n_f} \exp(-\beta/\alpha) \tag{5}$$

Here, ν, Y_u, W are the stoichiometric coefficient, the initial mass fraction, and the molecular mass of the deficient species. The molar concentration of the oxidant and the fuel in the fresh mixture are denoted by $C_{o,u}^{n_o}$ and $C_{f,u}^{n_f}$. In Eq. (4), n is the order of the reaction and X a variable of integration defined by $X = \beta(1-\theta)$ where $\theta = (T - T_u)/(T_b - T_u)$ represents the reduced temperature.

In the case of the global reaction (1), Eqs. (4) and (5) become:

$$\Gamma = 2 \tag{6}$$

$$\frac{1}{\tau_r} = \nu_{CH_4} \frac{W_{CH_4}}{Y_{CH_4,u}} B C_{O_2,u}^2 C_{CH_4,2} \exp(-\beta/\alpha) \tag{7}$$

To estimate the thermal diffusivity in the burnt gases, we use the classical relation:

$$\frac{\mu}{\mu_u} = \left(\frac{T}{T_u}\right)^b \tag{8}$$

with $b = 0.76$.

Reporting Eqs. (6-8) into Eq. (3), we obtain:

$$B = \frac{1}{4} S_L^2 \frac{Pr W_{O_2}^2}{\rho_u^2 Y_{O_2,u}^2 \nu_{CH_4}} (1-\alpha)^{b-1} \beta^3 \exp(\beta/\alpha) \tag{9}$$

Due to the assumptions used in the asymptotic analysis (constant calorific capacities, thermal, and species diffusivities), Eq. (9) constitutes a first approximation for B. The values for B given by Eq (9) are compared with the result obtained using PREMIX. Asymptotic analysis exhibits higher values for B compared to PREMIX. This is also noticed by Rutland (1989), who studied the propagation of a one-dimensional premixed laminar flame using a one-step chemical model and by considering constant transport properties.

2.3 Kinetics parameters of one- & two-step models for lean premixed laminar flame

In this section, the kinetic parameters for one- and two-step models are determined for the combustion of a methane-air premixed laminar flame with an equivalence ratio of 0.55 using the PREMIX code. Particular conditions for the transport properties are considered. The dynamic viscosity is expressed according Eq. (8) and constant Prandtl and Schmidt numbers are assumed. Calorific capacity is also assumed constant and the molecular weights of all the species are equal. To do so, the PREMIX code had to be modified to accept artificial species and modified transport properties.

The motivations of these choices are directly related to the DNS code applied to complex flows such as vortex-premixed flame or turbulence-premixed flame interactions.

2.3.1 The one-step model chemical model

In this model, the chemistry is described by a single step irreversible reaction:

$$\text{A(reactants)} \rightarrow \text{P(products)} \tag{10}$$

The reaction rate of this reaction is expressed using a classical Arrhenius law

$$\dot{w}_A = BC_A \exp(-E_a/R_oT) \tag{11}$$

For this simplest chemical model, 4 parameters appear: B, E_a, (ΔH), and Le_A ((ΔH) being the heat released by the reaction). Since Le_A and (ΔH) can easily be determined (by using binary diffusion coefficient for the Lewis number and by matching the fully burnt gas temperature for (ΔH)), we have to determine B and E_a.

2.3.2 The two-step chemical model

The two-step mechanism initially proposed by Zel'dovich (1948) consists of a first order chain branching reaction and a second-order termination reaction:

$$\text{A} + \text{X} \rightarrow 2\text{X} \tag{12}$$

$$\text{X} + \text{X} \rightarrow \text{P} \tag{13}$$

The use of a two-step mechanism significantly increases the number of unknowns. Now, 8 parameters have to be determined: B_1, B_2, E_{a_1}, E_{a_2}, $(\Delta H)_1$, $(\Delta H)_2$, Le_A, and Le_X where $(\Delta H)_1$ and $(\Delta H)_2$ represent the heat released by the first and by the second reaction. To reduce the number of unknowns, some realistic assumptions can be proposed:

- the first reaction has a high activation energy and is thermo-neutral (Liñán 1974)
- the second reaction has a zero activation energy and liberates all the heat (Liñán 1974) coefficients

These assumptions lead to simplified expression for the reaction rates of the reactions (12) and (13).

$$RR_1 = B_1C_AC_X \exp(-E_{a_1}/R_oT) \tag{14}$$

$$RR_2 = B_2C_X^2 \tag{15}$$

Moreover, since the H atom provides a crucial source of radicals and plays a determining role in the submechanism $H_2 - O_2$ (Glassman 1987), we relate the intermediate species of the two-step mechanism to the H atom. Thus, from binary diffusion coefficients, the Lewis numbers for A and X are: $Le_A = 1.0$, $Le_X = 0.15$. From these considerations, 3 parameters still have to be determined: B_1, B_2, and E_{a_1}.

To determine the remaining unknowns of the one- and two-step mechanisms, the methodology previously described is applied.

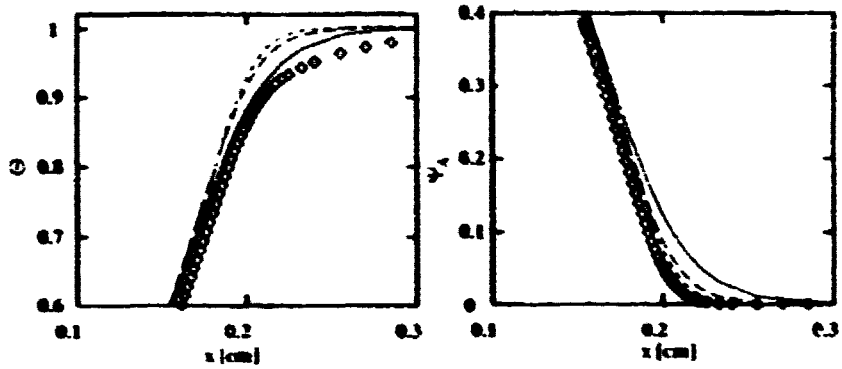

FIGURE 4. Temperature and A mass fraction obtained with the one-step model (reduced by its value in the fresh gas) at the trailing edge of the flame. ◇ : GRI-mech (CH_4 mass fraction); ——— : E_a = 30kcal/mol B = 1.82e8; ---- : E_a = 45kcal/mol 4.93e10; ····· : E_a = 60kcal/mol B = 1e13 (B in mol, s).

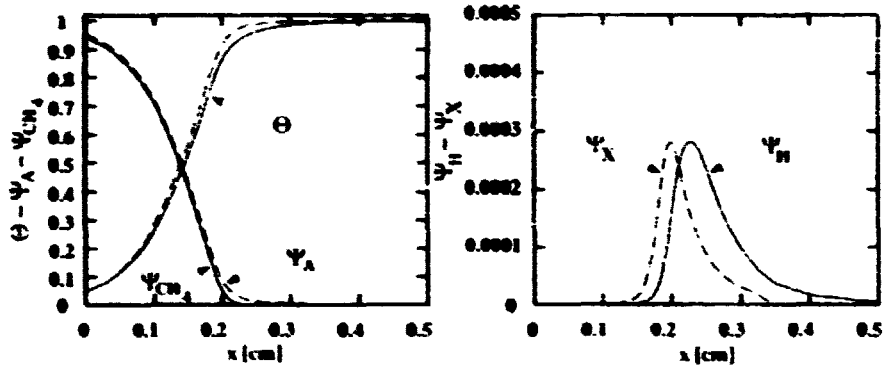

FIGURE 5. Reduced methane and H concentration and temperature profiles across the laminar flame front. ——— : GRI-mech; ---- : two step mechanism.

2.3.3 Results

First, the influence of kinetic parameters of one- and two-step models on the flame structure is analyzed. The flame structure is very sensitive to the couple (B, E_a) especially in the trailing edge of the flame (see Fig. 4). Since both B and E_a vary, it is difficult to know which of these two parameters influences the gradients of temperature and concentration. The profiles of $\Psi_{CH_4} = Y_{CH_4}/Y_{CH_4,u}$ in the burnt gas side seems to be very critical in the opposed jet configuration. When the flames interact between them, incomplete combustion by leakage of the fuel can lead to sudden extinction. This is particularly true for the case E_a = 30 kcal/mol, B = 1.82 10^8 $mol^{-1}s^{-1}$ for which the spreading of the CH_4 profile is more pronounced. For these values, the one step model predicts an extinction strain rate of $50s^{-1}$, whereas the experimental results give $K_{ext} = 200s^{-1}$ (Egolfopoulos 1994a).

This can be explained by noticing that for high activation energy, the thin reaction

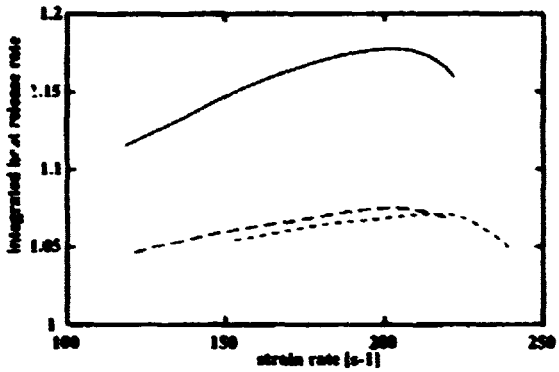

FIGURE 6. Evolution of the heat release integrated across the flame front (reduced by the unstrained value) in function of the strain. ——— : GRI-mech; - - - - : one-step mechanism; ····· : two-step mechanism.

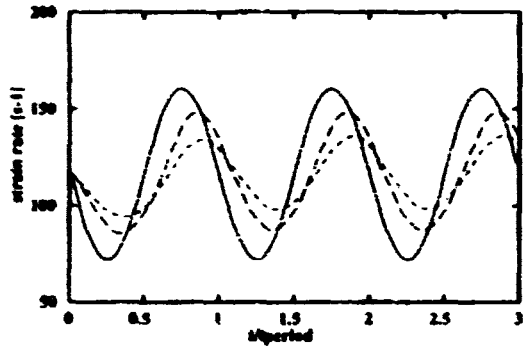

FIGURE 7. Evolution of the strain rate in function of time for different frequencies. ——— : 1 Hz; - - - - : 40 Hz; ····· : 80 Hz.

zone is located at the downstream end of the temperature and concentration profiles (since the reaction zone is proportional to β^{-1}). Thus, for larger values of E_a, low strain rates only affect the preheat zone. As the strain rate increases, the temperature and concentration profiles are steeper, and the reaction zone starts to be affected by the strain. This effect is emphasized in the twin flame configuration where the distance separating the two reaction zones is a key parameter in the processes leading to extinction. The determination of the extinction strain rate (in the opposed jet configuration) depends directly on the good prediction of the position of the reaction zone in function of the inlet mass flow rate and, consequently, the strain rate.

Figure (5) represents the flame structure using the two-step mechanism. Here, the concentration of the intermediate species is also of interest because of the quadratic dependence on Y_X on the heat release rate (see Eq. 15). The maximum value of X is chosen by matching the maximum value of the H atom concentration given by the GRI mechanism. Once B_1 and E_{a_1} are chosen to match the θ and Ψ_A profiles, the

maximum of Ψ_X is directly related to the frequency factor of the second reaction B_2. We also observe a space shift of the Ψ_X compared to the Ψ_H profile. This could be overcome by decreasing B_1 in order to change the production of X. However, the decrease of B_1 directly leads to a thickening of the flame in the burnt gas side of the flame and, consequently, to a different response of the flame to strain. Thus, a compromise between the profiles of θ, Ψ_A, and Ψ_X has to be found in order to obtain the right extinction strain rate in the opposed jet flame configuration. Finally, Fig. (6) shows the flame response to a steady strain rate obtained for the one- and two-step models and the comparison with the solution given by the GRI mechanism. Here, the heat release rate integrated across the flame (normalized by the unstrained value) is presented. Both the one- and two-step mechanisms allow us to find the correct extinction strain rate (within 10% of error). We also notice that the Lewis number effect is also observed by using the simple transport properties described in section (2.3). Since the Lewis number based on the limiting species (here CH_4) is less than unity ($Le_A = 0.95$), a positive stretch applied to the flame increases the heat release. As the stretch increases, the reaction zones are pushed toward the stagnation plane, and reaction cannot be sustained due to shorter residence time (Law 1988).

3. Lean premixed laminar flames submitted to an oscillating strain

3.1 Analysis of the flame response

The response of a laminar premixed methane-air flame to unsteady strain is numerically studied using one- and two step chemical models. The unsteadiness of the flow is obtained by imposing a sinusoidal velocity field at the inlet boundaries. The amplitude of the velocity variations is 20% of the mean value inlet velocity. Three different frequencies for the velocity fluctuations are studied (1, 40, and 80 Hz). The strain rate applied to the flame varies from 70 to 160 s^{-1}, corresponding to Karlovitz number varying from 0.33 to 0.75. Here, the Karlovitz number is defined by $Ka = \tau_c K$ where K is the strain rate and τ_c a chemical time scale defined by $\tau_c = \alpha_u / S_L^2$, α_u being the thermal diffusivity in the fresh gases. The order of magnitude of the Karlovitz number is typically representative of the flamelet regime defined by the Klimov-Williams criteria ($Ka < 1$).

The time evolution of the heat release rate integrated across the flame (non-dimensionalized by the unstrained value) is presented Fig. (8). As a first observation, no phase shift is observed between the one- and two-step chemical models and the solution given by the GRI mechanism. The slight asymmetry between the slopes corresponding to the extension and relaxation observed by the GRI mechanism is also described by the two-step model. Figure (9) represents the heat release amplitude (normalized by its steady strained value) for different frequencies. The amplitudes of the fluctuations are underestimated by the simple models even if the tendency is well reproduced. As previously observed by Egolfopoulos (1994a), at low frequencies the flame behaves like in the steady case whereas at higher frequencies, the amplitude of the fluctuations decreases. The attenuation of the heat release amplitude at higher frequencies is explained by the fact that the disturbances are

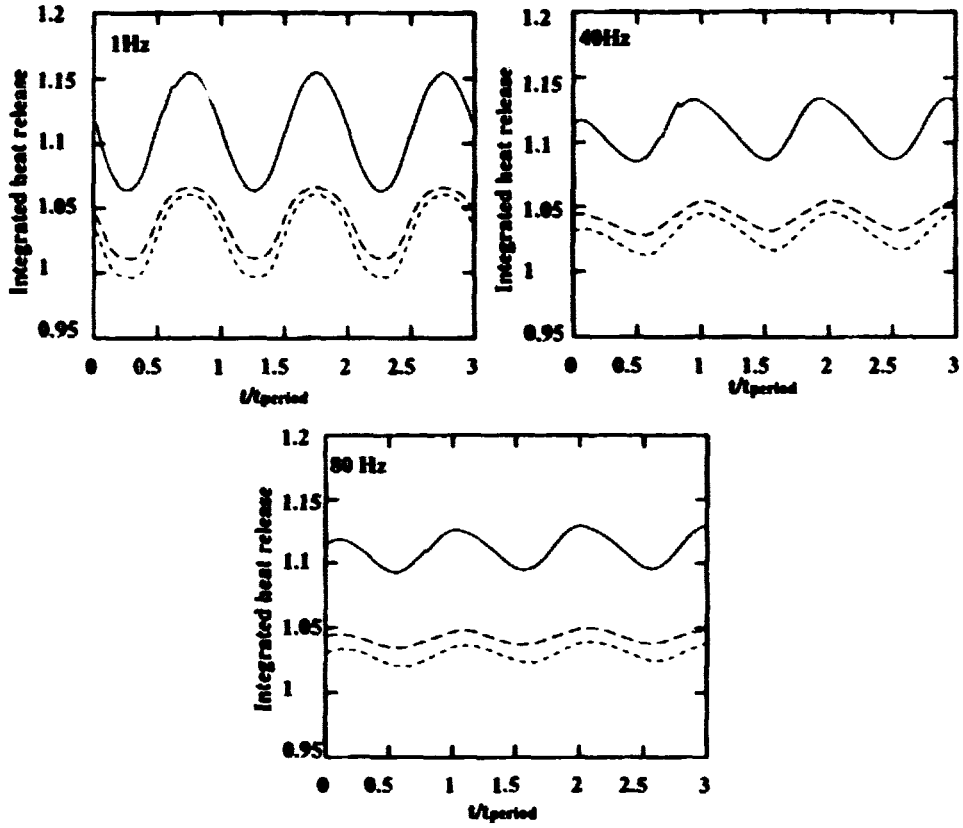

FIGURE 8. Evolution of the heat release integrated across the flame front (reduced by the unstrained value) in function of time ($Le_A = 0.95$). ——— : GRI-mech; - - - - : one-step mechanism; ····· : two-step mechanism.

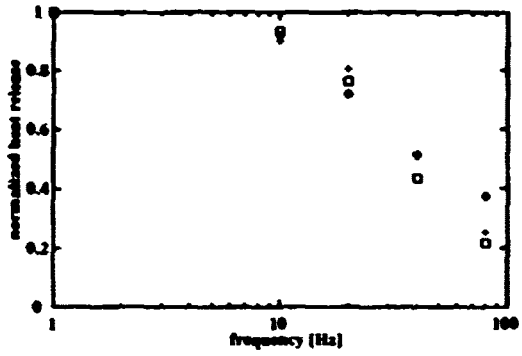

FIGURE 9. Evolution of the heat release amplitude (normalized by its unstrained value) in function of the frequency. ◇ : GRI-mech; + : one-step mechanism; □ : two-step mechanism.

rapidly attenuated by diffusion effects (Egolfopoulos 1994a).

3.2 Response of a flame with unity Lewis number to an oscillating strain

We also notice that the heat release rate given by the two-step mechanism is always lower than the results given by the one-step mechanism. This can be explained using the asymptotic analysis of Seshadri & Peters (1983) who studied the structure of a planar premixed laminar flame submitted to stretch. Considering a high activation energy for the first reaction, the authors derived an asymptotic expansion for the temperature. They found that the first order temperature can be expressed as a function of stretch and Lewis numbers for the reactant and the intermediate species:

$$T_0^1 = -K^* \left\{ \frac{Le_A - 1}{Le_A} + (-\Delta H_2^*) \left[\frac{1 - Le_X}{Le_X} I_0 \right] + \frac{Y_{X_0}^1}{Le_X} \right\} \tag{16}$$

The subscript 0 refers to the axial coordinate where Y_X is maximum, I_0 is a function always positive, K^* is a non-dimensionalized stretch, and $(-\Delta H_2^*)$ is the non-dimensionalized heat of reaction of the recombination step. The relation (16) points out the respective roles of the diffusivities of the reactant and of the intermediate species. Considering only the first term on the RHS of Eq. (16), for positive stretch the temperature increases for $Le_A < 1$. For $Le_A = 1$, the temperature remains constant equal to the zero order temperature regardless the value of the stretch. This recovers the classical conclusions of the role played by the Lewis number of the reactant on the dynamic of stretched flames (Clavin 1985, Law 1988). The second term on the RHS of (16) enhances the effects of diffusivity of the intermediate species on the dynamic of stretched flames. Since radicals are mostly very light species, they have high diffusivities leading to Lewis numbers significantly less than unity (here $Le_X = 0.15$). Thus, in the case of positive stretch, the diffusivity of the intermediate species tends to decrease the temperature and, consequently, the local laminar flame speed. This result points out that even for $Le_A = 1$ the flame can be sensitive to stretch effect and exhibits local variations of the laminar flame speed not only due to compression of the reaction zone.

Moreover, under some circumstances, a positive stretch can produce a decrease of the heat release rate when the Lewis number of the reactant is slightly less than unity. This is observed in Fig. (8) for the frequency 1 Hz and $Le_A = 0.95$ where the normalized heat release rate goes under unity.

In order to characterize the effect of a slight variation of the Lewis number, the response of the flame to unsteady strain is analyzed by imposing the Lewis number for the reactant equal to unity. This slight variation of Le_A has a strong consequence on the flame response. Figure 10 shows the evolution of the heat release integrated across the flame front for $Le_A = 1.0$ and for 1, 40, and 80 Hz. The results issued from the one- and two-step calculations are in opposition of phase compared to the solution given by the GRI mechanism. Due to the compression of the reaction zone, the integrated heat release is less than unity for both one- and two step-models. Moreover, for the two-step mechanism, the diffusion of the intermediate species also contributes to the decrease of the heat release as previously explained.

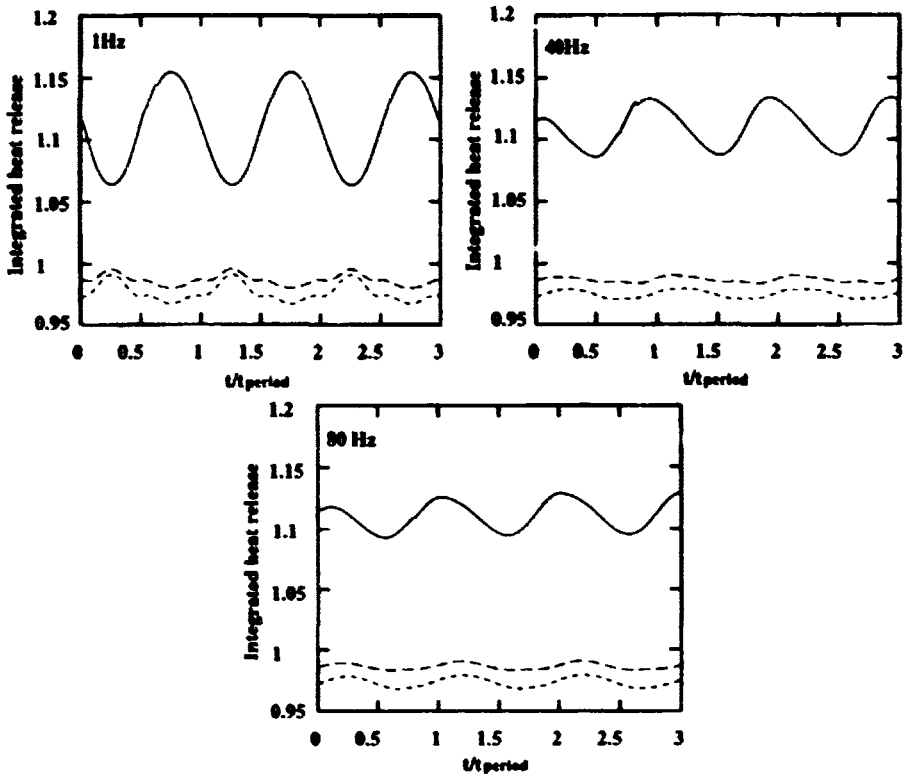

FIGURE 10. Evolution of the heat release integrated across the flame front (reduced by the unstrained value) in function of time ($Le_A = 1.0$). ——— : GRI-mech; - - - - : one-step mechanism; ····· : two-step mechanism.

This behavior is well summarized on Fig. 11, in which the scatter plot of the heat release rate versus the strain rate is represented for all the frequencies (1, 40, and 80 Hz). Very clear correlations are observed, and different signs for the slopes are found between the cases $Le_A = 0.95$ and $Le_A = 1.0$.

This seems to indicate that the thermo-diffusive properties of the mixture is a first order parameter in the behavior of strained laminar flames.

4. Vortex-premixed laminar flame interaction

The configuration investigated here concerns the interaction between a two-dimensional vortex pair generated by acoustic excitation and a V-shaped air-methane premixed laminar flame stabilized on a heated wire. A counter-rotating vortex pair propagating itself by mutual induction interacts with an initially planar premixed flame. Figure 12 shows the vorticity and heat release fields during the interaction (t = 5ms). Here, the Lewis number based on the reactants is taken equal to unity. This problem has been extensively studied both experimentally (Samaniego *et al.* 1996) and numerically (Mantel 1994). Here, a lean methane-air flame is investigated (equivalence ratio = 0.55). The initial conditions for the simulations are obtained from the

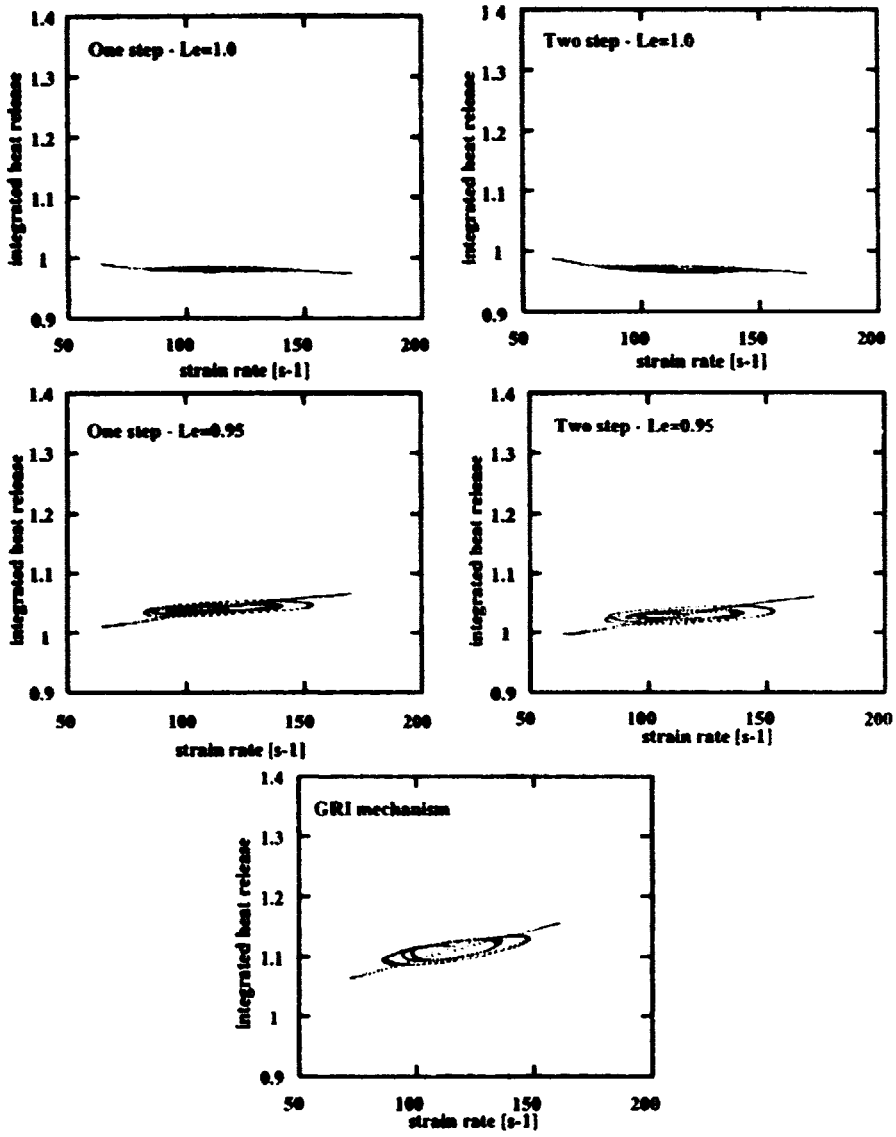

FIGURE 11. Scatter plot of the integrated heat release across the flame front (reduced by the unstrained value) vs strain rate.

experiment. The characteristics of the interaction are $V_D/S_L = 66.8$, $s/\delta_f = 25.7$, and $D/\delta_f = 104.8$, where V_D, S_L represent respectively the displacement velocity of the vortex pair and the laminar burning velocity; and s, δ_f, and D are the distance between the center of the vortices, the laminar flame thickness, and the distance separating the vortex pair from the laminar flame.

Details concerning the geometry and diagnostic techniques can be found in Samaniego *et al.* (1995). Information concerning the equations solved in the DNS code and

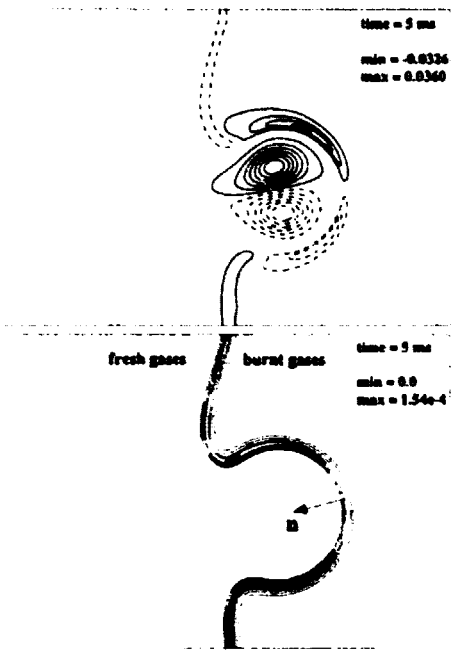

FIGURE 12. Vorticity (top) and heat release rate (bottom) fields at t = 5ms of the interaction (from Mantel *et al.* 1996).

the computational configuration are presented in Mantel (1994).

Since radiative heat losses effects have been found negligible during this interaction (Samaniego 1996, Mantel 1994), adiabatic conditions for the flame are taken for the simulations. Figure 13 shows the time evolution of the flame length (non-dimensionalized by its initial length). Comparison with the experimental results of Samaniego (1996) points out that the dynamic of the interaction is well reproduced by the simulations. The time evolution of the minimum heat release rate integrated along a normal to the flame and encountered along the flame is also shown Fig. 13. As long as the interaction goes on, the vortex pair increases the flame length and leads to a decrease of the heat release rate at a location in front of the vortex pair. This is qualitatively well described both by one- and two-step mechanism. In this configuration, the two-step model allows a significant improvement in the description of the decrease of the heat release rate.

5. Conclusions

This paper presents a new methodology to determine kinetic parameters of one- and two-step chemical models classically used in DNS of premixed combustion. By using a one-dimensional code in which simple chemical models and simple transport properties are implemented, the kinetic parameters are determined in order to verify (1) the laminar burning velocity, (2) the temperature and concentration profiles, and (3) the extinction strain rate of a laminar flame in the opposed jet configuration (counterflow flames). To do so, the results issued from these simple models are

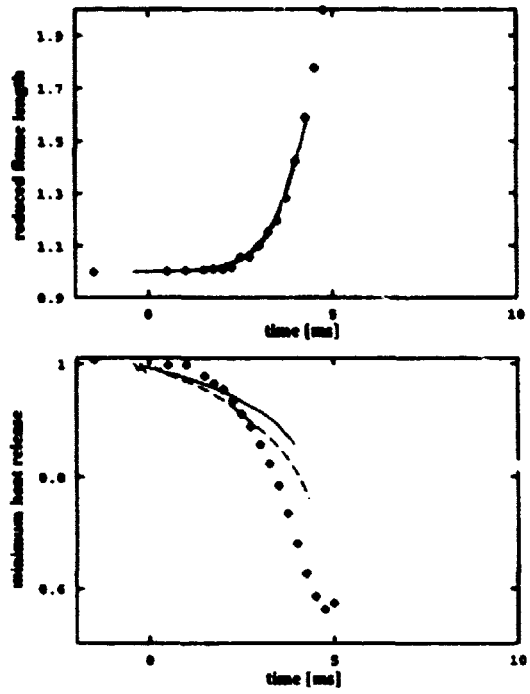

FIGURE 13. Time evolution of the flame length (top) and minimum heat release rate integrated across the flame. ——— : one-step mechanism; ---- : two-step mechanism.

compared in detail with results obtained from the GRI-mech 2.1 mechanism and multi-component transport properties.

Applications of these simple mechanisms and transport models on two unsteady configurations show good behavior of these models. In the case of a flame submitted to an unsteady strain, both one- and two-step models describe qualitatively well the dynamic of the flame and the heat release amplitude for different frequencies. In this configuration, no obvious improvement is obtained with the two-step model. However, the Lewis number based on the reactant seems to be a determining parameter for laminar strained flames. A slight variation of the Lewis number from 0.95 to 1.0 leads to a completely different behavior of the flame.

The interaction between a two-dimensional vortex pair with an initially planar premixed flame is also analyzed by DNS using the one- and two-step chemical models. In this case, comparisons with the experimental results of Samaniego *et al.* (1996) shows that the two-step chemical model allows a better description of the interaction. However, further work is needed to investigate the effects of a slight variation of the Lewis number on the behavior of the flame during the vortex-flame interaction.

This methodology can be improved by studying a configuration of laminar strained

flame more representative of turbulent premixed flames. This concerns the counterflow flame configuration, but with hot products on one side and reactants on the other side. Further work is in progress to examine the behavior of simple and transport models.

Acknowledgments

The authors wish to thank Dr. Jean-Michel Samaniego for his encouraging and fruitful support.

REFERENCES

CHEN, J. H., MAHALINGAM, S., PURI, I. K., & VERVISCH, L. 1992 Structure of turbulent non-premixed flames modeled with two-step chemistry. In *Proc. 1992 Summer Program*.Center for Turbulence Research, NASA Ames/Stanford Univ. 389-402.

CHUNG, S. H., KIM, J. S. & LAW, C. K. 1986 Extinction of interacting premixed flames: Theory and experimental comparisons. *21st Symp.(Int'l.) on Combust.* The Combustion Institute. 1845-1851.

CLAVIN, P. 1985 Dynamic behavior of premixed flame fronts in laminar and turbulent flows. *Progress in Energy and Combustion Science*. **11**, 1-59.

EGOLFOPOULOS, F. N. 1994a Dynamics and structure of unsteady, strained, laminar premixed flames. *25th Symp. (Int'l.) on Combust.*The Combustion Institute. 1365-1373.

EGOLFOPOULOS, F. N. 1994b Geometric and radiation effects on steady and unsteady strained laminar flames. *25th Symp. (Int'l.) on Combust.*The Combustion Institute. 1375-1381.

FRENKLACH, M., WANG, H., GOLDENBERG, M., SMITH, G. P., GOLDEN, D. M., BOWMAN, C. T., HANSON, R. K., GARDINER, W. C. & LISSIANSKI, V. 1995 GRI-Mech - An optimized detailed chemical reaction mechanism for methane combustion. *Gas Research Institute report* GRI-95/0058.

GLASSMAN, I. 1987 *Combustion*. Academic Press 2nd Ed.

HILKA, M., VEYNANTE, D., BAUM, M. & POINSOT, T. 1995 Simulation of flame-vortex interactions using detailed and reduced chemistry. *10th Symposium on Turbulent Shear Flows*.

KEE, R. J., GRCAR, J. F., SMOOKE, M.D. & MILLER, J. A. 1994 A fortran program for modeling steady laminar one-dimensional premixed flames. *Sandia National Laboratories - SAND85-8240*.

KEE, R. J., RUPLEY, F. M. & MILLER, J. A. 1989 Chemkin-II: A fortran chemical kinetics package for the analysis of gas phase chemical kinetics. *Sandia National Laboratories - SAND89-8009B*.

LAW, C. K. 1988 Dynamics of Stretched Flames. *22nd Symp. (Int'l.) on Combust.* The Combustion Institute. 1381-1402.

LAW, C. K., ZHU, D. L. & YU, G. 1986 Propagation and extinction of stretched premixed flames. *21st Symp. (Int'l.) on Combust.* The Combustion Institute.1419-1426.

LIÑAN, A. 1974 A Theoretical analysis of premixed flame propagation with an isothermal chain reaction. Instituto Nacional De Tecnica Aerospacial, Esteban Terradas, Madrid, Spain.

MANTEL, T. 1994 Fundamental Mechanisms in Premixed Flame Propagation Via Vortex Flame Interactions-Numerical Simulations. *Annual Research Briefs.* Center for Turbulence Research, NASA Ames/Stanford Univ. 45-75.

MANTEL, T., SAMANIEGO, J.-M., & BOWMAN, C. T. 1996 Fundamental mechanisms in premixed flame propagation via vortex flame interactions-Part II: Numerical Simulations. *In preparation.*

POINSOT, T. 1996 Using direct numerical simulations to understand premixed turbulent combustion. *26th Symp. (Int'l.) on Combust.* The Combustion Institute.

POINSOT, T., CANDEL, S., & TROUVÉ, A. 1996 Applications of direct numerical simulation to premixed turbulent combustion. *Progress in Energy and Combustion Science.* **21,** 531-576.

POINSOT, T., VEYNANTE, D. & CANDEL, S. M. 1991 Quenching processes and premixed turbulent combustion diagrams. *J. Fluid Mech.* **228,** 561-605.

RUTLAND, C. J., 1989 Effects of strain, vorticity and turbulence on premixed flames. *Ph-D Thesis,*Stanford University.

RUTLAND, C. J. & TROUVÉ, A. 1993 Direct simulations of premixed turbulent flames with non-unity Lewis numbers. *Combust. Flame.* **94,** 41-57.

SAMANIEGO, J.-M., MANTEL, T. & BOWMAN, C. T. 1996 Fundamental mechanisms in premixed flame propagation via vortex flame interactions-Part I: Experiment. Submitted to J. Fluid Mech.

SESHADRI, K. & PETERS, N. 1983 The influence of stretch on a premixed flame with two-step kinetics. *Combust. Sci. Tech.* **22,** 119-129.

TROUVÉ, A. & POINSOT, T. 1994 The evolution equation for the flame surface density in turbulent premixed combustion. *J. Fluid Mech.* **278,** 1-31.

VERVISCH, L. 1992 Study and Modeling of finite rate chemistry effects in turbulent non-premixed flames. *In Annual Research Briefs* Center for Turbulence Research, NASA Ames/Stanford Univ. 411-429.

WILLIAMS, F. A. 1985 *Combustion theory.* 2nd ed., Benjamin Cummings.

ZEL'DOVICH, Y. B. 1948 Theory of flame propagation. *Zhur. Fizi. Khi. (USSR),* **22,** 27-49.

NEXT
DOCUMENT

Evaluation of joint probability density function models for turbulent nonpremixed combustion with complex chemistry

By N. S. A. Smith[1], S. M. Frolov[2] AND C. T. Bowman[3]

Two types of mixing sub-models are evaluated in connection with a joint-scalar probability density function method for turbulent nonpremixed combustion. Model calculations are made and compared to simulation results for homogeneously distributed methane-air reaction zones, mixing and reacting in decaying turbulence within a two-dimensional enclosed domain. The comparison is arranged to ensure that both the simulation and model calculations a) make use of exactly the same chemical mechanism, b) do not involve non-unity Lewis number transport of species, and c) are free from radiation loss. The modified Curl mixing sub-model was found to provide superior predictive accuracy over the simple relaxation-to-mean sub-model in the case studied. Accuracy to within 10 – 20% was found for global means of major species and temperature; however, nitric oxide prediction accuracy was lower and highly dependent on the choice of mixing sub-model. Both mixing sub-models were found to produce non-physical mixing behavior for mixture fractions removed from the immediate reaction zone. A suggestion for a further modified Curl mixing sub-model is made in connection with earlier work done in the field.

1. Introduction

A large number of practical combustion systems can be said to operate in a nonpremixed turbulent regime. Under these conditions, fuel and oxidizer react concurrently as they are mixed together through the cascade of scales from turbulent stirring down to molecular diffusion. The nonpremixed mode of combustion is distinct from the premixed mode in that the propagation of reaction fronts through a flammable mixture is not encountered. This is by virtue of the concurrence of mixing of reactants to a flammable state, and reaction.

When put in the context of the partially premixed flame studies discussed elsewhere in this volume, nonpremixed combustion refers to all the phenomena that occurs after the passage of any initial igniting flame fronts. The bulk of chemical activity in gas turbine combustors, compression ignition internal combustion engines, and a great many other classes of devices, occurs downstream of stabilizing flow structures in a purely nonpremixed mode.

1 Center for Turbulence Research

2 N. N. Semenov Institute for Chemical Physics, Moscow, Russia

3 Stanford University

The critical design issues facing gas turbine combustor and diesel engine designers at present center on reducing pollutant formation in order to meet present and future emission regulations. In order to understand and be able to predict the occurrence of unwanted byproducts, such as oxides of nitrogen (NO_x) and soot, it is essential that allowances be made for the interactions which occur between finite rate chemical reactions and turbulent mixing processes. Nitric oxide (NO) is a species whose formation in flames is limited by chemical kinetic rates which are slow in comparison to typical mixing rates, and thus cannot be adequately predicted using a model assumption of mixing-limited chemistry.

Many methods have been proposed which seek to accurately predict the interaction of finite rate chemistry and turbulent mixing. One of the most promising groups is the Joint Probability Density Function (JPDF) methods as employed by Pope (1981, 1985, 1990) and others (see Chen & Kollmann 1988, 1992, 1994). The variants of the JPDF method have been used to successfully predict nitric oxide formation in turbulent jet diffusion flames of hydrogen (Chen & Kollmann 1992, Chen *et al.* 1995, Smith *et al.* 1993). The effectiveness of the JPDF model in these experimental comparisons for hydrogen and other tests involving hydrocarbon fuels (Chen 1996) make it a prime candidate for incorporation in design tools for use with more practical combustion systems.

Correa and Pope (1992) have already begun to take steps towards implementing JPDF methods in a computational framework more suited to practical calculations. They showed reasonable agreement between the predictions of a hybrid JPDF method in an elliptic flow solver, with experimental data gathered behind a bluff body stabilized flame. One difficulty with the experimental comparison of Correa and Pope (1992) and those of the jet flame experiments described above is that there are a number of other models and approximations that must be incorporated in order to produce useful predictions, but these other models make it difficult to ascertain the inherent accuracy of the JPDF method.

Where only a *scalar* JPDF method is employed (as in the studies cited), a turbulence model must be used to solve for the turbulent flow field. In the jet flame studies, radiation modeling can be problematic (Smith *et al.* 1993, 1996) and thus make it difficult to evaluate the performance of the JPDF model directly. Further, since the JPDF model cannot be easily employed with large chemical reaction mechanisms, due to computational constraints, it is often necessary to employ reduced chemical descriptions of the full reaction set. This modeled abbreviation of a chemical system also introduces uncertainty when comparing with physical experiments.

Extraneous modeling issues can be swept aside if direct numerical simulation (DNS) is used as an evaluation tool. With DNS it is possible to construct an idealized numerical experiment where unwanted physical effects can be excluded by design. For the case of mixing and reaction of fuel and oxidizer pockets in decaying isotropic turbulence, the flow field is at its simplest, radiation losses can be dropped from consideration, and commonality between the modeled and simulated chemical reaction schemes can be ensured.

The purpose of this study was to compare JPDF model predictions with DNS

observations for the nonpremixed combustion of methane and air in decaying turbulence. The chemical mechanism employed in both the DNS and in the JPDF model calculations included prompt and thermal NO formation pathways and so allowed an evaluation of the model's NO prediction capabilities to be made.

2. Joint scalar PDF equations

Given a chemical system of N species it is possible to construct a chemical composition vector, where each coordinate corresponds to a possible species mass fraction. It is then possible to define the probability F that the instantaneous composition vector at a time t at a sample point is in the immediate vicinity of $\underline{\psi}$.

$$F(\psi_1, \ldots, \psi_N; t) \equiv Prob\{\psi_1 < \phi_1 \leq \psi_1 + d\psi_1, \ldots, \psi_N < \phi_N \leq \psi_N + d\psi_N\} \quad (1)$$

The density-weighted joint scalar probability density function, $\tilde{f}$, in composition space is then defined as the partial derivative with respect to the species dimensions.

$$\tilde{f}(\psi_1, \ldots, \psi_N) \equiv \frac{\rho(\psi_1, \ldots, \psi_N)}{<\rho>} \frac{\partial^n F}{\partial\psi_1 \ldots \partial\psi_N} \quad (2)$$

For homogeneous flows, the evolution of the joint scalar PDF is then given by the following (see Chen and Kollmann 1994), where $\dot{Q}_k$ is the instantaneous reaction rate of the kth species at time t, and $\chi_{k,l}$ is the joint scalar dissipation rate for the kth and lth species.

$$\frac{\partial\tilde{f}}{\partial t} + \frac{\partial}{\partial\psi_k}(\dot{Q}_k\tilde{f}) = -\frac{\partial^2}{\partial\psi_k\partial\psi_l}(\chi_{k,l}\tilde{f}) \quad (3)$$

The influence of chemical reactions on the temporal evolution of the joint scalar PDF is similar to a convective velocity field in composition space. Dissipation of scalar fluctuations through mixing, as represented by the second right hand side term, lead to reductions in the variances and covariances of the species and a sharpening of the joint PDF at the mean composition.

As chemical systems of practical interest can have an extremely large number of important species, the dimensionality of the joint PDF can also be large. Stochastic methods recommend themselves as the solution method of choice in these cases (Pope 1981).

In a Monte Carlo approach, a large number of stochastic particles are operated upon by model processes in a Lagrangian frame of reference. The model processes are designed in such a way as to cause the joint PDF of all the particles to behave according to the evolution equation above.

Each stochastic particle has a definite location in composition space at any given time. The evolution of the ith chemical component of the jth stochastic particle can be expressed in terms of a chemical reaction source term, $\dot{Q}_i^j$, and molecular mixing term, $\dot{m}_i^j$, as given below.

$$\frac{\partial \phi_i^j}{\partial t} = \dot{Q}_i^j + \dot{m}_i^j \tag{4}$$

A significant advantage of the JPDF method over other models is that the chemical source terms $\dot{Q}_i^j$ can be evaluated exactly without need for a model. The difficulty with the Lagrangian formulation lies with the treatment of the molecular mixing terms $\dot{m}_i^j$.

2.1 Molecular mixing models

A wide variety of molecular mixing models have been proposed for $\dot{m}_i^j$ in the past (see Pope 1981, Chen and Kollmann 1994). The simplest useful model is a deterministic relaxation-to-the-mean (RTM) expression as given below, where ω denotes a turbulent mixing frequency.

$$\dot{m}_i^j \approx \omega(< \phi_i > - \phi_i^j) \tag{5}$$

The deterministic RTM model has the advantage of being simple to implement within a complex practical calculation and allows the mixing and reaction terms of the stochastic equations to be solved simultaneously. All particles are operated on by both the molecular mixing and reaction models at all stages of the computation. A disadvantage of the RTM model is that it does not predict the correct mixing behavior of two fluids in an isotropically decaying turbulent field. Instead of causing a mixture fraction PDF to tend towards a Gaussian distribution with increasing time, the RTM model allows the flatness of the PDF to increase without bound.

More sophisticated mixing models have been derived from the Curl coalescence-dispersion models for droplet mixing. Whereas the original Curl mixing model gives rise to discontinuous joint PDFs, the modified Curl model proposed by Janicka *et al.* (1979), and Dopazo (1979), yields the desired continuous joint PDFs. Mixing is modeled by operating on a small number of particles at each time step of the calculation. Particle pairs are chosen at random from the complete particle ensemble, and are caused to mix with one another to a randomly varying degree a. The resultant compositions of the jth and kth particle after mixing interaction are given by the following.

$$\phi_i^{j*} = a\phi_i^j + \frac{1}{2}(1-a)(\phi_i^k + \phi_i^j) \tag{6}$$

$$\phi_i^{k*} = a\phi_i^k + \frac{1}{2}(1-a)(\phi_i^k + \phi_i^j) \tag{7}$$

The number of random particle pair selections that must be made per timestep of the calculation is given by the following (see Pope 1982), where B is a constant number that depends on the pair selection scheme, and $\omega\delta t$ is the timestep nondimensionalized by the mixing frequency.

$$N_{pairs} = B\omega\delta t N_{particles} \tag{8}$$

The use of random particle interaction (RPI) models provides a framework for the implementation of schemes that reflect more of the physical nature of mixing. An example of the benefit that can be derived from RPI models can be found in the "particle age" modification suggested by Pope (1982). This model can be tuned to enforce asymptotic Gaussianity on conserved scalar PDFs in decaying isotropic turbulence.

One potential drawback incurred in using particle interaction models is that the mixing process can then no longer be solved simultaneously with the chemical reaction process. The two processes must be decoupled, and this can cause problems where the rates of mixing and reaction are both very large relative to the inverse of the timestep. Such problems are likely to occur when combustion occurs in the flamelet regime (see Anand & Pope 1987).

Both the RPI model and the simple RTM model were employed in JPDF calculations against the DNS data. The results of this comparison are presented in Section 4.

3. Simulation conditions

Due to resource and time constraints, the direct numerical simulation was limited to a two-dimensional calculation of nonpremixed combustion in a decaying turbulent field.

As the JPDF method is inherently statistical in nature, it was desirable to maximize the number of DNS data points in the domain that could be included in a single statistical set. To this end, the simulation was performed with an initially isotropic turbulent velocity field and distribution of fuel and oxidizer pockets. The initial distribution of chemical species was determined from a phase scrambled E^{-4} spectrum for a conserved scalar, known as mixture fraction ξ (see Fig. 1).

Mixture fraction is a normalized scalar that is equal to unity where all of the local has mass originated from the nominal fuel source, irrespective of its reacted state, and zero where all the local mass has originated from the oxidizer source.

Given the distribution of the conserved scalar, mixture fraction (ξ), reactive scalar profiles were mapped onto the domain according to adiabatic equilibrium profiles in mixture fraction space (see Fig. 2).

Zones on the domain with a stoichiometric mixture fraction ($\xi = 0.055$) were thus assigned a species and temperature composition corresponding to adiabatic equilibrium conditions at stoichiometric. Domain regions with higher or lower mixture fraction values were given correspondingly richer or leaner blends of equilibrated fluid.

Note that the richest mixture fraction allowed in the initialization of the simulation domain was $< \xi > = 0.15$. This mixture fraction is beyond the rich flammability limit of methane-air mixtures at standard temperature and pressure. Of all the species present in the simulation, only nitric oxide (NO) was initialized as being zero at all mixture fractions.

By initializing the simulation using the method described above, the flame zones were effectively ignited simultaneously, albeit artificially, prior to run time. This

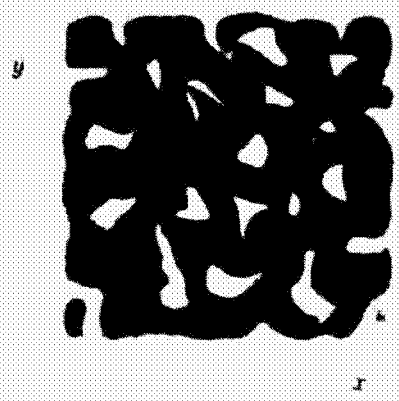

FIGURE 1. Initial distribution of the conserved scalar. Dark regions denote fuel rich zones $\xi = 1$ while light regions denote fuel lean zones $\xi = 0$.

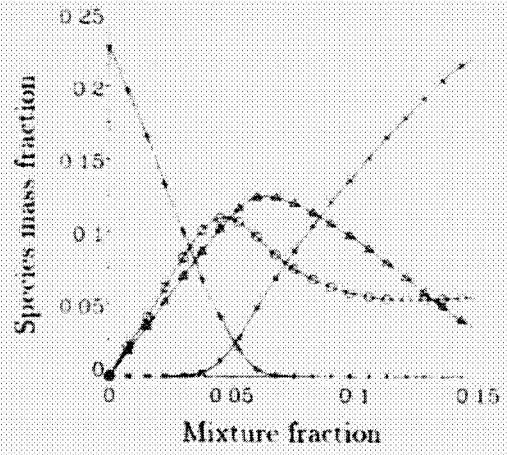

FIGURE 2. Adiabatic equilibrium species mass fraction profiles in mixture fraction space. Symbol key: O_2, × - CO, ○ - CO_2, △ - H_2O.

was done to avoid a potentially long transient period where (presumably) triple flames would propagate along the unburnt flammable ribbons between the fuel and oxidizer pockets away from the ignition points.

In order to avoid the establishment of intense pressure waves as a result of mapping flame zone temperatures onto an initial cold flow field, the local densities were adjusted everywhere to maintain a uniform initial pressure field. The existence of large density gradients after initialization caused a short period where the flow field reorganized to preserve continuity. It is difficult to draw a parallel in behavior between the decay of turbulent motions in the reacting case and the well known trends in inert grid turbulence. The former case is subject to dilatation, variable

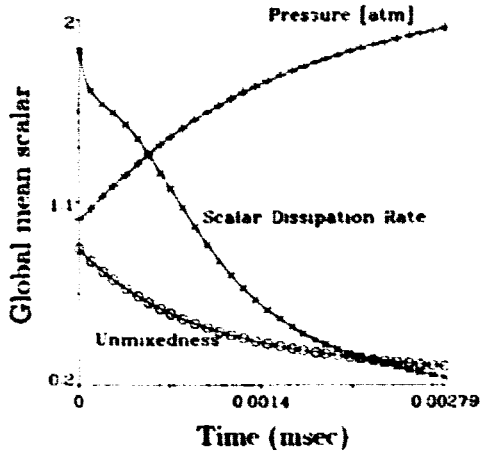

FIGURE 3. Variation in simulated global mean quantities with calculation time.

viscosity, and baroclinic torque effects that are absent in the latter.

Unfortunately, it was further found that it was not possible to perform simulations with a combination of periodic boundary conditions and the initialization technique described above. No satisfactory explanation for this restriction has been found. It was found, however, that the calculation could proceed without hindrance if the domain was instead bounded by adiabatic slip walls encompassing a small filter zone with initially damped wall-normal velocity.

Under the simulation conditions described above, the flow and mixing fields on a central portion of the grid (210^2) were found to be statistically homogeneous. All of these points were then used in each of the statistical samples taken periodically throughout the temporal evolution of the simulation. With the passage of time, turbulent motions caused parcels of fuel and oxidizer to be convected into close proximity while molecular diffusion fed the reaction zones present at the fuel/oxidizer interfaces.

Unmixedness, U, is defined here as the global variance of mixture fraction normalized by the maximum possible variance, which is given by the product of the differences between the global mean and the maximum and minimum possible values of conserved scalar. Unmixedness is thus equal to unity when no mixed fluid is present, and zero when all fluid has been mixed to a uniform state. The gradual decay in the unmixedness of the conserved scalar is plotted along with nondimensional scalar dissipation rate and mean pressure in Fig. 3.

It is evident that the molecular mixing processes promoted by turbulent stirring rapidly mixed the conserved scalar towards uniformity, but that at the end of the simulation the unmixedness was still substantial at approximately $U = 0.3$. As a result of the increase in the characteristic turbulent time scale and the decrease in local conserved scalar gradients, the scalar dissipation rate can be seen to decrease with time.

The simulation was carried out using a Fickian assumption for the molecular

transport of the species, as traces, in a background gas (N_2). All species were assigned uniform Lewis numbers of unity in order to allow a fair comparison with the JPDF model predictions. The JPDF model is not strictly valid where significant differential molecular diffusion between the species is present.

As the reactions proceeded, more and more fuel and oxidizer were consumed and progressively more sensible enthalpy was released into the system. The release of heat in the confined system caused the mean pressure in the domain to double over the course of the simulation (see Fig. 3). The change in global mean species mass fractions during the course of the simulation can be seen in Fig. 4.

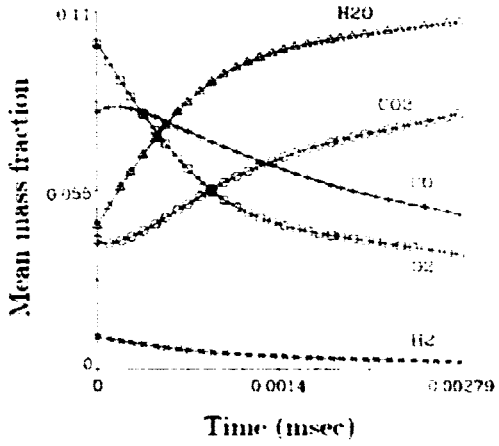

FIGURE 4. Variation in simulated global mean species mass fractions with calculation time.

The turbulent Reynolds number determined use of the mean molecular viscosity (recall that the local temperature variations give rise to a seven-fold variation in local dynamic viscosity) slowly from approximately 30 down to 20 over the duration of the simulation.

The simulation conditions correspond physically to a small area of intensely mixed fluid of the order of 3 millimeters on each side. In some ways the simulation conditions may be analogous to the kind of conditions experienced inside high power-density combustion devices of practical interest. The DNS domain might be thought of as representing a single computational cell in a much larger grid used in a practical model calculation. In this sense it is of some interest to observe how well the JPDF model performs in this single cell, as it could well have implications for use of the model in a large multi-cellular calculation.

With the assumption of isotropy, the JPDF model reduces to a dimensionally degenerate case devoid of mean gradients. The case is similar to those studied by Correa (1993) and Chen (1993), except that it is unsteady, whereas the earlier studies were for steady combustion.

3.1 Chemical reaction mechanism

An eight step reduced chemical mechanism for methane combustion was provided by Frolov (1996) for use in both the DNS and JPDF calculations. The mechanism consists of global steps which do not make explicit use of any radical species, such as hydroxyl (OH), methyl (CH_3), and so on, but instead employs tuning factors for the fuel oxidation and prompt NO_x steps. These tuning factors are incorporated into the pre-exponential coefficients in the Arrhenius expressions and make allowance for variations in local equivalence ratio, fuel species, and pressure. The tuning constants were derived by Frolov (1996) from comparison of the reduced mechanism with full mechanism calculations in counterflow laminar premixed flames.

$$CH_4 + 1.5O_2 \rightarrow CO + 2H_2O \qquad (I)$$

$$CO + H_2O \rightarrow CO_2 + H_2 \qquad (IIf)$$

$$CO_2 + H_2 \rightarrow CO + H_2O \qquad (IIb)$$

$$2H_2 + O_2 \rightarrow 2H_2O \qquad (III)$$

$$2CO + O_2 \rightarrow 2CO_2 \qquad (IV)$$

$$CH_4 + O_2 + N_2 \rightarrow CH_4 + 2NO \qquad (V)$$

$$N_2 + O_2 \rightarrow 2NO \qquad (VIf)$$

$$NO + NO \rightarrow N_2 + O_2 \qquad (VIb)$$

The Arrhenius rate constants corresponding to the above reaction steps are given below where A_i, n_i and E_i denote the pre-exponential factor, temperature index, and activation energy for reaction number i, and p is the local pressure in bar.

No.	$A_i(mol, L, s)$	n_i	$E_i(kcal/mol)$
I	A_1/p	0.0	50.0
IIf	$1.0 \times 10^{12}/p$	0.0	41.5
IIb	$3.1 \times 10^{13}/p$	0.0	49.1
III	$7.0 \times 10^{13}/p^2$	0.0	21.0
IV	$8.5 \times 10^{12}/p^2$	0.0	21.0
V	A_5/p^2	0.0	50.0
VIf	1.7×10^{17}	-0.5	136.0
VIb	4.1×10^{15}	-0.5	93.3

The pre-exponential factors for reactions I and V are functions of the local equivalence ratio β. Frolov (1996) determined the appropriate values of A_1 and A_5 at a range of equivalence ratios from $\beta = 0.67$ up to $\beta = 1.54$. The pre-exponential factors vary nonlinearly over the range such that the lean limit values are orders of magnitude greater than the rich limit values. The values under stoichiometric conditions for each is $A_1 = 2.57 \times 10^{15} L/(mol \cdot s)$ and $A_5 = 7.03 \times 10^{13} L^2/(mol^2 s)$.

At the suggestion of Frolov (1996), linear interpolation between the known values for A_1 and A_5 was used to determine values for intermediate mixing states.

At this stage there are some questions as to the accuracy of the chemical mechanism described above, since it appears to give quantitatively inaccurate values for unstrained laminar flame speed and extinction strain rate. However, as both the DNS and JPDF computations employed the same chemical mechanism, the quantitative accuracy of the mechanism is not an issue in comparing one with the other.

4. Comparison of predictions and simulation data

The JPDF model calculations were in each case initialized directly from the domain of the DNS data base. Each of the 2,000 stochastic particles used in the model were assigned compositions selected at random from the domain. Special care was taken to ensure that the initial particle distribution in composition space gave rise to the same statistics as was found in the simulation. As the particles used in the model were of equal mass, this required that the number of potential particle assignments for each domain cell be proportional to the local fluid density.

An assignment table was constructed for the purpose of particle initialization, where there was an equal probability of a particle being assigned the composition of any entry in the table. The number and composition of the table entries was determined from the simulation domain, such that a very low density cell would only provide a single entry whereas a high density cell would provide a number of repeated entries, each with the same composition as the originating cell. As the central portion of the simulation domain consisted of approximately 45,000 cells and the ratio of the mean cell density to the minimum cell density was of order 2 -- 3, this gave rise to a table containing around 100,000 entries. Of that number, 2,000 were selected at random, without replacement, for particle assignment.

Model calculations were then allowed to proceed according to Eq. 3, with a revised mean pressure calculated after every time step. Mixing time scales were drawn from the DNS for use in the model calculation.

4.1 Global mean behavior

Global mean species yields and pressure were predicted using RTM and RPI mixing sub-models (see Section 2.1) within the JPDF model.

Typical model predictions for mean pressure, initialized from the initial DNS data, are plotted in comparison with the DNS pressure record in Fig. 5. The RTM prediction displays too slow an initial pressure rise, indicating a too modest sensible energy release rate. Towards the end of the simulation period, the RTM-modeled mean pressure rises at a rate greater than that seen in the DNS.

The random particle interaction model prediction tends to lie substantially closer to the DNS curve than do the predictions of the RTM model. At its worst the RTM model exhibits an approximate 20% discrepancy below the DNS curve, while the RPI model exhibits a maximum underprediction on the order of 10%.

The model predictions for mean carbon dioxide (CO_2) mass fraction formation reflect the predicted mean pressure behavior (see Fig. 6). Carbon dioxide is one of

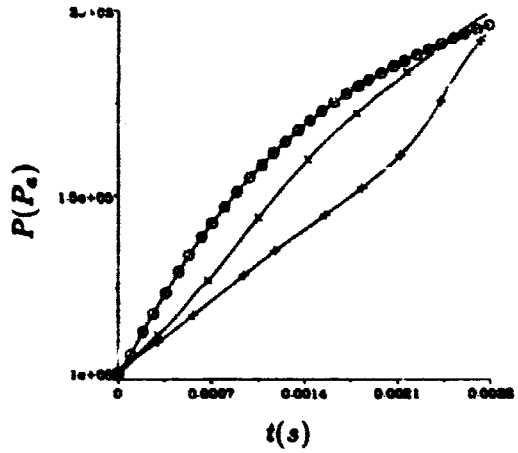

FIGURE 5. Comparison of simulated and predicted mean pressure rise. chemical description of H_2/N_2-air combustion. Symbol key : + - JPDF-RTM, × - JPDF-RPI, o - DNS.

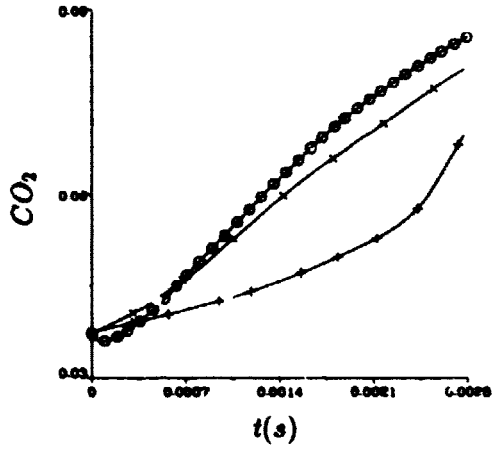

FIGURE 6. Comparison of simulated and predicted overall mean CO_2 production. Symbol key : + - JPDF-RTM, × - JPDF-RPI, o - DNS.

the principal exothermic products of hydrocarbon combustion, with the release of sensible energy being closely linked to its oxidation from carbon monoxide (CO).

The carbon dioxide mass fraction curve predicted by the RTM mixing model displays the same tendency as the corresponding mean pressure curve. The initial formation of CO_2 proceeds at a slow rate before sharply increasing towards the end of the simulation.

As was the case for the mean pressure, the RPI prediction for CO_2 formation does not display this kind of sharp increase. Instead the curve has the same kind of gradual decrease in slope that can be seen in the simulation data.

Carbon monoxide (CO) is in great abundance at the beginning of the simulation, having been initialized using adiabatic equilibrium values at each value of mixture fraction. These equilibrium values are not normally encountered in flames since any substantial level of molecular transport tends to move CO into reaction zones at leaner mixture fractions, where it is consumed.

As a result of the initially high levels of CO, it acts primarily as a fuel species in the simulation. It is oxidized to form CO_2, releasing heat in the process. Typical predicted mean mass fraction curves for carbon monoxide are compared with the simulation in Fig. 7. It is again evident that the JPDF model using the RTM mixing sub-model tends to underpredict the initial reaction rate, but displays a sharp increase in reactant consumption towards the end of the simulation.

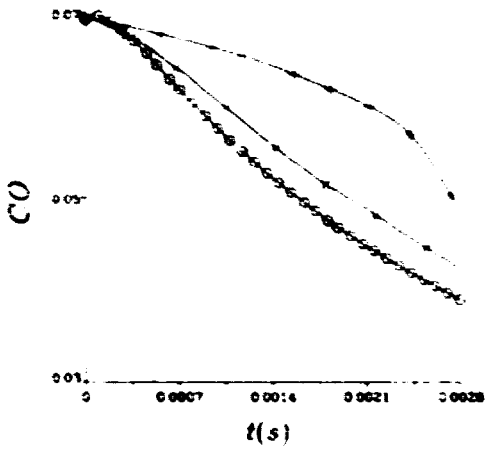

FIGURE 7. Comparison of simulated and predicted global mean CO consumption. Symbol key : + - JPDF-RTM, × - JPDF-RPI, o - DNS.

The prediction of nitric oxide (NO) formation is particularly difficult given its high sensitivity to local temperature and oxygen concentration. The equilibrium concentration for NO under hot combusting conditions is orders of magnitude greater than what is usually observed in practice. Unlike the major species, the formation of NO is limited not by the rate of mixing but by the chemical kinetic rate at which mixed species will react.

Typical JPDF model predictions for mean nitric oxide mass fraction, derived using RTM and RPI mixing submodels, are compared with simulation data in Fig. 8. The profiles from all three sources exhibit increases with time, which indicates the level of NO is far below its equilibrium condition. The second derivative with respect to time of all three profiles is positive over the course of the simulation.

The significance of small differences in model assumptions on NO prediction is highlighted by the fact that the RTM and RPI curves straddle the observed DNS curve. The nitric oxide formation rate predicted by the RTM submodel is substantially less than the simulated rate, whereas the RPI predicted rate is somewhat greater.

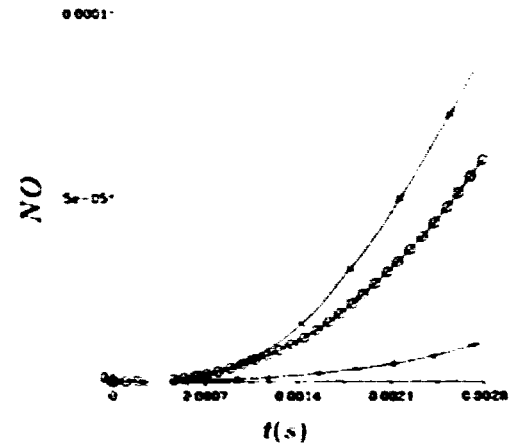

FIGURE 8. Comparison of simulated and predicted global mean NO formation. Symbol key : + - JPDF-RTM. < JPDF-RPI. o - DNS.

4.2 Behavior in mixture fraction space

The comparison of global mean statistics presented above indicates that substantial differences in model predictions arise from the choice of mixing submodel.

The characteristic differences that arise due to the choice of mixing model can be seen in Fig. 9. which depicts a typical comparison of the instantaneous scatter of stochastic particles in mixture fraction and CO_2 mass fraction space. The comparison of particle scatter is made at the end of the calculation ($t = 2.80ms$). bearing in mind that the particle scatter was identical at $t = 0$.

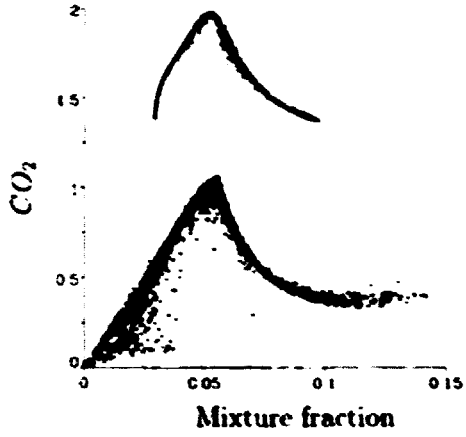

FIGURE 9. Comparison of predicted CO_2-mixture fraction distribution of stochastic particles at time $t = 2.80ms$. The RTM (upper) profile has been uniformly shifted by an offset in CO_2 mass fraction of 1.0 for the sake of clarity. The RPI (lower) profile is unshifted.

Despite the fact that both distributions have the same overall mixture fraction mean and variance, the range in particle values is much greater in the case of the RPI-modeled distribution. This is because, in contrast to RTM where all particles mix at every step, the RPI model only mixes a relatively small random selection to a potentially large degree. The random nature of the RPI mixing model allows unselected particles to remain far from the mean of the distribution. As a result, the kurtosis of the RPI-predicted mixture fraction distribution tends to be higher than that predicted by the RTM model, and for that matter the DNS data (not shown).

In addition, the qualitative forms of the two distributions are quite different. The RTM-predicted distribution exhibits far less scatter than its RPI-predicted counterpart at any given mixture fraction. This is because in the RTM model, all particles relax towards the mean position in composition space at a rate which depends only on the mixing frequency (same for all particles) and the distance between the particle and the mean position. Thus two particles that are initially very close together will both proceed towards the global mean composition, though they will never interact. In the absence of chemical reactions, the RTM mixing model causes the initial profile to contract with time in a self-similar fashion towards the mean position. Thus the distribution plotted in Fig. 9 is virtually a contracted image of the initial particle distribution, albeit somewhat perturbed by chemical reactions.

This self-similar behavior is in contrast to the RPI model where particle-to-particle interactions are what drive the overall distribution towards the mean position in composition space. Unlike with the RTM process, two particles which are initially very close in composition space may diverge substantially during the course of a single mixing step, as a result of random interaction with other particles. Conversely, two particles which are in close proximity in mixture fraction space may have widely different reactive species compositions as a result of their different individual time histories.

This is not possible under the RTM mixing model where nearby particles automatically have very similar time histories. The trajectories of all particles through composition space are constrained to approach the overall mean.

Under RPI, differences in particular reactive species compositions will be most pronounced in zones where the reaction rates pertaining to the particular species are slow compared to mixing rates. In the case of carbon dioxide (Fig. 9), scatter is greatest at mixture fractions corresponding to very rich and very lean stoichiometries where the CO_2 influencing reactions are comparatively weak.

The degree of freedom of movement of particles through composition space has implications for the accurate prediction of reactive species yields. Due to the nonlinear nature of non-isothermal chemical reactions, small fluctuations in local temperature and species concentrations can lead to large changes in the production rates of species and sensible energy. These changes in kinetic rates then have an impact on the mean behavior of the system through mixing.

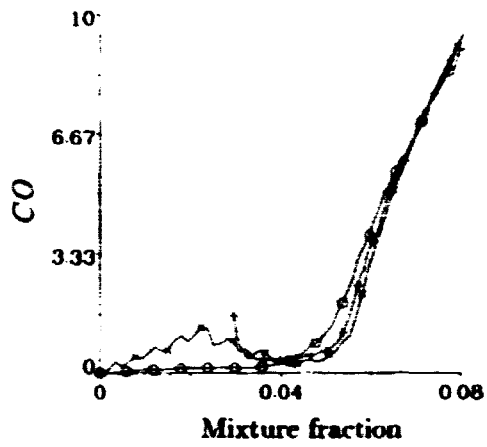

FIGURE 10. Comparison of predicted conditional mean normalized CO mass fraction profiles at time $t = 2.80ms$. Symbol key : + - JPDF-RTM, × - JPDF-RPI, o - DNS.

4.2.1 Conditionally averaged statistics

Conditional statistics were determined from both the predicted and simulated data by subdividing mixture fraction space into one hundred bins of equal width. Conditional means and root mean square deviations were computed within each bin for each data set at various calculation times.

The general behavior of the conditional mean profiles drawn from the simulation is one of a slow relaxation towards chemical equilibrium at an elevated pressure, after a rapid perturbation from the initial condition. The initial perturbation of the system resulted from the relatively strong mixing processes at the beginning of simulation which served to transport reactive scalars rapidly through mixture fraction space. As the level of turbulent mixing decayed with time, the degree of scalar transport decreased, thereby allowing the chemical system to return towards chemical equilibrium.

Characteristic trends in a return towards chemical equilibrium, (see Barlow *et al.* 1989, 1990) include upward relaxation in the conditional mean profiles for major product species (CO_2, H_2O) and temperature around stoichiometric. There is also a corresponding downward relaxation in fuel and oxidizer levels. Nitric oxide levels at stoichiometric increase rapidly, having been orders of magnitude below chemical equilibrium at the time of initialization.

Shortcomings in the current particle mixing models are apparent when predicted conditional mean profiles are compared with the simulation. The profiles for CO (normalized by the initial adiabatic equilibrium value at stoichiometric) at time $t = 2.80ms$ are plotted in Fig. 10. The elevated levels of CO at lean mixture fractions on the part of the models are anomalous and are not present in the simulation. The degree of this lean profile elevation decreases with increasing computation time, as the intensity of the turbulent mixing decreases.

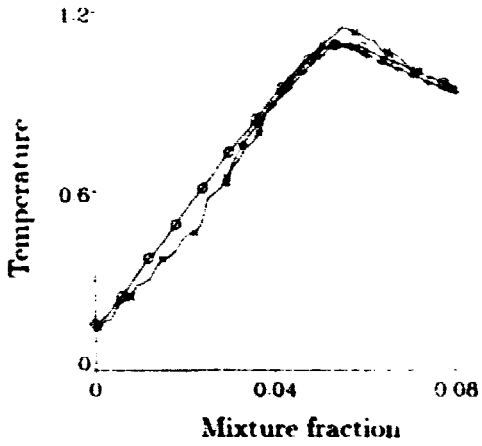

FIGURE 11. Comparison of predicted conditional mean normalized temperature profiles at time $t = 2.80ms$. Symbol key : + - JPDF-RTM, × - JPDF-RPI, o - DNS.

The equations for the diffusive transport of reactive scalar mass fractions in mixture fraction space (see Klimenko 1990) indicate that the negative curvature of the conditional mean CO profile in mixture fraction space must result in a local decrease in the CO mass fraction profile. Similarly, chemical reactions should drive conditional mean CO levels downward. There is no obvious *physical* explanation as to how the observed elevated profiles could have been produced from the initial condition.

A similar anomalous effect can be seen in the normalized conditional mean temperature profiles in Fig. 11, where the modeled mixing processes have caused the lean portion of the temperature profile to be depressed below the expected equilibrium line. The temperature depression is more substantial at earlier times and seems to be responsible for the early underprediction of mean pressure rise seen in Fig. 5.

It is evident that the profile deviations are due to shortcomings in both the RPI and RTM mixing models. In effect, the models allow particles to mix towards a mean position that can be very far from their local region of composition space. Thus, in the case of the RPI model, particles at very lean mixture fractions are just as likely to mix with other particles at very rich mixture fractions as those immediately adjacent to themselves. The RTM model effectively allows the same interaction by constraining particles to mix along trajectories towards the overall mean position.

In reality, a fluid parcel is not free to mix with any other fluid parcel; it is instead bound to interact with those in its immediate vicinity in composition space. Parcels in a fluid continuum cannot *jump* between separated locations in composition space, given a certain time step, without having an impact upon the intervening compositions. In the case of the conditional mean CO profile of Fig. 10, the elevated levels on the lean side of the reaction zone can only exist if the CO values at stoichiometric

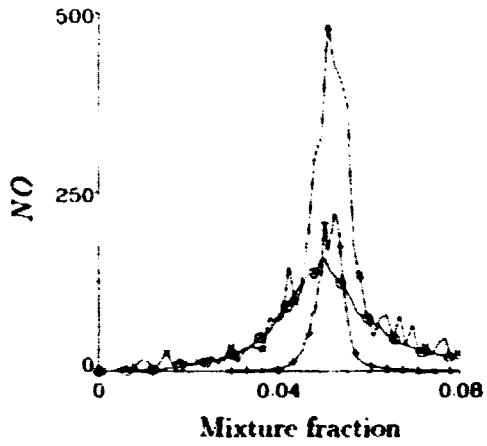

FIGURE 12. Comparison of predicted conditional mean NO mass fraction [ppm] profiles at time $t = 2.80ms$. Symbol key : + - JPDF-RTM, × - JPDF-RPI, o - DNS.

are more elevated still. There is no possibility of counter-gradient transport in the simulation given the assumptions employed.

Turning to the prediction of nitric oxide (NO) formation, a comparison of conditional mean profiles from the models and the simulation can be made from Fig. 12. It is clear that in all cases the formation of NO is strongly centered on the high temperature reaction zones around stoichiometric. Of the two predictions, those of the RPI model seem to best match the simulation profile at lean and rich mixture fractions in capturing the transport of NO to inert zones in mixture fraction space.

An explanation for the significant discrepancy between the two model predictions for NO can be found in the difference between the conditional mean and variance profiles of temperature. Throughout the calculations, the particles in the vicinity of the reaction zone have a slightly higher conditional mean temperature under the RPI model than the RTM model. Further, the level of conditional variance in the temperature under the RPI model is many times greater than what is observed under the RTM model.

The RPI model predicts a slightly higher conditional temperature variance than the simulation, around stoichiometric, while having conditional mean temperature values similar to the prediction. Given the high nonlinear sensitivity of NO formation to temperature, it is reasonable to speculate that this difference in conditional variance may be the cause of the observed NO discrepancy.

5. Discussion

It is reasonable to assert that the RPI mixing model as described above seems to perform better than the RTM mixing model under the conditions examined. The overall prediction of mean species yields by the RPI-JPDF combination is superior to that seen for the RTM-JPDF combination in the tests conducted.

The RPI model seems to incorporate significant conditional root mean square deviations in reactive species levels in mixture fraction space. This in turn may allow better prediction the formation of thermochemically sensitive species such as NO. Indeed, in cases where highly nonlinear phenomena such as extinction behavior is to be predicted, the RTM approach would be unable to capture the significant contributions made by particles that are far from the conditional mean profiles.

Both models, however, seem to suffer from a "long range mixing" problem. That is to say that particles are allowed to freely mix with other particles that are far removed in mixture fraction space, without having any effect at all on particles that lie in the intervening space.

The Kolmogorov *scalar* scale (η_k), defined below (where τ_k is the Kolmogorov time scale, and χ is the mean scalar dissipation rate), describes the characteristic fluctuations in a conserved scalar which are present at the smallest eddy sizes, i.e. the level of scalar fluctuations which are diminished by molecular diffusion alone.

$$\eta_k \equiv (\chi \tau_k)^{1/2} \tag{9}$$

After making an assumption about the relationship between the scalar dissipation rate, the scalar variance, and the turbulent time scale, it is possible to express η_k approximately as given below.

$$\eta_k \propto < \xi'^2 >^{1/2} / Re_t^{1/4} \tag{10}$$

As the turbulent Reynolds number (Re_t) in the simulation performed in this study was rather low, the Kolmogorov scalar scale was on the order of one fifth of the entire range of mixture fraction space. In practical turbulent reactors, one might expect this value to be substantially lower.

Using the Kolmogorov scalar scale as a guide for the case studied here, it seems unlikely that any particle would be able to mix on a molecular level with any other particle that is any further than $\Delta\eta = 0.03$ distant.

It may be appropriate to attempt to modify the RPI mixing model presented here so as to limit the range in mixture fraction space over which particles are allowed to interact. In so doing, a greater number of particle interactions would be required in each time step so as to correctly model the overall decay rate in mixture fraction variance.

Chen and Kollmann (1994) suggest a modified RPI model which better represents molecular diffusion by limiting the range over which particles can interact. No mention of a criteria for this critical range was mentioned, but perhaps the Kolmogorov scalar scale could be used in this capacity. To the best of the authors' knowledge, this scheme has yet to be implemented for testing.

6. Comments

This preliminary work has served to illustrate the effective differences between different mixing sub-models employed in a scalar JPDF model for nonpremixed turbulent combustion.

The simulation conditions were admittedly difficult to model, given that the non-premixed reaction zones were initially quite thin compared to both the physical and mixture fraction scales of the domain. Nevertheless, practical multi-cellular calculations using JPDF methods will likely involve discretizations with cell Reynolds and Damköhler numbers of the same order as that encountered in the simulation. In that regard, the insight obtained here could be of some use in selecting a mixing sub-model for practical usage.

It would seem that of the two mixing sub-models tested, the Random-Particle-Interaction (RPI) model proved both to be more accurate in prediction, and also to exhibit more of the qualitative characteristics of the mixing processes observed in the simulation. Both mixing sub-models were found to exhibit non-physical behavior in the sense that particles were free to interact over too wide a range in mixture fraction space.

The RPI model seems to be best suited for modification to include some limitation on mixing interaction distances in mixture fraction space. The implementation and testing of this modification as described in the discussion and by Chen and Kollmann (1994) is a project for future work in this area.

Further, as computational resources become available it would be valuable to simulate a three dimensional case of the conditions studied here. This would be done to determine if important effects have been neglected in the current simulation and would have the advantage of carrying a much larger number of statistical sample points in the analysis.

REFERENCES

ANAND, M. S., & POPE, S. B. 1987 Calculations of premixed turbulent flames by pdf methods. *Combust. Flame.* **67,** 127-142.

BARLOW, R. S., DIBBLE R. W., & FOURGETTE D. C. 1989 *Departure from chemical equilibrium in a lifted hydrogen flame.* Sandia Report SAND89-8627.

BARLOW, R. S., DIBBLE, R. W., CHEN, J.-Y., & LUCHT, R. P. 1990 Effect of Damköhler number on super-equilibrium OH concentration in turbulent non-premixed jet flames.. *Combust. Flame.* **82,** 235.

CHEN, J.-Y. 1993 Stochastic Modeling of Partially Stirred Reactors. Presented at the Fall Meeting of the Western States Section of the Combustion Institute. Menlo Park, California.

CHEN, J.-Y. 1996 Private communication.

CHEN, J.-Y., CHANG, W.-C., & KOSZYKOWSKI, M. L. 1995 Numerical Simulation and Scaling of NOx Emissions from Turbulent Hydrogen Jet Flames with Various Amounts of Helium Dilution. *Combust. Sci. Tech.* **110,** 505.

CHEN, J.-Y. & KOLLMANN, W. 1988 PDF Modeling of Chemical Nonequilibrium Effects in Turbulent Nonpremixed Hydrocarbon Flames. *Proceedings of the Twenty-Second Symposium (International) on Combustion.* The Combustion Institute. 645-653.

CHEN, J.-Y. & KOLLMANN, W. 1992 PDF Modeling and Analysis of Thermal NO Formation in Turbulent Nonpremixed Hydrogen-Air Jet Flames. *Combust. Flame.* **88,** 397-412.

CHEN, J.-Y. & KOLLMANN, W. 1994 *Comparison of prediction and measurement in nonpremixed turbulent flames.* in *Turbulent Reacting Flows*, F. A. Williams & P. A. Libby (eds). Academic Press Ltd. 211-308

CORREA, S. M. 1993 Turbulence-Chemistry Interactions in the Intermediate Regime of Premixed Combustion. *Combust. Flame.* **93,** 41-60.

CORREA, S. M., & POPE, S. B. 1992 Comparison of a Monte Carlo PDF/Finite Volume Mean Flow Model with Bluff-Body Raman Data. *Proceedings of the Twenty-Fourth Symposium (International) on Combustion.* The Combustion Institute. 279-285.

DOPAZO, C. 1975 Probability function approach for a turbulent axisymmetric heated jet: centerline evolution. *Phys. Fluids.* **18,** 397.

DOPAZO, C. 1979 On conditioned averages for intermittent turbulent flows. *J. Fluid Mech.* **81,** 433.

FROLOV, S. M. 1996 Private communication.

JANICKA, J., KOLBE W., & KOLLMANN W. 1979 Closure of the transport equation for the probability density of function of scalar fields. *J. Nonequilib. Thermodyn.* **4,** 27.

JANICKA, J., & KOLLMANN, W. 1978 A Two-Variables Formalism for the Treatment of Chemical Reactions in Turbulent H_2-Air Diffusion Flames. *Proceedings of the Seventeenth Symposium (International) on Combustion. The Combustion Institute. 421-430.*

KLIMENKO, A. YU. 1990 Multicomponent diffusion of various admixtures in turbulent flow. *Fluid Dynamics.* **25,** 327-334.

POPE, S. B. 1981 A Monte Carlo Method for the PDF Equations of Turbulent Reactive Flow. *Combust. Sci. Tech.* **25,** 159-174.

POPE, S. B. 1982 An improved turbulent mixing model. *Comb. Sci. Tech.* **28,** 131.

POPE, S. B. 1985 PDF Methods for Turbulent Flows. *Prog. Energy Sci. Comb.* **11,** 119-192.

POPE, S. B. 1990 Computations of Turbulent Combustion: Progress and Challenges. *Proceedings of the Twenty-Third Symposium (International) on Combustion.* The Combustion Institute. 591-612.

SMITH, N. S. A., BILGER, R. W., CARTER, C. D., BARLOW, R. S., & CHEN, J.-Y. 1993 A Comparison of CMC and PDF Modelling Predictions with Experimental Nitric Oxide LIF/Raman Measurements in a Turbulent H_2 Jet Flame. *Combust. Sci. Tech.* **105,** 357-375.

SMITH, N. S. A., BILGER, R. W., CARTER, C. D., BARLOW, R. S., & CHEN J.-Y. 1996 Radiation Effects on Nitric Oxide Formation in Turbulent Hydrogen Jet Flames Diluted with Helium. Submitted to *Combustion and Flame.*

NEXT
DOCUMENT

Effect of chemistry and turbulence on NO formation in oxygen-natural gas flames

By J.-M. Samaniego[1], F. N. Egolfopoulos[2] AND C. T. Bowman[3]

The effects of chemistry and turbulence on NO formation in oxygen-natural turbulent diffusion flames gas flames have been investigated. The chemistry of nitric oxides has been studied numerically in the counterflow configuration. Systematic calculations with the GRI 2.11 mechanism for combustion of methane and NO chemistry were conducted to provide a base case. It was shown that the 'simple' Zeldovich mechanism accounts for more than 75% of N_2 consumption in the flame in a range of strain-rates varying between 10 and 1000 s^{-1}. The main shortcomings of this mechanism are: 1) overestimation (15%) of the NO production rate at low strain-rates because it does not capture the reburn due to the hydrocarbon chemistry, and 2) underestimation (25%) of the NO production rate at high strain-rates because it ignores NO production through the prompt mechanism. Reburn through the Zeldovich mechanism alone proves to be significant at low strain-rates. A one-step model based on the Zeldovich mechanism and including reburn has been developed. It shows good agreement with the GRI mechanism at low strain-rates but underestimates significantly N_2 consumption (about 50%) at high strain-rates. The role of turbulence has been assessed by using an existing 3-D DNS data base of a diffusion flame in decaying turbulence. Two PDF closure models used in practical industrial codes for turbulent NO formation have been tested. A simpler version of the global one-step chemical scheme for NO compared to that developed in this study was used to test the closure assumptions of the PDF models, because the data base could not provide all the necessary ingredients. Despite this simplification, it was possible to demonstrate that the current PDF models for NO overestimate significantly the NO production rate due to the fact that they neglect the correlations between the fluctuations in oxygen concentration and temperature. A single scalar PDF model for temperature that accounts for such correlations based on laminar flame considerations has been developed and showed excellent agreement with the values given by the DNS.

1. Introduction

This study is an investigation of the effects of chemistry and turbulence on nitric oxide formation in oxygen-natural gas flames. The choice of oxygen as the oxidizer is related to current interest in use of oxygen for high temperature combustion in

1 Air Liquide, Centre de Recherche Claude-Delorme, France
2 University of Southern California, Los Angeles, CA
3 Stanford University, Stanford, CA

industry. In terms of NO emissions, oxygen is advantageous compared to preheated air in high-temperature processes such as those encountered in the glass and steel making industry due to the low nitrogen content. However, molecular nitrogen still is present in certain amounts in the natural gas (0.5% for Algerian gas to 11% for Groningue gas) and in the oxygen stream. In the latter case, the nitrogen content depends on the production method: from virtually 0% for cryogenic oxygen to 5% for vacuum swing absorption. Other sources of nitrogen for oxygen-natural gas combustion include air leaks into the furnace. Despite the relatively low levels of NO emissions from oxy-combustion, ever more stringent emission standards require a better understanding of NO formation in oxy-flames.

The chemical mechanisms controlling NO formation are well known (Fenimore 1971, De Soete 1974, Miller & Bowman 1989, Drake & Blint 1991, Bozelli *et al.* 1993, Bowman 1992). Nitric oxide is formed from two sources: molecular nitrogen, N_2, and fuel-bound nitrogen. In the case of oxygen-natural gas flames, the only source is molecular nitrogen since natural gas, whatever its origin, does not contain nitrogen-bound species. In this case, the three main pathways for NO formation are the Zeldovich, prompt, and N_2O mechanisms, and the main pathway for NO destruction is the reburn mechanism. The Zeldovich mechanism is based on O-atom attack of N_2 through $O + N_2 = NO + N$, and is active both in the flame zone and the postflame zone. It is strongly dependent on temperature due to the high activation energy, $E_{Zeldovich}$, of the N_2-consuming step ($E_{Zeldovich}$ = 76.5 $kcal/mole$). A particular case of the Zeldovich mechanism is the equilibrium Zeldovich mechanism, where O-atoms are in partial equilibrium with molecular O_2. In this case, a global one-step reaction for NO formation can be derived with an overall activation energy, $E_{equilibrium}$ = 138 $kcal/mole$. The prompt mechanism is active only within the flame zone since it requires the presence of CH_x radicals for consumption of molecular nitrogen, mainly through $CH + N_2 = HCN + N$. Subsequent elementary reactions lead to the formation of NO. This mechanism is weakly dependent on temperature due to the low activation energy of the main N_2-consuming step ($E_{prompt} \cong 20$ kcal/mole). The N_2O mechanism is due to reaction of O-atoms with N_2 in a three-body reaction, i.e. $O + N_2 + M = N_2O + M$, with the subsequent reaction of $N_2$0 to form mainly through $O + N_2O = NO + NO$. The reburn mechanism is responsible for consumption of NO within the flame zone to produce N_2, and it is controlled by CH, CH_2, and CH_3 radicals.

These various mechanisms are present in air flames and must be accounted for to predict accurately the level of nitric oxide emissions. The usual picture for NO production in air flames can be split in two parts: 1) production in the flame zone through a balance between the prompt, N_2O, and reburn mechanisms - in this zone, the Zeldovich mechanism can be neglected; 2) production of NO in the post-flame zone by the Zeldovich mechanism alone. The picture is different in oxygen flames since in this case, the destruction rate of N_2 is controlled by the Zeldovich mechanism, with a small contribution of the prompt mechanism (Samaniego *et al.* 1996). The main reason is that the higher temperatures of the oxygen flame tend to increase the destruction rates of N_2, and this acceleration is more pronounced

for the Zeldovich mechanism due to its higher activation energy. As a result, the Zeldovich mechanism becomes faster than the prompt NO mechanism in the flame zone of an oxygen flame, while it is slower than the prompt NO mechanism in the flame zone of an unpreheated air flame. However, it is not clear whether the NO production rates can be derived from the Zeldovich mechanism alone since reburn may be taking place as indicated by the high HCN concentration levels observed in the numerical study of Samaniego *et al.* (1996). Furthermore, it is necessary to clarify the role of non-equilibrium atomic oxygen since it is unclear whether the partial-equilibrium assumption holds (Samaniego *et al.* 1996).

The effect of turbulence on NO emissions in jet diffusion flames has been studied extensively (Peters & Donnerhack 1981, Turns & Myrh 1991, Chen & Kollman 1992, Driscoll *et al.* 1992). The turbulent mixing process results in temporal fluctuations in temperature and species composition which influence the NO formation rates. Since the relationships between NO formation rate, temperature, and species are highly non-linear, NO emissions cannot be predicted from mean temperature and species concentrations alone. Therefore, accurate predictions of NO formation rates require the knowledge of temperature and composition fluctuations. Modelers have derived PDF formulations that account for the effect of these fluctuations on the turbulent NO production rate (Janicka & Kollmann 1982, Pope & Correa 1986, Correa & Pope 1992). The closure of the turbulent source term for NO is made possible through the use of a joint PDF which, in the case of Zeldovich NO with the partial equilibrium assumption for atomic oxygen, can be expressed as:

$$\frac{d\overline{[NO]}}{dt} = \int k[O_2]^{1/2}[N_2]\exp(-E/RT)P([O_2],[N_2],T)\,d[O_2]\,d[N_2]\,dT \qquad (1)$$

where $P([O_2],[N_2],T)$ is a joint PDF of oxygen concentration, $[O_2]$, nitrogen concentration, $[N_2]$, and temperature, T. Usually, the nitrogen concentration is considered constant and $[N_2]$ is taken out of the PDF. Furthermore, in practice, $[O_2]$ and T are assumed to be independent variables and the joint PDF, P, can be expressed as the product of two single-variable PDF's, P_{O_2} and P_T, such as:

$$P([O_2],T) = P_{O_2}([O_2])P_T(T) \qquad (2)$$

In such a case, the turbulent NO production term becomes:

$$\frac{d\overline{[NO]}}{dt} = k\overline{[N_2]}\left(\int [O_2]^{1/2}P_{O_2}([O_2])d[O_2]\right)\left(\int \exp(-E/RT)P_T(T)dT\right) \qquad (3a)$$

In some cases, the same term is calculated from a single PDF by assuming that $[O_2]$ fluctuations can be neglected:

$$\frac{d\overline{[NO]}}{dt} = k\overline{[N_2][O_2]}^{1/2}\left(\int \exp(-E/RT)P_T(T)dT\right) \qquad (3b)$$

In both cases, this final assumption has a limited domain of validity since it presumes that the oxygen concentration fluctuations are not correlated with the temperature fluctuations. This may be valid in the post-flame zone where the combustion process is completed, but it is highly questionable in the flame zone where the temperature and oxygen concentration levels are obviously correlated. Since the amount of NO produced in the flame zone of oxygen flames can be very significant, it is expected that such PDF modeling approaches are inapplicable.

The goals of this study are to derive a simple chemical model for NO formation in oxygen diffusion flames and to propose a model for the closure of the turbulent NO production term based on a PDF approach. For this purpose, two complementary numerical approaches are used, one addressing the effects of chemistry, and another addressing the effect of turbulence.

2. Effects of chemistry

2.1 Numerical approach

Concerning chemistry, NO formation mechanisms are investigated using the counterflow flame problem. The counterflow configuration is often used to address chemistry-turbulence interactions with detailed chemistry, and it is well known that the strain-rate modifies the chemical pathways through reduced flame temperature reduction and residence times (Hahn and Wendt 1981, Haworth *et al.* 1988, Drake and Blint 1989, Chelliah *et al.* 1990, Mauss *et al.* 1990, Vranos *et al.* 1992, Takeno *et al.* 1993, Egolfopoulos 1994a, 1994b, Nishioka *et al.* 1994, Samaniego *et al.* 1995, Egolfopoulos & Campbell 1996). In such a geometry, the flow field is that of a strained flame where a jet of oxidizer impinges upon a jet of fuel. The oxidizer is a mixture of oxygen and nitrogen. Various mixtures are used: 100% O_2 and 0% N_2; 95% O_2 and 5% N_2; 21% O_2 and 79% N_2. The fuel is a mixture of methane and nitrogen. Two different mixtures are used: 100% CH_4 and 0% N_2; 95% CH_4 and 5% N_2.

The numerical simulation is conducted by solving the steady and unsteady equations of mass, momentum, energy, and species concentrations along the streamline. Details on the set of equations and numerical method can be found in Egolfopoulos (1994a and 1994b), and in Egolfopoulos & Campbell (1996). The chemical scheme that is used for combustion of methane is the latest GRI 2.11 mechanism, which accounts for 49 species and 277 reactions. Calculations are performed without radiative losses as it has been demonstrated that radiative losses from CO_2, H_2O, CO, and CH_4 play a negligible role in counterflow oxygen flames (Samaniego *et al.* 1996).

2.2 Results

The objective of this study is to check whether the Zeldovich mechanism alone is capable of predicting with sufficient precision the rate of formation of NO in an oxygen flame. In order to do so, two sets of calculations have been carried out, one with the full mechanism which includes all NO formation routes, and one with the three reactions of the Zeldovich mechanism, namely:

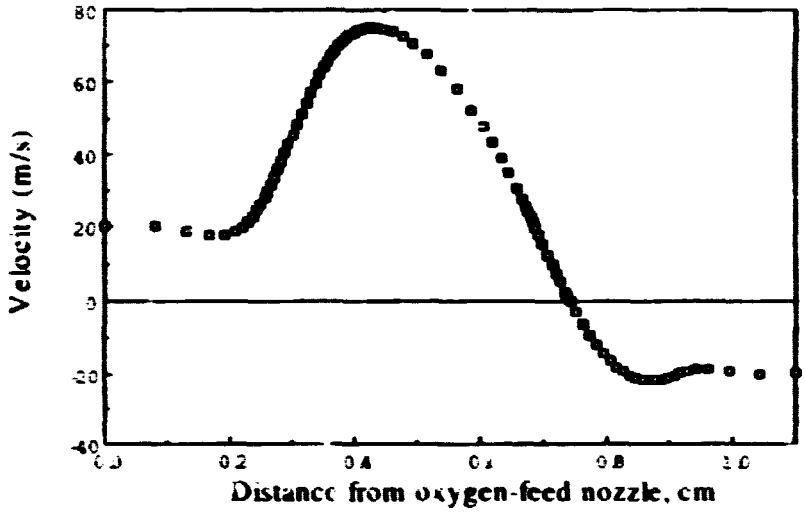

FIGURE 1. Computed velocity profile along the stagnation streamline of a counterflow O_2/CH_4 flame for a strain-rate of 25 s^{-1}.

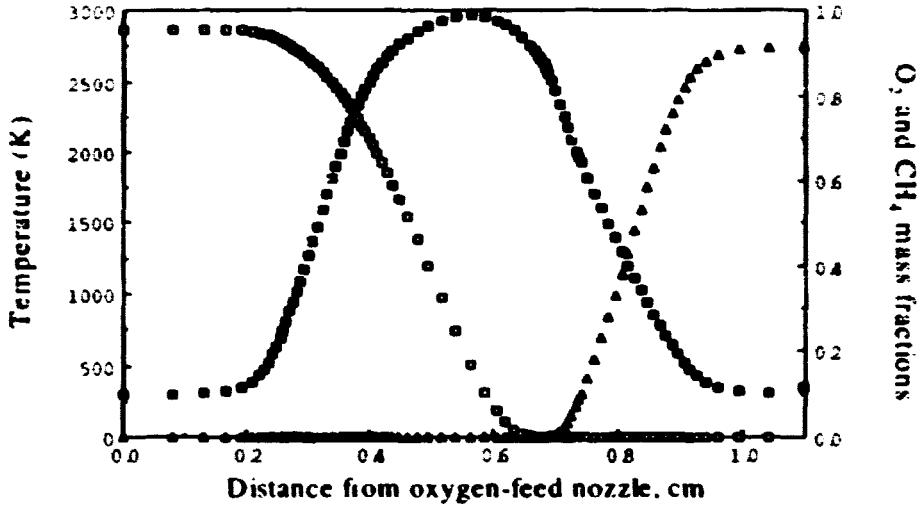

FIGURE 2. Computed profiles of temperature (■), oxygen mass fraction (□) and methane mass fraction (△) in a counterflow O_2/CH_4 flame for a strain-rate of 25 s^{-1}.

$$O + N_2 = NO + N \qquad (R1)$$

$$N + O_2 = NO + O \qquad (R2)$$

$$N + OH = NO + H \qquad (R3)$$

For both mechanisms, a series of about 400 steady strained flames is calculated for strain-rates varying from 10 to 1000 s^{-1}. The strain-rate is defined as the maximum velocity gradient in the oxidant stream. Figures 1 and 2 depict the flame structure for a strain-rate of 25 s^{-1}, which is typical of all the strain-rates computed in this study. This result is obtained with the full GRI 2.11 mechanism, and it is almost identical for the Zeldovich calculations since the NO chemistry does not significantly impact the fuel chemistry. The horizontal axis is the co-ordinate along the stagnation streamline, with oxidant being fed at $x = 0$ cm and fuel being fed at $x = 1.05$ cm. The feed velocities in this case are $V = 20$ cm/s for both streams. The velocity profile exhibits a stagnation point at $x = 0.74$ cm (Fig. 1). The velocity decreases from the oxygen nozzle feed, then increases due to thermal expansion and decreases again until crossing the stagnation point. The velocity profile has a similar behavior on the fuel side, and asymmetries are due to the different molecular weights of O_2 and CH_4 and to chemical effects. Figure 2 depicts the profiles of mass fractions of O_2, CH_4, and temperature. The maximum temperature is reached at $x = 0.56$ cm which corresponds to the flame zone. The consumption of oxygen and methane are almost complete at $x = 0.65$ cm, a location slightly on the fuel side relative to the maximum temperature. This can be attributed to the fact that some recombination reactions, which are exothermic, occur on the oxygen side. Figure 3 depicts the profile of NO mass fraction, Y_{NO}, in the case of the full and Zeldovich mechanisms, and in this case both mechanisms give similar maximum values but slightly different profiles in the fuel side.

To allow comparison with well known results, a series of strained unpreheated air flames also has been calculated. Figure 4 depicts the maximum NO mass fractions, $Y_{NO,max}$, as a function of strain-rate for the oxygen and air flames, and for the Zeldovich and full mechanisms. In all cases, $Y_{NO,max}$ decreases with increasing strain-rate, and this can be attributed to reduced residence times. In the case of the oxygen flame, $Y_{NO,max}$ is well predicted by the Zeldovich mechanism alone. In contrast, in the case of the air flame, $Y_{NO,max}$ is underpredicted by the Zeldovich mechanism by one to three orders of magnitude. The difference in behavior between the air and oxygen flames can be explained on the basis of the flame temperature as indicated in Samaniego *et al.* (1996). Oxygen flames are much hotter than air flames and, as a consequence, the Zeldovich mechanism, which is highly sensitive to temperature, is predominant over the prompt mechanism; in contrast, air flames are not as hot and the prompt mechanism is predominant over the Zeldovich mechanism at all strain-rates (Drake & Blint 1989, Nishioka *et al.* 1994).

A further comparison between full and Zeldovich mechanisms for the oxygen flame is performed by plotting the integral of the N_2 consumption rate, $\int(-d[N_2]/dt)dx$, as a function of strain-rate for both calculations. The reason for looking at this

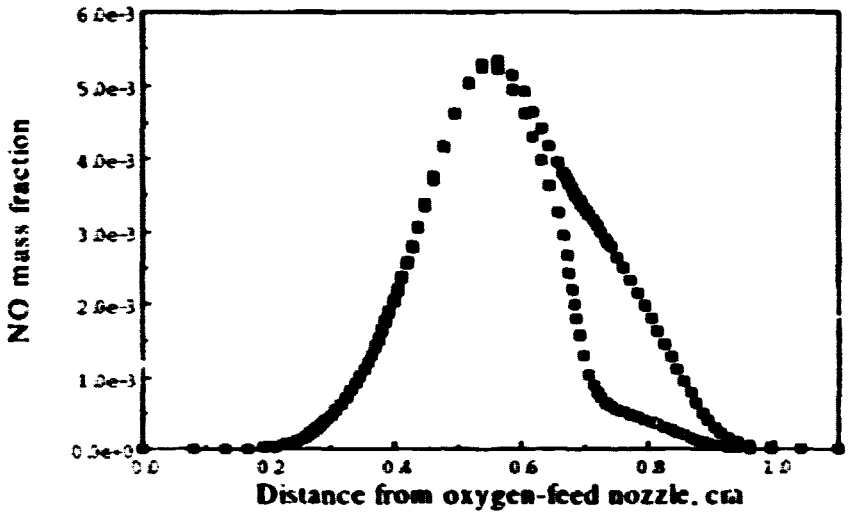

FIGURE 3. Computed profiles of NO mass fraction in a counterflow O_2/CH_4 flame with 5% N_2 addition in both streams for a strain-rate of 25 s^{-1}. Filled symbols: full GRI 2.11 mechanism. Open symbols: Zeldovich mechanism alone.

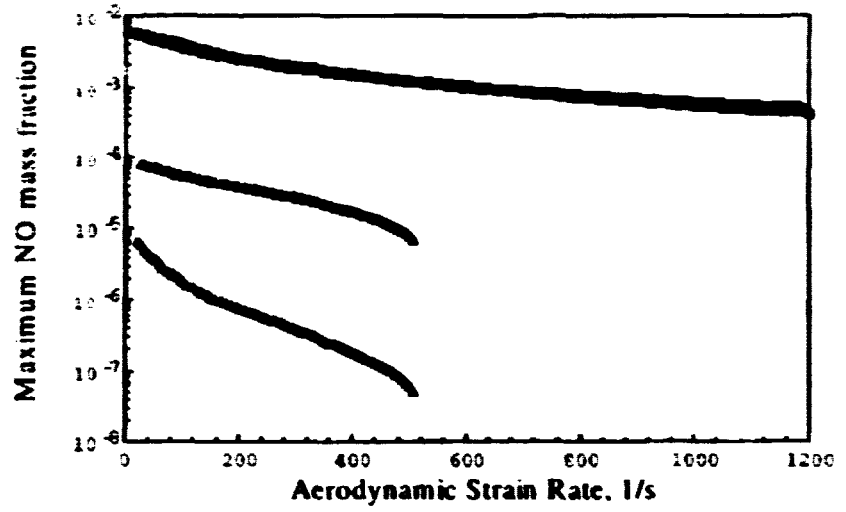

FIGURE 4. Effect of strain-rate on maximum NO mass fraction. □: Full GRI 2.11 mechanism for a O_2/CH_4 counterflow diffusion flame with 5% N_2 addition in both streams. ■: Zeldovich mechanism alone for a O_2/CH_4 counterflow diffusion flame with 5% N_2 addition in both streams. △: Full GRI 2.11 mechanism for an unpreheated Air/CH_4 counterflow diffusion flame. ▲: Zeldovich mechanism alone for an unpreheated Air/CH_4 counterflow diffusion flame.

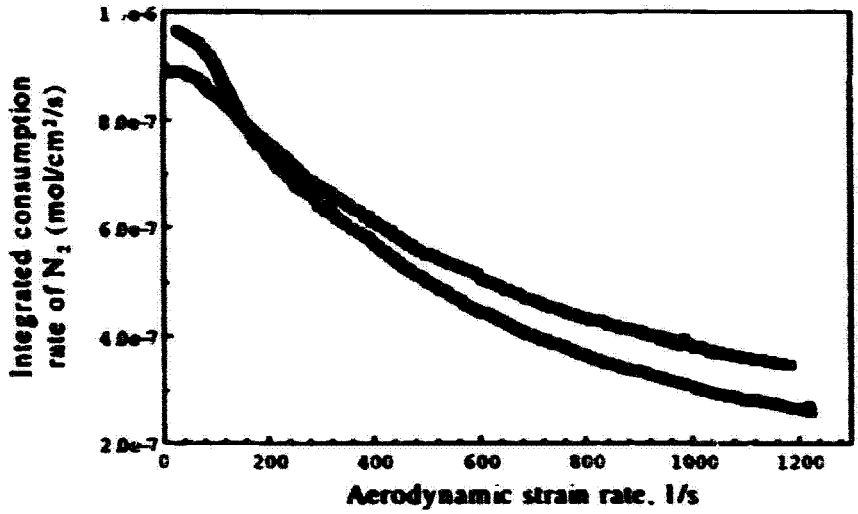

FIGURE 5. Effect of strain-rate on integrated consumption rate of N_2. □: Full GRI 2.11 mechanism for a O_2/CH_4 counterflow diffusion flame with 5% N_2 addition in both streams. ■: Zeldovich mechanism alone for a O_2/CH_4 counterflow diffusion flame with 5% N_2 addition in both streams.

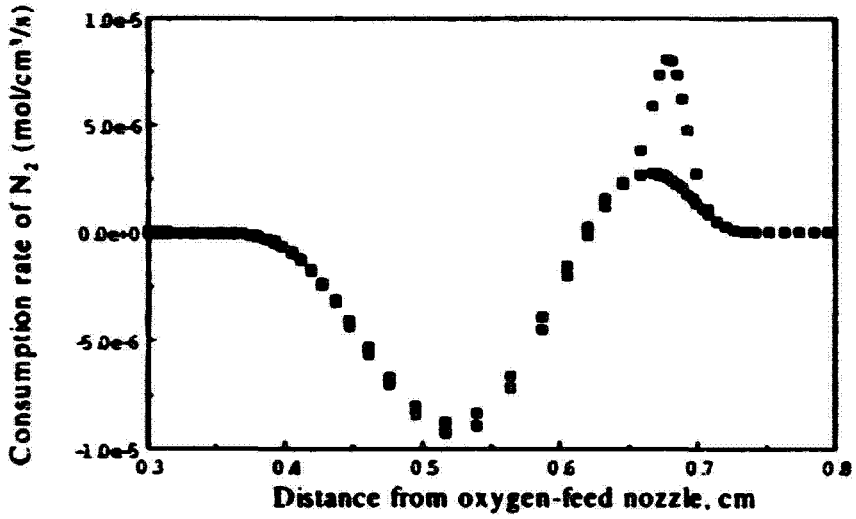

FIGURE 6. Profile of N_2 consumption rate in a strained O_2/CH_4 counterflow diffusion flame with 5% N_2 addition in both streams for a strain-rate of 25 s^{-1}. □: Full GRI 2.11 mechanism. ■: Zeldovich mechanism alone.

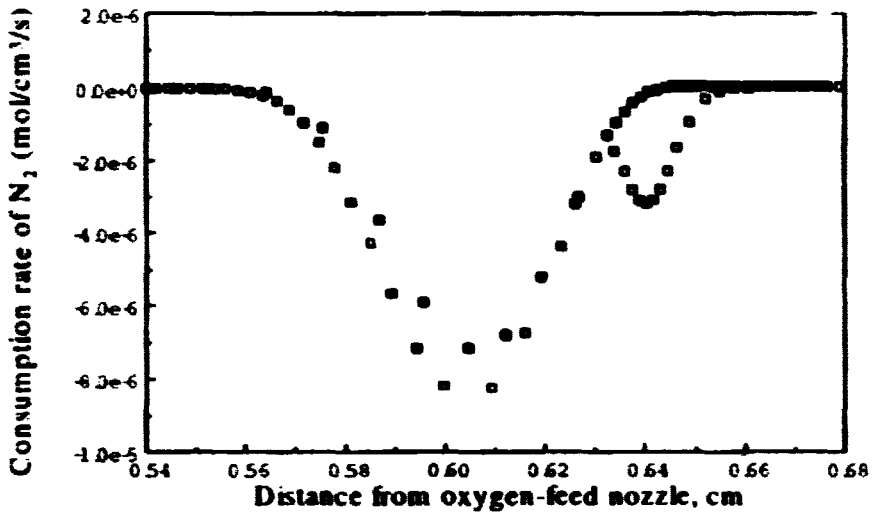

FIGURE 7. Profile of N_2 consumption rate in a strained O_2/CH_4 counterflow diffusion flame with 5% N_2 addition in both streams for a strain-rate of 1065 s^{-1}. □: Full GRI 2.11 mechanism. ■: Zeldovich mechanism alone.

quantity rather than the flux of NO is that reburn, i.e. production of N_2 from NO and other nitrogen-containing species, can be clearly identified. Figure 5 depicts that, in both cases, the consumption rate of N_2 is positive and decreases with strain-rate. Furthermore, the Zeldovich approach shows two weaknesses: 1) at low strain-rates, it overpredicts the consumption of N_2, and 2) at high strain-rates, it underpredicts it. Overprediction of N_2 consumption at low strain-rates is evidence that reburn through the hydrocarbon chemistry is active in these cases, and underprediction at high strain-rates indicates that N_2 consumption through the prompt mechanism is significant.

The discrepancies between the full and Zeldovich mechanisms may be explained by analyzing the profile of $d[N_2]/dt$ at low and high strain-rates. Figure 6 depicts the profiles of $d[N_2]/dt$ for both mechanisms and the profiles of temperature, oxygen mass fraction, and methane mass fraction for a strain-rate of 25 s^{-1}. For both mechanisms, $d[N_2]/dt$ is negative on the oxygen side and positive on the fuel side. On the oxygen side, N_2 is consumed to produce NO and other nitrogen-containing species and the two mechanisms give similar results. This indicates that N_2 consumption is mainly due to the Zeldovich mechanism via the reaction $O + N_2 \rightarrow NO + N$ and that the prompt and reburn mechanisms are not active. On the fuel side, N_2 is produced, which is evidence of reburn, and there is a significant discrepancy between the full and Zeldovich mechanisms. In this case, the Zeldovich pathway predicts some reburn through the reverse reaction ($N + NO \rightarrow O + N_2$) but misses the reburn through hydrocarbon chemistry which is accounted for by the full GRI 2.11 reaction mechanism. The picture is different at higher strain-rates. Figure 7 depicts the profiles of $d[N_2]/dt$ for both mechanisms and the profiles of temperature, oxygen

mass fraction and methane mass fraction for a strain-rate of 1065 s^{-1}. In this case, $d[N_2]/dt$ is always negative everywhere in the flame for both the Zeldovich and full mechanisms, indicating that there is no reburn. However, the full GRI 2.11 scheme predicts higher consumption rates of N_2 everywhere in the flame zone both on the oxygen side and in the fuel side. On the oxygen side, most of the N_2 is consumed via the Zeldovich mechanism, but additional reactions are also taking place. On the fuel side, the full mechanism exhibits a "bump" that is missed by the Zeldovich mechanism and which is due to the "prompt" reaction, $CH + N_2 \rightarrow N + HCN$.

Therefore, the following picture can be drawn for oxygen flames: 1) the amount of N_2 consumption and, consequently, NO production decreases by about 50% for strain-rates varying between 10 and 1000 s^{-1}; 2) in this range of strain-rates, the Zeldovich mechanism predicts N_2 consumption within ± 25% compared to the full GRI mechanism; 3) at low strain-rates, the Zeldovich mechanism overpredicts N_2 consumption by about 15% because it does not account for reburn through the hydrocarbon chemistry; 4) at high strain-rates, the Zeldovich mechanism underpredicts the N_2 consumption by about 25% because it does not account for N_2 consumption through the prompt mechanism.

2.3 An overall one-step model for N_2 consumption

The next step consists in deriving an overall one-step reaction mechanism for N_2 consumption based on the Zeldovich mechanism alone. The proposed model (model 1) includes reburn and considers the following reactions:

$$NO + N = N_2 + O \qquad (R1)$$

$$N + O_2 = O + NO \qquad (R2)$$

$$N + OH = H + NO \qquad (R3)$$

$$H + O_2 = OH + O \qquad (R4)$$

$$H + OH + M = H_2O + M \qquad (R5)$$

$$O + O + M = O_2 + M \qquad (R6)$$

The model is based on the following: 1) reaction 2 plays a negligible role (its net reaction rate is 1 to 2 orders of magnitude less than those of reactions 1 and 3); 2) atomic nitrogen is in steady-state ($d[N]/dt = 0$); 3) reactions 4 to 6 are assumed in partial equilibrium. After some algebra and considering N-atom conservation, one finds:

$$\frac{d[NO]}{dt} = -2\frac{d[N_2]}{dt} = 2\frac{k_1^+ k_3^- [H][NO]^2 - k_1^- k_3^+ [N_2][OH][O]}{k_1^+ [NO] + k_3^+ [OH]} \qquad (4)$$

with

$$[H] = \left[\frac{[H_2O][O]}{K_4 K_5 [O_2]}\right]^{1/2} \qquad (5)$$

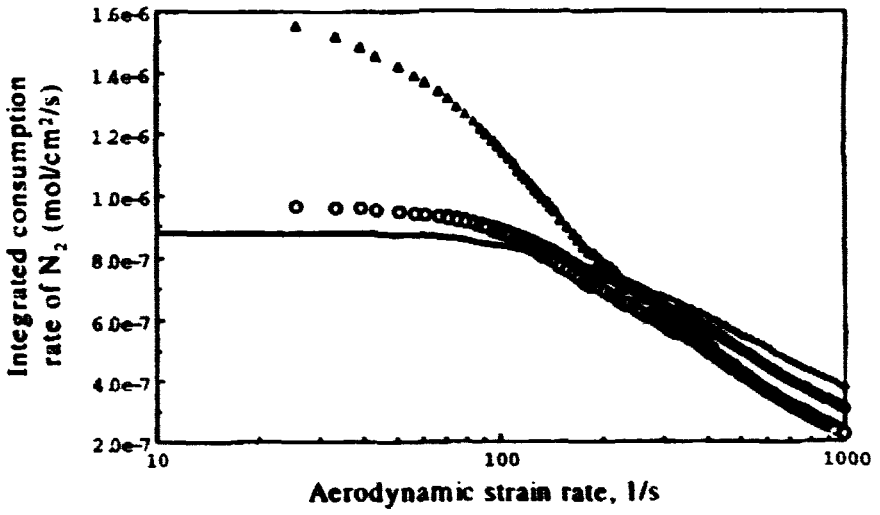

FIGURE 8. Effect of strain-rate on integrated consumption rate of N_2 in a O_2/CH_4 counterflow diffusion flame with 5% N_2 addition in both streams. Solid line: Full GRI 2.11 mechanism. • : Zeldovich mechanism alone. Δ: model with no reburn. ▲: model with reburn.

$$[OH] = \left[\frac{K_4[H_2O][O_2]}{K_5[O]}\right]^{1/2} \tag{6}$$

$$[O] = \left[\frac{[O_2]}{K_6}\right]^{1/2} \tag{7}$$

where bracketed quantities refer to concentrations, and where k is the specific reaction rate. K is the equilibrium constant. subscripts refer to reaction numbers, superscript '+' refers to forward rate of reaction, and superscript '-' refers to backward rate of reaction.

An alternative model (model 2) with no reburn effects and with the partial equilibrium assumption for atomic oxygen can be derived by assuming $k_1^+ = 0$. One obtains:

$$\left.\frac{d[NO]}{dt}\right|_{\text{no reburn}} = -2\left.\frac{d[N_2]}{dt}\right|_{\text{no reburn}} = 2\frac{k_1^-}{K_6^{-1/2}}[O_2]^{1/2}[N_2] \tag{8}$$

These global one-step models are compared with the full GRI 2.11 and the Zeldovich mechanisms by focusing on the evolution of the spatially-integrated N_2 consumption rate with strain-rate (Fig. 8). This figure also depicts the values of $\int(-d[N_2]/dt)dx$ of the full GRI 2.11 and Zeldovich mechanisms. As in Fig. 5. all models lead to a decrease of the integrated consumption rate of N_2 with strain-rate. Model 1 has a behavior similar to the Zeldovich mechanism except that at strain-rates greater than 200 s^{-1} it underpredicts N_2 consumption. This is due

to the fact that for the higher strain-rates the partial equilibrium assumption for atomic oxygen fails. Compared to the full GRI 2.11 scheme, model 1 overpredicts N_2 consumption at low strain-rates by about 15% due to the fact that it does not account for reburn through the hydrocarbon chemistry. At high strain-rates, it underpredicts N_2 consumption by about 50% due to the fact that it does not account for the prompt mechanism and for non-equilibrium effects of atomic oxygen. Model 2 overpredicts significantly N_2 consumption at low strain-rates and behaves like model 1 at high strain-rates. The overprediction of N_2 consumption is due to the fact that no reburn mechanism is included, neither that of the Zeldovich mechanism alone, nor that of the full GRI 2.11 scheme. This shows that inclusion of the reverse step, $N + NO \rightarrow N_2 + O$, is essential in getting correct estimates of N_2 consumption at low strain-rates.

3. Effect of turbulence

3.1 Numerical approach

Concerning turbulence, the closure method is investigated by post-processing the 3D data base of a turbulent diffusion flame developed by Vervisch (1992). This data base was the result of a direct numerical simulation of a turbulent non-premixed flame in decaying turbulence. The flow field was resolved accurately by solving the full Navier-Stokes equations. The flame was modeled by a one-step irreversible reaction, $O + F \rightarrow P$, where O is the oxidizer, F is the fuel, and P is the product, and the reaction rate follows an Arrhenius formulation:

$$\dot{w} = k\rho Y_O \rho Y_F \exp(-E/RT) \tag{9}$$

where $\dot{w}$ is the reaction rate, k is the pre-exponential factor, ρ is the density, Y_O is the oxidizer concentration, Y_F is the fuel concentration, E is the activation energy, R is the gas constant, and T is the temperature. The formalism that was used was that of Williams (1985): the quantities were non-dimensionalized in such a way that the heat of reaction was expressed in terms of a temperature jump, $\alpha = (T_b - T_u)/T_b$ and the activation energy was expressed in terms of a Zeldovich number, $\beta = E(T_b - T_u)/RT_b^2$. The values of these parameters are: $\alpha = 0.8$ and $\beta = 8$. The pre-exponential factor was selected such that the initial global Damköhler number was equal to one. This number is defined in Chen *et al.* (1992) as:

$$Da = \frac{l_t}{u_0}\left[\frac{1}{\delta_{fl}}\int_{\delta_{fl}} \dot{w}dx\right] \tag{10}$$

where l_t is the integral scale of turbulence, u_0 is the rms velocity, and δ_{fl} is the flame thickness. The Damköhler number expresses the ratio between the initial eddy turnover time and a characteristic chemical time. Furthermore, the molecular weights of the fuel and the oxidizer were taken to be equal.

At time $t = 0$, the flow field was initialized with a given spectrum for turbulence and with a planar laminar diffusion flame located at the center of the computational

domain. The calculations were carried out on a 129 × 65 × 65 grid. The resulting data base is composed of a series of eight different time intervals: they correspond to times 0, 2.1, 4.4, 6.8, 9.2, 10.0, 14.7, 17.2, where time is non-dimensionalized by the acoustic time, $t_a = L/c$ (c is the speed of sound in the fresh reactants and L is a reference length).

The approach for testing various modeling formulations consists of computing at each time-step the volume-average of $d[N_2]/dt$ and comparing this value with that given by the various closure models. To compute $d[N_2]/dt$, a chemical model is needed, and we use model 2 in this section. The reason for not using model 1 is that it is necessary to have the NO concentration for this model. However, the data base does not provide this information, but provides the oxidizer mass fraction and the temperature field, and, therefore, only model 2 can be used. Consequently, reburn is not accounted for. Since the objective is to assess closure formulations, it is expected that model 2 is sufficient. In this case, the consumption rate of NO is expressed from Eq. 8 as follows:

$$\frac{d[NO]}{dt} \sim \sqrt{\frac{Y_O}{T}} \frac{1}{T} \exp(-T_a/T) \tag{11}$$

where Y_O/T is assumed to be proportional to $[O_2]$, $1/T$ is assumed to be proportional to $[N_2]$, and T_a is the activation temperature. In this data base, T is non-dimensional and varies between 2.5 and 12.5; therefore, T_a is non-dimensional and is set equal to:

$$T_a = \frac{E_{Equilibrium}(cal/mol)}{R(cal/mol/K)} \times \frac{12.5}{T_b(K)} \tag{12}$$

Here, we take $T_b = 3000\ K$ in order to reproduce the temperature sensitivity of N_2 consumption occurring in an oxygen-methane flame, and this leads to $T_a = 287.5$. Consequently, the exact turbulent production of NO in the direct numerical simulation is taken to be:

$$\frac{d[NO]}{dt}\Big|_{exact} = \frac{1}{N_x N_y N_z} \Sigma_{N_x,N_y,N_z} \frac{\sqrt{Y_O}}{T^{3/2}} \exp(-T_a/T) \tag{13}$$

where N_x, N_y and N_z are the number of points in directions x, y and z, respectively.

3.2 Results

The PDF closure models of Eq. 3a, referred to as JPDF for joint PDF, and Eq. 3b, referred to as SPDF for single PDF, are assessed by comparing their predictions with the actual NO production rates as estimated from Eq. 13. The predictions by JPDF and SPDF are computed as follows:

$$\left.\frac{d[NO]}{dt}\right|_{JPDF} =$$

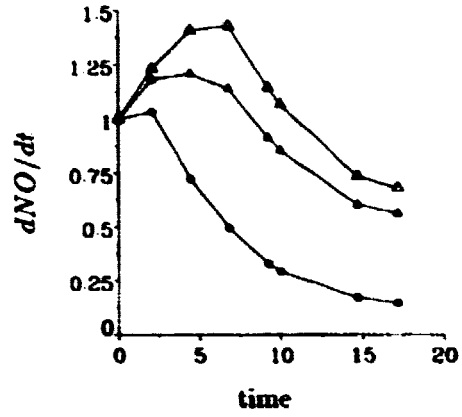

FIGURE 9. Time-evolution of turbulent NO production term. The terms are non-dimensionalized by the exact value at $t = 0$. • : Exact term. ▲: Joint PDF. △: Single scalar PDF.

$$\frac{1}{N_x}\Sigma_{N_x}\left(\frac{1}{N_yN_z}\Sigma_{N_y,N_z}\frac{1}{T}\right)\left(\frac{1}{N_yN_z}\Sigma_{N_y,N_z}\sqrt{\frac{Y_O}{T}}\right)\left(\frac{1}{N_yN_z}\Sigma_{N_y,N_z}\exp(T_a/T)\right) \tag{14a}$$

$$\left.\frac{d[NO]}{dt}\right|_{\text{SPDF}} =$$

$$\frac{1}{N_x}\Sigma_{N_x}\left(\frac{1}{N_yN_z}\Sigma_{N_y,N_z}\frac{1}{T}\right)\left(\sqrt{\frac{1}{N_yN_z}\Sigma_{N_y,N_z}\frac{Y_O}{T}}\right)\left(\frac{1}{N_yN_z}\Sigma_{N_y,N_z}\exp(T_a/T)\right) \tag{14b}$$

Figure 9 shows a comparison between the predictions of JPDF, SPDF, and the exact $d[NO]/dt$. In all cases, the production rate of NO starts increasing and then decreases at later times. This can be explained as follows: at initial times, the flame surface is wrinkled by turbulence, leading to an increase of flame surface area and, therefore, to an increase in NO production; at later times, the flame is strained by the turbulent flow field and is locally quenched, as can be seen in Chen *et al.* (1992), thereby reducing the rate of production of NO. The JPDF and SPDF models overestimate significantly the amount of NO production rates, with JPDF being slightly better than SPDF. The reason for this overestimation is that $[O_2]$ and T are assumed to be uncorrelated. This can be seen as follows (for simplicity, we consider $[N_2]$ as constant):

$$\frac{\overline{d[NO]}}{dt} \sim \overline{[O_2]^{1/2}\exp(T_a/T)} = ([O_2]^{1/2})^*\overline{\exp(-T_a/T)} \tag{15}$$

where $([O_2]^{1/2})^*$ is a weighted average of $[O_2]^{1/2}$ with:

$$([O_2]^{1/2})^* = \int_V [O_2]^{1/2}\left(\frac{\exp(-T_a/T)}{\int_V \exp(-T_a/T)dV}\right)dV \tag{16}$$

where V is the volume on which is conducted the averaging procedure, here, the computational domain. Equation 16 is a weighted average which is strongly biased towards the high temperatures and, therefore, strongly biased to low values of $[O_2]$, due to chemical reaction and dilatation. Consequently, we obtain:

$$([O_2]^{1/2})^{\sim} < \overline{[O_2]^{1/2}} \tag{17}$$

Furthermore, we have:

$$\overline{[O_2]^{1/2}} < \overline{[O_2]}^{1/2} \tag{18}$$

By combining Eq. 15, 17, and 18 and assuming that $[N_2]$ inhomogeneities do not modify the relationships, one finds:

$$\int_V [N_2][O_2]^{1/2} \exp(-T_a/T)dV < \overline{[N_2]}\left(\int_V [O_2]^{1/2}dV\right)\left(\int_V \exp(-T_a/T)dV\right)$$

$$< \overline{[N_2]}\,\overline{[O_2]}^{1/2} \int_V \exp(-T_a/T)dV \tag{19}$$

Therefore, not accounting for the correlation between $[O_2]$ and T leads necessarily to an overestimation of the turbulent production term of NO. In addition, the error is dependent on the averaging volume as is apparent in Eq. 16. In the case of Fig. 9, the averaging volumes over which are computed mean quantities are yz planes as indicated in Eq. 14a and 14b, and this corresponds to a case that minimizes the error. Additional computations have been carried where a single averaging volume corresponding to the whole computational domain has been used, and the corresponding estimates of $d\overline{[NO]}/dt$ by the SPDF and JPDF models are 20 times higher.

3.3 A model based on laminar flame structure

To improve the predictive capabilities of PDF formulations for NO formation, a correlation between $[O_2]$ and T is sought assuming a laminar flame structure. The goal is to express $[O_2]$ as a function of temperature. Figure 10 shows the correlation between Y_O and the reduced temperature θ at time $t = 0$ in the data base, where θ is defined by:

$$\theta = \frac{T - T_u}{T_b - T_u} \tag{20}$$

The relationship has two branches, one with high values of Y_O corresponding to the oxidizer side, and one with low values of Y_O corresponding to the fuel side. Matching the oxidizer branch leads to the following fit:

$$Y_O = 1. - 0.9 \times \theta \tag{21}$$

and the fuel branch is fit by:

$$Y_O = 0.05 \times \theta \tag{22}$$

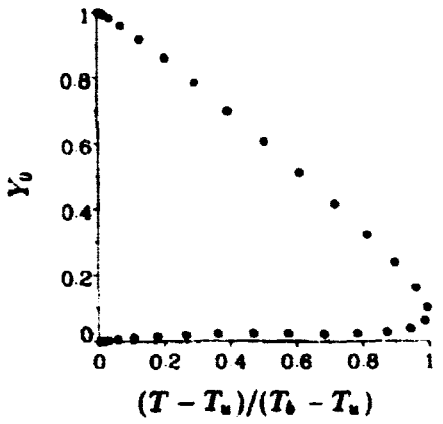

FIGURE 10. Relationship between θ and Y_O across the planar laminar diffusion flame at time $t = 0$ in the data base.

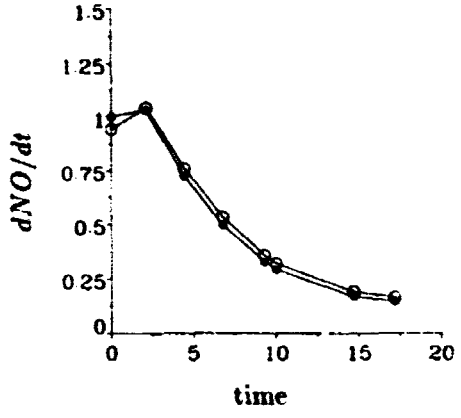

FIGURE 11. Time-evolution of turbulent NO production term. The terms are non-dimensionalized by the exact value at $t = 0$. • : Exact term. o : proposed single scalar PDF model.

Combining Eq. 13, 21, and 22 leads to the following alternate single PDF model:

$$\left.\frac{d[NO]}{dt}\right|_{\text{model}} = \frac{1}{N_x N_y N_z} \Sigma_{Nx,Ny,Nz} \frac{1}{2}\left(\frac{\sqrt{1-0.9\theta}}{T^{3/2}} + \frac{\sqrt{0.05\theta}}{T^{3/2}}\right) \exp(-T_a/T) \quad (23)$$

Figure 11 shows the evolution of the turbulent production term of NO for the new single PDF model. The agreement is very good and the predictions of this new model are insensitive to the choice of the averaging volume.

This test shows that this new model is promising and can be applied in practical codes that use single PDF formulations for NO production. In the case of an oxygen-natural gas flame, reburn should be accounted for and concentrations of O_2, H_2O, and NO should be included. Therefore, correlations between $[O_2]$ and

T, $[H_2O]$ and T.and $[NO]$ and T should be derived from, for example, a library of laminar strained flames.

In practice, this PDF model would be able to predict the amount of NO produced in the flame zone; however, it would not be appropriate in the post-flame zone since $[O_2]$ and T are no longer correlated. Therefore, two models should be used, one for the reaction zone, similar to that developed in this paper, and one for the post-flame zone of the kind of the SPDF or JPDF models.

4. Conclusion

The effects of chemistry and turbulence on the rate of production of nitric oxide in oxygen-natural gas diffusion flames has been investigated.

It has been shown that, due to the high temperatures encountered in these flames, the Zeldovich mechanism is dominant and accounts for more than 75% of the rate of production of NO over a large range of strain-rates. The limitations of predictions based on the Zeldovich mechanism alone have been identified. at low strain-rates, it overpredicts N_2 consumption, which is the source of NO, due to the fact that it does not account for reburn, and at high strain-rates it underpredicts N_2 consumption due to the fact that it does not account for the prompt mechanism. Despite these shortcomings, the Zeldovich mechanism is satisfactory for predicting NO formation rates within 25% and an overall one-step mechanism that accounts for reburn and which assumes partial equilibrium of atomic oxygen with O_2 has been developed. This simple model gives the same results as the Zeldovich mechanism at low strain-rates but leads to further underprediction of N_2 consumption due to the fact that it cannot reproduce non-equilibrium effects.

The effect of turbulence is to generate fluctuations of temperature and species concentrations as well as straining effects. It has been shown by postprocessing the 3D DNS data base of Vervisch (1992) that usual closure models based on single scalar PDF's or joint PDF's lead to significant overpredictions of NO formation rates. The main reason is that these models do not account for the intrinsic correlation between oxygen concentration and temperature in the reaction zone of a diffusion flame. A new single scalar PDF model incorporating such a correlation has been developed. The model assumes that the relationship between oxygen and temperature is that of a laminar diffusion flame. The predictions of this model are in excellent agreement with the results from the DNS, and it is expected that it can be implemented in practical codes that use single scalar PDF's for NO formation.

Acknowledgments

The first author would like to thank Prof. P. Moin for giving the opportunity to participate to this summer program. He would also like to thank Greg Ruetsch and Nigel Smith for their help. The second author would like to express his gratitude to Air Liquide and CTR for their partial financial support.

REFERENCES

BOWMAN, C. T. 1992 Control of combustion-generated nitrogen oxide emissions:

Technology driven by regulation. *24th Symposium (Int'l.) on Combustion*, The Combustion Institute, Pittsburgh, 859-878.

BOWMAN, C. T., HANSON, R. K., DAVIDSON, D. I., GARDINER, W. C., LISSIANSKI, V., FRENKLACH, M., GOLDENBERG, M., SMITH, G. P., GOLDEN, G. M. AND SERAISKAR, R. V. Optimized Kinetics for Natural Gas Combustion, NO_x Production and Reburning (GRI Mech 2.11) Poster 047, *26th* Int. Symposium on Combustion.

BOZELLI, J. W., KARIM, M. H. U. & DEAN, A. M. 1993 Reactions of CH2 and CH with N2 and CH with NO. In *Turbulence and Molecular Processes in Combustion*, Elsevier Science Publishers B. V., Amsterdam, 101.

CHELLIAH, H. K., LAW, C. K., UEDA, T., SMOOKE, M. D. & WILLIAMS, F. A. 1990 An experimental and theoretical investigation of the dilution, pressure and flow-field effects on the extinction condition of methane-air-nitrogen diffusion flames. *23rd Symposium (Int'l.) on Combustion*. The Combustion Institute, Pittsburgh, 503-511.

CHEN, J. H., MAHALINGAM, S., PURI, I. K. & VERVISCH, L. 1992 Effect of finite-rate chemistry and unequal Schmidt numbers on turbulent non-premixed flames modeled with single-step chemistry. *Proceedings of the 1992 Summer Program*, Center for Turbulence Research, Stanford Univ./NASA Ames, 367-387.

CHEN, J.-Y. & KOLLMANN, W. 1992 PDF modeling and analysis of thermal NO formation in turbulent nonpremixed hydrogen-air jet flames. *Combust. Flame* **88**, 37-49.

CORREA, S. M.& POPE, S. B. 1992 Comparison of a Monte Carlo PDF/Finite-Volume Mean Flow Model with Bluff-Body Raman Data. *Twenty-Fourth Symposium (Int'l.) on Combustion*,The Combustion Institute, 279-285.

DE SOETE, G. G. 1974 Overall reaction rates of NO and N2 formation from fuel dilution. *15th Symposium (Int'l.) on Combustion*. The Combustion Institute, Pittsburgh, 1093-1102.

DRAKE, M. C. & BLINT 1989 Thermal NOx in stretched laminar opposed-flow diffusion flames with CO/H2/N2 fuel. *Combust. Flame* **76**, 151-167.

DRAKE, M. C. & BLINT 1991 Relative importance of nitric oxide formation mechanisms in laminar opposed-flow diffusion flames. *Combust. Flame* **83**, 287-338.

DRISCOLL, J. F., CHEN, R.-H. & YOON, Y. 1992 Nitric oxide levels of turbulent jet diffusion flames: Effects of residence time and Damköhler number. *Combust. Flame* **88**, 37-49.

EGOLFOPOULOS, F. N. 1994a Dynamics and Structure of Unsteady, Strained, Laminar, Premixed Flames. *25th Symposium (Int'l.) on Combustion*. The Combustion Institute, Pittsburgh, 1365-1374.

EGOLFOPOULOS, F. N. 1994b Geometric and Radiation Effects on Steady and Unsteady Strained Laminar Flames. *25th Symposium (Int'l.) on Combustion*. The Combustion Institute, Pittsburgh, 1375-1381.

EGOLFOPOULOS, F. N. & CAMPBELL, C. S. 1996 Unsteady, Counterflowing, Strained Diffusion Flames: Frequency Response and Scaling. *J. of Fluid Mech.* **318**, 1-29.

FENIMORE, C. P. 1971 Formation of nitric oxide in premixed hydrocarbon flames. *13th Symposium (Int'l.) on Combustion* The Combustion Institute, Pittsburgh, 373-380.

HAHN, W. A. & WENDT, J. O. L. 1981 NOx formation in flat, laminar, opposed jet methane diffusion flames. *18th Symposium (Int'l.) on Combustion*. The Combustion Institute, Pittsburgh, 121-131.

HAWORTH, D. C., DRAKE, M. C., POPE, S. B. & BLINT, R. J. 1988 The importance of time-dependent flame structures in stretched laminar flamelet models for turbulent jet diffusion flames. *22nd Symposium (Int'l.) on Combustion*. The Combustion Institute, Pittsburgh, 589-597.

JANICKA, J. & KOLLMANN, W. 1982 The Calculation of Mean Radical Concentrations in Turbulent Diffusion Flames. *Combust. Flame*. **44**, 319-336.

MAUSS, F., KELLER, D. & PETERS, N. 1990 A lagrangian simulation of flamelet extinction and re-ignition in turbulent jet diffusion flames. *23rd Symposium (Int'l.) on Combustion*. The Combustion Institute, Pittsburgh, 693-698.

MILLER, J. A. & BOWMAN, C. T. 1989 Mechanism and modeling of nitrogen chemistry in combustion. *Prog. Energy Combust. Sci.* **15**, 287-338.

NISHIOKA, M., NAKAGAWA, S., ISHIKAWA, Y. & TAKENO, T. 1994 NO emission characteristics of methane-air double flame. *Combust. Flame* **98**, 127-138.

PETERS, N. & DONNERHACK, S. 1981 Structure and similarity of nitric oxide production in turbulent diffusion flames. *18th Symposium Int'l. on Combustion*. The Combustion Institute, Pittsburgh, 33-42.

POPE, S. B. & CORREA, S. M. 1986 Joint PDF Calculations of an Non-Equilibrium Turbulent Diffusion Flame. *21st Symposium (Int'l.) on Combustion*, The Combustion Institute, 1341-1348.

SAMANIEGO, J.-M., EGOLFOPOULOS, F. N. & BOWMAN, C. T. 1995 CO_2^* Chemiluminescence in Premixed Flames. *Combustion Science and Technology* **109**, 183-203.

SAMANIEGO, J.-M., LABÉGORRE, B., EGOLFOPOULOS, F. N., DITARANTO, M., SAUTET, J.-C. & CHARON, O. 1996 Mechanisms of Nitric Oxide Formation in Oxygen-Natural Gas Combustion. *In preparation.*

TAKENO, T., NISHIOKA, M. & YAMASHITA, H. 1993 Prediction of NOx emission index of turbulent diffusion flame. In *Turbulence and Molecular Processes in Combustion*, Elsevier Science Publishers B. V., Amsterdam, 375-392.

TURNS, S. R. & MYHR, F. H. 1991 Oxides of nitrogen emissions from turbulent jet flames: Part I-fuel effects and flame chemistry. *Combust. Flame* **87**, 319-335.

VERVISCH, L. 1992 Study and modeling of finite rate chemistry effects in turbulent non-premixed flames. *Annual Research Briefs*. Center for Turbulence Research, Stanford Univ./NASA Ames, 411-429.

VRANOS, A., KNIGHT, B. A., PROSCIA, W. M., CHIAPETTA, L. & SMOOKE, M. D. 1992 Nitric oxide formation and differential diffusion in a turbulent methane-hydrogen diffusion flame. *24th Symposium (Int'l.) on Combustion*. The Combustion Institute, Pittsburgh, 377-384.

WILLIAMS, F. A. 1985 *Combustion Theory*, Benjamin/Cummings, Menlo Park.

NEXT
DOCUMENT

Asymptotic solution of the turbulent mixing layer for velocity ratio close to unity

By F. J. Higuera[1], J. Jiménez[2] AND A. Liñán[1]

The equations describing the first two terms of an asymptotic expansion of the solution of the planar turbulent mixing layer for values of the velocity ratio close to one are obtained. The first term of this expansion is the solution of the well-known time-evolving problem and the second, which includes the effects of the increase of the turbulence scales in the stream-wise direction, obeys a linear system of equations. Numerical solutions of these equations for a two-dimensional reacting mixing layer show that the correction to the time-evolving solution may explain the asymmetry of the entrainment and the differences in product generation observed in flip experiments.

1. Introduction

Time evolving simulations of the mixing layer are believed to capture many important features of the dynamics of this flow, and are widely used because they are simpler to implement, less expensive, and less subject to uncertainties coming from approximate boundary conditions than the alternative space-evolving simulations. Some features of the real flow, however, are outside the framework of the time-evolving simulations. In particular, it is known that an incompressible mixing layer does not entrain equal amounts of fluid from each of the two free streams (Dimotakis, 1986 and references therein) and that, when the free streams carry passive scalars, the average composition in the molecularly mixed fluid in the mixing layer is nearer to the composition of the fast stream than to the composition of the slow stream. While it is not clear to what extent the second of these features is a consequence of the first or of some asymmetry of the process leading to molecular mixing inside the layer, none of the two can be captured by a time-evolving simulation, owing to the intrinsic symmetry of this artificial flow.

The amount of molecular mixing and the variation of the mixed fluid mean concentration across the layer depend on the Reynolds number, the degree of development of the layer, and the Prandtl or Schmidt number of the scalar; these factors determining in particular the extent to which free stream fluid is transported across the layer by the large scale motions before being molecularly mixed (Konrad 1976; Batt 1977; Mungal & Dimotakis 1984; Koochesfahani & Dimotakis 1986; Karasso & Mungal 1996), but the asymmetries mentioned above occur in any case.

1 E. T. S. Ingenieros Aeronáuticos, UPM, Madrid

2 Center for Turbulence Research

The effect of the scalar field asymmetry is specially obvious when the species carried by the two streams are reactive and lead to a diffusion flame inside the mixing layer, in which a unit of mass of a stream (the fuel stream say) reacts with S units of mass of the other (the oxidizer stream). Then, flip experiments, consisting in exchanging the reactive species between the two streams and keeping constant their concentrations and all the other operating conditions (Mungal & Dimotakis 1984; Koochesfahani & Dimotakis 1986; Karasso & Mungal 1996), clearly show that the amount of product generated by the chemical reaction is larger when the reactant that is more consumed (the oxidizer if $S > 1$) is carried by the fast stream.

To study the effect of these asymmetries, a correction to the time-evolving mixing layer formulation is worked out here using an asymptotic expansion for small differences of the two stream velocities. The analysis follows the lines of Spalart (1986, 1988). The new formulation is applied to a constant density two-dimensional reactive mixing layer with an infinitely fast, diffusion controlled reaction. In this limit, and assuming in addition that the Lewis numbers of the two reactants are equal to one, the chemical reaction can be easily accounted for following the evolution of a linear combination of the mass fractions of the reactants (the mixture fraction Z) which takes the values 0 and 1 in the oxidizer and fuel streams and is transported as a passive scalar. The mass fraction of the product (also with Lewis number equal to one) is a piecewise linear function of Z given by (6) below (see, e.g., Williams 1985).

2. Formulation

The turbulent mixing layer is a statistically stationary flow and, asymptotically, after an adjustment region, it is also statistically self-similar. Our aim here is to try to take advantage of these two properties to simplify the numerical computations.

The large length and time scales of the turbulence are proportional to the streamwise distance x in the self-similar state, and the variation of these scales is inextricably linked to the dynamics of the layer, being brought about by the process responsible for its evolution (vortex pairings in the classical view). This feature makes the numerical simulation costly because a long and wide stretch of the layer must be simulated in order to see the approach to its self-similar state.

The opening angle of the mixing layer is often small. Formally this is true when the velocities of the two streams are close to each other, but in fact the angle is fairly small in any case. On one hand, this feature makes the numerical simulations even more expensive, because a very long stretch is needed to see the initial size of a typical vortex grow by a given factor. On the other hand, this feature is the basis of a well known simplification of the numerical treatment, based on the fact that the changes of time and length scales are small, and can be taken into account as a perturbation, over distances of the order of the size of one or a few vortices.

This is so because for a layer growing by pairings of the large vortices, for which each vortex must undergo a number of these discrete events to approach the self-similar state, a small angle amounts to a small ratio of the size of a vortex to the distance it travels between successive pairings. But then, since the spacing of the large scale vortices is not much larger than their size, there are many neighboring

vortices to the left and to the right of a given vortex with sizes not very different from its own size, and it seems reasonable to think that the evolution of a vortex and of its nearest neighbors between successive pairings depends on the details of the evolution of only a number of other neighbors, whereas the effect of the rest of the mixing layer can be taken into account using a kind of mean field approximation without regard for individual features of the far vortices.

Since the vortices move with a velocity intermediate between the velocities of the two streams, these conditions can be better put to use in a reference frame moving with that intermediate velocity. In this reference frame the evolution of a vortex can be described following the detailed dynamics of the flow over a span containing only a limited number of neighbor vortices. Here, using periodicity conditions in the stream-wise direction amounts, of course, to a temporal simulation of the flow, but the equations describing the small perturbations due to the growth of the turbulent scales can be easily worked out and solved along with those of the temporal simulation. It is worth recalling, however, that a definite error of a different type is always associated to the use of periodic conditions because the self-similarity and stationarity of the flow are statistical properties not applicable to individual realizations. Hopefully, the importance of this error decreases as the number of vortices included in the simulation increases.

Restricting the computations to a finite span in the moving frame imposes a limitation on the time during which the evolution of the flow may be followed, owing to the growth of the vortices. In principle, a long span is required if the initial conditions are not close to the final self-similar state and a large number of pairings is necessary to approach that state. In practice, such a long span could perhaps be avoided carrying out computations on a shorter one for a moderate lapse of time and then replicating the results one or a few times in new adjacent spans, introducing appropriate phase shifts and a slight decrease of resolution before continuing the computation.

Consider then a plane self-similar mixing layer between two incompressible streams with velocities U_1 and $U_2 < U_1$. Assume that $\epsilon = (U_1 - U_2)/(U_1 + U_2) \ll 1$ to ensure that the angle of the layer, defined in any convenient way, is small of $O(\epsilon)$, though, as was mentioned before, this angle is probably small for any ϵ. The aim is to follow the evolution of a few adjacent vortices, of initial characteristic size δ say, during a time of order $t_c = 2\delta/(U_1 - U_2)$ corresponding to a few pairings. The growth of the mixing layer thickness is taken into account switching to the variables (x^*, η, z^*), where $\eta = y^*/(\epsilon x^*)$ and (x^*, y^*, z^*) are the usual Cartesian coordinates. The statistical properties of the flow imply then that the x-averages coincide with the time averages and both are functions of η only. Next, introducing a reference frame moving with velocity $U_m = (U_1 + U_2)/2$, the solution is sought in the form

$$\boldsymbol{v}^* = U_m(\mathbf{i} + \epsilon \mathbf{v}), \quad p^* = \rho U_m^2 \epsilon^2 p, \qquad \text{with} \quad x^* = U_m t_c(t + \epsilon x), \tag{1}$$

where the non-dimensional variables $(\mathbf{v}, p)$ are of order unity and the distances and time are scaled with δ and t_c, respectively. In terms of these variables the

Navier-Stokes equations and the equation for the mixture fraction are

$$\left.\begin{aligned} G_i v_i - \frac{\epsilon\eta}{t+\epsilon x}\partial_\eta u &= 0 \\ \partial_t v_i + (\tilde{v}_i G_i) v_i &= -G_i p + \frac{1}{Re}\nabla^2 v_i \\ \partial_t Z + (\tilde{v}_i G_i) Z &= \frac{1}{RePr}\nabla^2 Z \end{aligned}\right\} , \tag{2}$$

where $\mathbf{G} = (\partial_x,\ 1/(t+\epsilon x)\partial_\eta,\ \partial_z)$ is a symbolic vector, $\tilde{\mathbf{v}} = (u, v-\eta(1+\epsilon u), w)$, the Laplacian operator acting on each component of the velocity is $\nabla^2 = \partial_{xx} + (1+\epsilon^2\eta^2)/(t+\epsilon x)^2\partial_{\eta\eta} + \partial_{zz} - 2\epsilon\eta/(t+\epsilon x)\partial_{x\eta} + 2\epsilon^2\eta/(t+\epsilon x)^2\partial_\eta$. $Re = (U_1 - U_2)\delta/2\nu$, and Pr is the Prandtl number. The solution of (2) can be sought as a power series in ϵ, of the form $(\mathbf{v}, p, Z) = (\mathbf{v}_0, p_0, Z_0) + \epsilon(\mathbf{v}_1, p_1, Z_1) + \cdots$.

Carrying this expansion into (2) we find, at leading order,

$$\left.\begin{aligned} G_{0_i} v_{0_i} &= 0 \\ \partial_t v_{0_i} + (\tilde{v}_{0_j} G_{0_j}) v_{0_i} &= -G_{0_i} p_0 + \frac{1}{Re}\nabla_0^2 v_{0_i} \\ \partial_t Z_0 + (\tilde{v}_{0_j} G_{0_j}) Z_0 &= \frac{1}{RePr}\nabla_0^2 Z_0 \end{aligned}\right\} , \tag{3}$$

where $\mathbf{G}_0 = (\partial_x,\ 1/t\,\partial_\eta,\ \partial_z)$, $\tilde{\mathbf{v}}_0 = (u_0, v_0 - \eta, w_0)$, and $\nabla_0^2 = \partial_{xx} + 1/t^2\partial_{\eta\eta} + \partial_{zz}$.

At the next higher order linear equations are obtained for $(\mathbf{v}_1, p_1, Z_1)$ having some forcing terms proportional to x (arising from the expansion of the denominators in (2)) and other that do not contain x explicitly. The solution of these equations is of the form $(\mathbf{v}_1, p_1, Z_1) = x(\mathbf{v}_{10}, p_{10}, Z_{10}) + (\mathbf{v}_{11}, p_{11}, Z_{11})$, where, as can be easily verified, $(\mathbf{v}_{10}, p_{10}, Z_{10}) = \partial_t(\mathbf{v}_0, p_0, Z_0)$ in order for the time averages to be independent of x, and $(\mathbf{v}_{11}, p_{11}, Z_{11})$ satisfy

$$\left.\begin{aligned} G_{0_i} v_{11_i} + \partial_t u_0 - \frac{\eta}{t}\partial_\eta u_0 &= 0 \\ \partial_t v_{11_i} + (\tilde{v}_{0_j} G_{0_j}) v_{11_i} + (\tilde{v}_{11_j} G_{0_j}) v_{0_i} &= -G_{0_i} p_{11} + \frac{1}{Re}\nabla_0^2 v_{11_i} + F_i \\ \partial_t Z_{11} + (\tilde{v}_{0_j} G_{0_j}) Z_{11} + (\tilde{v}_{11_j} G_{0_j}) Z_0 + u_0\partial_t Z_0 - \frac{\eta u_0}{t}\partial_\eta Z_0 &= \\ \frac{1}{RePr}\left(\nabla_0^2 Z_{11} + 2\partial_{xt} Z_0 - \frac{2\eta}{t}\partial_{x\eta} Z_0\right) & \end{aligned}\right\} , \tag{4}$$

where $\mathbf{F} = -u_0\partial_t\mathbf{v}_0 + \eta u_0/t\,\partial_\eta\mathbf{v}_0 + 2/Re(\partial_{xt}\mathbf{v}_0 - \eta/t\,\partial_{x\eta}\mathbf{v}_0) + (-\partial_t p_0 + \eta/t\,\partial_\eta p_0,\ 0,\ 0)$. The velocity at this order is therefore $\mathbf{v} = \mathbf{v}_0 + \epsilon(x\,\partial_t\mathbf{v}_0 + \mathbf{v}_{11})$, which can be written as $\mathbf{v}_0(x, \eta, t + \epsilon x) + \epsilon\mathbf{v}_{11}$, and the pressure and mixture fraction are analogous. The first term admits a simple interpretation: as far as it is concerned the state of development of the flow is proportional to x, being slightly more evolved downstream of a point than it is upstream. Thus, even if periodic boundary conditions are used as an approximation for the leading order problem (3), as will be done in the

following section, this first term is not periodic. The effect of the second term will be discussed later.

Applying x- and t-averages in suitable order to Eqs. (3) and to the continuity equation in (4) yields

$$\left.\begin{aligned} \frac{d\bar{v}_0}{d\eta} &= 0 \\ \frac{d}{d\eta}(\overline{u_0 v_0}) - \eta\frac{d\bar{u}_0}{d\eta} &= 0 \\ \frac{d}{d\eta}(\overline{v_0^2} + \bar{p}_0) &= 0 \\ \frac{d}{d\eta}(\overline{u_0 Z_0}) - \eta\frac{d\bar{Z}_0}{d\eta} &= 0 \\ \frac{d\bar{v}_{11}}{d\eta} - \eta\frac{d\bar{u}_0}{d\eta} &= 0 \end{aligned}\right\}, \tag{5}$$

where the bars denote averaged variables. The first of these equations gives $\bar{v}_0 = 0$ (a constant v_0 has no effect on the dynamics; it can be set equal to zero by an $O(\epsilon)$ change in the orientation of the x axis). The last equation in (5) implies that the mean normal velocity is of order ϵ relative to the variation of the streamwise velocity, as could have been expected for a region of $O(\epsilon)$ aspect ratio. Using the second equation to eliminate $\eta\, d\bar{u}_0/d\eta$ and integrating, this equation yields $\bar{v}_{11} - \overline{u_0 v_0} =$ constant. Since $\overline{u_0 v_0} = 0$ for $\eta \to \pm\infty$, the normal velocity v_{11} tends to the same constant value on both sides of the mixing layer, and this constant can be set equal to zero as for v_0. Therefore the mixing layer does not introduce any perturbation in the free streams to this order and the ingestion of fluid by the layer is due only to the linear growth with x of its upper and lower apparent boundaries.

Since the orientation of the x-axis is well determined by the conditions $v_0 = v_1 = 0$ outside the mixing layer, the upper and lower boundaries can be defined on the basis of the usual thicknesses. For example, using the scaled momentum thickness $\Delta_m = \int_{-\infty}^{\infty} \overline{(U_1 - u^*)(u^* - U_2)}\, dy^*/[\epsilon x^*(U_1 - U_2)^2]$ and the scaled product thickness $\Delta_p = \int_{-\infty}^{\infty} \overline{Y_p(Z)}\, dy^*/(\epsilon x^*)$, where $Y_p(Z)$ is the product mass fraction given by the piecewise linear function

$$Y_p = \begin{cases} Z/Z_s & \text{for} \quad 0 \le Z \le Z_s \\ (1-Z)/(1-Z_s) & \text{for} \quad Z_s \le Z \le 1 \end{cases} \tag{6}$$

with $Z_s = 1/(1+S)$, the scaled upper and lower boundaries are

$$\begin{aligned} \Delta_m^{\pm} &= \pm\frac{1}{4}\int_0^{\pm\infty}(1 - \overline{u^2})\, d\eta = \pm\frac{1}{4}\int_0^{\pm\infty}(1 - \overline{u_0^2})\, d\eta \mp \frac{\epsilon}{2}\int_0^{\pm\infty}\overline{u_0 u_{11}}\, d\eta + \cdots \\ \Delta_p^{\pm} &= \pm\int_0^{\pm\infty}\overline{Y_p(Z)}\, d\eta \end{aligned} \tag{7}$$

and $\Delta_m = \Delta_m^+ + \Delta_m^-$, $\Delta_p = \Delta_p^+ + \Delta_p^-$.

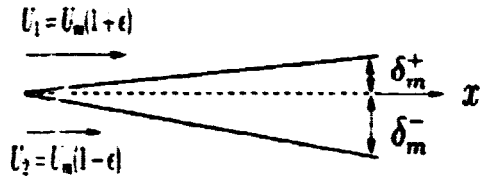

FIGURE 1. Sketch of the apparent boundaries and entrainment process.

3. Results

The two-dimensional forms of Eqs. (3) and (4) were numerically solved to find the effect of the first order corrections on the growth rate and the asymmetry of the layer. For this purpose the variable $y = \eta t$, which is the non-dimensional normal distance divided by the factor $1 + \epsilon x/t$, was used instead of η. The equations then take the form

$$\left.\begin{aligned} \nabla \cdot \mathbf{v}_0 &= 0 \\ \partial_t \mathbf{v}_0 + \nabla \cdot (\mathbf{v}_0 \mathbf{v}_0) &= -\nabla p_0 + \frac{1}{Re} \nabla^2 \mathbf{v}_0 \\ \partial_t Z_0 + \nabla \cdot (\mathbf{v}_0 Z_0) &= \frac{1}{RePr} \nabla^2 Z_0 \end{aligned}\right\} \tag{8}$$

$$\left.\begin{aligned} \nabla \cdot \mathbf{v}_{11} &= -\partial_t u_0 \\ \partial_t \mathbf{v}_{11} + \nabla \cdot (\mathbf{v}_0 \mathbf{v}_{11} + \mathbf{v}_{11} \mathbf{v}_0) &= -\nabla p_{11} + \frac{1}{Re} \nabla^2 \mathbf{v}_{11} + \partial_t \mathbf{R} \\ \partial_t Z_{11} + \nabla \cdot (\mathbf{v}_0 Z_{11} + \mathbf{v}_{11} Z_0) &= \frac{1}{RePr} \nabla^2 Z_{11} + \partial_t \left(-u_0 Z_0 + \frac{1}{RePr} \partial_x Z_0 \right) \end{aligned}\right\} \tag{9}$$

with $\mathbf{R} = -u_0 \mathbf{v}_0 + 2/Re\, \partial_x \mathbf{v}_0 - (p_0, 0)$, and were solved with the boundary conditions $\mathbf{v}_0 \mp \mathbf{i} = \mathbf{v}_{11} = Z_{11} = 0$ and $Z_0 = (1, 0)$ for $y \to \pm\infty$, and periodicity conditions in the stream-wise direction. The use of periodicity conditions is an approximation for which the only possible justification seems to be that in the present variables they are compatible with the spatial growth of the turbulence scales, and that, hopefully, they do not distort the solution too much if the period is sufficiently larger than the size of the vortices during most of the simulation. The initial conditions for the leading order variables were the hyperbolic tangent profiles $u_0 = \tanh 2y$ and $Z_0 = \frac{1}{2}(1 + \tanh 2y)$ plus perturbations proportional to the most unstable linear mode and one or two sub-harmonics with different amplitudes and phases. The variables $\mathbf{v}_{11}$ and Z_{11} were initially zero. In the simulations $Pr = 1$ and $Re = 500$-1000, based on the initial vorticity thickness.

With these conditions, $\mathbf{v}_0$, $Z_0 - 1/2$ and p_{11} change sign under the transformation $(x, y, t) \to (-x, -y, t)$ while $\mathbf{v}_{11}$, Z_{11}, and p_0 are left invariant. The mixing layer grows symmetrically in first approximation, leading to $\Delta^+_{m_0} = \Delta^-_{m_0} = \Delta_{m_0}/2$, whereas the correction to the growth rate is antisymmetric: $\Delta^+_{m_1} = -\Delta^-_{m_1} = \Delta_{m_1}$, say (the same relations hold for the product thickness when $S = 1$). Here Δ_{m_0} and Δ_{m_1} are the slopes of straight lines fitted to $\delta_{m_0} = \frac{1}{4}\int_{-\infty}^{\infty}(1 - \overline{u_0^2})\,dy$ and $\delta_{m_1} = -\frac{1}{2}\int_0^{\infty} \overline{u_0 u_{11}}\,dy$. The fluxes crossing the upper and lower apparent boundaries of

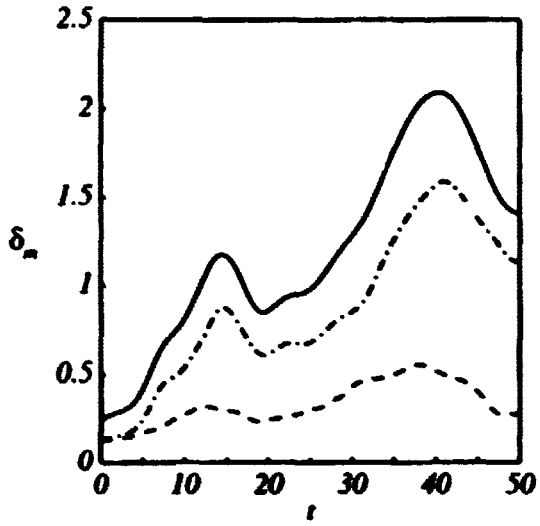

FIGURE 2. Momentum thickness (———) and upper and lower boundaries (---- and —·— , respectively) for $\epsilon = 0.45$ ($r = U_2/U_1 = 0.38$), $Re = 500$ and $Pr = 1$.

the layer, scaled with $\epsilon U_m x^*$, are (see Fig. 1) $\phi^{\pm} = (1 \pm \epsilon)\Delta_m^{\pm} = [\Delta_{m_0} \pm \epsilon(\Delta_{m_0} + 2\Delta_{m_1}) + \cdots]_{-}$, where the momentum thickness is used for definiteness, and the entrainment ratio, defined here as $E = \phi^+/\phi^-$, is

$$E = 1 + \epsilon\left[1 + 2\frac{\Delta_{m_1}}{\Delta_{m_0}}\right] + O(\epsilon^2). \tag{10}$$

The total momentum thickness $\delta_m = \delta_{m_0}$ and the upper and lower apparent boundaries, $\delta_m^+ = \delta_{m_0}/2 + \epsilon\delta_{m_1}$ and $\delta_m^- = \delta_{m_0}/2 - \epsilon\delta_{m_1}$ respectively, are given in Fig. 2 for a representative case displaying a pairing. The numerical results show that the layer opens more toward the slow stream ($\Delta_{m_1} < 0$), but this effect is overbalanced by the higher speed of the fast stream resulting in a E slightly greater than one.

Figure 3 shows the product thickness for $S = 1$ and for $S = 8$ and $1/8$. The last two values correspond to a flip experiment in which the fuel and the oxidizer streams are exchanged. The results show that the generation of product is higher when the reactant that is more consumed is carried by the fast stream.

Both results are in qualitative agreement with the experimental data. Quantitative comparisons are meaningless given the two-dimensional character of the present simulations.

The explanation of these results can be traced, of course, to the form of the forcing terms on the right hand sides of Eqs. (9). These terms depend only on time derivatives of the leading order solution, and the signs of some of them can be easily guessed. Thus, since the antisymmetric profile of $\overline{u}_0(y)$ (the bar meaning here x-average) gets thicker with time, $-\partial_t u_0$ in the continuity equation is more

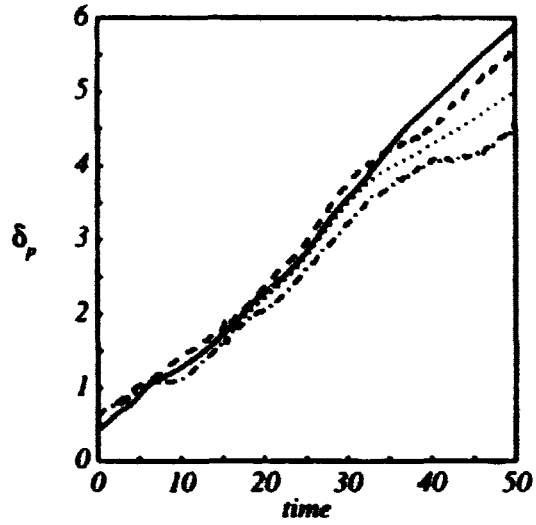

FIGURE 3. Product thickness for $S = 1$ (——— ; not affected by the asymmetry) and for $S = 8$ (— · —) and $1/8$ (- - - -), corresponding to a flip experiment, for $\epsilon = 0.45$, $Re = 500$ and $Pr = 1$. ····· : common value for $S = 8$ and $1/8$ when $\epsilon = 0$.

often positive than negative in the upper part of the layer, which amounts to a distribution of sources, and vice versa in the lower part, which amounts to sinks.

For the same reason, $-\partial_t u_0^2$ should be positive, on average, everywhere in the layer, and the numerical results show that this is also true of the whole forcing term $-\partial_t(u_0^2 + p_0) + 2/Re\,\partial_{xt} u_0$ in the x-momentum equation. This amounts to a force pushing the fluid in the stream-wise direction and leading to a u_{11} predominantly positive. Therefore the average velocity $\overline{u}_0 + \epsilon\overline{u}_{11}$ approaches its asymptotic value $+1$ in the upper stream faster than its asymptotic value -1 in the lower stream, which explains the results in Fig. 2.

The forcing term in the equation for Z_{11} has a complicated structure with bands of alternate signs. On average, however, it is positive (as could have been expected of the term $-\partial_t(\overline{u_0 Z_0})$, due to the increase of thickness of the profile of $\overline{Z}_0$ with time), leading to a Z_{11} with a banded structure but predominantly positive. Hence the region of $\overline{Z}$ near 1 in the upper part of the layer is wider than the region of $\overline{Z}$ near 0 in the lower part. This provides an explanation for the results in Fig. 3 because the upper region is responsible for a larger fraction of the product than the lower region when S is small and the average position of the flame is shifted toward the upper side, while the lower region is responsible for a larger fraction of the product than the upper region when S is large and the average position of the flame is shifted toward the lower side.

Since the forcing terms depend only on the leading order solution, they could perhaps be evaluated from the results of a three-dimensional time-evolving simulation (as that of Roger & Moser 1994), which would give indications on whether the

above observed trends hold also for that more realistic case.

Finally it may be noted that the condition $\epsilon \ll 1$, used here as the basis of a formal expansion, may not be necessary for some of the results to hold. As was mentioned before, the angle of the layer is moderately small for any value of ϵ because the eddy turn over time is always shorter than the time between pairings, and this alone provides the required scale separation.

REFERENCES

BATT, R. G. 1977 Turbulent mixing of passive and chemically reacting species in a low-speed shear layer. *J. Fluid Mech.* **82**, 53-95.

DIMOTAKIS, P. E. 1986 Two dimensional shear-layer entrainment. *AIAA J.* **24**, 1791-1796.

KARASSO, P. S. & MUNGAL, M. G. 1996 Scalar mixing and reaction in plane liquid shear layers. *J. Fluid Mech. In press.*

KONRAD, J. H. 1976 An experimental investigation of mixing in two-dimensional turbulent shear flows with applications to diffusion-limited chemical reactions. Ph.D. Thesis, Caltech.

KOOCHESFAHANI, M. M. & DIMOTAKIS, P. E. 1986 Mixing and chemical reactions in a turbulent liquid mixing layer. *J. Fluid Mech.* **170**, 83-112.

MUNGAL, M. G. & DIMOTAKIS, P. E. 1984 Mixing and combustion with low heat release in a turbulent shear layer. *J. Fluid Mech.* **148**, 349-382.

ROGERS, M. M. & MOSER, R. D. 1994 Direct simulation of a self-similar turbulent mixing layer. *Phys. Fluids.* **6**, 903-923.

SPALART, P. R. 1986 Numerical study of sink-flow boundary layers. *J. Fluid Mech.* **172**, 307-328.

SPALART, P. R. 1988 Direct simulation of a turbulent boundary layer up to $Re_\theta = 1410$. *J. Fluid Mech.* **187**, 61-98.

WILLIAMS, F. A. 1985 *Combustion Theory*, 2nd ed. Benjamin/Cumming, Menlo Park, CA.

NEXT
DOCUMENT

The effects of complex chemistry on triple flames

By T. Echekki[1] and J. H. Chen[1]

The structure, ignition, and stabilization mechanisms for a methanol (CH_3OH)-air triple flame are studied using Direct Numerical Simulations (DNS). The methanol (CH_3OH)-air triple flame is found to burn with an asymmetric shape due to the different chemical and transport processes characterizing the mixture. The excess fuel, methanol (CH_3OH), on the rich premixed flame branch is replaced by more stable fuels CO and H_2 which burn at the diffusion flame. On the lean premixed flame side, a higher concentration of O_2 leaks through to the diffusion flame. The general structure of the triple point features the contribution of both differential diffusion of radicals and heat. A mixture fraction-temperature phase plane description of the triple flame structure is proposed to highlight some interesting features in partially premixed combustion. The effects of differential diffusion at the triple point add to the contribution of hydrodynamic effects in the stabilization of the triple flame. Differential diffusion effects are measured using two methods: a direct computation using diffusion velocities and an indirect computation based on the difference between the normalized mixture fractions of C and H. The mixture fraction approach does not clearly identify the effects of differential diffusion, in particular at the curved triple point, because of ambiguities in the contribution of carbon and hydrogen atoms' carrying species.

1. Introduction

Triple flames arise in a number of practical configurations where the reacting mixture is partially premixed. The flame has three branches reflecting the extent of premixedness of the fuel and oxidizer. On the fuel side, a rich premixed flame forms, while on the oxidizer side, a lean premixed flame forms. Behind the two branches, a diffusion flame forms where 'excess' fuel and oxidizer burn. The premixed flame branches provide both a source of reactants (excess from the primary premixed flames) for the diffusion flame and a mechanism for its stabilization and ignition at the triple point (the location where the three branches meet).

During the last two decades a number of studies of triple flames have been carried out to understand the mechanisms of stabilization and their structure using simplified models of chemistry and transport (Hartley & Dold, 1991; Kioni *et al.*, 1993; Lakkaraju, 1996; Ruetsch *et al.*, 1995; Domingo & Vervisch, 1996; and Wichman, 1995). Recently, computations by Terhoeven & Peters (1996) have shown

1 Sandia National Laboratories

the significance of complex chemistry and realistic transport to the structure and stabilization of triple methane-air flames.

In the context of complex chemistry and transport effects, a number of questions pertaining to the flame structure, ignition at the triple point and propagation remain unanswered. The structure of the premixed flame on the rich and lean branches is expected to be asymmetrical because of the inherent asymmetry in the flammability limits, reacting mixture composition, and burning rates of the flame. In the diffusion branch, the primary fuel may not be the original fuel that burns on the premixed side. In the computations of Terhoeven & Peters (1996), only a small fraction of the primary fuel, methane, survives near the triple point. Instead, more stable molecules such as CO and H_2 provide the needed fuel to burn in the diffusion flame.

Moreover, the diffusion flame is anchored to the premixed branches at the triple point by both preheating and diffusion of radicals including H, O, and OH. These radicals diffuse at rates which are significantly different from diffusion rates of heat and result in differential diffusion effects at the triple point. The coupling of curvature and differential diffusion effects at the triple point may also display itself in enhanced burning rates and, thereby, enhanced propagation of the triple point. The same differential diffusion effects along with chemistry determine the structure and location of the diffusion branch of the triple flame.

The object of this study is to determine the structure and mechanisms of ignition and stabilization of triple methanol (CH_3OH)-air flames in a laminar free shear layer configuration using detailed chemistry and a realistic transport model. The choice of methanol as a fuel presents some advantages with regard to the complexity of the chemical system and the numerical treatment. The full range of flammability may be adequately described using C_1 chemistry. It displays some of the interesting features in its structure which are common among hydrocarbons (e.g. the two-layer structure corresponding to fuel and radical consumption, and H_2 and CO oxidation). In the following sections, the governing equations and numerical configuration are described. A discussion of the triple flame structure and the contribution of chemistry and transport to its ignition and stabilization is presented.

2. Governing equations and numerical configuration

The triple flame in a laminar mixing layer between methanol (CH_3OH) fuel and air as oxidizer is computed using DNS with a C_1 mechanism for chemistry (Warnatz *et al.*, 1996). The numerical scheme is based on the solution of the Navier-Stokes, species, and energy equations for a compressible gas mixture with temperature dependent properties. The equations are solved using an eighth-order explicit finite difference scheme (Kennedy & Carpenter, 1994) for approximating spatial derivatives and a fourth-order low storage Runge-Kutta scheme for time advancement (Kennedy & Carpenter, 1996). A modified version of the Navier-Stokes Characteristic Boundary Conditions (NSCBC) procedure originally developed by Poinsot & Lele (1992) is used to account for variable specific heats (Card *et al.*, 1994). The

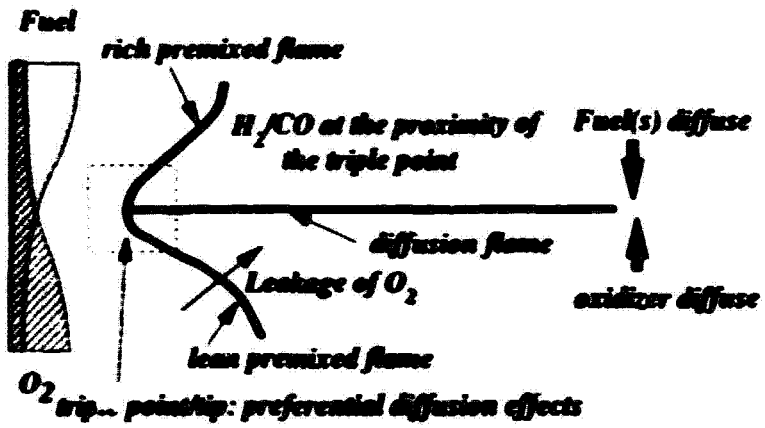

FIGURE 1. Numerical configuration.

boundary conditions are non-reflecting in all directions. The species mass diffusion is modeled with a Lewis number formulation and a prescription of the Lewis numbers for the different species (Smooke & Giovangigli, 1991). The values of the Lewis numbers for the species is given in Table 1. The Prandtl number, $Pr = \mu\overline{C}_p/\lambda$, is set to a constant of 0.708.

For the C_1 methanol (CH_3OH) mechanism, conservation equations for fifteen reacting species are considered (see Table 1), and the mass fraction of N_2 is obtained through the relationship $\sum_{a=1}^{N} Y_a = 1$, where $N = 16$. The computational configuration is shown in Fig. 1. The initial mixture is preheated to 800 K. The field is initialized with stoichiometric one-dimensional flame profiles which are modified spatially over a buffer domain of thickness L to reflect the desired inlet composition. The inlet conditions are maintained constant during the computations. The inlet velocity is fixed at the stoichiometric flame speed, S_L; no attempt to stabilize the flame is made. The methanol, oxygen, and its corresponding proportion of nitrogen (in air) in the buffer domain are based on self-similar solution profiles of the mixture fraction, ξ. They are prescribed as follows:

$$\xi(x, y, t = 0) = (1 - \xi_{st}) \cdot \left\{1 - \exp\left[-\left(\frac{x - L}{\Delta}\right)^2\right]\right\} \Big/ \left\{1 - \exp\left[-\left(\frac{L}{\Delta}\right)^2\right]\right\} \cdot \operatorname{erf}\left(\frac{y}{\delta}\right) + \xi_{st}. \tag{1}$$

Here, ξ is the mixture fraction expressed as follows:

$$\xi \equiv \frac{Z^* - Z_O^*}{Z_F^* - Z_O^*}.$$

where the subscripts F and O denote the fuel and oxidizer streams, respectively. Z^* is expressed in terms of the elemental mixture fraction (three elements make up the reacting species: C, H, and O), Z_i as follows (Warnatz *et al.*, 1996):

$$Z^* = \sum_{i=1}^{\text{elem.}} \beta_i Z_i. \tag{2}$$

The element mass fraction, Z_i, is defined as $Z_i = \sum_{\alpha=1}^{N} \mu_{i\alpha} Y_\alpha$. $\alpha = 1, \ldots, N$, where $\mu_{i\alpha}$ is the mass proportion of the element i in the species α (e.g. for hydrogen atom in methane, it is 1/4). In terms of the species mass fraction, Z^* may be written as $Z^* = \sum_{\alpha=1}^{N} \mu_\alpha^* Y_\alpha$, where $\mu_\alpha^* = \sum_{i=1}^{\text{elem.}} \beta_i \mu_{i\alpha}$.

species	Le
H_2	0.30
O_2	1.11
O	0.70
OH	0.73
H_2O	0.83
H	0.18
HO_2	1.10
H_2O_2	1.12
CO	1.10
CO_2	1.39
CH_2O	1.28
CHO	1.27
CH_2OH	1.30
CH_3OH	1.30
CH_3O	1.30

TABLE 1. Lewis Numbers of Reacting Species.

In Eq. 1, ξ_{st} denotes the stoichiometric mixture fraction; δ is the characteristic thickness of the mixing region in the y direction; Δ is the buffer region characteristic thickness. In the spatial and temporal variations, the rate of variations of mixture fraction profiles in x are specified as Gaussian functions with characteristic thicknesses, Δ. For hydrocarbon fuels, Bilger *et al.* (1990) propose $2/W_C$, $1/(2W_H)$ and $1/W_O$ as coefficients β_i (Eq. 2) for the carbon (C), hydrogen (H), and oxygen (O) elements. Here, W_C, W_H and W_O are the atomic weights of C, H, and O. The proposed coefficients have been used in turbulent methanol diffusion flames by Masri *et al.* (1992). The stoichiometric mixture fraction for the methanol-air mixture based on these coefficients is $\xi_{st} = 0.136$.

A single computation is carried out with a mixture fraction characteristic thickness of $\delta/\delta_F = 3.5$. The flame thermal thickness, δ_F, corresponds to the stoichiometric premixed methanol-air flame and is defined as follows:

$$\delta_F = \frac{T_b - T_u}{(dT/dx)_{max}},$$

where the subscripts u and b refer, respectively, to the unburat and burnt gases. The buffer domain size, L/δ_F, and its characteristic thickness, Δ/δ_F, are 5.4 and 0.7, respectively. The computational domain is 501 by 351 grid points.

3. Numerical diagnostics

The DNS yields detailed information about the flow field and various scalars characterizing the structure of the triple flame. In this section, diagnostic approaches used to identify the pertinent features of the triple flame are described.

3.1 Reaction flow analysis

The primary objective of reaction flow analysis (Warnatz *et al.*, 1996) is to identify the primary reactions which contribute to the production or consumption of a particular species or to the rate of heat release.

3.2 Quantitative analysis of differential diffusion effects

Differential diffusion represents a non-negligible phenomenon in hydrogen and hydrocarbon flames in regions of strong curvature. It contributes to the enhancement of the burning intensity due to the strong chemical role played by hydrogen atoms and molecules in these flames and their fast rate of diffusion. To identify the strength of differential diffusion effects, in particular at the triple point in the flame, two approaches are considered. The first is based on the computation of the diffusion velocities of the various reactive species in the mixture which represent a direct measure of differential diffusion effects. From the formulation described earlier, the diffusion velocity of species, α, may be written as follows:

$$V_{\alpha j} = -D_{\alpha N}\frac{1}{Y_\alpha}\frac{\partial Y_\alpha}{\partial x_j}, \quad \alpha = 1, \cdots, N-1.$$

An alternate and indirect method of identifying strong differential diffusion effects is to compute the difference between elemental mass fractions (Bilger, 1981; Bilger & Dibble, 1982; Drake & Blint, 1988; Smith *et al.*, 1995). In the present work, the difference, $z_{C,H}$, between elemental mass fractions of C atom and H atoms is computed:

$$z_{C,H} = \xi_C - \xi_H,$$

where

$$\xi_C \equiv \frac{Z_C - Z_{C,O}}{Z_{C,F} - Z_{C,O}} = \frac{Z_C}{\mu_{C,CH_3OH}}, \quad \xi_H \equiv \frac{Z_H - Z_{H,O}}{Z_{H,F} - Z_{H,O}} = \frac{Z_H}{\mu_{H,CH_3OH}}.$$

A different formulation of the differential diffusion parameters is to compute correlations between ξ_C and ξ_H.

It is important to note that there is a fundamental limitation in the interpretation of the difference between ξ_C and ξ_H in terms of differential diffusion effects alone. The contribution to these quantities comes from carbon-carrying and hydrogen-carrying species in which the particular C and H may not play a significant role in its transport properties.

3.3 Flame propagation

The propagation of the flame may be tracked by evaluating a displacement speed of the front relative to the flow field. This quantity may be evaluated exactly from the numerical results when a flame surface is tracked with a particular scalar isocontour (such as hydrogen molecule mass fraction). An expression for the displacement speed, S_d, based on tracking a constant mass fraction contour may be obtained (Ruetsch *et al.*, 1995) by writing the Hamilton-Jacobi equation and substitution of the governing species equation:

$$\rho S_d \equiv \rho_u S_d^* = \frac{1}{|\nabla Y_\alpha|}\left[\frac{\partial}{\partial x_j}\left(\rho D_\alpha \frac{\partial Y_\alpha}{\partial x_j}\right) + \dot{\omega}_\alpha\right]. \tag{3}$$

In this expression, S_d^* is the density-weighted displacement speed. In this general form, the displacement speed measures the velocity of a scalar iso-contour (i.e. the flame-front) relative to the local gas. The value of S_d depends on the location in the flame where it is measured. The use of the product ρS_d or S_d^* tends to reduce thermal expansion effects due to the choice of the location where S_d is measured. Under strictly one-dimensional planar flame condition, this quantity is constant. In the reaction zone, the value of the density-weighted displacement speed, S_d^*, reflects primarily the chemical contribution. However, with the exception of perhaps a narrow region in the reaction zone, ρS_d is subject to additional effects resulting from the processes in the preheat zone.

A measure of the triple flame stabilization mechanisms is its speed relative to the cold gas. It may be evaluated using the same approach adopted by Ruetsch & Broadwell (1995). This speed contains both the contributions from chemical and hydrodynamic-diffusive effects (Echekki, 1992 & 1996; Poinsot *et al.*, 1992). To evaluate the hydrodynamic-diffusion contribution, the velocity, V_f, of the triple point relative to the unburnt gas is evaluated. V_f, at the leading edge of the flame, may be evaluated using the following relation:

$$V_f = (S_d - u_f) + u_0, \tag{4}$$

where u_f is the gas velocity at the flame location where the displacement speed is computed. The term $-S_d + u_f$ represents the Lagrangian speed of the triple point. The speed u_0 is the unburnt gas velocity at the inlet of the computational domain prior to the onset of lateral flow expansion and cross-stream diffusion effects. Note that, although S_d and u_f vary along the flame, the combined speed, $-S_d + u_f$, is constant in the flame under steady flow conditions.

4. General structure of the triple flame

In what follows, a description of the general structure of the methanol (CH_3OH)-air triple flame is given in terms of reactant, radicals, and heat release rate profiles.

4.1. Reactants and products profiles

Figure 2 shows the isocontours of the major species (reactants and products) mass fractions in the triple flame. The figure shows no leakage of the fuel beyond the primary premixed flame (Fig. 2c). Beyond the premixed flame front, methanol (CH_3OH) is decomposed into more stable fuels which include CO, H_2, and H. On the lean side, O_2 survives through the premixed flame and diffuses towards the stable reactants from the fuel side. A reduction in the fuel concentration across the premixed flame has also been observed by Terhoeven & Peters (1996) in their methane-air flame, albeit to a lesser extent. In addition to its oxidation by radical species in the C_1 chain, methanol pyrolyzes in the preheat zone (Seshadri *et al.*, 1989).

The reaction rates governing the premixed flame chemistry exhibit additional asymmetries, as shown in Fig. 3. The oxidation of methanol proceeds down the C_1 path: $CH_3OH \rightarrow CH_2OH \rightarrow CH_2O \rightarrow HCO \rightarrow CO \rightarrow CO_2$. The oxidation of methanol through HCO occurs in the premixed branches, whereas the remaining oxidation steps are present in all three branches. In addition to CO, the stable molecule H_2, which is produced on the rich premixed flame side, is also oxidized in the diffusion flame. All fuels in the premixed and diffusion flame are being oxidized primarily by radical species H, OH, and O. While H and OH play a more important role in the oxidation process on the rich premixed branch, oxidation reactions involving O atom play a more significant role on the lean side.

The reaction rates governing the premixed flame chemistry exhibit additional asymmetries, as shown in Fig. 3. For example, the peak production rates of H_2 and CO occur on the fuel rich side due to the consumption of H atom and OH by hydrocarbon intermediates. A further asymmetry appears in the inclination of the diffusion flame towards the lean premixed flame. This inclination may be primarily attributed to the rates of diffusion of H_2 relative to O_2 such that the reaction zone of the diffusion flame is at the stoichiometric mixture. The consumption rate of CO, as shown in Fig. 3e, also exhibits some inclination towards the lean branch. CO is consumed primarily by OH in the water gas shift reaction, an important reaction contributing to the overall heat release; the asymmetry is due to the peak production of OH occurring on the lean side due to the elementary chain branching reaction, $O_2 + H \rightleftharpoons OH + O$.

4.2. Radical profiles

Figure 4 shows the radical profiles for H, O, OH, and CH_2O in the flame. This figure shows that O and H atoms peak at the triple point. OH, on the other hand, peaks behind the primary reaction zones of the premixed flames and along

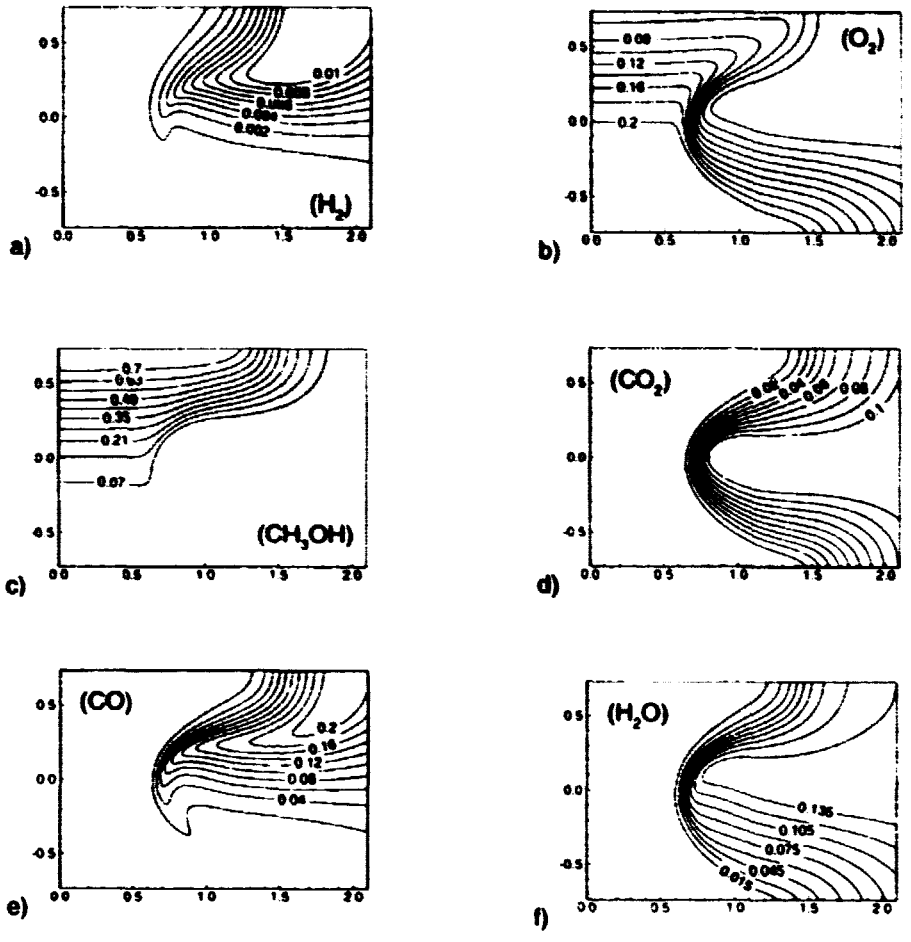

FIGURE 2. Major species mass fraction profiles (a) H_2, (b) O_2, (c) CH_3OH, (d) CO_2, (e) CO, and (f) H_2O.

the mean reaction zone of the diffusion flame branch. The radical OH has a slow recombination rate compared to O and H atoms and, therefore, accumulates and peaks in the diffusion flame.

Figure 5 shows the the contribution of the different reactions to the production and consumption of H, O, OH, and CH_2O. The radicals H, O, and OH are produced behind the fuel consumption layer near the burnt gas side of the flame, and diffuse upstream towards the unburnt gas to react in the fuel and radical consumption layer. The molecule H_2, on the other hand, is produced in the fuel and radical consumption layer and is consumed in the region of radical production in the H_2 oxidation layer. The convex shape of the triple point flame towards the burnt gas focuses H_2 towards its oxidation layer. The peak production of H_2 in the triple flame

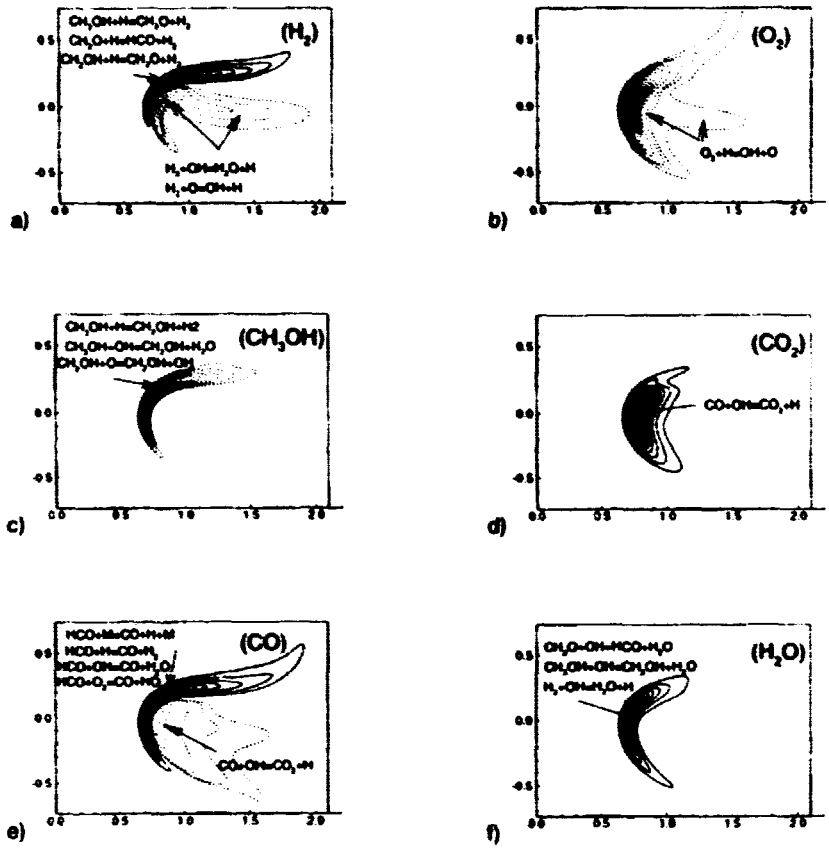

FIGURE 3. Major species reaction rate profiles (a) H_2, (b) O_2, (c) CH_3OH, (d) CO_2, (e) CO, and (f) H_2O. Production rates: ——— ; consumption rates: - - - - .

occurs at the triple point region on the rich side of the premixed flame. It results primarily from the break up of the fuel and its reactions with radicals, especially H. The primary mechanism for H_2 consumption results from radical production (in the H_2 oxidation layer) through the following reactions:

$$H_2 + OH \rightleftharpoons H_2O + H,$$

and

$$H_2 + O \rightleftharpoons OH + H.$$

The latter reaction is a significant chain branching reaction which plays a major role in the rate of flame propagation and radical production. By the focusing of H_2 towards its oxidation (consumption) zone, the rate of radical production is enhanced and the propagation speed is increased. An additional chain branching reaction which is responsible for the bulk of production of O and OH is the following reaction:

$$O_2 + H \rightleftharpoons O + OH.$$

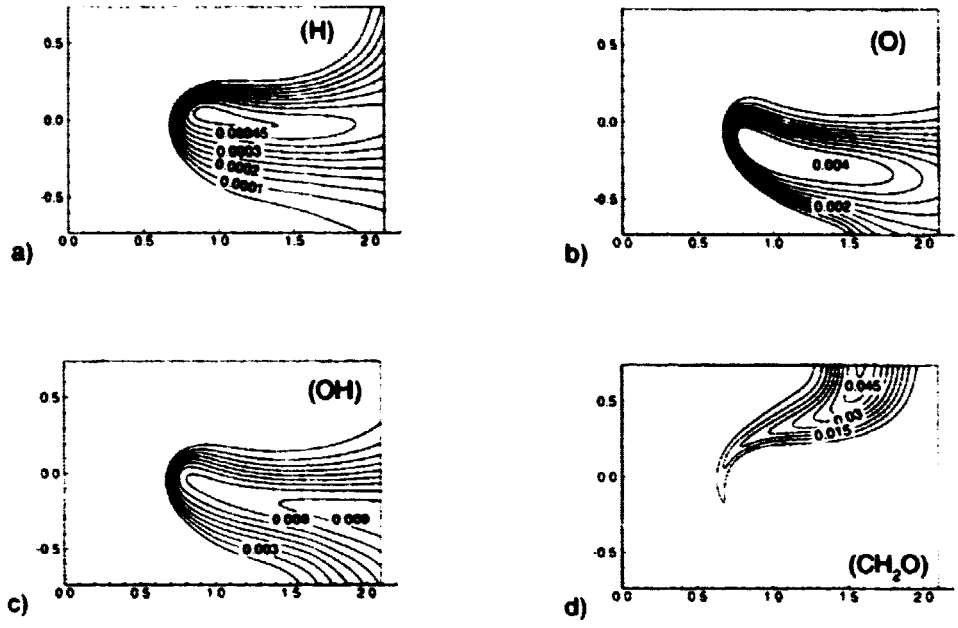

FIGURE 4. Minor species mass fraction profiles (a) H, (b) O, (c) OH, and (d) CH_2O.

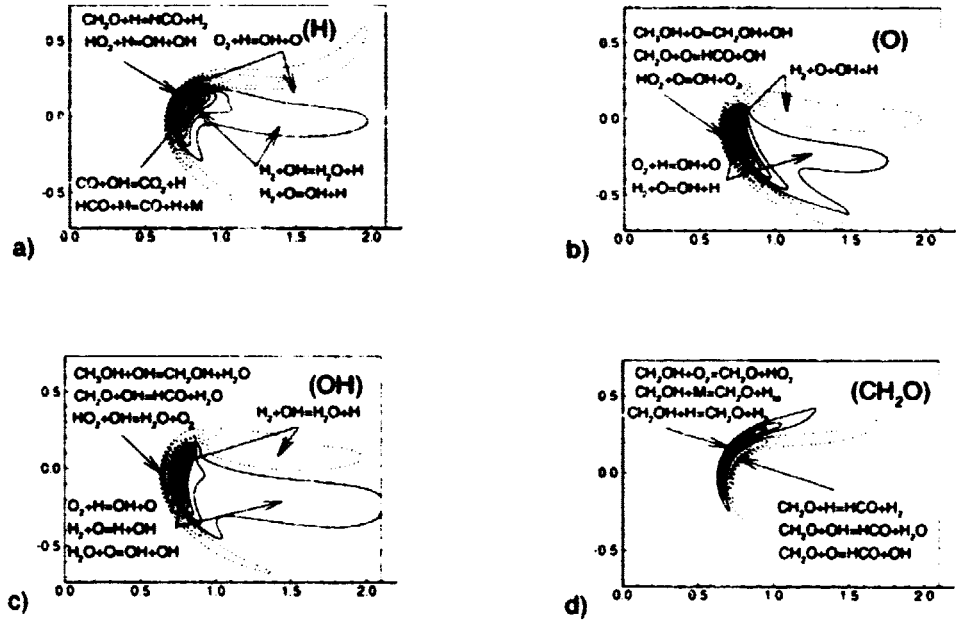

FIGURE 5. Minor species reaction rate profiles (a) H, (b) O, (c) OH, and (d) CH_2O. Symbols as in Fig. 3.

While the H atom in this reaction is defocused at the triple point by the same mechanism that focuses H_2, the net effect is the enhanced concentration of radical species at the triple point. The enhanced activity in this region also contributes to the ignition and anchoring of the trailing diffusion flame.

4.3. Parameterization of triple flame structure

The two-dimensional structure of the triple flame and the variation of the degree of premixedness in the reacting mixture suggest that at least two phase-space parameters may be required to fully describe the triple flame structure. Figure 6 shows overlays of the mixture fraction (Bilger *et al.*, 1990) profiles with H_2 reaction rate and temperature. The consumption rate of H_2 is used to illustrate the alignment of reaction rates in the diffusion flame with isocontours of the mixture fraction. The mixture fraction changes monotonically across the diffusion flame. This suggests that the mixture fraction may be a useful progress variable in this branch. Temperature plays a similar role in the premixed branches. In this section, we choose temperature and mixture fraction to parameterize the flame structure. The two parameters, ξ and T, effectively span the entire range of reaction and mixedness. The mixture fraction is a measure of the degree of mixedness, while the temperature is a measure of the extent of reaction.

Figures 7 and 8 show the mass fractions and reactions rates for the major species in phase space, while the corresponding figures for the minor species are shown in Figs. 9 and 10. Overlayed on these figures is the maximum consumption rate of O_2 in the premixed (thick solid lines) and the diffusion (thick dashed lines) branches. The maximum consumption rate of O_2, the only reactant which is consumed in the premixed and diffusion flames, is used to demarcate the three branches of the flame. These figures highlight the different topologies of the flame which may not be apparent in physical coordinates, particularly if the flame is distorted significantly by the flow field. Shifts in concentration or reaction peaks on the lean and rich sides and the delineation between diffusion and premixed branches are made more pronounced using this parameterization. Similarly the delineation of reactions and species that are present in the premixed branches versus the diffusion flame is made more clear. For example,

1. the peak production rates for formaldehyde (CH_2O), H_2 and CO occur on the rich side of the flame in the premixed branch, while the peak consumption of H_2 and CO persists to very lean conditions;

2. the peak consumption of H occurs on the rich side, whereas the peak consumption of O atoms occurs on the lean side of the flame;

3. the peak concentrations of CH_2O, H_2 and CO exist well into the rich side;

4. the peak radical concentrations for O and H exist near the triple point and on the lean sides respectively, whereas OH peaks in the diffusion flame;

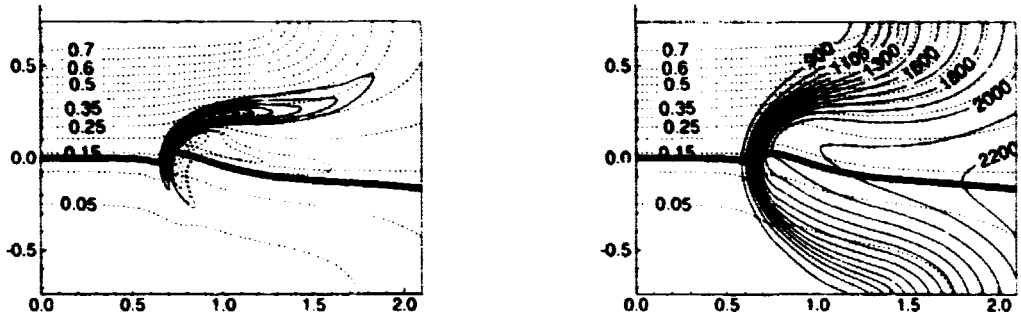

FIGURE 6. Overlay of mixture fraction profiles with H_2 reaction rate (left) and temperature (right). The wide solid line denotes the stoichiometric mixture fraction isocontour. The mixture fraction isocontours are shown in dashed lines.

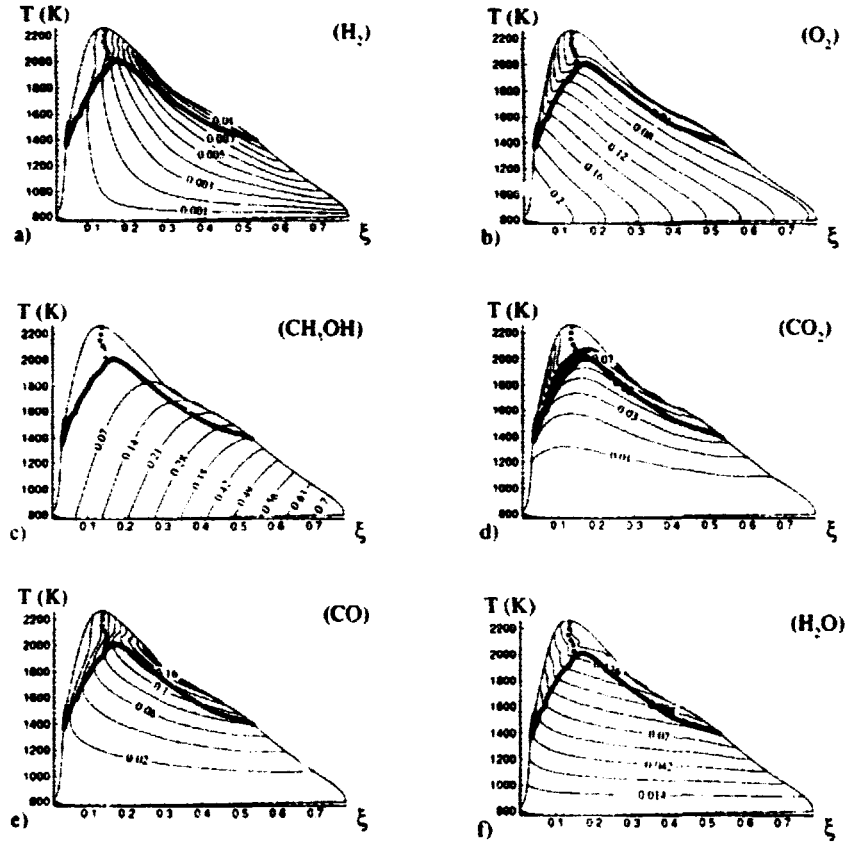

FIGURE 7. Major species mass fraction for H_2, O_2, CH_3OH, CO_2, CO and H_2O in ξ-T phase space. The bold solid line demarcates the premixed branches. The bold dashed line demarcates the diffusion branch.

5. while O_2 exists behind the premixed flame, there is no leakage of methanol or formaldehyde behind the premixed branches.

5. Propagation of the triple flame and its stabilization

In this section, the values of the propagation speeds are reported using the mass fraction of H_2 to track the flame surface. Other scalars yield similar results. The ratio of density-weighted displacement speed, S_d^*, to the laminar stoichiometric flame value, S_L, at the leading edge of the triple flame is 1.13. Since S_d^* is measured in the reaction zone, its enhancement relative to the laminar value is primarily attributed to an enhancement in the burning intensity of the flame (Sec. 3.3) due to the coupling of differential diffusion with curvature.

Another quantity of relevance to the stabilization mechanism of the triple flame is the flame speed relative to the unburnt gas, V_f (Sec. 3.3). The ratio, $V_f/S_{L,\phi=1}$, based on H_2 mass fraction is 1.79. The approximately 80% enhancement in V_f may be attributed primarily to hydrodynamic-diffusive effects associated with lateral flow expansion and cross-stream diffusion. Ruetsch *et al.* (1995) show that the ratio, $V_f/S_{L,\phi=1}$, may be approximated by the square-root of the inverse density ratio across the flame, $\sqrt{\rho_u/\rho_b}$, or by the temperature ratio, $\sqrt{T_b/T_u}$. In the current computation, the quantity $\sqrt{T_b/T_u} \sim \sqrt{2300/800} \sim 1.7$ compares well with the computational values for $V_f/S_{L,\phi=1}$ after subtraction of the chemical contribution.

6. Differential diffusion effects

In the previous sections, we have identified some contributions to the triple flame structure which result from differential diffusion effects: (a) the inclination of the diffusion branch towards the lean premixed branch, (b) the enhancement of the displacement speed, and (c) the ignition at the triple point. There are a number of approaches in the literature which attempt to quantify these effects. In this section, two approaches to investigate differential diffusion effects are compared. Figure 11 shows correlations of the elemental mixture fractions based on C and H in the triple flame. Elemental mixture fractions may only be modified by transport since reaction does not modify the atomic composition of a mixture. The figure shows that on the unburnt gas side, the values of ξ_C and ξ_H are the same, and that both reflect the local unburnt gas composition of the methanol (the correlation is shown by the diagonal line of ξ_C vs. ξ_H). In the reaction zone of the premixed branches, ξ_C is smaller than ξ_H, although this difference is not significant and it reflects the production of relatively fast diffusive species such as H_2. The difference between the two quantities is reversed behind the rich branch. There, the greatest contribution to ξ_C comes from CO, while the main contribution to ξ_H is from H_2O and H_2. In this region, the deficit in H may be a result of the diffusion of H_2 and H towards the diffusion flame. On the oxidizer side of the diffusion flame, ξ_C is lower than ξ_H. In this region, the main contribution to ξ_H is from H_2O, and for ξ_C is CO_2. There is no distinct behavior at the triple point from ξ_C and ξ_H contours. The

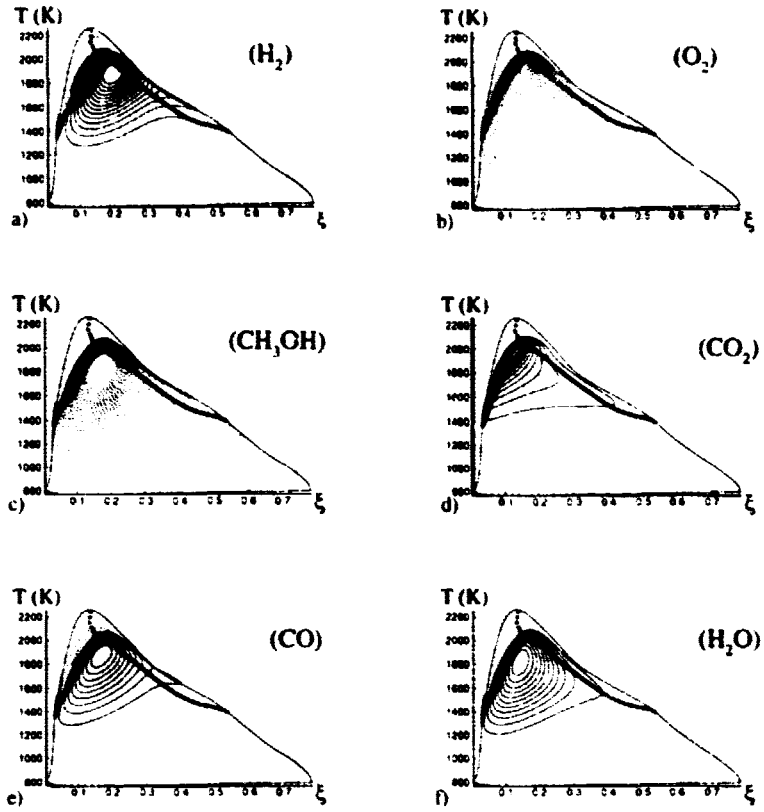

FIGURE 8. Major species reaction rate for H_2, O_2, CH_3OH, CO_2, CO and H_2O in ξ-T phase space. Symbols as in Fig. 7.

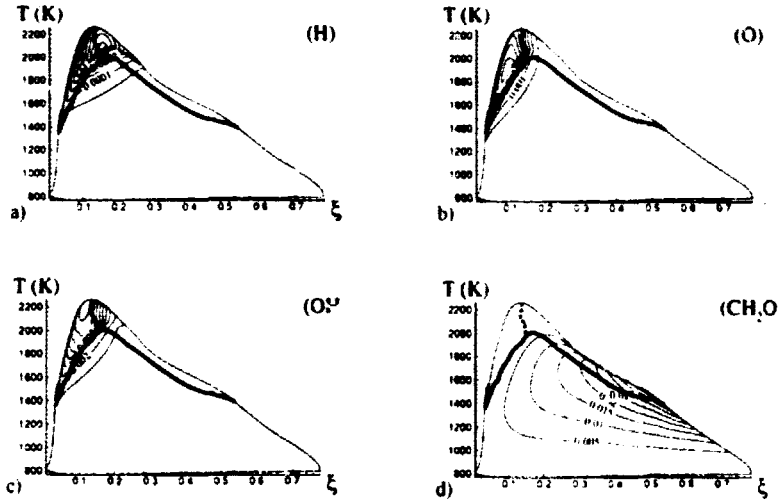

FIGURE 9. Minor species mass fraction for H, O, OH and CH_2O in ξ-T phase space. Symbols as in Fig. 7

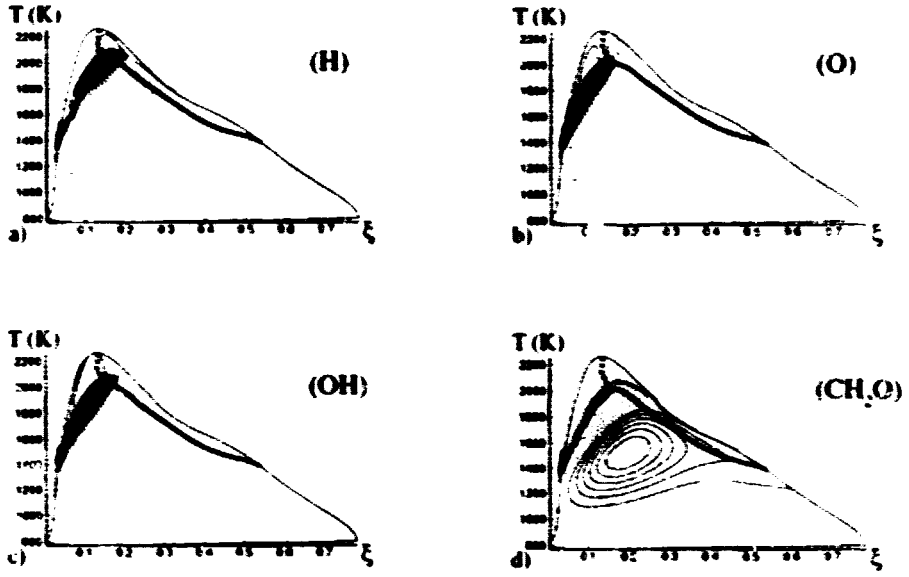

FIGURE 10. Minor species reaction rate for H, O, OH, and CH_2O in ξ-T phase space. Symbols as in Fig 7.

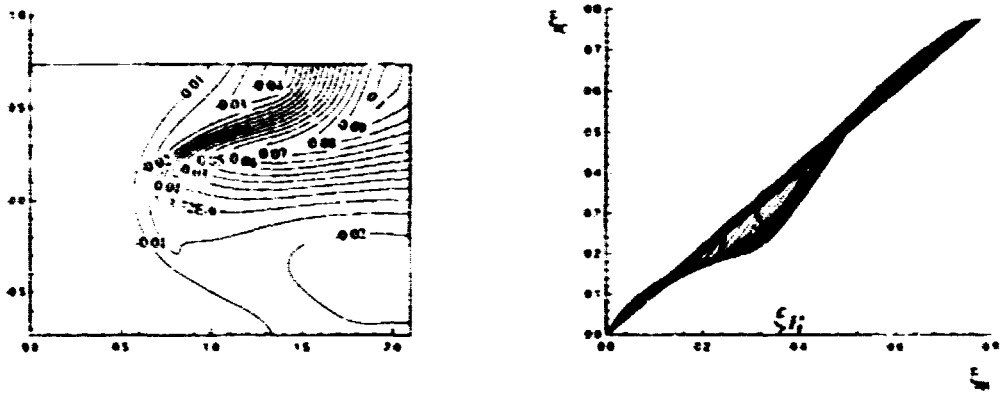

FIGURE 11. Correlation of C and H elemental mixture fractions. Left: $\xi_C - \xi_H$; right: ξ_C vs. ξ_H.

principal limitation of the mixture fraction approach as a measure of differential diffusion effects is now more apparent; the value of the elemental mixture fraction does not tell us whether the higher or lower element composition in a given region is a result of its transport by a species which is fast or slow diffusing. Hydrogen, for example, may be present in both H_2O or H_2, but the two species have very different diffusivities. At the triple point, minor species such as H atom may not contribute

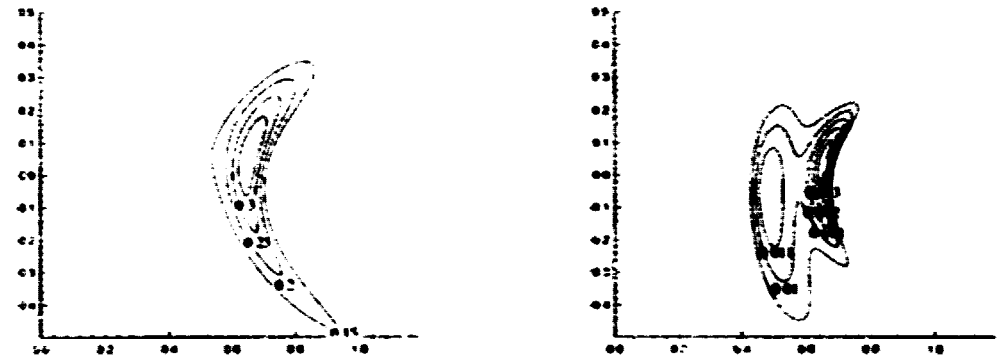

FIGURE 12. Diffusion velocities of H and CO normalized by the stoichiometric one-dimensional flame speed. Left: V_H/S_L; right: V_{CO}/S_L.

significantly to the elemental mixture fraction despite their important role in the chemistry of the flame.

Another indication of the role played by diffusional transport and its coupling with curvature may be demonstrated by the magnitudes of the diffusion velocity of H and CO shown in Fig. 12. This figure shows that the maximum diffusion velocity is found near the triple point of the flame. This velocity corresponds to more than a two-fold increase for H relative to the remaining premixed branches. The increase in the diffusion velocity of CO is only 30%. The peak value of the diffusive velocity for H is approximately thirty times higher than that of CO. The use of diffusion velocities to quantify differential diffusion effects shows significantly different trends than the elemental mixture fraction approach.

7. Concluding remarks

The structure, propagation and stabilization mechanisms of a methanol-air triple flame is investigated using DNS. The computations show that the primary fuel, methanol, is consumed entirely through the premixed branches of the flame and is converted to more stable fuels, H_2 and CO, for the diffusion flame behind the triple point.

In the triple point region, the coupling of curvature and differential diffusion of hydrogen molecules results in enhanced radical production and, in turn, an enhancement in the flame propagation speed. However, hydrodynamic effects (associated with heat release in the flame) are more important in the current computations. These effects are predicted adequately by the model by Ruetsch *et al.* (1995).

A mixture fraction-temperature parameterization of the triple flame structure is proposed. The approach attempts to separate mixedness and reactivity, and highlights some of the interesting features of partially-premixed combustion.

A comparison between two approaches to identify the effects of differential diffusion is carried out. The first approach is based on a direct computation of the magnitude of the diffusion velocity of the various species. The second is based on the comparison of elemental mixture fractions based on carbon and hydrogen atoms. The comparison between the two approaches shows that the second approach is strongly dependent on the species carrying the atoms and may not be a good indicator of differential diffusion effects.

Acknowledgments

This research was supported by the United States Department of Energy, Office of Basic Energy Sciences, Chemical Sciences Division. We would like to thank Profs. Amable Liñán and Forman Williams, and Drs. Greg Reutsch and Arnaud Trouvé for many fruitful discussions.

REFERENCES

BILGER, R. W. 1981 Molecular Transport effects in turbulent diffusion flames at moderate Reynolds number. *AIAA J.* **20**(7), 962-970.

BILGER, R. W. & DIBBLE, R. W. 1982 Differential molecular diffusion effects in turbulent mixing. *Combust. Sci. & Tech.* **28** 161-172.

BILGER, R. W., STARNER, S. H. & KEE, R. J. 1990 On Reduced Mechanisms for Methane-Air Combustion. *Combust. & Flame.* **80**, 135-149.

CARD, J. M., CHEN, J. H., DAY, M. & MAHALINGAM, S. 1994 Direct Numerical simulations of turbulent non-premixed methane-air flames modeled with reduced kinetics. *Proceedings of the 1994 Summer Program*,Center for Turbulence Research, NASA-Ames/Stanford University, 41-54.

DOMINGO, P. & VERVISCH, L. 1996 Triple Flames and partially premixed combustion in autoignition of nonpremixed turbulent mixtures. To appear in *Twenty-Sixth Symposium (International) on Combustion*, The Combustion Institute, Pittsburgh.

DRAKE, M. C. & BLINT, R. J. 1988 Structure of laminar opposed-flow diffusion flames with $CO/H_2/N_2$ Fuel. *Combust. Sci. & Tech.* **61**, 187-224.

ECHEKKI, T. 1992 Studies of curvature, strain and unsteady effects on laminar premixed flames. Ph.D. Thesis, Mechanical Engineering Dept., Stanford University.

ECHEKKI, T. 1996 A quasi-one dimensional premixed flame model with cross-stream diffusion. To appear in *Combust. & Flame.*

HARTLEY, L. J. & DOLD, J. W. 1991 Flame propagation in a nonuniform mixture: analysis of a propagating triple-flame. *Combust. Sci. & Tech.* **80**, 23-46.

KENNEDY, C. J. & CARPENTER, M. H. 1994 Several new numerical methods for compressible shear-layer simulations. *Appl. Num. Math.* **14**, 397-443.

KENNEDY, C. J. & CARPENTER, M. H. 1996 Several New ultra-low-storage, lower-order Runge-Kutta schemes. In preparation.

KIONI, P. N., ROGG, B., BRAY, N. C. & LIÑÁN, A. 1993 Flame spread in laminar mixing layers: the triple flame. *Combust. & Flame.* **95**, 276-290.

LAKKARAJU, N. K. 1996 Studies of quenched diffusion flames near cold, inert surfaces. *Master's Thesis*, Dept. of Mechanical Engineering, Michigan State University, Lansing, MI.

MASRI, A. R., DIBBLE, R. W. & BARLOW, R. S. 1992 The structure of turbulent nonpremixed flames of methanol over a range of mixing rates. *Combust. & Flame.* **89**, 167-185.

POINSOT T., ECHEKKI, T. & MUNGAL, M. G. 1992 A study of the laminar flame tip and implications for premixed turbulent combustion. *Combust. Sci. & Tech.* **81**, 45-73.

POINSOT, T. & LELE, S. 1991 Boundary Conditions for direct simulations of compressible viscous flows. *J. Comput. Phys.* **101**, 104-129.

RUETSCH, G. R. & BROADWELL, J. E. 1995 Effects of confinement on partially premixed flames. *Annual Research Briefs 1995*. Center for Turbulence Research, NASA-Ames/Stanford Univ.

RUETSCH, G. R., VERVISCH, L. & LIÑÁN, A. 1995 Effects of heat release on triple flames. *Phys. Fluids.* **7**(6), 1447-1454.

SESHADRI, K., TREVINO, C. & SMOOKE, M. D. 1989 Analysis of the structure and mechanisms of extinction of a counterflow methanol-air diffusion flame. *Combust. & Flame.* **76**, 111-132.

SMITH, L. L., DIBBLE, R. W., TALBOT, L., BARLOW, R. S. & CARTER, C. D. 1995 Laser Raman scattering measurements of differential molecular diffusion in turbulent nonpremixed jet flames of H_2/CO_2 Fuel. *Combust & Flame.* 100, 153-160.

SMOOKE, M. D. & GIOVANGIGLI, V. 1991 *Reduced kinetic mechanisms and asymptotic approximation for methane-air flames* (M. D. Smooke, Ed.), Lecture Notes in Physics 384, Spriuger-Verlag, New York, 1-28.

TERHOEVEN, P. & PETERS, N. 1996 Basic flame structures of turbulent combustion for applications in diesel engines. To appear in *Combust. & Flame.*

WARNATZ, J., MAAS, U. & DIBBLE, R. W. 1996 *Combustion: physical and chemical fundamentals, modeling and simulation, experiments, pollutant formation.* Springer-Verlag, Berlin Heidelberg, Germany.

WICHMAN, I. S. 1995 Basic features of triple flames in combustion theory. To appear in Eighth International Symposium on Transport Processes in Combustion (ISTP-8), San Francisco.

NEXT
DOCUMENT

Ensemble averaged dynamic modeling

By D. Carati[1], A. Wray[2] AND W. Cabot[3]

The possibility of using the information from simultaneous equivalent large eddy simulations for improving the subgrid scale modeling is investigated. An ensemble average dynamic model is proposed as an alternative to the usual spatial average versions. It is shown to be suitable independently of the existence of any homogeneity directions, and its formulation is thus universal. The ensemble average dynamic model is shown to give very encouraging results for as few as 16 simultaneous LES's.

1. Introduction

The equation for large eddy simulation (LES) is obtained by applying a spatial filter to the Navier-Stokes equation. The LES equation thus describes the evolution of a filtered velocity field $\overline{u}_i$ which explicitly depends on the small scales through the subgrid scale stress $\tau_{ij} = \overline{u_i u_j} - \overline{u}_i\,\overline{u}_j$:

$$\partial_t \overline{u}_i + \partial_j \overline{u}_j \overline{u}_i = -\partial_i \overline{p} + \nu_0 \nabla^2 \overline{u}_i - \partial_j \tau_{ij}. \tag{1.1}$$

For simplicity, we only consider incompressible flows. The pressure p is then chosen to satisfy the incompressibility condition. Clearly, τ_{ij} is a large scale quantity depending mainly on the small scale velocity field. However, it is usually modeled as a function of the resolved velocity field as in the Smagorinsky eddy viscosity model (Smagorinsky, 1963):

$$\tau_{ij} - \frac{1}{3}\tau_{kk}\delta_{ij} \approx -2C\overline{\Delta}^2 |\overline{S}| \overline{S}_{ij}, \tag{1.2}$$

where $\overline{S}_{ij} = \frac{1}{2}(\partial_i \overline{u}_j + \partial_j \overline{u}_i)$ and $|\overline{S}| = (2\overline{S}_{ij}\overline{S}_{ij})^{1/2}$. In the original formulation of the Smagorinsky model, the parameter C must be obtained from some fitting procedure. Recently, this model has been improved by the introduction of the dynamic procedure, which allows a self calibration of the parameter C and gives an explicit expression as a function of the resolved field $C = C(\overline{u}_k)$. However, any procedure that determines the subgrid scale stress in terms of the resolved field can only be an approximation. Indeed, the same resolved field may be compatible with many different small scale velocity fields. This is reflected in the *a priori* tests which show very poor correlations between the models $\tau_{ij} \approx \tau_{ij}^M(\overline{u}_k)$ and the actual τ_{ij} obtained from direct numerical simulations (see Winckelmans *et al.* in this volume).

1 Université Libre de Bruxelles
2 NASA Ames Research Center
3 Center for Turbulence Research

Clearly more information is needed to properly reconstruct the subgrid-scale stress. The introduction of stochastic model for τ_{ij} is a first attempt to introduce models that are not fully determined by the resolved field (Carati *et al*, 1995; Chasnov, 1991; Leith, 1990; Mason & Thomson, 1992). Here, we explore another approach which consists in running simultaneously several statistically equivalent LES's and constructing the model by using information from the set of resolved velocity fields:

$$\partial_t \overline{u}_i^r + \partial_j \overline{u}_j^r \overline{u}_i^r = -\partial_i \overline{p}^r + \nu_0 \nabla^2 \overline{u}_i^r - \partial_j \tau_{ij}^r \qquad r = 1, \ldots, R. \tag{1.3}A$$

Here, r is a new index corresponding to the realization and R is the total number of realizations. The concept of *statistically equivalent* LES's will be defined in Section 3. The model we propose to test should generalize the classical subgrid scale model ($\tau_{ij}^r = \tau_{ij}^r(\overline{u}_k^r)$) by allowing an explicit dependence on the velocity field from other members in the set:

$$\tau_{ij}^r = \tau_{ij}^r(\{\overline{u}_k^s\}) \tag{1.4}$$

Clearly, in that case the subgrid scale model in the LES labeled r will not be a function of the resolved velocity field $\overline{u}_k^r$ only.

In the following section, we will present the dynamic procedure and its generalization to several LES's. We also present an alternative formalism to the classical dynamic model. Some results for decaying and forced isotropic turbulence and for channel flow are discussed.

2. The dynamic procedure

The dynamic procedure is based on an exact relation between subgrid scale stresses for different filter widths (Germano, 1992; Ghosal *et al* 1995; Lilly, 1992). This relation is obtained by introducing a second filter G_t, usually referred to as the *test filter*, denoted by $\hat{}$; we will call the original filter G_1. The application of this new filter to Eq. (1.1) yields:

$$\partial_t \hat{\overline{u}}_i + \partial_j \hat{\overline{u}}_j \hat{\overline{u}}_i = -\partial_i \hat{\overline{p}} + \nu_0 \nabla^2 \hat{\overline{u}}_i - \partial_j \hat{\tau}_{ij} - \partial_j L_{ij}, \tag{2.1}$$

where $L_{ij} = \widehat{\overline{u}_i \overline{u}_j} - \hat{\overline{u}}_i \hat{\overline{u}}_j$ is the Leonard tensor. This equation governs the evolution of the field $\hat{\overline{u}}$ obtained by the application of the filter $G_2 \equiv G_t \star G_1$ to the fully resolved velocity. Thus, an equivalent equation should be obtained by applying G_2 directly to the Navier-Stokes equation:

$$\partial_t \hat{\overline{u}}_i + \partial_j \hat{\overline{u}}_j \hat{\overline{u}}_i = -\partial_i \hat{\overline{p}} + \nu_0 \nabla^2 \hat{\overline{u}}_i - \partial_j T_{ij}. \tag{2.2}$$

Here, the subgrid stress tensor is defined by $T_{ij} = \widehat{\overline{u}_i \overline{u}_j} - \hat{\overline{u}}_i \hat{\overline{u}}_j$. The comparison between equations (2.1) and (2.2) readily leads to the Germano identity:

$$L_{ij} + \hat{\tau}_{ij} - T_{ij} = 0. \tag{2.3}$$

When approximate models $\tau_{ij} \approx \tau_{ij}^M$ and $T_{ij} \approx T_{ij}^M$ are used, this identity is violated. However, the error $E_{ij} \equiv L_{ij} + \hat{\tau}_{ij}^M - T_{ij}^M \neq 0$ may be used to calibrate the models. When the Smagorinsky model is used at both grid and test levels, the error is a linear function of the Smagorinsky parameter:

$$E_{ij} = L_{ij} + C\widehat{\beta_{ij}} - C\alpha_{ij} \tag{2.4}$$

where

$$\alpha_{ij} = -2\widehat{\bar{\Delta}}^2 |\widehat{\bar{S}}|\widehat{\bar{S}}_{ij}$$
$$\beta_{ij} = -2\overline{\Delta}^2 |\overline{S}|\overline{S}_{ij}$$

The calibration of C is usually achieved by using a least square method for minimizing E_{ij}. The integral

$$I[C] = \int_V d\mathbf{y} \sum_{ij} E_{ij}^2(\mathbf{y}) \tag{2.5}$$

is thus minimized with respect to C.

A first difficulty encountered when using the dynamic procedure for determining C has been pointed out by Ghosal *et al* (1993,1995), who showed that this procedure requires the solution of an integral equation for C unless both of the following conditions are satisfied:

1. There are one or more directions of homogeneity in the flow.
2. The flow is fully resolved in the other direction(s).

In that case, C is assumed to be constant along the direction of homogeneity and can be taken out of the test filter operation $\widehat{\ }$. Moreover, the flow being fully resolved in the other direction(s), the test filter must only act in the homogeneous direction. The error (2.4) then reduces to:

$$E_{ij} = L_{ij} + CM_{ij} \tag{2.6}$$

where $M_{ij} = \alpha_{ij} - \widehat{\beta_{ij}}$ and the dynamic prediction for C reads:

$$C = \frac{\langle L_{ij} M_{ij} \rangle_h}{\langle M_{ij} M_{ij} \rangle_h}$$

where the brackets $\langle\ \rangle_h$ represent a spatial average in the homogeneous direction(s). If the two aforementioned conditions for replacing expression (2.4) by (2.6) are not fulfilled, one could argue that C is slowly varying in space and that (2.6) should be a valid approximation independently of the existence of a direction of homogeneity. The minimization of the global quantity $I[C]$ then leads to a local expression for C:

$$C = \frac{L_{ij} M_{ij}}{M_{ij} M_{ij}},$$

Unfortunately, this approximation has proved to be very poor, and the resulting C depends strongly on space. Since in almost all LES's at least one of the aforementioned conditions is violated, a mathematically clean implementation of the dynamic model always requires the solution of an integral equation (Ghosal *et al.* 1995).

A second difficulty with the dynamic model is that C takes negative as well as positive values. Positive values correspond to the classical eddy dissipation picture for the subgrid scales. The negative values were first interpreted as the capability of the dynamic model to predict reverse energy transfer (backscatter). Unfortunately, the modeling of backscatter by a negative Smagorinsky coefficient leads to numerical instabilities. This problem is easily solved by constraining *a priori* the minimization of $I[C]$ so that only positive values of C are accepted. The resulting C (obtained either by solving an integral equation or by using a spatial average) is the same as before but clipped to positive value. Thus, C must then be replaced by $(C + |C|)/2$. Although this clipping procedure can be derived properly from a constrained minimization procedure, it is usually considered an undesirable extension of the dynamic model. In particular, the clipping corresponds to turning off the model where the dynamic procedure "tries to build a model for backscatter." In some sense, the resulting model does not use all the information available from the dynamic procedure. Hence, it is desirable to have a dynamic model with as few clipped values as possible for C.

We will discuss in the following sections how the simultaneous use of several statistically equivalent LES's may solve these two difficulties.

3 Statistical LES & dynamic model

3.1 Definition of the ensemble

We first discuss the problem of defining the ensemble of runs needed for the statistical tests without considering the modeling problem. The equations (1.3) correspond to R different LES's. In order to have a "good" ensemble, these LES's should correspond to *statistically equivalent* and *statistically independent* realizations of the same problem. Although these requirements are intuitively clear, it is worthwhile to define them as properly as possible. The first step consists in defining precisely what is an "acceptable" simulation for a given problem. From the strict mathematical point of view, a flow described by the Navier-Stokes equation or by an LES equation is completely defined by the knowledge of

1. The domain $\mathcal{D}$ in which the flow is considered.
2. The conditions on the boundary $\partial\mathcal{D}$ of this domain $v(\partial\mathcal{D}, t) = f(t)$.
3. The initial conditions $v(\mathbf{x}, 0) = v_0(\mathbf{x}) \quad \forall x \in \mathcal{D}$.

However, in a simulation of a turbulent flow only the domain and the boundary conditions are rigorously fixed. Indeed, because of the lack of sensitivity to initial conditions in a turbulent flow, different simulations with different initial conditions sharing some properties are considered to characterize the same flow. Thus, the

requirement that the initial conditions are known is usually replaced by some weaker constraints, and point (3) is replaced by

3'. The initial conditions $v(\mathbf{x},0) = v_0(\mathbf{x}; w_l)$ are generated using random numbers w_l and satisfy some constraints: $P_s[v_0] = p_s, \quad s = 1,\ldots S.$

For example, in homogeneous turbulence, the first constraint $s = 1$ will be on the spectrum of v_0. For the channel flow, one could impose the profile of the velocity and of the fluctuation in each direction. We will not discuss in detail the minimal constraints that must be imposed on the initial conditions in order to have a reasonable simulation. We only suppose that these constraints do exist. Now, it is possible to give some precise definition of the ensemble of LES's:

Definition 1: *Two LES's are* **statistically equivalent** *if the domain of the flow and the boundary conditions are exactly the same and if the initial conditions satisfy the same set of constraints.*

Definition 2: *Two LES's are* **statistically independent** *if the initial conditions are generated with uncorrelated random numbers* w_l.

For a stationary flow, such equivalent and independent initial conditions can be obtained by running a single LES and recording several velocity fields separated by at least one large eddy turnover time when turbulence is fully developed.

3.2 Ensemble average dynamic model

In what follows, we will focus on a simple generalization of the Smagorinsky model which reads:

$$\tau^r_{ij} - \frac{1}{3}\tau^r_{kk}\delta_{ij} \approx -2C\overline{\Delta}^2|\overline{S}^r|\overline{S}^r_{ij}. \tag{3.2.1}$$

Thus, we basically use the Smagorinsky model in every realization with the following additional assumption :

Hypothesis 1: *The Smagorinsky coefficient is independent of the realization for statistically equivalent flows.*

This assumption defines the model in such a way that the unknown parameter in the LES is "universal". The formulation thus mixes some aspects of both LES and Reynolds average simulations.

The dynamic procedure can also be used to determine C when several LES's are run in parallel. In that case, the model depends on the resolved flow from other realizations (1.3). Indeed, the quantity that needs to be minimized is a straightforward generalization of $I[C]$:

$$\mathcal{I}[C] = \sum_r \int_V dy \sum_{ij} \left(E^r_{ij}(\mathbf{y})\right)^2 \tag{3.2.2}$$

where now E_{ij} as well as L_{ij}, β_{ij}, and α_{ij} depend on the realization ($E^r_{ij} = L^r_{ij} + \widehat{C\beta^r_{ij}} - C\alpha^r_{ij}$). We now make another assumption:

Hypothesis 2: *For large ensembles, the Smagorinsky coefficient is slowly dependent on space and can be taken out of the test filter.*

The quantity $I[C]$ then reduces to

$$I[C] = \sum_{r=1}^{R} \sum_{ij} (L_{ij}^r - C\, M_{ij}^r)^2 .$$

which leads to the same expression for C as in the spatial average version of the dynamic procedure:

$$C = \frac{\langle L_{ij} M_{ij} \rangle}{\langle M_{ij} M_{ij} \rangle},$$

where now the brackets represent an ensemble average. We will see in the next section that hypothesis 2 is very well justified by the numerical results.

3.3 Alternative formalism for the dynamic model

The usual formulation of LES Eq. (1.1) is not fully satisfactory because the evolution of the filtered velocity is given in terms of quantities that are not filtered, whereas all numerically computed quantities are filtered in some way. This is well known, but, to our knowledge, its effect on the dynamic model formulation has never been carefully considered. In this section, we propose an alternative dynamic model formulation which should be fully self-consistent with the filtered equation for the resolved field. First, we assume that all the quantities in the LES equation are filtered and Eq. (1.1) must then be replaced by

$$\partial_t \bar{u}_i = \nu_0 \nabla^2 \bar{u}_i - \partial_j \overline{\bar{u}_j \bar{u}_i} - \partial_j \bar{\tau}_{ij} - \partial_i \bar{p}. \tag{3.3.1}$$

This redefines the subgrid scale stress as

$$\bar{\tau}_{ij} = \overline{u_i u_j} - \overline{\bar{u}_i \bar{u}_j}$$

The application of the test filter to the LES equation (3.3.1) yields:

$$\partial_t \hat{\bar{u}}_i + \partial_j (\widehat{\hat{\bar{u}}_j \hat{\bar{u}}_i}) = \nu_0 \nabla^2 \hat{\bar{u}}_i - \partial_i \hat{\bar{p}} - \partial_j \hat{\bar{\tau}}_{ij} - \partial_j \hat{\bar{L}}_{ij},$$

and the comparison with the "one-step" application of G_2 to u_i leads to the following equality:

$$\hat{\bar{L}}_{ij} + \hat{\bar{\tau}}_{ij} - \hat{\bar{T}}_{ij} = 0. \tag{3.3.2}$$

where now

$$\hat{\bar{L}}_{ij} = \widehat{\overline{\bar{u}_i \bar{u}_j}} - \widehat{\overline{\hat{\bar{u}}_i \hat{\bar{u}}_j}},$$

$$\widehat{\bar{T}_{ij}} = \widehat{\overline{u_i u_j}} - \widehat{\overline{\hat{\bar{u}}_i \hat{\bar{u}}_j}}.$$

At this point it is important to ensure that the model for the subgrid scale is also expressed in terms of a filtered quantity. The simplest generalization of the Smagorinsky model would then be $\overline{\tau_{ij}} = \overline{C\beta_{ij}}$ and $\widehat{\overline{T_{ij}}} = \widehat{\overline{C}\alpha_{ij}}$. The dynamic procedure is then easily implemented and yields

$$C = \frac{\langle \widehat{\overline{L}}_{ij} \widehat{\overline{N}}_{ij} \rangle}{\langle \widehat{\overline{N}}_{ij} \widehat{\overline{N}}_{ij} \rangle} \tag{3.3.3}$$

where $N_{ij} = \beta_{ij} - \alpha_{ij}$. Of course, the expression (3.3.3) also relies on the assumption that C can be taken out from the filtering operators. This assumption is very important here because, in the equality (3.3.2), the Smagorinsky coefficient only appears in filtered quantities. This means that the integral equation formulation of this alternative dynamic model would be much more complicated than the classical formalism. However, if hypothesis 2 is valid, the present formalism appears to be more consistent with the LES equation.

4. Test on isotropic turbulence

4.1 Decaying turbulence

The statistical average dynamic model described in section 3.1 has been tested in decaying turbulence for 32^3 LES. A first series of numerical experiments have determined how large the ensemble of simultaneous LES's must be (*i.e.* how large R should be). The criteria used to determine the minimal size of the ensemble were focused on

1. The spatial variability of C.
2. The percentage of negative C.
3. Comparison with the volume average dynamic model.
4. Comparison with direct numerical simulations.

The first conclusion we have reached is quite encouraging. Indeed, it appears that with only 16 simultaneous LES's, the ensemble average dynamic model performs as well as the volume average model. The spatial variability of C decreases drastically when R increases (see Fig. 1). This is also reflected on the probability distribution function (PDF) of C (see Fig. 2).

The comparison between a 512^3 DNS and dynamic model shows good agreement both for the total resolved energy (see Fig. 3) and for the spectra. The results for $R = 16$ are indistinguishable for the volume average and for the ensemble average. Here the comparison with the dynamic model has been made by running an ensemble of unrelated volume average LES's. This allows comparison of the both the means and the standard deviations. The standard deviations are computed for the 3-d energy spectra at each k, and quantities such as total resolved energy and compensated spectra are then computed from the mean and mean$\pm\sigma$ spectra.

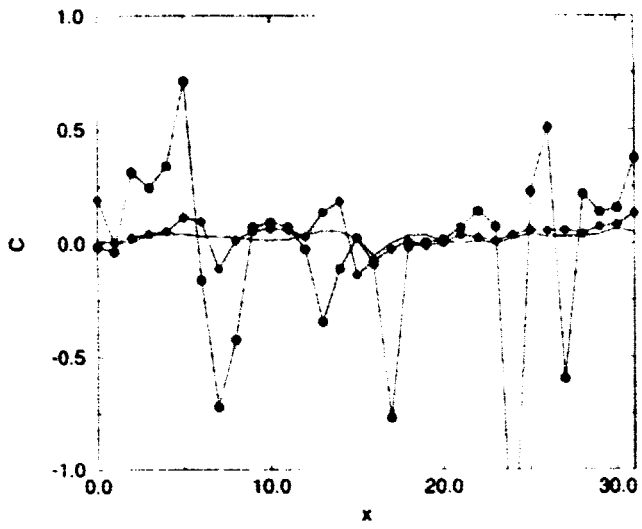

FIGURE 1. Typical profile of C in decaying isotropic turbulence. R=1:—● — ; R=4: — ◆ — ; R=16:—— .

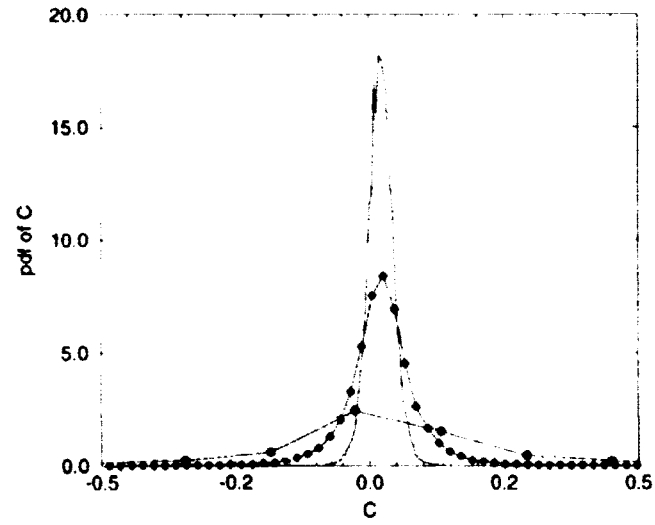

FIGURE 2. PDF of C in decaying isotropic turbulence. Symbols as in Fig. 1.

4.2 Forced turbulence

We have run an ensemble of 32^3 forced turbulence LES's with zero molecular viscosity. Fig. 4 shows that the mean resolved energy and the standard deviation evolve in a very similar way for both the volume and the ensemble average models.

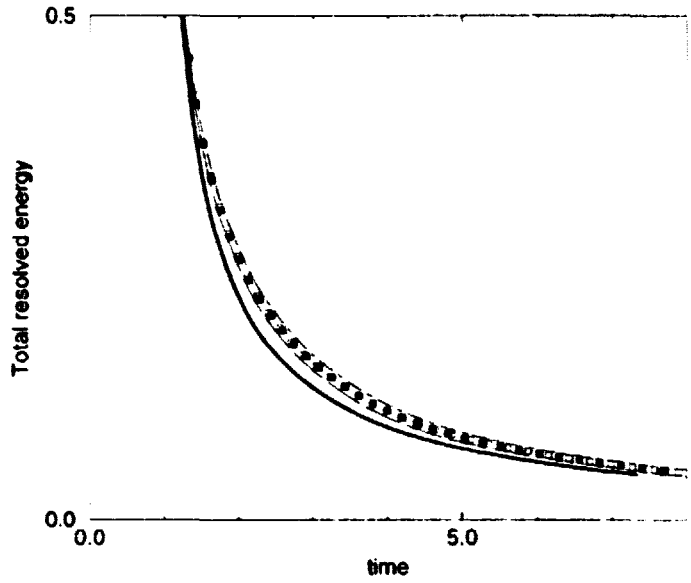

FIGURE 3. Energy decay: comparison with DNS and volume average. DNS:——— ; ensemble-averaged (mean):□ ; ensemble-averaged (mean+sigma):— · — ; ensemble-averaged (mean-sigma):— — — ; volume-averaged (mean):■ ; volume-averaged (mean+sigma):····· ; volume-averaged (mean-sigma):- - - -

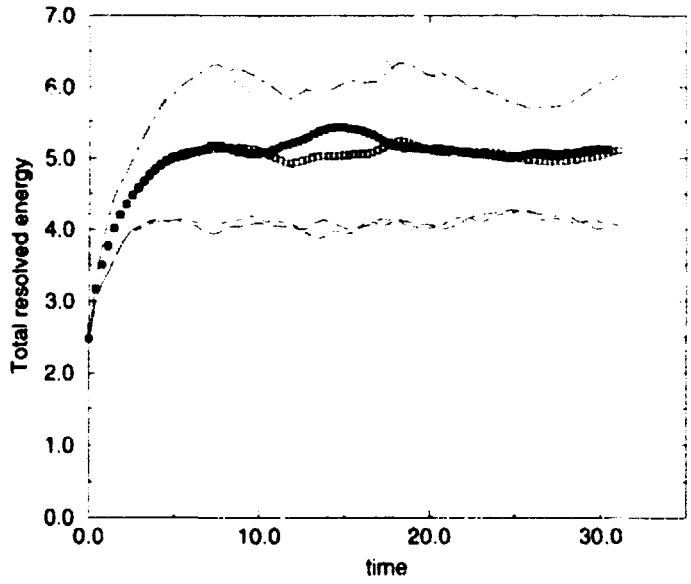

FIGURE 4. Resolved energy in forced isotropic turbulence: average vs volume. Symbols as in Fig. 3, without DNS.

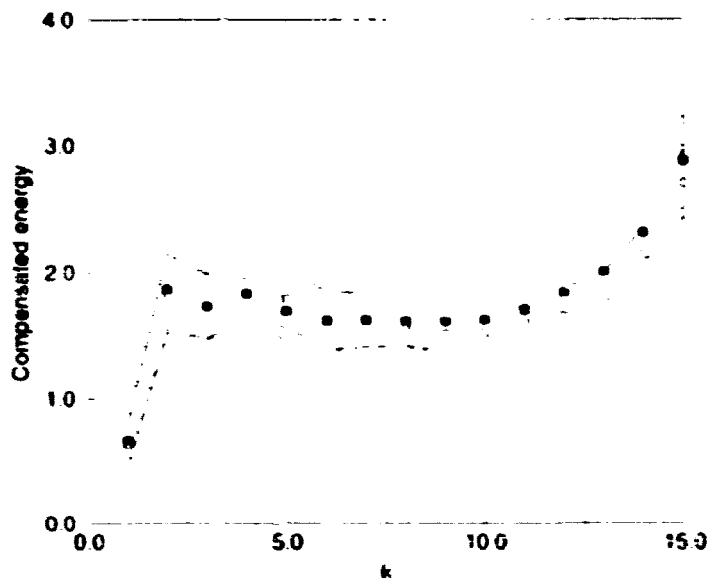

FIGURE 5. Compensated energy spectrum in forced isotropic turbulence: average vs volume. Symbols as in Fig. 3.

It is also very important to notice that the standard deviation saturates so that the LES's in the ensemble do not evolve towards very different states.

It is also interesting to compare the compensated energy spectrum to check if an inertial range is observed. Of course, with 32^3 LES, we do not expect to obtain a very good estimate of the Kolmogorov constant. However, the results in Fig. 5 show that the observed "Kolmogorov constant" is in a reasonable range of values. These spectra are at time ≈ 27 in the units of Fig. 4.

5. Tests in channel flow

We did not reach the stage of "production runs" for the channel flow, so the tests presented here are very preliminary and have been focused on the behavior of C as a function of the ensemble size (R). The data collected from the runs concern the PDF of C and the fraction of negative C. Because of the channel flow inhomogeneity, the PDF of C depends on the wall normal coordinate. However, the trends for increasing numbers of runs (R) is similar across the channel, and we only present in Fig. 6 the results for $y = 0.1$ near midchannel.

We also show the fraction of negative C (Fig. 7). Since the channel flow simulations used in these tests have a non-zero molecular viscosity, the relevant stability condition is the percentage of C leading to a total (molecular + eddy) negative viscosity. Here again, the results are encouraging for $R \approx 16$: less than 15% of the points need to be clipped, while the local version of the dynamic model for only one LES requires about 40% clipping.

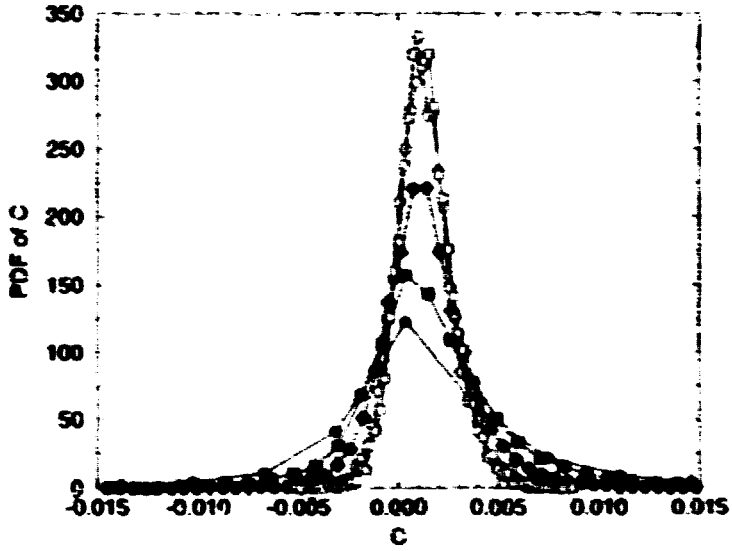

FIGURE 6. *Probability distribution function of C for different ensemble sizes at* $y = 0.1$ R=1:● : R=2:■ : R=4: ◆ : R=8:○ : R=16:□ .

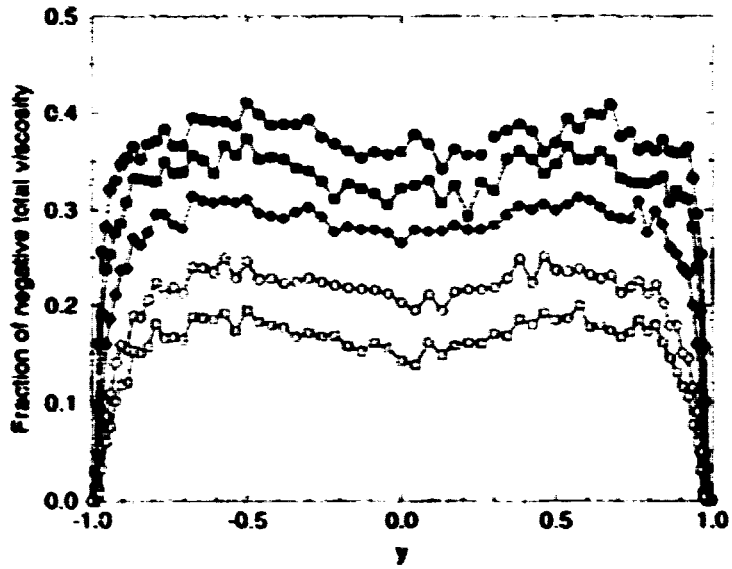

FIGURE 7. Fraction of negative total viscosity as a function of y for different ensemble sizes. Symbols as in Fig. 6.

6. Conclusion

The statistical tests presented in this report have shown that the knowledge of statistically equivalent resolved velocity fields may be useful in deriving new subgrid scale models. We have used the additional information available from the different LES's to create an ensemble average version of the dynamic model. This dynamic model has the following advantages:

1. A local version of the ensemble average dynamic model may be derived in the limit of large ensemble sets.
2. The local formulation does not rely on any homogeneity assumption. It can thus be adapted to any geometry, unlike to the classical volume (or surface or line) average dynamic model.
3. The theoretical limit of large ensemble sets is closely approached for $R \approx 16$. This is indicated by the PDF of C, which is very peaked for $R = 16$. Also, the spatial variations of C decrease drastically for increasing ensemble sizes and seem to be quite mild for $R = 16$.

For the examples treated in this work (decaying and forced isotropic turbulence), the volume average version of the dynamic model is justified. Remarkably, in those cases, the results from the ensemble average and the volume average versions are almost indistinguishable.

The next interesting step in the investigation of statistical LES is to apply this model to fully inhomogeneous problems (for which the mathematically consistent classical dynamic model requires the solution of an integral equation). The additional cost of multiple simultaneous LES's may be ameliorated by a reduction in the time of simulation since the statistics should converge more rapidly.

REFERENCES

CARATI, D., GHOSAL, S. & MOIN, P. 1995 On the representation of backscatter in dynamic localization model. *Phys. Fluids.* **7**, 606-616.

CHASNOV, J. 1991 Simulation of the Kolmogorov inertial subrange using an improved subgrid model. *Phys. Fluids A.* **3**, 188-200.

GERMANO, M. 1992 Turbulence: the filtering approach. *J. Fluid Mech.* **238**, 325-336.

GHOSAL, S., LUND, T. & MOIN, P. 1993 A local dynamic model for LES. *Annual Research Briefs 1992*. Center for Turbulence Research, Stanford Univ./NASA Ames, 3-25.

GHOSAL, S., LUND, T., MOIN, P. & AKSELVOLL, K. 1995 The Dynamic Localization Model for large eddy simulation of turbulent flows. *J. Fluid Mech.* **286**, 229-255.

LEITH, C. 1990 Stochastic backscatter in a subgrid-scale model: Plane shear mixing layer. *Phys. Fluids A.* **2**, 297-299.

LILLY, D. K. 1992 A proposed modification of the Germano subgrid-scale closure method. *Phys. Fluids* **4**, 633-635.

MASON, P. & THOMSON, D. 1992 Stochastic backscatter in large-eddy simulations of boundary layers. *J. Fluid Mech.* **242**, 51-78.

SMAGORINSKY, J. S. 1963 General circulation experiments with the primitive equations: I. The basic experiment. *Mon. Weather Rev.* **91**, 99-164.

NEXT
DOCUMENT

Anisotropic eddy viscosity models

By D. Carati[1] AND W. Cabot[2]

A general discussion on the structure of the eddy viscosity tensor in anisotropic flows is presented. The systematic use of tensor symmetries and flow symmetries is shown to reduce drastically the number of independent parameters needed to describe the rank 4 eddy viscosity tensor. The possibility of using Onsager symmetries for simplifying further the eddy viscosity is discussed explicitly for the axisymmetric geometry.

1. Introduction

Contrary to most of the works presented in this volume, this note does not result from a planned project for the summer program. It developed instead from discussions during the course of the workshop by many participants concerning the representation of anisotropy in the modeling of the subgrid-scale stress in Large Eddy Simulation (LES). This study is thus an attempt to present a systematic discussion of the influence of anisotropy on the structure of the eddy viscosity tensor. Some of the results presented here are not really original since they have been derived in other contexts (viscoelastic media or magnetized plasmas). However, we found several motivations for reproducing the general study of tensor symmetries in the special case of the eddy viscosity tensor.

First, we remark that there is often evidence of anisotropy at the subgrid level. The most obvious case arises when the grid itself is anisotropic. In that case, even if the flow does satisfy the classical local isotropy assumption, the subgrid velocity would be anisotropic by construction. Since most LES's use a non-uniform grid with anisotropic stretching, the effects of anisotropy should be taken into account in a very wide class of problems.

Second, the discussions we had during the workshop showed that few attempts have been made to introduce the anisotropy at the tensor level in the relation between the subgrid scale stress and the resolved strain tensor. On the contrary, most of the studies on the influence of anisotropy have focused on possible modifications to the isotropic eddy viscosity amplitude (Deardorff, 1970, 1971; Scotti *et al.*, 1993).

Finally, the development of the dynamic procedure (Germano, 1992; Ghosal *et al.*, 1995; Lilly, 1992) allows the introduction of multi-parameter models for the subgrid scale stress. Therefore, there is no practical reason for practitioners to limit their models to an isotropic eddy viscosity.

1 Université Libre de Bruxelles

2 NASA Center for Turbulence Research

2. Anisotropic eddy viscosity

In this work we only consider the subgrid scale modeling of an incompressible fluid. If the exact description of the large scale pressure is not required, the trace of the subgrid scale tensor may be added to the pressure, which is then calculated in order to ensure the incompressibility. The only tensor that needs to be modeled is

$$\tau_{ij}^* = \overline{u_i u_j} - \overline{u}_i \overline{u}_j - \frac{1}{3}(\overline{u_k u_k} - \overline{u}_k \overline{u}_k)\delta_{ij} . \tag{2.1}$$

The usual modeling procedure consists in giving an expression for τ_{ij}^* in terms of the spatial derivatives of the resolved velocity field $\partial_i \overline{u}_j$. These quantities are usually decomposed into a symmetric resolved strain tensor,

$$\overline{S}_{ij} = \frac{1}{2}(\partial_i \overline{u}_j + \partial_j \overline{u}_i) , \tag{2.2}$$

and an antisymmetric resolved rotation tensor,

$$\overline{R}_{ij} = \frac{1}{2}(\partial_i \overline{u}_j - \partial_j \overline{u}_i) = \frac{1}{2}\epsilon_{ijk}\overline{w}_k , \tag{2.3}$$

where $\overline{w}_k$ is the vorticity and ϵ_{ijk} is the Levi-Civita fully antisymmetric tensor with $\epsilon_{123} = 1$. The most general tensorial relation in an anisotropic system thus reads:

$$\tau_{ij}^* = \nu_{ijkl}\overline{S}_{kl} + \mu_{ijkl}\overline{R}_{kl} . \tag{2.4}$$

For three dimensional turbulence, a naive analysis of this relation would lead to the conclusion that both ν and μ are described by 81 independent parameters. However, very strong simplifications can be derived by using the *tensor symmetry properties* of τ_{ij}^*, $\overline{S}_{ij}$ and $\overline{R}_{ij}$, as well as the *symmetries of the flow*. These simplifications do not require any assumption (as far as the model (2.4) is accepted). A more debatable simplification might apply if the *Onsager reciprocal symmetries* (Onsager, 1931) are assumed to hold for the eddy viscosity tensors. This will be discussed at the end of this section.

2.1 Tensor symmetries

The tensors τ_{ij}^* and $\overline{S}_{ij}$ are symmetric and traceless while the tensor $\overline{R}_{ij}$ is antisymmetric. This implies that the eddy viscosity tensor ν_{ijkl} has the following properties:

$$\begin{aligned} \nu_{ijkl} &= \nu_{jikl} , \\ \nu_{ijkl} &= \nu_{ijlk} , \\ \nu_{iikl} &= 0 , \\ \nu_{ijkk} &= 0 . \end{aligned} \tag{2.5}$$

Thus, for a given value of $(k,l) = (k^*, l^*)$, the matrix $a_{ij} = \nu_{ijk^*l^*}$ is traceless and symmetric. Consequently, it has 5 independent components. Similarly, for a given

value of $(i,j) = (i^*, j^*)$, the matrix $b_{kl} = \nu_{i^*j^*kl}$ is also traceless and symmetric. The full tensor ν_{ijkl} is thus described by $5 \times 5 = 25$ independent parameters. The same analysis can be performed for the tensor μ_{ijkl}, which has the following symmetries:

$$\begin{aligned} \mu_{ijkl} &= \mu_{jikl}\,, \\ \mu_{ijkl} &= -\mu_{ijlk}\,, \\ \mu_{iikl} &= 0\,. \end{aligned} \tag{2.6}$$

Now, the tensor μ_{ijkl} is symmetric and traceless for its first two indices, while it is antisymmetric for its last two indices. Consequently, the full tensor μ_{ijkl} is described by $5 \times 3 = 15$ independent parameters.

2.2 Flow symmetries

This 25+15 parameter eddy viscosity tensor may be strongly simplified by using the symmetries of the flow. Let us consider some simple cases.

2.2.1 Isotropic turbulence

Any isotropic tensor can only be constructed with the unit tensor δ_{ij}. Thus, the most general isotropic tensor of rank 4 can be written as follows:

$$T_{ijkl} = a_1\delta_{ij}\delta_{kl} + a_2\delta_{ik}\delta_{jl} + a_3\delta_{il}\delta_{jk}\,. \tag{2.7}$$

If we impose the symmetry relations (2.5), it turns out that the eddy viscosity tensor ν reduces to

$$\nu_{ijkl} = -a\left(\delta_{ik}\delta_{jl} + \delta_{il}\delta_{jk} - \frac{2}{3}\delta_{ij}\delta_{kl}\right)\,, \tag{2.8}$$

while the symmetry relations (2.6) imply that the tensor μ vanishes. Consequently, the subgrid scale stress reads:

$$\tau^*_{ij} = -2a\overline{S}_{ij}, \tag{2.9}$$

where a is the usual isotropic eddy viscosity (Smagorinsky, 1963).

The simplest anisotropic situation arises when only one direction can be distinguished from the other. This axisymmetric geometry is thus characterized by a vector pointing to the anisotropy direction. We will show that the nature of this vector will strongly affect the structure of the eddy viscosity tensor. In particular, anisotropy induced by a pseudovector (like a magnetic field or a rotation) must be treated differently from the anisotropy induced by an axial vector (like a mean flow).

2.2.2 Axisymmetry induced by an axial vector

We first consider the case of an axisymmetry characterized by an axial vector $\mathbf{n}$. An axisymmetric tensor of rank 4 can only be a function of this vector $\mathbf{n}$ and of the unit tensor δ_{ij}. Its most general form, compatible with the symmetry between the first two indices, reads:

$$
\begin{aligned}
T'_{ijkl} = {} & b_1\delta_{ij}\delta_{kl} + b_2(\delta_{ik}\delta_{jl} + \delta_{il}\delta_{jk}) \\
& + b_3\delta_{ij}n_kn_l + b_4n_in_j\delta_{kl} + b_5(\delta_{ik}n_jn_l + \delta_{jk}n_in_l) \\
& + b_6(\delta_{il}n_jn_k + \delta_{jl}n_in_k) + b_7n_in_jn_kn_l .
\end{aligned} \tag{2.10}
$$

Imposing the constraints (2.5) and defining $b_2 = -c_1$, $b_6 = -c_2$ and $b_7 = -c_3$ lead to the following expressions:

$$
\begin{aligned}
b_1 &= (6c_1 - 4c_2n^2 - c_3n^4)/9 , \\
b_3 &= b_4 = (4c_2 + c_3n^2)/3 , \\
b_5 &= -c_2 .
\end{aligned} \tag{2.11}
$$

If the constraints (2.6) are imposed on μ_{ijkl}, only two parameters are different from zero and are opposite ($b_5 = -b_6$). Thus, by introducing $b_5 = c_4$ in μ, the subgrid-scale stress reads:

$$
\begin{aligned}
\tau^*_{ij} = {} & -2c_1\bar{S}_{ij} - 2c_2\left(n_i\bar{s}_j + \bar{s}_in_j - \frac{2}{3}\delta_{ij}\bar{s}_kn_k\right) \\
& - c_3\left(n_in_j - \frac{1}{3}\delta_{ij}n^2\right)\bar{s}_kn_k - 2c_4(\bar{r}_in_j + n_i\bar{r}_j) ,
\end{aligned} \tag{2.12}
$$

where $\bar{s}_i = \bar{S}_{ik}n_k$ and $\bar{r}_i = \bar{R}_{ik}n_k$. The effect on the resolved energy balance of the first three terms is fully determined by the sign of the parameters c_1, c_2, and c_3. Indeed, these terms correspond to dissipation (resp. creation) of resolved energy if and only if c_1, c_2, and c_3 are positive (resp. negative). On the contrary, the sign of the term proportional to c_4 in the resolved energy balance depends simultaneously on the sign of c_4 and on the flow through the factor $\bar{s}_k\bar{r}_k$:

$$
\tau^*_{ij}\bar{S}_{ij} = -c_1|\bar{S}|^2 - 4c_2\bar{s}^2 - c_3(\bar{s}_kn_k)^2 - 4c_4\bar{s}_k\bar{r}_k . \tag{2.13}
$$

If the anisotropy is weak (n is relatively small), only terms up to n^2 must be retained; since $\bar{s}_i, \bar{r}_i = O(n)$, the term proportional to c_3 can be neglected in this case.

2.2.3 Axisymmetry induced by a pseudovector

We now consider that the anisotropy direction is represented by a pseudovector **p**. The most general axisymmetric tensor of rank 4 will be a function of the vector p_i, the unit tensor δ_{ij}, and the Levi-Civita tensor ϵ_{ijk}. The situation is thus more complicated and more parameters need to be introduced. The notations will be simplified by introducing the antisymmetric tensor $V_{ij} = \epsilon_{ijk}p_k$ so that the most general tensor compatible with the symmetry between the first two indices reads:

$$
\begin{aligned}
T''_{ijkl} = {} & d_1\delta_{ij}\delta_{kl} + d_2(\delta_{ik}\delta_{jl} + \delta_{il}\delta_{jk}) + d_3\delta_{ij}V_{kl} + d_4(\delta_{ik}V_{jl} + \delta_{jk}V_{il}) \\
& + d_5(\delta_{il}V_{jk} + \delta_{jl}V_{ik}) + d_6(\epsilon_{ikl}p_j + \epsilon_{jkl}p_i) + d_7\delta_{ij}p_kp_l + d_8p_ip_j\delta_{kl} \\
& + d_9(\delta_{ik}p_jp_l + \delta_{jk}p_ip_l) + d_{10}(\delta_{il}p_jp_k + \delta_{jl}p_ip_k) \\
& + d_{11}(V_{ik}V_{jl} + V_{il}V_{jk}) + d_{12}(V_{ik}p_jp_l + V_{jk}p_ip_l) \\
& + d_{13}(V_{il}p_jp_k + V_{jl}p_ip_k) + d_{14}p_ip_jV_{kl} + d_{15}p_ip_jp_kp_l .
\end{aligned} \tag{2.14a}
$$

We will not discuss the complete tensor T'' with 15 independent parameters. Let us assume that the anisotropy is weak enough to keep only terms proportional to the vector p_i. In this case, T'' reduces to

$$\begin{aligned} T''_{ijkl} \approx\ & d_1\delta_{ij}\delta_{kl} + d_2(\delta_{ik}\delta_{jl} + \delta_{il}\delta_{jk}) \\ & + d_3\delta_{ij}V_{kl} + d_4(\delta_{ik}V_{jl} + \delta_{jk}V_{il}) \\ & + d_5(\delta_{il}V_{jk} + \delta_{jl}V_{ik}) + d_6(\epsilon_{ikl}p_j + \epsilon_{jkl}p_i)\,. \end{aligned} \tag{2.14b}$$

Imposing the constraints (2.5) and defining $d_2 = -e_1$, $d_5 = -e_2$ and $d_6 = -e_3$ lead to the following expression:

$$\begin{aligned} d_1 &= 2e_1/3\,, \\ d_3 &= 2e_3\,, \\ d_4 &= -2e_3 - e_2\,, \end{aligned} \tag{2.15}$$

while imposing the constraints (2.6) with the new definition $d_5 = -e_4$, and $d_6 = -e_5$ leads to

$$\begin{aligned} d_1 &= d_2 = 0\,, \\ d_3 &= (2e_5 - 4e_4)/3\,, \\ d_4 &= e_4\,. \end{aligned} \tag{2.16}$$

The subgrid scale stress thus reads:

$$\begin{aligned} \tau^*_{ij} = & -2e_1\overline{S}_{ij} - 2(e_2 + e_3)(\overline{S}_{ik}V_{jk} + \overline{S}_{jk}V_{ik}) \\ & + 2(e_4 + e_5)\left(\overline{R}_{ik}V_{jk} + \overline{R}_{jk}V_{ik} - \frac{2}{3}\delta_{ij}\overline{R}_{kl}V_{kl}\right)\,. \end{aligned} \tag{2.17a}$$

Although the total eddy viscosity contains 5 parameters, only three of them appear independently in the expression for τ^*_{ij}. Let us note that the expression of τ^*_{ij} can be simplified by using the resolved vorticity:

$$\begin{aligned} \tau^*_{ij} = & -2e_1\overline{S}_{ij} - 2(e_2 + e_3)(\overline{S}_{ik}V_{jk} + \overline{S}_{jk}V_{ik}) \\ & + 2(e_4 + e_5)\left(\overline{w}_ip_j + \overline{w}_jp_i - \frac{2}{3}\delta_{ij}\overline{w}_kp_k\right)\,. \end{aligned} \tag{2.17b}$$

It is interesting to note that the anisotropic corrections appear at first order in the anisotropy direction p_i. Thus, we conclude that a pseudovector anisotropy (like a rotation or a magnetic field) should affect the eddy viscosity more rapidly than an axial vector anisotropy (like a grid or a flow anisotropy).

2.3 Onsager reciprocal symmetries

Strictly speaking, the Onsager reciprocal symmetries do not apply to turbulence. Indeed, they have been derived for describing the irreversible return to equilibrium in macroscopic system, and they strongly rely on the microscopic reversibility of particle motions as well as on the linearity of the transport laws. However, in an

attempt to simplify the eddy viscosity picture as much as possible, it is tempting to assume the existence of such relations for the tensors ν and μ. We will not try to justify further the use of such relations and present the form of the eddy viscosity tensors fulfilling these relations as a approximate simplification. The Onsager reciprocal relation will imply the following additional relations:

$$\begin{aligned} \nu_{ijkl}(\mathbf{n}) &= \nu_{klij}(\mathbf{n}), \\ \mu_{ijkl}(\mathbf{n}) &= \mu_{klij}(\mathbf{n}), \\ \nu_{ijkl}(\mathbf{p}) &= \nu_{klij}(-\mathbf{p}), \\ \mu_{ijkl}(\mathbf{p}) &= \mu_{klij}(-\mathbf{p}). \end{aligned} \tag{2.18}$$

When applied to the previous results, these relations imply $c_4 = 0$ and $\epsilon_5 = -\epsilon_4$. Thus, they strongly simplify the tensor μ_{ijkl} but they do not affect the tensor ν_{ijkl} in the case presented here.

3. Anisotropic eddy viscosity and dynamic model

It has been mentioned in the introduction that the use of the dynamic procedure gives a direct access to a multiple-parameter eddy viscosity. In this section we present the dynamic derivation of the eddy viscosity tensor in the simplest anisotropic geometry: the weak axisymmetric anisotropy induced by an axial vector. Moreover, the problem is further simplified by assuming the existence of Onsager symmetries for the tensor ν_{ijkl} and μ_{ijkl}. In that case, we have shown in the previous section that the subgrid stress tensor reduces to

$$\tau^*_{ij} = -2c_1\overline{S}_{ij} - 4c_2 n^2 \overline{S}^{\parallel}_{ij}, \tag{3.1}$$

where

$$\overline{S}^{\parallel}_{ij} = \frac{1}{2n^2}\left(n_i\overline{S}_{jl}n_l + n_j\overline{S}_{il}n_l\right) - \frac{1}{3n^2}\overline{S}_{kl}n_k n_l \delta_{ij}. \tag{3.2}$$

With the new tensor† $\overline{S}^{\perp}_{ij} = \overline{S}_{ij} - \overline{S}^{\parallel}_{ij}$ and the parameters $\nu_1 = c_1 + 2n^2c_2$ and $\nu_2 = c_1$, the subgrid stress tensor may be rewritten as

$$\tau^*_{ij} = -2\nu_1\overline{S}^{\parallel}_{ij} - 2\nu_2\overline{S}^{\perp}_{ij}. \tag{3.3}$$

With this formulation, the resolved energy dissipation reads $\epsilon = -\tau^*_{ij}\overline{S}_{ij} = \nu_1 R_1 + \nu_2 R_2$, where

$$R_1 = \sum_{ij}\overline{S}_{ij}\hat{\overline{S}}^{\parallel}_{ij} = \frac{s^2}{n^2} \geq 0, \tag{3.4a}$$

$$R_2 = \sum_{ij}\overline{S}_{ij}\hat{\overline{S}}^{\perp}_{ij} = \sum_{ij}\overline{S}_{ij}\left(\hat{\overline{S}}_{ij} - \hat{\overline{S}}^{\parallel}_{ij}\right) = \frac{1}{2}|\overline{S}|^2 - \frac{s^2}{n^2} \geq 0. \tag{3.4b}$$

† This notation should not lead to the conclusion that $\overline{S}^{\perp}_{ij}$ and $\overline{S}^{\parallel}_{ij}$ are orthogonal. It is easy to show that $\sum_{ij}\overline{S}^{\parallel}_{ij}\overline{S}^{\perp}_{ij} \neq 0$ in general.

The last inequality is a direct consequence of the Cauchy-Schwartz inequality :

$$s^2 = \sum_i (\sum_k \overline{S}_{ik} n_k)^2 \leq \sum_i \sum_k \left(\overline{S}_{ik}^2\right) \left(\sum_l n_l^2\right) = n^2 |\overline{S}|^2 / 2 . \tag{3.5}$$

Sufficient conditions for having a positive resolved energy dissipation are thus $\nu_1 \geq 0$ and $\nu_2 \geq 0$. In order to devise the simplest dynamic procedure, we suppose that both ν_1 and ν_2 scale following the Kolmogorov law:

$$\nu_1 = -C_1 \Delta^{4/3} , \tag{3.6a}$$

$$\nu_2 = -C_2 \Delta^{4/3} . \tag{3.6b}$$

The choice for the length scale Δ in C_1 and C_2 (which are *not* dimensionless) is unimportant because the dynamic model will take care of the amplitudes. Only the power 4/3 is important. With these definitions, the model becomes

$$\tau_{ij}^* = C_1 \rho_{ij} + C_2 \eta_{ij} , \tag{3.7}$$

where

$$\rho_{ij} = -2\Delta^{4/3} \overline{S}_{ij}^{\parallel} , \tag{3.8a}$$

$$\eta_{ij} = -2\Delta^{4/3} \widehat{\overline{S}}_{ij}^{\perp} . \tag{3.8b}$$

Assuming a volume-averaged version of the dynamic model, the error with respect to the Germano identity is given by (Germano, 1992; Ghosal *et al.*, 1995; Lilly, 1992):

$$E_{ij}(C_1, C_2) \equiv L_{ij} + C_1 M_{ij} + C_2 N_{ij} , \tag{3.9}$$

where

$$\begin{aligned} M_{ij} &= -2\ \Delta^{4/3}\ (1 - \alpha^{4/3}) \widehat{\overline{S}}_{ij}^{\parallel} , \\ N_{ij} &= -2\ \Delta^{4/3}\ (1 - \alpha^{4/3}) \widehat{\overline{S}}_{ij}^{\perp} . \end{aligned} \tag{3.10}$$

where α is the ratio between test and grid filters. By minimizing E_{ij}^2, we have the two coupled equations:

$$\begin{aligned} \langle L_{ij} M_{ij} \rangle + C_1 \langle M_{ij} M_{ij} \rangle + C_2 \langle N_{ij} M_{ij} \rangle &= 0 , \\ \langle L_{ij} N_{ij} \rangle + C_1 \langle M_{ij} N_{ij} \rangle + C_2 \langle N_{ij} N_{ij} \rangle &= 0 . \end{aligned} \tag{3.11}$$

Since M_{ij} is not aligned with N_{ij}, these two equations are not linearly proportional and they may be used for determining both C_1 and C_2.

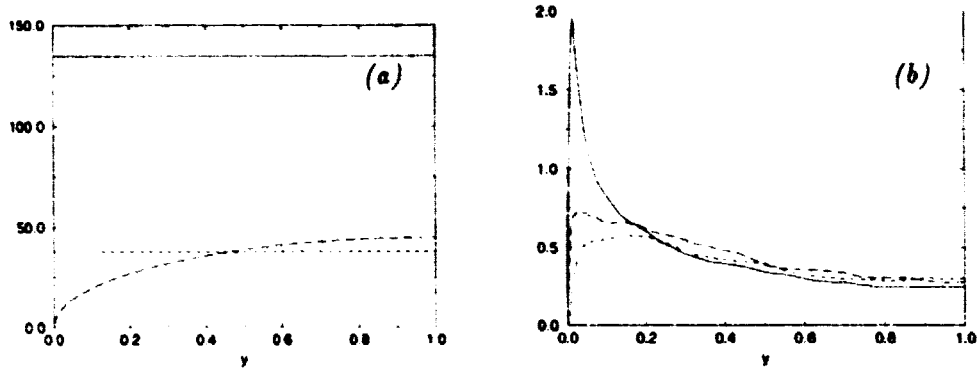

FIGURE 1. Comparison of the grid anisotropy described in terms of the grid spacing in each direction vs. the flow anisotropy described in terms of the square root of the diagonal components of the Leonard tensor. Clearly, the flow anisotropy is only important close to the wall in the streamwise direction. The grid anisotropy is also more important close to the wall, but mainly in the wall-normal direction. a) Dx+:——— ; Dy+:— — — ; Dz+:- - - - . b) Square root of Lxx:——— ; square root of Lyy:- - - - ; square root of Lzz:— — — .

4. Application to the channel flow

The dynamic formulation presented in the previous section has been implemented for channel flow with a friction Reynolds number of 1030 (cf. Cabot, 1994). The weak axisymmetric anisotropy is probably a very rough approximation for the channel geometry, so that the results presented here must be regarded as very preliminary tests. Moreover, it is not clear in channel flow which direction is the dominant anisotropic one (see Fig. 1). Indeed, channel flow is characterized by two anisotropic directions: the streamwise and the wall-normal directions. Both choices for $\mathbf{n}$ have been tested.

The rms values of streamwise velocity component (u') are presented in Fig. 2. The rms values of the wall-normal and spanwise velocity components (v' and w') seem to be insensitive to the model and are not shown here. It appears that the results from the isotropic model and the anisotropic model based on the wall-normal direction are almost indistinguishable. The results for the anisotropic model based on the streamwise direction seem to be better close to the wall. This could indicate that the flow anisotropy has more influence than the grid anisotropy. However, no definitive conclusion can be made since the model based on the streamwise direction does not perform well in the core region. Also, preliminary results indicate a long-time lack of stability for this latter model.

Finally, we present the results for the two eddy viscosity coefficients (ν_1 and ν_2) in Fig. 3. For both models, the condition of positive dissipation ($\nu_1 \geq 0$ and $\nu_2 \geq 0$) are mostly well satisfied. It is not known if the weakly negative values of ν_2 in the model based on the streamwise direction are responsible for its lack of stability.

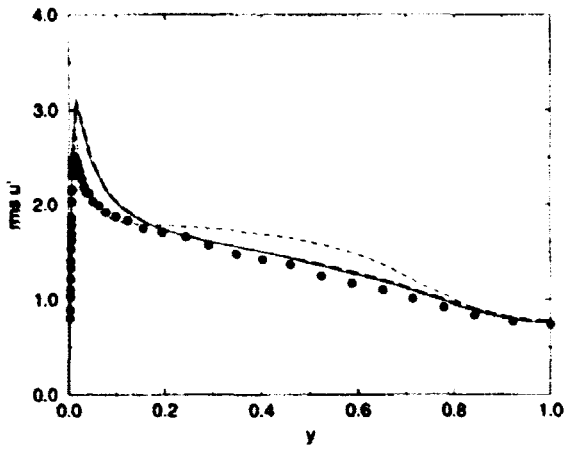

FIGURE 2. Comparison of profiles for the rms of streamwise velocity (u') between experimental data, the isotropic dynamic model and two versions of the anisotropic dynamic model based on the streamwise and wall-normal anisotropy directions. Experimental data (Hussain & Reynolds, 1970):• ; isotropic LES:——— ; anisotropic LES (n=str.dir.):---- ; anisotropic LES (n=wall norm. dir.):— — — .

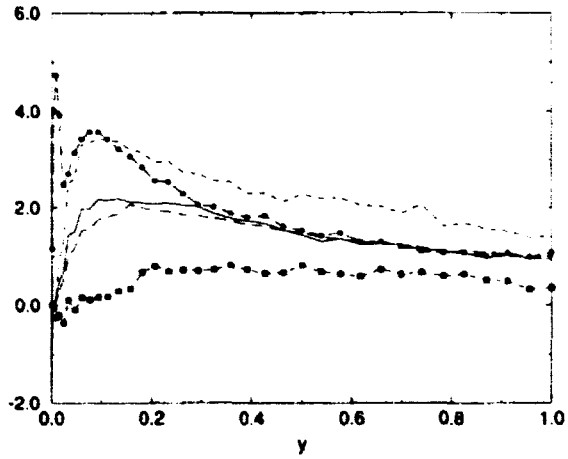

FIGURE 3. Comparison of eddy viscosity coefficients in three different models. Isotropic model: $\nu - t$ ——— ; anisotropic model (streamwise): ν_1 ---- , ν_2 ■; anisotropic model (wall normal): ν_1 ---- , ν_2 •

5. Discussion

The use of an anisotropic eddy viscosity model has been shown to complicate dramatically the relation between the subgrid stress tensor and the resolved velocity derivatives. In particular, in the fully anisotropic geometry, 40 independent effective transport coefficients must be introduced. However, when some approximations are used, it is possible to simplify the problem drastically. As an example, we have tested the weakly anisotropic axisymmetrical geometry. In that case, the eddy

viscosity tensor reduces to a two parameter quantity. A dynamic procedure has been proposed for this problem and some tests have been made in channel flow.

These numerical tests have clearly shown that the determination of the anisotropy direction remains an important issue in the simplified anisotropic model presented in §3. Indeed, even when the flow is fully anisotropic, the model discussed in §3 may be regarded as the first tensorial invariant correction to the isotropic eddy viscosity. The use of this model could then be seen as the result of a "local axisymmetric assumption" which should be at least as robust as the local isotropic assumption. However, in that case it is probably crucial to chose the vector $\mathbf{n}$ in an appropriate way. It is also possible that the vector $\mathbf{n}$ varies with space. An interesting extension to this work would be the derivation of a dynamic procedure giving explicit expressions not only for the eddy viscosity amplitudes but also for the vector $\mathbf{n}$.

At this point the simplest test for anisotropic models would be the homogeneous rotating turbulence. In that case, the anisotropy direction is clearly determined and is given in terms of the rotation pseudovector.

REFERENCES

CABOT, W. 1994 Local dynamic models in channel flow. In *CTR Annual Research Briefs 1994*, CTR, NASA Ames/Stanford Univ., 143–159.

DEARDORFF, J. W. 1970 A numerical study of three-dimensional turbulent channel flow at large Reynolds numbers. *J. Fluid Mech.* **41**, 453–480.

DEARDORFF, J. W. 1971 On the magnitude of the subgrid scale eddy coefficient. *J. Comp. Phys.* **7**, 120–133.

GERMANO, M. 1992 Turbulence: the filtering approach. *J. Fluid Mech.* **238**, 325–336.

GHOSAL, S., LUND, T., MOIN, P. & AKSELVOLL, K. 1995 The dynamic localization model for large eddy simulation of turbulent flows. *J. Fluid Mech.* **286**, 229–255.

HUSSAIN, A. K. M. F., & REYNOLDS, W. C. 1970 The mechanics of a perturbation wave in turbulent shear flow. Dept. of Mech. Eng. Tech. Rep. **FM-6**, Stanford Univ.

LILLY, D. K. 1992 A proposed modification of the Germano subgrid-scale closure method. *Phys. Fluids.* **4**, 633–635.

ONSAGER, L. 1931 Reciprocal relations in irreversible processes. I. *Phys. Rev.* **37**, 405–426.

ONSAGER, L. 1931 Reciprocal relations in irreversible processes. II. *Phys. Rev.* **38**, 2265–2279.

SCOTTI, A., MENEVEAU C., & LILLY D. K. 1993 Generalized Smagorinsky model for anisotropic grids. *Phys. Fluids.* **5**, 2306–2308.

SMAGORINSKY, J. S. 1963 General circulation experiments with the primitive equations: I. The basic experiment. *Mon. Weather Rev.* **91**, 99–164.

NEXT
DOCUMENT

Dynamic Smagorinsky model on anisotropic grids

By A. Scotti[1], C. Meneveau[1] AND M. Fatica[2]

Large Eddy Simulation (LES) of complex-geometry flows often involves highly anisotropic meshes. To examine the performance of the dynamic Smagorinsky model in a controlled fashion on such grids, simulations of forced isotropic turbulence are performed using highly anisotropic discretizations. The resulting model coefficients are compared with a theoretical prediction (Scotti *et al.*, 1993). Two extreme cases are considered: pancake-like grids, for which two directions are poorly resolved compared to the third, and pencil-like grids, where one direction is poorly resolved when compared to the other two. For pancake-like grids the dynamic model yields the results expected from the theory (increasing coefficient with increasing aspect ratio), whereas for pencil-like grids the dynamic model does not agree with the theoretical prediction (with detrimental effects only on smallest resolved scales). A possible explanation of the departure is attempted, and it is shown that the problem may be circumvented by using an isotropic test-filter at larger scales.

Overall, all models considered give good large-scale results, confirming the general robustness of the dynamic and eddy-viscosity models. But in all cases, the predictions were poor for scales smaller than that of the worst resolved direction.

1. Introduction

Since its introduction in the 1960's, a goal of LES has been to simulate complex turbulent flows. A complex flow is, by definition, characterized by regions where the physics of turbulence change, e.g., from homogeneous turbulence far from boundaries to near wall turbulence, etc. To capture the full gamut with a simple subgrid model without having to adjust constants in an *ad hoc* manner every time was a serious problem until recently. The introduction of the dynamic model (Germano *et al.*, 1991) to dynamically calculate the parameter(s) of the modeled sub-grid stress was a significant step towards making LES of complex flows possible without *ad hoc* adjustments. This model is able to self-adjust to the large scale flow in the correct fashion, for instance, shutting itself down near walls or in regions where the flow relaminarizes.

As a result, it has become possible to apply LES to study flows of increasing complexity (e.g. Akselvoll and Moin 1996 or see in this same volume Chan and Mittal, and Haworth and Jansen), which in turn requires the use of complex grids, either structured or unstructured. Complicated grid geometries in conjunction with

1 The Johns Hopkins University, Baltimore, MD 21218
2 Center for Turbulence Research

the dynamic model raise several questions. Consider, as an example, the flow past a 3-D bluff body: near the object, one needs to refine the grid in the spanwise directions. For a structured mesh, far downstream, the grid may be greatly expanded in the streamwise direction. Therefore, the grid can be strongly anisotropic, with the elements of the grid looking like sheets or pencils, depending on the kind of refinement imposed upstream. Hence, in the far-wake region one may have a situation where the turbulence is nearly isotropic, whereas the computational grid is highly anisotropic.

In LES, the grid filter is dictated by the computational mesh used to solve the equations (although, for methods other than spectral, it is difficult to give a precise definition of the filtering operator associated with a given discretization). Since classical eddy-viscosity models need as input a length-scale which is usually associated with the scale at which the filter operates, the problem arises in defining this length when, as a result of the anisotropy of the grid, the filter is defined by more than one length scale. For the Smagorinsky model, this problem was considered first by Deardoff (1970) and later by Schumann (1975). Lilly (1988) and Scotti *et al.* (1993), although the last two papers were only theoretical treatments.

On the other hand, other models such as the dynamic model do not in principle require a length scale to be specified. The question then arises whether the dynamic model is able to correctly simulate isotropic turbulence on anisotropic grids. The main goal of this work is to examine this question.

This issue is also of theoretical interest since, from the point of view of interaction among modes, local triadic interactions at small scales are fully available only to a limited amount of modes. Thus the small scales are exposed to a dynamic which is not the one typical of 3-D turbulence. It is natural then to expect that the SGS stress tensor should incorporate a correction originating only from the anisotropy of the grid.

The paper is organized as follows: in section 2 we briefly summarize the main result of Scotti *et al.* (1993) and set the notation that will be used throughout the paper; in Section 3 we discuss the simulations and how the results of different models will be compared. In showing the results, we have considered two categories of grids: pancake-like, when one direction is much better resolved than the other two, and pencil-like, when two directions are much better resolved than the third. Section 4 presents the results. Finally, in Section 5 a summary and discussion of the results is given.

2. Smagorinsky model on anisotropic grids

In this section, the results of Scotti *et al.* (1993) are briefly recalled. They are based on the assumption that the turbulence is isotropic and homogeneous, and that the largest and smallest scales at which the filter operates still lie within the inertial range. One begins by writing the Smagorinsky model as

$$\tau_{ij} = -2[L(\Delta_1, \Delta_2, \Delta_3)]^2 [2\tilde{S}_{lm}^2]^{1/2} \tilde{S}_{ij}. \tag{1}$$

Here Δ_1, Δ_2 and Δ_3 are the dimensions of the computational cell. For notational convenience and without lack of generality, let us assume $\Delta_1 \leq \Delta_2 \leq \Delta_3$. The

equivalent filter, via a collocation rule, is assumed to be a sharp cut-off filter in Fourier space, which corresponds to setting to zero all the modes outside the region $B = \{|k_1| < \pi/\Delta_1, |k_2| < \pi/\Delta_2, |k_3| < \pi/\Delta_3\}$, leaving the others unmodified.

By invoking an argument used first by Lilly (1967) an expression for $L(\Delta_1, \Delta_2, \Delta_3)$ was derived by requiring that

$$\varepsilon = - < \tau_{ij} \tilde{S}_{ij} >,$$

replacing τ_{ij} with the model and computing moments of the strain-rate tensor, assuming that the velocity field is characterized by a Kolmogorov isotropic spectrum on all resolved modes.

Introducing $\Delta_{eq} = (\Delta_1 \Delta_2 \Delta_3)^{1/3}$, $L(\Delta_1, \Delta_2, \Delta_3)$ can then be written as

$$L(\Delta_1, \Delta_2, \Delta_3) = C_s \Delta_{eq} f(a_1, a_2), \tag{2}$$

where $a_1 = \Delta_1/\Delta_3$ and $a_2 = \Delta_2/\Delta_3$ are the two aspect ratios of the grid, and $f \geq 1$ is a function equal to one if both ratios are equal to unity. C_s is the traditional Smagorinsky coefficient, which depends on the value of the Kolmogorov constant.

After evaluating the function f, a compact approximation for the result was given by Scotti *et al.* (1993)

$$f(a_1, a_2) \simeq \cosh \sqrt{4/27((\log a_1)^2 - \log a_1 \log a_2 + (\log a_2)^2)}. \tag{3}$$

Incidentally, we remark that the fact that $f \simeq 1$ for aspect ratios close to unity justifies the practice introduced by Deardoff (1970) of using Δ_{eq} as length scale, at least for aspect ratios close to unity. In the dynamic version of this model, with grid filtering denoted by tilde and test filtering by an overbar, the length-scale $L(\tilde{\Delta}_1, \tilde{\Delta}_2, \tilde{\Delta}_3)$ is computed according to

$$2[L(\tilde{\Delta}_1, \tilde{\Delta}_2, \tilde{\Delta}_3)]^2 = \frac{< L_{ij} M_{ij} >}{< M_{ij} M_{ij} >}, \tag{4}$$

where

$$L_{ij} = \overline{\tilde{u}_i \tilde{u}_j} - \bar{\tilde{u}}_i \bar{\tilde{u}}_j, \tag{4a}$$

and

$$M_{ij} = \left[\overline{[2\tilde{S}^2_{lm}]^{1/2} \tilde{S}_{ij}} - \left(\frac{\bar{\tilde{\Delta}}_{eq}}{\tilde{\Delta}_{eq}} \frac{f(\bar{a}_1, \bar{a}_2)}{f(\tilde{a}_1, \tilde{a}_2)} \right)^2 [2\bar{\tilde{S}}^2_{lm}]^{1/2} \bar{\tilde{S}}_{ij} \right], \tag{4b}$$

where we have made use of Eq. (2). If both test and grid filter have the same aspect ratios then Eq. (4) is closed; otherwise we can use Eq. (3) to compute f and check *a posteriori* its consistency.

3. Approach and validation

We run LES of isotropic turbulence in a box of side 2π with periodic boundary conditions. Turbulence is maintained by a forcing $\mathbf{f}$ that forces the largest modes ($k \leq 2$) with an intensity such that the energy injection rate $\mathbf{f} \cdot \mathbf{u}$ is fixed at a constant value $\varepsilon = 1.0$. The numerical scheme is the same as in Vincent and Meneguzzi (1991) and Briscolini and Santangelo (1994). It uses Adam-Bashforth 2 for time advancing, with $\Delta t = 0.001$. The nonlinear terms, written in rotational form, are evaluated pseudospectrally. Appendix A examines dealiasing for the AB2 scheme. The grids have mesh sides $(\Delta_1, \Delta_2, \Delta_3)$, with $\Delta_3 > \max\{\Delta_1, \Delta_2\}$ and aspect ratios $a_1 = \Delta_1/\Delta_3$, $a_2 = \Delta_2/\Delta_3$ ranging from 1 to 1/16. Grid filtering was performed with a sharp spectral cut-off setting to zero the modes outside the ellipsoid $B = \{\mathbf{k} \in R^3 \mid (k_1\Delta_1)^2 + (k_2\Delta_2)^2 + (k_3\Delta_3)^2 \leq 8/9\pi^2\}$, which has the advantage of partially removing aliasing errors (see appendix A). Test filtering was done at a scale twice as large in all directions.

For comparison, computations were performed using the classical non-dynamic Smagorinsky model with the Deardoff length scale and $C_s^2 = 0.026$, as well as with the Smagorinsky model corrected after Scotti *et al.* (1993) including $f(a_1, a_2)$ as evaluated from Eq. (3). In all cases the initial condition is assumed to be a random Gaussian field with $k^{-5/3}$ spectrum, random phase, and total kinetic energy equal to unity.

We wish to compare both large scale properties, such as total kinetic energy, derivative skewness in the worst resolved direction, and small scale properties, such as energy spectra near cut-off scale and the skewness in the best resolved direction (which is sensitive to the details of the small scales).

For isotropic turbulence we know that the spectral tensor in the inertial range is given by

$$Q_{ij}(\mathbf{k}) = < u_i(\mathbf{k}) u_j(-\mathbf{k}) > = (4\pi)^{-1} C_K \varepsilon^{2/3} k^{-11/3} P_{ij}(\mathbf{k}), \tag{5}$$

where ε is the average dissipation, C_K is the Kolmogorov constant, and $P_{ij}(\mathbf{k})$ is the projector on the space orthogonal to $\mathbf{k}$. Also, we know that the skewness of the derivative is $O(-.5)$, although for LES the value attained is typically smaller due to the incomplete resolution of the small scales. We will compute the skewness in the α-direction, defined as $S_\alpha = < (\partial \tilde{u}_\alpha / \partial x_\alpha)^3 > / < (\partial \tilde{u}_\alpha / \partial x_\alpha)^2 >^{3/2}$.

Due to the anisotropy of the grid, it is better to study 1-D premultiplied spectra, defined as

$$C(k_1) = \frac{\int_B 2\pi \varepsilon^{-2/3} k^{11/3} Q_{ii}(\mathbf{k}) dk_2 dk_3}{\int_B dk_2 dk_3}.$$

For ideal Kolmogorov turbulence, where the spectral tensor is given by Eq. (5), $C(k_1)$ is a constant equal to the Kolmogorov constant $C_K \simeq 1.6$.

4. Results

To obtain a self-consistent estimate for the Smagorinsky constant C_s, we first run LES with the dynamic model with isotropic spherical test and grid filter on a 32^3 grid. After an initial transient the value stabilizes at $C_s^2 = 0.023 \pm 5\%$. Next, we

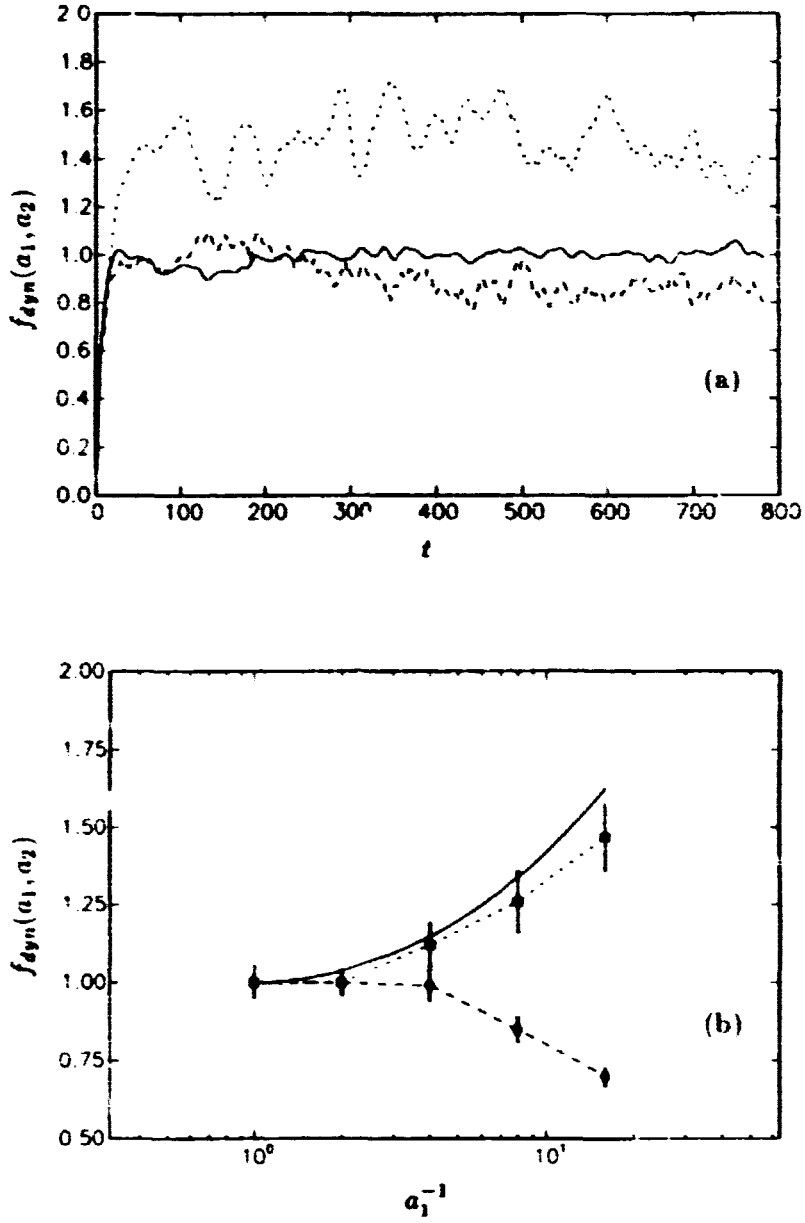

FIGURE 1. (a) Time traces of $f_{dyn}(a_1, a_2)$ as generated by the dynamic model during LES of forced turbulence on anisotropic grids. ---- : aspect ratios $a_1 = a_2 = 1, 8$; ——— : $a_1 = a_2 = 1$; ····· : $a_1 = 1/16$, $a_2 = 1$. (b) values of time averages of $f_{dyn}(a_1, a_2)$ computed between $400 \leq t \leq 800$, for pancake-like grids, $a_2 = 1$, (□) and pencil-like grids $a_2 = a_1$, (◇). The solid line represents the theoretically determined values, according to Eq. (3). Error bars are $\pm\sigma$, where σ is the standard deviation about the time average.

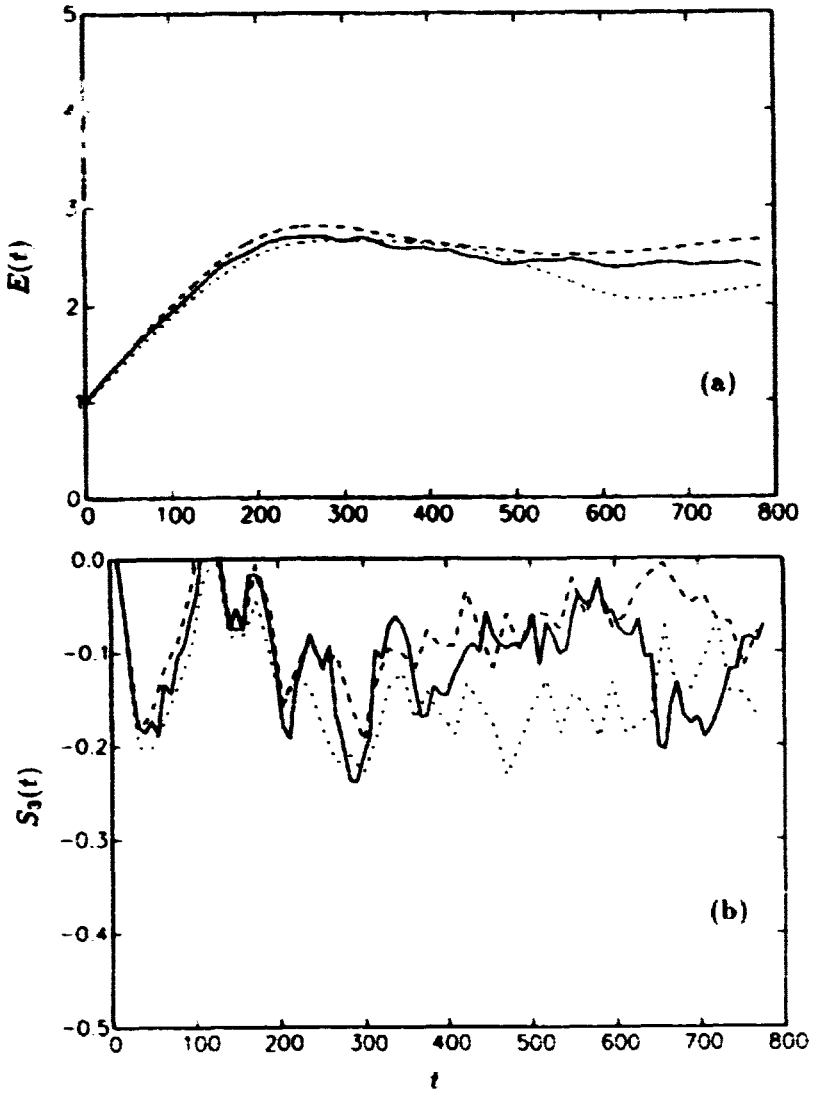

FIGURE 2. Eddy-viscosity models on pancake-like grids ($256 \times 16 \times 16$). (a) kinetic energy as a function of time for dynamic model (———), modified Smagorinsky (·····) and Smagorinsky-Deardoff (----). (b) skewness in the worst resolved direction, same symbols as in (a).

perform LES on anisotropic grids characterized by aspect ratios a_1 and a_2. The results are cast in terms of $f(a_1, a_2)$, by writing

$$f_{\mathrm{dyn}}(a_1, a_2) = \sqrt{\frac{< L_{ij} M_{ij} >}{2 < M_{ij} M_{ij} >}} \frac{0.023^{-1/2}}{\Delta_{eq}}.$$

Figure 1a shows the time evolution of $f_{\mathrm{dyn}}(a_1, a_2)$ for three cases: an isotropic grid

on 32^3 modes, a pancake-like grid using a $256 \times 16 \times 16$ grid, and a pencil-like grid using $128 \times 128 \times 16$ modes.

In the same way we have computed the time averages of f_{dyn} for aspect ratios varying from 1/2 to 1/16. They are plotted in Figure 1b together with the value obtained from Eq. (3). We see that the dynamic model reproduces the correct trend for pancake-like grids, but fails with pencil-like grids. To examine the simulations more closely, we now focus on two extreme cases: a $256 \times 16 \times 16$ grid (pancake) and a $128 \times 128 \times 16$ grid (pencil). For each case, we compare the dynamic model with predictions of the non-dynamic Smagorinsky model and with the non-dynamic model but including the correction of Eq. (3).

4.1 Pancake-like

Figure 2 shows the total kinetic energy versus time for the three models considered. We see that the three models agree quite well. Also, the skewness in the least resolved direction does not show marked differences. We conclude that at the large-scale level, there is no impact on the model variations even at this high level of grid anisotropy. Next, we consider the behavior near the grid scale. The premultiplied 1-D spectrum is shown in Fig. 3. The traditional Smagorinsky-Deardoff case shows a strong peak at wavenumber $k_1 \sim 10$. The modified Smagorinsky case remains constant at small wavenumbers and dies out at high wavenumbers without showing any pile-up. The dynamic model falls somewhere in between, but the value is higher than the expected value of C_K. All models show a rapid decay at wavenumbers above 10.

The fact that all three models decay for $k_1 > 10$ means that those modes that cannot have access to all the local triadic interactions experience a high drain of energy so that they do not display a Kolmogorov scaling. It appears unlikely that any modification of a scalar eddy-viscosity model could compensate for this behavior.

The analysis of the derivative skewness in the well-resolved direction shows no real difference.

4.2 Pencil-like

As already mentioned, the dynamic model gives a value for f_{dyn} which is smaller than one, in contrast with the theoretical expression, which implies that f must be bigger than one. If we look at the large-scale parameters of the flow, energy and skewness in the least resolved direction (Fig. 4) we see that the three models again give similar answers; note the small value of the skewness in the worst resolved direction. But if we consider parameters that are more sensitive to the small scale behavior, we notice marked differences. For the dynamic model the Kolmogorov constant is too large, about twice as much as expected (Fig. 5). Therefore, the "underestimation" of f brings consequences that cannot be ignored at the scales near the least resolved direction. Again, scales between the least and best resolved directions are much less energetic than the Kolmogorov spectrum, as is clear from the rapid drop of the premultiplied spectrum above $k_1 = 16$. On the other hand, the modified Smagorinsky model gives too small a value, probably due to overdamped

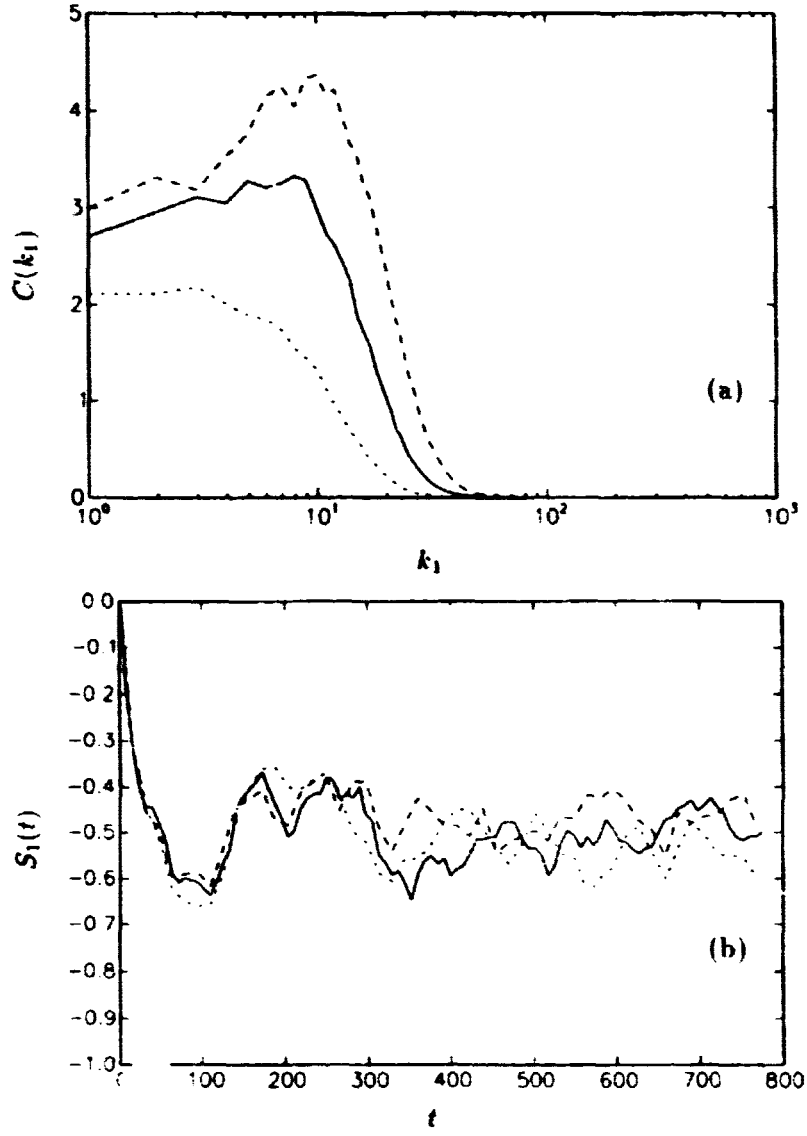

FIGURE 3. Eddy-viscosity models on a pancake-like grid. (a) premultiplied 1-D spectrum: dynamic model (——), modified Smagorinsky (·····) and Smagorinsky-Deardoff (- - - -). (b) derivative skewness in the best resolved direction. same symbols as in (a).

modes near $k \sim \frac{\pi}{\Delta_3}$. Finally, the skewness in the best resolved direction is consistent with these differences: the smaller the skewness is in magnitude, the more the energy piles up.

4.3 Discussion

The strongest discrepancy between the theoretically and dynamically determined

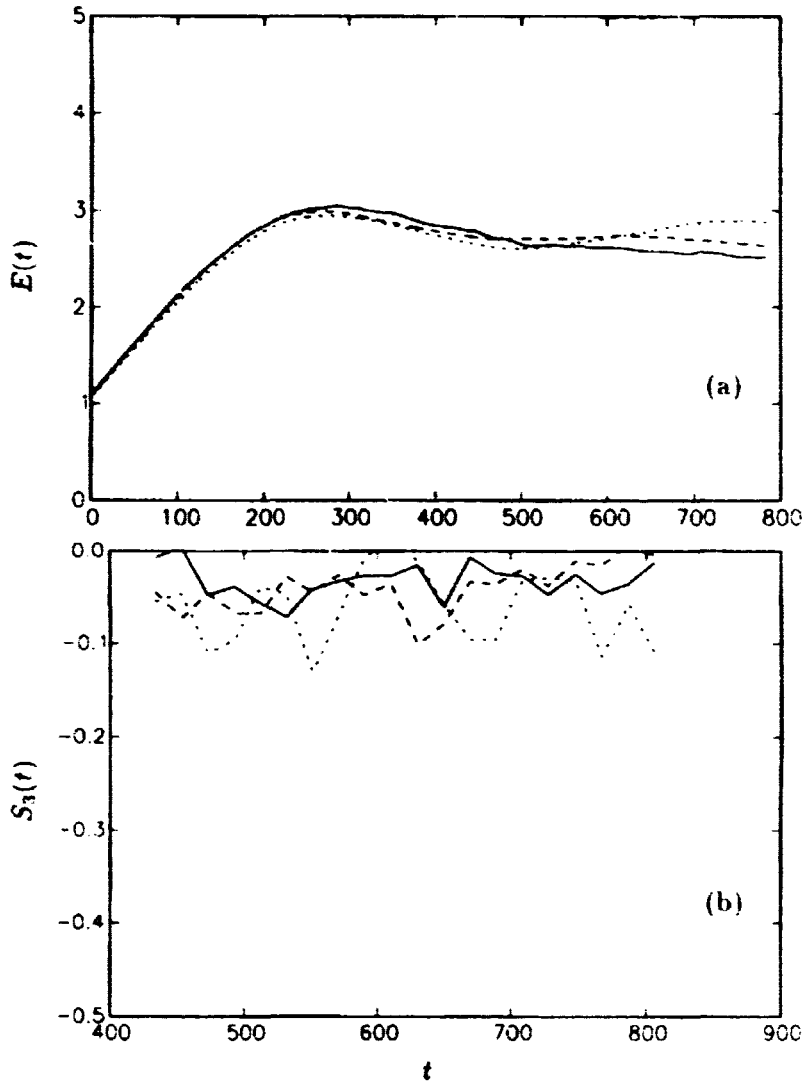

FIGURE 4. Eddy-viscosity models on pencil-like grid ($128 \times 128 \times 16$). (a) energy as a function of time for dynamic model (——), modified Smagorinsky (·····) and Smagorinsky-Deardoff (- - - -). (b) derivative skewness in the worst resolved direction, same symbols as above.

$f(a_1, a_2)$ was observed for the case of highly pencil-like grids. For this case, the premultiplied spectrum of the dynamic model case showed considerable pile-up, as evidenced by much higher values of $C(k_1)$. In order to understand the causes of this behavior, we recall that the dynamic model computes L by sampling the turbulence between grid and test filter. It could be argued that for pencil-like grids these modes behave essentially as 2D turbulence, with the vorticity aligned in the x_3 direction and a concomitant change in the dynamics. To focus on the relevant scales, we

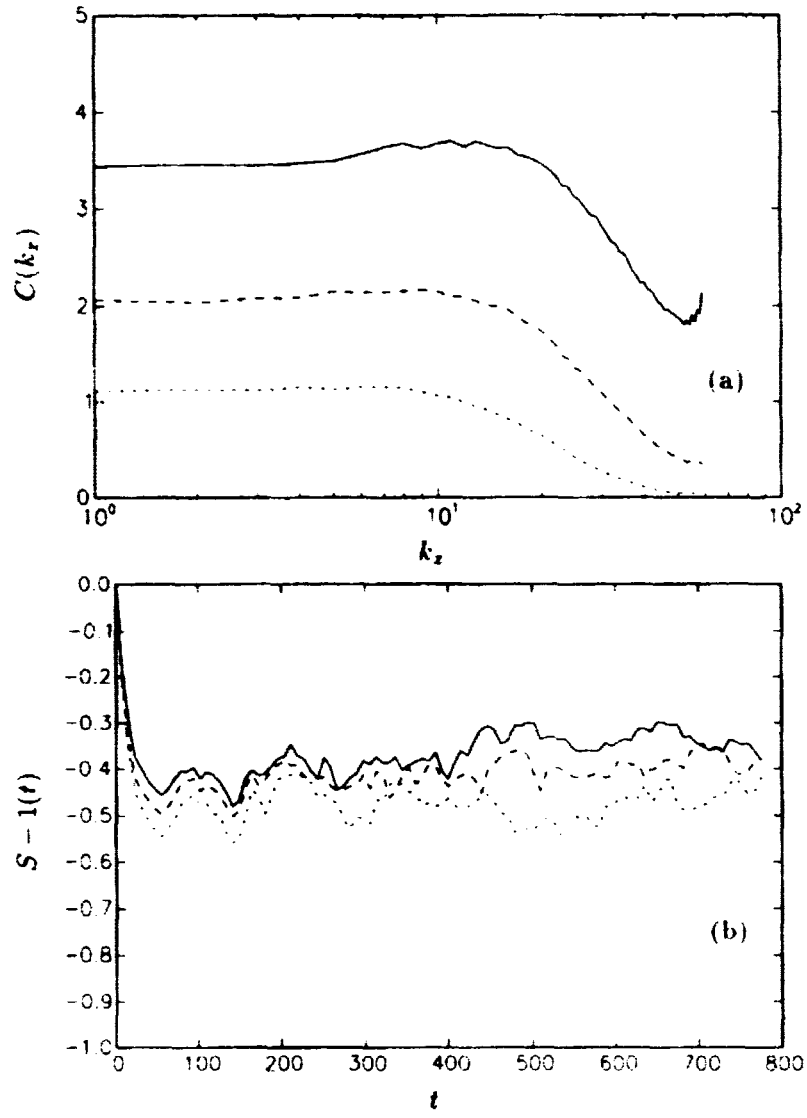

FIGURE 5. Pencil-like grid. (a) compensated 1-D spectrum: dynamic model (———), modified Smagorinsky (·····) and Smagorinsky-Deardoff (----). (b) derivative skewness in the best resolved direction, same symbols as above.

have analyzed the vorticity band-pass filtered between test and grid filter (i.e. the statistics of $\omega' = \tilde{\omega} - \bar{\omega}$). We find that the variances are not isotropic, and that $\omega_1'^2/\omega_3'^2 \sim \omega_2'^2/\omega_3'^2 \sim 0.75$, i.e. the flow is not quite 3-D but not 2-D either. More directly related to the small value of L or $f_{\rm dyn}$ obtained from the dynamic model, in Fig. 6 we show the PDF of $L_{ij}M_{ij}$ (solid line). The curve is almost symmetrically distributed around the origin, and the average value, while positive, is very small ($< L_{ij}M_{ij} >= 4.80$). $L_{ij}M_{ij}$ can be regarded as a measure of energy transfer from

large to small scales, with negative values meaning energy backscatter. If we now compute the same PDF but using an isotropic test filter at a scale $2\Delta_3$ in all three directions, we see that the shape of the PDF changes, being now skewed to the right (symbols in Fig. 6). The mean value is now $< L_{ij}M_{ij} >= 31.66$. Therefore, by sampling larger scales that are more isotropic, the dynamics of the energy transfer changes noticeably.

This observation suggests that in order to improve the performance of the dynamic model in such extreme cases of grid anisotropy, it may be advisable to use a test filter which is isotropic, with a length scale twice as large as the worst resolved scale. In this case, the grid and test anisotropies differ, and this must be taken into account explicitly in the dynamic model formulation. We now implement the dynamic model with Eq. (4b) for M_{ij}, using the expression given in Eq. (3) for $f(\bar{a}_1, \bar{a}_2)$ and $f(\hat{a}_1, \hat{a}_2)$. Using this formulation on a $128 \times 128 \times 16$ simulation yields the result shown in Fig. 6. The time trace of f (Fig. 6) shows that it oscillates around an average value of $1.44 \pm .067$, much closer to the expected value of 1.34 than the value of 0.8 obtained with pencil-like test filtering. At large scales the difference between this run and the previous one is small. On the other end, at small scales the situation changes as now the premultiplied spectrum (Fig. 7) lies flat at 1.4 for $k_1 < 10$, very close to the expected value for C_K. The skewness in the best resolved direction agrees well with the one calculated from the modified Smagorinsky model.

5. Conclusions

We have run several LES of forced isotropic turbulence on anisotropic grids, using three different Smagorinsky models. All three models are able to satisfactorily reproduce the very large scales of the flow. This result confirms the general robustness of the dynamic model even for the extreme cases considered in this work (see Jiménez (1995) for further observations on the dynamic model's robustness). However, none of the models considered is able to give a correct representation of the scales smaller than the worst resolved direction, where spectra are strongly damped below Kolmogorov values. This is probably due to the fact that the transfer of energy at very small scales is affected by the lack of similar modes in one or more directions. For a related study on the effect of grid anisotropy on velocity components and stress anisotropy, see Kaltenbach (1996).

For the model performance at scales near the cut-off in the worst resolved direction, we need to distinguish between pancake grids and pencil grids. For pancake-like grids, the non-dynamical Smagorinsky model modified after Scotti *et al.* (1993) and the dynamic model give reasonably good results, while the conventional Smagorinsky model using the Deardoff prescription for Δ_{eq} shows excessive pile up of energy at scales close to the largest mesh size. The anisotropy factor computed from the dynamic model shows an increasing trend with anisotropy in accord with the theoretical prediction, although the numerical value is somewhat smaller. For pencil-like grids, the Smagorinsky-Deardoff model as well as the modified version give good results, with the modified version yielding slightly better results. On the other

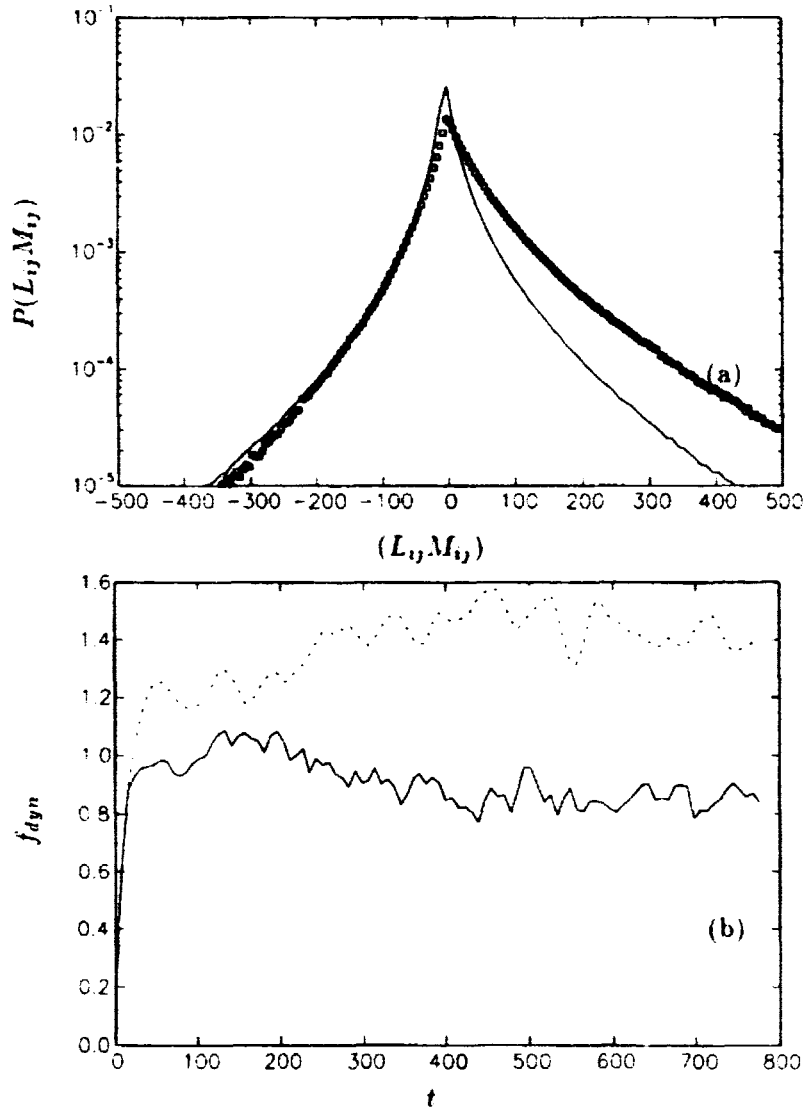

FIGURE 6. (a) PDF of $L_{ij}M_{ij}$ computed with same grid but different test filters. Both statistics were performed on the same fields simulated on a 128 × 128 × 16 grid and with test filter cutting off at $\bar{k}_i = 1/2\tilde{k}_i$. The solid line refers to $L_{ij}M_{ij}$ computed as in the simulation, while the symbols refer to $L_{ij}M_{ij}$ computed with a test filter cutting off at $\bar{k}_i = 1/2\tilde{k}_3$. (b) anisotropy factor f_{dyn} computed with an anisotropic test filter (——) and with an isotropic (larger scale) test filter (·····). The predicted value is 1.34.

hand, the dynamic model exhibits insufficient dissipation of energy, as shown by the fact that the anisotropy factor f_{dyn} becomes smaller than one, and reflected in that small scales have excessive energy as compared to the Kolmogorov value.

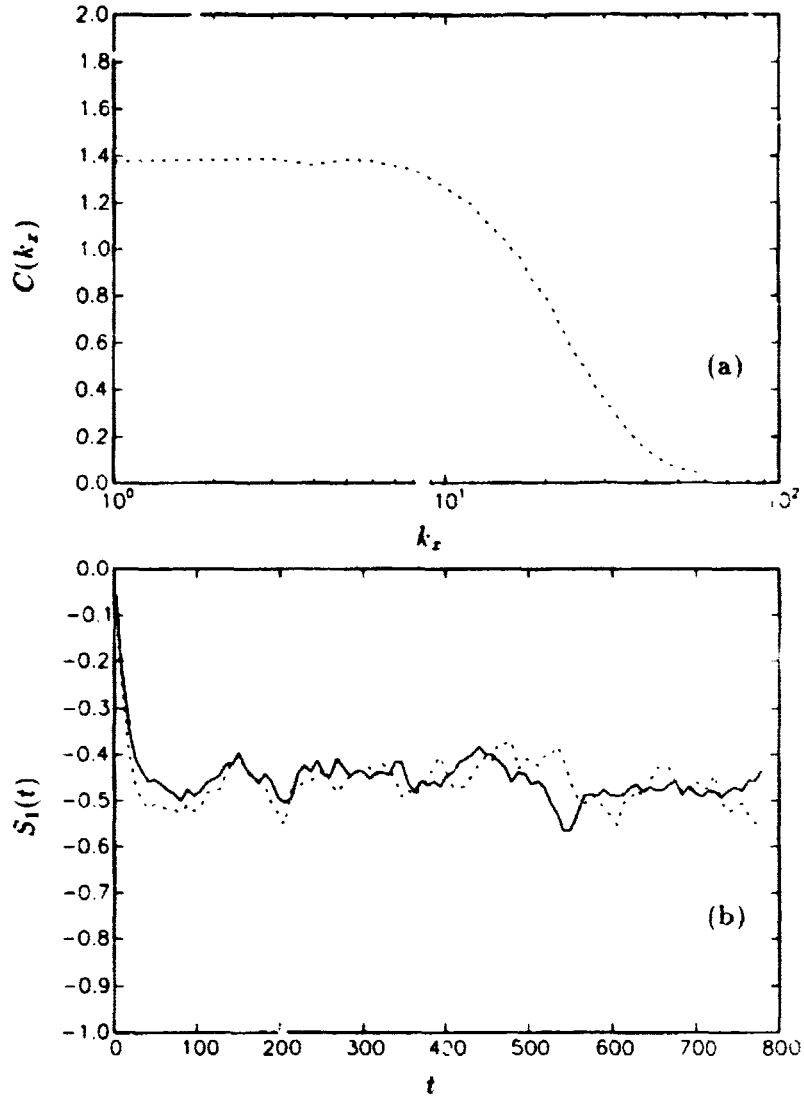

FIGURE 7. (a) compensated 1-D spectrum of dynamic model on pencil-like grid with isotropic test filter. (b) derivative skewness in the best resolved direction for dynamic model with isotropic test filter (——) and modified Smagorinsky-model (·····).

It would appear that in this particular case the strength of the dynamic model becomes its weak point. The dynamic model computes the unknown factor from information derived from the smallest resolved scales. But in the case of highly anisotropic grids, these scales experience a dynamic which is *different from* the usual one due to the missing modes at large wavenumbers. This in turn affects the resolved non-linear interactions embodied in the term $L_{ij}M_{ij}$, which is what the dynamic model samples. Specifically, the number of events during which energy

is transferred forward is decreased, which could actually be explained by a partial 2-dimensionalization of the flow at these scales.

A proposed improvement is to move the test filter towards larger scales, where the combination of more energetic modes and more realistic triadic coupling allows a more faithful representation of how energy is exchanged. Indeed, simulations done with an isotropic test filter at twice the worst resolved scale show improved results. Perhaps not surprisingly, this conclusion is similar to one reached by others in the context of dynamic LES using non-spectral numerical methods, such as low-order finite differences. There, it has been found advisable to "prefilter" the results and shift the test filter to larger scales (Ferziger 1996, Lund 1996) so that the dynamic model is not strongly affected by numerical errors occurring near the grid scale.

Acknowledgments

We thank Prof. J. Jiménez, Prof. P. Moin, Dr. W. Cabot, and Dr. D. Carati for interesting discussions on this subject. The support of CTR and of NSF (CTS-9408344) is gratefully acknowledged.

REFERENCES

AKSELVOLL, K. & MOIN, P. 1996 Large-eddy simulation of turbulent confined coannular jets. *J. Fluid Mech.* **315**, 387.

BRISCOLINI, M. & SANTANGELO, P. 1994 The non-Gaussian statistics of the velocity field in low-resolution large-eddy simulations of homogeneous turbulence. *J. Fluid Mech.* **270**, 199.

CANUTO, C., HUSSAINI, M.Y., QUARTERONI, A., ZANG, T.A. 1988 *Spectral methods in fluid dynamics. Springer-Verlag.*

DEARDOFF, J. W. 1970 A numerical study of three-dimensional turbulent channel flow at large Reynolds numbers. *J. Fluid Mech.* **41**, 453.

FERZIGER J. 1996 Personal communication.

GERMANO, M., PIOMELLI, U., MOIN, P. & CABOT, W. H. 1991 A dynamic subgrid-scale eddy viscosity model. *Phys. Fluid A.* **48**, 273-337.

JIMÉNEZ, J. 1995 On why dynamic subgrid-scale models work. *Annual Research Briefs.* Center for Turbulence Research, NASA Ames/Stanford Univ., 25-34.

KALTENBACH, H-J 1996 Cell aspect ratio dependence of anisotropy measures for resolved and subgrid scale stresses. Preprint.

LILLY, D. K. 1967 The representation of small-scale turbulence in numerical simulation experiments. *Proceedings of the IBM Scientific Computing Symposium on Environmental Science.* **320-1951**, 195.

LILLY, D. K. 1988 The length scale for sub-grid-scale parameterizaion with anisotropic resolution. *Annual Research Briefs.* Center for Turbulence Research, NASA Ames/Stanford Univ., 3-9.

LUND, T. 1996 Personal communication.

ROGALLO, R. S. 1977 An ILLIAC Program for the Numerical Simulation of Homogeneous Incompressible Turbulence. *NASA TM-81315.*

SCHUMANN, U. 1975 Subgrid scale model for finite difference simulations of turbulent flows in plane channels and annuli. *J. Comp. Phys.* **18**, 386.

SCOTTI, A., MENEVEAU, C. & LILLY, D. K. 1993 Generalized Smagorinsky model for anisotropic grids. *Phys. Fluid A.* **5**, 2306-2308.

VINCENT A. & MENEGUZZI M. 1991 The spatial structure and statistical properties of homogeneous turbulence. *J. Fluid Mech.* **225**, 1.

Appendix A

We assume that the computational domain is covered by $N_1 \times N_2 \times N_3$ points and $\mathbf{i}, \mathbf{j}$ and $\mathbf{l}$ are unit vectors in the x, y, and z directions. It is well known (see Canuto *et al.* (1987)) that the pseudospectral treatment of a 3-D convolution product $\sum_{\mathbf{m}+\mathbf{n}=\mathbf{k}} a(\mathbf{m})b(\mathbf{n})$ introduces an error. If we denote with $w_{\mathbf{k}}$ the true convolution product and with $W_{\mathbf{k}}$ the calculated one, the following relation holds:

$$W_{\mathbf{k}} = w_{\mathbf{k}} + \sum_{j=1}^{7} W_j$$

where the seven extra terms have the form

$$W_j = \sum_{\mathbf{m}+\mathbf{n}=\mathbf{k}+\mathbf{e}_j} a(\mathbf{m})b(\mathbf{n})$$

and

$$\mathbf{e}_1 = \pm N_1\mathbf{i},\ \mathbf{e}_2 = \pm N_2\mathbf{j},\ \mathbf{e}_3 = \pm N_3\mathbf{l},$$

$$\mathbf{e}_4 = \pm N_1\mathbf{i} \pm N_2\mathbf{j},\ \mathbf{e}_5 = \pm N_1\mathbf{i} \pm N_3\mathbf{l},\ \mathbf{e}_6 = \pm N_3\mathbf{l} \pm N_2\mathbf{j},$$

$$\mathbf{e}_7 = \pm N_1\mathbf{i} \pm N_2\mathbf{j} \pm N_3\mathbf{l}.$$

The last four terms, (double and triple aliased) can be set to zero if we adopt an elliptical truncation, i.e. , if we set to zero all the modes such that

$$\left(\frac{k_1}{N_1}\right) + \left(\frac{k_2}{N_2}\right) + \left(\frac{k_3}{N_3}\right) \geq \frac{2}{9}.$$

The proof is by inspection.

To remove the single aliased terms we can resort to phase shift. If we premultiply all the modes by a factor $e^{i\mathbf{k}\cdot\boldsymbol{\theta}}$, $\boldsymbol{\theta} \in [0, 2\pi] \times [0, 2\pi] \times [0, 2\pi]$, compute the convolution sum and multiply the result by $e^{-i\mathbf{k}\cdot\boldsymbol{\theta}}$, the aliased terms now are $e^{\pm i\theta_j N_j} W_j$, $j = 1, 2, 3$, i.e. we have shifted their phase by an amount $\pm\theta_j N_j$. If we do the same thing one more time, but this time $\boldsymbol{\theta} \rightarrow \boldsymbol{\theta} + (\pi/N_1, \pi/N_2, \pi/N_3)$ and take the average of the results, the aliased terms, being out of phase, will cancel exactly. However, this requires doubling the number of FFT's required for each term to be dealiased.

Rogallo (1977) showed that for a multistep scheme such as even-order Runge-Kutta, it is possible to control the growth of aliasing essentially at no extra cost. Indeed, let us consider the typical step of a 2nd order Runge-Kutta:

$$u^{n+1} = u^n + \frac{\Delta t}{2}(F_1 + F_2)$$

with F_i's being the non-linear terms evaluated recursively. It is important to notice that to 0th order in Δt they are identical. Therefore, if F_1 is evaluated with a shift θ and F_2 with shift $\theta + (\pi/N_1, \pi/N_2, \pi/N_3)$, their sum to 0th order is dealiased, leaving possibly a contribution to first order. Therefore, the global effect of aliasing is pushed to second order. Choosing θ randomly at each time step further ensures that the error does not accumulate over time. Nevertheless the RK-2 method requires doubling the FFT's for each time step.

In our computation we have used an AB2 scheme, which schematically can be written as

$$u^{n+1} = u^n + \frac{\Delta t}{2}(3F^n - F^{n-1})$$

with obvious meaning of the symbols. Although to 0th order the alias terms are identical in F^n and F^{n-1}, it is clear that there is no way in which a combination of phase shifts can cancel them exactly, since the equation

$$3e^{i\alpha N} - e^{i\beta N} = 0$$

does not have solutions for $\alpha, \beta \in [0, 2\pi]$.

However, by successive phase-shifts it is still possible to ensure that the error does not accumulate. If n is even, the shift is chosen randomly; if n is odd, the shift is chosen to be the shift of the previous time step plus $(\pi/N_1, \pi/N_2, \pi/N_3)$. After m time steps, the solution can be written as

$$u^{n+m} = u^n + \frac{\Delta t}{2}[3(F^n + F^{n+1} + F^{n+2} + \cdots + F^{n+m}) - (F^{n-1} + F^n + F^{n+1} + \cdots + F^{n+m-1})].$$

In the two bracketed sums, to the lowest order, all but a few aliased terms (typically the first and/or the last) cancel out. This proves that the error does not accumulate, and that after m steps the aliasing is still $O(\Delta t)$, no matter how big m is. Again, the randomness prevents accumulation at higher orders. We have compared results obtained with this dealiasing technique with results obtained by zero padding (2-rule in the worst resolved direction) without finding any noticeable difference.

NEXT
DOCUMENT

Dynamic model with scale-dependent coefficients in the viscous range

By C. Meneveau[1] & T. S. Lund[2]

The standard dynamic procedure is based on the scale-invariance assumption that the model coefficient C is the same at the grid and test-filter levels. In many applications this condition is not met, e.g. when the filter-length, Δ, approaches the Kolmogorov scale, and $C(\Delta \to \eta) \to 0$. Using *a priori* tests, we show that the standard dynamic model yields the coefficient corresponding to the *test-filter* scale ($\alpha\Delta$) instead of the grid-scale (Δ). Several approaches to account for scale dependence are examined and/or tested in large eddy simulation of isotropic turbulence: (a) Take the limit $\alpha \to 1$; (b) Solve for two unknown coefficients $C(\Delta)$ and $C(\alpha\Delta)$ in the least-square-error formulation; (c) The 'bi-dynamic model', in which two test-filters (e.g. at scales 2Δ and 4Δ) are employed to gain additional information on possible scale-dependence of the coefficient, and an improved estimate for the grid-level coefficient is obtained by extrapolation. (d) Use theoretical predictions for the ratio $C(\alpha\Delta)/C(\Delta)$ and dynamically solve for $C(\Delta)$. None of these options is found to be entirely satisfactory, although the last approach appears applicable to the viscous range.

1. Introduction

One of the underlying ideas of the dynamic procedure (Germano *et al.*, 1991) for large eddy simulation (LES) is scale-similarity, which allows information obtained from the resolved field to be utilized for modeling the subgrid scales. Typically, this information consists of a dimensionless model coefficient (e.g. the Smagorinsky coefficient) which is assumed to have the same value at the grid-scale Δ and test-filter scale $\alpha\Delta$, where $\alpha = 2$ in most applications. Concretely, within the context of the Smagorinsky model, the Germano identity leads to

$$L_{ij} = C(\alpha\Delta)A_{ij} - \widehat{C(\Delta)B^*_{ij}}, \tag{1}$$

where $A_{ij} = -2(\alpha\Delta)^2|\tilde{\bar{S}}|\tilde{\bar{S}}_{ij}$, $B^*_{ij} = -2\Delta^2|\bar{S}|\bar{S}_{ij}$, $|\bar{S}| = \sqrt{2\bar{S}_{ij}\bar{S}_{ij}}$, and $L_{ij} = \widehat{\bar{u}_i\bar{u}_j} - \tilde{\bar{u}}_i\tilde{\bar{u}}_j$ is the resolved stress. The fundamental scale-similarity assumption of the standard dynamic model is that the model coefficients $C(\Delta) = C(\alpha\Delta) = C$. With this assumption, C is obtained by minimizing the error in Eq. 1 averaged over the independent tensor components (Lilly, 1992) and, if it exists, over a region

1 The Johns Hopkins University
2 Center for Turbulence Research

of statistical homogeneity (Germano *et al.*, 1991; Ghosal *et al.*, 1995). For fully inhomogeneous flows, averaging can be performed over pathlines (Meneveau *et al.*, 1996).

As in other applications, it will be assumed here that the averaging operations sufficiently diminish spatial variations of C, so that one can neglect the error incurred in extracting C from the test-filter operation (see Ghosal *et al.*, 1995). Thus, the second term in the rhs of Eq. (1) is replaced with $C(\Delta)B_{ij}$, where $B_{ij} = \widehat{B^*}_{ij}$. Also, in this work we will examine the dynamic procedure in conjunction with the Smagorinsky model. While other base-models such as similarity models have been proposed (Bardina *et al.*, 1980; Liu *et al.*, 1994), they typically require an additional eddy-viscosity term (mixed model, Bardina 1983; Zang *et al.* 1993; Liu *et al.*, 1995). Thus, it is of interest to continue to examine the Smagorinsky model in parallel to other efforts on improved base models.

Under the assumption of scale-invariance, the dynamic Smagorinsky model yields

$$C = \frac{\langle M_{ij} L_{ij} \rangle}{\langle M_{ij} M_{ij} \rangle}, \tag{2}$$

where

$$M_{ij} = A_{ij} - B_{ij}, \tag{2a}$$

and where $\langle\rangle$ denotes an average over directions of statistical homogeneity or over pathlines.

When applied to the simple problem of either forced or decaying isotropic turbulence at large Reynolds number, the resulting coefficient is typically between $C \simeq 0.02$ and 0.03, independent of Δ. This agrees with the classical result by Lilly (1967) which relates C to the universal Kolmogorov constant c_K according to

$$C = \left(\frac{2}{3c_K}\right)^{3/2} \pi^{-2} \simeq 0.027, \quad \text{for} \quad c_K = 1.6. \tag{3}$$

This result is obtained from balancing the rate of SGS dissipation with the total dissipation, and evaluating moments of the resolved strain-rate tensor by requiring the resolved portion of the flow to display an inertial-range Kolmogorov spectrum. When the filter-scale is within the inertial range, this argument indeed yields a Δ-independent result.

While the above analysis is useful as a guide, it is not generally applicable to LES of complex flows, where the filter (grid) scale Δ may not fall inside a pure inertial range. For instance, in certain parts of the domain, Δ may approach the flow's integral scale, or the flow may be undergoing rapid distortions so that the inertial range is perturbed. In other regions of the flow, the grid scale may approach the viscous scale. In such situations, the coefficient may dependent on Δ, and the assumption $C(\Delta) = C(\alpha\Delta)$ used in the dynamic model is not strictly applicable.

The objective of this study is to examine the dynamic model when the coefficient depends on scale. A convenient application in which to examine this issue

numerically is forced isotropic turbulence, when $\Delta \to \eta$, where η is the Kolmogorov scale. We will study coefficient scale dependence using filtered DNS data (*a priori* test) and perform LES at varying viscosity, so that Δ/η, or the mesh-Reynolds number (McMillan & Ferziger, 1979), defined as $Re_\Delta = \Delta^2|\bar{S}|/\nu$, decreases towards $Re_\Delta \simeq 1$.

First, a review of the expected behavior of $C(\Delta \to \eta)$ is given in §2. In §3, we analyze highly-resolved DNS data at moderate Reynolds number and compare the real Smagorinsky coefficient to that obtained from the dynamic model under the assumption that $C(\Delta) = C(\alpha\Delta)$. The effect of varying α is also examined. In section §4, we report on several attempts to generalize the dynamic model to explicitly take into account the scale-dependence of the coefficient. Conclusions are outlined in §5.

2. Smagorinsky coefficient in the viscous range

Before considering the dynamic Smagorinsky model, it is useful to establish the expected behavior of the Smagorinsky coefficient as the grid-scale approaches the viscous range. The analysis is based on a generalization of the argument by Lilly (1967) and was recently carried out by Voke (1996) who expressed the results in terms of the mesh-Reynolds number Re_Δ. We shall also need results in terms of Δ/η, so the analysis is briefly repeated below. Examination of the equation for resolved kinetic energy in isotropic, statistically steady, and forced (force f_i) turbulence yields

$$\langle f_i \bar{u}_i \rangle = -\langle \tau_{ij}\bar{S}_{ij} \rangle + 2\nu \langle \bar{S}_{ij}^2 \rangle . \tag{4}$$

where $\langle\rangle$ denotes a volume average. The last term above is viscous dissipation of resolved motion, which was neglected in the traditional Lilly (1967) analysis as $\Delta >> \eta$. Using the fact that in steady turbulence the injection rate $\langle f_i \bar{u}_i \rangle$ equals the overall rate of dissipation ϵ, replacing the Smagorinsky model with a possibly scale-dependent coefficient $C(\Delta)$, and using the approximation $\langle |\bar{S}|^3 \rangle \simeq \langle |S|^2 \rangle^{\frac{3}{2}}$, one obtains

$$\epsilon = C(\Delta) 2^{3/2} \Delta^2 \langle \bar{S}_{ij}^2 \rangle^{3/2} + 2\nu \langle \bar{S}_{ij}^2 \rangle , \tag{5}$$

The moment $\langle \bar{S}_{ij}^2 \rangle \equiv \langle \bar{S}_{ij}\bar{S}_{ij} \rangle$ can be evaluated from the energy spectrum of the resolved field, which is assumed here to follow the Pao spectrum up to a sharp cutoff wavenumber $k_\Delta = \pi/\Delta$. The Pao spectrum, given by

$$E(k) = c_K \epsilon^{2/3} k^{-5/3} \exp\left(-\frac{3}{2} c_k k^{-4/3} \right)$$

is one of the cases considered by Voke (1996), and we use it here because resulting expressions are simple. Solving for C, one obtains

$$C(\Delta/\eta) = \epsilon^{-\frac{3}{2}c_K(\pi\eta/\Delta)^{4/3}} \left(\frac{\eta}{\Delta}\right)^2 \left(1 - \epsilon^{-\frac{3}{2}c_K(\pi\eta/\Delta)^{4/3}}\right)^{-3/2} . \tag{6}$$

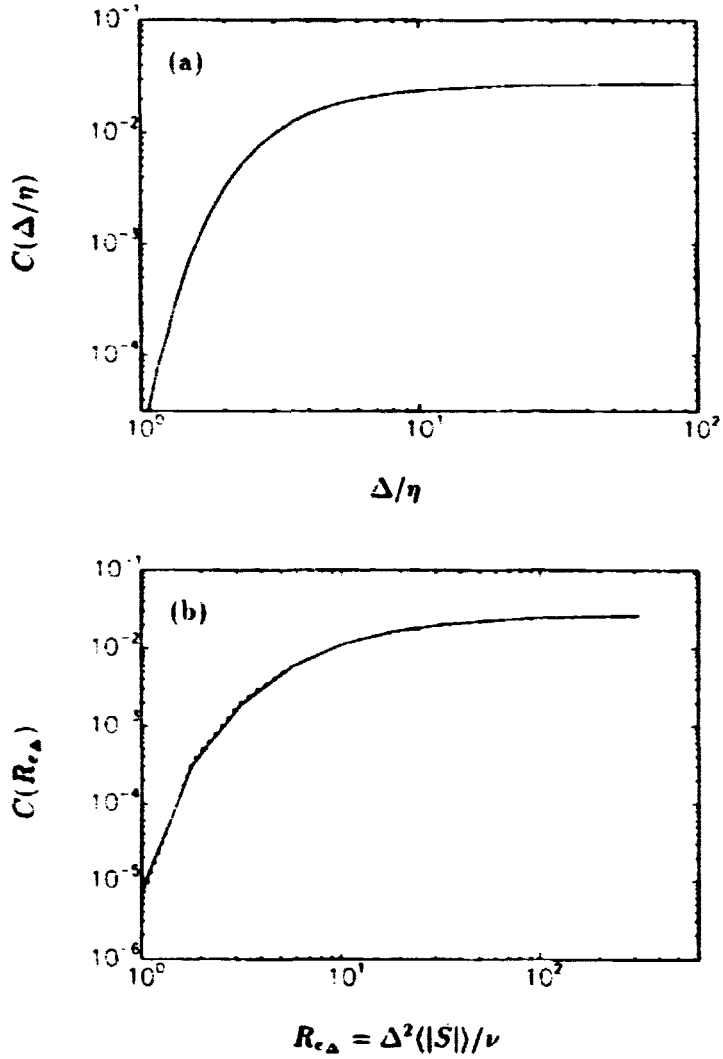

FIGURE 1. (a) Smagorinsky coefficient as calculated from the dissipation balance using the Pao spectrum (Eq. 6). (b) Same result but expressed in terms of mesh Reynolds number (solid line), obtained by solving Eq. 7. (see also Voke (1996), who expresses the same result in terms of the ratio of eddy to molecular viscosity). The dotted line is a convenient fit, namely $C_{\rm fit}(Re_\Delta) = 0.027 \times 10^{-3.23 Re_\Delta^{-0.92}}$.

The predicted variation in C is shown in Fig. 1a (for $c_K = 1.6$). As expected, the above estimate shows a rapid decrease in C as the grid-scale approaches the Kolmogorov scale.

For future reference, it is also useful to express the coefficient in terms of the mesh-Reynolds number $Re_\Delta = \Delta^2|\bar{S}|/\nu$ which (as opposed to Δ/η) is a variable that can be computed locally in LES. Using $\eta = (\nu^3/\epsilon)^{1/4}$ and replacing ϵ with the

r.h.s. of Eq. 5, one obtains

$$C(Re_\Delta) = \frac{\sinh^{-\frac{3}{4}}\gamma}{2^{\frac{3}{4}} Re_\Delta^{\frac{3}{4}} \sqrt{C(Re_\Delta) + Re_\Delta^{-1}}}\, e^{-\gamma/2}. \tag{7}$$

where

$$\gamma = \frac{3}{4} c_K \pi^{\frac{4}{3}} Re_\Delta^{-1} (C(Re_\Delta) + Re_\Delta^{-1})^{-\frac{1}{3}}.$$

In deriving this result it has been assumed that $\langle |S| \rangle \simeq \langle |\bar{S}|^2 \rangle^{\frac{1}{2}}$. Solving for $C(Re_\Delta)$ numerically ($c_K = 1.6$) one obtains the curve shown in Fig. 1b. This curve is not too different from the empirically obtained result of McMillan & Ferziger (1979).

While the precise nature of these curves depends strongly on the assumed Pao spectrum, which is not entirely realistic, the general trend is quite robust: The coefficient begins to drop from the asymptotic value starting from scales significantly greater than the Kolmogorov scale. Evidently, at the transition between inertial and viscous range, the assumption that C does not depend on scale is not accurate.

3. A priori tests

The aim of this section is to evaluate Smagorinsky coefficients computed with the dynamic model operating on filtered DNS data of forced isotropic turbulence. The dynamic coefficient is then compared with the 'real' coefficient obtained by requiring that the model dissipate the correct amount of energy. Velocity fields at microscale Reynolds number $R_\lambda = 85$ were generated with the pseudo-spectral code of Rogallo (1981) on a 256^3 mesh. This data base has a very well-resolved dissipation range and was used previously by Lund and Rogers (1994) in their study of the topology of dissipative motions. This feature is important for the present study since we are interested in the behavior near the Kolmogorov scale. The maximum wavenumber scaled in Kolmogorov units is $k_{max}\eta = 3$, which corresponds to a mesh spacing of $\Delta_m = 3/\pi\eta \simeq 1\eta$.

From the DNS, we evaluate the coefficient from the large-scale portion of the spectrum using the dynamic model (Eq. 1), assuming that $C(\Delta) = C(\alpha\Delta)$. The analysis is repeated at various filtering scales Δ (cutoff wavenumbers π/Δ) and several values of α. For comparison, the coefficient can be obtained from the condition that the model dissipates the proper amount of energy.

$$C(\Delta) = -\frac{\langle \tau_{ij}\bar{S}_{ij} \rangle}{\Delta^2 2^{3/2} \left\langle (\bar{S}_{ij}^2)^{\frac{3}{4}} \right\rangle}. \tag{8}$$

Results are shown in Fig. 2. As can be seen, the 'real' coefficient is near $C \simeq 0.02 \rightarrow 0.04$ when $\Delta > 30\eta$, i.e. for scales above the viscous range. At smaller Δ, the coefficient decreases rapidly, qualitatively in accord with the theoretical prediction based on the Pao spectrum (Fig. 1a). We do not ascribe much significance to the discrepancies between Fig.1a and 2 since we have verified that they are due to minor differences between the Pao and the actual spectrum, and also due to

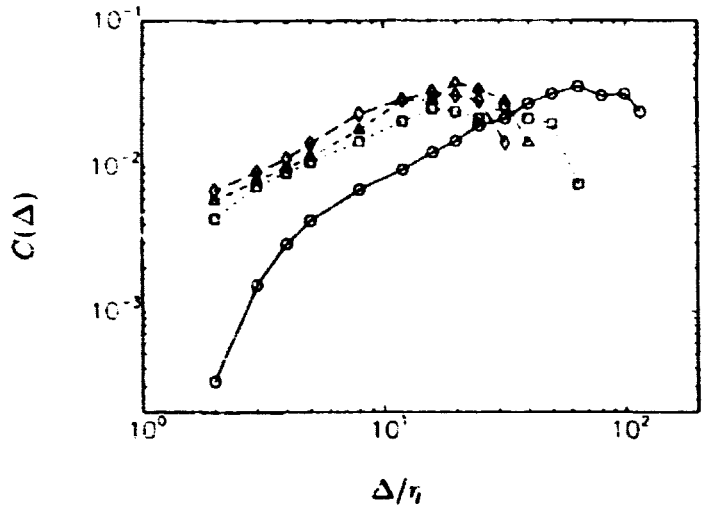

FIGURE 2. Coefficients obtained from *a priori* tests using well resolved DNS (256^3 simulation at $R_\lambda \simeq 85$ and $k_{max}\eta \simeq 3$). o , 'true coefficient' obtained from dissipation balance (Eq. 8). Other symbols: dynamic model coefficient (standard formulation) at various test-filters: □ , $\alpha = 2$; △ , $\alpha = 3$; ◇ , $\alpha = 4$.

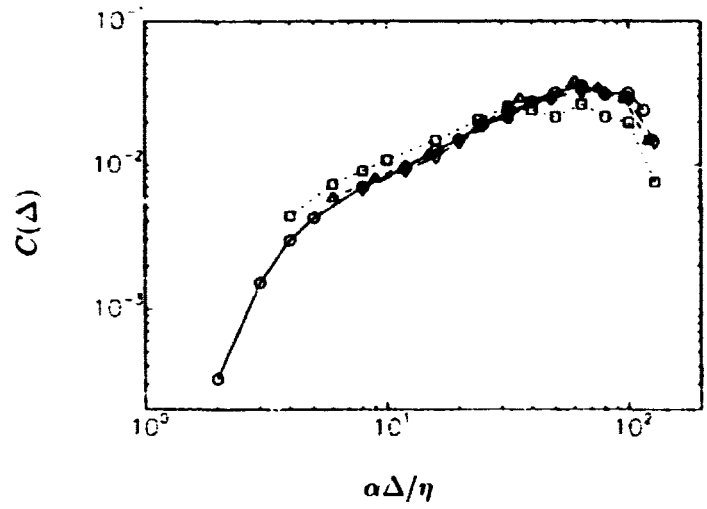

FIGURE 3. Same as Fig. 2, but plotted as function of $\alpha\Delta/\eta$. The near collapse means that the dynamic model yields the coefficient appropriate to the test-filter scale instead of the grid-scale.

residual unsteadiness in the simulations due to a limited sampling of velocity fields in time. At large scales a drop in coefficient can be seen, probably due to the effects of forcing.

The dynamic model predictions yield a similar trend for the coefficient, only that

the scale range appears to be shifted. Since the dynamic model samples the scales at the test-filter level, it is reasonable to expect that the resulting coefficient is the one corresponding to the test-filter scale instead of that of the grid-scale. To verify this idea, in Fig. 3 we plot the results of the dynamic model as function of the respective test-filter scales instead of the grid-scale (except for the coefficient obtained from Eq. 8). The collapse is quite good, indeed verifying that in this case the dynamic model yields the coefficient corresponding to the test-filter scale.

Similar results were obtained when using the strain-rate contraction (Germano *et al.*, 1991) for the dynamic model (for which $C = \langle L_{ij}\tilde{S}_{ij}\rangle / \langle M_{ij}S_{ij}\rangle$), or the least-square error approach to determine the 'real' coefficient (for which $C = -\langle \tau_{ij}|\tilde{S}|\tilde{S}_{ij}\rangle / 2\Delta^2 \langle |\tilde{S}|^2\tilde{S}_{ij}^2\rangle$). Therefore, the results are quite robust with regard to how the coefficients are determined.

At this point we conclude that the dynamic model is capable of reproducing the important trend that the coefficient should decrease as the filter-length approaches the Kolmogorov scale. Nevertheless, some discrepancy is observed between the 'real' and dynamic coefficient for scales at which the coefficient is strongly scale-dependent. From a practical perspective, this discrepancy is quite benign in the current application, since the dominant mechanism of energy drain when the filter is near the Kolmogorov scale is the resolved viscous dissipation. Indeed, simulations with resolutions in the viscous range run with the dynamically obtained coefficient (which according to Fig. 2 may be too high) did not show any significant difference from one using a lower coefficient, essentially because the SGS dissipation is negligible in these cases.

In what follows, we examine several reformulations of the dynamic model that attempt to explicitly include the scale-dependence of the coefficient. Because it affords relative ease of implementation and interpretation, the analysis is still conducted within the context of the viscous range, even though the impact of using different values for the coefficients is rather small.

4. Alternative formulations

In this section, we consider several alternative formulations of the dynamic model. None of the options considered will be found to be completely satisfactory, but the observations made along the way provide useful insights into the workings of the dynamic model.

4.1 The limit $\alpha \to 1$

Since we have found that (for $\alpha \geq 2$) the standard dynamic model yields the coefficient $C(\alpha\Delta)$ instead of $C(\Delta)$, an obvious possible remedy would be to allow the test filter scale to approach the grid scale. This issue was briefly addressed theoretically by Gao & O'Brien (1993), who noticed that while the resulting expressions would be indeterminate, the limit may be written in terms of higher-order gradients of the resolved velocity, thus emphasizing the scales closest to the grid-scale. A possible disadvantage of this approach is that the scales closest to the cutoff are often strongly affected by numerical errors.

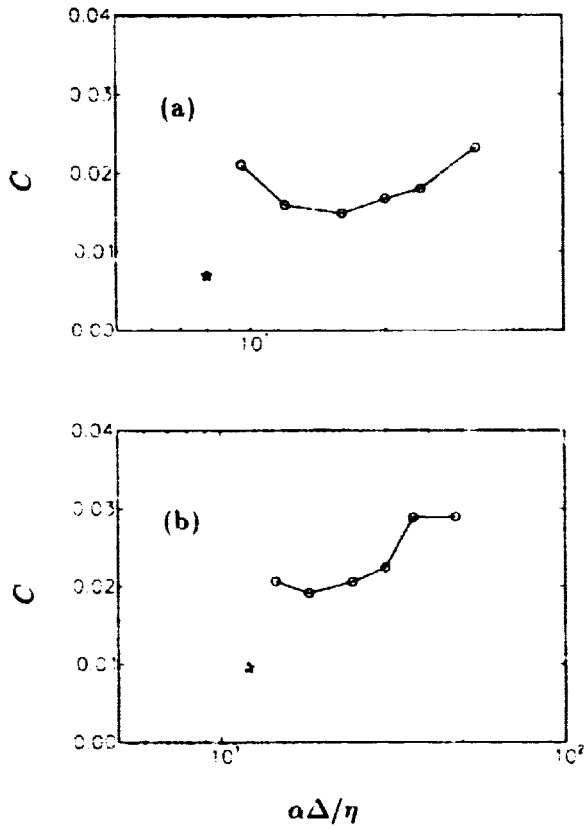

FIGURE 4. o , Coefficients obtained from the dynamic model at different test-filtering scales (from right to left, $\alpha = 4, 3, 2.5, 2, 1.5$ and 1.3). *, Coefficient value obtained from dissipation balance (Eq. 8) at the grid scale (a) Grid-scale is $\Delta = 8\eta$. (b) Grid-scale is $\Delta = 12\eta$.

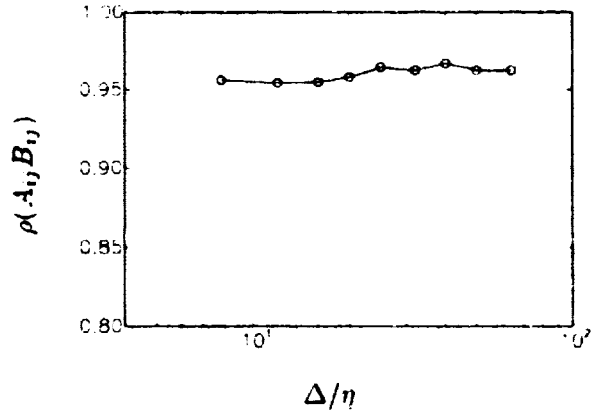

FIGURE 5. Correlation coefficient between the model tensors A_{ij} and B_{ij} measured from filtered DNS as function of filter scale. The correlation coefficient is computed according to $\rho(A, B) = \langle A_{ij} B_{ij} \rangle / \sqrt{\langle A_{ij}^2 \rangle \langle B_{ij}^2 \rangle}$.

To see if the limit $\alpha \to 1$ can be used to advantage in this case, we repeat the *a priori* test of the previous section and compute the dynamic model coefficient at the smaller filter-width ratios of $\alpha = 1.5$ and $\alpha = 1.3$. Figure 4a shows the results for a grid-scale $\Delta = 8\eta$, and 4b for $\Delta = 12\eta$. In both cases, it is apparent that for $\alpha \geq 2$ there is a smooth trend of the dynamic coefficient tending towards the 'true' coefficient as obtained from the dissipation balance. However, for $\alpha < 2$, there is a change in behavior and the coefficient increases again and does not tend towards the expected value as $\alpha \to 1$. While such a result may be specific to present conditions of analysis, it suggests that as the width of the band between grid and test filter becomes small, the procedure can yield unphysical results. For this reason, we do not consider this approach further.

Before proceeding however, we notice from Fig. 4 that for $\alpha > 2$ the approach towards the 'true' coefficient appears to be exponential. This observation will be used in §4.3.

4.2 Solving for two coefficients

Here we return to the case $\alpha = 2$. Instead of assuming that $C(\Delta) = C(2\Delta)$, we investigate the proposal of Moin & Jiménez, (1993) where the least-square-error approach is used to solve for the two coefficients. Upon solving the linear set of equations, one obtains (using, say, volume averaging)

$$C(\Delta) = \frac{\langle A_{ij}L_{ij}\rangle\langle B_{ij}^2\rangle - \langle B_{ij}L_{ij}\rangle\langle A_{ij}B_{ij}\rangle}{\langle A_{ij}^2\rangle\langle B_{ij}^2\rangle - \langle A_{ij}B_{ij}\rangle^2}, \tag{9a}$$

$$C(2\Delta) = \frac{\langle A_{ij}L_{ij}\rangle\langle A_{ij}B_{ij}\rangle - \langle B_{ij}L_{ij}\rangle\langle A_{ij}^2\rangle}{\langle A_{ij}^2\rangle\langle B_{ij}^2\rangle - \langle A_{ij}B_{ij}\rangle^2}. \tag{9b}$$

The averages can be evaluated from the DNS (as in §3) at different scales, and the coefficients computed from the above expressions. However, the results appear to be unphysical: both $C(\Delta)$ and $C(2\Delta)$ were found to be negative, with large scatter from one scale to another.

The cause for this problem can be traced to the fact that the two tensors A_{ij} and B_{ij} (or $\alpha^2|\hat{\tilde{S}}|\hat{\tilde{S}}_{ij}$ and $|\widehat{\tilde{S}|\tilde{S}}_{ij}$) are strongly correlated. The correlation coefficient between them is evaluated from the DNS and plotted in Fig. 5, for different scales. Due to the strong tensor-alignment, the system of equations is ill conditioned. It is interesting to point out that in the standard dynamic model, the coefficient is determined mainly by the fact that both tensors have significantly different magnitudes (due to the coefficient α^2). However, to use additional (directional) information from the Germano identity, at least in the context of the Smagorinsky model, appears not feasible.

4.3 The bi-dynamic model

This version of the dynamic model is motivated by our observation that the model provides the coefficient at the test-filter level $\alpha\Delta$. While this suggested taking the

limit $\alpha \to 1$, it was shown in §4.1 that then the Germano identity relied on less and less modes between test and grid filter, modes that are often most affected by numerical errors. Another alternative formulation is to compute coefficients from two different test filters and use these to extrapolate to the grid scale. Briefly, one assumes that the dynamic coefficient obtained by the traditional method (with M_{ij} given by Eq. 2) is a smooth function of the test-to-grid filter ratio α. In fact, noting the exponential behavior in Figs. 4 for $\alpha > 2$, it is more convenient to write that C is a smooth function of β, where $\alpha\Delta = 2^\beta\Delta$. The usual case $\alpha = 2$ corresponds to $\beta = 1$, while the limit $\alpha \to 1$ is obtained as $\beta \to 0$. Let us therefore denote the coefficient obtained from the traditional method as $C(\beta)$. Next, we expand $C(\beta)$ in Taylor series around $\beta = 1$,

$$C(\beta) = C(\beta = 1) + \frac{dC}{d\beta}|_1(\beta - 1). \tag{10}$$

To evaluate $dC/d\beta$ we introduce a secondary test-filter at scale, say, 4Δ ($\beta = 2$), evaluate the corresponding coefficient $C(\beta = 2)$, and compute the coefficient derivative using one-sided finite-difference, $(dC/d\beta)|_1 \simeq C(2) - C(1)$. The information employed has been obtained at and above scale 2Δ, where according to the results of §4.1 robust results can be expected. Since we are interested in the limit $\beta \to 0$, we now propose to simply evaluate Eq. 10 at $\beta = 0$. The resulting coefficient can be written as follows:

$$C = 2\frac{\langle M_{ij}L_{ij}\rangle}{\langle M_{ij}M_{ij}\rangle} - \frac{\langle N_{ij}F_{ij}\rangle}{\langle N_{ij}N_{ij}\rangle}, \tag{11}$$

where the tensors F_{ij} and N_{ij} are defined exactly as the tensors L_{ij} and M_{ij} respectively, only using a test-filter scale equal to 4Δ instead of 2Δ.

This basic formulation is first tested *a priori*: The DNS data is filtered at an additional test-filter scale to compute F_{ij} and N_{ij}. The coefficient C is evaluated according to Eq. 11 using volume averaging, and the analysis is repeated at several grid-scales Δ. Figure 6 shows the results. As can be seen, the 'bi-dynamic' model is very noisy since it is based on extrapolation. Nevertheless, the procedure does improve the prediction of the standard dynamic model. Importantly, this approach preserves the basic foundation of the dynamic model which only uses information from the resolved scales, instead of relying on equilibrium arguments to calibrate the coefficient and its dependence on scale.

The approach is implemented in LES of forced isotropic turbulence on 32^3 modes. The code and methodology is the same as that described in Meneveau *et al.* (1996), but using volume averaging. The primary and secondary test-filtering are performed using cutoff filters at scales 2Δ and 4Δ, and 14 simulations are run with various viscosities to vary the mean mesh Reynolds number. The results are shown in Fig. 7, where the volume averaged terms $C(1) = \langle LM\rangle / \langle MM\rangle$, $C(2) = \langle FN\rangle / \langle NN\rangle$ and the extrapolated result $C(0) = 2\langle LM\rangle / \langle MM\rangle - \langle FN\rangle / \langle NN\rangle$ are shown. The latter coefficient is used in the subgrid model. As can be seen, the results appear to display the correct trend, although some features are noteworthy: At

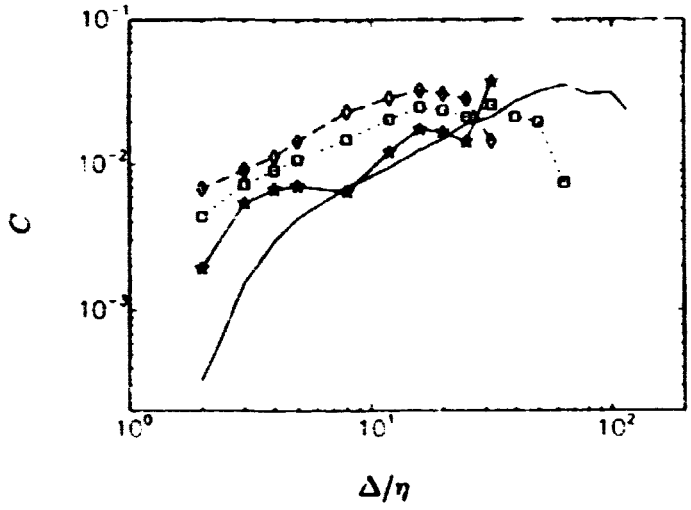

FIGURE 6. *A priori* test of extrapolation procedure, based on DNS results described in Fig. 2. ——— , 'Real' coefficients from dissipation balance; ◇ and □ , Dynamic coefficients at $\alpha = 4$ and $\alpha = 2$; ⋆, extrapolated values according to Eq. 11.

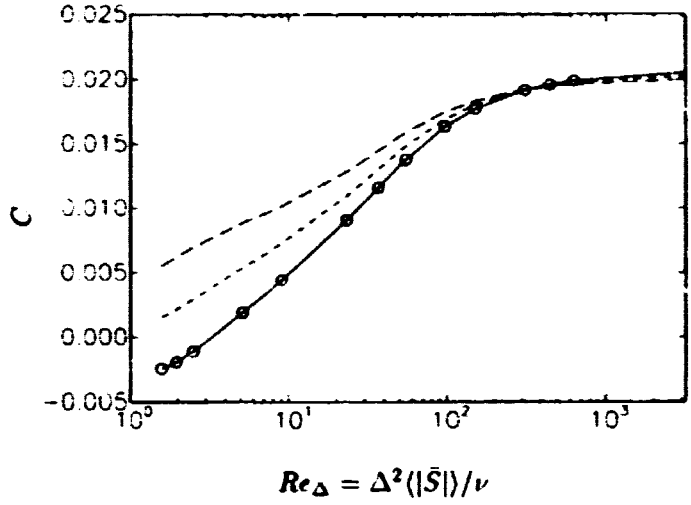

FIGURE 7. Coefficients obtained in LES of forced isotropic turbulence at various Reynolds numbers, using the bi-dynamic model with volume averaging. ——— , Value at scale 4Δ, $\langle FN\rangle / \langle NN\rangle$; ---- , Value at scale 2Δ, $\langle LM\rangle / \langle MM\rangle$; ○ , 'Bi-dynamic' coefficient obtained by extrapolation to scale Δ, $2\langle LM\rangle / \langle MM\rangle - \langle FN\rangle / \langle NN\rangle$. This coefficient is used in the LES. As reference, the Taylor-microscale Reynolds number $R_\lambda = \sqrt{15u'^4/(\nu\epsilon)}$ (where ϵ is the total dissipation) ranges from $R_\lambda = 17$ to $R_\lambda = 2,300$.

large Reynolds numbers, the coefficient value asymptotes to a slightly smaller value than the standard dynamic model. No simple explanation for this trend has been found.

Qualitatively, one expects the model to be quite stable because if, say, $C(\beta = 1)$ falls below its appropriate value while $C(\beta = 2)$ remains fixed, the extrapolated coefficient will drop significantly. This will cause more 'pile-up' of energy near the grid-scale, raising the value of $C(1)$ and raising the extrapolated coefficient. This in turn damps the smallest scales. The opposite occurs if $C(1)$ is initially increased, with excessive damping causing $C(1)$ to diminish. However, the equilibrium point of this version of the model appears to establish itself at a slightly smaller value than that of the traditional approach, even at very large Reynolds numbers where viscosity does not affect the results. Another observation is that at very small Re_Δ, the extrapolation process yielded negative coefficients. This is essentially an extrapolation error. In this application, this error had no impact on the simulation due to the smallness of the SGS term at such low mesh Reynolds numbers.

Finally, an attempt was made to replace the volume averaging with Lagrangian averaging (Meneveau *et al.*, 1996). The motivation is to enable applications of the dynamic model to LES of complex-geometry flows, where no directions of statistical homogeneity exist, but where some averaging must still be performed. In the 'Lagrangian bi-dynamic model', one would compute four variables $\mathcal{I}_{LM}$, $\mathcal{I}_{MM}$, $\mathcal{I}_{FN}$, and $\mathcal{I}_{NN}$, which correspond to the pathline averages of the source terms $L_{ij}M_{ij}$, M_{ij}^2, $F_{ij}N_{ij}$ and N_{ij}^2 respectively. They are obtained by integrating relaxation transport equations with a prescribed relaxation time-scale (Meneveau *et al.*, 1996). To be consistent with this reference, we must choose two relaxation time-scales, $T_1 = 1.5\Delta(\mathcal{I}_{LM}\mathcal{I}_{MM})^{-1/8}$ and $T_2 = 1.5\Delta(\mathcal{I}_{FN}\mathcal{I}_{NN})^{-1/8}$. T_1 is used in the equations for $\mathcal{I}_{LM}$ and $\mathcal{I}_{MM}$, while T_2 is used for $\mathcal{I}_{FN}$ and $\mathcal{I}_{NN}$. With these time-scales it is assured that the numerators $\mathcal{I}_{LM}$ and $\mathcal{I}_{FN}$ never become negative. Then, the coefficient at the grid-scale is computed by extrapolation at every point according to $C(0) = 2\mathcal{I}_{LM}/\mathcal{I}_{MM} - \mathcal{I}_{FN}/\mathcal{I}_{NN}$.

Overall, this approach resulted in several difficulties due to the spatial variability of the local coefficient coupled with the extrapolation procedure. Even though the method guarantees the individual coefficients at the two test-filter levels to be positive, there were many instances in which $\mathcal{I}_{FN}/\mathcal{I}_{NN} > 2\mathcal{I}_{LM}/\mathcal{I}_{MM}$, and therefore the extrapolated coefficient was negative causing instability or unphysical results.

To stabilize the simulation it was necessary to perform an additional pathline averaging of the coefficient $C(0)$ itself, with an appropriately selected relaxation time-scale so that it would not become negative. Denoting the Lagrangian average of the coefficient by $\mathcal{I}_C$, the time-scale chosen was $T_3 = 1.5\Delta[(\mathcal{I}_C\mathcal{I}_{MM})\mathcal{I}_{MM}]^{-1/8}$. On average, this time-scale is of the same order as T_1 and T_2. Results are shown in Fig. 8. The average of the coefficient shows the appropriate trend, although the extrapolated coefficient is not much smaller than the value at scale 2Δ, and at low Re_Δ is considerably higher than the expected values (compare with Fig. 5). Given the extra expense (carrying five relaxation transport equations instead of two) and

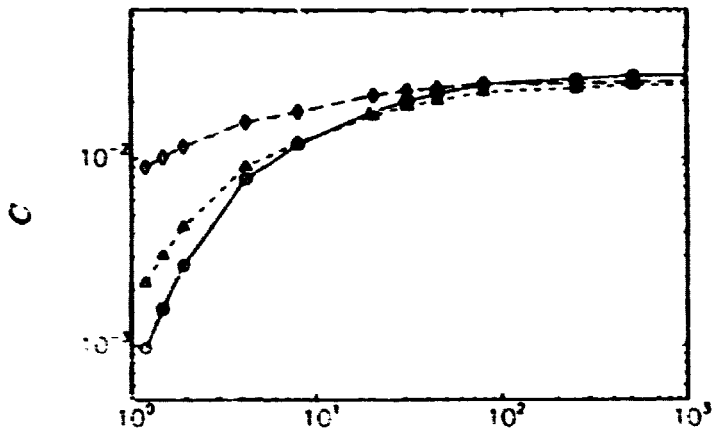

FIGURE 8. Coefficients obtained during LES of forced isotropic turbulence at various Reynolds numbers, using the bi-dynamic model with Lagrangian averaging of numerators and denominators, and additional averaging of extrapolated coefficient. Shown is the volume average of the coefficient (which varies locally). ◇, Value at scale 4Δ, (I_{FN}/I_{NN}); △, Value at scale 2Δ, (I_{LM}/I_{MM}). ○, Mean 'bi-dynamic coefficient' obtained by extrapolation to scale Δ.

the small improvement, this approach does not seem to constitute a method of choice.

4.4 Using non-dynamic estimates for scale-dependency

A more robust method is to explicitly build scale-dependence into the dynamic model. This is accomplished by rewriting Eq. 1 (for $\alpha = 2$) as follows

$$L_{ij} = C(\Delta)\left(\frac{C(2\Delta)}{C(\Delta)}A_{ij} - \hat{B}_{ij}\right), \tag{12}$$

and solve for $C(\Delta)$ as in Eq. 2, but with M_{ij} given by

$$M_{ij} = f(\Delta)A_{ij} - B_{ij}, \tag{13}$$

where

$$f(\Delta) = \frac{C(2\Delta)}{C(\Delta)}.$$

The idea is to solve for the coefficient $C(\Delta)$ but to use prior knowledge about the possible scale dependence to evaluate the function $f(\Delta)$. In the present case of approaching the viscous range, this function depends on the dimensionless parameters Δ/η or Re_Δ. As mentioned previously, the latter case is more convenient during LES since it is based on the strain-rate magnitude, which may be evaluated locally.

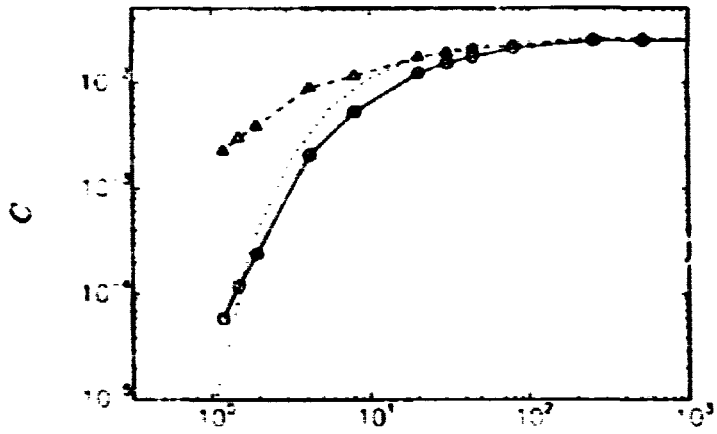

FIGURE 9. Coefficients obtained in LES of forced isotropic turbulence, using the Lagrangian dynamic model in which scale dependence is incorporated non-dynamically. Shown are the mean values of the coefficients. Average mesh Reynolds number is varied systematically by changing ν. Δ , mean coefficient using standard formulation. Eq. 2 and 2a; o , modified dynamic model, in which M_{ij} is given by Eq. 11; ---- , prediction based on Pao spectrum (Eq. 7).

Using Eq. 7, we evaluate the ratio $C(2\Delta)/C(\Delta)$, which can be fitted quite well by the following expression:

$$f(Re_\Delta) = 10^{-3.23|Re_{2\Delta}^{-0.92} - Re_\Delta^{-0.92}|}, \tag{14}$$

where $Re_{2\Delta} = 4\Delta^2|\tilde{S}|/\nu$. When the mesh Reynolds number is evaluated based on the local strain-rate magnitude, it may locally approach zero. Then Eq. 14 diverges, which can cause numerical difficulties. Thus, the expression is clipped at $f(Re_\Delta) = \max[f; Re_\Delta), 100]$. This approach was tested *a priori* and gave good results in the sense that the coefficient obtained by this modified method is indeed smaller than the value that would have been obtained by assuming $C(\Delta) = C(2\Delta)$.

The approach was then implemented in LES of forced isotropic turbulence on 32^3 modes using the Lagrangian method of averaging (Meneveau *et al.*, 1996), accumulating two variables I_{LM} and I_{MM} instead of five as in §4.3. The code and methodology was the same as that described in the above reference, except for the definition of M_{ij}. The local values of M_{ij} were computed from Eq. 13, and the local mesh Reynolds number Re_Δ was based on the local strain-rate magnitude. In order to span a significant range of Re_Δ, 14 simulations with different values of ν were carried out. For comparison, simulations were also done with the standard definition of M_{ij}, i.e. assuming that $C(\Delta) = C(2\Delta)$. Results are shown in Fig. 9 as function of the average value of the cell Reynolds number. Each symbol represents the result of a simulation that was run to a statistically stationary state. For comparison, the

dotted line shows the theoretical prediction of Eq. 7. As can be seen, the approach provides improved prediction of the coefficient compared to the standard dynamic model. As stated before, the difference in coefficient had no appreciable effect on the resolved scales or their energy spectrum.

This approach provides robust predictions of the coefficient for this case (in the viscous range), and is very easy to implement. However, it requires input based on theoretical arguments. It can thus only be applied to cases in which one knows *a priori* the dependence of the ratio of coefficient on scale. Therefore, this approach is not entirely dynamic, in the sense that important information about model coefficients must be specified and is not determined during the simulation.

5. Conclusions

The dynamic Smagorinsky model has been examined in a case where it is known *a priori* that the coefficient depends on scale, namely in the viscous range. Theoretical arguments were reviewed giving the coefficient's expected dependence on scale or on mesh Reynolds number. *A priori* tests using well-resolved DNS data revealed an important property of the standard dynamic model as applied to such a case: The method gives the coefficient corresponding to the test-filter scale instead of the grid-scale.

Several possible reformulations of the dynamic model were examined and/or tested in LES of isotropic turbulence. In the first, the limit $\alpha \to 1$ was considered. Using *a priori* tests at test-filter scales near the grid scale ($\alpha = 1.5$ and 1.3), it was shown that unphysical behavior can result. This limit is also expected to be susceptible to numerical errors. Another proposal was studied in which the Germano identity is used to solve for two unknown coefficients $C(\Delta)$ and $C(2\Delta)$ in the least-square-error sense. For implementations with the Smagorinsky model, this procedure was shown to be ill-conditioned essentially because the eigenvectors of the two basis tensors $|\hat{\bar{S}}|\hat{\bar{S}}_{ij}$ and $|\widehat{\bar{S}}|\widehat{\bar{S}}_{ij}$ are almost 'co-linear' (their correlation coefficient is about $\rho \simeq 0.96$).

A new procedure, the bi-dynamic model, was proposed and tested. It is based on extrapolating coefficients obtained at two test-filters. When implemented with volume averaging, the method gave fair results. Some complications arose when the method was coupled with Lagrangian averaging. We conclude that while the idea of using more than one test-filter scale to sample the resolved field in more detail appears to be promising in principle, in the present application the added complications outweigh the benefits. Finally, we tested a modified formulation in which one solves for a single coefficient at the grid-scale but must prescribe the ratio of coefficients at test and grid scales non-dynamically. This method proved quite practical, and it gave good results. However, it is not completely dynamic since prior theoretical information about scale dependence must be employed (a similar approach was employed to account for grid anisotropy in Scotti *et al.* in this volume).

Acknowledgments

This work profited from fruitful discussions with Prof. P. Moin. The financial support of CTR and ONR (N00014-92-J-1109, monitored by Dr. P. Purtell) is gratefully acknowledged.

REFERENCES

BARDINA, J., FERZIGER, J. H., & REYNOLDS, W. C. 1980 Improved subgrid scale models for large eddy simulation. *AIAA-80-1357*.

LILLY, D. K. 1967 The representation of small-scale turbulence in numerical simulation experiments. In *Proc. IBM Scientific Computing Symposium on Environmental Sciences*.

LIU, S., MENEVEAU, C., & KATZ, J. 1994 On the properties of similarity subgrid-scale models as deduced from measurements in a turbulent jet. *J. Fluid Mech.* **275**, 83-119.

LIU, S., MENEVEAU, C., & KATZ, J. 1995 Experimental study of similarity subgrid-scale models of turbulence in the far-field of a jet. *Appl. Sci. Res.* **54**, 177.

LUND, T. S. & ROGERS, M. M. 1994 An improved measure of strain state probability in turbulent flows. *Phys. Fluids.* **6**, 1838-1847.

MCMILLAN, O. J. & FERZIGER, J. 1979 Direct testing of subgrid-scale models. *AIAA-79-0072*.

MENEVEAU, C., LUND, T. S., & CABOT, W. H. 1996 A Lagrangian dynamic subgrid-scale model of turbulence. *J. Fluid Mech.* **319**, 353.

MOIN, P. & JIMÉNEZ, J. 1993 Large Eddy Simulation of Complex Turbulent Flows. *AIAA-93-3099*.

VOKE, P. R. 1996 Subgrid-scale modeling at low mesh Reynolds number. *Theor. Comp. Fluid Dyn.* **8**, 131-143.

ROGALLO, R. S. 1981 Numerical experiments in homogeneous turbulence. NASA Tech. Memo. 81315, NASA Ames Research Center.

ZANG, Y., STREET, R. L., & KOSEFF, J. 1993 A dynamic mixed subgrid-scale model and its application to turbulent recirculating flows. *Phys. Fluids A.* **5**, 3186-3196.

NEXT
DOCUMENT

The incremental unknowns–a multilevel scheme for the simulation of turbulent channel flows

By M. Chen[1], H. Choi[2], T. Dubois[3], J. Shen[1] AND R. Temam[4]

In numerical simulation of complex flows, it is important to identify different length scales of the flow and treat them differently. In this report, we introduce a new multilevel scheme for simulating turbulent channel flows. Two different versions of the scheme, namely the spectral and finite difference versions, are presented. The spectral version of the scheme is based on a spectral-Galerkin formulation which provides a natural decomposition of the flow into small and large wavelength parts, and which leads to linear systems that can be solved with quasi-optimal computational complexity. In the finite difference version, the "Incremental Unknown" (IU) is used to separate the length scales. Preliminary numerical results indicate that the scheme is well suited for turbulence computations and provides results which are comparable to that by Direct Numerical Simulation (DNS) but with significantly less CPU time.

1. Motivation

The numerical simulation of turbulent flows is an extremely challenging task for both the numerical analysts and computational fluid dynamicists. The computing power required to resolve the enormous number of degrees of freedom and their nonlinear interactions involved in a turbulent flow is often near or beyond reach of the current computer capacity so that conventional numerical schemes are often impractical for turbulence simulations.

The aim of this paper is to introduce a new multilevel scheme which is based on a differentiated treatment for small and large wavelength parts. It is well known in turbulence theory that the large number of small wavelengths only carry a small part of the total kinetic energy of the flow, however, the effect of their nonlinear interactions with large wavelengths over a long term integration can not be neglected and must be adequately resolved. Nevertheless, the small wavelength part, especially their nonlinear interactions, do not need to be represented in the same accuracy as the large wavelength part. Our multilevel scheme is specially designed such that it would produce results comparable to that by DNS but at significantly less cost so that one can simulate more complicated flows with limited capability of

1 Department of Mathematics, Penn State University, University Park, PA 16802
2 Department of Mechanical Engineering, Seoul National University, Seoul 151-742, Korea
3 Lab. de Mathématiques Appliquées, Univ. Blaise Pascal & CNRS, 63177 Aubière, France
4 Lab. d'Analyse Numérique, Université de Paris-Sud, 91405 Orsay, France; and Institute of Scientific Computing and Applied Mathematics, Indiana University, Bloomington, IN 47405

the computer. The method can be applied to a class of dissipative equations and can be combined with a large number of existing numerical methods.

The method starts with separating the length scales of the solution u as

$$u = f + g + r$$

where f is the large length scale, g is the intermediate length scale, and r is the small scale. Then the different scales of the solution are treated differently, which could involve (a) neglecting some higher-order terms involving the small scales, (b) updating small scales with lager time interval. The effect of these further approximations would, if done correctly, reduce the CPU time for each time step, improve the stability (the CFL condition will be only related to the large wavelengths), and allow larger time steps.

There are two ways to look at this method. One is that we neglect some effect of the small scale terms. Another way is we think that large scale approximation is not enough, so we take into account the effect of small scale terms in an efficient way instead of simply adding more mesh points.

This method has been applied to the simulation of 2D and 3D forced homogeneous turbulence (see Jauberteau & Temam 1995a, 1995b, 1996 and the references therein). In the 3D case, it has been shown that the main statistical properties of homogeneous turbulence is well predicted with multilevel schemes. Indeed, while a saving in CPU time of 50-75% versus a classical Galerkin method is obtained, the energy and enstrophy spectra as well as the high-order moments of the velocity and its derivatives are accurately computed. The comparison of these results has been done with the results of direct simulations.

In the case of homogeneous turbulence, when Fourier expansion of the velocity is used, the separation of the flow into large and small scales is trivial. However, this is not obvious for the channel flow problem because of the no-slip boundary conditions at the walls. In particular, the popular spectral-tau (Gottlieb & Orszag 1977) method is not suitable for this purpose. We shall use the spectral-Galerkin method developed by Shen (1994, 1995) for the non-homogeneous direction. This spectral-Galerkin formulation not only provides a natural decomposition of the flow into small and large wavelength parts, but also leads to linear systems that can be solved with quasi-optimal computational complexity.

In the finite difference case, we will use the IU's developed by Chen & Temam (1991). The IU method has been used for steady equations, and the result is similar to preconditioning the associated matrix. The scheme was shown theoretically convergent and has an improved efficiency (Chen & Temam 1993). Here for the first time, the IU method is applied to unsteady problems.

This report is an interim report: more detailed results using the new scheme for the turbulent channel flows will be reported later.

2. Incremental unknowns in the spectral case

2.1 Formulation of the equations

We consider the Navier-Stokes equations

$$\frac{\partial \mathbf{u}}{\partial t} - \nu \Delta \mathbf{u} + (\mathbf{u} \cdot \nabla)\mathbf{u} + \frac{1}{\rho}\nabla P = 0, \tag{2.1}$$

$$\operatorname{div} \mathbf{u} = 0, \tag{2.2}$$

in a channel $\Omega = (0, L_x) \times (-1, 1) \times (0, L_z)$ with the boundary conditions: $\mathbf{u} = (u, v, w)$ is periodic in x and z, and no slip on the walls. For this channel flow, we assume that the pressure P takes the form $P = \hat{P} + K_P\, x$, where $\hat{P}$ is periodic in directions x and z and K_P is a given constant.

Following Kim, Moin & Moser (1987), we set

$$\begin{aligned}
\Lambda &= (\mathbf{u} \cdot \nabla)\mathbf{u} = (\Lambda_x, \Lambda_y, \Lambda_z), \\
f &= \frac{\partial u}{\partial x} + \frac{\partial w}{\partial z}, \\
g &= \frac{\partial u}{\partial z} - \frac{\partial w}{\partial x}, \\
h_v(\mathbf{u}, \mathbf{u}) &= \frac{\partial}{\partial x}\left(\frac{\partial \Lambda_x}{\partial y} - \frac{\partial \Lambda_y}{\partial x}\right) - \frac{\partial}{\partial z}\left(\frac{\partial \Lambda_y}{\partial z} - \frac{\partial \Lambda_z}{\partial y}\right), \\
h_g(\mathbf{u}, \mathbf{u}) &= -\left(\frac{\partial \Lambda_x}{\partial z} - \frac{\partial \Lambda_z}{\partial x}\right) = -(\mathbf{u} \cdot \nabla)g + g\,\frac{\partial v}{\partial y} + \frac{\partial v}{\partial x}\,\frac{\partial w}{\partial y} - \frac{\partial v}{\partial z}\,\frac{\partial u}{\partial y},
\end{aligned} \tag{2.3}$$

then, (2.1)-(2.2) are equivalent to the following equations (cf. Kim *et al.* 1987):

$$\begin{aligned}
&\frac{\partial}{\partial t}\Delta v - \nu \Delta^2 v = h_v(\mathbf{u}, \mathbf{u}), \\
&\frac{\partial g}{\partial t} - \nu \Delta g = h_g(\mathbf{u}, \mathbf{u}), \\
&f + \frac{\partial v}{\partial y} = 0.
\end{aligned} \tag{2.4}$$

From the boundary conditions of $\mathbf{u}$ and the continuity equation (2.2), we deduce boundary conditions for v and g:

$$v(x, \pm 1, z, t) = \frac{\partial}{\partial y} v(x, \pm 1, z, t) = 0,$$

$$g(x, \pm 1, z, t) = 0.$$

We emphasize that $h_v(\cdot, \cdot)$ and $h_g(\cdot, \cdot)$ are indeed bilinear forms since they are derived from the original bilinear form by linear differential operations.

Writing the Fourier expansion in directions x and z for $\mathbf{u}$

$$\mathbf{u}(\mathbf{x},t) = \sum_{\mathbf{k}\in Z^2} \hat{\mathbf{u}}_{\mathbf{k}}(y,t)e^{i\left(k_x\frac{2\pi}{L_x}x + k_z\frac{2\pi}{L_z}z\right)},\quad \mathbf{k} = (k_x,k_z),$$

where $\hat{\mathbf{u}}_{\mathbf{k}} = (\hat{u}_{\mathbf{k}}, \hat{v}_{\mathbf{k}}, \hat{w}_{\mathbf{k}})$, and similarly for f, g and h_v, h_g, we derive from (2.4) that

$$\begin{aligned} &\frac{\partial}{\partial t}(k^2 - \frac{\partial^2}{\partial y^2})\hat{v}_{\mathbf{k}} + \nu\left(k^4 - 2k^2\frac{\partial^2}{\partial y^2} + \frac{\partial^4}{\partial y^4}\right)\hat{v}_{\mathbf{k}} = \hat{h}_{v,\mathbf{k}}(\mathbf{u},\mathbf{u}),\\ &\hat{v}_{\mathbf{k}}(\pm 1) = \frac{\partial \hat{v}_{\mathbf{k}}}{\partial y}(\pm 1) = 0, \end{aligned} \tag{2.5}$$

and

$$\begin{aligned} &\frac{\partial \hat{g}_{\mathbf{k}}}{\partial t} + \nu(k^2 - \frac{\partial^2}{\partial y^2})\hat{g}_{\mathbf{k}} = \hat{h}_{g,\mathbf{k}}(\mathbf{u},\mathbf{u}),\\ &\hat{g}_{\mathbf{k}}(\pm 1) = 0, \end{aligned} \tag{2.6}$$

where $k^2 = \left(\frac{2\pi}{L_x}\right)^2 k_x^2 + \left(\frac{2\pi}{L_z}\right)^2 k_z^2$.

From the equations relating the velocity components u and w to f and g in (2.3), we derive

$$\begin{aligned} &ik_x\frac{2\pi}{L_x}\hat{u}_{\mathbf{k}} + ik_z\frac{2\pi}{L_z}\hat{w}_{\mathbf{k}} = \hat{f}_{\mathbf{k}},\\ &ik_z\frac{2\pi}{L_z}\hat{u}_{\mathbf{k}} - ik_x\frac{2\pi}{L_x}\hat{w}_{\mathbf{k}} = \hat{g}_{\mathbf{k}}, \end{aligned} \qquad \text{for all } (k_x,k_z)\neq(0,0). \tag{2.7}$$

For $(k_x,k_z)\neq(0,0)$, the relations (2.7) can be used to determine $\hat{u}_{\mathbf{k}}(y,t)$ and $\hat{w}_{\mathbf{k}}(y,t)$ in terms of $\hat{f}_{\mathbf{k}}(y,t)$ and $\hat{g}_{\mathbf{k}}(y,t)$. Hence, to complete the system, we still need additional relations for $\hat{u}_0(y,t)$ and $\hat{w}_0(y,t)$. To this end, we integrate the first and last components of the Navier-Stokes equations with respect to x and z to obtain

$$\begin{aligned} &\frac{\partial \hat{u}_0}{\partial t} - \nu\frac{\partial^2 \hat{u}_0}{\partial y^2} + \frac{1}{L_xL_z}\int_0^{L_x}dx\int_0^{L_z} v(\mathbf{x})\frac{\partial u}{\partial y}(\mathbf{x})dz + K_P = 0,\\ &\frac{\partial \hat{w}_0}{\partial t} - \nu\frac{\partial^2 \hat{w}_0}{\partial y^2} + \frac{1}{L_xL_z}\int_0^{L_x}dx\int_0^{L_z} v(\mathbf{x})\frac{\partial w}{\partial y}(\mathbf{x})dz = 0. \end{aligned} \tag{2.8}$$

The time discretization of (2.5), (2.6), and (2.8) is achieved by using a semi-implicit scheme with the second-order Crank-Nicolson for the linear terms and a third order explicit Runge-Kutta scheme for the nonlinear terms. Hence, we only have to solve a sequence of one-dimensional second-order equations for $\hat{g}_{\mathbf{k}}(y,t)$ and fourth-order equations for $\hat{v}_{\mathbf{k}}(y,t)$.

Kim, Moin & Moser (1987) applied a Chebyshev-tau approximation to the y–direction. Since the direct application of tau method to fourth-order equations is unstable (Gottlieb & Orszag, 1977), they proposed a time splitting scheme which consists of solving several successive second-order problems to enforce the boundary conditions on v by using a technique similar to the influence matrix method.

Based on a sequence of recent work by Shen (1994, 1995, 1996), we present below a spectral-Galerkin scheme for these second-order and fourth-order equations. Using this method, the system (2.5)-(2.6) can be directly solved.

2.2 A spectral-Galerkin approximation of the Kim-Moin-Moser formulation

A Fourier-Galerkin approximation in the x and z directions is first applied to the problems (2.5) and (2.6), i.e. we look for

$$\boldsymbol{u}_N(\boldsymbol{x},t) = \sum_{\boldsymbol{k}\in S_N} \hat{\boldsymbol{u}}_{\boldsymbol{k}}(y,t)e^{i\left(k_x\frac{2\pi}{L_x}x + k_z\frac{2\pi}{L_z}z\right)}, \tag{2.9}$$

(where $N = (N_x, N_z)$ and $S_N = \left\{\boldsymbol{k}\in\mathcal{Z}^2/(k_x,k_z)\in\left[1-\frac{N_x}{2},\frac{N_x}{2}\right]\times\left[1-\frac{N_z}{2},\frac{N_z}{2}\right]\right\}$) as a solution of the system of

$$\begin{aligned}&\frac{\partial}{\partial t}(k^2-\frac{\partial^2}{\partial y^2})\hat{v}_{\boldsymbol{k}} + \nu\left(k^4 - 2k^2\frac{\partial^2}{\partial y^2} + \frac{\partial^4}{\partial y^4}\right)\hat{v}_{\boldsymbol{k}} = \hat{h}_{v,\boldsymbol{k}}(\boldsymbol{u}_N,\boldsymbol{u}_N),\\ &\hat{v}_{\boldsymbol{k}}(\pm1) = \frac{\partial\hat{v}_{\boldsymbol{k}}}{\partial y}(\pm1) = 0,\end{aligned} \tag{2.10}$$

and

$$\begin{aligned}&\frac{\partial\hat{g}_{\boldsymbol{k}}}{\partial t} + \nu(k^2-\frac{\partial^2}{\partial y^2})\hat{g}_{\boldsymbol{k}} = \hat{h}_{g,\boldsymbol{k}}(\boldsymbol{u}_N,\boldsymbol{u}_N),\\ &\hat{g}_{\boldsymbol{k}}(\pm1) = 0,\end{aligned} \tag{2.11}$$

for all $\boldsymbol{k}\in S_N$.

We now describe Galerkin approximations of (2.10) and (2.11) in the y–direction. Let us denote

- P_M: the space of polynomials of degree less than or equal to M,
- $V_M = \text{span}\{\varphi(y)\in P_M : \varphi(\pm1) = 0\}$,
- $W_M = \text{span}\{\varphi(y)\in P_M : \varphi(\pm1) = 0,\ \frac{\partial\varphi}{\partial y}(\pm1) = 0\}$.

Let $p_j(y)$ be either the Legendre or Chebyshev polynomial of degree j, then

$$V_M = \text{span}\{\phi_0,\phi_1,\ldots,\phi_{M-2}\}$$

with $\phi_j(y) = p_j(y) - p_{j+2}(y)$. Moreover, following Shen (1996), we can determine (a_j,b_j) such that

$$\psi_j(y) = p_j(y) + a_jp_{j+2}(y) + b_jp_{j+4}(y)$$

satisfies the boundary conditions $\psi_j(\pm1) = \frac{\partial\psi_j}{\partial y}(\pm1) = 0$, i.e. $\psi_j\in W_M$. Therefore

$$W_M = \text{span}\{\psi_0,\psi_1,\ldots,\psi_{M-4}\}.$$

The spectral-Galerkin scheme in the y–direction for (2.10) and (2.11) is to find $v_{N,M}(\boldsymbol{x},t)$ such that $\hat{v}_{\boldsymbol{k},M}(y,t)\in W_M$, and $u_{N,M}(\boldsymbol{x},t)$ (similarly for w and g) such that $\hat{u}_{\boldsymbol{k},M}(y,t)\in V_M$, for all $\boldsymbol{k}\in S_N$, such that

$$\begin{aligned}&\frac{\partial}{\partial t}\left((k^2-\frac{\partial^2}{\partial y^2})\hat{v}_{\boldsymbol{k}},\psi_j\right)_\omega + \nu\left(\left(k^4 - 2k^2\frac{\partial^2}{\partial y^2} + \frac{\partial^4}{\partial y^4}\right)\hat{v}_{\boldsymbol{k}},\psi_j\right)_\omega\\ &\qquad = \left(\hat{h}_{v,\boldsymbol{k}}(\boldsymbol{u}_{N,M},\boldsymbol{u}_{N,M}),\psi_j\right)_\omega\end{aligned} \tag{2.12}$$

for all $j = 0,\ldots,M-4$,

and

$$\frac{\partial}{\partial t}(\hat{g}_k, \phi_j)_\omega + \nu\left((k^2 - \frac{\partial^2}{\partial y^2})\hat{g}_k, \phi_j\right)_\omega = \left(\hat{h}_{g,k}(\mathbf{u}_{N,M}, \mathbf{u}_{N,M}), \phi_j\right)_\omega, \quad (2.13)$$

for all $j = 0, \ldots, M-2$,

where $(\varphi, \psi)_\omega = \int_{-1}^{1} \varphi(y)\,\psi(y)\,\omega\,dy$ with $\omega(y) \equiv 1$ in the Legendre case and $\omega(y) = (1-y^2)^{-\frac{1}{2}}$ in the Chebyshev case.

It is easy to see that in (2.13) the mass matrix $\mathcal{M}$ with entries $m_{jl} = (\phi_l, \phi_j)_\omega$ is a sparse symmetric matrix with three nonzero diagonals, and that the stiffness matrix $\mathcal{S}$ with entries $s_{jl} = (\frac{\partial^2}{\partial y^2}\phi_l, \phi_j)_\omega$ is diagonal in the Legendre case, and is a special upper triangular matrix in the Chebyshev case such that the linear system $(\alpha\mathcal{M} + \mathcal{S})\boldsymbol{x} = \boldsymbol{b}$ associated with (2.13) can be solved in $O(M)$ operations (Shen 1995). Similarly, the linear systems in (2.12) can be solved in $O(M)$ operations, see Shen (1994, 1995). We emphasize that the above spectral-Galerkin scheme is superior, in both efficiency and accuracy, to the tau-method used in Kim, Moin & Moser (1987), and is, in particular, suitable for multilevel decomposition.

The Legendre-Galerkin method has been implemented and tested. In this code, the pseudo-spectral computation of the nonlinear terms is done at the Chebyshev-Gauss-Lobatto points in the normal direction (see Shen 1996). A $128 \times 129 \times 128$ simulation at the Reynolds number of 180 has been conducted. The statistics have been compared to the one presented by Kim, Moin & Moser (1987).

2.3 A multilevel spectral-Galerkin scheme

We now describe a multilevel scheme for the time integration of (2.12) and (2.13). For the sake of simplicity, we will only present a scheme based on a first-order semi-implicit scheme for the time discretization. However, one can easily generalize it to higher-order semi-implicit scheme.

The basic idea of the multilevel scheme is to decompose the solution into several length scales and treat them differently in order to improve the efficiency and stability of the classical Galerkin approximation. The special basis functions $\{\phi_j, \psi_j\}$ provide a natural decomposition of small and large wavelengths for this purpose. Furthermore, the small and large wavelengths are quasi-orthogonal in the following sense:

$$\begin{aligned}
&(\phi_l, \phi_j)_\omega = 0, \quad \text{for } j \neq l, l \pm 2, \\
&(\frac{\partial^2 \phi_l}{\partial y^2}, \phi_j)_\omega = 0, \quad \text{for } l \neq j \text{ (Legendre case)}, \\
&(\frac{\partial^2 \phi_l}{\partial y^2}, \phi_j)_\omega = 0, \quad \text{for } l < j \text{ or } l + j \text{ odd (Chebyshev case)},
\end{aligned} \quad (2.14)$$

and

$$\begin{aligned}
&(\psi_l, \psi_j)_\omega = 0, \quad \text{for } j \neq l, l \pm 2, l \pm 4,\\
&(\frac{\partial^2 \psi_l}{\partial y^2}, \psi_j)_\omega = 0, \quad \text{for } l \neq j, l \neq j \pm 2,\\
&(\frac{\partial^4 \psi_l}{\partial y^4}, \psi_j)_\omega = 0, \quad \text{for } l \neq j \text{ (Legendre case)},\\
&(\frac{\partial^4 \psi_l}{\partial y^4}, \psi_j)_\omega = 0, \quad \text{for } l < j \text{ or } l + j \text{ odd (Chebyshev case)}.
\end{aligned} \tag{2.15}$$

Given two appropriate cut-off numbers M_p, M_q such that $0 < M_p < M_q < M$, we may decompose $\hat{u}_{\boldsymbol{k},M}(y,t) \in V_M$ as follows

$$\begin{aligned}
\hat{u}_{\boldsymbol{k},M}(y,t) &= \sum_{j=0}^{M-2} \hat{u}_{\boldsymbol{k},j}(t)\phi_j(y)\\
&= \sum_{j=0}^{M_p-2} \hat{u}_{\boldsymbol{k},j}\phi_j(y) + \sum_{j=M_p-1}^{M_q-2} \hat{u}_{\boldsymbol{k},j}\phi_j(y) + \sum_{j=M_q-1}^{M-2} \hat{u}_{\boldsymbol{k},j}\phi_j(y)\\
&= p_u(y,t) + q_u(y,t) + r_u(y,t),
\end{aligned} \tag{2.16}$$

and similarly for $\hat{w}_{\boldsymbol{k},M}(y,t)$ and then for $\hat{g}_{\boldsymbol{k},M}(y,t)$, for all $\boldsymbol{k} \in S_N$. Note that for the sake of simplicity, the dependence of p_u, q_u, and r_u in $\boldsymbol{k}$ is omitted. We may also decompose $\hat{v}_{\boldsymbol{k},M}(y,t) \in W_M$ as

$$\begin{aligned}
\hat{v}_{\boldsymbol{k},M}(y,t) &= \sum_{j=0}^{M-4} \hat{v}_{\boldsymbol{k},j}\psi_j(y)\\
&= \sum_{j=0}^{M_p-4} \hat{v}_{\boldsymbol{k},j}\psi_j(y) + \sum_{j=M_p-3}^{M_q-4} \hat{v}_{\boldsymbol{k},j}\psi_j(y) + \sum_{j=M_q-3}^{M-4} \hat{v}_{\boldsymbol{k},j}\psi_j(y)\\
&= p_v(y,t) + q_v(y,t) + r_v(y,t).
\end{aligned} \tag{2.17}$$

We finally obtain the following decomposition for $\hat{\boldsymbol{u}}_{\boldsymbol{k},M}$:

$$\hat{\boldsymbol{u}}_{\boldsymbol{k},M} = \boldsymbol{p} + \boldsymbol{q} + \boldsymbol{r},$$

where $\boldsymbol{p} = (p_u, p_v, p_w)$ and similarly for $\boldsymbol{q}$ and $\boldsymbol{r}$. The decomposition (2.16) on $\hat{u}_{\boldsymbol{k},M}$ and $\hat{w}_{\boldsymbol{k},M}$ induces a decomposition of $\hat{g}_{\boldsymbol{k},M}$ into

$$\hat{g}_{\boldsymbol{k},M}(y,t) = p_g + q_g + r_g.$$

Then, thanks to (2.15) (resp. (2.14)), we can *approximate* the system (2.12) (resp. (2.13)) in W_{M_p} (resp. V_{M_p}) as follows

$$\begin{aligned}
\frac{\partial}{\partial t}\left((k^2 - \frac{\partial^2}{\partial y^2})p_v, \psi_j\right)_\omega + \nu\left(\left(k^4 - 2k^2\frac{\partial^2}{\partial y^2} + \frac{\partial^4}{\partial y^4}\right)p_v, \psi_j\right)_\omega\\
= (\hat{h}_{v,\boldsymbol{k}}(\boldsymbol{p}+\boldsymbol{q}+\boldsymbol{r}, \boldsymbol{p}+\boldsymbol{q}+\boldsymbol{r}), \psi_j)_\omega,\\
\text{for } j = 0, \ldots, M_p - 4.
\end{aligned} \tag{2.18}$$

$$\frac{\partial}{\partial t}(p_g, \phi_j)_\omega + \nu k^2 (p_g, \phi_j)_\omega - \nu \left(\frac{\partial^2 p_g}{\partial y^2}, \phi_j\right)_\omega = (\hat{h}_{g,k}(p+q+r, p+q+r), \phi_j)_\omega, \quad \text{for } j = 0, \ldots, M_p - 2, \tag{2.19}$$

and in W_{M_q} (resp. V_{M_q}) as follows

$$\frac{\partial}{\partial t}\left((k^2 - \frac{\partial^2}{\partial y^2})(p_v + q_v), \psi_j\right)_\omega + \nu\left(\left(k^4 - 2k^2\frac{\partial^2}{\partial y^2} + \frac{\partial^4}{\partial y^4}\right)(p_v + q_v), \psi_j\right)_\omega = (\hat{h}_{v,k}(p+q+r, p+q+r), \psi_j)_\omega, \quad \text{for } j = 0, \ldots, M_q - 4. \tag{2.20}$$

$$\frac{\partial}{\partial t}(p_g + q_g, \phi_j)_\omega + \nu k^2 (p_g + q_g, \phi_j)_\omega - \nu(\frac{\partial^2}{\partial y^2}(p_g + q_g), \phi_j)_\omega = (\hat{h}_{g,k}(p+q+r, p+q+r), \phi_j)_\omega, \quad \text{for } j = 0, \ldots, M_q - 2. \tag{2.21}$$

Note that in (2.18)-(2.19) and (2.20)-(2.21) linear interaction terms coming from $(p_g, \phi_j)_\omega$ (resp. $(q_v, \phi_j)_\omega$) and similarly for r_g (resp. r_v) are neglected. Until numerical tests are performed it is not clear whether or not these terms have to be neglected. However, for the sake of simplicity we do not take them into account in the large or intermediate scale equations.

By projecting (2.12) (resp. (2.13)) onto the space $W_M \backslash W_{M_q}$ (resp. $V_M \backslash V_{M_q}$) we obtain the small scale equation

$$\begin{aligned}\frac{\partial}{\partial t}\left((k^2 - \frac{\partial^2}{\partial y^2})r_v, \psi_j\right)_\omega + \nu\left((k^4 - 2k^2\frac{\partial^2}{\partial y^2} + \frac{\partial^4}{\partial y^4})r_v, \psi_j\right)_\omega \\ = (\hat{h}_{v,k}(p+q, p+q), \psi_j)_\omega \\ - \frac{\partial}{\partial t}\left((k^2 - \frac{\partial^2}{\partial y^2})q_v, \psi_j\right)_\omega - \nu\left((k^4 - 2k^2\frac{\partial^2}{\partial y^2})q_v, \psi_j\right)_\omega, \\ \text{for } j = M_q - 3, \ldots, M - 4.\end{aligned} \tag{2.22}$$

$$\frac{\partial}{\partial t}(r_g, \phi_j)_\omega + \nu k^2 (r_g, \phi_j)_\omega - \nu(\frac{\partial^2 r_g}{\partial y^2}, \phi_j)_\omega = (\hat{h}_{g,k}(p+q, p+q), \phi_j)_\omega - \frac{\partial}{\partial t}(q_g, \phi_j)_\omega - \nu k^2 (q_g, \phi_j)_\omega, \quad \text{for } j = M_q - 1, \ldots, M - 2. \tag{2.23}$$

We note that in (2.22)-(2.23) the nonlinear interaction between the small wavelength part r and the larger wavelength parts $(p+q)$ is neglected.

Since $h_g(\cdot,\cdot)$ is a bilinear form, we can write

$$\begin{aligned}h_g(\varphi+\psi, \varphi+\psi) &= h_g(\varphi,\varphi) + (h_g(\varphi,\psi) + h_g(\psi,\varphi) + h_g(\psi,\psi)) \\ &= h_g(\varphi,\varphi) + h_{g,\text{int}}(\varphi,\psi),\end{aligned}$$

and similarly for $h_r(\cdot,\cdot)$.

We may now define the multilevel scheme based on the approximation (2.18)-(2.23).

Given $U^n_{N,M} = p^n + q^n + r^n$, the approximation of $u_{N,M}(n\Delta t)$, and an integer n_*, we define $U^{n+2n_*}_{N,M} = p^{n+2n_*} + q^{n+2n_*} + r^{n+2n_*}$ by using the following multilevel scheme:

For $j = 0, 1, \ldots, n_* - 1$,

$$\begin{aligned} &k^2(1+\nu k^2\Delta t)(p_v^{n+2j+1}, v_l)_\omega - (1+\nu k^2\Delta t)(\frac{\partial^2}{\partial y^2}p_v^{n+2j+1}, v_l)_\omega \\ &\qquad + \nu\Delta t\left(\frac{\partial^4}{\partial y^4}p_v^{n+2j+1}, v_l\right)_\omega = \left((k^2 - \frac{\partial^2}{\partial y^2})p_v^{n+2j}, v_l\right)_\omega \\ &\qquad + \Delta t(\hat h_v(p^{n+2j}, p^{n+2j}), v_l)_\omega + \Delta t(\hat h_{v,int}(p^n, q^n + r^n), v_l)_\omega, \\ &\qquad\qquad \text{for } l = 0, \ldots, M_p - 4. \end{aligned} \tag{2.24}$$

$$q_v^{n+2j+1} = q_v^{n+2j},$$

$$r_v^{n+2j+1} = r_v^{n+2j} = r_v^n;$$

$$\begin{aligned} &(1+\nu k^2\Delta t)(p_g^{n+2j+1}, o_l)_\omega - \nu\Delta t(\frac{\partial^2}{\partial y^2}p_g^{n+2j+1}, o_l)_\omega = (p_g^{n+2j}, o_l)_\omega \\ &\qquad + \Delta t(\hat h_g(p^{n+2j}, p^{n+2j}), o_l)_\omega + \Delta t(\hat h_{g,int}(p^n, (q+r)^n), o_l)_\omega, \\ &\qquad\qquad \text{for } l = 0, \ldots, M_p - 2. \end{aligned} \tag{2.25}$$

$$q_g^{n+2j+1} = q_g^{n+2j},$$

$$r_g^{n+2j+1} = r_g^{n+2j} = r_g^n;$$

$$\begin{aligned} &k^2(1+\nu k^2\Delta t)((p_v+q_v)^{n+2j+2}, v_l)_\omega - (1+\nu k^2\Delta t)(\frac{\partial^2}{\partial y^2}(p_v+q_v)^{n+2j+2}, v_l)_\omega \\ &+ \nu\Delta t\left(\frac{\partial^4}{\partial y^4}(p_v+q_v)^{n+2j+2}, v_l\right)_\omega = \left((k^2 - \frac{\partial^2}{\partial y^2})(p_v+q_v)^{n+2j+1}, v_l\right)_\omega \\ &\qquad + \Delta t(\hat h_v((p+q)^{n+2j+1}, (p+q)^{n+2j+1}), v_l)_\omega \\ &\qquad + \Delta t(\hat h_{v,int}(p^n + q^n, r^n), v_l)_\omega, \\ &\qquad\qquad \text{for } l = 0, \ldots, M_q - 4. \end{aligned}$$

$$r_v^{n+2j+2} = r_v^{n+2j+1} = r_v^n; \tag{2.26}$$

$$\begin{aligned} &(1+\nu k^2\Delta t)((p_g+q_g)^{n+2j+2}, o_l)_\omega - \nu\Delta t(\frac{\partial^2}{\partial y^2}(p_g+q_g)^{n+2j+2}, o_l)_\omega \\ &\qquad = ((p_g+q_g)^{n+2j+1}, o_l)_\omega \\ &\qquad + \Delta t(\hat h_g((p+q)^{n+2j+1}, p^{n+2j+1}), o_l)_\omega \\ &\qquad + \Delta t(\hat h_{g,int}(p^n + q^n, r^n), o_l)_\omega, \\ &\qquad\qquad \text{for } l = 0, \ldots, M_q - 2. \end{aligned} \tag{2.27}$$

$$r_g^{n+2j+2} = r_g^{n+2j+1} = r_g^n.$$

Once we obtain p^{n+2n_s} and q^{n+2n_s} from above, we compute r^{n+2n_s} as follows

$$\begin{aligned}
&k^2(1+2n_s\nu k^2\Delta t)(r_v^{n+2n_s},\varphi_l)_\omega-(1+2n_s\nu k^2\Delta t)(\frac{\partial^2}{\partial y^2}r_v^{n+2n_s},\varphi_l)_\omega\\
&+2n_s\nu\Delta t\left(\frac{\partial^4}{\partial y^4}r_v^{n+2n_s},\varphi_l\right)_\omega=\left((k^2-\frac{\partial^2}{\partial y^2})r_v^n,\varphi_l\right)_\omega\\
&+2n_s\Delta t(h_v((\boldsymbol{p}+\boldsymbol{q})^{n+2n_s},(\boldsymbol{p}+\boldsymbol{q})^{n+2n_s}),\varphi_l)_\omega\\
&-\left((k^2-\frac{\partial^2}{\partial y^2})(q_v^{n+2n_s}-q_v^n),\varphi_l\right)_\omega\\
&-2n_s\Delta t\left((k^4-2k^2\frac{\partial^2}{\partial y^2})q_v^{n+2n_s},\varphi_l\right)_\omega\\
&\qquad\text{for } l=M_q-3,\ldots,M-4,
\end{aligned}\tag{2.28}$$

and

$$\begin{aligned}
&(1+2n_s\nu k^2\Delta t)(r_g^{n+2n_s},\varphi_l)_\omega-2n_s\nu\Delta t(\frac{\partial^2}{\partial y^2}r_g^{n+2n_s},\varphi_l)_\omega\\
&\qquad=(r_g^{n+2n_s},\varphi_l)_\omega\\
&\qquad+2n_s\Delta t(h_g((\boldsymbol{p}+\boldsymbol{q})^{n+2n_s},(\boldsymbol{p}+\boldsymbol{q})^{n+2n_s}),\varphi_l)_\omega\\
&\qquad-(q_g^{n+2n_s}-q_v^n,\varphi_l)_\omega-2n_sk^2\Delta t(q_g^{n+2n_s},\varphi_l)_\omega\\
&\qquad\qquad\text{for } l=M_q-1,\ldots,M-2.
\end{aligned}\tag{2.29}$$

Note that the computation of the right-hand side of (2.24)-(2.25) (resp. (2.26)-(2.27)) requires only fast Chebyshev transforms (FCT) with $O(M_p log_2(M_p))$ (resp. $O(M_p log_2(M_p))$) operations in the normal direction. The nonlinear interaction terms $h_{v,int}$ and $h_{g,int}$ are computed once at the time iteration $j=n$. Hence, during the $2n_s$ time iterations described above, FCT with $O(Mlog_2(M))$ are required only at $j=n$ and $j=n+2n_s$. Compared to a classical Galerkin (or tau) approximation the multilevel scheme proposed here allows to significantly reduce the CPU time needed for channel flow simulations. In the case of forced homogeneous turbulence, savings of the order of 50-70% have been obtained (see Dubois, Jauberteau & Temam 1995b, 1996).

3. Incremental unknowns in the finite difference case

The main idea of the multilevel scheme is to treat the large and small scales differently in numerical simulation. Therefore, it is important to have an appropriate decomposition of the flow into different length scales. In Section 3.1, we describe a procedure to decompose the solution into large and small scales in finite difference method. To illustrate the method, we start by applying the IU's to the Burger's equation. In Section 3.2, we test the method of separating scales using turbulent channel flow database. In Section 3.3, we suggest an algorithm to implement the scheme for the turbulent channel flow.

3.1 Incremental unknowns on Burger's equation

In this section, we start with the two-level IU's, namely, we decompose the solution u into

$$u = y + z.$$

The second-order IU's in one-dimensional case are defined as in Chen & Temam (1991) by

$$y_{2j} = u_{2j},$$
$$z_{2j+1} = u_{2j+1} - \frac{1}{2}(u_{2j+2} + u_{2j}).$$

Multilevel IU's can be defined recursively. Three-level IU's will be defined in Section 3.2.

Let us consider the Burger's equation,

$$\frac{\partial u}{\partial t} + \frac{\partial}{\partial x}(\frac{u^2}{2}) = \nu \frac{\partial^2 u}{\partial x^2} + \mathcal{X}(x,t), \quad u(0,t) = u(1,t) = 0.$$

When the second order central difference scheme is used for the space derivatives and the explicit Euler is used for the time advancing, the finite difference scheme reads

$$\frac{u_i^{n+1} - u_i^n}{\Delta t} + \frac{1}{4\Delta x}[(u_{i+1}^n)^2 - (u_{i-1}^n)^2] = \frac{\nu}{\Delta x^2}[u_{i+1}^n - 2u_i^n + u_{i-1}^n] + \mathcal{X}(x_i, t^n).$$

Writing y and z components separately, one finds that y satisfies

$$u_{2j+1}^n = z_{2j+1}^n + \frac{1}{2}(y_{2j+2}^n + y_{2j}^n),$$
$$\frac{y_{2j}^{n+1} - y_{2j}^n}{\Delta t} + \frac{1}{4\Delta x}[(u_{2j+1}^n)^2 - (u_{2j-1}^n)^2]$$
$$= \frac{\nu}{\Delta x^2}[u_{2j+1}^n - 2y_{2j}^n + u_{2j-1}^n] + \mathcal{X}(x_{2j}, t^n),$$

and z satisfies

$$\frac{z_{2j+1}^{n+1} - z_{2j+1}^n}{\Delta t} + \frac{1}{2\Delta t}[(y_{2j+2}^{n+1} + y_{2j}^{n+1}) - (y_{2j+2}^n + y_{2j}^n)]$$
$$+ \frac{1}{4\Delta x}[(y_{2j+2}^n)^2 - (y_{2j}^n)^2] = \frac{\nu}{\Delta x^2}[-2z_{2j+1}^n] + \mathcal{X}(x_{2j+1}, t^n).$$

Instead of evaluating z at each time step, we propose to fix z for m steps and then evaluate once to save CPU time and memory. Therefore, as m increases, so does the saving of CPU time. On the other hand, we are also at the risk of losing accuracy as m increases. It is clear that when $m = 0$, the scheme is the same as the original standard method with the fine mesh, while if we never update z and let it be 0, the scheme is simply the original standard method in the coarse mesh and $u = y$.

To illustrate how much savings one could obtain by freezing z systematically, we list in Table 1 the ratio of the work with freezing z m times vs. 0 times, with the assumption that the work per time step per grid point is independent of the mesh size. As an example, if one freezes z for one time step in a three-dimensional problem, the work by using IU's is only 56.25% of that by using the standard finite difference method.

Table 1. Ratio of the work with freezing z m times vs. 0 times

m	0	1	2	3	···	N_t
1-D	1	0.75	0.67	0.625	···	0.50
2-D	1	0.625	0.5	0.44	···	0.25
3-D	1	0.5625	0.42	0.34	···	0.125

We now test this scheme on a model problem, in which we try to recover the steady solution $u_s(x) = f(20x) - f(0) + (f(0) - f(20))x$ of Burger's equation, where

$$f(t) = \sum_{k=1}^{15} \exp(\cos(k\sqrt{k}(2.5 + 0.5t)\pi/10) - 0.3\sin(0.8k\sqrt{k}t\pi/10)).$$

The forcing function $X(x,t) = X(x)$ is calculated by substituting $u_s(x)$ into the equation. Initial condition is taken as $u(x,0) = \sin(2x)$ with the boundary conditions $u(0,t) = u(1,t) = 0$. By comparing the graphs of $u_s(x)$ with $N_x = 512$, $N_x = 256$, and $N_x = 128$, one finds that $N_x = 256$ is approximately the minimum number of grid points required to adequately resolve $u_s(x)$.

The numerical results using the original scheme and the proposed scheme with different m are compared (Fig. 1). For $m = 1$ to 4, the results are almost identical. However, for $m = 5$, the approximate solution is significantly less accurate. Therefore, the proposed scheme has to be used with caution and m can not be too large.

3.2 Small scales in IU

In the multilevel scheme given in Section 2, a spectral method is used to decompose scales. However, it is not easy to define small scales in finite difference methods. In Section 3.1, the small scale component of the flow is defined in the context of IU's. In this section, we examine this concept.

For simplicity, we will only treat the three-level IU. As is done in Section 2, the method starts with separating the length scales of the flow into

$$u = f + g + r, \tag{3.1}$$

where u is the velocity in the streamwise direction, f, g, and r are respectively the large, intermediate, and small scales. The definitions of f, g, and r are given below (see Fig. 2):

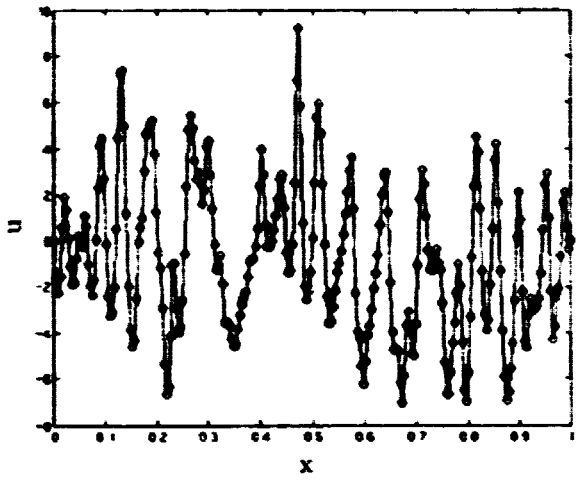

FIGURE 1. An exact steady state solution of the Burger's equation. N=256 is the minimum for resolution.

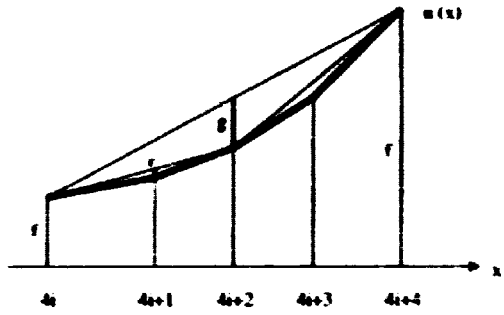

FIGURE 2. Schematic diagram of separating scales in a finite difference method.

$$
\begin{aligned}
f_{4i} &= u_{4i} \\
g_{4i+2} &= u_{4i+2} - \frac{1}{2}(u_{4i+4} + u_{4i}) \\
r_{4i+1} &= u_{4i+1} - \frac{1}{2}(u_{4i+2} + u_{4i}).
\end{aligned}
\tag{3.2}
$$

where i is the index for the streamwise (or wall-normal, or spanwise) direction ($i = 0, 1, 2, ..., N_x/4$). The wall-normal and spanwise velocities can be defined in a similar way. We require the condition

$$|f| > |g| > |r| \tag{3.3}$$

in order to validate the assumption of separating length scales.

In the present study, the magnitudes of f, g, and r are estimated using the database of turbulent channel flow. Turbulent flow in a channel is simulated using

DNS. The convection and diffusion terms are integrated in time using a third-order Runge-Kutta method and the Crank-Nicolson method, respectively. A second-order central difference is used in space. A fractional step method is used to decouple the pressure from the velocity. The Reynolds number used is $Re_\tau = u_\tau \delta/\nu = 150$ and the computational domain is $4\pi\delta\,(x) \times 2\delta\,(y) \times 4\pi/3\delta\,(z)$, where u_τ is the wall shear velocity, δ is the channel half width, and ν is the kinematic viscosity. The number of grid points used is $128\,(x) \times 129\,(y) \times 128\,(z)$.

Figure 3 shows the energy spectra of the velocity components in the streamwise and spanwise directions, where $E(f_i)$, $E(g_i)$ and $E(r_i)$ are shown at three y-locations ($y^+ = 6, 33, 177$). It is clear that r_i's have the energy of small scales, while g_i's have the energy of intermediate scales. Both g_i and r_i have orders of magnitude smaller energies in small wavenumbers as compared to f_i. Therefore, the IU's defined in (3.2) properly describe the small and intermediate scales of the velocity.

3.3 Implementation of IU in turbulent channel flow

Implementation of IU for the Navier-Stokes equations is very similar to that of IU for the Burger's equation (see Section 3.1), once the approximating factorization scheme is used (see below). The only difference is the coupling between the velocity and the pressure.

The governing equations for an incompressible flow are

$$\frac{\partial u_i}{\partial t} + \frac{\partial}{\partial x_j} u_i u_j = -\frac{\partial p}{\partial x_i} + \frac{1}{Re}\frac{\partial}{\partial x_j}\frac{\partial u_i}{\partial x_j}, \tag{3.4}$$

$$\frac{\partial u_i}{\partial x_i} = 0. \tag{3.5}$$

The integration method used to solve (3.4) and (3.5) is based on a semi-implicit fractional step method, i.e., third-order Runge-Kutta method for the convection terms and Crank-Nicolson method for the diffusion terms:

$$\begin{aligned}\frac{\hat{u}_i^k - u_i^{k-1}}{\Delta t} =& (\alpha_k + \beta_k) L_i(u^{k-1}) + \beta_k L_i(\hat{u}^k - u^{k-1}) \\ & - \gamma_k N_i(u^{k-1}) - \zeta_k N_i(u^{k-2}).\end{aligned} \tag{3.6}$$

$$\nabla^2 \phi^k = \frac{1}{\Delta t}\frac{\partial \hat{u}_i^k}{\partial x_i}, \tag{3.7}$$

$$\frac{u_i^k - \hat{u}_i^k}{\Delta t} = -\frac{\partial \phi^k}{\partial x_i}, \tag{3.8}$$

where L_i and N_i are the diffusion and convection terms of (3.4), $k = 1, 2, 3$, and

$$\begin{aligned} &\alpha_1 = \beta_1 = \frac{4}{15}, && \gamma_1 = \frac{8}{15}, && \zeta_1 = 0 \\ &\alpha_2 = \beta_2 = \frac{1}{15}, && \gamma_2 = \frac{5}{12}, && \zeta_2 = -\frac{17}{60} \\ &\alpha_3 = \beta_3 = \frac{1}{6}, && \gamma_3 = \frac{3}{4}, && \zeta_3 = -\frac{5}{12}. \end{aligned}$$

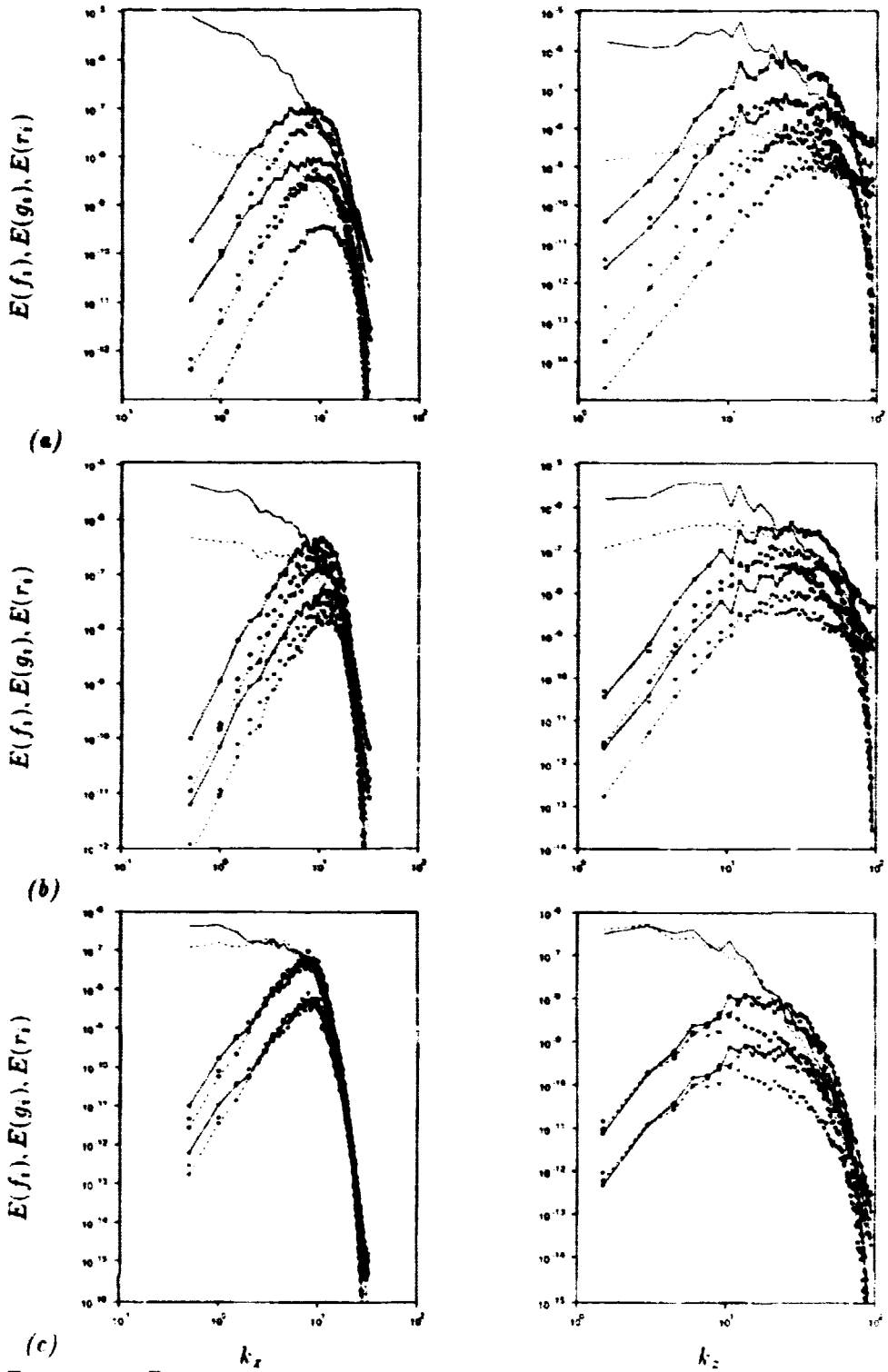

FIGURE 3. Energy spectra of the velocities, u_1 (——), u_2 (- - - -), u_3 (·····): no symbol, f_i: •, g_i: ▼, r_i. (*a*) $y^+ = 6$; (*b*) $y^+ = 33$; (*c*) $y^+ = 177$.

Here, $(\alpha_k + \beta_k)p^k = \phi^k - (\Delta t\beta_k/Re)\nabla^2\phi^k$.

Rearranging (3.6) in delta form ($\delta\hat{u}_i^k = \hat{u}_i^k - u_i^{k-1}$) gives

$$(1 - \Delta t\beta_k \frac{1}{Re}\nabla^2)\delta\hat{u}_i^k = \Delta t\big[(\alpha_k + \beta_k)L_i(\mathbf{u}^{k-1}) - \gamma_k N_i(\mathbf{u}^{k-1}) - \zeta_k N_i(\mathbf{u}^{k-2})\big].$$

Approximating factorization of this equation gives

$$\begin{aligned}&(1 - \Delta t\beta_k \frac{1}{Re}\frac{\partial^2}{\partial x^2})(1 - \Delta t\beta_k \frac{1}{Re}\frac{\partial^2}{\partial y^2})(1 - \Delta t\beta_k \frac{1}{Re}\frac{\partial^2}{\partial z^2})\delta\hat{u}_i^k \\ &= \Delta t\big[(\alpha_k + \beta_k)L_i(\mathbf{u}^{k-1}) - \gamma_k N_i(\mathbf{u}^{k-1}) - \zeta_k N_i(\mathbf{u}^{k-2})\big] \\ &\equiv R_i(\mathbf{u}^{k-1}, \mathbf{u}^{k-2}).\end{aligned} \tag{3.9}$$

Let us define χ_i as

$$\chi_i \equiv (1 - \Delta t\beta_k \frac{1}{Re}\frac{\partial^2}{\partial y^2})(1 - \Delta t\beta_k \frac{1}{Re}\frac{\partial^2}{\partial z^2})\delta\hat{u}_i. \tag{3.10}$$

Then, (3.9) becomes

$$(1 - \Delta t\beta_k \frac{1}{Re}\frac{\partial^2}{\partial x^2})\chi_i = R_i. \tag{3.11}$$

For simplicity, we only focus on the velocity in the streamwise component. Note that in turbulent channel flow the periodic boundary conditions are applied in the streamwise and spanwise directions (x, z) and the no-slip condition is applied in the wall-normal direction (y).

Now, let us decompose χ (streamwise component of χ_i) into three different scales as was introduced in Section 3.2:

$$\chi \equiv f + g + r \tag{3.12}$$

As a first step, (3.11) is approximated at each fourth grid point using a second-order central difference scheme:

$$\chi_{4i} - \Gamma(\chi_{4i+1} - 2\chi_{4i} + \chi_{4i-1}) = R_{1_{4i}}. \tag{3.13}$$

where $\Gamma = \Delta t\beta_k/(Re\Delta x^2)$.

Using a similar relation to (3.2), it can be easily shown that (3.13) becomes

$$\begin{aligned}&-\frac{\Gamma}{4}\chi_{4i+4} + (1 + \frac{\Gamma}{2})\chi_{4i} - \frac{\Gamma}{4}\chi_{4i-4} \\ &= R_{1_{4i}} + \Gamma(\frac{1}{2}g_{4i+2} + \frac{1}{2}g_{4i-2} + r_{4i+1} + r_{4i-1}).\end{aligned} \tag{3.14}$$

The χ at every fourth grid point is obtained by solving (3.14). The $\chi_{4i\pm1}$ and $\chi_{4i\pm2}$ are updated with the newly obtained χ_{4i} from (3.14): e.g.,

$$\begin{aligned}\chi_{4i+2} &= g_{4i+2} + \frac{1}{2}(\chi_{4i} + \chi_{4i+4}) \\ \chi_{4i+1} &= r_{4i+1} + \frac{1}{2}(\chi_{4i} + \chi_{4i+2}),\end{aligned} \tag{3.15}$$

where g and r are frozen for the periods of Δt_g and Δt_r, respectively. Δt_g and Δt_r are called as the frozen times for the intermediate and small scales, respectively.

As a second step, (3.11) is approximated at every other grid point at $t = l\Delta t_g$ (l is an integer) using a second-order central difference:

$$-\frac{\Gamma}{2}\chi_{2i+2} + (1+\Gamma)\chi_{2i} - \frac{\Gamma}{2}\chi_{2i-2} = R_{1_{2i}} + \Gamma(r_{2i+1} + r_{2i-1}). \tag{3.16}$$

The χ at every other grid point is obtained by solving (3.16). The $\chi_{2i\pm1}$ are then updated with the frozen r, and $g_{4i\pm2}$ are updated: e.g.,

$$\chi_{2i+1} = r_{2i+1} + \frac{1}{2}(\chi_{2i} + \chi_{2i+2}) \tag{3.17}$$

$$g_{4i+2} = \chi_{4i+2} - \frac{1}{2}(\chi_{4i} + \chi_{4i+4}). \tag{3.18}$$

As a third step, (3.11) is approximated at every point at $t = l\Delta t_r$:

$$-\Gamma\chi_{i+1} + (1+2\Gamma)\chi_i - \Gamma\chi_{i-1} = R_{1_i}. \tag{3.19}$$

The χ at every grid point is obtained by solving (3.19). The $r_{2i\pm1}$ are then updated as

$$r_{2i+1} = \chi_{2i+1} - \frac{1}{2}(\chi_{2i} + \chi_{2i+2}). \tag{3.20}$$

Once χ's are obtained at either $4i$, $2i$, or i points, similar procedures are applied to the other two directions. It is straightforward to extend the procedure described above in the spanwise and wall-normal directions. At the end of these procedures, the streamwise velocity is obtained. Again, the same procedure can be easily applied to the other two velocity components.

Let us write the numerical algorithm of IU:

1. Start with an initial velocity field u^0 or a previous time step $u^{n,k-1} = u^{n-1}$.
2. Solve the discretized momentum equations at $(4i, 4j, 4k)$ grid points (similar to (3.14)) to obtain $\boldsymbol{u}$ at $(4i, 4j, 4k)$ points.
3. Update $\boldsymbol{u}$ at non-$(4i, 4j, 4k)$ points with frozen $\boldsymbol{g}$ and $\boldsymbol{r}$ (see (3.15)).
4. If $t = l\Delta t_g$, go to Step 5. If not, go to Step 2.
5. Solve the discretized momentum equations at $(2i, 2j, 2k)$ grid points (similar to (3.16)) to obtain $\boldsymbol{u}$ at $(2i, 2j, 2k)$ points.
6. Update $\boldsymbol{u}$ at $(2i \pm 1.2j \pm 1, 2k \pm 1)$ points with frozen $\boldsymbol{r}$ and also update $\boldsymbol{g}$ at $(4i \pm 2, 4j \pm 2, 4k \pm 2)$ points (see (3.17) - (3.18)).
7. If $t = l\Delta t_r$, go to Step 8. If not, go to Step 2.
8. Solve the discretized momentum equations at all the grid points (similar to (3.19)) *to obtain* $\boldsymbol{u}$ at all points.
9. Update $\boldsymbol{r}$ at $(2i \pm 1, 2j \pm 1, 2k \pm 1)$ points (see (3.20)).
10. Solve the Poisson Eq. (3.7) at all points, update the velocity (3.8), and go to Step 2.

Note that it is not necessary for us to decompose the velocity into the same levels of scales in all the directions. That is, one may decompose the flow into two scales in the wall-normal direction and three scales in the streamwise and spanwise directions.

The interpolation used in obtaining the neighboring velocity (e.g., (3.15)) deteriorates the momentum conservation property, and the mass conservation is easily violated unless the Poisson Eq. (3.7) is solved at each time step. However, the requirement of the Poisson solution at each time step clearly diminishes the advantage of using the IU method.

The modification and application of the present multilevel scheme to the turbulent channel flow are in progress and will be reported in the future.

REFERENCES

CHEN, M. & TEMAM, R. 1991 Incremental Unknowns for Solving Partial Differential Equations. *Numer. Math.* **59**, 255-271.

CHEN, M. & TEMAM, R. 1993 Nonlinear Galerkin Method with Multilevel Incremental Unknowns. *Contributions in Numerical Mathematics, WSSIAA.* **2**, 151-164.

DEBUSSCHE, A., DUBOIS, T., & TEMAM, R. 1995a The Nonlinear Galerkin Method: A multiscale method applied to the simulation of homogeneous turbulent flows. *Theoretical and Computational Fluid Dynamics.* **7(4)**, 279-315.

DUBOIS, T., JAUBERTEAU, F., & TEMAM, R. 1995b Dynamic multilevel methods in turbulence simulations. *Computational Fluid Dynamics Review*, M. Hafez and K. Oshima ed., Wiley Publishers.

DUBOIS, T., JAUBERTEAU, F., & TEMAM, R. 1996 A Comparative Study of Multilevel Schemes in Homogeneous Turbulence. *Proceeding of ICNMFD.* **15.**

GOTTLIEB, D. & ORSZAG, S. A. 1977 Numerical Analysis of Spectral Methods: Theory and Applications. *SIAM-CBMS, Philadelphia.*

KIM, J., MOIN, P., & MOSER, R. 1987 Turbulence statistics in fully developed channel flow at low Reynolds number. *J. Fluid Mech.* **177**, 133-166.

SHEN, J. 1994 Efficient spectral-Galerkin method I. direct solvers for second- and fourth-order equations by using Legendre polynomials. *SIAM J. Sci. Comput.* **15**, 1489-1505.

SHEN, J. 1995 Efficient spectral-Galerkin method II. direct solvers for second- and fourth-order equations by using Chebyshev polynomials. *SIAM J. Sci. Comput.* **16**, 74-87.

SHEN, J. 1996 Efficient Chebyshev-Legendre Galerkin methods for elliptic problems. *Proceedings of ICOSAHOM'95. Houston J. Math.*, 233-239.

NEXT
DOCUMENT

A priori testing of subgrid-scale models for the velocity-pressure and vorticity-velocity formulations

By G. S. Winckelmans[1], T. S. Lund[2], D. Carati[3] AND A. A. Wray[4]

Subgrid-scale models for large eddy simulation (LES) in both the velocity-pressure and the vorticity-velocity formulations were evaluated and compared in *a priori* tests using spectral Direct Numerical Simulation (DNS) databases of isotropic turbulence: 128^3 DNS of forced turbulence ($Re_\lambda = 95.8$) filtered, using the sharp cutoff filter, to both 32^3 and 16^3 synthetic LES fields; 512^3 DNS of decaying turbulence ($Re_\lambda = 63.5$) filtered to both 64^3 and 32^3 LES fields. Gaussian and top-hat filters were also used with the 128^3 database. Different LES models were evaluated for each formulation: eddy-viscosity models, hyper eddy-viscosity models, mixed models, and scale-similarity models. Correlations between exact versus modeled subgrid-scale quantities were measured at three levels: tensor (traceless), vector (solenoidal 'force'), and scalar (dissipation) levels, and for both cases of uniform and variable coefficient(s). Different choices for the $1/T$ scaling appearing in the eddy-viscosity were also evaluated. It was found that the models for the vorticity-velocity formulation produce higher correlations with the filtered DNS data than their counterpart in the velocity-pressure formulation. It was also found that the hyper eddy-viscosity model performs better than the eddy viscosity model, in both formulations.

1. Velocity-pressure formulation and models investigated

Consider the Navier-Stokes equations for incompressible fluid in the velocity-pressure formulation:

$$\frac{\partial u_i}{\partial t} + \frac{\partial}{\partial x_j}(u_i u_j) + \frac{\partial P}{\partial x_i} = \nu \frac{\partial}{\partial x_j}\frac{\partial u_i}{\partial x_j} \,.$$

Filtering, using a low-pass filter G of characteristic length Δ,

$$\overline{\psi}(\boldsymbol{x}) = \int \psi(\boldsymbol{y}) G\left(\frac{\boldsymbol{x}-\boldsymbol{y}}{\Delta}\right) \frac{d\boldsymbol{y}}{\Delta^3} \,, \qquad \psi'(\boldsymbol{x}) = \psi(\boldsymbol{x}) - \overline{\psi}(\boldsymbol{x}) \,.$$

1 Dept. of Mechanical Engineering, Université catholique de Louvain, Belgium
2 Center for Turbulence Research
3 Dept. of Statistical Physics, Université libre de Bruxelles, Belgium
4 NASA Ames Research Center

with $\overline{\psi}$ the filtered value and ψ' the remainder, leads to the following evolution equation for the filtered velocity field:

$$\frac{\partial \overline{u}_i}{\partial t} + \frac{\partial}{\partial x_j}(\overline{u_i u_j}) + \frac{\partial \overline{P}}{\partial x_i} = \nu \frac{\partial}{\partial x_j}\frac{\partial \overline{u}_i}{\partial x_j} .$$

which is rewritten either as

$$\frac{\partial \overline{u}_i}{\partial t} + \frac{\partial}{\partial x_j}(\overline{u}_i \overline{u}_j) + \frac{\partial \overline{P}}{\partial x_i} + \frac{\partial \tau_{ij}}{\partial x_j} = \nu \frac{\partial}{\partial x_j}\frac{\partial \overline{u}_i}{\partial x_j} ,$$

or as

$$\frac{\partial \overline{u}_i}{\partial t} + \frac{\partial}{\partial x_j}(\overline{\overline{u}_i \overline{u}_j}) + \frac{\partial \overline{P}}{\partial x_i} + \frac{\partial \overline{\tau}_{ij}}{\partial x_j} = \nu \frac{\partial}{\partial x_j}\frac{\partial \overline{u}_i}{\partial x_j} .$$

where the 'subgrid-scale stress' (sgs) tensor is defined as

$$\tau_{ij} \stackrel{\text{def}}{=} \overline{u_i u_j} - \overline{u}_i \overline{u}_j = \overline{C}_{ij} + \overline{R}_{ij} + L'_{ij} ,$$
$$\overline{\tau}_{ij} \stackrel{\text{def}}{=} \overline{u_i u_j} - \overline{\overline{u}_i \overline{u}_j} = \overline{C}_{ij} + \overline{R}_{ij} ,$$

with the usual definitions for the cross term, the Reynolds term, and the Leonard's term:

$$\overline{C}_{ij} = \overline{\overline{u}_i u'_j} + \overline{u'_i \overline{u}_j} ,$$
$$\overline{R}_{ij} = \overline{u'_i u'_j} ,$$
$$L'_{ij} = \overline{\overline{u}_i \overline{u}_j} - \overline{u}_i \overline{u}_j = -(\overline{u}_i \overline{u}_j)' .$$

Here, $\overline{C}_{ij}$ and $\overline{R}_{ij}$ are purposely written with the 'overline' as they are the filtered value of some quantity. L'_{ij} is purposely written with the 'prime' as it is the remainder, after filtering, of some quantity and thus contains high spatial frequencies.

The notation $\overline{\tau}_{ij}$ is somewhat misleading (but will nevertheless be retained). Indeed, although it is the filtered value of some quantity, it is not necessarily the result of filtering τ_{ij}. In the case of sharp cutoff filter in wave space, $\overline{\overline{\psi}} = \overline{\psi}$ and $\overline{\psi'} = 0$ so that $\overline{\tau}_{ij}$ is indeed the result of filtering τ_{ij}. In the case of smooth filters such as the Gaussian, the filtering of τ_{ij} produces $\overline{\overline{C}}_{ij} + \overline{\overline{R}}_{ij} + \overline{L'}_{ij}$, which is not equal to $\overline{C}_{ij} + \overline{R}_{ij}$.

When doing LES with a computational grid which is of the same size as the assumed filter size Δ, one cannot accurately evaluate quadratic terms such as $(\overline{u}_i \overline{u}_j)$ using the coarse grid only, as such quantities have a high frequency content. One can only hope to resolve, on the coarse grid, quantities such as $(\overline{\overline{u}_i \overline{u}_j})$ (and even that requires using an appropriate reconstruction scheme, e.g., the need for dealiasing in spectral codes). The second form of the filtered equation is thus the one to consider in LES computations. It is assumed throughout this paper unless otherwise specified. (Notice that, if one were to use a computational grid smaller than the assumed filter size, then quantities such as $\overline{u}_i \overline{u}_j$ could be partially resolved.)

The trace of the subgrid-scale tensor does not influence the dynamics of the filtered flow and is usually lumped into the pressure term:

$$\overline{\tau}^*_{ij} = \overline{\tau}_{ij} - \frac{1}{3}\overline{\tau}_{kk}\delta_{ij}\,, \qquad \overline{P}^* = \overline{P} + \frac{1}{3}\overline{\tau}_{kk}\,.$$

$$\frac{\partial \overline{u}_i}{\partial t} + \frac{\partial}{\partial x_j}(\overline{\overline{u}_i\overline{u}_j}) + \frac{\partial \overline{P}^*}{\partial x_i} + \frac{\partial \overline{\tau}^*_{ij}}{\partial x_j} = \nu\frac{\partial}{\partial x_j}\frac{\partial \overline{u}_i}{\partial x_j}\,.$$

Only the subgrid scale force, the divergence of the subgrid-scale tensor $\overline{f}^*_i = \frac{\partial \overline{\tau}^*_{ij}}{\partial x_j}$, needs to be modeled: 3 degrees of freedom instead of 5, (or 6 if one were also interested in modeling $\overline{\tau}_{kk}$). The modified pressure is solution of

$$-\frac{\partial}{\partial x_i}\frac{\partial \overline{P}^*}{\partial x_i} = \frac{\partial}{\partial x_i}\frac{\partial}{\partial x_j}(\overline{\overline{u}_i\overline{u}_j}) + \frac{\partial \overline{f}^*_i}{\partial x_i}\,.$$

Finally, the solenoidal (i.e., divergence-free) part of the subgrid-scale force is the only one that affects the flow dynamics. Defining $\overline{g}^*_i$ as the solenoidal part of $\overline{f}^*_i$, the other part being the gradient of a potential $\overline{\phi}$ which is lumped into a new 'pressure', $\overline{P}^* = \overline{P}' + \overline{\phi}$, we write:

$$\frac{\partial \overline{u}_i}{\partial t} + \frac{\partial}{\partial x_j}(\overline{\overline{u}_i\overline{u}_j}) + \frac{\partial \overline{P}^*}{\partial x_i} + \overline{g}^*_i = \nu\frac{\partial}{\partial x_j}\frac{\partial \overline{u}_i}{\partial x_j}\,,$$

$$-\frac{\partial}{\partial x_i}\frac{\partial \overline{P}^*}{\partial x_i} = \frac{\partial}{\partial x_i}\frac{\partial}{\partial x_j}(\overline{\overline{u}_i\overline{u}_j})\,.$$

Correlations of different LES models with filtered DNS data in isotropic turbulence were obtained and investigated. This was done at three levels: tensor level (traceless sgs tensor), vector level (solenoidal force), and scalar level (dissipation), for two different DNS data sets, using the sharp cutoff filter in wave space (with spherical truncation):

a) 128^3 DNS of forced isotropic turbulence ($Re_\lambda = 95.8$) that was filtered to both 32^3 and 16^3 synthetic LES fields, see Fig. 1.
b) 512^3 DNS of decaying isotropic turbulence ($Re_\lambda = 63.5$) that was filtered to both 64^3 and 32^3 synthetic LES fields, see Fig. 2.

In addition, correlations at the tensor level were also obtained when using smooth filters (here applied in wave space) with $G(\boldsymbol{x}/\Delta) = \prod_{i=1,3} G(x_i/\Delta)$, $G(\boldsymbol{k}\Delta) = \prod_{i=1,3} G(k_i\Delta)$, such as the Gaussian (of same standard deviation as the top-hat),

$$G\left(\frac{x_i}{\Delta}\right) = \left(\frac{6}{\pi}\right)^{1/2}\exp\left(-6\left(\frac{x_i}{\Delta}\right)^2\right)\,; \quad G(k_i\Delta) = \exp\left(-\frac{1}{6}\left(\frac{k_i\Delta}{2}\right)^2\right)\,.$$

and the top-hat,

$$G\left(\frac{x_i}{\Delta}\right) = 1 \quad \text{if } \left|\frac{x_i}{\Delta}\right| < \frac{1}{2}\,, \quad 0 \quad \text{otherwise}\,; \quad G(k_i\Delta) = \frac{\sin\left(\frac{k_i\Delta}{2}\right)}{\left(\frac{k_i\Delta}{2}\right)}\,.$$

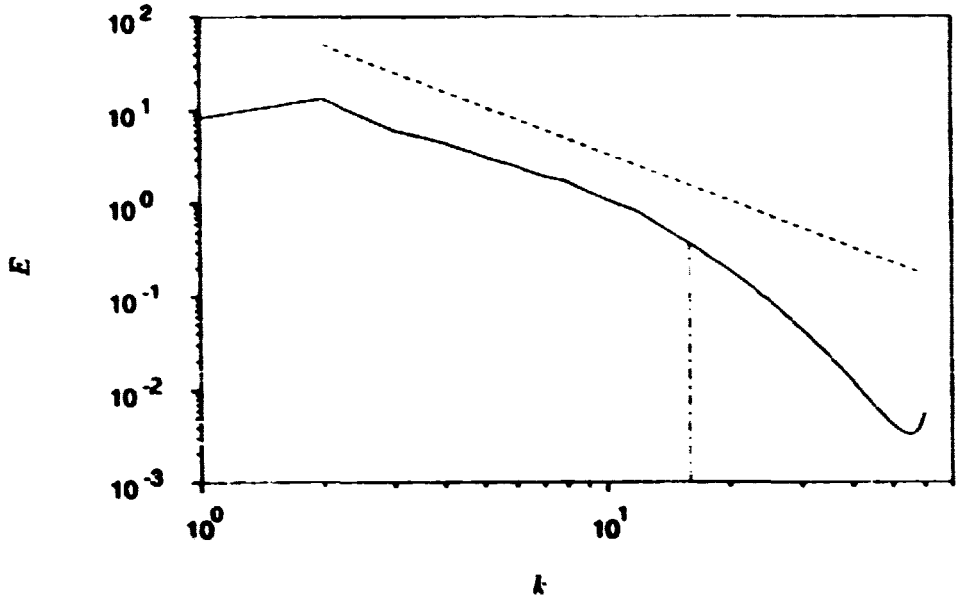

FIGURE 1. Spectrum of the 128^3 DNS ($Re_\lambda = 95.8$). Also shown is the cut used to produce the 32^3 synthetic LES field. ——— , $E(k)$; ---- , $k^{-5/3}$.

to generate synthetic LES fields from the 128^3 DNS data (i.e., DNS with $k_{max} = 64$). The cutoff wavenumber was set to $k_{max} = 16$, hence $\Delta = \pi/k_{max} = \pi/16$. Notice that, with smooth filters, the synthetic LES field still contains contributions from all original modes.

Many different LES models were investigated:

Model 1 (eddy-viscosity type, tensor modeling):

$$\overline{\tau}_{ij}^{\,M} = -2\overline{\nu_t \bar{S}_{ij}} \qquad \text{with} \qquad \bar{S}_{ij} = \frac{1}{2}\left(\frac{\partial \bar{u}_i}{\partial x_j} + \frac{\partial \bar{u}_j}{\partial x_i}\right) .$$

Different choices for the $1/T$ scaling that appears in the eddy-viscosity were investigated:

$$\nu_t = C\,\Delta^2\,(2\bar{S}_{ij}\bar{S}_{ij})^{1/2} , \tag{a}$$

$$\nu_t = C\,\Delta^2\,(\bar{\omega}_i\bar{\omega}_i)^{1/2} , \tag{b}$$

$$\nu_t = C\,\Delta^2\,(\epsilon/\Delta^2)^{1/3} , \tag{c}$$

$$\nu_t = C\,\Delta^2\,(2\bar{\omega}_i\bar{S}_{ij}\bar{\omega}_j)\,/\,(\bar{\omega}_i\bar{\omega}_i) , \tag{d}$$

$$\nu_t = C\,\Delta^2\,(2\bar{\omega}_i\bar{S}_{ij}\bar{\omega}_j)^{1/3} , \tag{e}$$

where ϵ is the rate of energy transfer within the inertial range (assumed constant) and $\bar{\omega} = \nabla \times \bar{\mathbf{u}}$ is the large-scale vorticity. The first choice is the classical Smagorinsky's scaling based on local dissipation by the large scales (e.g., see reviews by

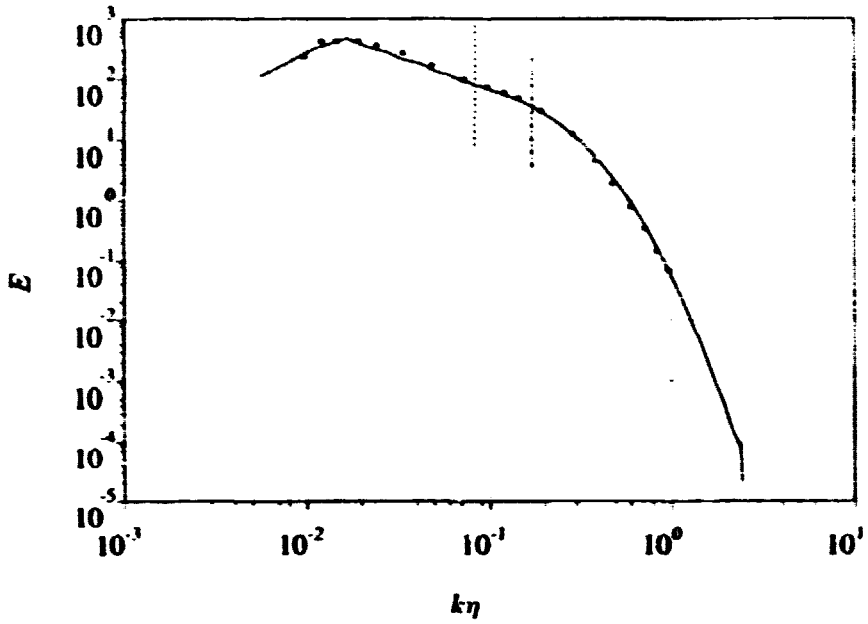

FIGURE 2. Spectrum of the 512^3 DNS ($Re_\lambda = 63.5$). Also shown are the cuts used to produce the 64^3 and 32^3 synthetic LES fields. • : Comte-Bellot and Corrsin experimental data at $Re_\lambda = 65.1$. k normalized by Kolmogorov scale η.

Rogallo & Moin 1984, Lesieur *et al.* 1995). Consider the eigenvalues λ_1, λ_2 and λ_3 of the rate-of-strain tensor, with $\lambda_1 + \lambda_2 + \lambda_3 = S_{kk} = 0$. The scaling then produces an eddy-viscosity proportional to $\left(2\left(\lambda_1^2 + \lambda_2^2 + \lambda_3^2\right)\right)^{1/2}$.

The second choice is based on local enstrophy of the large scales (e.g., Mansour *et al.* 1978). Recalling the identity

$$2\,S_{ij}S_{ij} = \omega_i\omega_i + 2\,\frac{\partial}{\partial x_i}\frac{\partial}{\partial x_j}\left(u_i u_j\right) ,$$

together with the Poisson equation for pressure, it appears that, to first order, the two scalings differ by the local pressure Laplacian (which can have either sign).

The third choice was proposed by Carati *et al.* (1995b) and is referred to as the 'Kolmogorov' scaling. If, following Smagorinsky, local equilibrium between the rate of energy transfer within the inertial range is identified with the subgrid-scale dissipation $\epsilon \approx -\overline{\tau}_{ij}^{\,M}\,\overline{S}_{ij}$, one recovers the classical Smagorinsky's model for the eddy-viscosity. The Kolmogorov scaling has the practical advantage over the other models that fewer filtering operations are required when implementing the dynamic procedure as in Germano *et al.* (1991), Ghosal *et al.* (1992), Moin & Jiménez (1993), Moin *et al.* (1994), Ghosal *et al.* (1995), Carati *et al.* (1995a). When

developing the dynamic procedure in the present formulation, one obtains

$$-2\,\Delta^{4/3}\left[\left(\frac{\hat{\Delta}}{\Delta}\right)^{4/3} C'\,\hat{\bar{S}}_{ij} - C'\,\widehat{\bar{S}}_{ij}\right] = \left(\widehat{\bar{u}_i\bar{u}_j} - \widehat{\bar{u}}_i\widehat{\bar{u}}_j\right)^{*} .$$

where $\hat{\cdot}$ is an additional 'test filter' of the LES field, at scale $\hat{\Delta}$, where C' stands for the *dimensional* product $C\,\epsilon^{1/3}$, and where it has been assumed that both filters lie in the inertial range so that ϵ is indeed the same at both filter sizes. Since the dynamic procedure also assumes that the model coefficient C is invariant with filtering scale in that range, it turns out that C' is also invariant with filtering scale and is, in fact, what is determined by the dynamic procedure.

The fourth scaling was proposed by Winckelmans (1995) and is based on the relative rate of change of the large scale enstrophy due to 3-D stretching,

$$\frac{1}{\bar{\omega}_i\bar{\omega}_i}\frac{D}{Dt}(\bar{\omega}_i\bar{\omega}_i) = 2\,\frac{\bar{\omega}_i\bar{S}_{ij}\bar{\omega}_j}{\bar{\omega}_i\bar{\omega}_i} .$$

This scaling selects the eigenvalues used to compute the eddy-viscosity according to the relative orientation between $\bar{\boldsymbol{\omega}}$ and the principal axes (eigenvectors) of the rate-of-strain tensor. Indeed, writing the components of $\bar{\boldsymbol{\omega}}$ in the system of principal axes as $(\bar{\omega}_1, \bar{\omega}_2, \bar{\omega}_3)$, this scaling produces an eddy-viscosity proportional to $2\,(\lambda_1\bar{\omega}_1^2 + \lambda_2\bar{\omega}_2^2 + \lambda_3\bar{\omega}_3^2)\,/\,(\bar{\omega}_1^2 + \bar{\omega}_2^2 + \bar{\omega}_3^2)$. Hence a vorticity-weighted average of the eigenvalues is used to produce the eddy-viscosity. This scaling produces a negative eddy viscosity scaling in regions where enstrophy is decreasing. To ensure positivity, one can use either $|d|$ or $d_+ = \max(d, 0)$.

For completeness, a fifth scaling is considered, which is based on the rate of change of enstrophy, hence an eddy viscosity proportional to $\{2\,(\lambda_1\bar{\omega}_1^2 + \lambda_2\bar{\omega}_2^2 + \lambda_3\bar{\omega}_3^2)\}^{1/2}$.

Models other than the classical LES model (Model 1) were also investigated:

Model 2 (eddy-viscosity type, solenoidal force modeling):

$$\bar{\boldsymbol{q}}^{*M} = -\nabla\times(\overline{\bar{\nu}_t\bar{\boldsymbol{\omega}}}) .$$

Model 3 (hyper eddy-viscosity type, tensor modeling):

$$\bar{\tau}_{ij}^{*M} = 2\Delta^2\,\overline{\bar{\nu}_t\nabla^2\bar{S}_{ij}} .$$

Model 1+3 (mixed eddy-viscosity and hyper eddy viscosity type, tensor modeling):

$$\bar{\tau}_{ij}^{*M} = -2\left(\overline{\bar{\nu}_{t1}\bar{S}_{ij}} - \Delta^2\,\overline{\bar{\nu}_{t2}\nabla^2\bar{S}_{ij}}\right) .$$

Model 1+4 (mixed, simplest non eddy-viscosity type, tensor modeling):

$$\bar{\tau}_{ij}^{*M} = -2\left(\overline{\bar{\nu}_t\bar{S}_{ij}} + C_2\Delta^2\,\overline{(\bar{S}_{il}\bar{S}_{lj})^{*}}\right) .$$

We are unaware of any published results describing Model 3 or Model 1+3. However, Cerutti and Meneveau (1996, private communication) have also considered this

model. Model 1+4 is one of the many models investigated by Lund and Novikov (1992) where they considered all possible models with the sgs tensor function only of the strain and rotation rate tensors.

Notice that one can even build models that give a decent (i.e., as good as other models) correlation at the tensor level but give zero solenoidal force, hence zero effect on the dynamics of the filtered velocity field, e.g.,

$$\bar{\tau}_{ij}{}^{M} = C\Delta^2 \frac{\partial}{\partial x_i}\frac{\partial}{\partial x_j}(\bar{u}_l\bar{u}_l) .$$

Such models should, of course, never be used. Nevertheless, they make the point that correlation at the tensor level does not necessarily mean good dynamics. What really matters is the solenoidal forcing.

Finally, scale similarity models of Bardina's type. Models B, were also investigated (e.g., see Horiuti 1993, Zang et al. 1993, Liu et al. 1994, Salvetti & Banerjee 1995). The combinations considered were:

$$C\left(\widehat{\bar{u}_i\bar{u}_j} - \widehat{\bar{u}}_i\widehat{\bar{u}}_j\right) . \qquad (a)$$

$$C\left(\widehat{\bar{u}_i\bar{u}_j} - \widehat{\bar{u}}_i\widehat{\bar{u}}_j\right) . \qquad (b)$$

$$C\left(\bar{u}_i\bar{u}_j - \widehat{\bar{u}}_i\widehat{\bar{u}}_j\right) . \qquad (c)$$

$$C\left(\widehat{\bar{u}_i\bar{u}_j} - \widehat{\bar{u}}_i\widehat{\bar{u}}_j\right) . \qquad (d)$$

where the additional filtering of the LES field was done at twice the size of the original filter, and with the same filter type. Model Ba is the filtering of $\bar{u}_i\bar{u}_j - \widehat{\bar{u}}_i\widehat{\bar{u}}_j$ and is 'similar' to $\bar{\tau}_{ij}$, which is the original filtering of $u_iu_j - \bar{u}_i\bar{u}_j$. Model Bb is similar to $\tau_{ij} = \overline{u_iu_j} - \bar{u}_i\bar{u}_j$. Model Bc was also investigated, in *a priori* testing, in Meneveau & Lund (1992). Model Bd is the remainder, after second filtering, of $\widehat{\bar{u}}_i\widehat{\bar{u}}_j$, and is thus not expected to perform well.

2. Optimization of the coefficient(s) and correlations

We first consider optimization of the model's coefficient(s) when no spatial variation is allowed. This is a natural requirement as the models are being compared with DNS data in isotropic turbulence. For each level, the value of C that provides the minimum error, in the least square sense, between 'exact' and 'modeled' subgrid-scale quantities is evaluated. Defining

$$\bar{\tau}^{\circ}_{ij}{}^{M} = C_\tau\,\overline{m}^{\circ}_{ij} , \quad \bar{g}^{\circ}_{i}{}^{M} = C_g\,\overline{m}^{\circ}_{i} ,$$

and $\langle\cdot\rangle$ as integration over physical space, one then obtains:
At the traceless tensor level:

$$C_\tau = \frac{\langle\bar{\tau}^{\circ}_{kl}\,\overline{m}^{\circ}_{kl}\rangle}{\langle\overline{m}^{\circ}_{kl}\,\overline{m}^{\circ}_{kl}\rangle} .$$

At the solenoidal force level:

$$C_g = \frac{\langle \overline{g}_k^{\,*}\, \overline{m}_k^{\,*} \rangle}{\langle \overline{m}_k^{\,*}\, \overline{m}_k^{\,*} \rangle} .$$

At the scalar level (= dissipation level):

$$\overline{d}^{\,*} = \overline{u}_k \overline{g}_k^{\,*} . \qquad \overline{d}^{\,*M} = \overline{u}_k \overline{g}_k^{\,*M} = C_d\, \overline{m}^{\,*} . \qquad C_d = \frac{\langle \overline{d}^{\,*}\, \overline{m}^{\,*} \rangle}{\langle \overline{m}^{\,*}\, \overline{m}^{\,*} \rangle} .$$

For models with two coefficients, defining

$$\overline{\tau}_{ij}^{\,*M} = C_{\tau 1}\, \overline{m}_{ij}^{\,*} + C_{\tau 2}\, \overline{n}_{ij}^{\,*} .$$

the least-square optimization then leads to

$$\begin{pmatrix} \langle \overline{m}_{kl}^{\,*}\, \overline{m}_{kl}^{\,*} \rangle & \langle \overline{m}_{kl}^{\,*}\, \overline{n}_{kl}^{\,*} \rangle \\ \langle \overline{m}_{kl}^{\,*}\, \overline{n}_{kl}^{\,*} \rangle & \langle \overline{n}_{kl}^{\,*}\, \overline{n}_{kl}^{\,*} \rangle \end{pmatrix} \begin{pmatrix} C_{\tau 1} \\ C_{\tau 2} \end{pmatrix} = \begin{pmatrix} \langle \overline{\tau}_{kl}^{\,*}\, \overline{m}_{kl}^{\,*} \rangle \\ \langle \overline{\tau}_{kl}^{\,*}\, \overline{n}_{kl}^{\,*} \rangle \end{pmatrix} .$$

and similarly for the coefficients at the force and dissipation levels.

The correlations between 'exact' and 'modeled' subgrid-scale quantities are defined in the usual way.

$$\eta_\tau = \frac{\langle \overline{\tau}_{kl}^{\,*}\, \overline{\tau}_{kl}^{\,*M} \rangle}{\langle \overline{\tau}_{kl}^{\,*}\, \overline{\tau}_{kl}^{\,*} \rangle^{1/2} \langle \overline{\tau}_{kl}^{\,*M}\, \overline{\tau}_{kl}^{\,*M} \rangle^{1/2}} .$$

$$\eta_g = \frac{\langle \overline{g}_k^{\,*}\, \overline{g}_k^{\,*M} \rangle}{\langle \overline{g}_k^{\,*}\, \overline{g}_k^{\,*} \rangle^{1/2} \langle \overline{g}_k^{\,*M}\, \overline{g}_k^{\,*M} \rangle^{1/2}} .$$

$$\eta_d = \frac{\langle \overline{d}^{\,*}\, \overline{d}^{\,*M} \rangle}{\langle \overline{d}^{\,*}\, \overline{d}^{\,*} \rangle^{1/2} \langle \overline{d}^{\,*M}\, \overline{d}^{\,*M} \rangle^{1/2}} .$$

One interesting question is posed when using mixed models instead of the simplest models (e.g., using Model 1+3 instead of Model 1 alone or Model 3 alone): by how much can one expect to improve the correlation? Part of the answer lies in the following identity:

$$(\eta_\tau^{m+n})^2 = \frac{(\eta_\tau^m)^2 + (\eta_\tau^n)^2 - 2\,\eta_\tau^m\, \eta_\tau^n\, \eta_m^n}{1 - (\eta_m^n)^2} ,$$

where η_a^b stands for the correlation between a and b. Upper and lower bounds are obtained as:

$$\max\left((\eta_\tau^m)^2 , (\eta_\tau^n)^2 \right) \le (\eta_\tau^{m+n})^2 \le (\eta_\tau^m)^2 + (\eta_\tau^n)^2 .$$

The above formulas also hold for correlations at the force or energy dissipation levels by replacing η_τ by η_g or η_d. The best situation occurs when the two terms used

in the models (a) each correlate well with the exact subgrid-scale quantity, and (b) are not highly correlated with each other. This is unfortunately not the case for all models tested in this paper (see results), as well as in other papers (e.g., Lund & Novikov 1992).

We then go on to consider local optimization of the model's coefficient(s) where spatial variation is allowed. Although one usually uses dynamic LES models with coefficient(s) that are averaged (and hence uniform) in the directions of flow homogeneity (here all three directions), the present study is justified by the hope that some model, in some formulation, might exhibit a better behavior than the others in terms of coefficient(s) uniformity. In the same spirit, it is believed that dynamic models will then have to work less hard, e.g., require less averaging of the coefficient(s) obtained dynamically.

The above least square optimization is then carried out locally, at the tensor level. For models with one coefficient, the local optimization leads to

$$C_\tau = \frac{\overline{\tau}^*_{kl}\,\overline{m}^*_{kl}}{\overline{m}^*_{kl}\,\overline{m}^*_{kl}} .$$

For models with two coefficients, the linear system is solved locally to determine $C_{\tau 1}$ and $C_{\tau 2}$. The local optimization can be done only at the tensor level. Indeed, the force, being the divergence of the sgs tensor, must remain written in conservative form (so as to have zero global integral in the case of isotropic turbulence). Since C_τ now depends on space, it cannot be pulled out of a derivative such as $\partial\left(C_\tau \overline{m}^*_{ij}\right)/\partial x_j$. (If one were to relax the constraint that the force be conservative, an optimization at the force level would, of course, be possible.)

Correlations are then computed in the same way as above, at all three levels. At the tensor level, they are now artificially much higher than those obtained with uniform C. Since the Cs are optimized locally, their spatial variation is quite high, including regions of negative values. Interesting quantities are evaluated and reported: mean, rms $\left(\langle C^2\rangle - \langle C\rangle^2\right)^{1/2}$, and normalized pdf, the better models exhibiting a sharper (i.e. smaller rms) pdf which is also more skewed towards positive C.

3. Vorticity-velocity formulation and models investigated

Consider LES in the vorticity-velocity formulation:

$$\frac{\partial \overline{\omega}_i}{\partial t} + \frac{\partial}{\partial x_j}\left(\overline{\overline{\omega}_i \overline{u}_j} - \overline{\overline{\omega}_j \overline{u}_i}\right) + \frac{\partial \overline{\gamma}_{ij}}{\partial x_j} = \nu \frac{\partial}{\partial x_j}\frac{\partial \overline{\omega}_i}{\partial x_j} .$$

with the subgrid-scale antisymmetric tensor defined as

$$\gamma_{ij} \overset{\text{def}}{=} \left(\overline{\omega_i u_j} - \overline{\omega_j u_i}\right) - \left(\overline{\omega}_i \overline{u}_j - \overline{\omega}_j \overline{u}_i\right) = \overline{C}_{ij} + \overline{R}_{ij} + L'_{ij} .$$

$$\overline{\gamma}_{ij} \overset{\text{def}}{=} \left(\overline{\omega_i u_j} - \overline{\omega_j u_i}\right) - \left(\overline{\overline{\omega}_i \overline{u}_j} - \overline{\overline{\omega}_j \overline{u}_i}\right) = \overline{C}_{ij} + \overline{R}_{ij} ,$$

where

$$\overline{C}_{ij} = \left(\overline{\overline{\omega}_i u'_j} - \overline{\overline{\omega}_j u'_i}\right) + \left(\overline{\omega'_i \overline{u}_j} - \overline{\omega'_j \overline{u}_i}\right) ,$$

$$\overline{R}_{ij} = \overline{\omega'_i u'_j} - \overline{\omega'_j u'_i} ,$$

$$L'_{ij} = \left(\overline{\overline{\omega}_i \overline{u}_j} - \overline{\overline{\omega}_j \overline{u}_i}\right) - \left(\overline{\omega}_i \overline{u}_j - \overline{\omega}_j \overline{u}_i\right) = \left(\overline{\omega}_i \overline{u}_j - \overline{\omega}_j \overline{u}_i\right)' .$$

Scaling	C_r	C_g	C_d	C_d'	η_r	η_g	η_d	$\langle C_r \rangle$	$\frac{\text{rms}}{\text{mean}}$	η_r	η_g	η_d
a	0.0086	0.016	0.013	0.0098	0.12	0.29	0.34	0.014	4.4	0.57	0.60	0.59
b	0.012	0.019	0.016	0.013	0.13	0.28	0.32	0.016	4.1	0.56	0.59	0.58
c	0.21*	0.35*	0.29*	0.21*	0.13	0.28	0.33	0.23*	4.0	0.57	0.59	0.59
d	0.013	0.037	0.036	0.041	0.07	0.20	0.27	0.012	15.0	0.57	0.60	0.59
$\lvert d \rvert$	0.019	0.043	0.036	0.031	0.10	0.26	0.32	0.036	5.8	0.57	0.60	0.59
d_+	0.019	0.037	0.031	0.024	0.11	0.27	0.33	0.032	4.8	0.57	0.60	0.59
e	0.011	0.029	0.028	0.039	0.07	0.20	0.27	0.0082	16.0	0.57	0.59	0.58
$\lvert e \rvert$	0.017	0.032	0.027	0.028	0.11	0.26	0.31	0.028	5.1	0.56	0.59	0.58
e_+	0.017	0.028	0.022	0.022	0.13	0.27	0.33	0.023	4.2	0.56	0.59	0.58

Table 1. Investigation of the influence of scaling. Model 1, $128^3 \rightarrow 32^3$ with sharp cutoff. (*: value of $C\epsilon^{1/3}$).

LES in the vorticity-velocity formulation is a natural choice which requires modeling only three quantities. Defining $\bar{\beta}_1 = \bar{\gamma}_{23} = -\bar{\gamma}_{32}$, $\bar{\beta}_2 = \bar{\gamma}_{31} = -\bar{\gamma}_{13}$, $\bar{\beta}_3 = \bar{\gamma}_{12} = -\bar{\gamma}_{21}$, together with $\bar{\gamma}_{11} = \bar{\gamma}_{22} = \bar{\gamma}_{33} = 0$, one obtains $\nabla \cdot \bar{\gamma} = \nabla \times \bar{\beta}$. Hence, modeling is already at the 'vector' level, since modeling $\bar{\gamma}$ is really modeling $\bar{\beta}$. Moreover, it is already in the form of a solenoidal 'forcing', $\nabla \times \bar{\beta}$. For instance, the equivalent of the classical Smagorinsky's model is simply:
Model 1 (eddy-viscosity type):

$$\bar{\gamma}_{ij}{}^{M} = -2\overline{\bar{\nu}_t \bar{r}_{ij}} \qquad \text{with} \qquad \bar{r}_{ij} = \frac{1}{2}\left(\frac{\partial \bar{\omega}_i}{\partial x_j} - \frac{\partial \bar{\omega}_j}{\partial x_i}\right) .$$

which is identical to doing:

$$\frac{\partial \bar{\omega}}{\partial t} + \nabla \cdot (\overline{\bar{\omega}\bar{u}} - \overline{\bar{u}\bar{\omega}}) = \nabla \times \left(\overline{\bar{\nu}_t \nabla^2 \bar{u}}\right) + \nu \nabla^2 \bar{\omega} .$$

Another model investigated is:
Model 2 (hyper eddy-viscosity type):

$$-\Delta^2 \nabla \times \left(\overline{\bar{\nu}_t \nabla^4 \bar{u}}\right) .$$

4. Results and discussion

The velocity-pressure LES formulation is considered first, with the classical Model 1 but different scalings. The results are compiled in Table 1 for the case $128^3 \rightarrow 32^3$ with sharp cutoff.

For models that can produce local negative scaling, s, it is always better to restrict it to positive values by using $|s|$ or $s_+ = \max(s, 0)$: better correlations are obtained in the case of uniform C, and sharper distribution of C in the case of variable C_r (smaller ratio 'rms/mean', e.g., 4-6 instead of 15-16). Of the two options, $|s|$ is always slightly better than s_+.

For cases with uniform C (optimized at each level), the correlations are different at each level, typically $\eta_r \approx 0.12$, $\eta_g \approx 0.27$, and $\eta_d \approx 0.33$. The choice for the $1/T$

scaling is found to be unimportant as it does not affect the correlations significantly. Since the model represents only a crude estimate of the sgs stresses, the correlations obtained at the tensor level are quite low. Things improve a bit when considering correlation at the force level, and even more so at the dissipation level. This is to be expected as one has to work less hard in the modeling effort: 5 degrees of freedom versus 3 versus 1. Results in Lund & Novikov (1992) and Clark *et al.* (1979) for isotropic turbulence report $\eta_\tau \approx 0.2$ (such correlations are also obtained here, as presented at the end of this section). Piomelli *et al.* (1988) for turbulent channel flow, and McMillan & Ferziger (1979) for homogeneous shear flow reporting $\eta_\tau \approx 0.1$. In the case of uniform C, the correlations only measure the 'alignment' between the model and the exact quantities, not the magnitude. Indeed, C drops out of the three equations defining the correlations. In particular, one could use a value which is such that the global dissipation obtained with the model, $\langle \bar{d}^{*M} \rangle$, be equal to the exact global dissipation, $\langle \bar{d}^* \rangle$: $C_d' = \langle \bar{d}^* \rangle / \langle \bar{d}^{*M} \rangle$. These values are also reported in the tables.

For cases with variable C_τ (optimized locally at the tensor level), the correlations are pretty much the same at all levels. To attain correlations in the range 0.56-0.60, the model has to 'work hard': highly varying C_τ field as seen in the ratio rms/mean 4-5 and in the normalized pdf of Fig. 3.

An investigation is also carried out to evaluate the relative participation of the two terms $\bar{C}^*_{ij}$ and $\bar{R}^*_{ij}$ in in the correlations, see Table 2. As expected from the mathematical definitions of these terms, the model correlates better with $\bar{C}^*_{ij}$ than with $\bar{R}^*_{ij}$. It also correlates better with $\bar{C}^*_{ij} + \bar{R}^*_{ij}$ than with $\bar{C}^*_{ij}$ alone.

$\bar{C}^*_{ij}$	$\bar{R}^*_{ij}$	η_τ	η_g	η_d
no	yes	0.066	0.102	0.171
yes	no	0.108	0.278	0.317
yes	yes	0.116	0.286	0.339

Table 2. Contributions of $\bar{C}^*_{ij}$ and $\bar{R}^*_{ij}$ to the correlations: Model 1 with scaling (a); $128^3 \rightarrow 32^3$ with sharp cutoff.

Model 2 is considered next. This model is not obtained by taking the curl of Model 1 (it would if ν_t were uniform). Nevertheless, since the choice of scaling was found to be unimportant with Model 1, which means that very local variation of ν_t are unimportant, Model 2 is expected to perform as Model 1. This is indeed found to be the case. For scaling (a): $C_g = 0.020$, $C_d = 0.016$, $\eta_g = 0.29$, $\eta_d = 0.34$.

Model 3 is considered next. The results are reported in Table 3 and in Fig. 3. This model performs significantly better than Model 1 at all three levels, and for both cases of uniform and variable coefficient. In particular, with variable C_τ, the pdf is sharper (ratio rms/mean of 3.3 instead of 4.4) and more skewed to the right.

Model 1+3 with uniform coefficients does not perform substantially better than Model 3 alone ($\eta_g = 0.344$ instead of 0.334). This is due to the fact that $\bar{S}_{ij}$

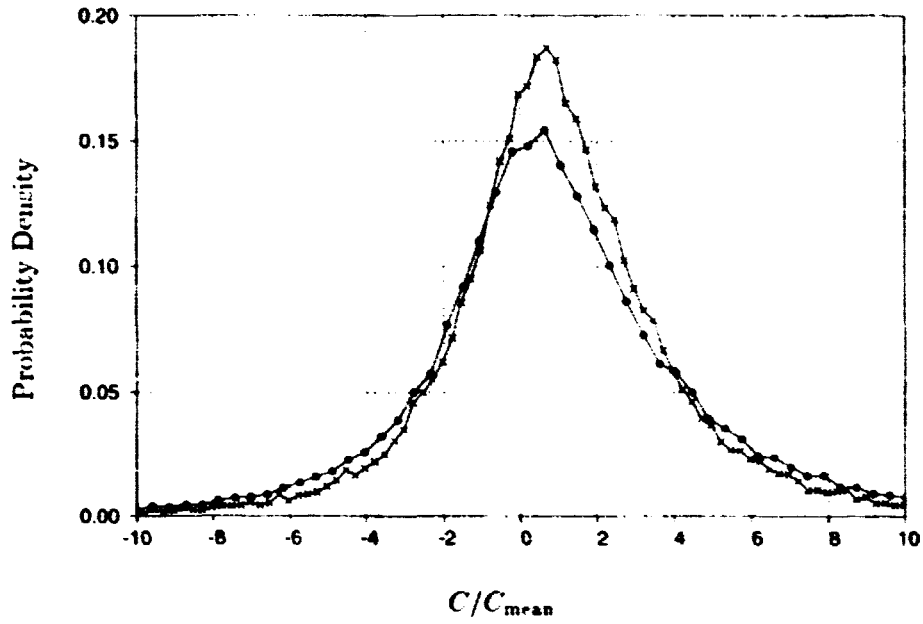

FIGURE 3. Normalized pdf for Model 1 (•) and Model 3 (×) with scaling (a): $128^3 \rightarrow 32^3$ with sharp cutoff.

Model	C_τ	C_g	C_d	η_τ	η_g	η_d	(C_τ)	$\frac{\text{rms}}{\text{mean}}$	η_τ	η_g	η_d
1	0.0086	0.016	0.013	0.12	0.29	0.34	0.014	4.4	0.57	0.60	0.59
3	0.0030	0.0037	0.0034	0.16	0.33	0.39	0.0040	3.3	0.59	0.62	0.63
1+3	-0.0077	-0.014	-0.012	0.17	0.34	0.40	-0.0059	24	0.75	0.76	0.76
	0.0046	0.0062	0.0060				0.0053	5.6			
4	0.0089	-0.073	-0.076	0.031	-0.21	-0.29	0.019	12	0.57	0.54	0.53
1+4	0.014	0.015	0.012	0.16	0.29	0.34	0.019	1.6	0.75	0.74	0.73
	0.039	-0.04	-0.012				0.047	6.9			

Table 3. Comparison of Model 3 and Model 1+3, Model 4 and Model 1+4, with Model 1: scaling (a): $128^3 \rightarrow 32^3$ with sharp cutoff.

and $\nabla^2 \overline{S}_{ij}$ are highly correlated to each other (relative correlations $\eta_\tau = 0.87$, $\eta_g = 0.94$, $\eta_d = 0.95$). It is found that this model corresponds to diffusion with the hyperviscosity term ($C_2 > 0$) corrected by some antidiffusion with the viscosity term ($C_1 < 0$). In the case with variable coefficients, it is found that $C_{\tau 1}$ must vary a lot in order to bring the correlations to 0.75 0.76: very high ratio of rms/mean for $C_{\tau 1}$.

Finally, Model 1+4 is investigated. Model 4 alone performs very poorly: in the case of uniform coefficient, the optimization leads to a coefficient of different sign whether the correlation is formed at the tensor level, or at the force and dissipation levels; in the case with variable coefficient, a ratio rms/mean of 12 is obtained.

Model 1+4 with uniform coefficients does not perform better than Model 1 alone. This is in accordance with results in Lund & Novikov (1992). This is due not only to the high correlations between the two terms (relative correlations $\eta_\tau = -0.55$, $\eta_g = -0.67$, $\eta_d = -0.82$), but also to the low correlations of Model 4 alone. In that respect, Model 1+3 performs significantly better than Model 1+4. In the case with variable coefficients, the correlations for Model 1+4 are in the 0.73-0.75 level, with not much of an increase in the ratio rms/mean for $C_{\tau 1}$, and even a decrease in the ratio for $C_{\tau 2}$. This is in contrast with what was obtained with Model 1+3.

The case where smooth filters are applied to the DNS data is also investigated. In that case, correlations are obtained at the tensor level only. The reason being that the filtered data for the τ_{ij} was computed on the original 128^3 grid, but was only sampled, for output, on a 32^3 subset of that grid. Since it still contains very significant contributions from all original modes, this data cannot be properly differentiated to obtain the forces. All possible contributions to the sgs tensor were considered and were correlated with Model 1, see Table 4.

$L_{ij}^{*\prime}$	$\overline{C}_{ij}^{*}$	$\overline{R}_{ij}^{*}$	C_τ	η_τ	$\langle C_\tau \rangle$	$\frac{\text{rms}}{\text{mean}}$	η_τ
no	no	yes	0.00062	0.083	0.0014	7.2	0.41
no	yes	no	0.0054	0.080	0.011	12	0.42
no	yes	yes	0.0060	0.084	0.012	11	0.42
yes	no	no	0.0047	0.067	-0.0027	47	0.41
yes	no	yes	0.0053	0.077	-0.0014	92	0.41
yes	yes	no	0.010	0.27	0.0083	2.8	0.34
yes	yes	yes	0.011	0.26	0.0097	2.6	0.33

Table 4. Gaussian filtering of the 128^3 DNS; Model 1 with scaling (a).

We feel that the cutoff filter is the most appropriate for generating synthetic LES fields from DNS data as it completely eliminates the 'small scale' information that will never be present in a large eddy simulation. In that sense, *a priori* tests using smooth filters such as the Gaussian are of a more academic interest. Indeed, an LES simulation would not be able to capture with the 32^3 grid the 'small scale' information which is still present after smooth filtering of the 128^3 DNS data. With the Gaussian, the filter value at the cutoff wavenumber (i.e., at the edge of the 32^3 grid) is $0.663^3 = 0.291$, which is still very significant. At twice that wavenumber, it has dropped to $0.193^3 = 0.0072$. It thus can be argued that a 64^3 grid (or so) would be needed to correctly capture the important part of the fine grain information left after Gaussian filtering.

Proceeding nevertheless with this study, one finds that the case where Model 1 is correlated with $\overline{C}_{ij}^{*} + \overline{R}_{ij}^{*} + L_{ij}^{*\prime}$ $(= \tau_{ij}^{*})$ performs quite well: $\eta_\tau = 0.26$ for the case with uniform coefficient, rms/mean of only 2.6 to reach $\eta_\tau = 0.33$ for the case with variable coefficient. Similarly for the case $\overline{C}_{ij}^{*} + L_{ij}^{*\prime}$. The cases $L_{ij}^{*\prime}$ and $\overline{R}_{ij}^{*} + L_{ij}^{*\prime}$ perform very poorly: very low correlation in the case with uniform coefficient, extremely high value of rms/mean in the case with variable coefficient.

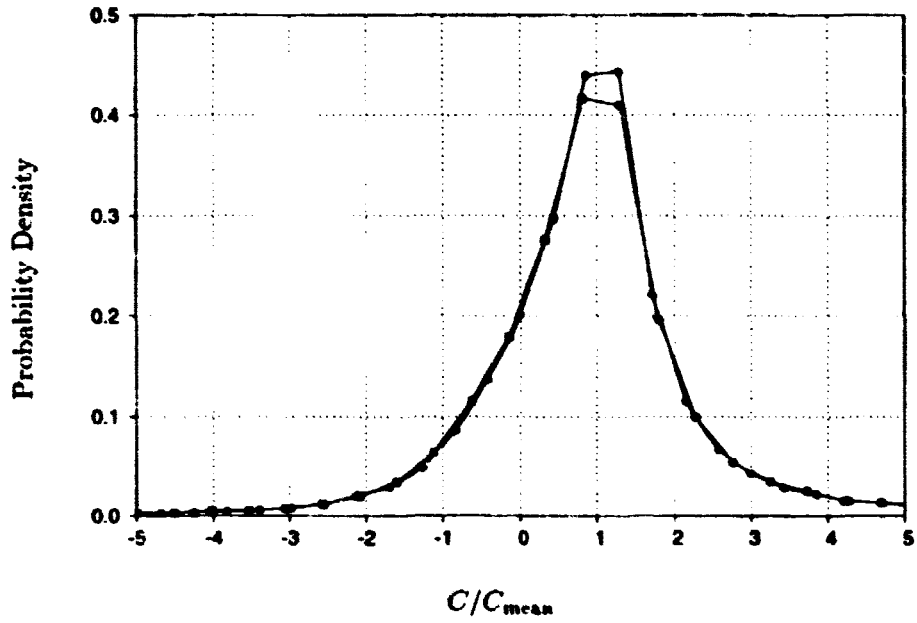

FIGURE 4. Normalized pdf for Model 1 with scaling (a); Gaussian (•) and top-hat (•) filtering of the 128^3 DNS.

All other case are such that $L_{ij}^{*\prime}$ is not included and perform very poorly, e.g., the case $\overline{C}_{ij}^{*} + \overline{R}_{ij}^{*}$ $(= \overline{\tau}_{ij}^{*})$, which has only $\eta_\tau = 0.084$. In conclusion, the correlation with τ_{ij}^{*} is significantly higher than what was obtained with sharp cutoff ($\eta_\tau = 0.26$ instead of 0.12) but the correlation with $\overline{\tau}_{ij}^{*}$ is significantly lower ($\eta_\tau = 0.084$ instead of 0.12). Finally, very similar results are obtained when using the top-hat filter instead of the Gaussian, see e.g., Fig. 4 for very similar pdf's.

The scale similarity models, Models B, are considered next, first with sharp cutoff filter, then with Gaussian filter.

Type	C_τ	C_g	C_d	C_d'	η_τ	η_g	η_d
a	0.028	0.022	0.084	0.68	0.043	0.017	0.070
b	0.015	0.031	0.083	0.43	0.039	0.034	0.098
c	-0.0054	-0.044	-0.073	1.20	-0.022	-0.12	-0.14
d	0.0076	0.039	0.090	1.2	0.015	0.031	0.075

Table 5. Scale similarity models, $128^3 \rightarrow 32^3$ with sharp cutoff.

With sharp cutoff, Models B are only compared to $\overline{\tau}_{ij}^{*}$ (since $L_{ij}^{*\prime}$ cannot be captured on the 32^3 grid), see Table 5. It is seen that very low levels of correlations are obtained regardless of the Model's type. This is in accordance with results by Meneveau & Lund (1992). Again, one must recall that, in the case of uniform C,

the correlation is independent of C. Nevertheless, when C is optimized as usual, one obtains a very large difference between C_d' and C_τ, C_g, C_d, which is also indicative of very poor models. Thus, with sharp cutoff filter, Bardina's type models show essentially no correlation with the relevant sgs quantities: trace-free tensor $\overline{\tau}^*_{ij}$, solenoidal force $\overline{g}^*_i$. In fact, if anything, Models Ba and Bb only correlate a little when the trace of $\overline{\tau}_{ij}$ is kept ($\eta_\tau = 0.13$ and 0.11 respectively).

Type	sgs	C_τ	η_τ	$\langle C_\tau \rangle$	$\frac{\text{rms}}{\text{mean}}$	η_τ
a	τ^*_{ij}	0.14	0.29	0.21	1.8	0.61
	$\overline{\tau}^*_{ij}$	0.57	0.70	0.51	0.93	0.73
b	τ^*_{ij}	0.47	0.70	0.38	0.90	0.74
	$\overline{\tau}^*_{ij}$	0.29	0.25	0.33	2.8	0.53
c	τ^*_{ij}	0.014	0.062	0.0073	48	0.47
	$\overline{\tau}^*_{ij}$	0.37	0.92	0.36	0.57	0.78
d	τ^*_{ij}	0.095	0.20	0.15	2.8	0.57
	$\overline{\tau}^*_{ij}$	-0.47	-0.55	-0.40	1.44	0.64

Table 6. Scale similarity models: Gaussian filtering applied to the 128^3 DNS.

With Gaussian smoothing, things are completely different, see Table 6. Models B are here compared to both τ^*_{ij} and $\overline{\tau}^*_{ij}$. Model Ba is 'similar' to $\overline{\tau}^*_{ij}$ and correlates indeed very well with it: $\eta_\tau = 0.70$ for the case with uniform C, very low rms/mean of 0.93 for the case with variable C. Model Bb is 'similar' to τ^*_{ij} and correlates indeed very well with it: $\eta_\tau = 0.70$ for the case with uniform C, rms/mean of 0.90 for the case with variable C. Model Bc correlates very poorly with τ^*_{ij}, but extremely well with $\overline{\tau}^*_{ij}$: $\eta_\tau = 0.92$ for the case with uniform C, rms/mean of 0.57 for the case with variable C. This is the highest correlation encountered in the course of this study. It is consistent with the 0.8 correlation reported in Meneveau & Lund (1992). Model Bd does not perform well, as expected, since it is the remainder of some quantity after second filtering.

These impressive results are misleading. Indeed, Gaussian filtering of the DNS data produces a synthetic LES field that still contains considerable contributions from the small scales. As this small scale information will not be present in an real LES, results obtained with the sharp cutoff filter are more representative of what might be expected from using Bardina's models in LES.

The vorticity-velocity LES formulation is now considered. The correlation at the antisymmetric tensor level, γ_{ij}, is denoted as C_γ, at the 'forcing' level as C_g, at the 'enstrophy dissipation' level as C_d. The results obtained with the eddy-viscosity model, Model 1, and with the hyper eddy-viscosity model, Model 2, are presented in Table 7.

The eddy-viscosity model in the vorticity-velocity formulation produces significantly higher correlations than its counterpart in the velocity-pressure formulation: in the case of uniform coefficient, $\eta_\gamma = 0.19$ instead of $\eta_\tau = 0.12$, $\eta_g = 0.32$ instead of 0.29, $\eta_d = 0.46$ instead of 0.34; in the case of variable coefficient, $\eta_\gamma = 0.71$

Model	C_γ	C_g	C_d	C_d'	η_γ	η_g	η_d	$\langle C_\gamma \rangle$	$\frac{\text{rms}}{\text{mean}}$	η_γ	η_g	η_d
1	0.019	0.026	0.019	0.021	0.19	0.32	0.46	0.023	4.6	0.71	0.74	0.80
2	0.0041	0.0046	0.036	0.039	0.23	0.35	0.48	0.0045	4.3	0.73	0.75	0.79

Table 7. Vorticity-velocity formulation; Model 1 and Model 2 with scaling (a); $128^3 \rightarrow 32^3$ with sharp cutoff.

instead of $\eta_r = 0.57$, $\eta_g = 0.74$ instead of 0.60, $\eta_d = 0.80$ instead of 0.59, with essentially the same ratio rms/mean as before, and a pdf which is more skewed towards positive C, see Fig. 5.

Again, the hyper eddy-viscosity version of the model performs even better than the eddy-viscosity version, see Table 7 and pdf of Fig. 5.

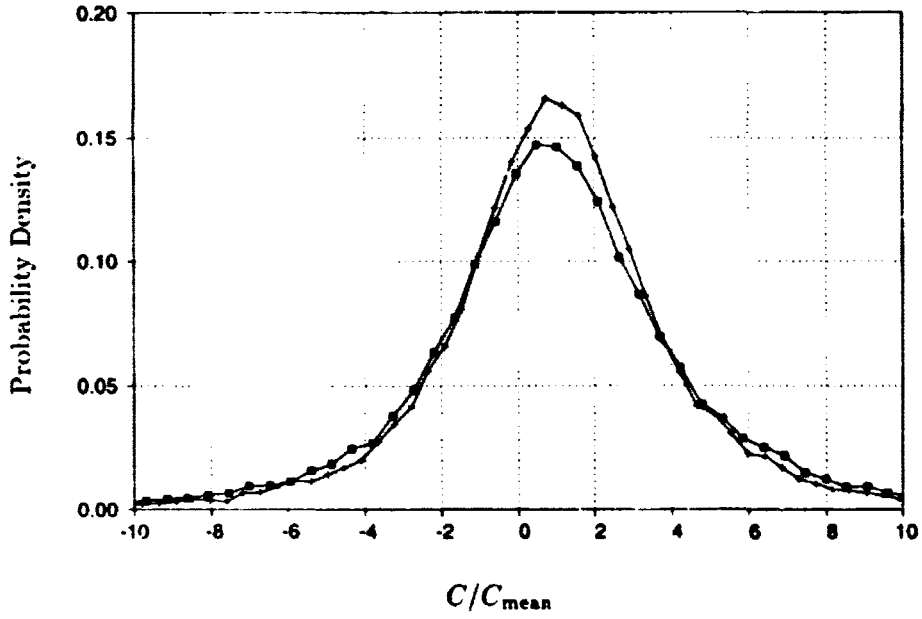

FIGURE 5. Normalized pdf for Model 1 (■) and Model 2 (+) with scaling (a) in the vorticity-velocity formulation; $128^3 \rightarrow 32^3$ with sharp cutoff.

Moreover, one finds for both models that the coefficients optimized globally are close to each other, and that they are also close to the average of the coefficient optimized locally. This is also indicative of good candidate models for LES.

For completeness, the case of smooth filtering of the DNS data is also investigated, see Table 8. The Gaussian and top-hat filter produce similar results. The eddy-viscosity model in the vorticity-velocity formulation performs slightly better than in the velocity-pressure formulation: in the case of uniform coefficient, $\eta_\gamma = 0.28$ instead of 0.26; in the case of variable coefficient, $\eta_\gamma = 0.55$ instead of 0.33, with

Type	sgs	C_γ	η_γ	$\langle C_\gamma \rangle$	$\frac{\text{rms}}{\text{mean}}$	η_γ
Gaussian	γ_{ij}	0.014	0.28	0.014	2.1	0.55
top-hat	γ_{ij}	0.015	0.24	0.016	2.3	0.53
Gaussian	$\bar{\gamma}_{ij}$	0.042	0.051	0.0009	140	0.52
top-hat	$\bar{\gamma}_{ij}$	0.050	0.057	0.0029	42	0.53

Table 8. Vorticity-velocity formulation: Gaussian and top-hat filtering of the 128^3 DNS: Model 1 with scaling (a).

a smaller ratio rms/mean (2.1 instead of 2.6). Again, when the L'_{ij} term is not included (i.e., when using $\bar{\gamma}_{ij}$ instead of γ_{ij}), the model correlates very poorly.

So far, all correlations have been obtained using the same 128^3 DNS database in forced isotropic turbulence ($Re_\lambda = 95.8$). With sharp cutoff filter, the filtering was always done from 128^3 DNS to a 32^3 synthetic LES field. An investigation is now done (a) using the same database, but filtering to a 16^3 synthetic LES field, and (b) filtering the 512^3 DNS database in decaying isotropic turbulence ($Re_\lambda = 63.5$) to both 64^3 and 32^3 synthetic LES fields. The regions of the spectra where the cut is done are marked in Figs. 1 and 2. Although there is no pure $k^{-5/3}$ 'inertial range' in this 512^3 computation at such Re_λ, there is 'almost' an inertial range, the 64^3 cut being to the far right of it, and the 32^3 cut being within it. With the 128^3 database, the 32^3 cut is also to the far right of the 'inertial range' (actually probably more at the beginning of the 'dissipation range'), and the 16^3 cut is within the inertial range. Results of this investigation done in the velocity-pressure formulation are reported in Table 9 and in Fig. 6. The results corresponding to the vorticity-velocity formulation are presented in Table 10.

Data	C_τ	C_g	C_d	C_d'	η_τ	η_g	η_d	$\langle C_\tau \rangle$	$\frac{\text{rms}}{\text{mean}}$	η_τ	η_g	η_d
$128^3 \to 32^3$	0.0086	0.016	0.013	0.0098	0.12	0.29	0.34	0.014	4.4	0.57	0.60	0.59
$128^3 \to 16^3$	0.061	0.077	0.070	0.069	0.18	0.32	0.46	0.11	3.5	0.49	0.38	0.38
$512^3 \to 64^3$	0.016	0.019	0.018	0.018	0.18	0.30	0.42	0.022	3.1	0.59	0.60	0.61
$512^3 \to 32^3$	0.029	0.028	0.028	0.031	0.29	0.39	0.59	0.036	2.0	0.61	0.64	0.73

Table 9. Investigation of different databases and of different cut locations in each database: velocity-pressure formulation: Model 1 with scaling (a); sharp cutoff.

We concentrate on correlations obtained with uniform coefficients. When considering different cuts within the same database, one finds that the cut within the inertial range produces higher correlations than the cut to the far right of that range. We don't see any obvious reason at this time why this should be the case. *Nevertheless*, this finding holds for both databases investigated and for both formulations.

Notice that the superior performance of the vorticity-velocity formulation over the velocity-pressure formulation is not as marked in the 512^3 runs as it is in the

Data	C_s	C_g	C_d	C_d'	η_s	η_g	η_d	$\langle C_s \rangle$	$\frac{\text{rms}}{\text{mean}}$	η_s	η_g	η_d
$128^3 \rightarrow 32^3$	0.019	0.026	0.019	0.021	0.19	0.32	0.46	0.023	4.6	0.71	0.74	0.80
$512^3 \rightarrow 64^3$	0.022	0.025	0.023	0.024	0.21	0.29	0.50	0.025	4.3	0.71	0.73	0.81
$512^3 \rightarrow 32^3$	0.032	0.033	0.033	0.035	0.28	0.35	0.62	0.037	3.0	0.73	0.74	0.84

Table 10. Investigation of different databases and of different cut locations in each database: vorticity-velocity formulation: Model 1 with scaling (a); sharp cutoff.

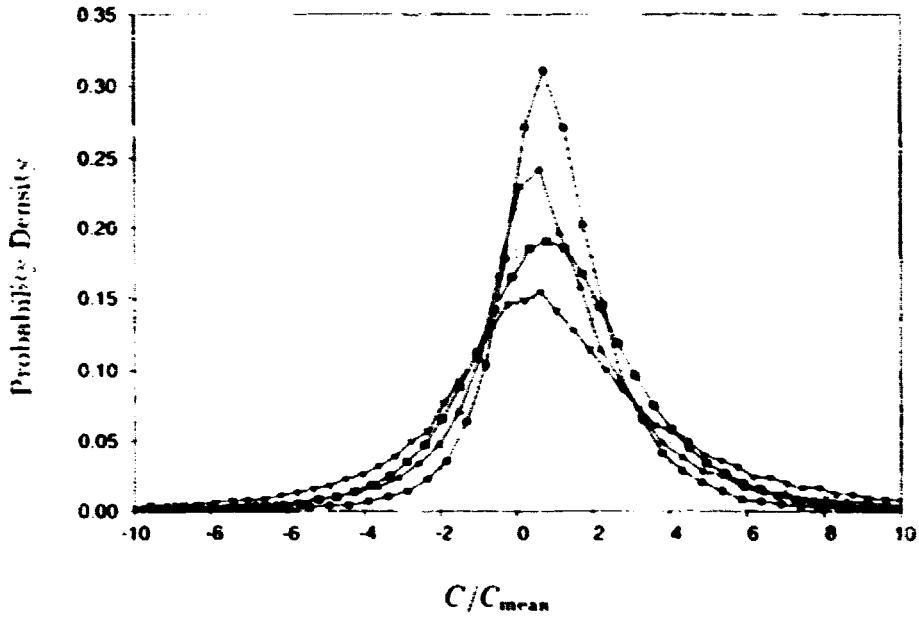

FIGURE 6. Normalized pdf for Model 1 with scaling (a) in the velocity-pressure formulation. $128^3 \rightarrow 32^3$ (τ). $128^3 \rightarrow 16^3$ ($\blacktriangle$). $512^3 \rightarrow 64^3$ ($\blacksquare$). $512^3 \rightarrow 32^3$ ($\bullet$) with sharp cutoff.

128^3 runs. In particular, the $512^3 \rightarrow 32^3$ cases are very comparable when C is uniform (still slightly better when C is allowed to vary).

5. Conclusions

A few conclusions can be made from the investigations done using the sharp cutoff filter to produce the synthetic LES fields from the DNS databases. The choice for the $1/T$ scaling in the eddy-viscosity is found to be unimportant as it does not significantly affect the correlations between modeled and exact sgs quantities at any of the three levels: trace-free tensor, solenoidal forcing, dissipation. It is found that the hyper eddy-viscosity model yields higher correlations than the eddy-viscosity model in both the velocity-pressure and the vorticity-velocity formulations. It thus appears as a good candidate for real LES and should be tested numerically. Scale similarity models exhibit essentially no correlation with the exact sgs quantities

when the sharp cutoff filter is used. The correlations obtained with simple LES models in the vorticity-velocity formulation are higher than those obtained with the counterpart models in the velocity-pressure formulation. This suggests that the vorticity-velocity formulation might be a good candidate for real LES, with reduced sgs modeling error. It certainly appears as a natural choice. It should also be tested numerically in real LES.

Some conclusions are also reached from the investigations done using the Gaussian and top-hat filters in order to produce the synthetic LES fields. It is found that the L'_{ij} contribution is essential in order to produce significant correlations. The correlations are then artificially higher than those obtained with sharp cutoff. Indeed, the filtered field still contains significant small-scale information that would not be available in a real LES. In particular, some scale similarity models exhibit remarkably high correlations when smooth filters are used.

Finally, it is found that the level of obtained correlation is quite sensitive to the database investigated, and to the location of the spectral 'cut' used to produce the synthetic LES field. If anything, our investigation shows that one must exercise caution when comparing correlations reported by different authors and when working with different databases and with different models or formulations.

REFERENCES

CARATI, D., GHOSAL, S. & MOIN, P. 1995 On the representation of backscatter in dynamic localization models. *Phys. Fluids.* **7(3)**, 606-16.

CARATI, D., JANSEN, K. & LUND, T. 1995 A family of dynamic models for large-eddy simulation. *Ann. Res. Briefs*, Center for Turbulence Research (Stanford University/NASA Ames), 35-40.

CERUTTI, S. & MENEVEAU, C. 1996 Statistical equilibrium in 3-D turbulence: implications for hyperviscous and nonlocal subgrid models. *In preparation for journal submission.*

CLARK, R. A., FERZIGER, J. H. & REYNOLDS, W. C. 1979 Evaluation of subgrid-scale models using an accurately simulated turbulent flow. *J. Fluid Mech.* **91**, 1.

COMTE-BELLOT, G. & CORRSIN, S. 1971 Simple Eulerian time-correlation full and narrow-band velocity signals in grid-generated 'isotropic' turbulence. *J. Fluid Mech.* **48**, 273-337.

GERMANO, M., PIOMELLI, U., MOIN, P. & CABOT, W. 1991 A dynamic subgrid-scale eddy-viscosity model. *Phys. Fluids A.* **3(7)**, 1760-65.

GHOSAL, S., LUND, T. S. & MOIN, P. 1992 A local dynamic model for large eddy simulation. *Ann. Res. Briefs*, Center for Turbulence Research (Stanford University and NASA Ames), 3-25.

GHOSAL, S., LUND, T. S., MOIN, P. & AKSELVOLL, K. 1995 A dynamic localization model for large-eddy simulation of turbulent flows. *J. Fluid Mech.* **286**, 229-255.

HORIUTI, K. 1993 A proper velocity scale for modeling subgrid-scale eddy viscosities in large eddy simulation. *Phys. Fluids A.* **5(1)**, 146-57.

LESIEUR, M., COMTE, P. & MÉTAIS, O. 1995 Numerical simulations of coherent vortices in turbulence. *Appl. Mech. Rev.* **48(3)**, 121-149.

LIU, S., MENEVEAU, C. & KATZ, J. 1994 On the properties of similarity subgrid-scale models as deduced from measurements in a turbulent jet. *J. Fluid Mech.* **275**, 83-119.

LUND, T. S. & NOVIKOV, E. A. 1992 Parameterization of subgrid-scale stress by the velocity gradient tensor. *Ann. Res. Briefs*, Center for Turbulence Research (Stanford University/NASA Ames), 27-43.

MCMILLAN, O. J. & FERZIGER, J. H. 1979 Direct testing of subgrid-scale models. *AIAA J.* **17**, 1340.

MENEVEAU, C. & LUND, T. S. 1992 Search for subgrid-scale parameterization by projection pursuit regression. *Proceedings of the 1992 Summer Program* Center for Turbulence Research (Stanford University/NASA Ames), 61-82.

MANSOUR, N. N., FERZIGER, J. H. & REYNOLDS, W. C. 1978 *Large-eddy simulation of a turbulent mixing layer*. Report TF-11, Thermosciences Div., Dept. of Mech. Eng., Stanford University.

MOIN, P. & JIMÉNEZ, J. 1993 Large eddy simulation of complex turbulent flows. *AIAA 24th Fluid Dynamics Conference*, Orlando, Fl., AIAA paper 93-3099.

MOIN, P., CARATI, D., LUND, T., GHOSAL, S. & AKSELVOLL, K. 1994 Developments and applications of dynamic models for large eddy simulation of complex flows. *74th Fluid Dynamics Symposium on Application of Direct and Large Eddy Simulation to Transition and Turbulence*, Chania, Crete, Greece, AGARD-CP-551, 1:1-9.

PIOMELLI, U., MOIN, P. & FERZIGER, J. H. 1988 Model consistency in large eddy simulation of turbulent channel flows. *Phys. Fluids.* **31(7)**, 1884-91.

ROGALLO R. S. & MOIN, P. 1984 Numerical simulation of turbulent flows. *Ann. Rev. Fluid Mech.* **16**, 99-137.

SALVETTI, M. V. & BANERJEE, S. 1995 A priori tests of a new dynamic subgrid-scale model for finite-difference large-eddy simulations. *Phys. Fluids.* **7(11)**, 2831-47.

WINCKELMANS, G. S. 1995 Some progress in large-eddy simulation using the 3-D vortex particle method. *Ann. Res. Briefs*, Center for Turbulence Research (Stanford University/NASA Ames), 391-415.

ZANG, Y., STREET, R. L. & KOSEFF, J. R. 1993 A dynamic mixed subgrid-scale model and its application to turbulent recirculating flows. *Phys. Fluids A.* **5(12)**, 3186-96.

NEXT
DOCUMENT

LES on unstructured deforming meshes: towards reciprocating IC engines

By D. C. Haworth[1] AND K. Jansen[2]

A variable explicit/implicit characteristics-based advection scheme that is second-order accurate in space and time has been developed recently for unstructured deforming meshes (O'Rourke & Sahota 1996a). To explore the suitability of this methodology for large-eddy simulation (LES), three subgrid-scale turbulence models have been implemented in the CHAD CFD code (O'Rourke & Sahota 1996b): a constant-coefficient Smagorinsky model, a dynamic Smagorinsky model for flows having one or more directions of statistical homogeneity, and a Lagrangian dynamic Smagorinsky model for flows having no spatial or temporal homogeneity (Meneveau *et al.* 1996). Computations have been made for three canonical flows, progressing towards the intended application of in-cylinder flow in a reciprocating engine. Grid sizes were selected to be comparable to the coarsest meshes used in earlier spectral LES studies. Quantitative results are reported for decaying homogeneous isotropic turbulence, for linear (non-solenoidal) strain of homogeneous isotropic turbulence, and for a planar channel flow. Computations are compared to experimental measurements, to direct-numerical simulation (DNS) data, and to rapid-distortion theory (RDT) where appropriate. Generally satisfactory evolution of first and second moments is found on these coarse meshes; deviations are attributed to insufficient mesh resolution. Issues include mesh resolution and computational requirements for a specified level of accuracy, analytic characterization of the filtering implied by the numerical method, wall treatment, and inflow boundary conditions. To resolve these issues, finer-mesh simulations and computations of a simplified axisymmetric reciprocating piston-cylinder assembly are in progress.

1. Introduction

Contemporary three-dimensional time-dependent models for flow and combustion in reciprocating IC engines are based on solutions to Reynolds-averaged governing equations ('RANS' based modeling; Amsden *et al.* 1989, Haworth *et al.* 1990). In RANS, the local instantaneous value of a computed dependent variable represents an ensemble- or phase-average over many engine cycles at a specified spatial location and crank phasing. In general, two-equation ($k-\epsilon$) closures have been used to model turbulent transport, with standard equilibrium wall functions. Shortcomings of RANS models have been documented by several generations of turbulence

1 GM R&D Center
2 Center for Turbulence Research, currently at Rensselaer Polytechnic Institute

researchers. Discussion of engine-specific issues can be found in the reviews by El Tahry & Haworth (1992, 1996).

An alternative to RANS is large-eddy simulation (LES). Here the governing equations are spatially filtered rather than ensemble averaged. Explicit account is taken of flow structures larger than the filter width, which is on the order of the mesh spacing, while the influence of unresolved scales is modeled using a subgrid-scale (SGS) model. Because statistics of small-scale turbulence are expected to be more universal than those of the large scales, LES offers the promise of wider generality and reduced modeling uncertainty.

LES is particularly appealing for IC engine applications. Turbulence model formulation and calibration traditionally have been carried out in statistically stationary and/or homogeneous flows for simple geometric configurations. To bring these models to bear in a phase-averaged formulation implies an equivalence between ensemble- and spatial- or temporal-averages (ergodicity) that has been demonstrated neither experimentally nor analytically. Use of conventional models also demands a reasonable degree of commonality in turbulence structure between the benchmark flow and the engine. While universality has been argued in the limit of fully-developed high-Reynolds-number broad-inertial-range turbulence, it is dubious for the low Reynolds numbers (Section 4) and complex three-dimensional transient flows that characterize the engine.

The same moderate Reynolds numbers that make IC engine flow problematic for RANS render it an appealing candidate for LES. It has been estimated that grid-independent (to a 10%-20% level) RANS computations of in-cylinder flow and combustion require at least 100^3 mesh points using second-order or higher numerical methods. This corresponds to sub-millimeter mesh spacings in a typical automotive IC engine, and is not far beyond current practice of 250,000 to 500,000 nodes. This mesh density should suffice to capture large- and intermediate-scale flow structures. Thus for IC engines, LES mesh requirements are expected to be comparable to those of RANS.

LES also promises more direct access to physical processes. Cycle-to-cycle variability in flow and combustion is one phenomenon that has proven elusive to ensemble-mean modeling and analysis. The result has been a number of largely ad hoc attempts to distinguish among 'mean,' 'turbulence,' and 'cyclic variability' components of the flow (El Tahry & Haworth 1992). This distinction becomes moot in a spatially-filtered formulation.

A drawback of LES is that substantially more computational effort may be required compared to RANS. In the engine, for example, accumulating ensemble-mean statistics via LES requires computations through multiple engine cycles. Other issues include geometric complexity (moving piston and valves) and the relatively immature state of LES for modeling complex engineering flows. It is the purpose of the present research to advance LES on several of these fronts. First, we seek to establish the limitations and resolution requirements of a particular numerical methodology (Section 2). Second, we implement and evaluate the performance of state-of-the-art subgrid-scale turbulence models on unstructured deforming meshes

(Section 3). And third, we consider several other physical modeling issues that arise in engines, including treatment of solid walls and inflow/outflow boundaries (Section 4).

2. Numerical methodology

The high-order finite difference schemes and spectral methods that traditionally have been used for DNS and LES are not suited to complex geometric configurations with moving boundaries. On the other hand, the first-order time, second-order space discretizations typically employed for engineering RANS computations (Amsden *et al.* 1989, Haworth *et al.* 1990) are overly dissipative for LES. Here we require both that the numerical methodology be compatible with the intended application of in-cylinder flow and combustion, and that it be sufficiently accurate for meaningful large-eddy simulation.

A novel discretization scheme called NO-UTOPIA (NOde-Centered Unstructured TOpology, Parallel Implicit Advection) has been developed recently by O'Rourke & Sahota (1996a, 1996b). NO-UTOPIA is a variable explicit/implicit advection scheme that differences along characteristic directions to yield formal second-order accuracy in space and time, provided that the material-speed Courant number is less than unity. It has been implemented using node-centered variables and an edge-based data structure, allowing fully unstructured meshes.

For the present study, the equations solved are those of conservation of mass, momentum, and enthalpy; the equation of state is that of an ideal gas with constant specific heats. Computations are compressible, although the Mach number is small for all cases considered here. To accommodate arbitrary mesh deformation, advective terms in the governing equations are written using velocities relative to the moving grid. A pressure-based iterative solution procedure patterned after SIMPLE is used.

The momentum equation for a control volume is obtained by integrating the Navier-Stokes equations over an arbitrary volume V with bounding surface S that is moving with velocity $\underline{v}$. Density, Cartesian velocity components, and pressure are denoted by ρ, u_i, and p, respectively; the (constant) laminar viscosity is μ_L. Adopting Cartesian tensor notation with summation over repeated lower-case Roman indices, the momentum equation has the form,

$$\frac{d}{dt}\int_V \rho u_i d\tau + \int_S \rho u_i (u_j - v_j) dA_j = -\int_S p dA_i + \int_S \tau_{\mathrm{eff}\,ji} dA_j + \int_V \rho g_i d\tau \quad (1)$$

Here g_i is a body force per unit mass. The effective stress $\tau_{\mathrm{eff}\,ji}$ is the sum of a viscous or laminar stress $\tau_{\mathrm{L}\,ji}$ and the subgrid scale stress $\tau_{\mathrm{SGS}\,ji}$,

$$\tau_{\mathrm{eff}\,ji} = \tau_{\mathrm{L}\,ji} + \tau_{\mathrm{SGS}\,ji}\ , \text{ with } \tau_{\mathrm{L}\,ji} = 2\mu_{\mathrm{L}} S_{ji} - 2\mu_{\mathrm{L}} \frac{\partial u_l}{\partial x_l}\delta_{ji}/3\ . \quad (2)$$

Here S_{ji} is the rate-of-strain tensor, $Sji = \left(\frac{\partial u_j}{\partial x_i} + \frac{\partial u_i}{\partial x_j}\right)/2$, and δ_{ji} is Kronecker's delta. No supplementary turbulence model transport equations are carried for the subgrid-scale models considered here (Section 3).

Care is needed in the specification of initial conditions. For each flow, we select a reference velocity and length U_0 and L_0 (Section 4). Fluid properties $\gamma = c_p/c_v$ (ratio of specific heats) and R (specific gas constant) are set to nominal values for air. The Mach number based on U_0 is $M_0 = U_0/c_0$ where $c_0^2 = \gamma R T_0$ is the square of the reference sound speed and T_0 the reference temperature. Reference density and pressure are ρ_0 and p_0, respectively. Laminar viscosity μ_L is set to match the desired reference Reynolds number Re_0. Remaining reference quantities and fluid properties are specified as:

$$\begin{gathered} \gamma = 1.4\ ,\ R = 288.291\ \mathrm{J/kg-K}\ ,\ M_0 = 0.1\ , \\ \rho_0 = 1.0\ ,\ p_0 = (\gamma M_0^2)^{-1}\ ,\ \mu_L = \rho_0 U_0 L_0 Re_0^{-1}\ . \end{gathered} \tag{3}$$

Initial nodal velocities and pressures are prescribed, and nodal temperatures are set such that the initial entropy is uniform, $T = T_0(p/p_0)^{(\gamma-1)/\gamma}$.

3. Subgrid-scale models

The three models considered are of the Smagorinsky type. Here the influence of unresolved (subgrid-scale) motions on the resolved scales is treated as an additional viscosity, so that $\tau_{SGS\ ji}$ has a form identical to that of $\tau_{L\ ji}$,

$$\tau_{SGS\ ji} = 2\mu_{SGS} S_{ji} - 2\mu_{SGS} \frac{\partial u_l}{\partial x_l} \delta_{ji}/3\ . \tag{4}$$

The subgrid-scale viscosity μ_{SGS} is taken to be proportional to a norm of the local rate-of-strain $|S|$ and to a filter width Δ,

$$\mu_{SGS} = \rho C_s \Delta^2 |S|\ ,\ \text{with } |S| \equiv 2(S_{ij}S_{ij})^{1/2}\ . \tag{5}$$

The single model coefficient is C_s. It is the specification of C_s and Δ that distinguishes the three models.

3.1 Constant-coefficient Smagorinsky model

The simplest model results from taking C_s to be a constant and Δ to be equal to the mesh spacing. To accommodate non-uniform mesh spacing, Δ in Eq. (5) is specified as.

$$\Delta = V^{1/3}\ . \tag{6}$$

where V is the volume associated with a computational element.

Calibration with respect to benchmark turbulent flows has led modelers to adopt different values of C_s. For homogeneous isotropic decaying turbulence, the value $C_s = 0.17^2$ is found to result in a good match with the measurements of Comte-Bellot & Corrsin (1971) (Section 4.1). For planar channel flow, a value of $C_s = 0.1^2$ yields better agreement with measurements and DNS data (Section 4.3). The non-universality of C_s motivates the need for a more general model.

3.2 Dynamic Smagorinsky model

Germano *et al.* (1991) proposed an approach for evaluating subgrid-scale model coefficients from information contained in the resolved fields. Two filter widths are introduced, $\overline{\Delta}$ and $\widehat{\Delta}$, where $\widehat{\Delta} > \overline{\Delta}$. Dependent variables filtered at scale $\overline{\Delta}$ are denoted by the overbar notation $\overline{()}$ while the hat notation $\widehat{()}$ denotes filtering at the larger scale. Formally, the first filter corresponds to an explicit filtering of the governing equations at the scale $\overline{\Delta}$. In practice, the first filter is implicit in the numerical method. That is, the quantity $\overline{u}_i(\underline{x}, t)$ denotes the computed velocity delivered by the numerical method at position $\underline{x}$ and time t.

The second filter, or 'test filter,' corresponds to a hypothetical second filtering at a larger scale. Thus $\widehat{\overline{u}}_i(\underline{x}, t)$ represents the LES-computed velocity field filtered at scale $\widehat{\overline{\Delta}}$. Stress tensors τ_{ji} and T_{ji} represent the subgrid-scale stresses for the two filter widths, respectively: $\tau_{ji} \equiv \rho\overline{u_j u_i} - \rho\overline{u}_j\overline{u}_i$, and $T_{ji} \equiv \rho\widehat{u_j u_i} - \rho\widehat{\overline{u}}_j\widehat{\overline{u}}_i$. Here the fluid density ρ can vary in time, but is nearly uniform in space (low Mach number). Filtering τ_{ji} through the second filter yields the quantity $\hat{\tau}_{ji} = \rho\widehat{\overline{u_j u_i}} - \rho\widehat{\overline{u}}_j\widehat{\overline{u}}_i$. Then subtracting $\hat{\tau}_{ji}$ from T_{ji} yields a second-order tensor L_{ji}, which can be thought of as the stresses resulting from turbulent motions at scales intermediate between $\overline{\Delta}$ and $\widehat{\overline{\Delta}}$:

$$L_{ji} = T_{ji} - \hat{\tau}_{ji} = \rho\widehat{\overline{u}_j\overline{u}_i} - \rho\widehat{\overline{u}}_j\widehat{\overline{u}}_i \,. \tag{7}$$

Equation (7) is the Germano identity.

In the Smagorinsky model, subgrid-scale stresses at both scales are modeled consistently as,

$$\tau_{ji} = 2\rho C_s\overline{\Delta}^2|\overline{S}|\overline{S}_{ji} \,, \text{ and } T_{ji} = 2\rho C_s\widehat{\overline{\Delta}}^2|\widehat{\overline{S}}|\widehat{\overline{S}}_{ji} \,. \tag{8}$$

Equation (8) is substituted into Eq. (7) to yield,

$$L_{ji} = 2\rho C_s\widehat{\overline{\Delta}}^2|\widehat{\overline{S}}|\widehat{\overline{S}}_{ji} - 2\widehat{\rho C_s\overline{\Delta}^2|\overline{S}|\overline{S}_{ji}} \,. \tag{9}$$

Under the assumption that C_s and $\overline{\Delta}$ are constants with respect to the second (test) filtering operation,

$$L_{ji} = 2\rho C_s\overline{\Delta}^2\left((\widehat{\overline{\Delta}}/\overline{\Delta})^2|\widehat{\overline{S}}|\widehat{\overline{S}}_{ji} - \widehat{|\overline{S}|\overline{S}_{ji}} \right) = -2\rho C_s\overline{\Delta}^2 M_{ji} \,. \tag{10}$$

Equation (10) defines the second-order tensor M_{ji} which, like L_{ji}, is directly computable from the LES resolved velocity field.

The quantity $C_s\overline{\Delta}^2$ is chosen in a manner that minimizes the error in satisfying Eq. (10), $\epsilon_{ji} \equiv L_{ji} + 2C_s\overline{\Delta}^2 M_{ji}$. Here we follow Lilly (1992) in minimizing this error in a least-squares sense with the constraint that $C_s\overline{\Delta}^2$ does not vary over homogeneous directions to yield,

$$C_s\overline{\Delta}^2 = \frac{\langle L_{ij}M_{ij}\rangle}{2\langle M_{kl}M_{kl}\rangle} \,. \tag{11}$$

The angled brackets ( ) represent an average over homogeneous directions.

The dynamic model offers several advantages compared to the constant-coefficient model. Subgrid-scale viscosity increases locally in areas of low grid resolution in response to the high energy found between the two filter scales (large L_{ji}). And, μ_{SGS} decreases to zero in case all scales of motion are fully resolved locally ($L_{ji} \to 0$). A second advantage of the model as formulated here is that the filter width itself $\overline{\Delta}$ need not be explicitly specified. It is the ratio of the filter widths $\widehat{\overline{\Delta}}/\overline{\Delta}$ that appears in M_{ij} (Eq. 10). It is expected that the ratio of filter widths should be more uniform than the filter width itself on nonuniform deforming meshes.

A fundamental limitation of the model as outlined here is that it requires at least one direction of statistical homogeneity. We therefore consider a third variant of the Smagorinsky model that addresses this shortcoming.

3.3 *Lagrangian dynamic Smagorinsky model*

Meneveau *et al.* (1996) proposed to accumulate the averages required in the dynamic model over flow pathlines rather than over directions of statistical homogeneity. In this case, the error incurred by substituting the Smagorinsky model (Eq. 8) into the Germano identity (Eq. 7) is minimized along fluid-particle trajectories. The error to be minimized is the accumulated local squared error E along the pathline followed by the fluid particle that is located at position $\underline{x}$ at time t: $E = \int_{-\infty}^{t} \epsilon_{ij}(\underline{z}(t'),t')\epsilon_{ij}(\underline{z}(t'),t')W(t-t')dt'$, where $\underline{z}(t') = \underline{x} - \int_{t'}^{t} \overline{\underline{u}}(\underline{z}(t''),t'')dt''$ is the trajectory followed by the fluid particle at times $t' < t$. The quantity $W(t-t')$ is a weighting function that determines the relative importance of past events, and the error ϵ_{ij} is the difference between left- and right-hand sides of Eq. (10). As in the previous formulation (Section 3.2), it is assumed that $C_s\overline{\Delta}^2$ does not vary strongly over the scale of the test filter. Then the value of $C_s\overline{\Delta}^2$ that minimizes the error E is,

$$C_s\overline{\Delta}^2 = \frac{\mathcal{I}_{LM}}{\mathcal{I}_{MM}} , \tag{12}$$

where,

$$\begin{aligned} \mathcal{I}_{LM}(\underline{x},t) &= \int_{-\infty}^{t} L_{ij}M_{ij}(\underline{z}(t'),t),t')W(t-t')dt' , \\ \mathcal{I}_{MM}(\underline{x},t) &= \int_{-\infty}^{t} M_{ij}M_{ij}(\underline{z}(t'),t),t')W(t-t')dt' . \end{aligned} \tag{13}$$

An expedient choice of weighting function is one that decays exponentially backwards in time, $W(t-t') = T^{-1}\exp[-(t-t')/T]$, T being a memory or relaxation time scale. This choice allows the integral quantities $\mathcal{I}_{LM}$ and $\mathcal{I}_{MM}$ to be expressed as solutions to transport-relaxation equations. Meneveau *et al.* (1996) observed that high numerical accuracy is not needed in the solutions of these equations, and adopted the expedient of updating nodal values of $\mathcal{I}_{LM}$ and $\mathcal{I}_{MM}$ by interpolating

from surrounding nodes at the upstream position:

$$\begin{aligned} \mathcal{I}_{LM}^{n+1}(\underline{x}) &= \max\Big(0\ ,\ a[L_{ij}M_{ij}]^{n+1}(\underline{x}) + (1-a)\mathcal{I}_{LM}^{n}(\underline{x} - \overline{\underline{u}}^{n}\Delta t) \Big)\ , \text{ and} \\ \mathcal{I}_{MM}^{n+1}(\underline{x}) &= a[M_{ij}M_{ij}]^{n+1}(\underline{x}) + (1-a)\mathcal{I}_{MM}^{n}(\underline{x} - \overline{\underline{u}}^{n}\Delta t)\ . \end{aligned} \tag{14}$$

where $a = (\Delta t/T^n)/(1 + \Delta t/T^n)$. Here superscript $n+1$ denotes quantities evaluated at the current time, superscript n quantities at the previous time, and Δt is the computational time step. Trilinear interpolation is used to evaluate quantities at the upstream position $\underline{x} - \overline{\underline{u}}\Delta t$ from computed values at the surrounding nodes.

We adopt the relaxation time T selected by Meneveau *et al.* (1996),

$$T = \theta\overline{\Delta}[\ (2\overline{\Delta}^2)^3\mathcal{I}_{LM}\mathcal{I}_{MM}\ ]^{-1/8}\ , \tag{15}$$

where the value of the model coefficient is $\theta = 1.5$. This choice for T tends to reduce the memory time in regions of high strain (large $M_{ij}M_{ij}$) and in regions of large nonlinear energy transfer (large $L_{ij}M_{ij}$). The memory time increases to reach back further in time along the particle's trajectory in case $L_{ij}M_{ij}$ remains negative over a persistent period. Negative $L_{ij}M_{ij}$ might otherwise result in negative subgrid-scale viscosity, implying energy transfer from small to large scales and numerical instability.

4. Flow configurations

In a reciprocating engine, all flow velocities scale with the mean piston speed, which is proportional to the crankshaft rotational speed; length scales are independent of engine speed. Thus the mean-flow Reynolds number Re_b (based on bore diameter and mean piston speed) and the turbulence Reynolds number Re_l (based on turbulence intensity and integral length scale) increase in proportion to engine speed. At 2,000 r/min, these are estimated to be $Re_b \approx 36{,}000$ and $Re_l \approx 1{,}000$, respectively. In-cylinder turbulence, particularly at low engine speeds, is a low-to-moderate Reynolds number phenomenon.

The number of turbulence 'eddy-turnover' times available for the decay of induction-generated turbulence in the engine is estimated to be greater than ten. Induction-generated turbulence has largely decayed by the time of ignition: it is the breakdown of the large-scale induction-generated flow structure that has the major influence on near-TDC turbulence and flame propagation. During compression and expansion, the in-cylinder flow is subjected to linear mean strains. The mean strain due to piston motion is slow compared to turbulence time scales, but persists for a large number of eddy-turnover times. These observations guide our choice of test cases for LES.

4.1 Decay of homogeneous isotropic turbulence

This canonical configuration is of relevance to the engine by virtue of the long times available for turbulence decay between intake-valve closure and ignition. Benchmark measurements were reported by Comte-Bellot & Corrsin (1971). There

the temporal decay of homogeneous isotropic turbulence was approximated by grid-generated turbulence in a wind tunnel.

Here we compare computed turbulence kinetic energy decay $\bar{k} = \langle \bar{u}_i \bar{u}_i \rangle / 2$ and three-dimensional energy spectra to the experimental data of Comte-Bellot & Corrsin (1971). Turbulence was generated using a grid spacing of $M = 5.08$ cm in a uniform mean flow of velocity $U_\infty = 10$ m/s, yielding a Reynolds number of $U_\infty M/\nu = 34{,}000$. Data were reported at three downstream stations: $U_\infty t/M = 42$, 98, and 171.

Computations are done on triply-periodic uniform cubic meshes of length 2π along each edge. Scalings are such that the edge of the computational box 2π corresponds to a physical length of 0.55 m, and the computational reference velocity $U_0 = 1.0$ corresponds to the physical velocity $U_\infty = 10.0$ m/s. Other scalings and parameters are summarized in Eq. (3).

The initial velocity field is prescribed by a procedure similar to that used for incompressible spectral simulations. We begin with a superposition of Fourier modes having a prescribed energy spectrum but random phases; this is projected onto the divergence-free space. The resulting field represents the flow upstream of the first measurement station. It is advanced in time over several turbulence eddy turnover times to adjust to compressibility and to build phase coherence. The process is repeated with different initial fields until a satisfactory match is obtained between the computed and measured energy spectrum at the first measurement station $U_\infty t/M = 42$.

Comparisons between model and measurement are made on the basis of filtered quantities. Energy spectra are filtered based on our limited understanding of the nature of the filtering implied by the numerical method. We assume that $\tilde{()}$ corresponds to a top-hat filter in physical space at the mesh spacing with trapezoidal-rule integration.

Initial computations are for a mesh of 32^3 nodes. This has been the traditional starting point for new numerical methodologies in LES, but is marginal for resolving the physics of the flow. At the initial measurement station $U_\infty t/M = 42$, the computational box edge corresponds to between ten and twenty integral length scales of the turbulence: fewer than three mesh points span an integral scale. By the final measurement station $U_\infty t/M = 171$, the turbulence integral scale has roughly doubled. The computational time step is prescribed such that material Courant numbers are less than unity.

4.2 Linear strain of initially isotropic turbulence

Homogeneous strain of initially homogeneous isotropic turbulence has been a second canonical configuration for analysis, modeling, and experiment. Here we consider the linear expansion and the linear compression for their particular relevance to the IC engine. Results are compared to rapid-distortion theory (RDT), a linearized theory of turbulence that is appropriate in the limit where the mean strain rate is large compared to an inverse turbulence eddy turnover time (Kassinos & Reynolds 1994). Although IC engines appear to be far from the RDT limit, this nonetheless provides a sound basis for model evaluation. This configuration also

exercises the code's mesh deformation capability.

The behavior that we seek to capture is the distribution of energy among the three normal-stress components. We monitor the evolution of the normalized anisotropy tensor $\bar{b}_{ij}$ as a function of the total strain C^*,

$$\bar{b}_{ij} = \langle \bar{u}_i \bar{u}_j \rangle / \langle \bar{u}_l \bar{u}_l \rangle - \delta_{ij}/3 \quad , \quad C^* = \exp[\int |S^*| dt \,] \, . \tag{16}$$

Here S^* is the dominant eigenvalue of the modified rate-of-strain tensor S^*_{ij}, where $S^*_{ij} = S_{ij} - S_{ll}\delta_{ij}/3$. In the absence of mean rotation, the evolution of $\bar{b}_{ij}(C^*)$ in the RDT limit for a non-solenoidal mean strain S_{ij} is the same as the evolution of $\bar{b}_{ij}(C^*)$ for the corresponding divergence-free rate-of-strain S^*_{ij} (Kassinos & Reynolds 1994).

The linear expansion is the superposition of spherical (isotropic) expansion and irrotational axisymmetric contraction. Experiments (see Kassinos & Reynolds 1994 for references) show that the anisotropy $\bar{b}_{ij}$ depends weakly on the magnitude of the mean rate of strain. Thus even for slow linear expansions, the evolution of $\bar{b}_{ij}(C^*)$ is expected to be similar to that predicted by RDT. The linear compression is the superposition of spherical compression and irrotational axisymmetric expansion. In this case, experiments reveal that stronger anisotropy develops at slower mean rates of strain.

Initial meshes and velocity fields are the same as those for decaying turbulence simulations (Section 4.1). The mean strain rate is imposed by deforming the domain in a manner that maintains a constant rate-of-strain S_{33} along the x_3 coordinate direction. The mesh deformation rate varies linearly from zero at $x_3 = 0$ to $S_{33} \cdot L_3(t)$ at $x_3 = L_3(t)$, yielding exponential expansion or contraction of the mesh with time, $L_3(t) = L_3(0) \cdot \exp[S_{33}t]$.

4.3 Planar channel flow

The planar channel flow adds the complexity of walls and a single statistically nonhomogeneous direction. Computations are performed on a rectangular prism of dimension L_1 (streamwise) by L_2 (normal to the wall) by L_3. Relevant dimensionless parameters are Reynolds numbers based on the wall friction velocity u_τ, and on the bulk velocity: $Re_\tau \equiv u_\tau \delta/\nu$, and $Re_B \equiv U_B \delta/\nu$ where $U_B = \int_0^{L_2} \langle \bar{u}_1(x_2) \rangle dx_2/L_2$, and δ is the channel half-width. Here angled brackets $\langle \, \rangle$ denote averages over planes parallel to walls.

Results are computed for a low Reynolds number of $Re_\tau = 180$ ($Re_B \approx 2.800$). The computational domain is $4\pi\delta$ by 2δ by $4\pi\delta/3$. The initial mesh of 33 × 65 × 33 nodes is comparable to that adopted by earlier researchers for this Reynolds number, although higher-order numerical methods have been used in most previous work (e.g., Piomelli 1993). Mesh spacing is uniform in x_1 and x_3 and follows a tanh distribution in x_2. Grid spacing varies from a minimum of $\Delta y^+ = 0.87$ at the wall to a maximum of $\Delta y^+ = 11.7$ at the channel centerline, where the $^+$ notation denotes standard wall-units scaling ($y^+ \equiv y u_\tau/\nu$). Computations are periodic in x_1 and x_3, with no-slip boundaries at $x_2 = 0$ and $x_2 = L_2$.

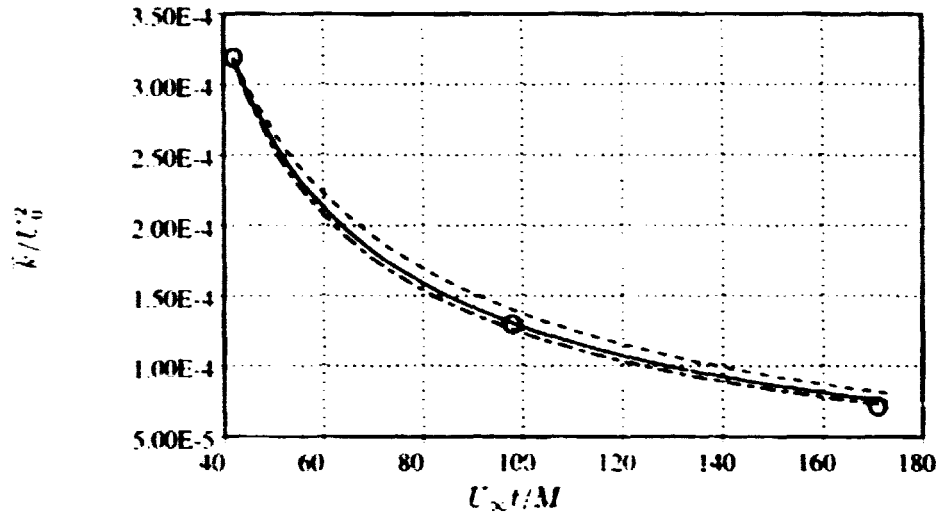

FIGURE 1. Decay of filtered turbulence kinetic energy for homogeneous isotropic decaying turbulence. Filter corresponds to a top-hat in physical space on a 32^3 uniform mesh with trapezoidal-rule integration. Symbols are measurements of Comte-Bellot & Corrsin (1971): ○. Lines are computations: ---- no subgrid-scale model; — — constant coefficient Smagorinsky model with $C_s = 0.17$; —— dynamic Smagorinsky model.

Periodicity in the streamwise direction is maintained by imposing a streamwise body force g_1 (Eq. 1) consistent with the desired Re_τ. A global force balance in the x_1 direction yields,

$$g_1 = 2L_2^{-1}(\nu Re_\tau/\delta)^2 . \tag{17}$$

Fluid viscosity is set to maintain the desired bulk Reynolds number Re_B. Velocity and length scales are $U_0 = U_B$ and $L_0 = \delta$; remaining parameters are set according to Eq. (3). The flow is allowed to develop for about 20 flow-through times $t_{dev}U_b/L_1 \approx 20$ ($t_{dev}u_\tau/\delta \approx 15$). Profiles of mean velocity, Reynolds stresses, and other statistics as functions of x_2 then are accumulated by averaging over planes parallel to walls and over time using averaging times t_{avg} of at least $t_{avg}u_\tau/\delta = 5$. Computed results are compared to DNS results of Kim *et al.* (1987) at the same Re_τ.

4.4 *Axisymmetric piston-cylinder assembly*

The target configuration for establishing the feasibility of in-cylinder LES is the simplified piston-cylinder assembly of Morse *et al.* (1978). There flow enters a pancake (flat head and piston) chamber through a central pipe of inside diameter 18.75 mm and length 1.8 m. The piston is driven in simple harmonic motion at a speed of 200 r/min through a 60 mm stroke; there is no compression. Bore diameter is 75-mm bore, and top-dead-center clearance height is 20 mm. Laser-Doppler anemometry has been used to obtain ensemble mean (phase-averaged) radial profiles of mean and rms axial velocity at 10 mm axial increments starting at the

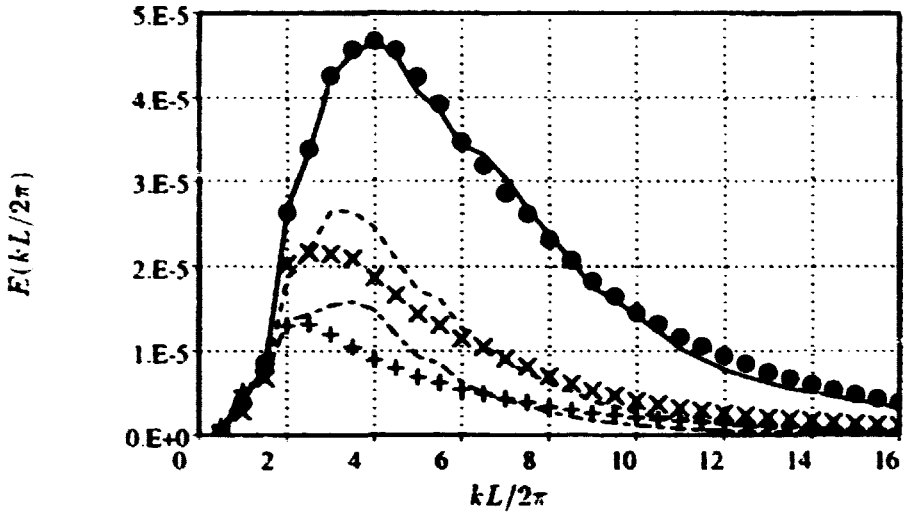

FIGURE 2. Evolution of filtered three-dimensional energy spectra for homogeneous isotropic decaying turbulence. The filter is a top-hat of width $2\pi/16$ in physical space with trapezoidal-rule integration. Symbols are experimental measurements of Comte-Bellot & Corrsin (1971): • $U_\infty t/M = 42$; × $U_\infty t/M = 98$; + $U_\infty t/M = 171$. Lines are computations for the constant-coefficient Smagorinsky model with $C_s = 0.17^2$ on 32^3 meshes: —— $U_\infty t/M = 42$; - - - - $U_\infty t/M = 98$; — - — $U_\infty t/M = 171$.

head for crank positions of 36°, 90°, 144°, and 270° after top-dead-center. This flow can be thought of as an extension of the classic statistically stationary sudden expansion/contraction to a statistically periodic case.

Several pieces of information are sought from these computations. First, we can evaluate the performance of subgrid-scale turbulence models in a configuration approaching that of an engine on a deforming unstructured mesh. Second, we will build experience with explicit phase- (ensemble-) averaging compared to spatial filtering and traditional RANS modeling. Third, we can establish mesh resolution requirements, particularly in the vicinity of walls. This includes a determination of the need for explicit wall models beyond that provided by the subgrid-scale model. And fourth, we will explore the nature of inflow forcing required to generate realistic in cylinder flow variability.

5. Results

All displayed results represent the resolved motion delivered by the numerical method in combination with the specified subgrid-scale model. These are the $\overline{(\,)}$-filtered quantities as defined in Section 3. No attempt has been made to add explicit subgrid-scale contributions to the stresses.

5.1 Decay of homogeneous isotropic turbulence

The effect of filtering on the fraction of resolved turbulence kinetic energy in the experiments of Comte-Bellot & Corrsin (1971) has been computed. For the filtering

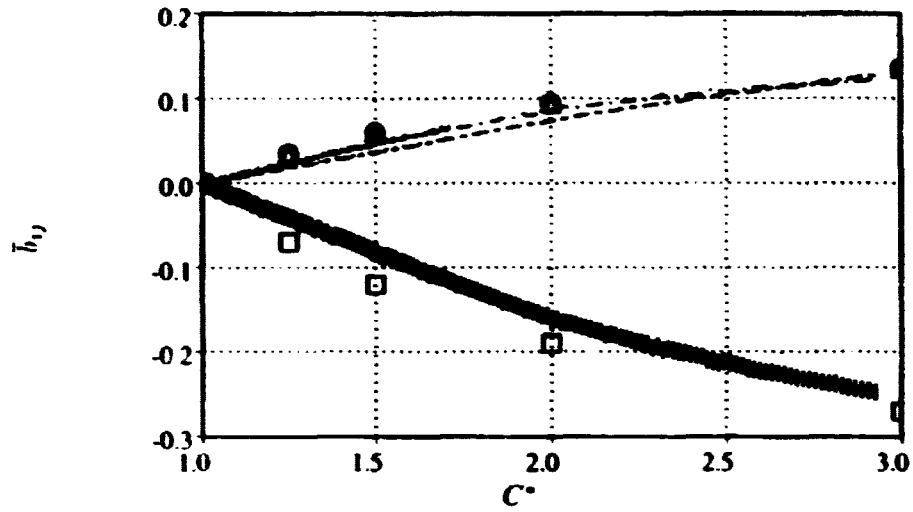

FIGURE 3. Evolution of the normalized anisotropy tensor $\bar{b}_{ij}$ as a function of total strain C^* for the linear expansion. Open symbols are RDT results (Kassinos & Reynolds 1994): ○ RDT, b_{11}; △ RDT, b_{22}; □ RDT, b_{33}. Lines are computations for the constant-coefficient Smagorinsky model with $C_s = 0.17^2$ on 32^3 meshes: —— $S_{33} \cdot \bar{k}/\bar{\epsilon} \approx 4$, b_{11}; ····· $S_{33} \cdot \bar{k}/\bar{\epsilon} \approx 4$, b_{22}; - - - - $S_{33} \cdot \bar{k}/\bar{\epsilon} \approx 4$, b_{33}; —·— $S_{33} \cdot \bar{k}/\bar{\epsilon} \approx 8$, b_{11}; —··— $S_{33} \cdot \bar{k}/\bar{\epsilon} \approx 8$, b_{22}; +++++ $S_{33} \cdot \bar{k}/\bar{\epsilon} \approx 8$, b_{33}. (Results for the lower rate-of-strain S_{33} are indistinguishable from those at the higher S_{33}.)

assumed to be closest to our numerical method (top-hat filter with trapezoidal-rule integration) only about 45% of the energy is resolved at the first measurement station on the 32^3 mesh.

The decay of filtered turbulence kinetic energy versus time for the 32^3 mesh is displayed in Figure 1. With no subgrid-scale model, there already is substantial decay resulting mainly from numerical dissipation. Constant-coefficient Smagorinsky adds sufficient additional dissipation to yield good agreement with measurements, using the standard value of the model coefficient ($C_s = 0.17^2$). The dynamic Smagorinsky model yields similar results, returning a value of $C_s \approx 0.16^2$, close to the standard value.

Filtered three-dimensional energy spectra are plotted in Figure 2. There is a pile-up of energy at wave numbers just beyond the peak of the spectrum in the computations. Thus while we are able to match the energy decay rate on this coarse mesh, the dynamics of the system are not fully captured. This is not surprising in a computation where less than half of the energy is resolved.

5.2 Linear strain of initially isotropic turbulence

Evolution of the normalized anisotropy tensor as a function of total strain is given in Figs. 3 and 4. Results are presented for two different values of $S_{33} \cdot \bar{k}/\bar{\epsilon}$ to show the influence of mean rate-of-strain. All numerical results are for a 32^3 mesh using the constant-coefficient Smagorinsky model ($C_s = 0.17^2$). RDT data are shown for

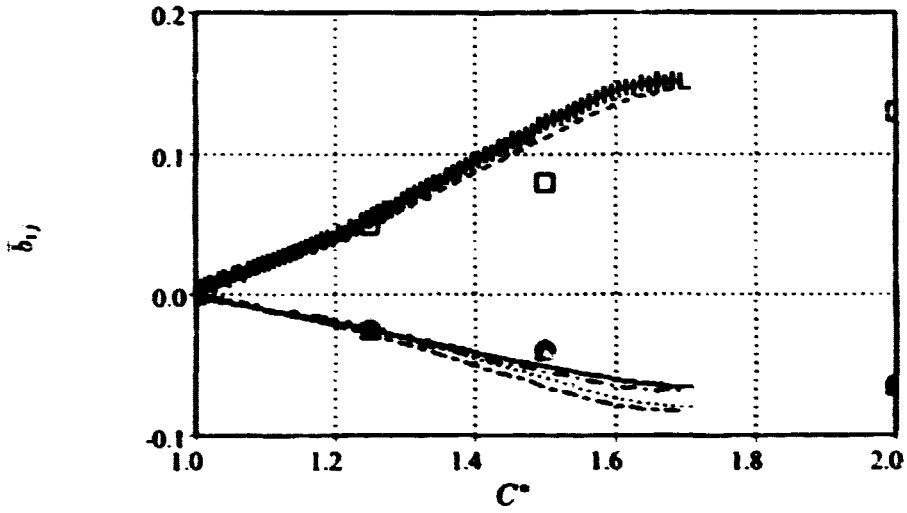

FIGURE 4. Evolution of the normalized anisotropy tensor $\bar{b}_{ij}$ as a function of total strain C^* for the linear compression. Open symbols are RDT results (Kassinos & Reynolds 1994): ○ RDT, b_{11}; △ RDT, b_{22}; □ RDT, b_{33}. Lines are computations for the constant-coefficient Smagorinsky model with $C_s = 0.17^2$ on 32^3 meshes: —— $S_{33} \cdot \bar{k}/\bar{\epsilon} \approx -4$, b_{11}; ····· $S_{33} \cdot \bar{k}/\bar{\epsilon} \approx -4$, b_{22}; ---- $S_{33} \cdot \bar{k}/\bar{\epsilon} \approx -4$, b_{33}; —·— $S_{33} \cdot \bar{k}/\bar{\epsilon} \approx -8$, b_{11}; —·— $S_{33} \cdot \bar{k}/\bar{\epsilon} \approx -8$, b_{22}; +++++ $S_{33} \cdot \bar{k}/\bar{\epsilon} \approx -8$, b_{33}.

comparison.

For the linear expansion, computations are in good quantitative agreement with RDT and are insensitive to the applied mean rate-of-strain (Fig. 3). This is consistent with experimental trends reviewed by Kassinos & Reynolds (1994).

Results for the linear compression warrant further discussion (Fig. 4). In this case computed results are closer to RDT for the slower mean rate-of-strain, and the degree of anisotropy increases with increasing mean rate-of-strain. This is contrary to experimental trends, which show increasing anisotropy at slower rates of strain (Kassinos & Reynolds 1994).

The Reynolds-averaged turbulence stress transport equation for homogeneous turbulence subjected to a uniform mean strain rate is derived by standard procedures.

$$\frac{d(\rho\langle\overline{u}_k'\overline{u}_l'\rangle)}{dt} = -\rho\langle\overline{u}_i'\overline{u}_k'\rangle\frac{\partial\langle\overline{u}_l\rangle}{\partial x_i} - \rho\langle\overline{u}_i'\overline{u}_l'\rangle\frac{\partial\langle\overline{u}_k\rangle}{\partial x_i} + \overline{T}_{kl}^r + \overline{T}_{kl}^s - \bar{\epsilon}_{kl}\,. \qquad (18)$$

The prime notation emphasizes that there is non-zero mean flow, $\overline{u}_i' \equiv \overline{u}_i - \langle\overline{u}_i\rangle$. Here the first two terms on the right-hand side represent the rate of production, $\overline{T}_{kl}^r$ and $\overline{T}_{kl}^s$ are the 'rapid' and 'slow' pressure-rates-of-strain, respectively, and $\bar{\epsilon}_{kl}$ is the viscous dissipation. In the limit of rapid distortion, $\bar{\epsilon}_{kl}$ and $\overline{T}_{kl}^s$ are negligible.

For the present linear mean strains, $\partial\langle\overline{u}_i\rangle/\partial x_j = S_{33}\delta_{i3}\delta_{j3}$. Thus all turbulence production goes directly into $\langle\overline{u}_3'^2\rangle$ and is redistributed to the other two components

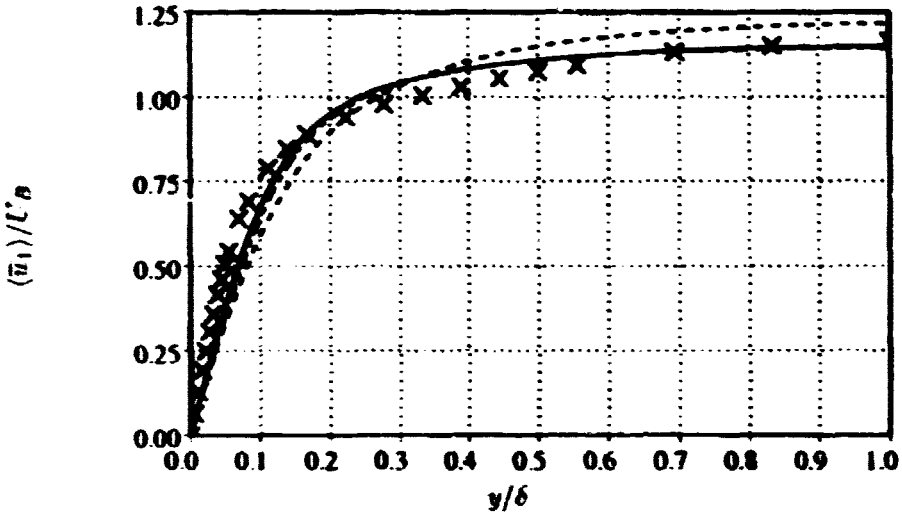

FIGURE 5. Streamwise mean velocity profiles normalized by the bulk velocity U_B for the planar channel flow at $Re_\tau = 180$. Symbols ($\times$) are the DNS data of Kim *et al.* (1987). Lines are computations on the $33\times65\times33$ mesh: ---- constant-coefficient Smagorinsky, $C_s = 0.17^2$; — · — dynamic Smagorinsky; —— Lagrangian dynamic Smagorinsky.

$\langle\bar{u}_1'^2\rangle$ and $\langle\bar{u}_2'^2\rangle$ via the pressure-rate-of-strain terms. For the low-resolution LES computations of linear compression, the effective rapid pressure-rate-of-strain model does not redistribute sufficient energy from the 'direct' production component to the other two. Moreover, the effective slow pressure-rate-of-strain model responds incorrectly to a decrease in the mean rate-of-strain.

5.3 Planar channel flow

Mean velocity profiles from the dynamic Smagorinsky and Lagrangian dynamic Smagorinsky models are very similar to one another, and show better agreement with DNS than the constant-coefficient model (Fig. 5). All three models deviate from DNS in the logarithmic region ($y^+ > 10$). Ratios of centerline mean velocity to bulk velocity $\langle\bar{u}_1(y=\delta)\rangle/U_B$ are 1.22 for constant-coefficient Smagorinsky, 1.15 for dynamic Smagorinsky, 1.15 for Lagrangian dynamic Smagorinsky, and 1.16 for the DNS of Kim *et al.* (1987).

Both dynamic models effectively 'turn down' the subgrid-scale viscosity in the vicinity of the wall. The mesh spacing $\overline{\Delta}$ decreases close to the wall, as does the model coefficient C_s. The latter behavior is demonstrated in Fig. 6. There computed profiles of $C_s^{1/2}$ extracted from the dynamic model and the Lagrangian dynamic model are shown. For the former model, the standard value of 0.1 is recovered in the center of the flow, with a rapid drop-off to zero at the walls. The Lagrangian dynamic model behaves similarly out to a distance of about $y^+ \approx 40$, but levels off to a lower value of $C_s^{1/2} \approx 0.06$ at the centerline.

Computed Reynolds-stress profiles from the Lagrangian dynamic model are given

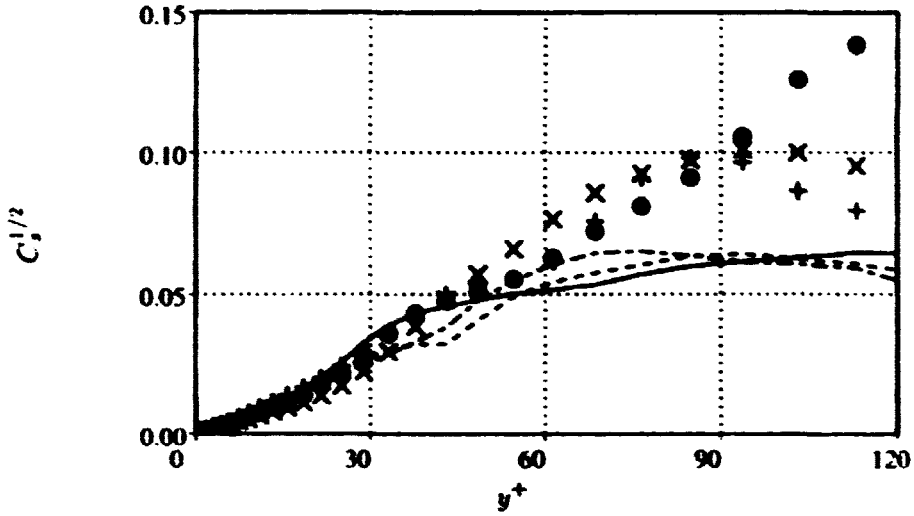

FIGURE 6. Computed profiles of $C_s^{1/2}$ adjacent to the lower wall for the planar channel flow at $Re_\tau = 180$. Symbols (• , × , +) are planar-averaged profiles from the dynamic Smagorinsky model at three instants of time. Lines (——, - - - - , ——) are planar-averaged profiles from the Lagrangian dynamic Smagorinsky model at three instants of time.

in Figs. 7 and 8. Results from the dynamic model are similar, while the constant-coefficient model yields somewhat poorer profiles (not shown). This is consistent with our findings from the mean velocity profiles of Fig. 5. Normal stress components display qualitatively correct behavior (Fig. 7), but there are significant quantitative departures from the DNS data. In particular, on this coarse mesh, all models tend to leave too much energy in the direct production component $\langle \overline{u}_1'^2 \rangle$ at the expense of $\langle \overline{u}_2'^2 \rangle$ and $\langle \overline{u}_3'^2 \rangle$. The value of the peak shear stress is computed reasonably well, although the LES profile is shifted outward from the wall compared to the DNS data (Fig. 8). These findings suggests that the present mesh resolution is marginal for computing second-order statistics, especially in the log-law region.

5.4 Axisymmetric piston-cylinder assembly

Computations are in progress at the time of this writing. Quantitative comparisons with measurements of Morse *et al.* (1978) are forthcoming.

6. Discussion and conclusions

This research has explored a candidate numerical methodology and subgrid-scale stress models for LES of flow in reciprocating IC engines. The present results have been obtained using coarse meshes that are representative of minimal mesh requirements for spectral LES. Generally reasonable evolution of first and second moments has been found nevertheless. This is an encouraging finding, given the low formal accuracy of the numerics. Based on these early results, it is anticipated that acceptable accuracy can be obtained using practical mesh densities.

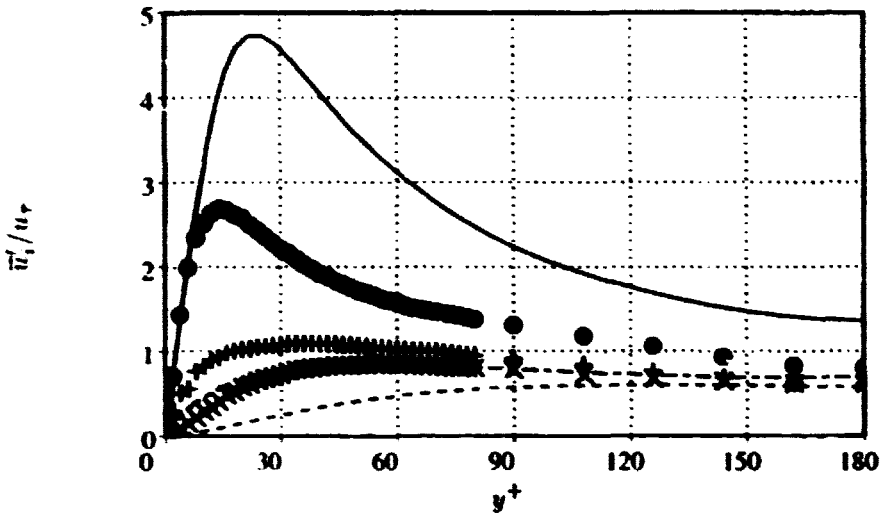

FIGURE 7. Turbulence intensities normalized by the wall friction velocity u_τ for the planar channel flow at $Re_\tau = 180$. Symbols are the DNS data of Kim *et al.* (1987): • streamwise (x_1) component; × wall-normal (x_2) component; + cross-stream (x_3) component. Lines are computations using the Lagrangian dynamic Smagorinsky model (resolved portion): —— streamwise (x_1) component; ---- wall-normal (x_2) component; – – – cross-stream (x_3) component.

Specific deficiencies have been attributed to inadequate spatial resolution. These include the energy spectrum decay for isotropic turbulence and insufficient energy transfer from the 'direct' production component for linear compression and planar channel flow. The two dynamic models have demonstrated an advantage compared to the constant-coefficient model in the planar channel flow. No specific deficiencies of the dynamic subgrid-scale models have been identified. In some cases, model results are not much different than those obtained in the absence of any explicit subgrid-scale model. This is consistent with earlier LES work for coarse meshes and low-order numerical methods. It remains to establish that these deficiencies can be overcome through mesh refinement, and to quantify resolution requirements for a specified level of fidelity to experiment or to benchmark computations. Short of explicitly filtering the governing equations at a scale much larger than the mesh spacing, it will remain difficult to isolate numerical inaccuracy from subgrid-scale model performance in LES.

Beyond spatial resolution, the most pressing outstanding issue is the lack of analytic characterization of the filtering implied by non-spectral numerical methods: what is $\bar{u}_i$? While it is straightforward to analyze and implement a variety of filters in spectral methods (e.g., spectral cutoff, spatial top-hat, spatial/spectral Gaussian), there has been little analysis to guide the implementation of filters implicit in finite-difference, finite-volume, or finite-element schemes on unstructured meshes. Our experience with the initial spectrum for decaying turbulence shows that the present discretization scheme affects all wavenumbers to some extent. The same has

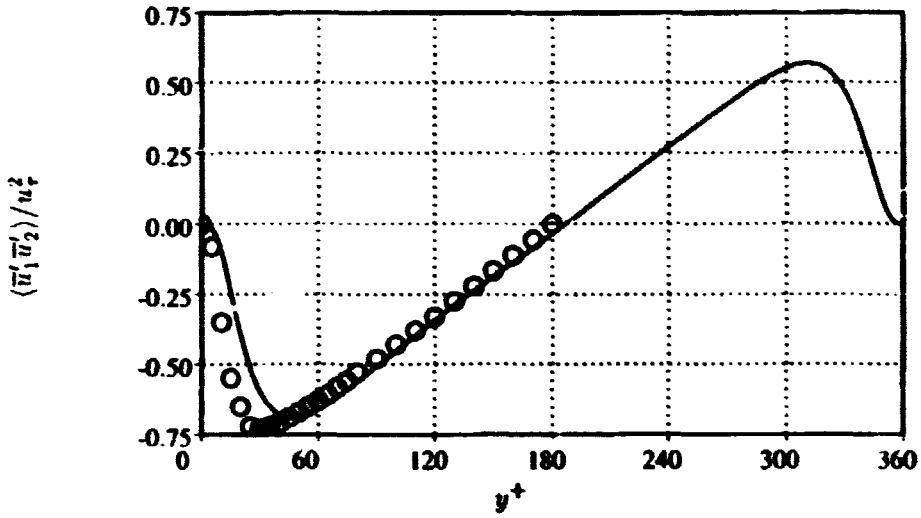

FIGURE 8. Turbulence shear stress normalized by the square of the wall friction velocity for the planar channel flow at $Re_\tau = 180$. Symbols (o) are the DNS data of Kim *et al.* (1987). Lines (———) are computations using the Lagrangian dynamic Smagorinsky model (resolved portion).

been found for other non-spectral methods that are being explored for unstructured LES (Jansen 1995).

Other outstanding issues for in-cylinder LES include wall treatment and inflow boundary conditions. Piomelli (1993) has shown that accurate LES results can be obtained using the dynamic model at high Reynolds numbers without further explicit wall modeling. The challenge at inflow boundaries is to establish the nature of forcing needed to yield in-cylinder velocity statistics representative of measured 'cyclic variability.' A final determination of suitability awaits the results of finer-mesh simulations for the three canonical configurations, and multiple-cycle results for the axisymmetric piston-cylinder assembly.

Acknowledgments

The first author thanks Drs. M. S. Sahota and P. J. O'Rourke of Los Alamos National Laboratory for many helpful discussions related to the use of CHAD. This project benefited immeasurably from the opportunity to interact with the other CTR Summer Program visitors and hosts. In particular, we thank Prof. Parviz Moin for the opportunity to participate.

REFERENCES

AMSDEN, A. A., O'ROURKE, P. J. & BUTLER, T. D. 1989 KIVA-II: a computer program for chemically reactive flows with sprays. *Los Alamos National Laboratory Report LA-11560-MS.*

COMTE-BELLOT, G. & CORRSIN, S. 1971 Simple Eulerian time correlation of full- and narrow-band velocity signals in grid-generated, 'isotropic' turbulence. *J. Fluid Mech.* **48**, 273-337.

EL TAHRY, S. H. & HAWORTH, D.C. 1992 Directions in turbulence modeling for in-cylinder flows in reciprocating IC engines. *AIAA J. Prop. & Power.* **8**, 1040-1048.

EL TAHRY, S. H. & HAWORTH, D.C. 1996 A perspective on the state-of-the-art in IC engine combustion modeling. *SIAM Sixth International Conference on Combustion, New Orleans, LA.* (To be submitted for publication.)

GERMANO, M., PIOMELLI, U., MOIN, P. & CABOT, W.H. 1991 A dynamic subgrid-scale eddy viscosity model. *Phys. Fluids A.* **3**, 1760-1765.

HAWORTH, D. C., EL TAHRY, S. H., HUEBLER, M. S. & CHANG, S. 1990 Multidimensional port-and-cylinder flow calculations for two- and four-valve-per-cylinder engines: influence of intake configuration on flow structure. *SAE Paper No. 900257.* (Also *SAE Trans., J. of Engines*, 1990.)

JANSEN, K. 1995 Preliminary large-eddy simulations of flow around a NACA 4412 airfoil using unstructured grids. *CTR Annual Research Briefs - 1995.* NASA Ames/Stanford Univ.,61-72.

KASSINOS, S. C. & REYNOLDS, W. C. 1994 A structure-based model for the rapid distortion of homogeneous turbulence. *Stanford University Dept. of Mech. Eng. Thermosciences Division Report TF-61.*

KIM, J., MOIN, P. & MOSER, R. 1987 Turbulence statistics in fully developed channel flow at low Reynolds number. *J. Fluid Mech.* **177**, 133-166.

LILLY, D.K. 1992 A proposed modification of the Germano subgrid-scale closure method. *Phys. Fluids A.* **4**, 633-635.

MENEVEAU, C., LUND, T. S. & CABOT, W. H. 1996 A Lagrangian dynamic subgrid-scale model of turbulence. *J. Fluid Mech.* **319**, 353-385.

MORSE, A. P., WHITELAW, J. H. & YIANNESKIS, M. 1978 Turbulent flow measurement by laser Doppler anemometry in a motored reciprocating engine. *Imperial College Dept. Mech. Eng. Report FS/78/24.*

O'ROURKE, P. J. & SAHOTA, M. S. 1996a A variable explicit/implicit numerical method for calculating advection on unstructured grids. (Submitted to *J. Comput. Phys.*)

O'ROURKE, P. J. & SAHOTA, M. S. 1996b NO-UTOPIA: the flow solver for the CHAD computer library. *Los Alamos National Laboratory Report.* (In preparation.)

PIOMELLI, U. 1993 High Reynolds number calculations using the dynamic subgrid-scale stress model. *Phys. Fluids A.* **5**, 1484-1490.

NEXT
DOCUMENT

Large-eddy simulation of a backward facing step flow using a least-squares spectral element method

By Daniel C. Chan[1] AND Rajat Mittal[2]

We report preliminary results obtained from the large eddy simulation of a backward facing step at a Reynolds number of 5100. The numerical platform is based on a high order Legendre spectral element spatial discretization and a least squares time integration scheme. A non-reflective outflow boundary condition is in place to minimize the effect of downstream influence. Smagorinsky model with Van Driest near wall damping is used for sub-grid scale modeling. Comparisons of mean velocity profiles and wall pressure show good agreement with benchmark data. More studies are needed to evaluate the sensitivity of this method on numerical parameters before it is applied to complex engineering problems.

1. Introduction

Many aerospace and commercial products operate in a dynamic flow environment. The structural integrity, performance, and development costs of these products are affected by the unsteady flowfields they encounter. In rocket propulsion systems, dynamic loads are the cause of many life limiting and failure mechanisms. For instance, a number of dynamic load related issues manifested themselves during the development of the space shuttle main engine, resulting in hundreds of millions of dollars of program development costs in terms of hardware redesign and testing. Unsteady flows can also be a very effective sound generating mechanism; George (1990) states that the aerodynamically generated noise increases approximately as velocity to the 6^{th} power. Therefore, the aerodynamic noise generated by vehicles traveling at high speeds can be very annoying to both passengers and communities located in the proximity of major highways and railroads. In some European countries where trains can travel in excess of 200 MPH, the responsible agency has to erect sound walls along the railroads to minimize the effects of noise pollution. This requirement can drastically increase the construction and maintenance costs of a railway system. For passenger cars, unacceptable noise levels inside the compartment can have adverse effects on sales.

In light of the importance in characterizing the dynamic flow environment in both aerospace and commercial applications, Rocketdyne has initiated a multi-year effort to develop a general purpose computational fluid dynamics based analysis system for dynamic load prediction. This system will provide high-fidelity predictive capability through the development of a novel numerical algorithm and

1 CFD Technology Center, Rocketdyne Division, Rockwell International Corporation
2 Center for Turbulence Research

utilization of distributed parallel computing. The numerical algorithm is a high order spectral method which provides the unique capability to accurately model complex geometries and rapidly varying flowfields. Parallel computing provides the necessary memory capacity and speed required for large scale computations. All these features have been incorporated in the Rocketdyne Unstructured Implicit Flow (UniFlo) solver. The UniFlo code is capable of performing a hierarchy of fluid dynamic analyses including direct numerical simulation (DNS), large eddy simulation (LES) and Reynolds average Navier-Stokes solution (RANS). Only DNS and LES can provide time accurate information that is needed for unsteady turbulent simulations. LES models flow features that are not directly captured by the grid resolution employed. This technique is also known as subgrid scale (SGS) modeling. The LES approach (vs. DNS) can relax the requirement on grid resolution that is normally very demanding for turbulent flow simulations making it an effective tool for engineering analyses. However, one also has to be concerned with the numerical errors that increase as the grid is coarsened. If not controlled properly, these errors can overwhelm the advantage offered by LES. Therefore, the purpose of this work is to first evaluate the numerical accuracy of UniFlo in predicting time dependent flows. Once this is accomplished, we then assess the capability of the Smagorinsky SGS model in predicting turbulent flow. The backward facing step configuration is chosen as the benchmark case since it mimics the flowfield in a rocket engine combustor and existing numerical and experimental data are available for comparison.

In what follows, we describe the numerical method, boundary condition and SGS model employed by UniFlo. Numerical results demonstrating accuracy of the method and effectiveness of the Smagorinsky model are also provided.

2. Numerical method

The Navier-Stokes equations are written as a first order system and can be represented as $\mathcal{L}\vec{u} = \vec{f}$ in a domain $\Omega \subset \Re^{n_d}$ which is subjected to the condition $\mathcal{B}\vec{u} = \vec{g}$ along a piecewise smooth boundary Γ. $\mathcal{L}$ is a first-order partial differential operator:

$$\mathcal{L}\vec{u} = \sum_{i=1}^{n_d} \mathcal{A}_i \frac{\partial \vec{u}}{\partial x_i} + \mathcal{A}_0 \vec{u}$$

$n_d = 2$ or 3, depending on the spatial dimensions, $x_i's$ are the Cartesian coordinates, $\vec{u}$ has a length n, where n is the number of dependent variables, $\vec{f}$ is the forcing function, and both B and $\vec{g}$ describe the appropriate boundary conditions. $\mathcal{A}$'s are $m \times n$ matrices which describe the characteristics of the system of equations being solved. The idea behind the least squares spectral element method (LSSEM) is to minimize the residual

$$R = \mathcal{L}\vec{u} - \vec{f}$$

in a least squares sense within the domain of interest and construct the functional as

$$I(\vec{u}) = \frac{1}{2} \| \mathcal{L}\vec{u} - \vec{f} \|_0^2 = \left(\mathcal{L}\vec{u} - \vec{f}, \mathcal{L}\vec{u} - \vec{f} \right)$$

By setting $\delta I = 0$ and $\delta \vec{u} = \vec{w}$, one can reduce the problem to

$$(\mathcal{L}\vec{w}, \mathcal{L}\vec{u}) = \left(\mathcal{L}\vec{w}, \mathcal{L}\vec{f}\right) \qquad \vec{w} \in S$$

where, $S = \{\vec{u} \in H_0^1(\Omega); \mathcal{B}\vec{u} = g \text{ on } \Gamma\}$, and H_0^1 is the Sobolev space with a compact support. For incompressible viscous flows, the working variables are velocity, pressure, and vorticity. By using this system of equations, one can employ any of the C^0 functions to approximate the spatial variation of the dependent variables. UniFlo employs isoparametric mapping to transform the governing equations from the Cartesian coordinate system to a generalized coordinate system where the spatial discretization is performed. The domain of interest is divided into a set of non-overlapping elements and within each element, basis function derived from Legendre polynomials is used for spatial discretization. The spatial accuracy depends on the choice of the order of Legendre polynomial basis function and can vary from element to element. This approach, also known as spectral element, has been formulated by Rønquist and Patera (1987). LSSEM uses a common interpolating function to approximate all of the dependent variables. Even with the presence of the convective terms, the resulting set of algebraic equations are positive definite and symmetric. LSSEM maintains a tight coupling among all of the governing equations and provides a set of well-defined boundary conditions that are consistent with flow physics and mathematical constraints. It does not require any user defined artificial damping factor to maintain numerical stability. To maintain high spatial accuracy at the domain boundary, UniFlo does not need special treatment such as the utilization of ghost points. The convective terms are linearized with the Newton-Raphson procedure so that the spatial derivatives can be discretized implicitly. Sub-iterations are required at each time step for the purpose of minimizing the effect of linearization errors. For most problems, the residual can be reduced by four orders of magnitude in less than three iterations. The accuracy is second order in time with the application of a backward differencing scheme. For instance, the temporal derivative of the velocity component, u, can be discretized as

$$\frac{\partial u}{\partial t} = \frac{u^{s-1} - 4u^s + 3u^{s+1}}{2\delta t}$$

where superscripts represent different time levels. The resulting algebraic equations are solved by the conjugate gradient method with Jacobi preconditioning. The structure of the coefficient matrix is completely arbitrary and the solution procedure does not rely on any pre-defined order. More details of this method is given by Chan (1996).

The boundary conditions are: (1) specified velocity at the inlet, (2) no slip along solid walls, (3) stress free and vanishing normal velocity component along the plane of symmetry and (4) 'free boundary' along an outflow plane. For a Cartesian grid, stress free condition is imposed by setting the horizontal vorticity components to zero. Points located on a 'free boundary' are treated as unknowns and solved directly.

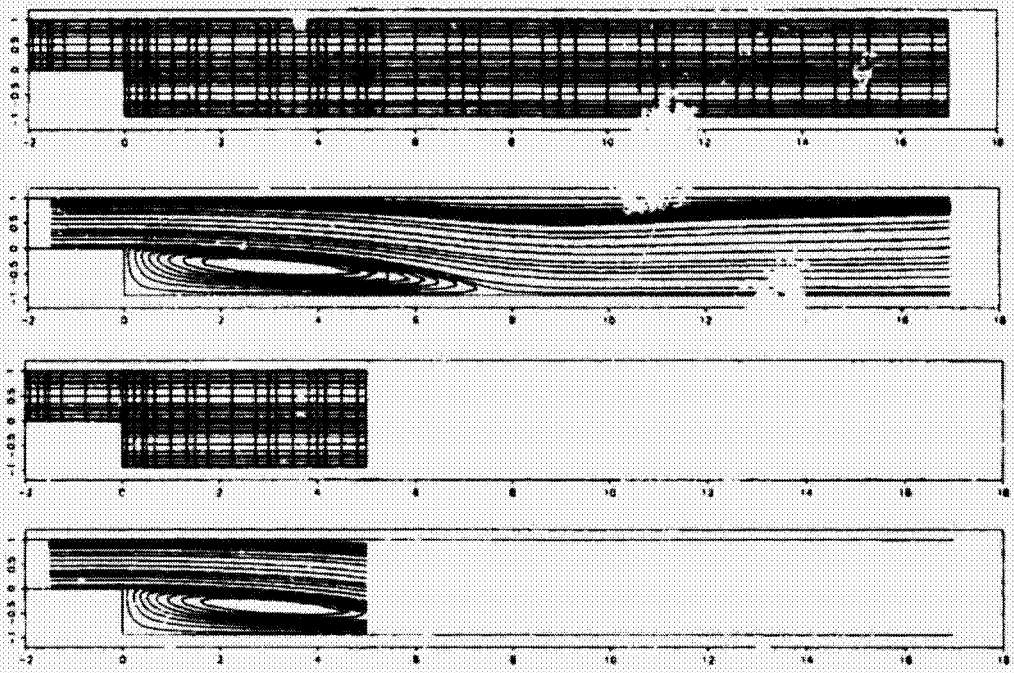

FIGURE 1. Streamlines behind a backward facing step at $Re = 389$; top half: result for long domain: bottom half: result for truncated domain.

For turbulent flows, we relate the subgrid scale stresses to the strain rate of the resolved velocity field via Boussinesq approximation. The diffusion term of the Navier-Stokes equations then becomes

$$-(\frac{1}{Re} + \nu_t)\epsilon_{ijk}\frac{\partial \omega_k}{\partial x_j} - \frac{\partial \nu_t}{\partial x_j}2S_{ij}$$

where ν_t is the eddy viscosity, S_{ij} is the strain rate, and ω is the vorticity. The value of ϵ_{ijk} is equal to zero unless each of the number 1,2, and 3 occurs as a subscript. Furthermore, ϵ_{ijk} is equal to 1 if the order of subscripts is cyclic, it becomes -1 if the order of subscripts is not cyclic. The eddy viscosity is computed as

$$\nu_t = (C_s\Delta)^2|S_{ij}|f_s$$

$$\Delta = (\delta x \delta y \delta z)^{1/3}$$

where $C_s = 0.1$ and f_s is the Van Driest damping function defined as

$$f_s = 1.0 - exp(\frac{-\delta^+}{26})$$

In reality the value of C_s is not constant and can change in time and space. Near a corner, δ^+ is determined with the shortest normal distance from the adjacent walls. This procedure is somewhat *ad hoc* and is problem dependent.

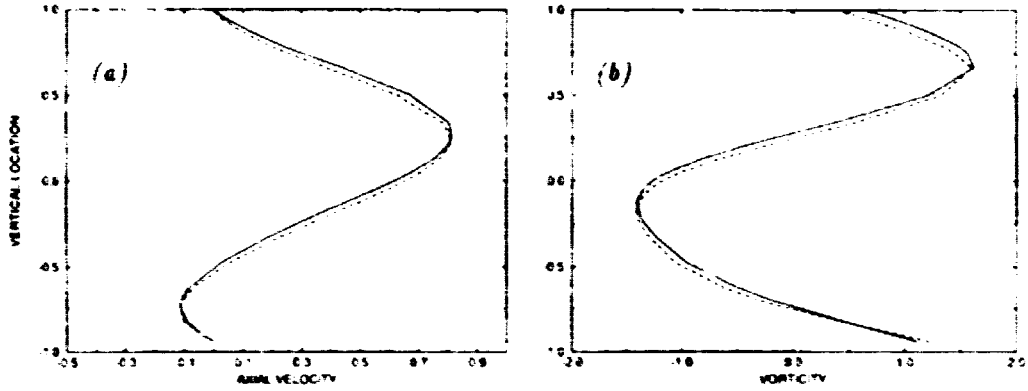

FIGURE 2. Predicted profiles at an axial distance of 5 inlet heights behind a backward-facing step with Re = 389. —— results obtained with long domain ---- results obtained with truncated domain. *(a)* axial velocity profile and *(b)* vorticity profile.

3. Numerical results and discussion

To demonstrate the effectiveness of the current outflow boundary condition, we apply it to compute the laminar flow behind a backward facing step studied experimentally by Armaly *et al.* (1983). The Reynolds number, based on the inlet height and average velocity, is 389. The ratio between the inlet and step heights is 0.94. Flow separates behind the step and reattaches at an axial distance that is equal to about eight step heights from the plane of expansion. Two exit domains, one long and one short, are used. For the long domain case, the axial length behind the step is 17, the flow has room to reattach after separation and recover to a fully-developed flow; therefore, the downstream influence on the flowfield near the step is small, and for comparison we can use the predicted profiles as the baseline. For the short domain case, the outflow plane, which cuts through the separated region, is located at 5 inlet heights behind the step. Because of this, accuracy of the predicted profiles is strongly influenced by the outflow boundary condition. For time dependent turbulent flow, this situation is similar to having an eddy pass across an outflow boundary. A parabolic profile is imposed along the inlet plane which is located at 2 inlet heights upstream of the expansion. Figure 1 shows the grid systems and streamlines predicted by UniFlo for both the short and long domains. In both cases, 5 collocation points are placed within each element. The total number of elements is 72 for the long domain and 36 for the short domain. The flow pattern is almost the same in both cases. For the short domain case, having a reverse flow on part of the outflow boundary does not present numerical convergence problem, and this further demonstrates the robustness of the current numerical method and outflow boundary condition. The predicted reattachment is 8.0 times the inlet height and is in good agreement with the test data. Armaly *et al.* also reports that at Re = 389, the flow begins to separate from the upper wall and becomes three-dimensional, but the separation region is so small that its size

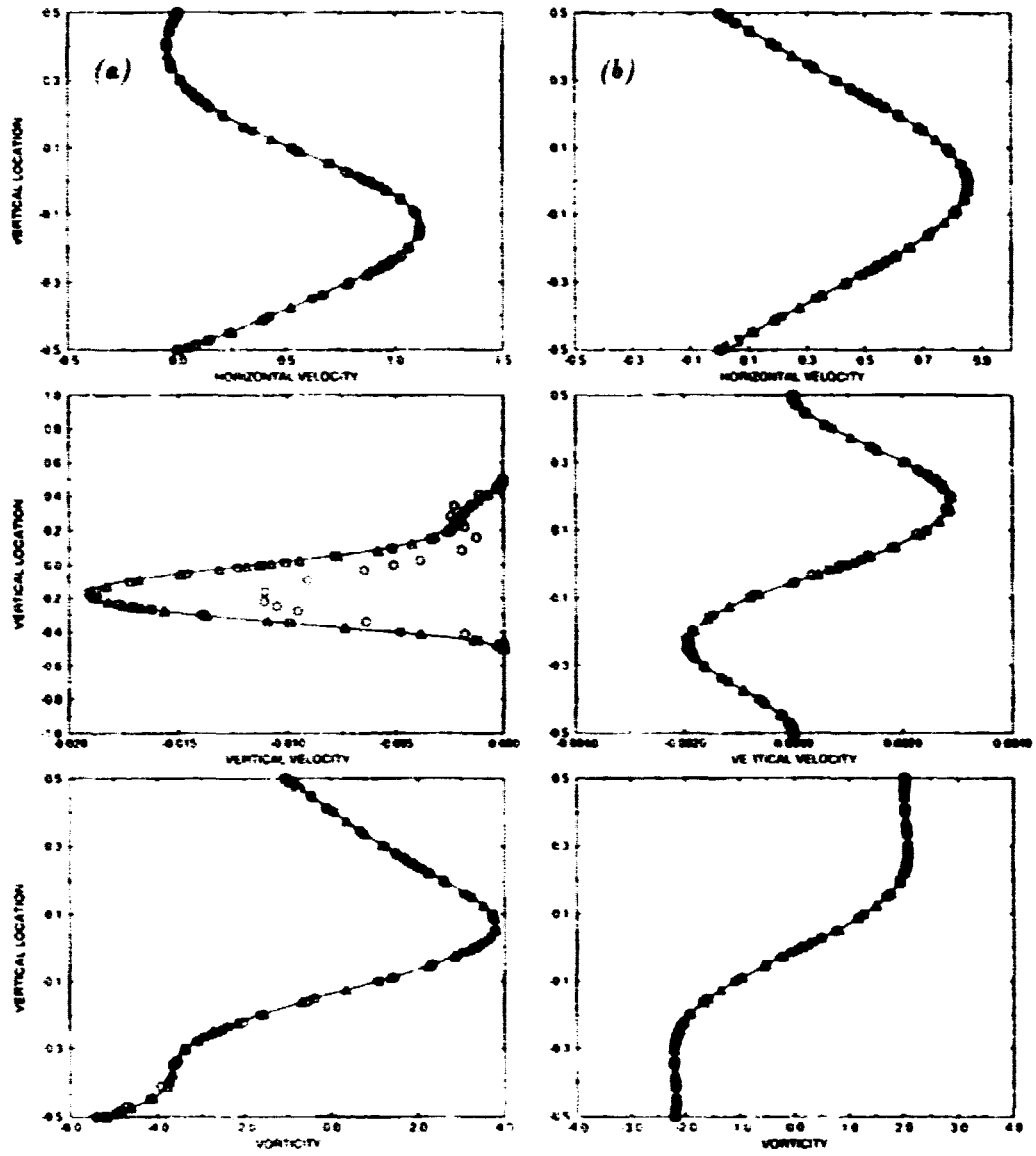

FIGURE 3. Predicted profiles behind a backward-facing step with Re = 800: —— Gartling's results, ○ 5^{th} order, △ 6^{th} order, and □ 7^{th} order: *(a)* axial location of 7 and *(b)* axial location of 15.

could not be measured. This phenomena is correctly predicted by UniFlo. Figure 2 shows the axial velocity and vorticity profiles at an axial location of 5 inlet heights behind the step. The trend in both cases is identical, with only less than 20 percent discrepancy on the magnitude.

The next test case is due to Gartling (1990) and Gresho *et al.* (1993). The purpose of this exercise is to answer some of the questions raised by Gresho *et al.* as

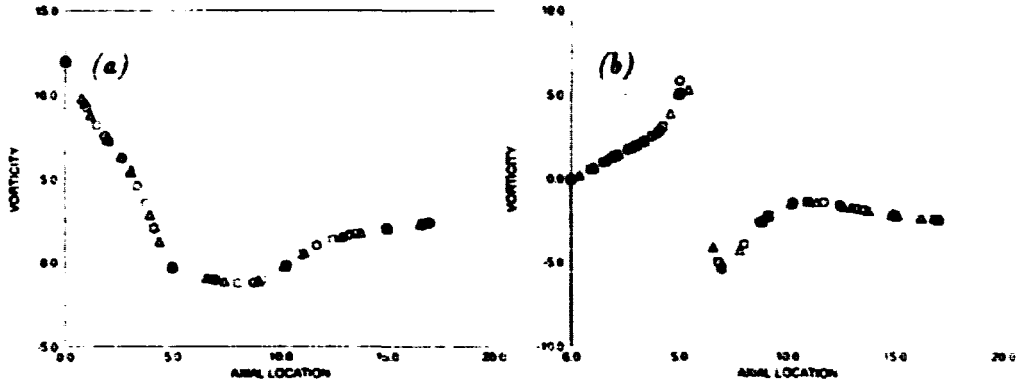

FIGURE 4. Predicted wall vorticity distribution for a backward-facing step with $Re = 800$, o 5^{th} order, Δ 6^{th} order, and $\square$ 7^{th} order, *(a)* upper wall and *(b)* lower wall.

to whether spectral methods can handle flow geometries with a sharp corner and predict the correct flow behavior. Through careful numerical studies and stability analysis, they conclude that at a Reynolds number of 800, the flow behind a backward facing step with 1:2 expansion ratio is indeed steady. With this in mind, we first perform the simulation as a steady state problem by turning off the transient terms in the Navier-Stokes equations. The rectangular flow domain is 17 units long and 1 unit high. The flow enters the domain along the top half portion of the left boundary with a parabolic profile. The Reynolds number based on the step height and mean velocity is 800. Figure 4 shows the grid skeleton employed; there are 4 elements in the vertical direction and 11 elements in the streamwise direction. Within each element, we apply 5^{th}, 6^{th}, and 7^{th} order polynomials, respectively, in each of the two directions. Figure 3 shows the comparison between the predicted profiles and benchmark data at two different streamwise locations. All except the vertical velocity profile at the axial location of 7 show an excellent agreement with the benchmark data of Gartling. Figure 4 shows the vorticity distribution, which is proportional to shear stress, along the bottom and top boundaries. By examining these plots, one can determine both the separation and reattachment points. Along the lower wall, UniFlo predicts a reattachment length of 6.1, whereas along the upper wall, it predicts a separation at the streamwise location of 4.8 and a reattachment at the streamwise location of 10.5. These predictions are in excellent agreement with the benchmark data. These results also indicate that for steady flow computation, numerical error incurred from using an under-resolving grid is very localized.

We then compute the same problem by treating it as an unsteady flow. Initially, the flow is stagnant inside the domain. Figure 5 shows the temporal evolution of the streamlines for the case where 6^{th} order polynomials are used inside each element. Overall this grid resolution produces satisfactory results for steady state calculation, however, this is not the case for time accurate simulation. A transient process, which involves a sequence of vortex shedding, takes place along the upper

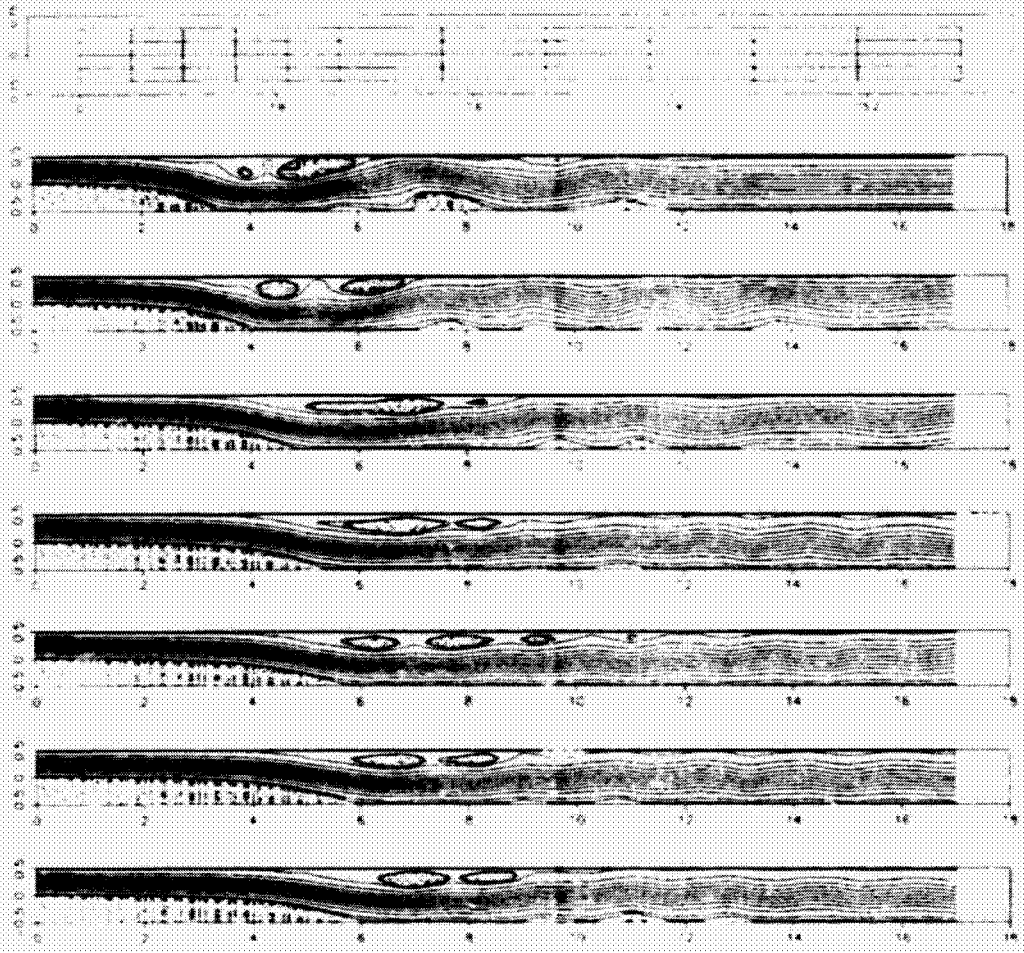

FIGURE 5. Streamlines showing the time evolution of the flowfield behind a backward facing step at a Reynolds number of 800; computation performed with a 11×4 grid and 6^{th} order Legendre polynomials; final state is a temporally periodic flow; from top to bottom: time=10, 20, 30, 50, 80, 100, and 140.

wall at the streamwise location where the steady state result show a discrepancy in the vertical velocity profile prediction. This result demonstrates that numerical error that develops in a small region can grow over time and contaminate the entire flowfield. We then refine the grid by increasing the number of elements in the streamwise direction to 18 while maintaining 6^{th} order polynomials in each element. The result shown in Fig. 6 indicates that the initial transient flow features decay rapidly in time and the flow evolves asymptotically towards a steady state. This prediction agrees with the finding of Gresho *et al.* It is apparent that the transient flow predicted above is a numerical artifact. Unfortunately, the flow features generated by this numerical error look so real, making them difficult to detect. Therefore, for unsteady flow simulation one must perform grid dependence study

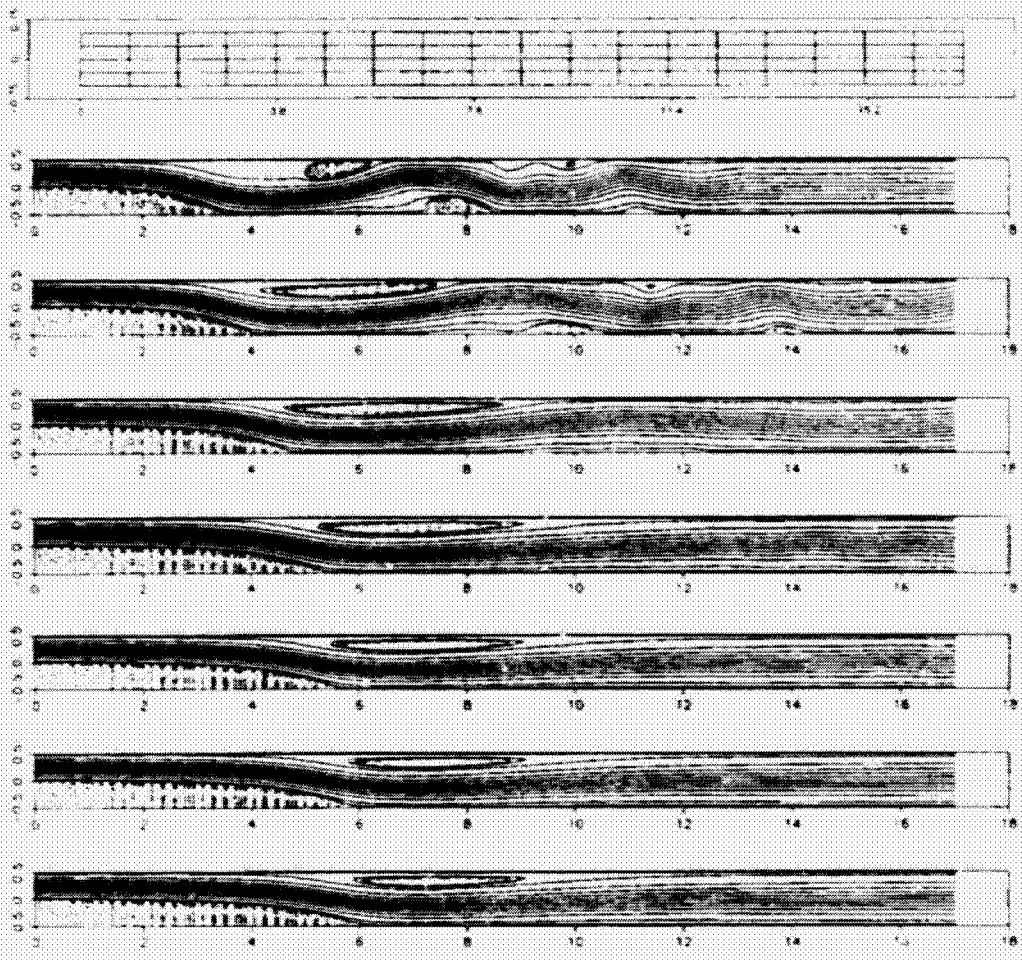

FIGURE 6. Streamlines showing the time evolution of the flowfield behind a backward facing step at a Reynolds number of 800: computation performed with a 18×4 grid and 6^{th} order Legendre polynomials; asymptotic state is steady; from top to bottom: time=10, 20, 30, 50, 80, 100, and 140.

before attempting to explain the underlying flow physics.

Having addressed some of the relevant numerical issues, we then use UniFlo to simulate the three-dimensional backward facing step configuration where experimental data of Jovic and Driver (1994), DNS data of Le and Moin (1994), and LES data of Akselvoll and Moin (1995) are available for comparison. The grid system employed is shown in Fig. 7. There are 13 elements in the streamwise direction, 6 elements in the vertical direction and 6 elements in the spanwise direction. Within each element, 6^{th} order Legendre polynomials are used in each of the three directions. The expansion ratio is 5:6. The geometry is scaled with the step height, H. The inlet plane is located at $5H$ upstream of the expansion, and the outflow plane is located at $17H$ downstream of the expansion plane. The spanwise width is $4H$ and

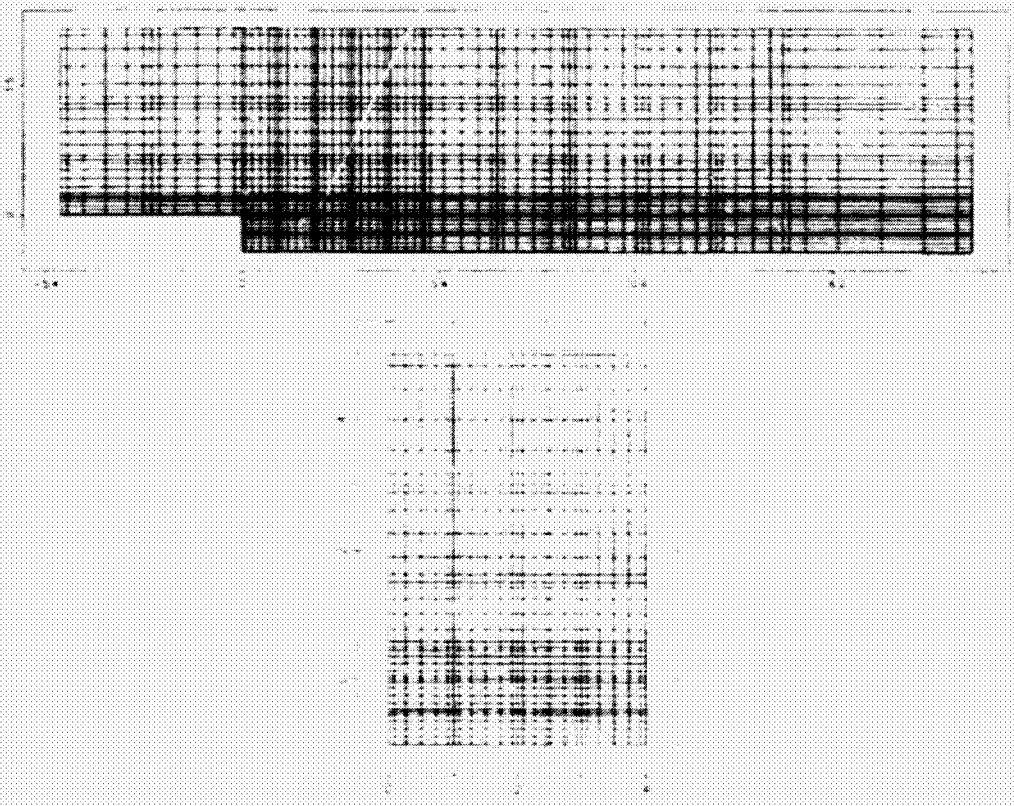

FIGURE 7. Grid system for the three-dimensional backward facing step. top: through flow plane, bottom: cross-sectional plane.

a periodic boundary condition is imposed in this direction. Stress free condition is imposed along the top boundary, and no slip condition is imposed along the bottom wall. At the inlet plane, we take the time dependent turbulent boundary layer profiles computed by Akselvoll and Moin and interpolate them onto the current grid. The freestream velocity is taken to be one, and the time it takes for the flow to travel one step height is also one. Since our implicit flow solver is not restricted by the CFL condition for numerical stability, we can take a larger time step size of 0.1, which is five times higher than that employed by Akselvoll and Moin. As a result, each through flow takes 220 time steps. Time average quantities are collected after the flow has evolved through the domain 5 times. For comparison, we further average the data in the spanwise direction and show them in Fig. 8. The predicted wall pressure distribution is in good agreement with the experimental data inside the recirculating region behind the step. However, in the recovery region, all the numerical methods, including UniFlo, predict a faster recovery rate than that of the experimental measurements. The velocity profiles are compared to the DNS data of Le and Moin. The agreement is good for all five streamwise locations.

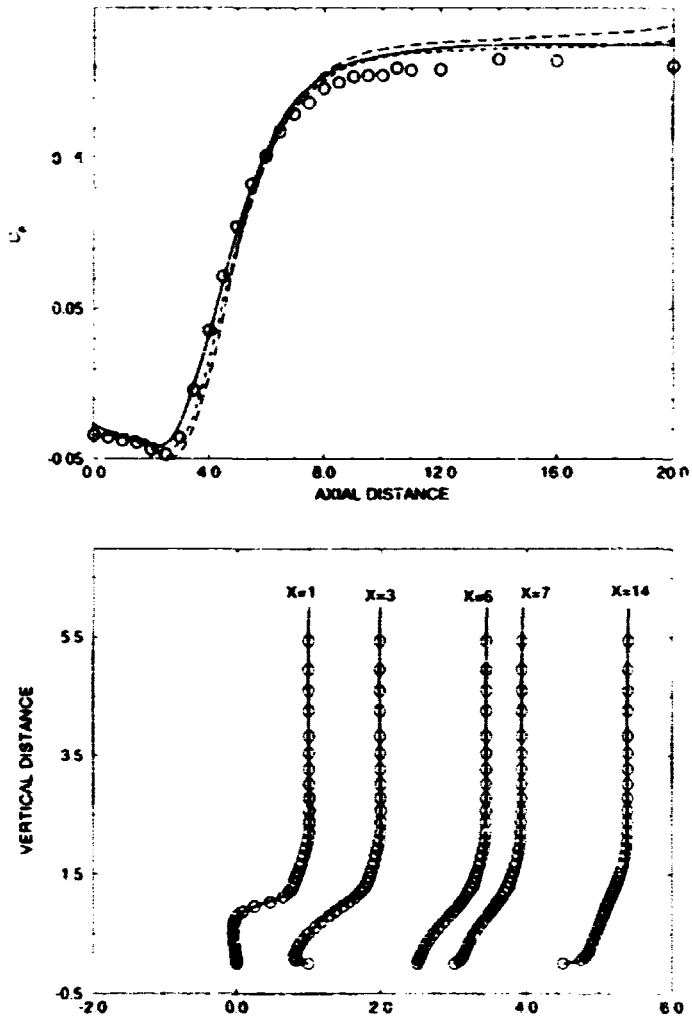

FIGURE 8. Time and spanwise average flow quantities predicted by UniFlo for a three-dimensional backward facing step at $Re = 5100$, top: pressure coefficient along bottom wall, —— UniFlo prediction, — - — DNS result of Le & Moin - - - - LES result of Akselvoll & Moin, and o experimental result of Jovic & Driver; bottom: axial velocity profiles at selected streamwise locations; —— UniFlo, o DNS result of Le & Moin.

4. Summary

We have demonstrated that a spectral based flow solver can be used to simulate the flow behind a backward-facing configuration. The weak singularity located at the corner does not present numerical problem to the least squares method. Numerical error can generate unsteady flow phenomena that could be mistaken as 'real' flow physics. Therefore, grid dependence study is paramount (more so than

the steady state flow calculation) in unsteady flow simulation. The preliminary results obtained from the LES show good agreement with both experimental data and numerical data. Further studies are needed in order to understand the role of the subgrid scale model in these simulations. The Smagorinsky model with Van Driest wall damping is, however, difficult to implement for complex geometries. Future work will include the implementation of dynamic models that do not require wall damping function and user specified model constant.

5. Acknowledgments

The first author is supported by the Rocketdyne IR&D program and he would like to thank Munir Sindir and Steve Barson for their continuing interest in his work. Technical discussion with Charles Meneveau, Ken Jensen, and Dan Haworth provided many insightful ideas on LES. Parviz Moin made all this possible and his hospitality is greatly appreciated.

REFERENCES

AKSELVOLL, KNUT & MOIN, PARVIZ 1995 Large eddy simulation of turbulent confined coannular jets and turbulent flow over a backward facing step. TF-63. Department of Mechanical Engineering, Stanford University.

ARMALY, B. F., DURST, F., PEREIRA, J. C. F., & SCHONUNG, B. 1983 Experimental and theoretical investigation of backward-facing step flow. *J. Fluid Mech.* **127**, 473-496.

CHAN, DANIEL C. 1996 A least squares spectral element method for incompressible flow simulations. *Proceedings of the Fifteen International Conference on Numerical Methods in Fluid Dynamics*. Springer-Verlag.

GARTLING, DAVID 1990 A test problem for outflow boundary conditions Flow over a backward-facing step. *Int'l. J. for Num. Meth. in Fluids*. **11**, 953-967.

GEORGE, ALBERT R. 1990 Automobile Aerodynamic Noise. *SAE Transactions*. **99-6**, 434-457.

GRESHO, P. M., GARTLING, D. K., CLIFFE, K. A., GARRAT, T. J., SPENCE, A., WINTERS, K. H., GOODRICH, J. W. & TORCZYNSKI, T. R. 1993 Is the steady viscous incompressible 2D flow over a backward-facing step at Re=800 stable? *Int'l. J. for Num. Meth. in Fluids*. **17**, 501-541.

JOVIC, S. & DRIVER, D. M. 1994 Backward-facing step measurement at low Reynolds number $Re_h = 5000$. NASA Technical Memorandum 108807. Ames Research Center, Moffett Field, CA 94035-1000.

LE, HUNG & MOIN, PARVIZ 1994 Direct numerical simulation of turbulent flow over a backward-facing step, TF-58. Dept. of Mechanical Engr., Stanford University.

RONQUIST, EINAR M. & PATERA, ANTHONY 1987 A Legendre spectral element method for the Stefan Problem. *Int'l. J. for Num. Meth. in Engr.* **24**, 2273-2299.

NEXT
DOCUMENT

Evaluation of a vortex-based subgrid stress model using DNS databases

By Ashish Misra[1] AND Thomas S. Lund[2]

The performance of a subgrid stress (SGS) model for large-eddy simulation (LES) developed by Misra & Pullin (1996) is studied for forced and decaying isotropic turbulence on a 32^3 grid. The physical viability of the model assumptions are tested using DNS databases. The results from LES of forced turbulence at Taylor Reynolds number $R_\lambda \simeq 90$ are compared with filtered DNS fields. Probability density functions (pdfs) of the subgrid energy transfer, total dissipation, and the stretch of the subgrid vorticity by the resolved velocity-gradient tensor show reasonable agreement with the DNS data. The model is also tested in LES of decaying isotropic turbulence where it correctly predicts the decay rate and energy spectra measured by Comte-Bellot & Corrsin (1971).

1. Introduction

The aim of this study is to use DNS data of isotropic turbulence to evaluate the performance of a new subgrid-stress model. LES is performed for both forced and decaying turbulence, and statistics are compared with appropriately filtered DNS fields and with some experimental results. The SGS stresses are calculated from a structural model of the subgrid vorticity proposed by Pullin & Saffman (1994), henceforth PS. This model has some similarity to the eddy-axis structure model for one-point closure proposed independently by Reynolds & Kassinos (1995). PS assume that the subgrid structure consists of an ensemble of straight stretched vortex structures each with an arbitrary internal vorticity distribution. Some support for this type of structure of the fine scales is provided by the observed tendency, in several numerical simulations, for the alignment between the vorticity vector and the eigenvector corresponding to the algebraically intermediate value of the principal rate-of-strain. Moreover, stretched-vortices have been used to make quantitative predictions for a range of fine-scale turbulence properties (Lundgren 1982, Pullin & Saffman, 1993, 1994). Misra & Pullin (1996) have examined and implemented several different versions of the locally anisotropic model of PS. In this report we will discuss one such model and examine its performance when measured against experiment and filtered DNS.

1 Graduate Aeronautical Laboratory, California Institute of Technology Pasadena CA 91125

2 Center for Turbulence Research

2. Vortex orientation model

In the PS model, the orientations of the structures are given by a pdf of the distribution of Euler-angles describing the transformation from laboratory to structure-fixed axes. The Reynolds stresses are proportional to the turbulent kinetic energy of the vortex collection times a tensor-moment of the pdf. For example, a delta-function pdf in which all vortices in a subgrid domain have a common direction described by the unit vector $\hat{\mathbf{e}}$ gives Reynolds stresses,

$$\tau_{ij} = (\delta_{ij} - \hat{e}_i \hat{e}_j) \int_{k_c}^{\infty} E(k) dk \tag{1}$$

where k_c is the cutoff wavenumber and the subgrid kinetic energy is given by $K = \int_{k_c}^{\infty} E(k) dk$. PS proposed a simplified version of the model using a rapid-distortion-like approximation in which the orientation of the subgrid vortices have a two-delta function pdf defined by the eigenvectors corresponding to the largest two eigenvalues of the resolved rate-of-strain tensor $\tilde{S}_{ij}$. It can be shown that such a model can not produce backscatter. In this report we study the performance of a slight variant of their original model wherein there is alignment between the eigenvector corresponding to the maximum eigenvalue of the rate-of-strain tensor, $\hat{\mathbf{e}}_3$, and the resolved vorticity vector, $\tilde{\omega}$. The Reynolds stresses are then given by

$$T_{ij} = (\mu(\delta_{ij} - \hat{e}_{3i}\hat{e}_{3j}) + (1-\mu)(\delta_{ij} - e^{\omega}_i e^{\omega}_j)) \int_{k_c}^{\infty} E(k) dk, \tag{2}$$

where μ is the fraction of structures aligned with the maximally extensive eigenvector and $\mathbf{e}^{\omega}$ is the unit vector along $\tilde{\omega}$. As partial justification for (2) we remark that one should expect complete alignment with $\tilde{\omega}$ in the DNS limit. We currently take $\mu = 0.5$. In order to calculate the subgrid energy, K, a local balance between production by the resolved scales, and the sum of subgrid and resolved scale dissipation is assumed. When coupled to an assumed Kolmogorov subgrid energy spectrum produced by the (unknown) internal structure of the vortices with a cut-off at $k\eta = 1$, where $\eta = (\nu^3/\epsilon)^{1/4}$ is the local Kolmogorov length, an equation sufficient to determine the dissipation is obtained. This is given by

$$\epsilon = 2\nu \tilde{S}_{ij}\tilde{S}_{ij} - \frac{3\,K_0}{2\,k_c^{2/3}}\,\epsilon^{2/3}\left(1 - (k_c\eta)^{2/3}\right)\tilde{S}_{ij} \times \left(\frac{1}{2}(\delta_{ij} - \hat{e}_{3i}\hat{e}_{3j}) + \frac{1}{2}(\delta_{ij} - e^{\omega}_i e^{\omega}_j)\right). \tag{3}$$

where K_0 is the Kolmogorov constant. When the model parameter K_0 is specified, (3) can be solved for the total dissipation ϵ and the subgrid energy determined from the Kolmogorov spectrum. This gives closure.

Equation (3) has the dimensions of L^2T^{-3}; we therefore divide (3) by $k_c^4\nu^3$ which results in two non-dimensional parameters (see Misra & Pullin for details),

$$\hat{S}_1 = \frac{2\tilde{S}_{ij}\tilde{S}_{ij}}{k_c^4\nu^2}, \qquad \hat{S}_2 = \tilde{S}_{ij}\frac{\left(\frac{1}{2}(\delta_{ij} - \hat{e}_{3i}\hat{e}_{3j}) + \frac{1}{2}(\delta_{ij} - e^{\omega}_i e^{\omega}_j)\right)}{2\,k_c^2\nu}. \tag{4}$$

where $\hat{S}_1$ represents the resolved scale dissipation while $\hat{S}_2$ represents the stretch experienced by the subgrid vortices by the resolved velocity-gradient tensor. The SGS dissipation may be written as,

$$\begin{aligned} \varepsilon_{sgs} &\equiv -\tilde{S}_{ij}T_{ij}, \\ &= -\tilde{S}_{ij}\left(\frac{1}{2}(\delta_{ij}-\tilde{e}_{3i}\tilde{e}_{3j})+\frac{1}{2}(\delta_{ij}-e_i^w e_j^w)\right)K, \\ &\sim -\hat{S}_2 K, \\ &= \tilde{S}'_{str} K, \end{aligned} \tag{5}$$

where $\tilde{S}'_{str}$ is the component of $\tilde{S}_{ij}$ aligned with the vortex. Hence backscatter, defined by $\varepsilon_{sgs} < 0$ occurs whenever $\hat{S}_2 > 0$ - the subgrid vortices are being compressed on the average - while $\hat{S}_2 < 0$ - the vortices are axially stretched - gives cascade.

This model has been implemented for both forced and decaying box turbulence by Misra & Pullin. They examine several alternative scenarios for determining the instantaneous orientations of vortices in a given cell.

3. Results and discussions

The incompressible, filtered Navier-Stokes equations are solved in a 32^3 box, with and without forcing, using periodic boundary conditions in all three directions. A Fourier-Galerkin pseudo-spectral method is used with '3/2 dealiasing rule' for the non-linear terms, i.e. 32 Fourier modes in each direction were advanced in time, the computation of the non-linear terms were done using 48 modes in each direction. A second order explicit Runge-Kutta scheme is used for time advancement.

3.1 Decaying turbulence

We study decaying isotropic turbulence in order to compare our results to the experiment of Comte-Bellot and Corrsin. They measured the energy spectrum at three downstream locations in grid turbulence. One can relate this to decaying isotropic turbulence by invoking the Taylor approximation. We mimic their experiment by studying turbulence in a cubical box with periodic boundary conditions. In a frame of reference moving with the mean flow speed,

$$t = \int_0^x \frac{dx'}{\overline{U}(x')}$$

where x is the downstream distance from the grid and $\overline{U}(x)$ is the mean flow velocity over the cross-section of the tunnel. We have non-dimensionalized the experimental data by the following characteristic velocity, length and time scales: $U_{ref} = \sqrt{3U_0'^2/2}$, $L_{ref} = L/2\pi$ and $t_{ref} = L_{ref}/U_{ref}$. In their experiments the velocity fluctuation at the first measuring station is $\sqrt{U_0'^2} = 22.2$ cm/s, the free-stream speed is $U_\infty = 10^3$ cm/s and the spacing of the turbulence generating mesh

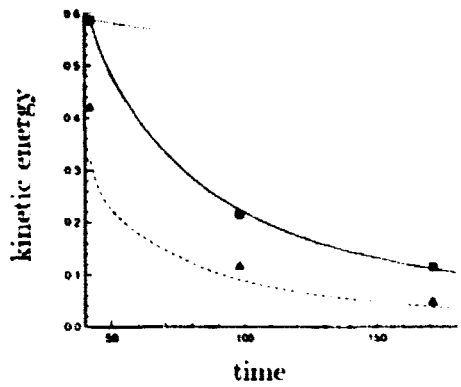

FIGURE 1. Decay of resolved (———) and subgrid (- - - -) kinetic energy. No model: ····· . Experiment: Resolved, ■; subgrid, ▲.

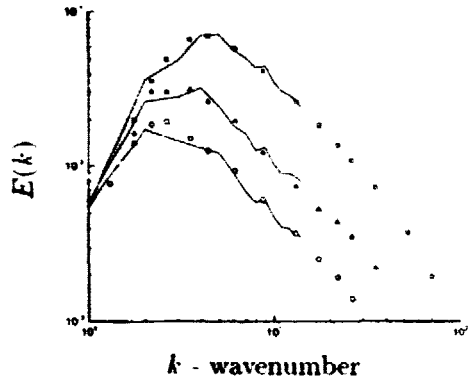

FIGURE 2. Time evolution of spectra in decaying turbulence. Experiment: □ , t=42; △ , t=98; ○ , t=171. Simulation at corresponding times: ——— .

is $M = 5.08$ cm. The size of the computational box, $L = 11M$, was chosen to contain roughly four integral scales. The times at the three stations were measured in terms of $U_\infty t/M$. The initial Taylor Reynolds number is $R_\lambda \simeq 80$. In order to compare the resolved and the subgrid part of the turbulent energy produced by the computation, the measured spectra have been integrated over the relevant scale ranges.

Figure 1 shows the decay of the resolved energy with time. The LES gives good agreement with experiment. The dotted line is the result of running the simulation with the model switched off. It is evident that the model plays an important role in predicting the correct decay of the kinetic energy. Aside from the parameter μ (set to 0.5), the model requires a value of the Kolmogorov constant. While acceptable results were obtained with the standard value of $K_0 = 1.5$, a slight improvement was observed when higher values were used. The results in Fig. 1 were obtained with $K_0 = 1.6$. While this value is on the edge of the uncertainty band from experimental measurements (Sreenivasan 1995), it is well within the predicted range

from numerical simulation; Jiménez *et al.* report a value of $K_0 \approx 2$ in a 256^3 DNS of isotropic turbulence at $R_\lambda = 94.1$. It is possible that elevated values of the Kolmogorov constant in numerical simulations is a low Reynolds number effect. If this is the case, it stands to reason that a larger value should be used in the present simulations which are also performed at relatively low Reynolds number.

The decay of the subgrid energy with time is also shown in Fig. 1. Note that the subgrid energy is obtained from the model without the solution of additional field equations. The subgrid energy is a quantity derived from a knowledge of the resolved field and the chosen subgrid energy spectrum; it therefore can not be initialized to match the experimental value. Figure 2 shows a plot of the resolved energy spectra with the measurements at the initial time and then at the two later instants. The initial spectrum is generated to match the experimental data, while the later two curves are the predicted spectra arising from the LES calculation. Figure 1 gives the area under the curve of Fig. 2 at the three time instants, over the resolved range of scales.

3.2 Forced turbulence

Forcing is achieved by exciting low wavenumbers such that the total energy injection rate is constant in time. A certain selected number of Fourier modes are chosen from a wavenumber shell $|\mathbf{k}| = k_0$. The Fourier coefficient of the forcing term is then written as,

$$\widehat{\mathbf{f}}_k = \frac{\delta}{N} \frac{\widehat{\widetilde{\mathbf{U}}}_k^*}{|\widehat{\widetilde{\mathbf{U}}}_k|^2} \tag{6}$$

for all modes in the specified shell. The above choice of $\widehat{\mathbf{f}}_k$ ensures that the energy injection rate, $\sum \widehat{\mathbf{f}}_k \cdot \widehat{\widetilde{\mathbf{U}}}_k$, is a constant and equal to δ. We have chosen $k_0 = 2, N = 20$, and $\delta = 0.1$ for all the runs. (See Carati *et al.* 1995)

Simulations with forcing were performed such that a statistical steady state is reached when statistics are collected. Results in this report are presented for Taylor Reynolds number, $R_\lambda \simeq 85$ in order to make comparisons with 128^3 DNS results at approximately the same Taylor Reynolds number.

Figure 3a-b shows scatter plots of $\hat{S}_1$ versus $\hat{S}_2$ from the LES as well as from filtered DNS data. These plots show the intensity of the vortex stretch as a function of the resolved dissipation rate. Notice that the DNS data displays a significant fraction of points with positive stretch parameter, $\hat{S}_2$, (backscatter) whereas the model rarely predicts these events. Quantitatively, the DNS shows roughly 30% backscatter, which is consistent with previous measurements (Piomelli *et al.* 1991). In contrast, our model yields only $\sim 3\%$ backscatter. While there is clearly a large discrepancy in the prediction of backscatter in Fig. 3, it should be noted that the percentage of backscatter can be controlled through the parameter μ in Eq. 2. $\mu = 1$ corresponds to complete alignment with $\tilde{\mathbf{e}}_3$ and results in no backscatter, while $\mu = 0$ corresponds to complete alignment with $\tilde{\omega}$ and gives about 40% backscatter. When $0 \leq \mu < 0.4$, the decay of the kinetic energy appears correct, but the decay of the energy spectra is somewhat unsatisfactory with a trend towards flattening of the

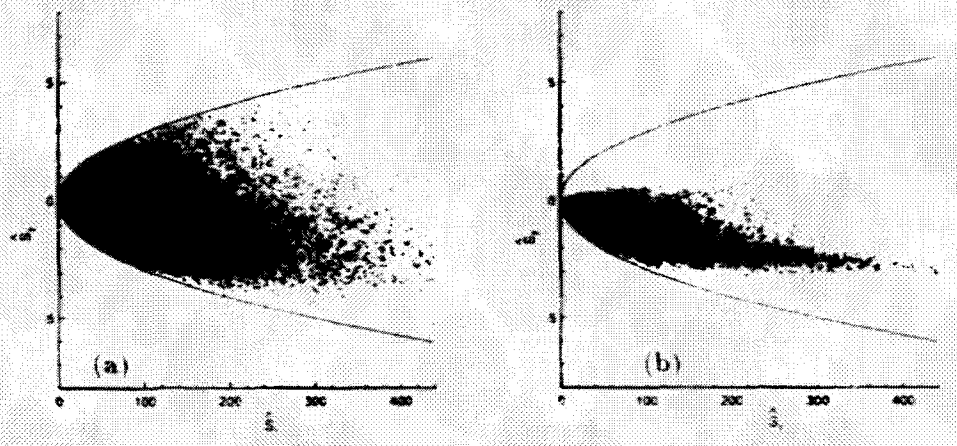

FIGURE 3. Scatter plot of $\hat{S}_1$ and $\hat{S}_2$ in filtered DNS (a) and LES (b).

spectrum at later times. In the range $0.4 \leq \mu \leq 1$, there is a general insensitivity to μ, leading to correct statistics and diminishing backscatter. The performance of the model for all values of μ in forced turbulence is satisfactory. Presently we show results for $\mu = 0.5$ which are typical of the behavior of the decay of the resolved energy spectrum and of the resolved and subgrid energy for $0.4 \leq \mu \leq 1.0$.

An interesting feature of Fig. 3 is that all points lie within a bounding parabola. An estimate based on a locally two-dimensional 'maximum stretch' scenario for $\hat{S}_{ij}$ gives a bounding parabola $\hat{S}_1 = 16\ \hat{S}_2^2$. We find however that $\hat{S}_1 = 12\ \hat{S}_2^2$ gives a slightly better boundary and so this curve is displayed in the figure. The importance of backscatter has been a question of debate though there is some evidence in the literature of its importance in wall-bounded flows. The backscatter property of the model is also illustrated in Fig. 4a, which shows a pdf of the 'stretch', that part of the velocity-gradient tensor which stretches the subgrid vorticity. The stretch is suitably normalized by $\sqrt{\bar{\epsilon}/\nu}$. While the two curves peak at approximately the same location, the LES shows predominant stretching. Figure 4b is a plot of the pdf of the subgrid energy transfer, $\varepsilon_{sgs}/\bar{\epsilon}$; points on the left of the origin exhibit backscatter. It is clear from the figure that the LES does well in the cascade region. The pdf of the total dissipation $\log_{10}(\epsilon/\bar{\epsilon})$ is displayed in Fig. 4c. The total dissipation ϵ is a positive definite quantity by construction as defined in (3). The distribution of ϵ appears to be approximately log-normal.

4. Concluding remarks

The behavior of an SGS model for LES has been tested against filtered DNS fields at similar Reynolds numbers. The model is stable and appears to produce a good quantitative description of the resolved flow and of the subgrid energy. It shows the right decay rate and gives good agreement with the experiments of Comte-Bellot and Corrsin. The model seems to work well for forced turbulence. Misra

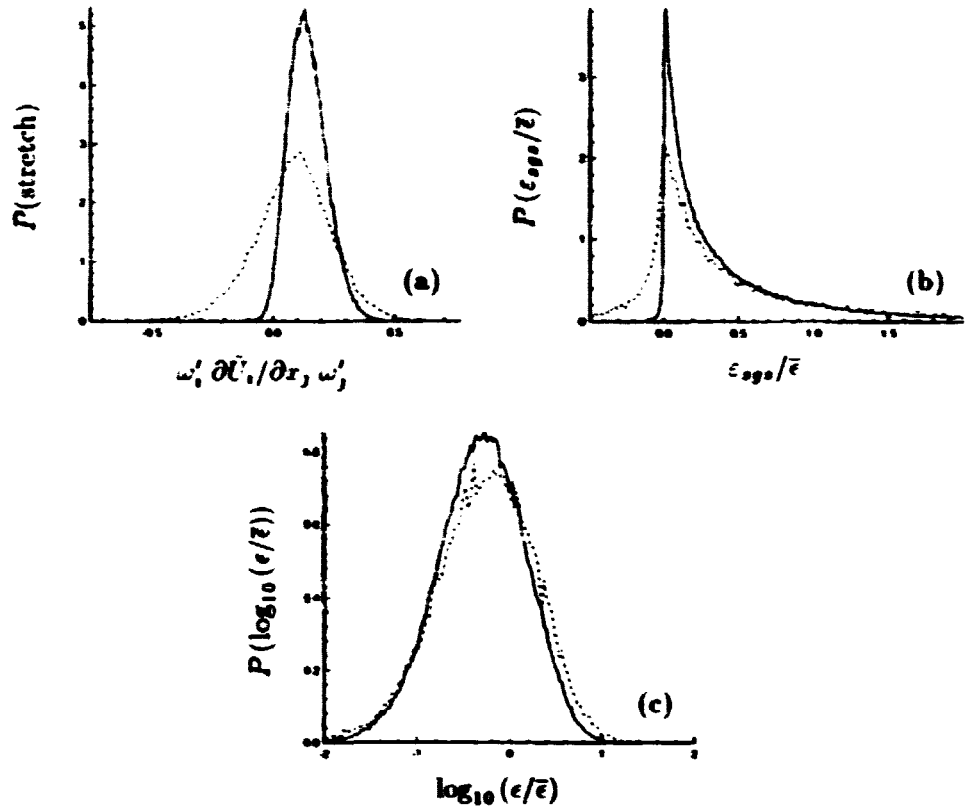

FIGURE 4. Pdf of: (a) stretch, (b) subgrid energy transfer, (c) total dissipation. —— LES, ---- DNS.

& Pullin demonstrate that it produces negligible SGS dissipation in the limit of fully resolved flow. A small amount of backscatter is produced by the version of the model tested presently albeit not as much as is indicated by the filtered DNS field. An adjustable parameter in the model is the Kolmogorov constant. The value presently used is within the bounds of experimental values. The model is about 25% more expensive in CPU time than the simple Smagorinsky model. Some subgrid model features show qualitative but not strong quantitative agreement with the equivalent quantities from filtered DNS fields at a similar Reynolds number. It remains to be seen how well the model will function for free-shear or wall-bounded flows. Future work will aim at constructing models with alternative representations of the subgrid vortex orientations.

Acknowledgments

AM was partially supported under NSF Grant CTS-9634222 and wishes to acknowledge fruitful discussions with Prof. D. I. Pullin. Hospitality provided by CTR during the 1996 Summer Program is gratefully acknowledged.

REFERENCES

COMTE-BELLOT, G. & CORRSIN, S. 1971 Simple Eulerian time correlation of full and narrow-band velocity signals in grid-generated 'isotropic' turbulence. *J. Fluid Mech.* **48**, 273-337.

CARATI, D., GHOSAL, S. & MOIN, P. 1995 On the representation of backscatter in dynamic localization models. *Phys Fluids* **7**(3), 606-616.

JIMÉNEZ J., WRAY A., SAFFMAN, P. G. & ROGALLO, R. S. 1993 The structure of intense vorticity in homogeneous isotropic turbulence. *J. Fluid Mech.* **255**, 65-90.

LUNDGREN, T. S. 1982 Strained spiral vortex model for turbulent fine structure. *Phys Fluids* **25**, 2193-2203.

MASON, P. AND THOMSON, D. 1992 Stochastic backscatter in large-eddy simulation of boundary layers. *J. Fluid Mech.* **242**, 51-78.

MISRA, A. & PULLIN, D. I. 1996 A vortex-based subgrid stress model for large-eddy simulation. Submitted to *Phys Fluids*

PIOMELLI, U., CABOT, W. H., MOIN, P., LEE, S. 1991 Subgrid-scale backscatter in turbulent and transitional flows. *Phys Fluids* **8**, 215-224.

PIOMELLI, U., YU, Y. & ADRIAN, R. J96 Subgrid-scale energy transfer and near-wall turbulence. *Phys Fluids* **8**, 215-224.

PULLIN, D. I. & SAFFMAN, P. G. 1993 On the Lundgren-Townsend model of turbulent fine scales. *Phys Fluids A* **5**, 126-145.

PULLIN D. I. & SAFFMAN, P. G. 1994 Reynolds stresses and one-dimensional spectra for a vortex model of homogeneous anisotropic turbulence. *Phys Fluids* **6**, 3010-3027.

REYNOLDS, W. C. & KASSINOS, S. 1995 One-point modeling of rapidly deformed homogeneous turbulence. *Proc. R. Soc. London* **A**, 87-104.

SMAGORINSKY, J. 1963 General circulation experiments with primitive equations. *Mon. Weather Rev.* **91**, 99.

SREENIVASAN, K. R. 1995 On the universality of the Kolmogorov constant. *Phys Fluids* **7**(11), 2778-2784.

VINCENT, A. & MENEGUZZI, M. 1994 The dynamics of vorticity tubes in homogeneous turbulence. *J. Fluid Mech.* **258**, 245-254.

NEXT
DOCUMENT

Hydroacoustic forcing function modeling using DNS database

By I. Zawadzki[1], J. L. Gershfeld[1], Y. Na[2] AND M. Wang[3]

A wall pressure frequency spectrum model (Blake 1971) has been evaluated using databases from direct numerical simulations (DNS) of a turbulent boundary layer (Na & Moin 1996). Good agreement is found for moderate to strong adverse pressure gradient flows in the absence of separation. In the separated flow region, the model underpredicts the directly calculated spectra by an order of magnitude. The discrepancy is attributed to the violation of the model assumptions in that part of the flow domain. DNS computed coherence length scales and the normalized wall pressure cross-spectra are compared with experimental data. The DNS results are consistent with experimental observations.

1. Introduction

Understanding the physics of the interaction of the airfoil turbulent boundary layers incident to the trailing edge is of interest to the designers of practical airframe components and lifting surfaces. Flow at trailing edges involves complex phenomena including adverse pressure gradient effects, flow separation, vortex shedding, and pressure scattering at the edge boundary discontinuity. It is not surprising then, that even an approximate treatment of practical cases, particularly from the vantage point of sound generation, encounters serious difficulties. Inviscid flow theories that capture the purely acoustic interaction of the flow with the trailing edge have been developed (Howe 1978,1988). Several experiments have also been performed (Brooks & Hodgson 1981, Blake 1986) which shed some light on the physics of the viscous flow problem. Well designed experimental efforts are invaluable in improving our understanding of the phenomena as demonstrated by Gershfeld *et al.* (1988) and Blake & Gershfeld (1989). They are, however, limited in terms of providing global information about the flow. One of the principal weaknesses of the experimental estimations of the flow acoustic source terms is that they are essentially ad hoc. The experimentalist must assume *a priori* which of the several potential flow acoustic sources are relevant so that estimates of the dipole source strength may be made. It is only when the direct dipole sound field is measured that the empirical estimates of the forces associated with the direct dipoles can be determined to be relevant. Unfortunately, there have been very few successful measurements of the trailing edge direct dipole sound field. When the inviscid

1 David Taylor Model Basin, NSWC/CD
2 University of Illinois at Urbana Champaign
3 Center for Turbulence Research

turbulent flow dipole sound formulations of Howe (1978, 1988) are applied with a Kutta condition, the predicted dipole sound field does not agree with experimental data (Brooks & Hodgson 1981). Only when the Kutta condition is removed does his model agree. Viscous DNS calculations may add insight into this modeling dilemma. The advantage of flow databases obtained by means of numerical simulations is that they contain spatial and temporal data throughout the flow domain which is not attainable in laboratory experiments.

Trailing edge flows of interest often include both attached and separated flow regimes (Brooks & Hodgson 1981, Blake 1984). With that in mind, we utilize the numerical database developed by Na & Moin (1996). Since the database includes flow with adverse pressure gradient and separation, it was well suited as a first step towards modeling of the more complex flow – trailing edge interactions. Our goals were two-fold. First, we wanted to re-examine the database from the point of view of an aeroacoustician to complement the results already presented by Na & Moin. (There is a certain degree of skepticism among the applied community as to whether relatively low Reynolds number DNS calculations can be of use for predicting high Reynolds number flows found in practical realizations. Wall pressure spectra reported by Na & Moin show many features and trends observed in the experiments, a hint that DNS calculations are, in fact, relevant.) Our second goal was to revisit a wall pressure model developed long before there were means of reliably assessing its accuracy or limits of applicability. DNS database provides such means since it contains both the complete flow data necessary for the input to the model as well as directly calculated wall pressures which can be used to verify or invalidate the model predictions.

2. Wall pressure model

In the following sections x, y, and z (or x_i, $i = 1,2,3$) will denote the streamwise, wall-normal, and spanwise coordinate, respectively, while u, v, w (or u_i, $i = 1,2,3$) will be the corresponding fluctuating velocity components. Other quantities pertaining to a given coordinate direction will carry an appropriate coordinate subscript (e.g. k_x is the streamwise component of the wave-number vector $\mathbf{k}$). For an incompressible flow invoking the usual boundary layer approximation, evaluation of pressure can be reduced to solving the Poisson's equation (see, for example, Blake 1986)

$$\nabla^2 p(\mathbf{x},t) = -2\rho_0 \frac{\partial v}{\partial x}\frac{\partial U(\mathbf{x},t)}{\partial y} - \rho_0 \frac{\partial^2 u_i u_j}{\partial x_i \partial x_j} \tag{1}$$

where U is the mean streamwise velocity. Lilley (1960) derived a solution of Eq. (1) in terms of the wave number frequency spectrum of the wall pressure,

$$\Phi_{pp}(\mathbf{k},\omega) = \frac{4\rho_0^2 k_x^2}{k_x^2 + k_z^2}\int_0^\infty dy \int_0^\infty dy' e^{-(y+y')\sqrt{k_x^2+k_z^2}}\tau(y)\tau(y')\Phi_v(y,y';\mathbf{k},\omega). \tag{2}$$

where $\mathbf{k} = (k_x, k_z)$ is the wave number vector in the plane parallel to the wall, $\tau(y) = \frac{\partial U}{\partial y}$ is the mean shear, and $\Phi_v(y,y';\mathbf{k},\omega)$ is the cross-spectral density of

the vertical velocity field. Equation (2) was derived under the assumption that the second term on the right hand side of Eq. (1) is negligible compared with the first term, and that the source field is spatially homogeneous in the (k_x, k_z) plane. Blake (1971) further modified Lilley's solution by introducing a separable model for the vertical velocity spectrum:

$$\Phi_v(y, y'; \mathbf{k}, \omega) = \overline{v^2}(y)\hat{R}_{vv}(y, y')\phi^x_{vv}(k_x)\phi^z_{vv}(k_z)\phi_m(\omega - k_x U_c). \tag{3}$$

Here, $\overline{v^2}(y)$ is the mean square of vertical fluctuating velocity, $\hat{R}_{vv}(y, y')$ is a normalized correlation in the y-direction, $\phi_m(\omega - k_x U_c)$ is the moving axis spectrum, U_c is the convection velocity, and $\phi^x_{vv}(k_x)$ and $\phi^z_{vv}(k_z)$ are wave number spectra defined as the Fourier transforms of, respectively, normalized streamwise and spanwise separation correlation functions of vertical velocity. (We use the lowercase symbol ϕ to denote the normalized spectrum functions. The normalization is: $\int_{-\infty}^{\infty} \phi(k_i)dk_i = 1.$)

Using (3) Blake (1971) obtains the wall pressure frequency spectrum by integrating Eq. (2) with respect to the wave number components k_x, k_z. The final result can be written in the form

$$\Phi_{pp}(\omega) = 4\rho_0^2 \int_0^{\infty} dy \int_0^{\infty} dy' \overline{v^2}(y)\hat{R}_{vv}(y, y')\tau(y)\tau(y')\frac{1}{U_C}\phi^x_{vv}(\frac{\omega}{U_C})I(\frac{\omega}{U_C}, y, y'). \tag{4}$$

where

$$I(k_x, y, y') = \int_{-\infty}^{\infty} dk_z \frac{k_x^2}{k_x^2 + k_z^2} e^{-(y+y')\sqrt{k_x^2+k_z^2}}\phi^z_{vv}(k_z). \tag{4a}$$

Taylor's hypothesis of frozen convection was used in the integration leading to Eq. (4). Mathematically, the hypothesis states that $\phi_m(k_x - \frac{\omega}{U_c}) = \delta(k_x - \frac{\omega}{U_c})$, which leads to the following equivalence of the normalized wave number spectrum $\phi^x_{vv}(k_x)$ and the frequency spectrum $\phi_{vv}(\omega)$:

$$\phi^x_{vv}(k_x) = \frac{1}{U_c}\phi_{vv}(\frac{\omega}{U_C}). \tag{5}$$

In order to evaluate Eq. (4.4a) one needs to compute the vertical correlation $\overline{v^2}(y)\hat{R}_{vv}(y, y')$, the mean shear $\tau(y)$, and the wave number spectra $\phi^x_{vv}(k_x)$ and $\phi^z_{vv}(k_z)$ (See discussion in sections 4.2 and 4.3 on selecting the location at which the spectra should be evaluated). Calculation of these quantities from the DNS database is a straightforward matter. We should point out that in principle one could compute the cross-spectral density function $\Phi_v(y, y'; \mathbf{k}, \omega)$ without resorting to the separable model (Eq. (3)) and integrate numerically Eq. (2) directly to obtain the pressure frequency spectrum. Besides not being physically revealing, such a procedure, however, would be prohibitively expensive in terms of computational time and memory.

We should also point out the modeling described above is applicable only to convective wave numbers near $k_x = \omega/U_C$. In other words, Eq. (4) does not encompass sources outside of the convective range. Other models of wall pressure

spectrum (Chase 1980) could be used to include broader range of wave numbers. However, trailing edge noise is dominated by scattering of convective wall pressures (with boundary discontinuity providing the conversion mechanism to acoustic wave numbers - Howe (1979)). Therefore, from the standpoint of acoustic radiation, Blake's simplified approach to computing the wall pressure spectrum should be sufficient.

3. DNS database

Most of the data presented here (with the exception of Fig. 2a) will refer to the separated flow calculation in the Na & Moin (1996) database. Following Na & Moin, we introduce the non-dimensional variables given by

$$u_i^* = \frac{u_i}{U_0}, \qquad x_i^* = \frac{x_i}{\delta_{in}^*}, \qquad t^* = \frac{tU_0}{\delta_{in}^*}, \qquad p^* = \frac{p}{\rho U_0^2} \tag{6}$$

where U_0 is the mean velocity at inlet and δ_{in}^* is the (dimensional) inlet displacement thickness. All quantities discussed in the following sections, including the wave number and frequency spectra, incorporate this nondimensionalization. The superscript $*$, denoting non-dimensional quantities, has been dropped to simplify notation.

In order to establish for the reader the reference coordinates for different flow regimes, the mean streamlines were reproduced in Fig. 1.

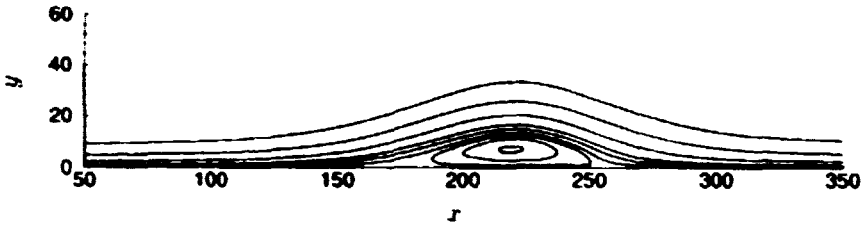

FIGURE 1. Mean flow streamlines.

In non-dimensional units (Eq. 6) the streamwise and spanwise extent of the computational domain is, respectively, 350 and 50. The vertical height is 64. Flow separation is induced by prescribing suction-blowing velocity profile along the upper boundary. As a result, strong adverse pressure gradient exists between the non-dimensional coordinates $x = 90$ and $x = 150$. Boundary layer separation occurs around $x = 160$. Coordinate $x = 220$ corresponds to the center of the separation bubble. Grid resolution is $513 \times 193 \times 129$ points in the streamwise, wall-normal, and spanwise directions, respectively. The Reynolds number based on inlet momentum thickness and free stream inlet velocity is 300. For additional details of the flow calculations, including description of the computational method, we refer the reader to Na & Moin (1996).

4. Results and discussion

4.1 Wall pressure data analysis

Standard tools of correlation analysis were utilized to analyze the DNS calculated wall pressure data. We wanted to establish whether DNS results, which are obtained for a relatively low Reynolds number, are in agreement with experimental data. The comparisons also served to validate our numerous computer codes. Let $\mathbf{r} = (r_x, r_z)$ be a separation vector in a plane parallel to the wall. Defining the cross-correlation function of a field quantity q as an ensemble average,

$$R_{qq}(\mathbf{x}, \mathbf{r}, \tau) = \langle q'(\mathbf{x}, t) q'(\mathbf{x} + \mathbf{r}, t + \tau) \rangle, \tag{7}$$

the cross spectrum function is the Fourier transform of (7) with respect to the time delay:

$$\Phi_{qq}(\mathbf{x}, \mathbf{r}, \omega) = \int_{-\infty}^{\infty} R_{qq}(\mathbf{x}, \mathbf{r}, \tau) e^{-i\omega\tau} d\tau. \tag{8}$$

Coherence is defined as the cross spectrum squared, normalized by the local autospectrum:

$$\gamma^2(\mathbf{x}, \mathbf{r}, \omega) = \frac{|\Phi_{qq}(\mathbf{x}, \mathbf{r}, \omega)|^2}{|\Phi_{qq}(\mathbf{x}, 0, \omega)||\Phi_{qq}(\mathbf{x} + \mathbf{r}, 0, \omega)|}. \tag{9}$$

The Corcos (1963) model of the cross-spectrum of the wall pressure, p, has the form

$$\Phi_{pp}(r_x, r_z, \omega) = \Phi(\omega) A\left(\frac{\omega r_x}{U_C}\right) e^{-i\frac{\omega r_x}{U_C}} B\left(\frac{\omega r_z}{U_C}\right), \tag{10}$$

with A and B modeled as exponentially decaying functions. These functions are calculated by expressing the square root of the coherence (Eq. 9) in terms of the similarity variable $\omega r / U_C$. The results for the streamwise component are shown in Fig. 2.

As a reference, the results for the zero pressure gradient flow, obtained using a separate DNS database (Na & Moin 1996, Chapter 3), are plotted in Fig. 2a. They are closely described by the experimentally observed exponential function with decay constant $a = -0.125$ (Brooks & Hodgson 1981). Abraham & Keith (1995) report similar agreement with the experimental results for DNS simulated turbulent channel flow. When an adverse pressure gradient is present, however, the streamwise coherence curves decay at a much faster rate (Fig. 2b) and the Corcos constant has to be altered. A reasonable fit is obtained with a decay constant $a = 0.4$. This trend is in agreement with the observations of Schloemer (1967). We evaluated the Corcos "A" function for several streamwise locations corresponding to varying degree of pressure gradient and found that the decay constant increases monotonically with the pressure gradient.

By contrast, we found the rate of decrease for the spanwise Corcos similarity function "B" to be practically independent of the pressure gradient. As shown in Fig. 3a, the results at $x = 120$ agree reasonably with the experimentally observed exponential rate of decrease $b = -0.7$. The situation changes dramatically, however,

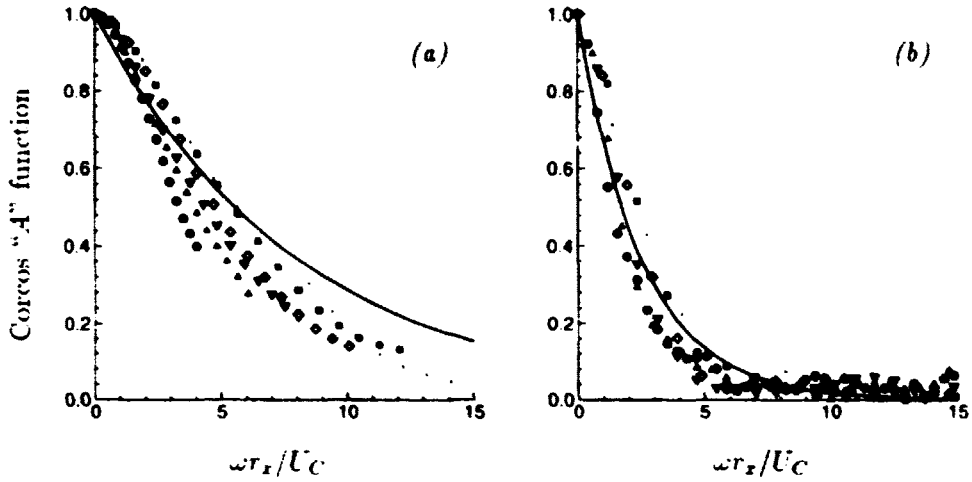

FIGURE 2. Streamwise coherence in Corcos similarity form. (a) Zero pressure gradient flow for selected values of frequency ω: • 0.31, ▲ 0.47, ▽ 0.63, ◇ 0.79, ■ 0.94, × 1.1; —— $e^{-0.125\omega r_x/U_C}$. (b) Adverse pressure gradient flow at $x = 120$; ω = • 0.21, ▲ 0.31, ▽ 0.42, ◇ 0.52, ■ 0.63, × 0.73; —— $e^{-0.4\omega r_x/U_C}$.

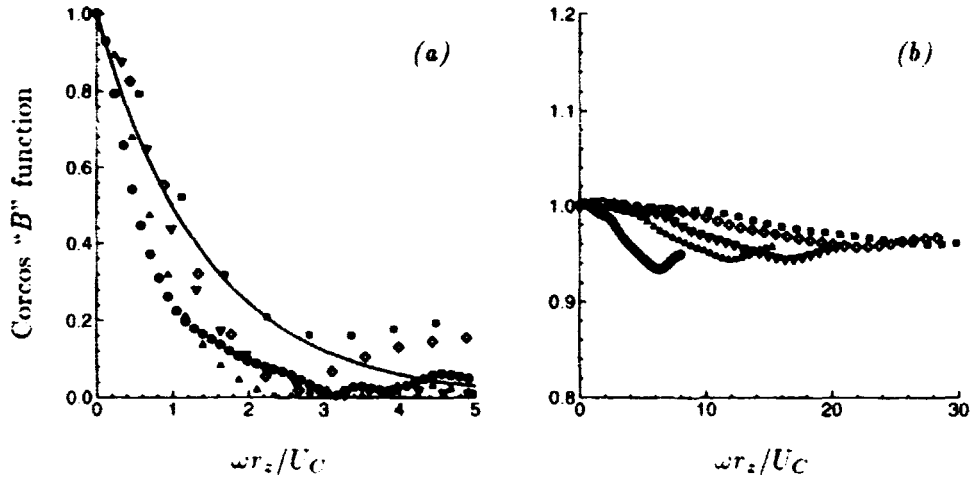

FIGURE 3. Spanwise coherence in Corcos similarity form. (a) $x = 120$, (b) $x = 220$; for selected values of frequency: • 0.21, ▲ 0.42, ▽ 0.59, ◇ 0.8, ■ 1.0; —— $e^{-0.7\omega r_z/U_C}$.

when the function is evaluated inside the separation bubble (Fig. 3b). All the curves stay very close to a constant value of unity which demonstrates that the wall pressure in the separated flow region is essentially two-dimensional.

Another experimentally measurable characteristic of the wall pressure is given by the frequency dependent streamwise and spanwise length scales. These are obtained by calculating the coherence for a suitably chosen separation vector and integrating

the result over the separation distance. For example, the spanwise length scale is given by:

$$\Lambda_z(\mathbf{x},\omega) = \int_0^\infty \sqrt{\gamma^2(\mathbf{x},r_z,\omega)}dr_z \tag{11}$$

where r_z is the spanwise separation distance. Gershfeld *et al.* (1988) have calculated both spanwise and streamwise coherence length scales for their trailing edge measurements which included adverse pressure gradient effects. They have assumed the Corcos relation: $\Lambda = C\frac{U}{\omega}$ and proceeded to calculate the proportionality constant C for varying flow conditions. They have found the constant value to range between 0.5 and 1.5 for the spanwise length scales and between 1.75 and 6.0 for the streamwise length scales. Figure 4 shows that the DNS calculated length scales fall within the range observed by Gershfeld *et al.*

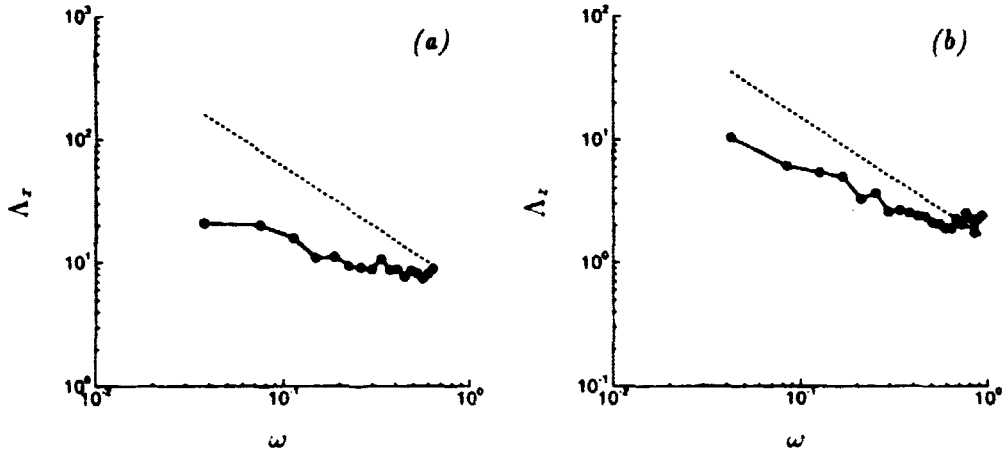

FIGURE 4. (a) Streamwise coherence length scales: • DNS, ····· $1.75U/\omega$, ---- $6.0/\omega$. (b) Spanwise coherence length scales: • DNS, ····· $1.5U/\omega$, ---- $0.5U/\omega$.

One of the quantities required for the integrand of Eq. (4) is the two-point correlation of vertical velocity. Hunt *et al.* (1987) have demonstrated that for boundary layer flows the normalized correlation has an approximately self-similar form when expressed as a function of y/y', $(0 \leq y \leq y')$. In Fig. 5 we plot the correlation with the normalization as prescribed by Hunt *et al.*

In the attached region (Fig. 5a) the self-similarity can be clearly observed for values of y' up to 4. At the streamwise location where the correlation in Fig. 5a was calculated ($x = 80$), the $y' = 8$ position lies too close to the boundary layer edge so the self-similarity is not expected to be preserved there. On the other hand, at the center of the separation bubble the boundary layer thickness is much larger than 8, and as a result none of the curves plotted in Fig. 5b shows drastic departure from the other curves. However, the collapse is not as good as for the first four y-locations in Fig. 5a. This is not surprising as the flow in the separated region does not at all resemble a typical boundary layer profile.

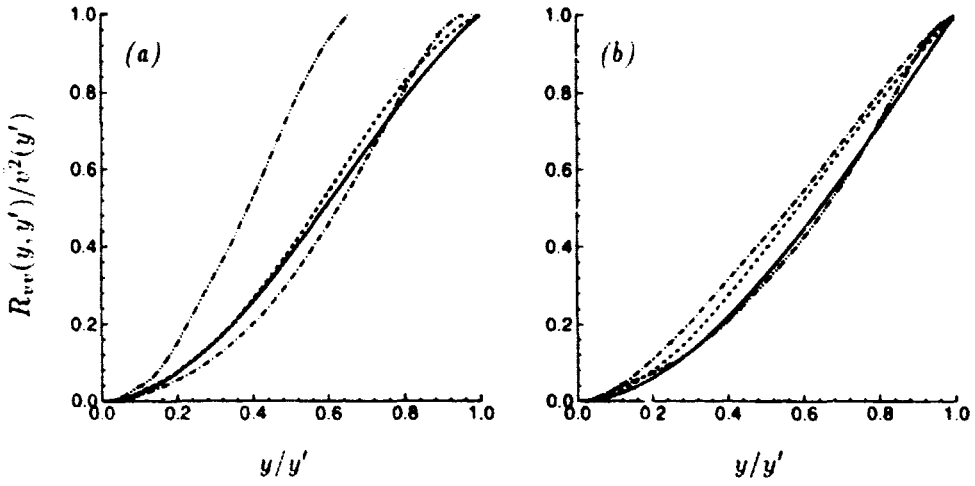

FIGURE 5. Two-point correlation of wall-normal velocity component, (a) $x = 80$. (b) $x = 220$: —— y'=0.5, - - - - y'=1.0, ····· y'=2.0, — — y'=4.0, — ·· — y'=8.0.

4.2 Discussion of the wall pressure model assumptions

For the sake of completeness we list the assumptions made in deriving the wall pressure model Eq. (4):

1 . Boundary layer approximation.
2 . Spatial homogeneity of the source term in the planes parallel to the wall.
3 . Dominance of the linear source term over the nonlinear part.
4 . Spatial localization (in the wall-normal direction) of the sources.
5 . Spectral separability of the source field.
6 . Taylor's hypothesis of frozen convection.

Assumption 1 is readily satisfied before the flow separation. This allows neglecting certain terms when deriving the Eq. (1). In the separated region, instantaneous velocity vector plots (Na & Moin 1996, Fig 5.14) show very small velocity vectors with frequent flow reversal in the region between the wall and the separated shear layer. Therefore, in this region the boundary layer approximation, which presumes preferable mean flow direction with the streamwise component being much larger than the other components, is no longer valid.

Assumption of spatial homogeneity is implicit in expressing the pressure and velocity fields in terms of wave number spectra (Eqs. (2) and (3)). Strictly speaking one cannot expect to find homogeneity in the streamwise direction in a spatially developing flow. All we can hope for is for the flow to be "locally homogeneous", in the sense that the streamwise variation is locally small enough so that computing the ensemble average (Eq. 7) and taking the Fourier transform with respect to the streamwise separation is physically meaningful at least for a certain range of the wave numbers. Figure 6 shows one of the diagnostics of the spatial homogeneity. It shows two-point streamwise separation correlation contours of the wall pressure. One can see that up to the point of separation ($x < 150$) and inside the separated

region ($190 < x < 260$), the field is nearly homogeneous (contour lines are nearly parallel to the abscissa). In the vicinity of the separation point, ($150 < x < 190$) the correlation function is strongly dependent on the streamwise location.

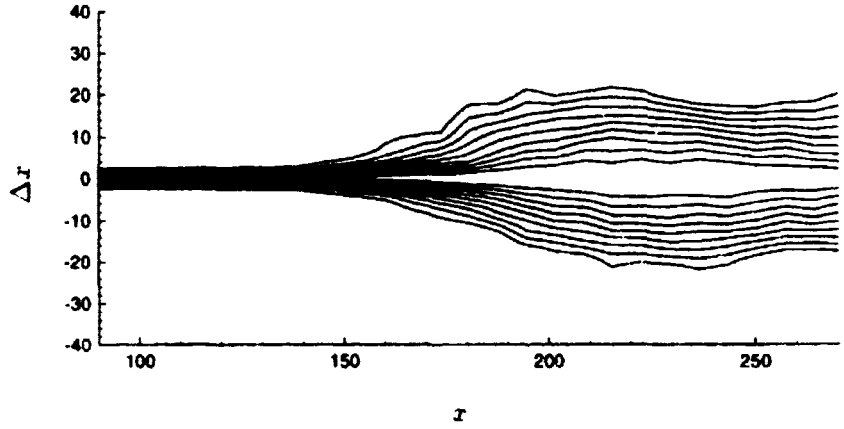

FIGURE 6. Wall pressure two-point streamwise separation correlation contours.

The next approximation - neglecting the nonlinear term in Eq. (1) - used to be considered very plausible until the work of Kim (1989). Kim has demonstrated that the contributions of both terms to the wall pressure are of comparable magnitude, with the total pressure exceeding both the linear component's contribution by about 30 percent. Therefore, we expect Eq. (2) to underestimate the spectral levels of the wall pressure.

Spatial localization of the sources is the key to representing the vertical velocity spectrum via Eq. (3), which de-facto puts all the dependence on the y-coordinate in the correlation term and makes the remaining terms independent of y. We plotted the magnitude of the y-coordinate dependent part of the source term in Fig. 7.

One can see a clearly pronounced peak very close to the wall for locations upstream of the separation bubble (Fig. 7a). At the detachment point (Fig. 7b, $x = 160$), the height of the peak has decreased by an order of magnitude and its effective width has become comparable with the thickness of the boundary layer. In the center of the separated region ($x = 220$), the maximum of the source term has moved away from the wall to coincide with the location of the shear layer and the peak has become even broader. In the reattachment region ($x = 280$), a new maximum begins to reappear near the wall.

The assumption of spectral separability states that the wave number spectrum in the plane parallel to the wall can be expressed as a product of two functions, each dependent on, respectively, only the streamwise and spanwise wave number component. It is a convenient tool which allows obtaining the final result (Eq. (4)) in a simple form. In principle, one could compute the exact two-dimensional spectrum by calculating two-point correlation for all possible pairs of streamwise and spanwise separations and taking two-dimensional Fourier transform of the result.

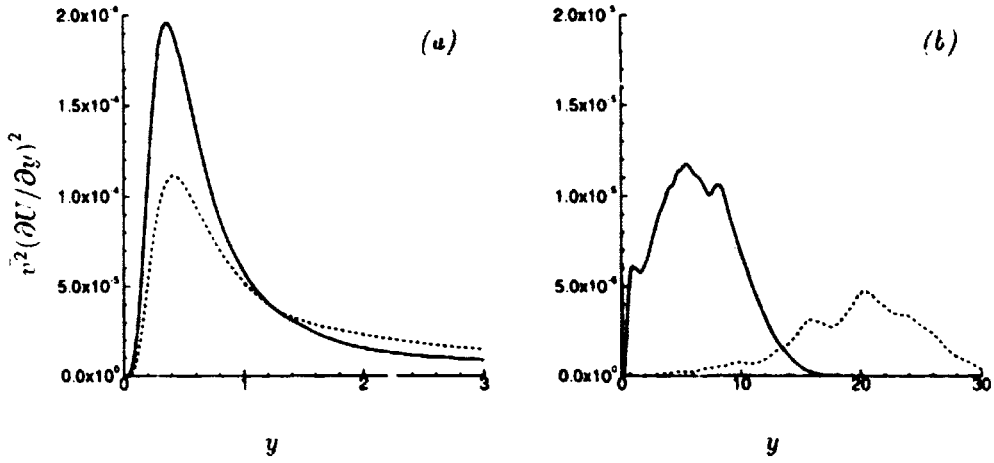

FIGURE 7. Wall pressure model source term as a function of the distance from the wall, (a): —— $x = 80$, ---- $x = 120$, (b): —— $x = 160$, ---- $x = 220$, ····· $x = 280$.

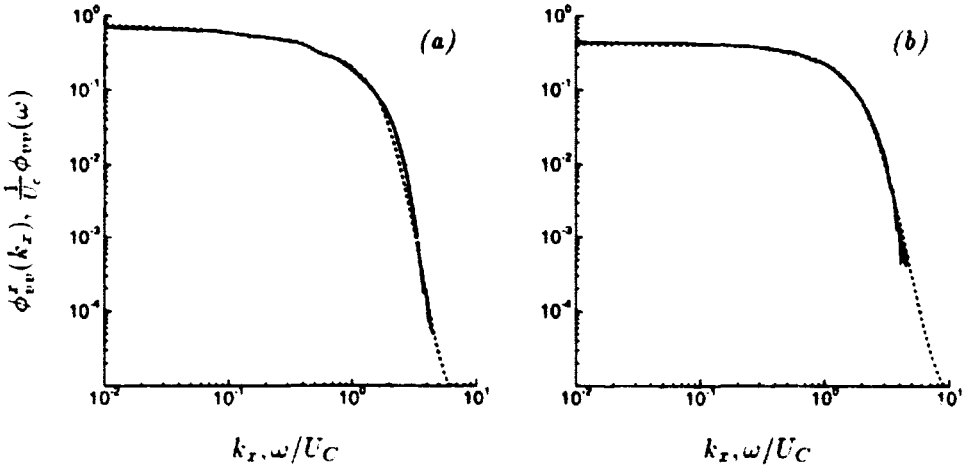

FIGURE 8. Normalized spectra of vertical velocity component at (a) $(x, y) = (80, 0.76)$, (b) $(x, y) = (130, 0.76)$; —— $\phi^x_{vv}(k_x)$, ---- $\frac{1}{U_c}\phi_{vv}(\omega)$.

We have not performed such calculations and, therefore, cannot comment on the errors incurred by using the separable representation.

The last approximation, the Taylor's hypothesis of frozen convection, can be tested by calculating and comparing the spectra in Eq. (5). Before making the comparison, one must choose a proper value for the convection velocity U_C. A natural choice is the local mean velocity. The normalized spectra calculated in the $y = 0.76$ plane at two selected streamwise locations, $x = 80$ and $x = 130$, are shown in Fig. 8a,8b. The local mean velocity U_{local} at these coordinates is, respectively,

0.56 and 0.29. Clearly, with this choice of $U_C = U_{local}$, the spectra agree very well even when evaluated at the location with a severe local adverse pressure gradient (Fig. 8b).

4.3 Comparison of model predictions with DNS data

The model predictions are calculated by numerically integrating (4). The integration is straightforward once all the ingredients of the integrand are known. There are, however, issues concerning the determination of the convection velocity U_C and the wavenumber spectra $\Phi^r_{vv}(k_x)$ and $\Phi^z_{vv}(k_z)$ in the integrand, which deserve a brief discussion.

Using the wall pressure convection velocity inferred from time-space correlations calculated by Na & Moin would not be compatible with the spirit of this work. One would prefer to rely exclusively on the velocity field data and not to use any variable that is a characteristic of the quantity that we are trying to predict. With regard to the normalized velocity wavenumber spectra, one expects them to be independent of y, since the y-dependence has been included in the vertical correlation function in the separable representation (3). Under this premise it appears reasonable to pick a single constant-y plane and take the $\Phi^r_{vv}(k_x)$ and $\Phi^z_{vv}(k_z)$ there as the representative wavenumber spectra required in (4). The convective velocity U_C can be approximated by the local mean velocity, as demonstrated by Fig. 8. Ideally, one would prefer the selected y-plane to coincide with the location of maximum source magnitude, as the contribution from the vicinity of the source peak is expected to dominate over contributions from all other locations (Blake 1984). (Of course, the notion that the maximum source magnitude contributes most to the wall pressure is valid only when the shear layer is close enough to the wall. Otherwise, the effects of the exponential factor in Eq. (4a) may become significant). However, the difference should be small even if the selected plane deviates from the source peak, so long as it lies within the active source region where the separable representation (3) holds.

In the present calculations, the vertical-velocity wavenumber spectra are approximated by those at $y \approx 0.76$ for the streamwise stations $x = 80$ and 120, $y = 7.07$ for $x = 160$, and $y = 19.67$ for $x = 220$. Our choices of the y-planes are limited by the available DNS data (there are only five y-planes with complete space-time velocity information saved in the original DNS database). The U_C value is approximated by the local mean velocity at the given (x, y)-position.

The model predictions at four different streamwise locations, representing different flow regimes, are shown in Figs. 9 and 10. The directly computed pressure spectra are also plotted for comparison. In the attached flow region at $x = 80$ (Fig. 9a) and $x = 120$ (Fig. 9b), the agreement between model and DNS is very good. The under-prediction at low frequencies may be attributed to neglecting the nonlinear terms in Eq. (1). Considering that the contributions from the retained and neglected term are of comparable magnitude (Kim 1989), and given the approximations involved in the evaluation of the integrand, a discrepancy (underestimate) should be expected.

At the flow separation point $x = 160$ (Fig. 10a) familiar underprediction at low frequencies is again observed. There is also a marked difference at the high end of

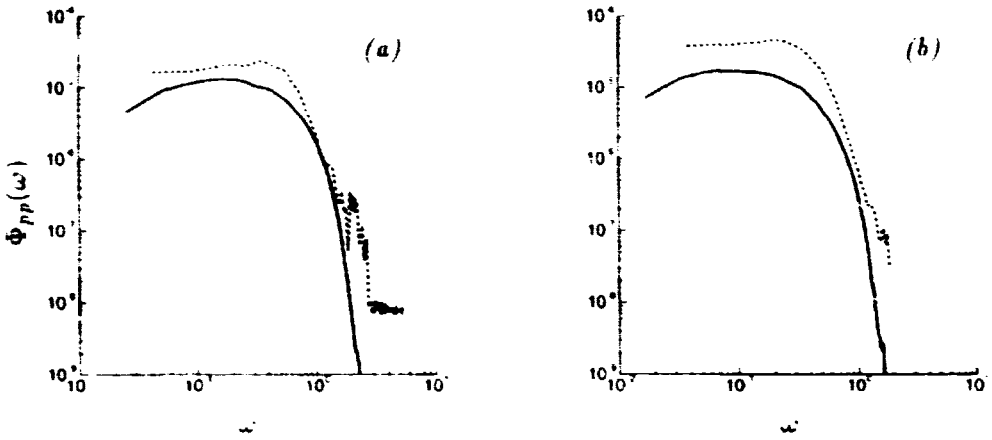

FIGURE 9. Wall pressure frequency spectrum. (a) $x = 80$. (b) $x = 120$; —— model (Eq. 4), ---- DNS.

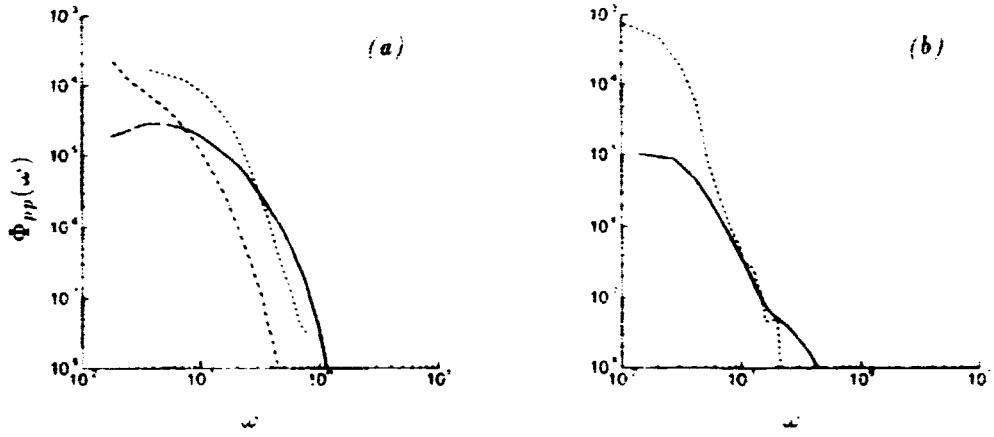

FIGURE 10. Wall pressure frequency spectrum. (a) $x = 160$; —— model (Eq. 4 using velocity spectrum at $y = 7.07$), — — model (Eq. 4 using velocity spectrum at $y \approx 2.28$), ---- DNS. (b) $x = 220$; —— model (Eq. 4), ---- DNS.

the frequency spectrum (compare solid and dashed lines in Fig. 10). One possible reason for the "misalignment" of the spectra could be an improper choice (restricted by the limited available data) of the representative wavenumber spectrum $\Phi^x_{vv}(k_x)$ and the corresponding convection velocity U_c. Indeed, if we use the $y \approx 2.28$ plane instead of our first choice $y = 7.07$, the model spectrum shifts towards lower frequencies (Fig. 10a). These results seem to confirm that the optimum choice would be $y \approx 5$, i.e. near the location of the peak of the source term (cf Fig. 7b).

In the separated region (Fig. 10b), the model and DNS results differ by more than an order of magnitude. As discussed in section 4.2 the model failure may be

attributed to the fact that the nature of the flow in this regime is largely incompatible with the model assumptions. For the model to perform well, the wall pressure has to be the signature of a spectrally separable source localized in the y-direction (cf. (3)), moving at a constant speed. This condition is violated, given the large vertical extent and the wide range of flow characteristics in the separated zone. The exponential decay of the Green's function (cf Eq. 4a) accentuates the contribution of the eddies closer to the wall than the detached shear layer, particularly in the high frequency range. In other words, less energetic eddies may compete, in terms of their contribution to the wall pressure, with higher intensity sources depending on their relative proximity to the wall. For the separated flow, therefore, a "representative" source y-layer with a single convective velocity is difficult, if not impossible, to identify.

5. Conclusions and future work

There is an ongoing need for an accurate prediction of wall pressure spectrum in aeroacoustic engineering applications. Since current computational capabilities cannot provide the necessary space and time resolution for computing the pressure spectrum directly (for the Reynolds numbers of interest), appropriate models have to be utilized. In this project we have demonstrated that a simplified model developed for a flat plate turbulent boundary layer can be used for predicting wall pressure frequency spectrum of a flow with a strong adverse pressure gradient. In practical cases RANS calculations could provide the mean shear and wall-normal turbulence intensity required by the model. Hunt *et al's.* (1987) similarity model can be used for the correlation function of vertical velocity. The wave number spectra of vertical velocity, also needed as input to the model, can be calculated from experimental two-point correlation flow measurement.

Our results also show that in the separated region the model's performance is unsatisfactory. It is perhaps premature to assume that the model would fail for any separated flow scenario. From the exponential form of the Green's function in Eq. (4a), it is apparent that the contribution of the shear layer as a source term of the wall pressure rapidly diminishes with the distance from the wall. Therefore, the accuracy of the model's prediction should depend on the distance between the shear layer and the wall as well as on the strength of the shear layer relative to the turbulence level in the separation bubble. In any event, the non-linear pressure source terms need to be included in order to obtain accurate wall pressure spectrum predictions for a broad class of separated flows.

We plan to use the experience gained during the course of this work as a stepping stone towards modeling, with the aid of DNS and LES simulations, of wall pressure spectra of more complex trailing edge flows.

Acknowledgements

The authors are thankful to Dr. W. Blake for his guidance and many enlightening discussions, and to Prof. P. Moin for helpful suggestions during the summer program. Support for this work provided by ONR, with P. Purtell as program manager, is gratefully acknowledged.

REFERENCES

ABRAHAM, B. M. AND KEITH, W. K. 1995 Analysis of the wall pressure field from a numerical simulation of turbulent channel flow. ASME NCA-Vol **19**/FED-Vol. **230**. ***Flow Noise Modeling, Measurement and Control.*** **55-65.**

BLAKE, W. K. 1971 Turbulent velocity and pressure fields in boundary layer flows over rough surfaces. ***Symposium on Turbulence in Liquids***, Univ. of Missouri, Rolla, 114-122.

BLAKE, W. K. 1984 Trailing edge flow and aerodynamic sound, Part 1 and Part 2, DTNSRC Report - 83/113.

BLAKE, W. K. 1986 Mechanics of flow-induced sound and vibration I, II Academic Press, London.

BLAKE, W. K. AND GERSHFELD J. L. 1989 The aeroacoustics of trailing edges. ***Ch. 10. Lecture Notes in Engineering***, Springer Verlag. **46,** 457-532.

BROOKS, T. F. AND HODGSON, T. H. 1981 Trailing edge noise prediction using measured surface pressures. ***J. Sound Vibr.*** **78,** 69-117.

CHASE, D. M. 1980 Modeling the wave-vector frequency spectrum of turbulent boundary layer wall pressure. ***J. Sound Vibr.*** **70,** 29-68.

CORCOS, G. M. 1963 On the resolution of pressure in turbulence. . ***J. Acoust. Soc. Am.*** **35,** 192-199.

GERSHFELD, J. L., BLAKE, W. K. AND KNISLEY, C. K. 1988 Trailing edge flows and aerodynamic sound. AIAA-88-3826-CP ***First National Fluid Dynamics Congress***, 2133-2140.

HOWE, M. S. 1978 A review of the theory of trailing edge noise. ***J. Sound Vibr.*** **61,** 473-465.

HOWE, M. S. 1979 The influence of surface rounding on trailing edge noise. ***J. Sound Vibr.*** **126(3),** 503-523.

HUNT, J. C., MOIN, P., MOSER, R. D. AND SPALART, P. R. 1987 Self similarity of two point correlations in wall bounded turbulent flows. ***Proceedings of the 1987 Summer Program***, Center for Turbulence Research, NASA Ames/Stanford Univ., 25-36.

KIM, J. 1989 On the structure of pressure fluctuations in turbulent channel flow. ***J. Fluid Mech.*** **205,** 421-451.

LILLEY, G. M. 1960 Pressure fluctuations in an incompressible turbulent boundary layer. ***College of Aeronautics, Cranfield. Report No.*** **133**.

NA, Y. AND MOIN, P. 1996 Direct numerical simulation of turbulent boundary layers with adverse pressure gradient and separation. Report No. TF-68, Thermosciences Division, Dept. of Mech. Eng., Stanford Univ.

SCHLOEMER, H. H. 1967 Effects of pressure gradients on turbulent boundary wall pressure fluctuations. ***J. Acoust. Soc. Am.*** **42,** 93-113.

NEXT
DOCUMENT

A study of the turbulence structures of wall-bounded shear flows

By M. S. Chong[1] J. Soria[2] A. E. Perry[1]
J. Chacin[3] Y. Na[4] AND B. J. Cantwell[5]

This project extends the study of the structure of wall-bounded flows using the topological properties of eddying motions as developed by Chong *et al.* (1990), Soria *et al.* (1992, 1994), and as recently extended by Blackburn *et al.* (1996) and Chacin *et al.* (1996). In these works, regions of flow which are focal in nature are identified by being enclosed by an isosurface of a positive small value of the discriminant of the velocity gradient tensor. These regions resemble the attached vortex loops suggested first by Theodorsen (1955). Such loops are incorporated in the attached eddy model versions of Perry & Chong (1982), Perry *et al.* (1986), and Perry & Marusic (1995), which are extensions of a model first formulated by Townsend (1976). The DNS data of wall bounded flows studied here are from the zero pressure gradient flow of Spalart (1988) and the boundary layer with separation and reattachment of Na & Moin (1996). The flow structures are examined from the viewpoint of the attached eddy hypothesis.

1. Introduction

In the attached eddy hypothesis, eddying motions are envisaged to consist of vortex tubes or cores which form loops as first proposed by Theodorsen (1955). These loops are referred to by many names depending on the shape one believes they possess, e.g. horseshoes, hairpins, $\cap$, Λ or Π eddies, etc. A problem immediately arises as to what constitutes a vortex core. There has been some debate regarding this over the years and many workers have been involved, e.g. Truesdell (1954), Cantwell (1979), Vollmers (1983), Dallman (1983), Chong, Perry & Cantwell (1989, 1990), Robinson (1991), Lugt (1979), and Jeong & Hussain (1995), to mention a few. To avoid endless discussion and debate the authors will simply identify those regions in the flow which are "focal", to be shortly defined, and refer to them as "focal regions". The attached eddies postulated in the attached eddy hypothesis need not necessarily be focal since this condition depends on the relative strengths of the local rate of rotation tensor and the local rate of strain tensor (defined in Eqs. (8) and (9)). The results of the attached eddy hypothesis are derived purely from the

1 Department of Mechanical and Manufacturing Engineering, University of Melbourne.
2 Department of Mechanical Engineering, Monash University.
3 Department of Mechanical Engineering, Stanford University.
4 Department of Theoretical and Applied Mechanics, Univ. of Illinois at Urbana-Champaign.
5 Department of Aeronautics and Astronautics, Stanford University.

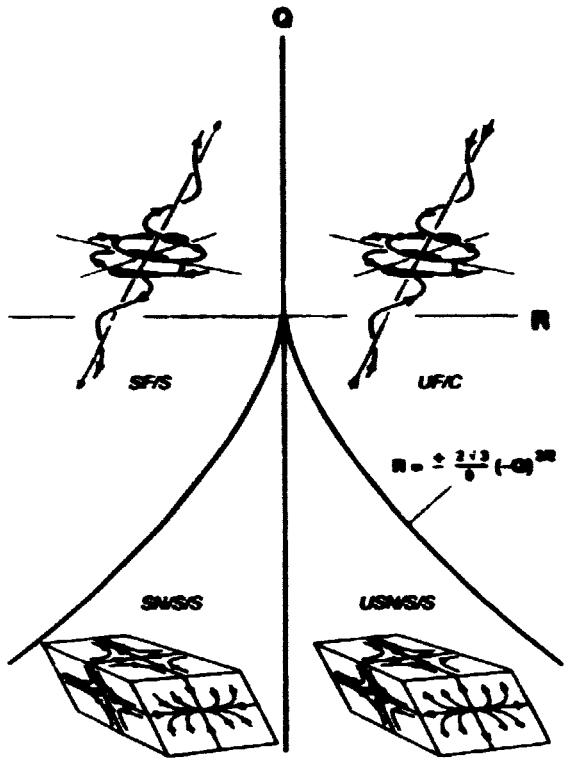

FIGURE 1. Local non-degenerate topologies in the $Q - R$ plane. SF/S: *stable focus/stretching*, UF/C: *unstable focus/contracting*, $SN/S/S$: *stable node/saddle/saddle* and $USN/S/S$: *Unstable node/saddle/saddle.*

Biot-Savart law and in no way depend on the above relative strengths. Whether or not a region of vorticity is focal depends on the rate of strain environment in which it is embedded and so also do all definitions for a vortex core. Nevertheless it is felt that most if not all of the attached eddies should display extensive focal regions as a result of the work of Blackburn, Mansour & Cantwell (1996), who examined the data from channel flow computations of Kim (1989). Here focal regions were found to exist in tubes, some of which extended from very close to the wall to the center plane of the channel. The authors consider these to be the clearest and most spectacular indicators of eddying motions so far seen in DNS data and at first sight look like the attached eddies envisaged by Perry and Chong (1982).

Following Chong, Perry & Cantwell (1989, 1990), the geometry of the streamline pattern at any point in the flow, as seen by a non-rotating observer moving with the velocity of that point, can be classified by studying certain invariants of the velocity gradient tensor $A_{ij} = \partial u_i/\partial x_j$ at that point. Here u_i is the velocity vector and x_i is the space vector. The characteristic equation of A_{ij} is

$$\lambda^3 + P\lambda^2 + Q\lambda + R = 0 \tag{1}$$

where P, Q and R are the tensor invariants. These are

$$P = -trace(\mathbf{A}) \tag{2}$$

$$Q = \frac{1}{2}(P^2 - trace(\mathbf{A}^2)) \tag{3}$$

and

$$R = -det(\mathbf{A}). \tag{4}$$

For incompressible flow, $P = 0$ from continuity and so

$$\lambda^3 + Q\lambda + R = 0. \tag{5}$$

The eigenvalues λ which determine the topology of the local flow pattern are determined by the invariants R and Q. In fact the $R - Q$ plane, shown in Fig. 1, is divided into regions according to flow topology.

The discriminant of A_{ij} is defined as

$$D = \frac{27}{4}R^2 + Q^3 \tag{6}$$

and the boundary dividing flows with complex eigenvalues from real is

$$D = 0 \tag{7}$$

Figure 2 shows contours of D on the $R - Q$ plane. For $D > 0$, Eq. (5) admits two complex and one real solution for λ. Such points are called foci and are part of the focal regions mentioned earlier. If $D < 0$, all 3 solutions for λ are real and the associated pattern is referred to as a node-saddle-saddle point according to the terminology adopted by Chong *et al.* (1990).

As implied earlier, the velocity gradient tensor can be split into two components thus:

$$A_{ij} = S_{ij} + W_{ij} \tag{8}$$

where S_{ij} is the symmetric rate of strain tensor and W_{ij} is the skew symmetric rate of rotation tensor. These are given by

$$S_{ij} = \frac{1}{2}\left(\frac{\partial u_i}{\partial x_j} + \frac{\partial u_j}{\partial x_i}\right) \tag{9}$$

and

$$W_{ij} = \frac{1}{2}\left(\frac{\partial u_i}{\partial x_j} - \frac{\partial u_j}{\partial x_i}\right). \tag{10}$$

The invariants of S_{ij} are P_s, Q_s, and R_s and are defined in an analogous way as the invariants of A_{ij}. For incompressible flow $P_s = 0$,

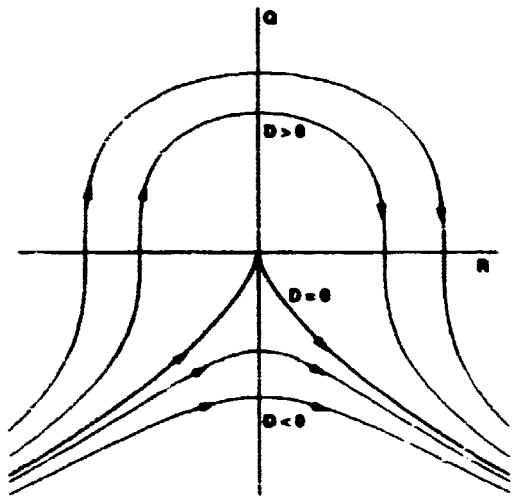

FIGURE 2. Trajectories of constant D in the $R-Q$ plane.

$$Q_s = -\frac{1}{2}S_{ij}S_{ij} \tag{11}$$

and

$$R_s = -\frac{1}{3}S_{ij}S_{jk}S_{ki} \tag{12}$$

The corresponding invariants of W_{ij} are P_w, Q_w and R_w. $P_w = R_w = 0$ but Q_w is non zero and is given by

$$Q_w = \frac{1}{2}W_{ij}W_{ij} \tag{13}$$

and is proportional to the enstrophy density. Other relations of interest are

$$\phi = 2\nu S_{ij}S_{ij} = -4\nu Q_s \tag{14}$$

where ϕ is the dissipation of kinetic energy into heat per unit mass and it should be noted that Q_s is always a negative quantity.

It can be shown that

$$Q = Q_w + Q_s = \frac{1}{2}(W_{ij}W_{ij} - S_{ij}S_{ij}) \tag{15}$$

According to the work of Vieillefosse (1982, 1984) and the more recent work of Cantwell (1992), the evolution of the velocity gradient tensor A_{ij} for a fluid particle is given by the following :

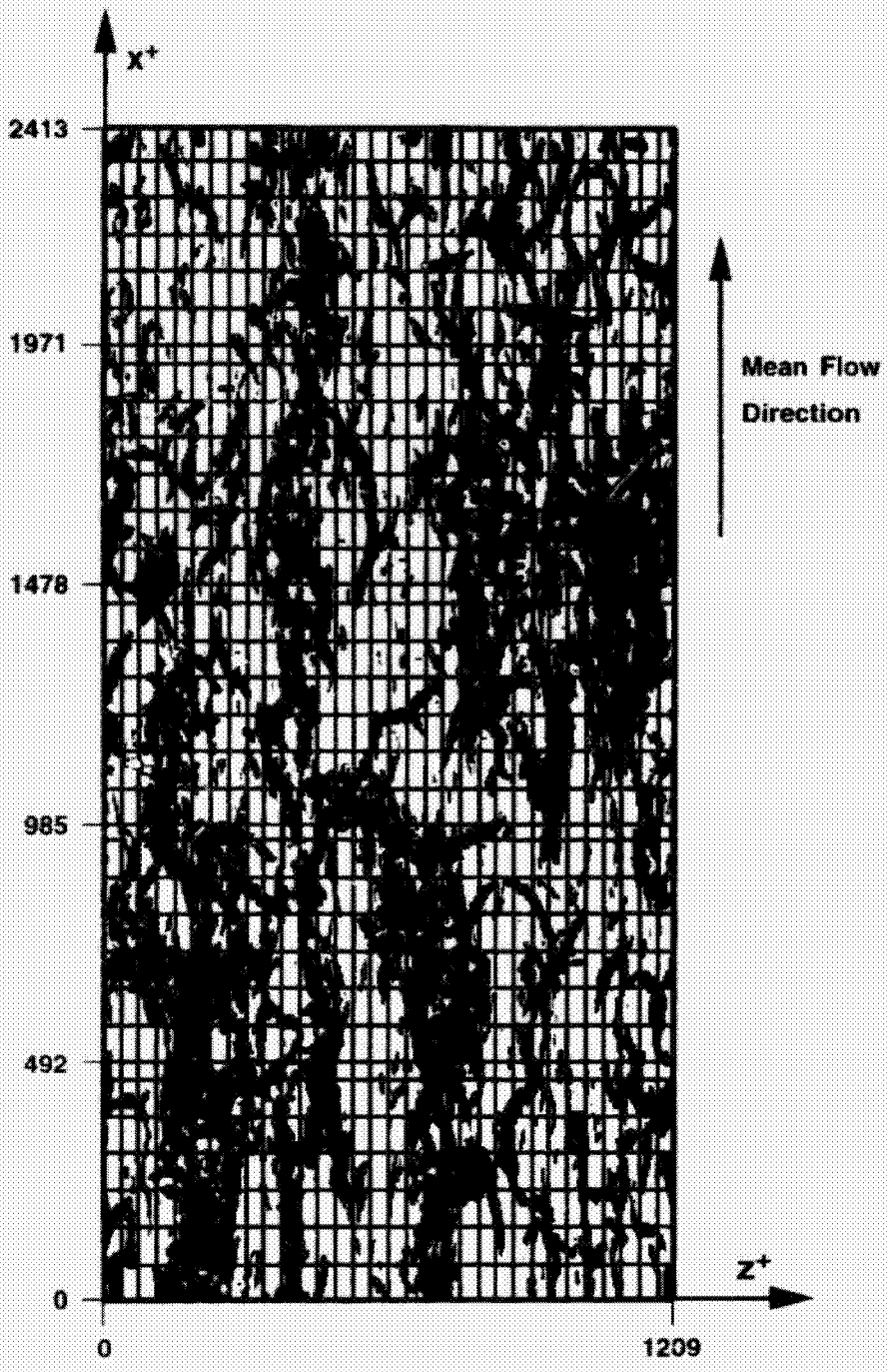

FIGURE 3. Isosurfaces of discriminant ($D \approx 0$) for zero pressure gradient data of Spalart for $Re_\theta = 670$ (from Chacin *et al.* (1996)).

$$\frac{\partial A_{ij}}{\partial t} + u_k \frac{\partial A_{ij}}{\partial x_k} + A_{ik}A_{kj} - A_{km}A_{mk}\frac{\delta_{ij}}{3} = H_{ij} \tag{16}$$

Here δ_{ij} is the Kronecker delta and

$$H_{ij} = -\left(\frac{\partial^2 p}{\partial x_i \partial x_j} - \frac{\partial^2 p}{\partial x_k \partial x_k}\frac{\delta_{ij}}{3}\right) + \nu \frac{\partial^2 A_{ij}}{\partial x_k \partial x_k} \tag{17}$$

If the viscous term and the pressure Hessian terms are small, the evolution of A_{ij} for fluid particles follows the so called restricted Euler equation, and solution trajectories of such particles follow the contours of constant D on the $R-Q$ plane as shown in Fig. 2. It is thought that this might be an appropriate description of the motions for fine scale eddies at high Reynolds numbers. It is found here that this restricted Euler equation is not valid for the Spalart (1988) data, which is of course at low Reynolds number. However, computations show that once a particle is focal it is highly probable it will remain focal. This study of particle trajectories on the $R-Q$ plane gives us a first glimpse of how fluid dynamics might be combined with the usual kinematic description of eddy structures as has been used in the attached eddy hypothesis.

It has been pointed out that three-dimensional plots of vortex lines or particle trajectories are extremely complex and confusing and not very helpful in gaining an insight into eddying motions (Cantwell (1979)). However, a very interesting feature of the isosurfaces of constant D found by Blackburn *et al.* (1996) is that they enclose a rather concentrated and well-ordered bundle of vortex lines. Finally, Blackburn *et al.* found that isosurfaces of constant D were superior to isosurfaces of enstrophy density or dissipation of kinetic energy for showing clear, well defined structures. The authors do not fully understand why this should be and this is a question which needs to be pursued in future work.

2. Results

2.1 Normalization of the discriminant

The raw values of the discriminant D were used in the case of the Spalart DNS data without any additional normalization. In the case of the Na & Moin DNS data, it is assumed that the inflow free-stream velocity is unity and that all length scales in the database are normalized by δ^*_{in}, the displacement thickness of the inflow boundary layer. The computed raw values of D were normalized by a velocity gradient representative of the mean separation bubble flow to the power of 6. This resulted in the raw values of D being multiplied by a factor of 10^6, and so maximum values of normalized D were of order 10^6. Typical values of D used in the isosurface visualization of D were of the order of $1-10$.

2.2 Zero pressure gradient boundary layer

Figure 3 shows a very clear picture (from Chacin *et al.* 1996) of isosurfaces of the discriminant for part of the Spalart (1988), $Re_\theta = 670$, zero pressure gradient turbulent boundary layer simulation data. Some Theodorsen-type vortices are apparent

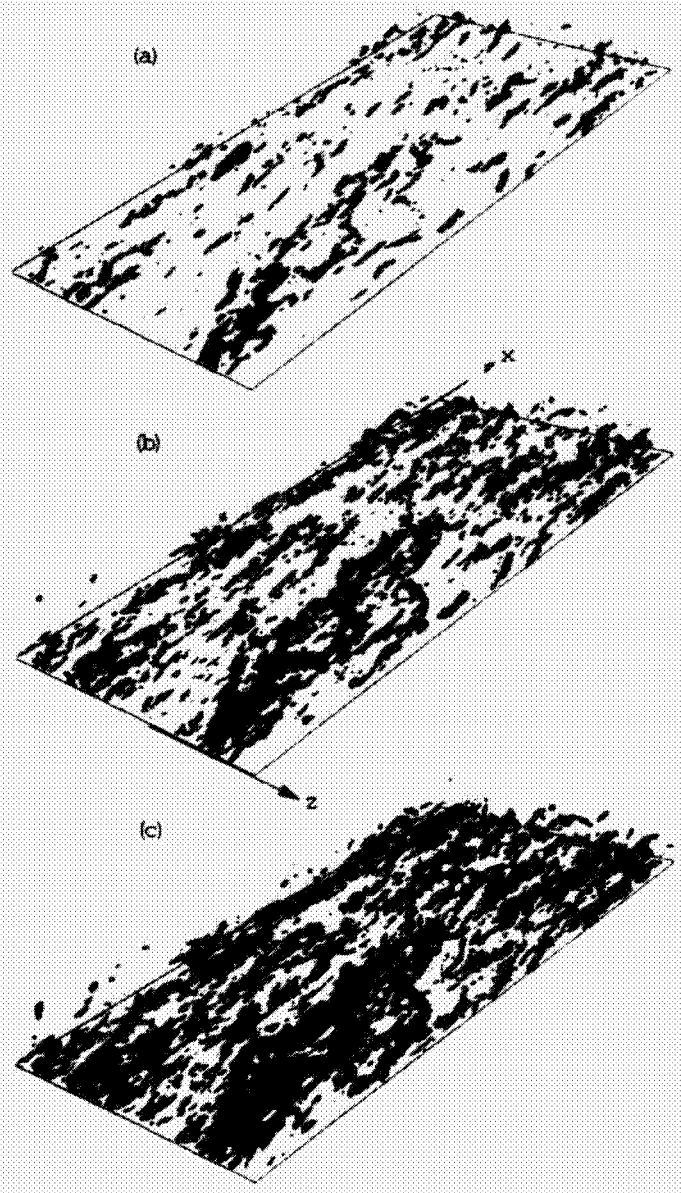

FIGURE 4. Isosurface of constant discriminant, D, for zero pressure gradient turbulent boundary layer flow at $R_\theta = 670$ for different threshold values of (a) $D = 1.0$, (b) $D = 0.25$ and (c) $D = 0.1$. The displayed boundary layer structures cover $\Delta x^+ = 2442$, $y^+_{min} = 6.4$, $y^+_{max} = 375$ and $\Delta z^+ = 1221$. Here $^+$ denotes viscous lengths.

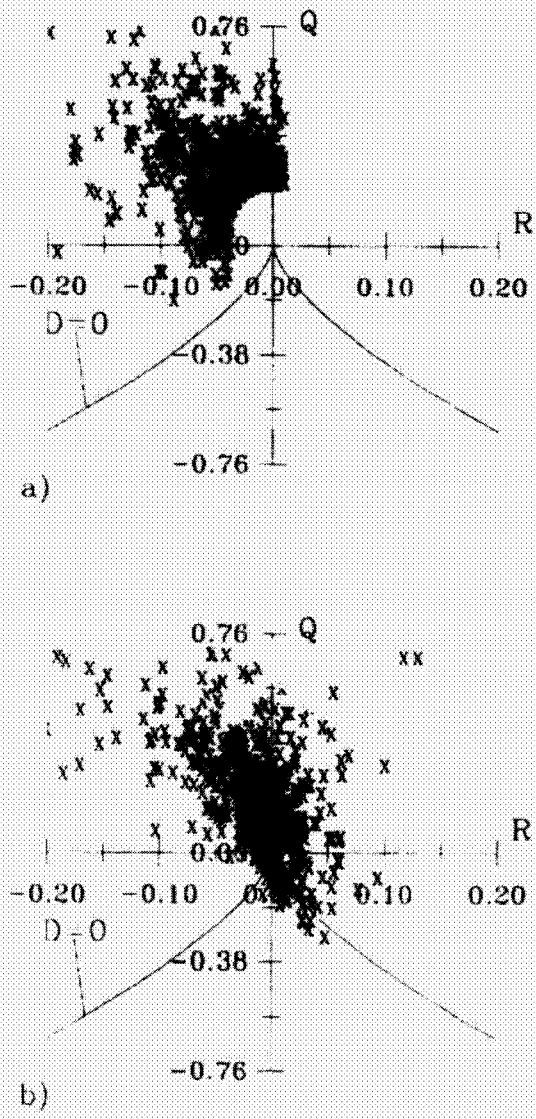

FIGURE 5. Particle trajectories on the $R - Q$ plane computed from the zero pressure gradient turbulent boundary layer data of Spalart (1988).

together with intertwining tubes forming braids which are near the surface and are aligned with the streamwise direction. Figures 4(a), (b), and (c) show the same flow case of Spalart but for a different time frame covering a larger field of data. The figures are ordered for diminishing values of D. Figure 4(a) shows structures which could be interpreted as $\cap$ or Λ eddies when viewed from upstream. These loops appear to lean in the streamwise direction. As the "threshold" is reduced (i.e. as the value of D for the isosurface is reduced), more attached vortex loops become apparent, but the picture becomes confusing. The structures are not as smooth as

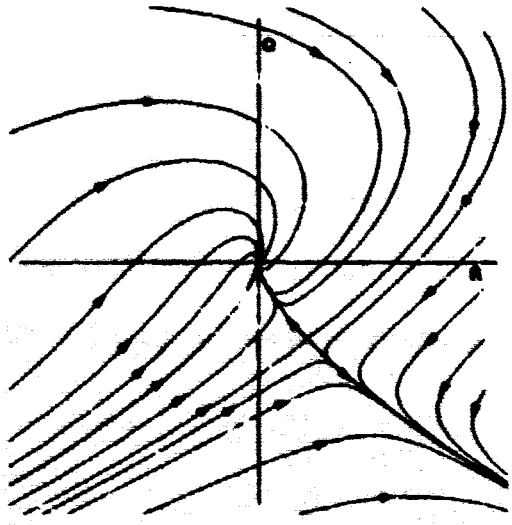

FIGURE 6. Particle trajectories using a linear diffusion model for H_{ij} of Martin & Dopazo (1995).

the Chacin *et al.* (1996) data, and this is because of computer storage problems. There is nonetheless a suggestion of Theodorsen type structures with focal tubes coming down to the wall and running along it in the streamwise direction. Superposition of vortex lines (done at the computer terminal) is confusing, but they tend to loop and lean in the streamwise direction in a manner similar to the isosurfaces of D.

Particle trajectories on the $R-Q$ plane show that there is a rapid convergence to small but positive D. Figure 5 shows a typical calculation for a selection of particles with $D > 0$ at the initial time. These particles are identified at $t = 0$ and then followed in space as the DNS code is run forward in time for several eddy characteristic turnover times. These calculations show that once a particle has a positive discriminant (i.e. once it is focal), it has a high probability of remaining focal over several eddy turnover times. Various models for the H_{ij} term are currently being formulated. One recent model by Martin & Dopazo (1995) shows ensemble averaged $R-Q$ trajectories with the topology sketched in Fig. 6, and this is consistent with the above findings. Time evolution computations and animations of the isosurfaces of the discriminant show that such surfaces retain their shape and identity for considerable streamwise distances. When viewing a movie made up of successive frames, these structures appear to convect downstream in close accordance with Taylor's hypothesis. Smaller structures close to the wall appear to be convecting at smaller velocities than the larger structures further away from the wall. All of this is consistent with aspects of the attached eddy model discussed by Perry *et al.* (1986).

In zero pressure gradient layers, there seems to be a strong link between these attached eddies and the Reynolds shear stress. Perry and Chong (1982) showed that

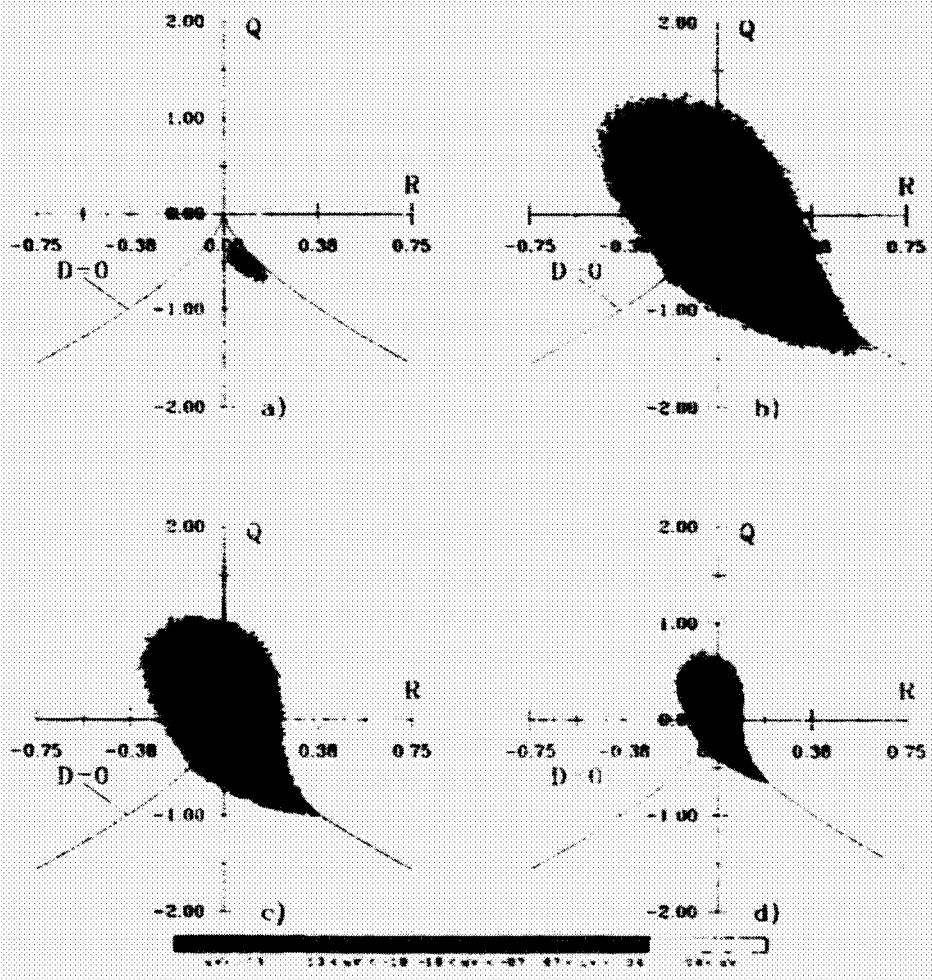

FIGURE 7. Time-averaged values of $-u'v'$ for zero pressure gradient turbulent boundary layer flow with $Re_\theta = 670$ in (a) viscous sub-layer $y^+ < 5.0$ (b) buffer layer, $5.0 < y^+ < 41$, (c) logarithmic region, $41 < y^+ < 107$ and (d) wake region, $y^+ > 107$. The contour levels shown are normalized by u_τ^2.

it is likely that they contribute almost entirely to the mean vorticity distribution and the Reynolds shear stress distribution. Figure 7 shows that peaks in the time averaged values of $-u'v'$ occur near to and on either side of the contour $D = 0$ on the $R > 0$ branch of the $R - Q$ plane. Here u' and v' are the streamwise and wall-normal components of the velocity fluctuations respectively.

Chacin *et al.* (1996) found that the contributions to the Reynolds shear stress by an attached eddy come from regions close in physical space to the isosurface of D, which is small and positive as seen in Fig. 9 of that reference. They found that high Reynolds stress events are strongly correlated with changes in sign of the discriminant. This is important near the wall where the discriminant and the

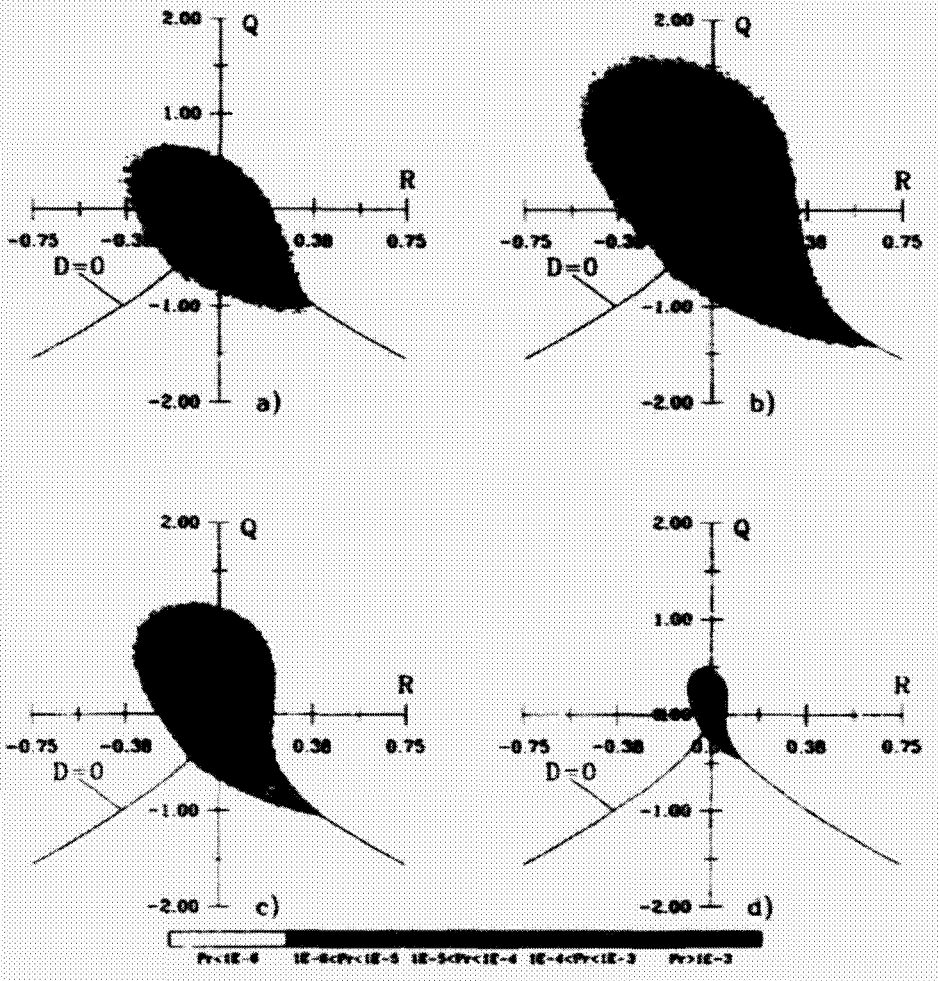

FIGURE 8. Joint probability density function betweer Q and R for zero pressure gradient turbulent boundary layer flow with $R_\theta = 670$ in (a) viscous sub-layer $y^+ < 5.0$ (b) buffer layer, $5.0 < y^+ < 41$. (c) logarithmic region, $41 < y^+ < 107$ and (d) wake region, $y^+ > 107$.

vorticity have completely different character. The role of the discriminant needs to be clarified. One approach would be to analyze the velocity gradient tensor induced by artificial isolated eddies of various shapes using the Biot-Savart law in the manner of Perry and Marusic (1995).

Figures 8, 9, 10, and 11 show joint probability distribution diagrams of the various topological invariants. On these diagrams are shown contours of the joint pdf's of various pairs of quantities. Figure 8 shows the joint pdf's of R and Q and Figs. 8(a) through to 8(d) show results for the sublayer, buffer zone, logarithmic region, and wake region respectively. Figure 9 shows the joint pdf of R_s and Q_s. In the sublayer, Fig. 9(a) shows that most of the rate of strain is two dimensional, since the data

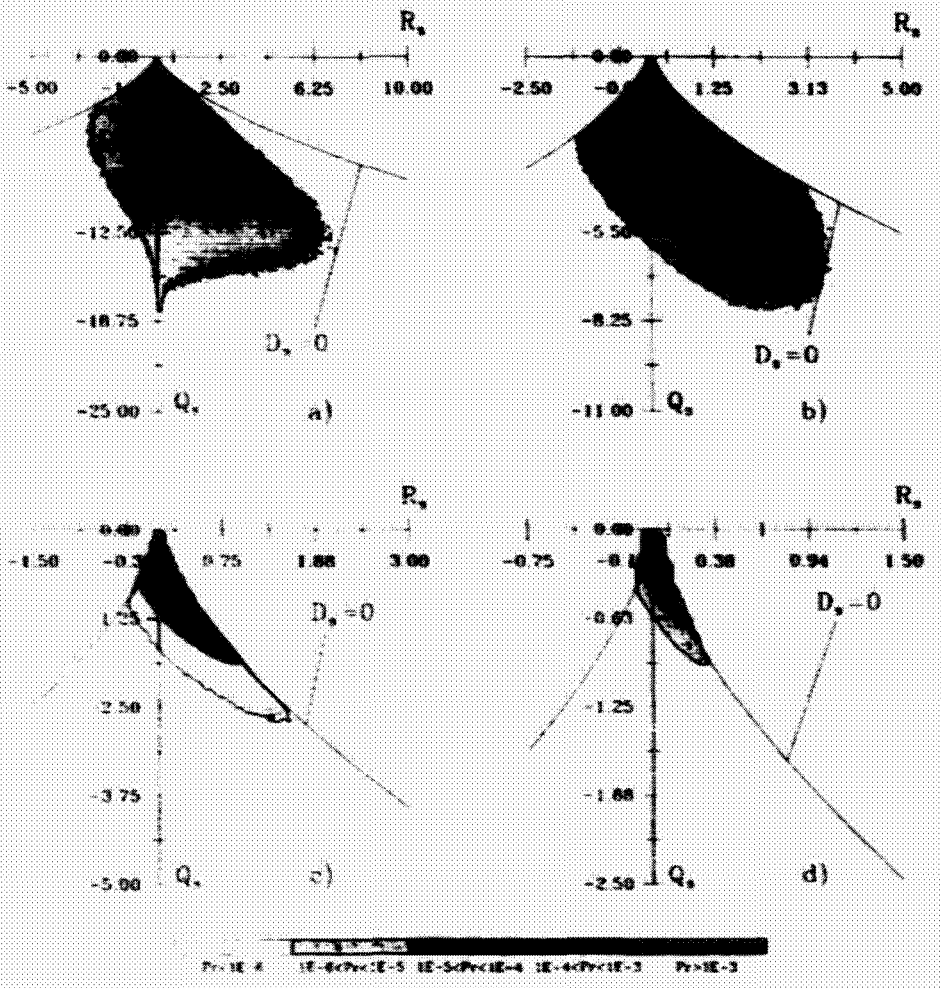

FIGURE 9. Joint probability density function between Q_S and R_S for zero pressure gradient turbulent boundary layer flow with $R_\theta = 670$ in (a) viscous sub-layer $y^+ < 5.0$ (b) buffer layer, $5.0 < y^+ < 41$, (c) logarithmic region, $41 < y^+ < 107$ and (d) wake region, $y^+ > 107$.

collects along the Q_s axis and very high Q_s values are encountered. In the buffer zone results shown in Fig. 9(b) there is a drift towards $D = 0$, and $|Q_s|$ is half that of the sublayer. In Fig. 9(c), the logarithmic region, there is a further decrease in $|Q_s|$ and further movement towards the $D = 0$ contour. The rate of strain is very three dimensional. In the wake region shown in Fig. 9(d), $|Q_s|$ is orders of magnitude smaller than the other regions and very little dissipation is occurring there.

Figure 10 shows the joint pdf between $-Q_s$ and Q_w. A line of 45° through the origin is symptomatic of vortex sheet behavior or two dimensional shearing. Data running close to the Q_w axis could be interpreted as belonging to vortex tubes, and

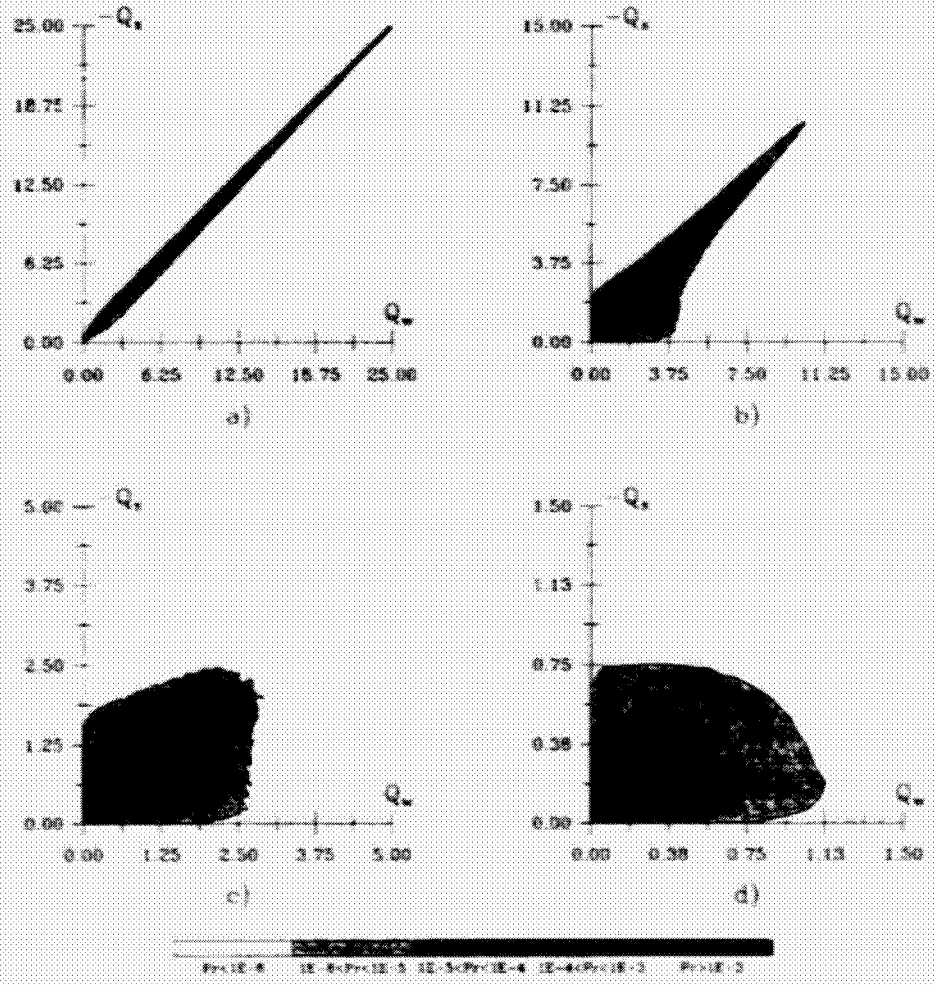

FIGURE 10. Joint probability density function between Q_W and $-Q_S$ for zero pressure gradient turbulent boundary layer flow with $R_\theta = 670$ in (a) viscous sublayer $y^+ < 5.0$ (b) buffer layer, $5.0 < y^+ < 41$, (c) logarithmic region, $41 < y^+ < 107$ and (d) wake region, $y^+ > 107$.

data close to the $-Q_s$ axis corresponds to irrotational rates of strain which cause dissipation. In Fig. 10(a) the sublayer results give sheet-like behavior which is not surprising. In Fig. 10(b), the buffer zone results are shown and there is a mixture of various types of motions, but vortex sheet behavior still dominates. Figure 10(c) shows a complete mixture of motion types and so also does Fig. 10(d). These results are consistent with the results of Blackburn *et al.* (1996).

Figure 11 shows the pdf between $|\sigma|\sigma/2$ and Q_w. Here

$$\sigma = \frac{\omega_i S_{ij} \omega_j}{\omega_k \omega_k} \tag{17}$$

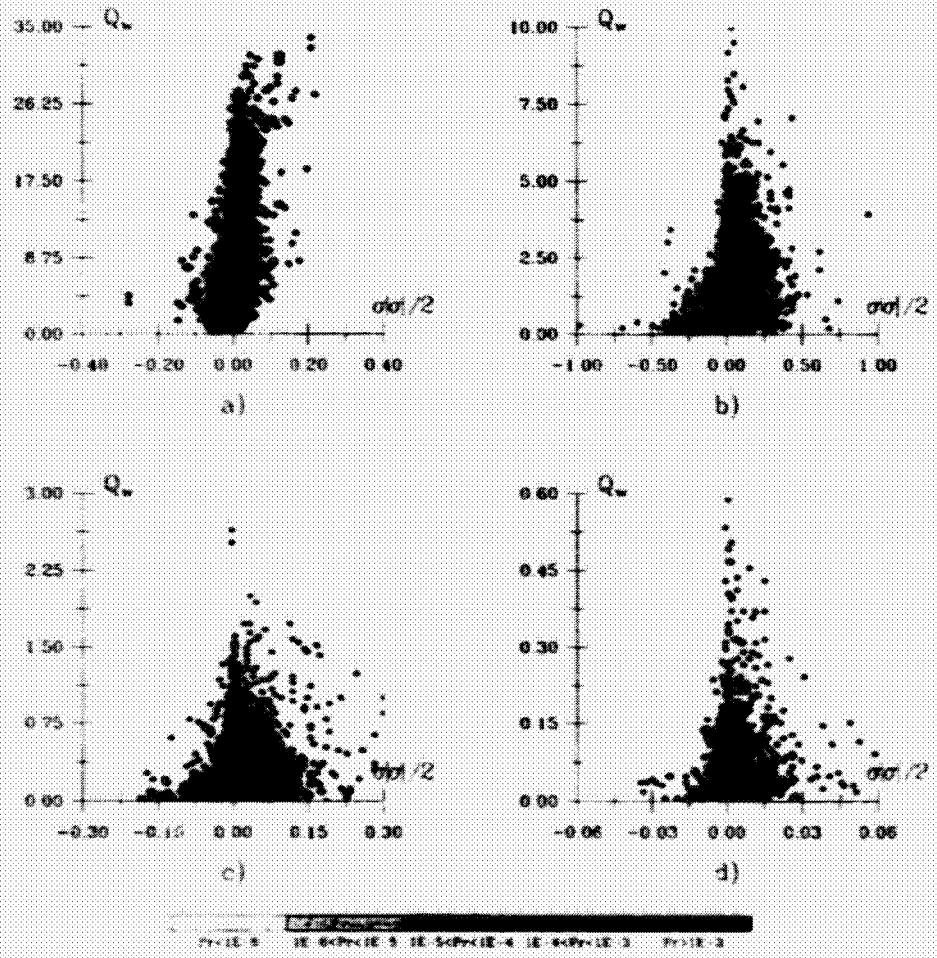

FIGURE 11. Joint probability density function between $|\sigma|\sigma/2$ and Q_w for zero pressure gradient turbulent boundary layer flow with $R_\theta = 670$ in (a) viscous sublayer $y^+ = 1.2$ (b) buffer layer, $y^+ = 16$, (c) logarithmic region, $y^+ = 87$ and (d) wake region, $y^+ = 243$.

where ω_i is the vorticity vector. Also it can be shown (e.g. see Soria and Chong (1993)) that

$$\omega_i S_{ij}\omega_j = R - R_s \tag{17}$$

The quantity $|\sigma|\sigma/2$ is a measure of the stretching and contracting in the direction of the vorticity vector. For all cases in Fig. 11 the highest vorticity has no stretching. Figure 12 shows the conditional volume integrated Q_w and Q_s for D greater than a specified threshold value as a function of this threshold value of D. These volume integrals have been normalized by the total volume integral of Q_w and Q_s respectively. In addition to the cases including the viscous zone, these normalized

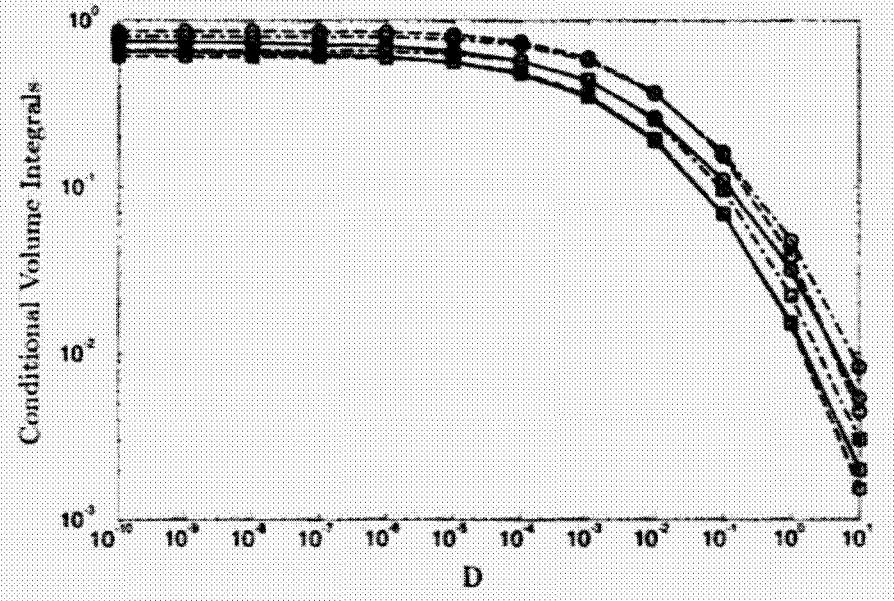

FIGURE 12. Conditional volume integrals of Q_s and Q_w normalized by the volume integrals of Q_s and Q_w respectively as a function of the cut-off value of the discriminant (D). —●— $\int Q_s(D > D_{given})dV / \int Q_s dV$. —●— $\int Q_w(D > D_{given})dV / \int Q_w dV$. —●—$\int Q_s(D > D_{given})dV / \int Q_s dV$ and $y^+ > 6.4$. —●—$\int Q_w(D > D_{given})dV / \int Q_w dV$ and $y^+ > 6.4$. --■- $\int Q_s(D > D_{given})dV / \int Q_s dV$ and $y^+ > 37$. --■- $\int Q_w(D > D_{given})dV / \int Q_w dV$ and $y^+ > 37$.

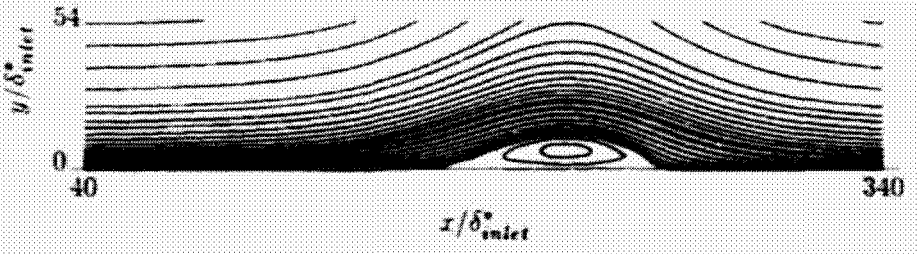

FIGURE 13. Mean streamline pattern for turbulent boundary layer with separation and reattachment. The dimensions shown were normalized by the displacement thickness at the inlet plane.

conditional integrals have been computed for $y^+ > 6.4$, thus eliminating the viscous sublayer contribution, and for $y^+ > 37.4$, thus eliminating the entire viscous zone contribution. The results show that independent of the y^+ threshold, focal regions account for approximately 75% of all volume integrated Q_w (i.e. enstrophy) and 66% of all volume integrated Q_s (i.e. dissipation of mechanical energy).

2.3 Separating and reattaching boundary layer

Figure 13 shows the mean flow streamlines of a turbulent boundary layer which nominally starts as a zero pressure gradient layer using the Spalart data of $R_\theta = 330$ as an inflow boundary condition. These computations were carried out using a finite differences method. As the flow moves downstream, the pressure gradient is arranged to be zero, then adverse, and then favorable, resulting in a separation bubble. The flow bears a strong resemblance to the experiment of Perry and Fairlie (1975), but the Reynolds number for that experiment was orders of magnitude higher than this computation.

Figure 14 (left side) shows an elevation view of the isosurfaces of the discriminant, and one can see a myriad of structures, many of which extend through from the wall to the outer edge of the boundary layer and generally lean in the streamwise direction. The structures leave the wall completely downstream of the mean separation point and ride over the separation bubble and then reattach. In the separation bubble there is an extensive region which seems to be devoid of fluid particles with positive discriminant. Figure 15 (left side) shows the instantaneous surface limiting streamlines or "skin friction lines". In the upstream part of the flow, bifurcation lines (curves towards which neighboring trajectories asymptote) are most evident. The precise definition and property of such lines are given by Hornung and Perry (1984) and Perry and Hornung (1984). As the pressure gradient becomes adverse, the skin friction lines reveal critical points all over the surface prior to the mean flow separation region. Under the bubble, the scale or spacing of the critical points is much larger than in the mean attached flow and large "nodes" of separation and reattachment are evident near the mean flow separation and reattachment "lines" respectively. After reattachment, bifurcation lines are reformed after a short streamwise distance with a much wider spanwise spacing than upstream of the separation bubble. This spacing is no doubt related to the viscous scaling as a lower shear velocity gives rise to the wider spacing.

Figure 15 (right side) shows the surface vortex lines which are orthogonal to the skin friction lines. In regions far upstream and downstream of the separation bubble, kinks in the vortex lines indicate a bifurcation line in the skin friction lines. Hornung and Perry (1984) showed that near a bifurcation line, neighboring skin friction lines are exponential curves and the vortex lines are orthogonal parabolas. Figure 16 shows skin friction lines and vortex lines superimposed for selected parts of the flow and the bifurcation patterns just mentioned are apparent. This orthogonality property throughout the limiting wall field acts as a useful check on the correctness in our data processing and in some aspects of the computations. Critical points in the limiting surface streamlines are also critical points in vorticity. In the separation region, the large velocity field nodes which are apparent are foci in the vorticity field.

In Figure 14, the side and plan views of the isosurfaces of the discriminant show that the structures appear to be pulled apart and stretched as they ride over the separation bubble. Coles (1956, 1957) formulated a hypothesis for the mean velocity profiles which considers a turbulent boundary layer to consist of two components superimposed – namely a wall component which follows the universal law of the

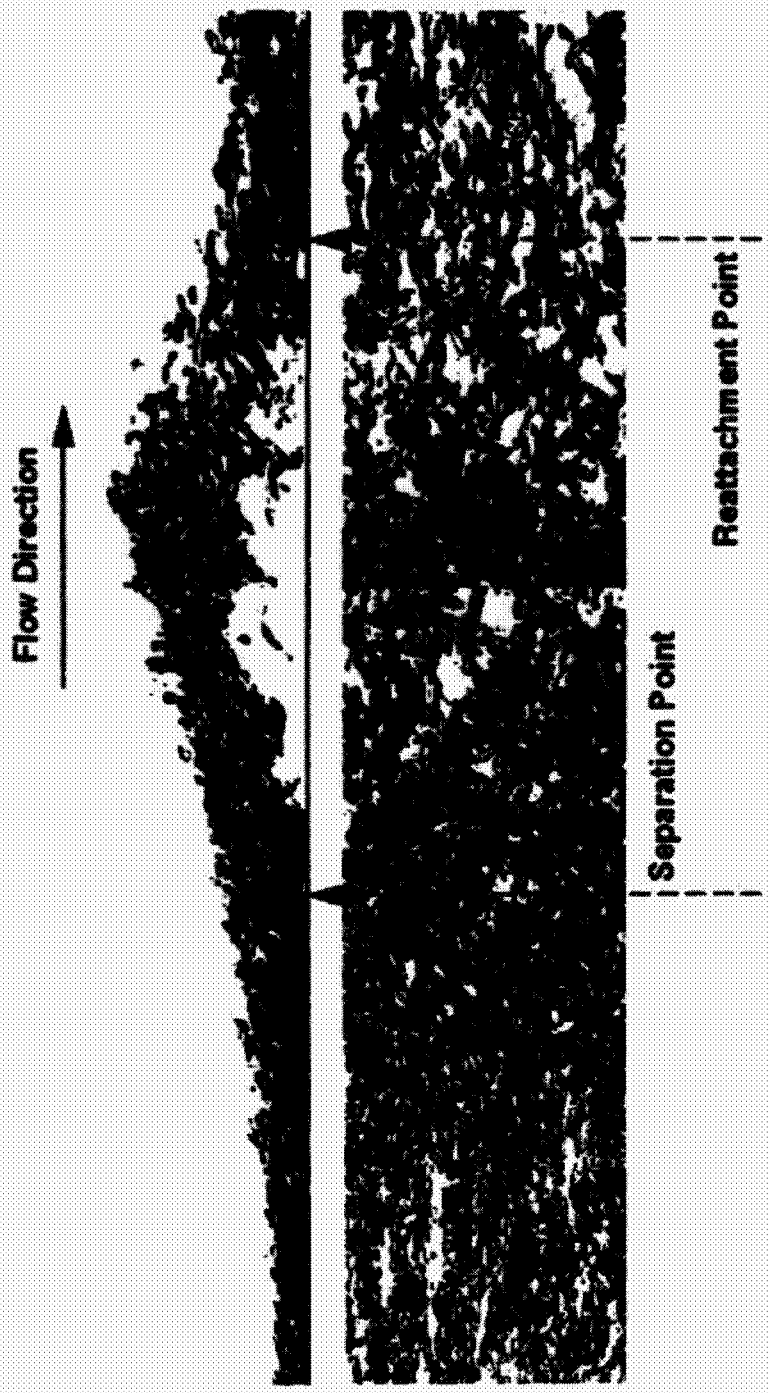

FIGURE 14. Isosurfaces of constant $D \sim 1$ to 10 showing focal structures in turbulent boundary layer with separation and reattachment from $x/\delta^*_{in} \approx 90$ to $x/\delta^*_{in} \approx 300$. Left) Elevation views. Right) Plan views.

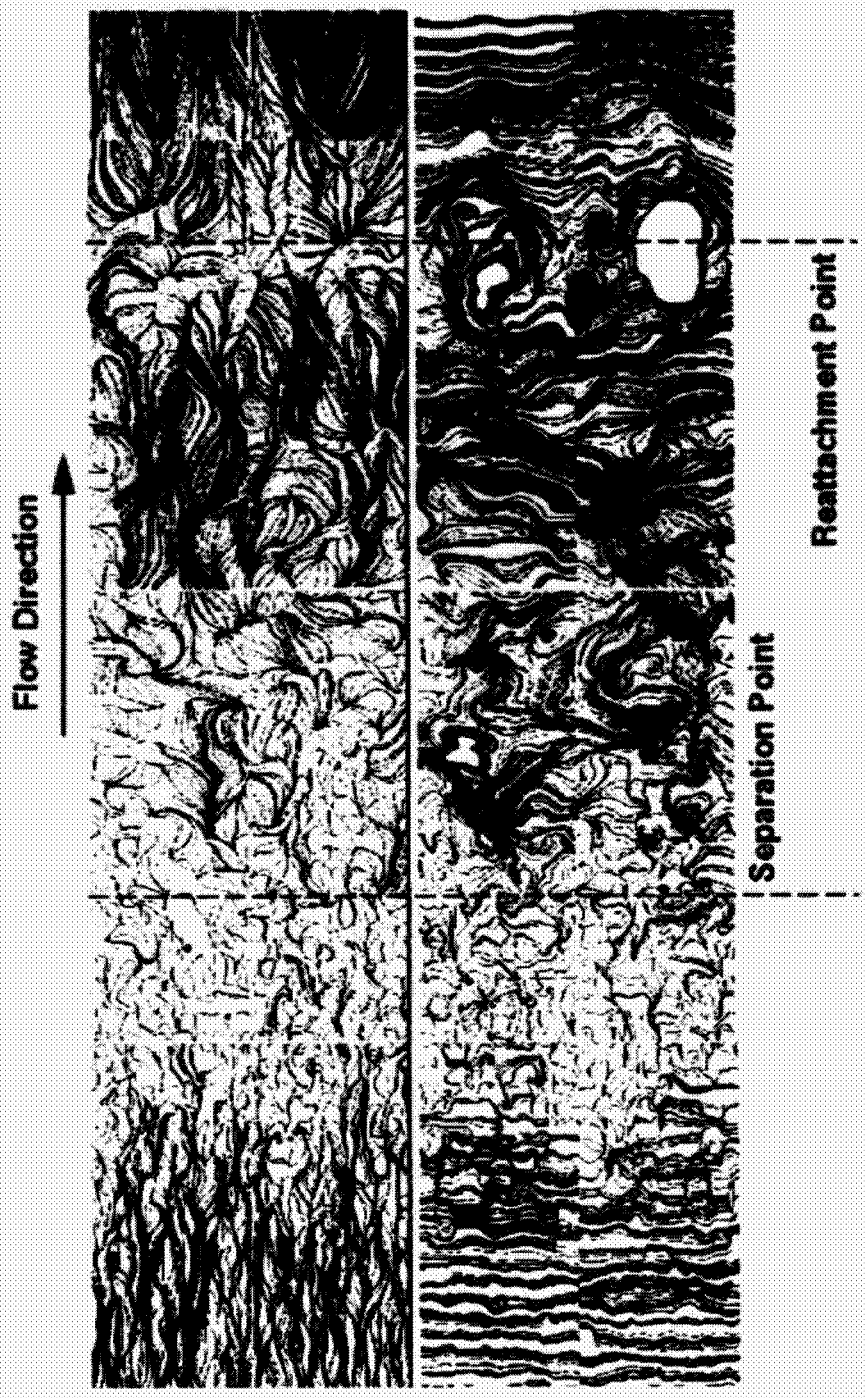

FIGURE 15. Skin friction lines and surface vorticity lines from $x/\delta^*_{in} \approx 90$ to $x/\delta^*_{in} \approx 309$. Left) Skin friction lines. Right) Vorticity lines.

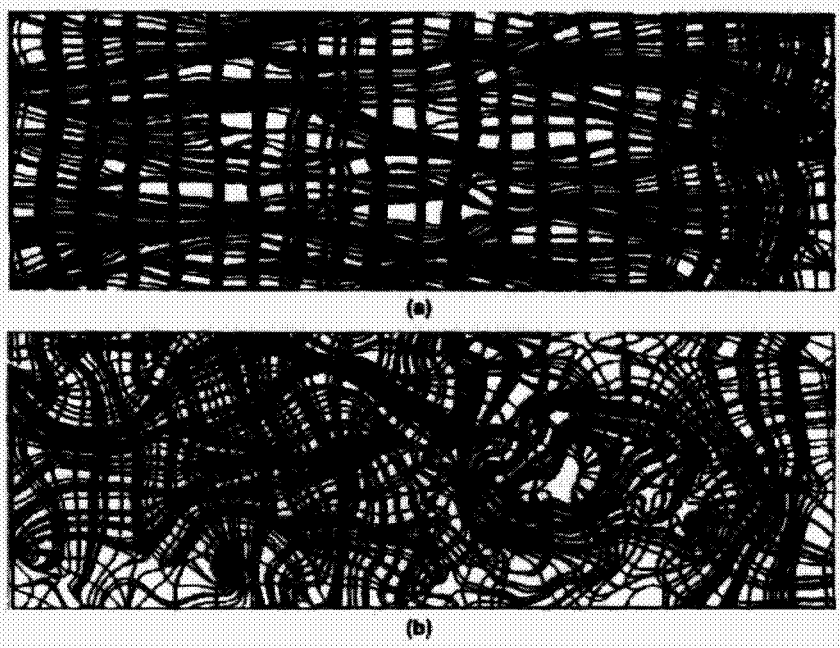

FIGURE 16. (a) and (b). Skin friction lines and surface vorticity lines superimposed. (a) Unseparated region. (b) Separated region.

wall and a wake component which follow a universal law of the wake. Recently this has been extended to include the turbulence structure by Perry and Marusic (1995) and Marusic and Perry (1995) where the wall component for both mean flow and Reynolds stress is considered to be generated by wall attached eddies where the vortex lines connect to the wall like the Theodorsen type eddies as shown sketched in Fig. 17(a). The wake component of velocity and the peak in the Reynolds shear stress which occurs well away from the wall when the Coles wake factor is appreciable is considered to be generated by wake eddies which are thought to consist of spanwise undulating vortex cores as shown in Fig. 17(b). This model is supported by mean flow, broadband turbulence and spectral measurements and an analysis using convolution integrals for computing the effect of a random array of eddies with a range of scales (see Perry & Marusic (1995) for details). It is almost obvious from the picture of the isosurface of the discriminant in Fig. 14 that as the flow develops in the adverse pressure gradient and as the Coles wake factor increases, more of the eddies which contribute to the Reynolds shear stress and mean flow vorticity are eddies which are not connected to the boundary. Once separation has occurred, there are no eddies connected with the wall. Unfortunately, memory limitations of the flow visualization software prevented a full rendering of the details of the flow field causing the isosurfaces to appear lumpy and unstructured. More work on this is required.

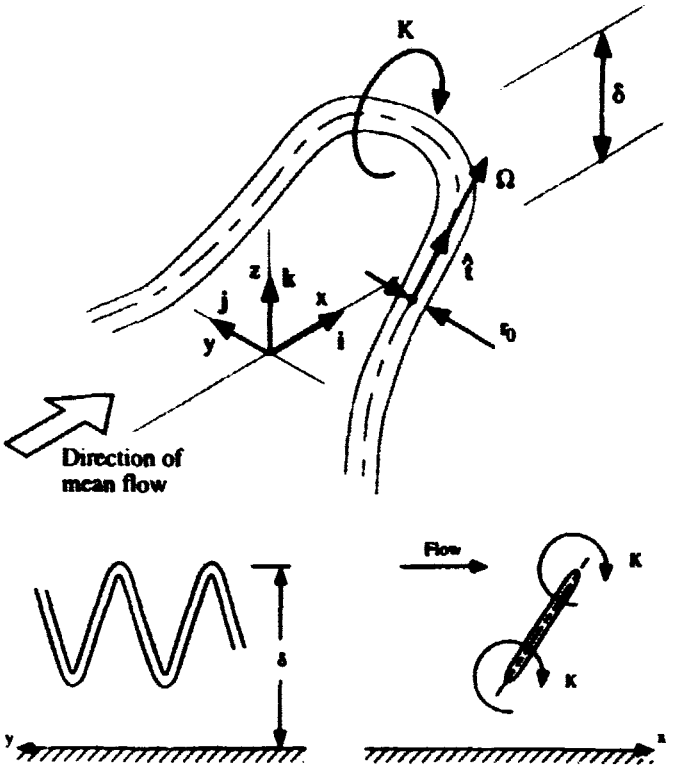

FIGURE 17. (a) Wall eddies and (b) wake eddies, after Perry & Marusic (1995). Note that here, unlike earlier convention, z is the coordinate normal to the wall rather than y.

3. Conclusions

This study has shown that there exists evidence for the Reynolds shear stress carrying structures in zero pressure gradient turbulent boundary layers, and they consist of attached eddies in the form of tubes of positive discriminant connected to the wall. The vortex loops envisioned by Theodorsen, the vortex tubes used in the model of Perry and Marusic (1995), and the tubes or arches of positive discriminant observed in simulations all bear striking resemblance to one another. But there are important differences which still need to be reconciled. The evidence presented here indicates that Reynolds stress generation is correlated, not with the vorticity, but with the discriminant of the velocity gradient tensor, especially near the wall where these two quantities have quite different character.

For adverse pressure gradients, there is evidence of wake structures which are not connected to the wall. However, because of the early stages of the present work and the difficulties encountered with the resolution of the stored data (if not the computed data), the evidence, although encouraging, is not conclusive. Furthermore we should keep in mind at all times that we are dealing with low Reynolds number flows where the range of eddy length scales is relatively small.

Acknowledgments

This work was supported by the Center for Turbulence Research, NASA AMES-Stanford Joint Institute for Aeronautics and Acoustics, NASA Grant NAG-1-1610 and the Australian Research Council. Additional supercomputing resources were provided by the San Diego Supercomputer Center.

REFERENCES

BLACKBURN, H. M., MANSOUR, N. N. & CANTWELL, B. J. 1996 Topology of fine-scale motions in turbulent channel flow. *J. Fluid Mech.* **310**, 269-292.

CANTWELL, B. J. 1979 Coherent turbulent structures as critical points in unsteady flow. *Archiwum Mechaniki Stosowanej. (Archives of Mechanics).* **31**, 5, 707-721.

CANTWELL, B. J. 1992 Exact solution of a restricted Euler equation for the velocity gradient tensor. *Phys. of Fluids.* **4(4)**, 782-793.

CHACIN, J. M., CANTWELL, B. J. & KLINE, S. J. 1996 Study of turbulent boundary structure using the invariants of the velocity gradient tensor. To appear in the *Journal of Experimental, Thermal and Fluid Science.* **November.**

CHONG, M. S., PERRY, A. E. & CANTWELL, B. J. 1989 A general classification of three-dimensional flow fields. *Proceedings of the IUTAM Symposium on Topological Fluid Mechanics, Cambridge* (Edited by H. K. Moffatt and A. Tsinober), 408-420.

CHONG, M. S., PERRY, A. E. & CANTWELL, B. J. 1990 A general classification of three-dimensional flow fields. *Phys. of Fluids.* **A4(4)**, 765-777.

DALLMANN, U. 1983 Topological structures of three-dimensional flow separations. *DFVLR Rep. IB 221-82-A07.* Gottingen, West Germany.

HORNUNG, H. G. & PERRY, A. E. 1984 Some aspects of three-dimensional separation. Part I. Streamsurface bifurcations. *Z. Flugwiss. Weltraumforsch.* **8**, 77-87.

JEONG, J. & HUSSAIN, F. 1995 On the identification of a vortex. *J. Fluid Mech.* **285**, 69-94.

KIM, J. 1989 On the structure of pressure fluctuations in simulated turbulent channel flow. *J. Fluid Mech.* **205**, 421-451.

LUGT, H. J. 1979 The dilemma of defining a vortex. In *Recent Developments in Theoretical and Experimental Fluid Mechanics* (ed. U. Muller, K.G. Roesner & B. Schmidt), Springer, 309-321.

MARTIN, J. & DOPAZO, C. 1995 Velocity gradient invariant evolution from a linear diffusion model. *Proceedings of the Twelfth Australasian Fluid Mechanics Conference.* 743-746.

MARUSIC, I. & PERRY, A. E. 1995 A wall-wake model for the turbulent structure of boundary layers. Part 2. Further experimental support. *J. Fluid Mech.* **298**, 389-407.

NA, Y. & MOIN, P. 1996 Direct numerical simulation of turbulent boundary layers with adverse pressure gradient and separation. *Stanford University Report TF-68.*

PERRY, A. E. & FAIRLIE, B. D. 1975 A study of turbulent boundary-layer separation and reattachment. *J. Fluid Mech.* **69,** 657-672.

PERRY, A. E. & CHONG, M. S. 1982 On the mechanism of wall turbulence. *J. Fluid Mech.* **119,** 173-217.

PERRY, A. E. & HORNUNG, H. G. 1984 Some aspects of three-dimensional separation. Part II. Vortex skeletons. *Z. Flugwiss. Weltraumforsch.* **8,** 155-160.

PERRY, A. E., HENBEST, S. M. & CHONG, M. S. 1986 A theoretical and experimental study of wall turbulence. *J. Fluid Mech.* **165,** 163-199.

PERRY, A. E. & MARUSIC, I. 1995 A wall-wake model for the turbulent structure of boundary layers. Part 1 Extension of the attached eddy hypothesis. *J. Fluid Mech.* **298,** 361-388.

ROBINSON, S. K. 1991 Coherent motions in the turbulent boundary layer. *Ann. Rev. Fluid Mech.* **23,** 601-639.

SORIA, J., CHONG, M. S., SONDERGAARD, R., PERRY, A. E. & CANTWELL, B. J. 1992 Topology of time-developing incompressible mixing layers. *Proceedings of the Center for Turbulence Research Summer Program, 1992.* Stanford Univ./NASA Ames, 101-121.

SORIA, J. & CHONG, M. S. 1993 The structure of intense focal regions in a direct numerical wake flow calculation. *Proceedings of the Ninth Symposium on Turbulent Shear Flows.* 3.1.1-3.1.6.

SORIA, J., CHONG, M. S., SONDERGAARD, R., PERRY, A. E. & CANTWELL, B. J. 1994 A study of the fine scale motions of incompressible time-developing mixing layers. *Phys. of Fluids.* **6(2),** 871-884.

SPALART, P. R. 1988 Direct simulation of a turbulent boundary layer up to Re_θ = 1410. *J. Fluid Mech.* **187,** 61-98.

THEODORSEN, T. 1955 The structure of turbulence. *50 Jahre Grenzschichtforsung.*

TOWNSEND, A. A. 1976 *The Structure of Turbulent Shear Flow* 2nd edn. Cambridge University Press.

TRUESDELL, C. 1954 *The Kinematics of Vorticity. Indiana University Press.*

VIEILLEFOSSE, P. 1982 Local interaction between vorticity and shear in a perfect incompressible fluid. *J. Phys. (Paris).* **43,** 837-842.

VIEILLEFOSSE, P. 1984 Internal motion of a small element of fluid in an inviscid flow. *Physica A.* **150,** 150-162.

VOLLMERS, H. 1983 Separation and vortical-type flow around a prolate spheroid. Evolution of relevant parameters. *AGARD Symposium on Aerodyn. of Vortical Type Flow in Three-Dimensional. Rotterdam.* **AGARD-CP342,** 14.1-14.14.

NEXT
DOCUMENT

Optimal and robust control of transition

By T. R. Bewley[1] AND R. Agarwal[2]

Optimal and robust control theories are used to determine feedback control rules that effectively stabilize a linearly unstable flow in a plane channel. Wall transpiration (unsteady blowing/suction) with zero net mass flux is used as the control. Control algorithms are considered that depend both on full flowfield information and on estimates of that flowfield based on wall skin-friction measurements only. The development of these control algorithms accounts for modeling errors and measurement noise in a rigorous fashion; these disturbances are considered in both a structured (Gaussian) and unstructured ("worst case") sense. The performance of these algorithms is analyzed in terms of the eigenmodes of the resulting controlled systems, and the sensitivity of individual eigenmodes to both control and observation is quantified.

1. Introduction

The behavior of infinitesimal perturbations in simple laminar flows is an important and well-understood problem. As the Reynolds number is increased, laminar flows often become unstable and transition to turbulence occurs. The effects of the turbulence produced in such flows are very significant and often undesirable, resulting in increased drag and heat transfer at the flow boundaries. Thus, a natural engineering problem is to study methods of flow control such that transition to turbulence can be delayed or eliminated.

Transition often occurs at a Reynolds number well below that required for linear instability of the laminar flow. Orszag & Patera (1983) demonstrate that finite amplitude two-dimensional perturbations can highly destabilize infinitesimal three-dimensional perturbations in the flow. Butler & Farrell (1992) show that the non-orthogonality of the eigenmodes of subcritical flows implies that perturbations of a particular initial structure will experience large amplification of energy before their eventual decay, and suggest that such amplification can sometimes lead to flow perturbations large enough for nonlinear instability to be triggered. Such nonlinear instabilities can lead to transition well below the critical Reynolds number at which linear instability occurs. Results such as these have renewed interest in the control of the small (linear) perturbations, as the mitigation of linear perturbations also lessens the potency of these nonlinear "bypass" mechanisms.

A firm theoretical basis for the control of small perturbations in viscous shear flows is only beginning to emerge. An important step in this direction is provided

1 Mechanical Engineering Department, Stanford University
2 Aerospace Engineering Department, Wichita State University

by Joslin *et al.* (1995) and Joshi, Speyer, & Kim (1996), who analyze this problem in a closed-loop framework, in which the dynamics of the flow system together with the controller are examined. Joslin *et al.* (1995) apply optimal control theory to a problem related to the one presented here; in their approach, the control is determined through an adjoint formulation requiring full flowfield information. Joshi, Speyer, & Kim (1996) consider essentially the same problem analyzed in this paper, and show that a simple constant gain feedback with an integral compensator may be used in a single-input/single-output (SISO) sense to stabilize the flow: a single output (the appropriate Fourier component of the streamwise drag) is multiplied by some scalar K and summed with a reference signal to determine the corresponding component of the control velocity. This proportional approach is a special case of a class of proportional-integral-derivative (PID) controllers, which combine terms which are proportional, integrals, and derivatives of a scalar output of a system.

The present work extends these analyses to rigorously account for state disturbances and measurement noise. A two-step control approach is used. First, a state estimate is developed from a (potentially inaccurate) model of the flow equations, with corrections to this state estimate provided by (noisy) flow measurements fed back through an output injection matrix L. This state estimate is then multiplied by a feedback matrix K to determine the control. Potentially, this approach can yield better results than a PID controller. In comparison to the PID approach, the present approach has many more parameters in the control law (specifically, the elements of the matrices K and L), which are rigorously optimized for a clearly defined objective. In this manner, multiple-input/multiple-output (MIMO) systems are handled naturally and the controller is coupled with an estimator which models the dynamics of the system itself.

Many problems in fluid mechanics, especially those involving turbulence, are dominated by nonlinear behavior. In such problems, the linear analysis performed in this paper is not valid. However, optimal control approaches, which use full state information, may still be formulated (Abergel & Temam 1990) and performed (Moin & Bewley 1995) with impressive results. In order to make such schemes practical, one must understand how to account for disturbances in a rigorous fashion and how to estimate accurately the necessary components of the state (for instance, the location and strength of the near-wall coherent structures) based on limited flow measurements. The current paper makes these concepts clear in a fluid-mechanical sense, albeit for a linear problem, and thus provides a step in this development.

The controllers and estimators used in this work are determined by $\mathcal{H}_2$ and $\mathcal{H}_\infty$ approaches. These techniques have recently been cast in a compact form by Doyle *et al.* (1989), and are well suited to the current problem, in which the issue of interest is the ability of a closed-loop system to reject disturbances to a laminar flow when only a few noisy measurements of the flow are available.

In §2, we derive the governing equations for the present flow stability problem and cast these equations in a standard notation. In §3, the control problem is analyzed in terms of the controllability and observability of each individual eigenmode of the system developed in §2. In §4, the control approach developed in Doyle *et al.* (1989)

is summarized and applied to the present system. In this control approach, two Riccati equations describe a family of $\mathcal{H}_2$ and $\mathcal{H}_\infty$ controllers which take into account structured (Gaussian) and unstructured ("worst case") disturbances. Results of these approaches are presented in §5, and §6 presents some concluding remarks.

2. Governing equations

This chapter derives the equations governing the perturbations to a laminar channel flow and casts them in a form to which standard control techniques may be applied. This familiar discussion is presented to precisely define the control problem under consideration.

2.1 Continuous form of flow equations

Consider a steady plane channel flow with maximum velocity U_0 and channel half-width δ. Non-dimensionalizing all velocities by U_0 and lengths by δ, the mean velocity profile in the streamwise direction (x) may be written $U(y) = 1 - y^2$ on the domain $y \in [-1, 1]$. The equations governing small, incompressible, three-dimensional perturbations (v, ω) are

$$\dot{\Delta v} = \{-ik_x U \Delta + ik_x U'' + \Delta(\Delta/Re)\}\, v \tag{1a}$$

$$\dot{\omega} = \{-ik_z U'\}\, v + \{-ik_x U + \Delta/Re\}\, \omega, \tag{1b}$$

where k_x is the streamwise wavenumber, k_z is the spanwise wavenumber, $\Delta \equiv \partial^2/\partial y^2 - k_x^2 - k_z^2$ is the Laplacian, $Re \equiv U_0\delta/\nu$ is the Reynolds number, v is the Fourier component of the wall-normal velocity, and ω is the Fourier component of the wall-normal vorticity. Equation (1a) is the (fourth order) Orr-Sommerfeld equation for the wall-normal velocity modes, and (1b) is the (second order) equation for the wall-normal vorticity modes. Note the one-way coupling between these two equations. Also note that, from any solution (v, ω), the streamwise velocity u and spanwise velocity w may be extracted by manipulation of the continuity equation and the definition of wall-normal vorticity into the form

$$u = \frac{i}{k_x^2 + k_z^2}\left(k_x \frac{\partial v}{\partial y} - k_z \omega\right) \tag{2a}$$

$$w = \frac{-i}{k_x^2 + k_z^2}\left(k_z \frac{\partial v}{\partial y} - k_x \omega\right). \tag{2b}$$

Control will be applied at the wall as a boundary condition on the wall-normal component of velocity v. The boundary conditions on u and w are no-slip ($u = w = 0$), which implies that $\omega = 0$ and (by continuity) $\partial v/\partial y = 0$ on the wall.

In this development, it is assumed that an array of sensors, which can measure streamwise and spanwise skin friction, and actuators, which provide wall-normal blowing and suction with zero net mass flux, are mounted on the walls of a laminar channel flow. It is also assumed that a sufficient number of sensors and actuators are installed such that individual Fourier components of wall skin friction and wall transpiration may be approximated, and the analysis is carried through for a particular Fourier mode.

2.2 Discrete form of flow equations

The continuous problem described above is discretized on a grid of $N+1$ Chebyshev-Gauss-Lobatto points such that

$$y_l = \cos(\pi l/N) \qquad \text{for } 0 \le l \le N.$$

An $(N+1) \times (N+1)$ matrix $\mathcal{D}$ may be expressed (Canuto *et al.* 1988, eqn. 2.4.31) such that the derivative of ω with respect to y on the discrete set of $N+1$ points is given by

$$\omega' = \mathcal{D}\omega \qquad \text{and} \qquad \omega'' = \mathcal{D}\omega',$$

where the prime ($'$) now indicates the (partial) derivative of the discrete quantity with respect to y. The homogeneous Neumann boundary condition on v is accomplished by modifying the first derivative matrix such that

$$\tilde{\mathcal{D}}_{lm} = \begin{cases} 0 & l = 0, N \\ \mathcal{D}_{lm} & 1 \le l \le N-1. \end{cases}$$

Differentiation of v with respect to y is then given by

$$v' = \tilde{\mathcal{D}}v, \qquad v'' = \mathcal{D}v', \qquad v''' = \mathcal{D}v'', \qquad \text{and} \qquad v'''' = \mathcal{D}v'''.$$

With these derivative matrices, it is straightforward to write (1) in matrix form. This is accomplished by first expressing the matrix form of (1) on all $N+1$ collocation points such that:

$$\dot{v} = \mathcal{L}v \tag{3a}$$

$$\dot{\omega} = \mathcal{C}v + \mathcal{S}\omega. \tag{3b}$$

where $\mathcal{L}$, $\mathcal{C}$, and $\mathcal{S}$ are $(N+1) \times (N+1)$. (Note that, for $k_x^2 + k_z^2 \neq 0$, the matrix form of the LHS of (1a) is invertible, so the form (3a) is easily determined.) The Dirichlet boundary conditions are explicitly prescribed as separate "forcing" terms. To accomplish this, decompose $\mathcal{L}$, $\mathcal{C}$, and $\mathcal{S}$ according to

$$\mathcal{L} = \begin{pmatrix} \cdot & \cdot & \cdot \\ b_{11} & A_{11} & b_{12} \\ \cdot & \cdot & \cdot \end{pmatrix} \quad \mathcal{C} = \begin{pmatrix} \cdot & \cdot & \cdot \\ b_{21} & A_{21} & b_{22} \\ \cdot & \cdot & \cdot \end{pmatrix} \quad \mathcal{S} = \begin{pmatrix} \cdot & \cdot & \cdot \\ \cdot & A_{22} & \cdot \\ \cdot & \cdot & \cdot \end{pmatrix}$$

where A_{11}, A_{21}, and A_{22} are $(N-1) \times (N-1)$ and b_{11}, b_{12}, b_{21}, and b_{22} are $(N-1) \times 1$. Noting that $\omega_0 = \omega_N = 0$ by the no-slip condition, and defining

$$x \equiv \begin{pmatrix} v_1 \\ \vdots \\ v_{N-1} \\ \omega_1 \\ \vdots \\ \omega_{N-1} \end{pmatrix} \quad A \equiv \begin{pmatrix} A_{11} & 0 \\ & \\ A_{21} & A_{22} \end{pmatrix} \quad B \equiv \begin{pmatrix} b_{11} & b_{12} \\ & \\ b_{21} & b_{22} \end{pmatrix} \quad u \equiv \begin{pmatrix} v_0 \\ v_N \end{pmatrix},$$

where x is $2(N-1)\times 1$, A is $2(N-1)\times 2(N-1)$, B is $2(N-1)\times 2$, and u is 2×1, we may express (3) in the standard form

$$\dot{x} = Ax + Bu. \tag{4}$$

The vector x is referred to as the "state", and the vector u is referred to as the "control".

2.3 Wall measurements

We will consider control algorithms using both full flowfield information and wall information only. For the latter case, we will assume that measurements made at the wall provide information proportional to the streamwise and spanwise skin friction

$$y_{m1} = \left.\frac{\partial u}{\partial y}\right|_{\text{upper wall}} \qquad y_{m2} = \left.\frac{\partial u}{\partial y}\right|_{\text{lower wall}}$$
$$y_{m3} = \left.\frac{\partial w}{\partial y}\right|_{\text{upper wall}} \qquad y_{m4} = \left.\frac{\partial w}{\partial y}\right|_{\text{lower wall}}.$$

Equations (2a) and (2b) allow us to express these measurements as linear combinations of v and ω. Defining $a \equiv i k_x/(k_x^2 + k_z^2)$ and $b \equiv -i k_z/(k_x^2 + k_z^2)$ and using the derivative matrices, the measurements are expressed as

$$y_{m1} = \left(a\tilde{D}^2 v + b D\omega\right)_{\text{upper wall}} \qquad y_{m2} = \left(a\tilde{D}^2 v + b D\omega\right)_{\text{lower wall}}$$
$$y_{m3} = \left(b\tilde{D}^2 v + a D\omega\right)_{\text{upper wall}} \qquad y_{m4} = \left(b\tilde{D}^2 v + a D\omega\right)_{\text{lower wall}}.$$

Now decompose $\tilde{D}^2$ and D according to

$$\tilde{D}^2 = \begin{pmatrix} d_1 & c_1 & d_3 \\ * & * & * \\ d_2 & c_2 & d_4 \end{pmatrix} \qquad D = \begin{pmatrix} * & c_3 & * \\ * & * & * \\ * & c_4 & * \end{pmatrix},$$

where c_1, c_2, c_3, and c_4 are $1\times(N-1)$ and d_1, d_2, d_3, and d_4 are 1×1. Finally, defining

$$y_m \equiv \begin{pmatrix} y_{m1} \\ y_{m2} \\ y_{m3} \\ y_{m4} \end{pmatrix} \quad C \equiv \begin{pmatrix} a c_1 & b c_3 \\ a c_2 & b c_4 \\ b c_1 & a c_3 \\ b c_2 & a c_4 \end{pmatrix} \quad D \equiv \begin{pmatrix} a d_1 & b d_3 \\ a d_2 & b d_4 \\ b d_1 & a d_3 \\ b d_2 & a d_4 \end{pmatrix},$$

where y_m is 4×1, C is $4\times 2(N-1)$, and D is 4×2, allows us to express y_m in the standard form of a linear combination of the state x and the control u

$$y_m = Cx + Du. \tag{5}$$

The vector y_m is referred to as the "measurement".

3. Analysis of control problem

In §2, it was shown that the equations governing small perturbations in a laminar channel flow may be expressed in the standard form

$$\dot{x} = Ax + Bu \tag{6a}$$

$$y_m = Cx + Du, \tag{6b}$$

where all variables are complex and the system matrix A is dense and non-self-adjoint. We now discuss the eigenmodes of A and identify which of these modes may be modified by the control u and which may be detected by the measurements y_m.

It has been shown (Orszag 1971) that, for $Re \leq 5772$, the uncontrolled problem itself is stable and, for $Re > 5772$, weak instability is seen (though most of the eigenvalues remain stable), with the greatest instability near $k_x = 1.0$ and $k_z = 0.0$. We seek a method to determine the control u which stabilizes the system in a manner which is robust to system uncertainties. To simplify our discussion, we will restrict our attention in the remainder of this work to the particular case $Re = 10{,}000$, $k_x = 1.0$, and $k_z = 0.0$. Joshi, Speyer, & Kim (1996) explore the (Re, k_x, k_z) parameter space further.

For $k_z = 0$ (two-dimensional perturbations), $C = 0$ in (3), entirely decoupling the ω eigenmodes from both the v eigenmodes and from the control $u = (v_0, v_N)^T$. In the language of control theory, the ω eigenmodes are thus "uncontrollable" by the control u. (However, it is also seen that the ω eigenmodes are stable, so these modes will, so to speak, "take care of themselves".) Thus, for the remainder of this paper, we will restrict our attention to the v eigenmodes according to system (6) with

$$x = \begin{pmatrix} v_1 \\ \vdots \\ v_{N-1} \end{pmatrix} \qquad A = \begin{pmatrix} & A_{11} & \\ & & \end{pmatrix} \qquad B = \begin{pmatrix} b_{11} & b_{12} \\ & \end{pmatrix} \qquad u = \begin{pmatrix} v_0 \\ v_N \end{pmatrix},$$

where x is $(N-1) \times 1$, A is $(N-1) \times (N-1)$, B is $(N-1) \times 2$, and u is 2×1, and

$$y_m = \begin{pmatrix} y_{m1} \\ y_{m2} \\ y_{m3} \\ y_{m4} \end{pmatrix} \qquad C = \begin{pmatrix} & ac_1 & \\ & ac_2 & \\ & bc_1 & \\ & bc_2 & \end{pmatrix} \qquad D = \begin{pmatrix} ad_1 & bd_3 \\ ad_2 & bd_4 \\ bd_1 & ad_3 \\ bd_2 & ad_4 \end{pmatrix},$$

where y_m is 4×1, C is $4 \times (N-1)$, and D is 4×2. (All the constituent matrices, vectors, and flow measurements are described in the previous section.)

3.1 System analysis

We now address whether or not all of the current system's $N-1$ eigenmodes may be controlled by the $m = 2$ control variables, and whether or not all of these eigenmodes may be observed with the $p = 4$ measurements. To accomplish this, it

is standard practice to consider two matrices which characterize the controllability and observability of the system as a whole (Lewis 1995). These are the system controllability Gramian L_c of $(A\ B)$ and the system observability Gramian L_o of (C, A), which may be found by solution of

$$A L_c + L_c A^* + B B^* = 0$$
$$A^* L_o + L_o A + C^* C = 0.$$

Note that stable numerical techniques to solve equations of this form, referred to as Lyapunov equations, are well developed.

If L_c is (nearly) singular, there is at least one eigenmode of the system which is (nearly) unaffected by any choice of control u, and the system is called "uncontrollable". If all uncontrollable eigenmodes are stable, and a controller may be constructed such that the dynamics of the system may be made stable by the application of control, the system is called "stabilizable".

Similarly, if L_o is (nearly) singular, there is at least one eigenmode of the system which is (nearly) indiscernible by the measurements y_m, and the system is called "unobservable". If all unobservable eigenmodes are stable, and an estimator may be constructed such that the dynamics of the error of the estimate may be made stable by appropriate forcing of the estimator equation, the system is called "detectable".

For the present system, the smallest eigenvalue of both L_c and L_o are computed to be near machine zero, indicating that the present system as derived above is both uncontrollable and unobservable. Gramian analysis can not identify which of the eigenmodes are uncontrollable or unobservable, however, so it is impossible to predict from this analysis alone whether or not the system is stabilizable and detectable. For this reason, we now develop a method to determine which of the eigenmodes of a system may be affected by the control u and, similarly, which eigenmodes may be discerned by the measurements y_m.

3.2 Individual eigenmode analysis

We will now make use of the modal canonical form of the system (6) to quantify the sensitivity of each eigenmode of A to both control and observation (Kailath 1980). In order to clarify the derivation, we shall examine each eigenmode of the system separately. Define the eigenvalues λ_i and the right and left eigenvectors, ξ_i and η_i, of A such that

$$\text{right eigenvectors:} \qquad A\xi_i = \lambda_i \xi_i$$
$$\text{left eigenvectors:} \qquad \eta_i^* A = \lambda_i \eta_i^*,$$

where the eigenvectors are normalized such that $\|\xi_i\| = \|\eta_i\| = 1$ for all i. Assume A has distinct eigenvalues (this may be verified for the present system described above). Then any x may be decomposed as a linear combination of the (independent but not orthogonal) right eigenvectors such that

$$x = \sum_i a_i \xi_i. \tag{7a}$$

Differentiating with respect to time,

$$\dot{x} = \sum_i \dot{a}_i \xi_i. \tag{7b}$$

Also, note that left and right eigenvectors corresponding to different eigenvalues are orthogonal, but those corresponding to the same eigenvalues are not

$$(\eta_j, \xi_i) = 0 \quad j \neq i \tag{8a}$$

$$(\eta_j, \xi_i) \neq 0 \quad j = i. \tag{8b}$$

3.2.1 Definition of modal control sensitivity

By (6a) and (7), we have

$$\sum_i \dot{a}_i \xi_i = A \sum_i a_i \xi_i + B u$$

$$= \sum_i a_i \lambda_i \xi_i + B u.$$

Taking the inner product with η_j and noting (8a) yields

$$(\eta_j, \dot{a}_j \xi_j) = (\eta_j, a_j \lambda_j \xi_j) + (\eta_j, B u).$$

Noting (8b), this yields

$$\dot{a}_j = \lambda_j a_j + \frac{(B^* \eta_j)^* u}{\eta_j^* \xi_j}.$$

If the vector $B^* \eta_j = 0$, then $\dot{a}_j = \lambda_j a_j$ for any u. In terms of equation (7a), the component of x parallel to ξ_j is not affected by the control u, and the eigenmode is said to be "uncontrollable". Further, the norm of the coefficient of u

$$f_j = \frac{|\eta_j^* B B^* \eta_j|^{1/2}}{|\eta_j^* \xi_j|}, \tag{9}$$

which we shall call the control sensitivity of mode j, is a quantitative measure of the sensitivity of the eigenmode j to the control u. Note the dependence of this expression on the matrix $B B^*$, which is the same term which drives the Lyapunov equation for controllability Gramian L_c.

3.2.2 Definition of modal observation sensitivity

By (6b) and (7) and assuming, for the moment, that $u = 0$, we have

$$y_m = \sum_j a_j C \xi_j.$$

If the vector $C \xi_j = 0$, then y_m will not be a function of a_j. In terms of equation (7a), the component of x parallel to ξ_j does not contribute to the measurements y_m, and the eigenmode is said to be "unobservable". Further, the norm of $C \xi_j$

$$g_j = |\xi_j^* C^* C \xi_j|^{1/2}, \tag{10}$$

which we shall call the observation sensitivity of mode j, is a quantitative measure of the sensitivity of the measurement y_m to eigenmode j. Note the dependence of this expression on the matrix $C^* C$, which is the same term which drives the Lyapunov equation for observability Gramian L_o.

j	λ_j	f_j	g_j
1	$0.00373967 - 0.23752649\,i$	0.266545	102.61
3	$-0.03516728 - 0.96463092\,i$	0.000215	72.85
4	$-0.03518658 - 0.96464251\,i$	0.000005	1.45
5	$-0.05089873 - 0.27720434\,i$	0.026606	347.98
6	$-0.06320150 - 0.93631654\,i$	0.000513	81.39
7	$-0.06325157 - 0.93635178\,i$	0.000021	2.90
8	$-0.09122274 - 0.90798305\,i$	0.000931	83.36
9	$-0.09131286 - 0.90805633\,i$	0.000056	4.32
10	$-0.11923285 - 0.87962729\,i$	0.001587	77.67
11	$-0.11937073 - 0.87975570\,i$	0.000124	5.37
12	$-0.12450198 - 0.34910682\,i$	0.171859	69.50
13	$-0.13822653 - 0.41635102\,i$	0.037660	252.09
14	$-0.14723393 - 0.85124584\,i$	0.002833	63.31
15	$-0.14742560 - 0.85144938\,i$	0.000268	5.59
16	$-0.17522868 - 0.82283504\,i$	0.005581	44.14
⋮	⋮	⋮	⋮
38	$-0.32519719 - 0.63610486\,i$	5.659801	0.78
39	$-0.34373267 - 0.67764346\,i$	4.685315	0.64
⋮	⋮	⋮	⋮
53	$-0.66286552 - 0.67027520\,i$	0.259581	11.58
⋮	⋮	⋮	⋮

TABLE 1. Least stable eigenmodes of A (no control) and the associated control and observation sensitivities. Note that all eigenvalues agree precisely with those reported by Orszag (1971). Calculation used Chebyshev collocation technique with $N = 140$ in quad precision (128 bits per real number). The second eigenmode, which is not shown here, is spurious (see text). Note that the only unstable mode ($j = 1$) for the present system is both sensitive to the control u and easily detected by the measurements y_m.

3.3 Sensitivity of eigenmodes of A to control and observation

The least stable eigenvalues of A and their corresponding control and observation sensitivities f_j and g_j are tabulated in Table 1. Note that the fourth eigenmode is five orders of magnitude less sensitive than the first eigenmode to modifications in the control. In general, those modes in the upper branch of Fig. 1a (large $|\Im(\lambda)|$) are much less sensitive to control than those in the lower branch (small $|\Im(\lambda)|$). Near the intersection of the two branches ($\Re(\lambda) \approx -0.3$), the control sensitivity is maximum, with this sensitivity decreasing slowly to the left of this intersection ($\Re(\lambda) < -0.3$). It can be predicted that the eigenmodes corresponding to the largest f_j may be affected most upon application of some feedback control u.

Note that the flow measurements are two orders of magnitude less sensitive to the fourth eigenmode as they are to the first eigenmode. It can be predicted that the state estimates of the eigenmodes corresponding to the largest g_j will be most

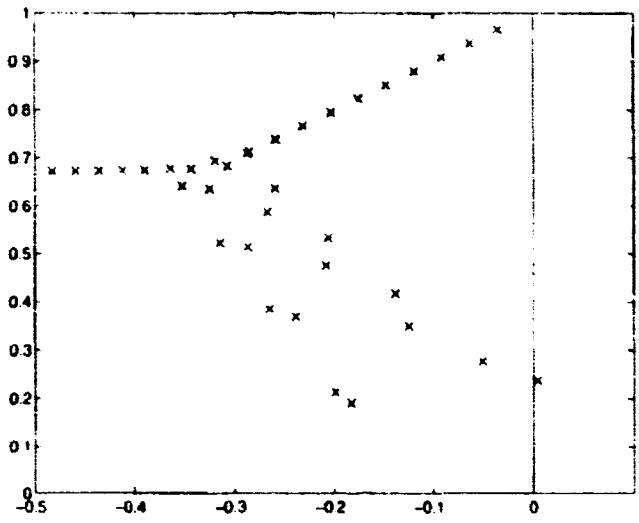

FIGURE 1a. Least stable eigenvalues: $|\Im(\lambda_j)|$ versus $\Re(\lambda_j)$.

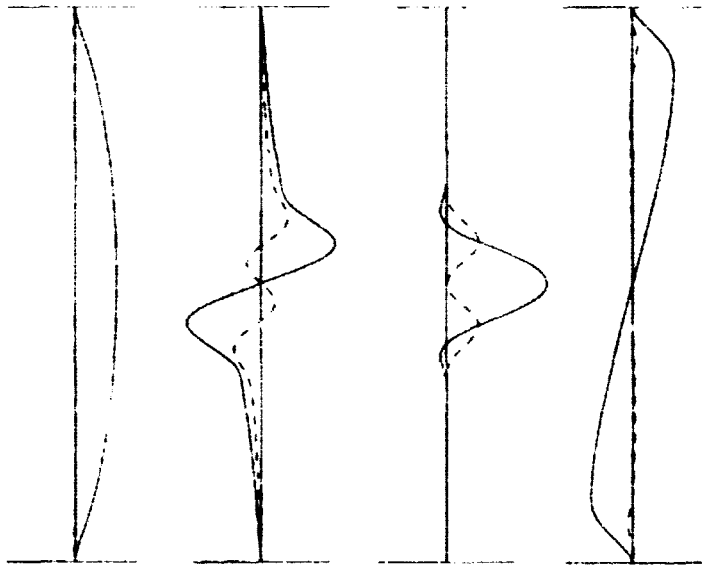

FIGURE 1b. Eigenvectors corresponding to (left to right): $j = 1$ (unstable, lower branch), $j = 3$ (stable, upper branch), $j = 4$ (stable, upper branch), and $j = 5$ (stable, lower branch), plotted as a function of y from the lower wall (bottom) to the upper wall (top). Real component of eigenvector is shown solid and imaginary component dashed. Corresponding eigenvalues are reported in Table 1.

accurate when estimating the state based on noisy measurements.

An important observation from Fig. 1b is that eigenvalues in the upper branch of Fig. 1a have corresponding eigenvectors with variations primarily in the center of the channel, and are thus less controllable via wall transpiration and less observable

via wall measurements than eigenvalues in the lower branch. This observation is quantified by reduced values of f_j and g_j for these modes in Table 1.

The second eigenvalue computed, at $\lambda_2 = -0.0235 + 1.520\,i$ is spurious. Spurious eigenmodes may be easily identified two ways: i) the eigenvalue moves significantly when N is modified slightly, though the eigenvalues reported in Table 1 remain converged, and ii) when plotted, spurious modes are dominated by large oscillations from grid point to grid point across the entire domain, though converged eigenmodes are well resolved. Spurious eigenmodes are expected using this approach and may be disregarded.

4. Summary of $\mathcal{H}_2$ and $\mathcal{H}_\infty$ control theories

In §2, the equations governing the stability of a laminar channel flow were derived and cast in the form

$$\dot{x} = Ax + Bu \tag{11a}$$

$$y_m = Cx + Du, \tag{11b}$$

where the constituent matrices A, B, C, and D were summarized and discussed in §3. We now seek a simple method to determine a control u based on the measurements y_m to force the state x towards zero in a manner which rigorously accounts for state disturbances, to be added on the RHS of (11a), and measurement noise, to be added on the RHS of (11b).

The flow of information in this problem is illustrated schematically in the following block diagram.

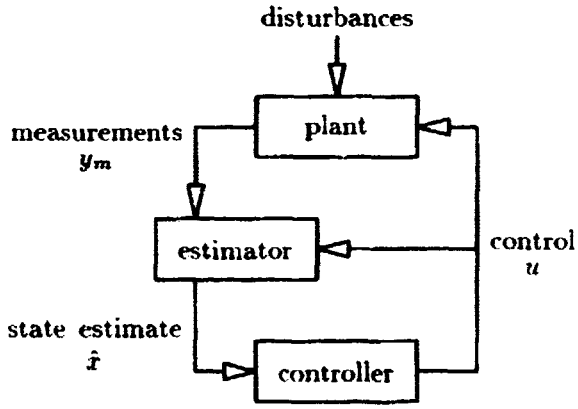

The plant, which is forced by external disturbances, has an internal state x which cannot be observed. Instead, a few noisy measurements y_m are made, and with these measurements an estimate of the state $\hat{x}$ is determined. This state estimate is then fed back to through the controller to determine the control u to apply back on the plant in order to regulate x to zero

To be more precise, we will consider feedback on the measurements y_m such that a state estimate $\hat{x}$ is first determined by the system model

$$\dot{\hat{x}} = A\hat{x} + Bu - \hat{u} \tag{12a}$$

$$\hat{y}_m = C\hat{x} + Du, \tag{12b}$$

$$\hat{u} = \mathcal{L}(y_m - \hat{y}_m), \tag{12c}$$

then this state estimate is used to produce the control

$$u = \mathcal{K}(\hat{x}). \tag{13}$$

Equation (11), with added disturbance terms on the RHS, is referred to as the "plant", (12) is referred to as the "estimator", and (13) is referred to as the "controller". The problem at hand is to compute linear time-invariant (LTI) functions $\mathcal{L}$ and $\mathcal{K}$ such that i) the "output injection" term $\hat{u}$ forces the state estimate $\hat{x}$ in the estimator (12) towards the state x in the plant (11), and ii) the control u computed by the controller (13) forces the state x towards zero in the plant (11).

We will now demonstrate how to apply $\mathcal{H}_2$ and $\mathcal{H}_\infty$ control theories to determine $\mathcal{L}$ and $\mathcal{K}$. (Note that we will redefine several variables used in §2 to derive the Orr-Sommerfeld equation. Considered in the context of this chapter, this should present no confusion.) With this presentation, one set of control equations, involving the solution of two Riccati equations, describes a family of $\mathcal{H}_2$ and $\mathcal{H}_\infty$ control algorithms. The reader is referred to Doyle *et al.* (1989), Dailey *et al.* (1990), and Zhou, Doyle, & Glover (1996) for derivation and further discussion of the control theories summarized here.

4.1 $\mathcal{H}_2$ control theory

4.1.1 Optimal control (LQR)

The first step in considering the system (11) is to consider the problem with no disturbances and measurements which identically determine full information about the state, so that $\hat{x} = x$ (*i.e.* no estimation of the state is necessary). These assumptions are quite an idealization and can rarely be accomplished in practice, but this exercise is an important step to determine the best possible system performance. It is for this reason that the controller in this limit is referred to as optimal. Under these assumptions about the system, the objective of the optimal controller, of the form in (13), is to regulate (*i.e.* return to zero) some measure of the flow perturbation x from an arbitrary initial condition as quickly as possible without using excessive amounts of control forcing. Mathematically, a cost function for this problem may thus be expressed as

$$\mathcal{J}_{LQR} \equiv \int_0^\infty (\|x\|^2 + \ell^2 u^* u)\, dt. \tag{14}$$

The term involving $\|x\|^2$ is a measure of the state disturbance x integrated over the time period over which the initial perturbation decays, which is taken as $t \in [0, \infty)$. The term involving u^*u is an expression of the magnitude of the control. These two terms are weighted together with a scalar ℓ^2, which represents the price of the control. This quantity is small if the control is "cheap" (which generally results in

larger control magnitudes), and large if applying the control is "expensive". As the state equation is linear, the cost quadratic, and the control objective regulation, this controller is also referred to as a linear quadratic regulator (LQR).

The mathematical statement of the present control problem, then, is the minimization of $\mathcal{J}_{LQR}$. This results in regulation of x without excessive use of control effort. Note that minimization of $\mathcal{J}_{LQR}$ is equivalent to minimization of the integral of $z^* z$, where

$$z \equiv \begin{pmatrix} Q^{1/2} x/\ell \\ u \end{pmatrix}.$$

and where Q is a diagonal matrix with diagonal entries $Q_{jj} = \pi/N$, as required by the appropriate definition of the inner product (Canuto *et al.* 1988). In order to arrive at a form which is easily generalized in later sections, define

$$B_2 \equiv B \qquad C_1 \equiv \begin{pmatrix} Q^{1/2}/\ell \\ 0 \end{pmatrix} \qquad D_{12} \equiv \begin{pmatrix} 0 \\ I \end{pmatrix}.$$

For notational convenience, the state equation (11a) will be considered as "forced" with a right hand side forcing term r which shall be set to zero, as this regulation problem simply drives the state towards zero without external command input. The state equation (11a), the performance measure z, and the state estimate $\hat{x}$ then may be written

$$\dot{x} = Ax + r + B_2 u \tag{15a}$$

$$z = C_1 x \quad + D_{12} u \tag{15b}$$

$$\hat{x} = x. \tag{15c}$$

The optimal controller $\mathcal{K}_{LQR}$ is sought to relate the (precise) state estimate $\hat{x}$ to the control u, which is applied to control the evolution of the state x such that the cost $\mathcal{J}_{LQR}(z)$ is minimized. The important matrices of the system described by (15) may be summarized in the shorthand form

$$\mathcal{P}_{LQR} = \begin{array}{c} \\ \dot{x} \\ z \\ \hat{x} \end{array} \begin{array}{c} \begin{array}{ccc} x & r & u \end{array} \\ \left[\begin{array}{c|cc} A & I & B_2 \\ \hline C_1 & 0 & D_{12} \\ I & 0 & 0 \end{array}\right] \end{array}.$$

The flow of information is represented by the block diagram

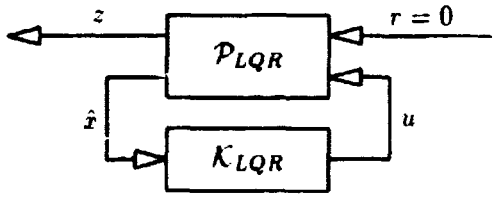

where $\mathcal{P}_{LQR}$ is the flow system given by (15) and $\mathcal{K}_{LQR}$ is the optimal controller, which is still to be determined. The system output z may be used to monitor the

performance of the system. Note that the command input is $r = 0$ and there are no disturbance inputs; the task of the control u is simply to regulate the state x from nonzero initial conditions back to zero. The state $x = \hat{x}$ is fed back through the controller $\mathcal{K}_{LQR}$ to control the system.

Given this general setup, a Hamiltonian is defined such that

$$H_2 \equiv \begin{pmatrix} A & -B_2 B_2^* \\ -C_1^* C_1 & -A^* \end{pmatrix}. \tag{16a}$$

As shown in Doyle *et al.* (1989), the Hermetian positive-definite solution X_2 to the algebraic Riccati equation defined by this Hamiltonian

$$A^* X_2 + X_2 A - X_2 (B_2 B_2^*) X_2 + (C_1^* C_1) = 0, \tag{16b}$$

denoted $X_2 = \mathrm{Ric}(H_2)$, then yields the optimal LTI state feedback matrix

$$K_2 = -B_2^* X_2. \tag{16c}$$

The optimal LTI controller $\mathcal{K}_{LQR}$ is then given simply by

$$u = K_2 \hat{x}. \tag{17}$$

This controller minimizes $\int_0^\infty z^* z \, dt$ in a system with no disturbances and arbitrary initial conditions. Note that standard numerical techniques to solve equations of the form (16b) are well developed (Laub 1991).

4.1.2 Kalman-Bucy filter (KBF)

When there are disturbances to the system, and thus the state is not precisely known, the state (or some portion thereof) must first be estimated, then the control determined based on this state estimate. The Kalman-Bucy filter, of the form (12), accomplishes the required state estimation by assuming that the state disturbances and the measurement noise are uncorrelated white Gaussian processes. To accomplish this, we introduce two zero-mean white Gaussian processes w_1 and w_2 with covariance matrices $E[w_1^* w_1] = I$, $E[w_2^* w_2] = I$, where $E[\cdot]$ denotes the expectation value. With these new disturbance signals, and with G_1 defined as the square root of the covariance of the disturbances to the state equation and G_2 defined as the square root of the covariance of measurement noise, the system (11) takes the form

$$\dot{x} = Ax + G_1 w_1 + Bu \tag{18a}$$

$$y_m = Cx + G_2 w_2 + Du. \tag{18b}$$

The objective of the Kalman-Bucy filter is to estimate the state x as accurately as possible based solely on the measurements y_m. Put another way, the Kalman-Bucy filter attempts to regulate the norm of the state estimation error x_E to zero, where

$$x_E \equiv x - \hat{x}$$

and where the state estimate $\hat{x}$ shall be determined by a filter of the form (12). Mathematically, a cost function for this problem may thus be expressed as

$$\mathcal{J}_{KBF} \equiv E[\|z_E\|^2],$$

where $z_E \equiv x_E$ for notational convenience. (As Gaussian disturbances w_1 and w_2 continually drive this system, an integral on $t \in [0, \infty)$, as used to define $\mathcal{J}_{LQR}$, is not convergent for this problem, and the expectation value is the relevant measure.)

The mathematical statement of the present control problem, then, is the minimization of $\mathcal{J}_{KBF}$. This results in a "best possible" estimate of the state x. In order to arrive at a form which is easily generalized in later sections, assume G_2 is nonsingular and define

$$B_1 \equiv (G_1 \quad 0) \qquad C_2 \equiv G_2^{-1}C \qquad D_{21} \equiv (0 \quad I)$$

and the vector of disturbances

$$w \equiv \begin{pmatrix} w_1 \\ w_2 \end{pmatrix}.$$

Also, define new "observation" vectors y and $\hat{y}$ by a simple change of variables such that

$$y \equiv G_2^{-1}(y_m - Du) \qquad \hat{y} \equiv G_2^{-1}(\hat{y}_m - Du).$$

Note that this change of variables does not represent any real limitation, for whenever any flow measurement y_m is made in a physical implementation, the control u at that moment is also known, so the observation y is easily determined from the flow measurement y_m. With this change of variables, (18b) and (12b) may be expressed as

$$y = C_2 x + D_{21} w \tag{19a}$$

$$\hat{y} = C_2 \hat{x}. \tag{19b}$$

As we are developing the equations for an estimator, it is appropriate now to examine the equations for the state estimation error x_E and the ouput estimation error $y_E \equiv y - \hat{y}$. Subtracting (12a) from (18a) and (19b) from (19a) yields the system

$$\dot{x}_E = Ax_E + B_1 w + \hat{u} \tag{20a}$$

$$z_E = x_E \tag{20b}$$

$$y_E = C_2 x_E + D_{21} w. \tag{20c}$$

The Kalman-Bucy filter $\mathcal{L}_{KBF}$ is sought to relate the output estimation error y_E to the output injection term $\hat{u}$, which is used to control the evolution of the state estimation error x_E such that the cost $\mathcal{J}_{KBF}(z_E)$ is minimized in the presence of Gaussian disturbances w. The important matrices of the system described by (20) may be summarized in the shorthand form

$$\mathcal{P}_{KBF} = \begin{array}{c} \\ \dot{x}_E \\ z_E \\ y_E \end{array} \begin{array}{c} \begin{array}{ccc} x_E & w & \hat{u} \end{array} \\ \left[\begin{array}{c|cc} A & B_1 & I \\ \hline I & 0 & 0 \\ C_2 & D_{21} & 0 \end{array}\right] \end{array}$$

The flow of information is represented by the block diagram

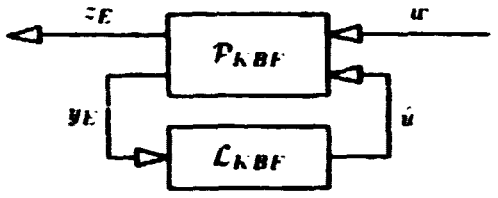

where $\mathcal{P}_{KBF}$ is the flow system given by (18) and $\mathcal{L}_{KBF}$ is the Kalman-Bucy filter, which is still to be determined. The system output z_E may be used to monitor the performance of the system. This system accounts for Gaussian disturbances w and noisy observations y_E of the system, which are fed back through the filter $\mathcal{L}_{KBF}$ to produce the state estimate. Note the striking similarity of the structure of $\mathcal{P}_{KBF}$ to the structure of the conjugate transpose of $\mathcal{P}_{LQR}$. For this reason, these two problems are referred to as "duals", and their solutions are closely related.

Given this general setup, another Hamiltonian is defined such that

$$J_2 \equiv \begin{pmatrix} A^* & -C_2^* C_2 \\ -B_1 B_1^* & -A \end{pmatrix}. \tag{21a}$$

As shown in Doyle *et al.* (1989), the Hermetian positive-definite solution Y_2 to the algebraic Riccati equation defined by this Hamiltonian

$$A Y_2 + Y_2 A^* - Y_2 (C_2^* C_2) Y_2 + (B_1 B_1^*) = 0. \tag{21b}$$

denoted $Y_2 = \mathrm{Ric}(J_2)$, then yields the LTI estimator feedback matrix

$$L_2 = -Y_2 C_2^*. \tag{21c}$$

The LTI Kalman-Bucy filter $\mathcal{L}_{KBF}$ is then simply given by

$$\hat{u} = L_2 y_E,$$

and thus the complete state estimator is given by

$$\dot{\hat{x}} = A\hat{x} + B_2 u - L_2 (y - C_2 \hat{x}) \tag{22}$$

This estimator minimizes $E[\|x - \hat{x}\|^2]$ in a system with Gaussian disturbances in the state equation and Gaussian noise in the measurements.

4.1.3 $\mathcal{H}_2$ control (LQG = LQR + KBF)

A controller/estimator of the form (12)—(13) for the complete system described by (18) with Gaussian disturbances may now be constructed. The objective of the control is to minimize

$$\mathcal{J}_2 \equiv E[\,\|z\|^2 + \ell^2 u^* u\,],$$

where $\|\cdot\|$ denotes the standard Euclidian norm, also known as a "2-norm". Note that minimization of $\mathcal{J}_2$ is equivalent to minimization of the expectation value of $z^* z$, where

$$z \equiv \begin{pmatrix} Q^{1/2} x/\ell \\ u \end{pmatrix},$$

and Q is a diagonal matrix with diagonal entries $Q_{jj} = \pi/N$ as required by the appropriate definition of the inner product. As the control objective is the minimization of the expectation value of the square of a 2-norm, this type of controller/estimator is referred to as $\mathcal{H}_2$. As the state equation is linear, the cost quadratic, and the disturbances Gaussian, this type of controller/estimator is also referred to as linear quadratic Gaussian (LQG).

Combining the notation developed in the previous two sections

$$B_1 \equiv (G_1 \quad 0) \qquad C_1 \equiv \begin{pmatrix} Q^{1/2}/\ell \\ 0 \end{pmatrix} \qquad D_{12} \equiv \begin{pmatrix} 0 \\ I \end{pmatrix}$$
$$B_2 \equiv B \qquad C_2 \equiv G_2^{-1} C \qquad D_{21} \equiv (0 \quad I),$$

with the vector of disturbances w and the observation vectors y and $\hat{y}$ defined such that

$$w \equiv \begin{pmatrix} w_1 \\ w_2 \end{pmatrix} \qquad y \equiv G_2^{-1}(y_m - D u)$$
$$\hat{y} \equiv G_2^{-1}(\hat{y}_m - D u),$$

the system (18) and the control objective for the minimization of $\mathcal{J}_2$ take the form

$$\dot{x} = A x + B_1 w + B_2 u \tag{23a}$$
$$z = C_1 x + D_{12} u. \tag{23b}$$
$$y = C_2 x + D_{21} w. \tag{23c}$$

An $\mathcal{H}_2$ controller/estimator is sought to relate the observations y to the control u, which is applied to control the evolution of the state x such that the cost $\mathcal{J}_2(z)$ is minimized in the presence of Gaussian disturbances w.

The remarkable result from control theory (Lewis 1995) is that the $\mathcal{H}_2$ controller/estimator of the form (12)—(13) which minimizes $\mathcal{J}_2$ for this system is formed by simple combination of the optimal controller and the Kalman-Bucy filter such that

$$u = K_2 \hat{x} \tag{24a}$$
$$\dot{\hat{x}} = A \hat{x} + B_2 u - L_2 (y - C_2 \hat{x}) \tag{24b}$$

where K_2 is given by (16)

$$K_2 = -B_2^* X_2 \qquad X_2 = \mathrm{Ric}\begin{pmatrix} A & -B_2 B_2^* \\ -C_1^* C_1 & -A^* \end{pmatrix} \tag{24c}$$

and L_2 is given by (21)

$$L_2 = -Y_2 C_2^* \qquad Y_2 = \mathrm{Ric}\begin{pmatrix} A^* & -C_2^* C_2 \\ -B_1 B_1^* & -A \end{pmatrix}. \tag{24d}$$

Note the separation structure of this solution. The computation of K_2 does not depend upon the influence of the disturbances, which are accounted for in B_1 and C_2. The computation of L_2 does not depend upon the weightings in the cost function, which are accounted for in C_1, or the manner in which the control u affects the state, which is accounted for in B_2. In other words, the problem of control and the problem of state estimation are entirely decoupled.

4.2 $\mathcal{H}_\infty$ control

The $\mathcal{H}_\infty$ controller/estimator described in this section is very similar to the $\mathcal{H}_2$ controller/estimator described previously. Consideration is now given to disturbances, which we shall distinguish with a new variable $\backslash$, of the "worst" possible structure (as made precise below), rather than the Gaussian structure assumed in the $\mathcal{H}_2$ case. Considered in the frequency domain, the controller/estimators developed in this section provide a system behavior in which the maximum singular value of the closed-loop transfer function, also known as the "∞-norm", is less than some constant, which shall be referred to as γ. As this approach may be interpreted as bounding the ∞-norm of the transfer function from the disturbances to the performance measure, it is referred to as $\mathcal{H}_\infty$ control. For further details of the frequency-domain explanation of $\mathcal{H}_\infty$, the reader is referred to Doyle *et al.* (1989) and Zhou, Doyle, & Glover (1996).

The governing equations to be considered in this section are identical to (23):

$$\dot{x} = A x + B_1 \backslash + B_2 u \tag{25a}$$

$$z = C_1 x + D_{12} u. \tag{25b}$$

$$y = C_2 x + D_{21} \backslash. \tag{25c}$$

An $\mathcal{H}_\infty$ controller/estimator is sought to relate the observations y to the control u, which is applied to control the evolution of the state x such that the cost $\mathcal{J}_\infty(z)$ is minimized in the presence of some "worst case" disturbance $\backslash$. As before, the G_1 and G_2 matrices used to define this system describe any covariance structure of the disturbances known or expected *a priori* (for instance, if one measurement is known to be noisier than another). These matrices are taken as identity matrices if no such structure is known in advance.

Effectively, the cost function considered for $\mathcal{H}_\infty$ control is

$$\mathcal{J}_\infty \equiv E[x^* Q x + \ell^2 u^* u - \gamma^2 \backslash^* \backslash]. \tag{26}$$

A u is sought, through a controller/estimator of the form (12)–(13), to *minimize* J_∞, while *simultaneously* an external disturbance λ is sought to *maximize* J_∞. (In this manner, λ is the "worst possible" disturbance, as it is exactly that disturbance which increases the relevant cost function the most.) Thus, the $\mathcal{H}_\infty$ problem is a "min-max" problem. The term involving $-\gamma^2$ limits the magnitude of the unstructured disturbance in the maximization of J_∞ with respect to λ in a manner analogous to the term involving ℓ^2, which limits the magnitude of the control in the minimization of J_∞ with respect to u.

The result (Doyle *et al.* 1989) is that an $\mathcal{H}_\infty$ controller/estimator of the form (12)–(13) which minimizes J_∞ in the presence of some component of the worst case unstructured disturbance λ for this system is given by

$$u = K_\infty \hat{x} \tag{27a}$$

$$\dot{\hat{x}} = A\hat{x} + B_2 u - L_\infty (y - C_2 \hat{x}) \tag{27b}$$

where K_∞ is given by

$$K_\infty = -B_2^* X_\infty \qquad X_\infty = \mathrm{Ric}\begin{pmatrix} A & \gamma^{-2} B_1 B_1^* - B_2 B_2^* \\ -C_1^* C_1 & -A^* \end{pmatrix} \tag{27c}$$

and L_∞ is given by

$$L_\infty = -Y_\infty C_2^* \qquad Y_\infty = \mathrm{Ric}\begin{pmatrix} A^* & \gamma^{-2} C_1^* C_1 - C_2^* C_2 \\ -B_1 B_1^* & -A \end{pmatrix}. \tag{27d}$$

Note first that, in the $\gamma \to \infty$ limit, the $\mathcal{H}_2$ controller/estimator is recovered, so the set of two Riccati equations in (27) describes both the $\mathcal{H}_2$ (optimal control + Kalman-Bucy filter) and the $\mathcal{H}_\infty$ problems.

It may also be shown that, as the upper-right blocks of the Hamiltonians may not be negative definite, a solution to these Riccati problems exists only for sufficiently large γ; the smallest $\gamma = \gamma_0$ for which a solution to these equations exists may be found by trial and error (Doyle *et al.* 1989). An $\mathcal{H}_\infty$ controller/estimator for $\gamma > \gamma_0$ is referred to as suboptimal.

4.3 Comparison of $\mathcal{H}_2$ and $\mathcal{H}_\infty$ control equations

Most of the robustness problems associated with $\mathcal{H}_2$ stem from the state estimation. Optimal (LQR) controllers themselves, provided with full state information, generally have excellent performance and robustness properties (Dailey *et al.* 1990). Recall from §4.1.3 that the problems of control and state estimation in the $\mathcal{H}_2$ formulation are decoupled.

An important observation of §4.2 is that the problems of control and state estimation in the $\mathcal{H}_\infty$ formulation are coupled. Specifically, the computation of K_∞ depends on the expected covariance of the state disturbances, which are accounted for in B_1, and the computation of L_∞ depends on the weightings in the cost function, which are accounted for in C_1. This is one of the essential features of $\mathcal{H}_\infty$ control.

By taking into account the expected covariance of the state disturbances, reflected in B_1, when determining the state feedback matrix K_∞, the components of $\hat{x}$ corresponding to the components of x that are expected to have the smallest forcing by external disturbances are weighted least in the feedback control relationship $u = K_\infty \hat{x}$.

Similarly, by taking into account the weightings in the cost function, reflected in C_1, when determining the estimator feedback matrix L_∞, the components of $\hat{x}$ corresponding to the components of x that are least important in the computation of J_∞ are forced with the smallest corrections by the output injection term $L_\infty(y - \hat{y})$ in the equation for the estimator.

By applying strong control only on those components of $\hat{x}$ significantly excited by external disturbances, and by applying strong estimator corrections only to those components of $\hat{x}$ important in the computation of the cost function, $\mathcal{H}_\infty$ feedback gains for components of the system not relevant to the control problem are reduced from those in the $\mathcal{H}_2$ case. With such feedback gains reduced, the stability properties of $\mathcal{H}_\infty$ controller/estimators in the presence of state disturbances and measurement noise may be expected to be better than their $\mathcal{H}_2$ counterparts, at the cost of a (hopefully, small) degradation of performance in terms of the 2-norm of the output z for the undisturbed system.

4.4 *Numerical method*

Standard numerical techniques are now applied to all aspects of this problem. In order to simplify both the theory to be presented and the numerical algorithm to be coded, no further manipulation of the equations is used beyond the matrix representations (25) and (27). It was observed that the minimal realization approach (Kailath 1980) is well suited to reduce the computation time necessary to determine effective control algorithms by the present approach; however, such an approach was not found to be necessary in the present case.

The algebraic Riccati equations are solved using the method of Laub (1991), which involves a Schur factorization. This is found to be a stable numerical algorithm for all cases tested. The implementation of Laub's method is written in Fortran-90 and follows closely the algorithm used by the Matlab function `are.m` (Grace *et al.* 1992). A Lyapunov solver, modeled after the Matlab function `lyap.m`, is used to compute the system Gramians.

Two LAPACK routines (Anderson *et al.* 1995), `zgeev.f` and `zgees.f`, are used to compute eigenvalues/eigenvectors and Schur factorizations. These routines are compiled in quad precision (128 bits per real number) to ensure sufficient numerical precision in the eigenvalue computation. All computations are carried out with $N = 140$ to ensure good resolution of all significant eigenmodes. The eigenvalues of A match all those tabulated by Orszag (1971) to all eight decimal places, as shown in Table 1, indicating that this numerical method is sufficiently accurate.

5. Performance of controlled systems (no disturbances)

We now examine the behavior of the "closed-loop" systems obtained by application of the above controllers and estimators to the "nominal" (*i.e.* no disturbances)

channel flow stability problem. In other words, we examine the behavior of the flow and the controller/estimators operating together as a single dynamical system. By looking at "root locus" plots which map the movement of the eigenvalues of these systems in the complex plane with respect to the relevant parameters, this behavior is well quantified. We shall also examine the control and observation sensitivities defined in §3.2 for two special cases in order to better understand the fundamental limitations of controllers and estimators applied to the present system.

5.1 $\mathcal{H}_2$ control

5.1.1 Optimal control (LQR)

In order to investigate the controllability of the closed-loop eigenmodes when all modes are observable, consider the system described in §4.1.1. With $r = 0$ and examining only the equations for $\dot{x}$ and $\dot{x}$, the plant is given (in the shorthand notation used in §4) by

$$\mathcal{P}_{LQR} = \begin{matrix} \dot{x} \\ \dot{x} \end{matrix} \left[\begin{array}{c|c} \begin{matrix} x \end{matrix} & \begin{matrix} u \end{matrix} \\ \hline A & B_2 \\ \hline I & 0 \end{array}\right]$$

with the control now given by

$$u = K_2 x + u',$$

where an additional control term u' has been added to study the sensitivity of the closed-loop system to further modification of the control. Putting the plant and the controller together, the closed-loop system may be represented by

$$\mathcal{P}_{LQR(closed\ loop)} = \begin{matrix} \dot{x} \\ \dot{x} \end{matrix} \left[\begin{array}{c|c} \begin{matrix} x \end{matrix} & \begin{matrix} u' \end{matrix} \\ \hline A + B_2 K_2 & B_2 \\ \hline I & 0 \end{array}\right].$$

The eigenmodes of $A_{K_2} \equiv A + B_2 K_2$ describe the dynamics of the closed loop system for the unmodified control rule ($u' = 0$). Figure 2 shows the movement of these eigenvalues with respect to the free parameter of the control problem, ℓ, used to determine K_2. The eigenvalues for $\ell \to \infty$ are very near those of the uncontrolled system A in Fig. 1, with the previously unstable mode moved just to the left of the imaginary axis. The eigenvalues generally move to the left as ℓ is decreased. Comparing Fig. 2b with Fig. 1b, it is seen that the control modifies most those eigenmodes with significant variations near the wall.

The sensitivity of the eigenmodes of the closed loop LQR system to modification of the control rule may be quantified by performing the analysis of §3.2.1, replacing the eigenmodes of A by the eigenmodes of A_{K_2}. The result of this analysis for small ℓ is shown in Table 2. This table shows that, in the $\ell \to 0$ limit, the system matrix is modified to the point that the eigenmodes are no longer sensitive to further modification of the control. In other words, all the controllable dynamics of the system have been modified by K_2 and are accounted for in the closed loop system in this limit. This is one demonstration that the optimal controller extracts the best possible performance from a given (full-information) system.

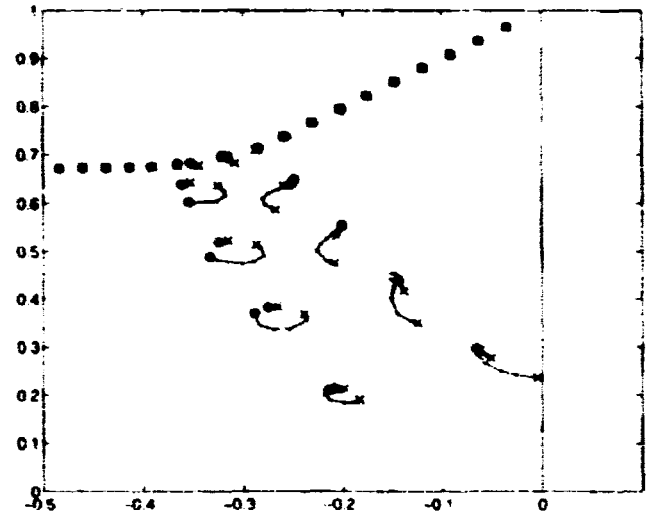

FIGURE 2a. Root locus of least stable eigenvalues of A_{K_2} as a function of the free parameter of the $\mathcal{H}_2$ controller, ℓ. The eigenvalues for $\ell \to \infty$ are marked with an (x).

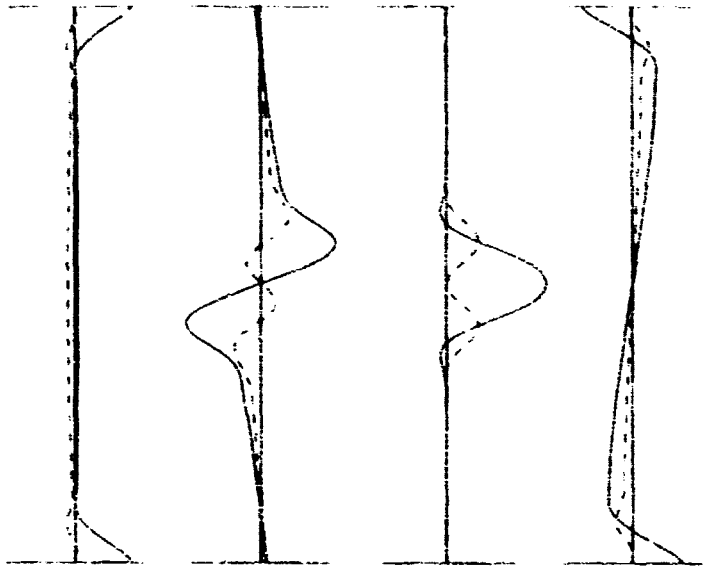

FIGURE 2b. Eigenvectors of A_{K_2}, with $\ell = 10^{-4}$, corresponding to (left to right): $j = 1$, $j = 3$, $j = 4$, and $j = 5$. Real component of eigenvector is shown solid and imaginary component dashed. Corresponding eigenvalues are reported in Table 2.

5.1.2 Kalman-Bucy filter (KBF)

The estimator itself has its own set of dynamics. These dynamics are captured by the equations for the state estimator error, as described in §4.1.2. We now make use of this system in order to investigate the observability of closed-loop eigenmodes

j	λ_j	f_j
3	−0.03513233 − 0.96462128*i*	0.000000029
4	−0.03518652 − 0.96464261*i*	0.000000001
5	**−0.06255259 − 0.29262711*i***	**0.000001101**
6	−0.06310358 − 0.93629329*i*	0.000000070
7	−0.06325089 − 0.93635257*i*	0.000000003
1	**−0.06644730 − 0.29721403*i***	**0.000001116**
8	−0.09102975 − 0.90793951*i*	0.000000129
9	−0.09130964 − 0.90805917*i*	0.000000008
10	−0.11890731 − 0.87955083*i*	0.000000226
11	−0.11936036 − 0.87976246*i*	0.000000020
12	**−0.14335180 − 0.43962023*i***	**0.000002303**
14	−0.14673294 − 0.85111508*i*	0.000000414
15	−0.14739907 − 0.85146161*i*	0.000000045
13	**−0.14803996 − 0.44586838*i***	**0.000003081**
16	−0.17450455 − 0.82261690*i*	0.000000842

TABLE 2. Least stable eigenmodes of the closed-loop system A_{K_2} and their sensitivity to control for the optimal controller in the cheap control limit ($\ell = 10^{-4}$). The numbering of the eigenvalues shown is the same as the numbering of the eigenvalues of Table 1 to which they are connected by the root locus of Fig. 2. Note that the control in this limit drives all eigenmodes to positions at which they are insensitive to further modifications of the control, as illustrated by the large reductions in f_j. Note also that those eigenmodes with the largest values of f_j in Table 1 (specifically, those in the lower branch) have moved the most.

when all modes are controllable. With $w = 0$ and examining only the equations for $\dot{x}_E$ and y_E, this plant is given by

$$\mathcal{P}_{KBF} = \begin{array}{c} \\ \dot{x}_E \\ y_E \end{array} \begin{array}{c} \begin{array}{cc} x_E & \hat{u} \end{array} \\ \left[\begin{array}{c|c} A & I \\ \hline C_2 & 0 \end{array}\right] \end{array}$$

with the output injection now given by

$$\hat{u} = L_2 y_E + \hat{u}',$$

where an additional output injection term $\hat{u}'$ has been added to study the sensitivity of the closed-loop system to further modification of the output injection rule. Putting the plant and the estimator together, the closed-loop system may be represented by

$$\mathcal{P}_{KBF\,(closed\ loop)} = \begin{array}{c} \\ \dot{x}_E \\ y_E \end{array} \begin{array}{c} \begin{array}{cc} x_E & \hat{u}' \end{array} \\ \left[\begin{array}{c|c} A + L_2 C_2 & I \\ \hline C_2 & 0 \end{array}\right] \end{array}.$$

The eigenmodes of $A_{L_2} \equiv A + L_2 C_2$ describe the dynamics of the closed-loop system for the unmodified output injection rule ($\hat{u}' = 0$). Figure 3 shows the movement of

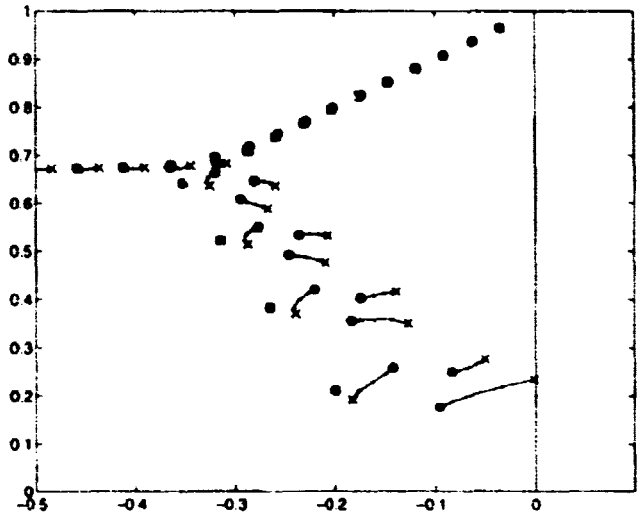

FIGURE 3. Root locus of least stable eigenvalues of A_{L_2} as a function of the free parameters of the $\mathcal{H}_2$ estimator, g_1 and g_2 (note that we take $g_1 = g_2$ for the purpose of drawing the root locus). The eigenvalues for $g_1 = g_2 \to 0$, marked with (x), are very near those of the uncontrolled system A in Fig. 1, with the previously unstable mode moved just to the left of the imaginary axis. The eigenvalues generally move to the left as g_1 and g_2 are increased.

these eigenvalues with respect to the free parameters of the estimator problem. This is done by assuming that the matrices describing the covariance of the disturbances have the simple form $G_1 = g_1 I$ and $G_2 = g_2 I$, where g_1 and g_2 are real scalars.

The sensitivity of measurements y_E to the eigenmodes of the closed loop KBF system may be quantified by performing the analysis of §3.2.2, replacing the eigenmodes of A by the eigenmodes of A_{L_2}. The result of this analysis for large $g_1 = g_2$ is shown in Table 3. This table shows that, in the $g_1 = g_2 \to \infty$ limit, the system matrix is modified to the point that the measurements are no longer sensitive to the eigenmodes of the closed-loop system. In other words, all the measurable dynamics of the system have been extracted by L_2 and are accounted for in the closed loop system in this limit. This is one demonstration that the Kalman-Bucy filter extracts the best possible state estimate from a given (fully-controllable) state estimator.

5.1.3 $\mathcal{H}_2$ control (LQG = LQR + KBF)

It was mentioned in §4.1.3 that the controller/estimator which minimized the relevant cost functional ($\mathcal{J}_2$) in the presence of Gaussian disturbances could be found by considering the controller and estimator problems separately. In this section, it is shown that the closed-loop performance of a system of the form (23) (without disturbances)

$$\dot{x} = A x + B_2 u$$
$$y = C_2 x$$

j	λ_j	g_j
3	−0.03505745 − 0.96474093*i*	0.000000568
4	−0.03518656 − 0.96464253*i*	0.000000004
6	−0.06287931 − 0.93668086*i*	0.000000644
7	−0.06325136 − 0.93635193*i*	0.000000008
5	**−0.08362450 − 0.25066856*i***	**0.000002858**
8	−0.09059621 − 0.90874817*i*	0.000000673
9	−0.09131196 − 0.90805689*i*	0.000000011
1	**−0.09565183 − 0.17658643*i***	**0.000000094**
10	−0.11823779 − 0.88095122*i*	0.000000646
11	−0.11936807 − 0.87975709*i*	0.000000014
12	**−0.14209547 − 0.25910275*i***	**0.000000130**
14	−0.14584717 − 0.85329567*i*	0.000000549
15	−0.14741926 − 0.85145223*i*	0.000000014
16	−0.17347707 − 0.82577419*i*	0.000000399
13	**−0.17418920 − 0.40314656*i***	**0.000002002**

TABLE 3. Least stable eigenmodes of the closed-loop system A_{L_2} and their sensitivity to observation for the Kalman-Bucy filter in the large disturbance limit ($g_1 = g_2 = 10^2$). The numbering of the eigenvalues shown is the same as the numbering of the eigenvalues of Table 1 to which they are connected by the root locus of Fig. 1. Note that the estimator in this limit modifies all eigenmodes until the measurements are no longer sensitive to them, as illustrated by the large reductions in g_j. Note also that those eigenmodes with the largest values of g_j in Table 1 (specifically, those in the lower branch) have moved the most.

combined with an estimator/controller of the form (24)

$$u = K_2 \hat{x}$$
$$\dot{\hat{x}} = A\hat{x} + B_2 u - L_2(y - C_2\hat{x})$$

may also be evaluated by considering the controller and estimator problems separately. To accomplish this, simply combine the above equations into the closed-loop composite system

$$\begin{pmatrix} \dot{x} \\ \dot{\hat{x}} \end{pmatrix} = \begin{pmatrix} A & B_2 K_2 \\ -L_2 C_2 & A + B_2 K_2 + L_2 C_2 \end{pmatrix} \begin{pmatrix} x \\ \hat{x} \end{pmatrix}.$$

Gaussian elimination, first on the rows and then on the columns, reveals that the eigenvalues of this system are the same as the eigenvalues of the system

$$\begin{pmatrix} A + B_2 K_2 & B_2 K_2 \\ 0 & A + L_2 C_2 \end{pmatrix}.$$

In other words, the eigenvalues of the closed-loop composite system for the $\mathcal{H}_2$ problem are simply the union of the eigenvalues of the controlled system $A_{K_2} = A + B_2 K_2$ and the eigenvalues of the estimated system $A_{L_2} = A + L_2 C_2$ discussed in the previous two sections and illustrated in Fig. 4.

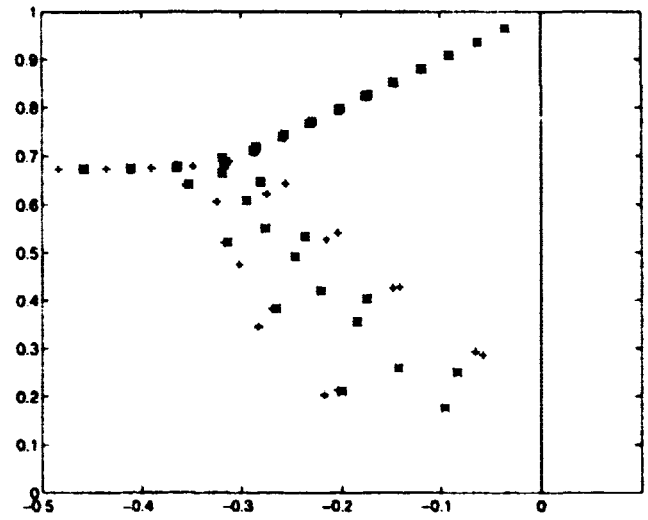

FIGURE 4. Least stable eigenvalues of the composite closed-loop system with the $\mathcal{H}_2$ controller/estimator, taking $\ell = g_1 = g_2 = 1$. Note that the eigenvalues are simply the eigenvalues of the closed loop controller (+) together with those of the closed loop estimator (*).

5.2 $\mathcal{H}_\infty$ control

As with the $\mathcal{H}_2$ controller/estimator, the performance of the closed loop composite system with the $\mathcal{H}_\infty$ controller/estimator

$$\begin{pmatrix} \dot{x} \\ \dot{\hat{x}} \end{pmatrix} = \begin{pmatrix} A & B_2 K_\infty \\ -L_\infty C_2 & A + B_2 K_\infty + L_\infty C_2 \end{pmatrix} \begin{pmatrix} x \\ \hat{x} \end{pmatrix}.$$

may be evaluated by considering the performance of the controlled system $A_{K_\infty} = A + B_2 K_\infty$ and the performance of the estimated system $A_{L_\infty} = A + L_\infty C_2$ separately. The root locus of the eigenvalues of A_{K_∞} are plotted with respect to the parameter γ of the H_∞ problem in Fig. 5, clearly illustrating the tendency of $\mathcal{H}_\infty$ controllers to modify only the least stable components of the system, as opposed to the $\mathcal{H}_2$ controller of Fig. 2, which modifies all controllable modes of the system.

6. Conclusions

Optimal and robust control theories have been successfully applied to the Orr-Sommerfeld equation. Given control on the wall-normal component of boundary velocity only, the flow system is shown to be stabilizable but not controllable. Given measurements of wall skin-friction only, the flow system is shown to be detectable but not observable. It is shown that $\mathcal{H}_2$ controllers/estimators modify all of the controllable/observable modes of the system. In contrast, the $\mathcal{H}_\infty$ controllers modify the corresponding $\mathcal{H}_2$ controllers only in the most unstable component, as $\mathcal{H}_\infty$ targets a bound only on the maximum value of the transfer function.

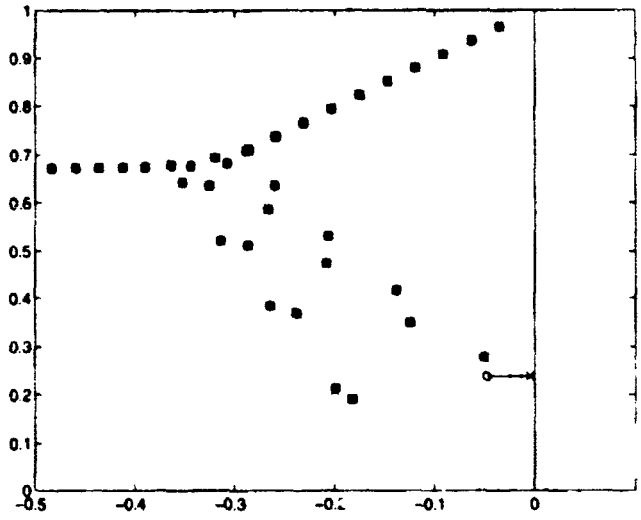

FIGURE 5. Root locus of least stable eigenvalues of the $\mathcal{H}_\infty$ controller versus γ, taking $\ell = 100$, $g_1 = g_2 = 0.001$. The result with $\gamma \to \infty$, marked with the (x), gives the corresponding $\mathcal{H}_2$ controller. Note that the $\mathcal{H}_\infty$ controller modifies only the least stable eigenmode of this $\mathcal{H}_2$ result, without expending any extra control effort to control those eigenmodes not associated with the maximally unstable component of the system. Note also that $\gamma = \gamma_0$, marked with the (o), is reached by reducing γ until the least stable eigenvalue corresponds to one of the uncontrollable eigenmodes in the upper branch, which cannot be moved further left; in the present case, this corresponds to a numerical value of $\gamma_0 = 0.26$.

In the $\ell \to 0$ limit of the $\mathcal{H}_2$ controller, corresponding to cheap control and thus large values of u, all eigenmodes of the closed-loop controlled system are shown to be modified to points at which they are no longer sensitive to further modifications of the control. Similarly, in the $g_1 = g_2 \to \infty$ limit of the $\mathcal{H}_2$ estimator, accounting for large disturbances on both the state and the measurements, all eigenmodes of the closed-loop system for the estimator error are shown to be modified to points at which they are not discernible by flow measurements.

These results indicate that $\mathcal{H}_2$ controllers and estimators are optimal for their desired purposes, but may contain large feedback gains. On the other hand, $\mathcal{H}_\infty$ controllers only target the least stable components of the system, and thus have smaller feedback gains while still achieving the same worst case performance for the nominal plant. Such reduced feedback gains generally result in improved robustness to inaccuracies in the system model.

Acknowledgements

The authors thank Profs. Parviz Moin and Steven Crow for inspiration during the genesis of this project, Prof. Alan Laub for advice on the numerical approach to the Riccati equation, Miss Sharon Liu and Mr. Yogesh Tupe for useful discussions of the control theory, Mr. S. Scott Collis for recommending the weak formulation

for the Neumann b.c., Dr. R. K. Owen for assistance with quad precision, and Dr. Krishnan Mahesh for comments on a draft copy of this manuscript.

REFERENCES

ABERGEL, T. & TEMAM, R. 1990 On some control problems in fluid mechanics. *Theor. and Comp. Fluid Dynamics.* **1**, 303-325.

ANDERSON, E., BAI, Z., BISCHOF, C., DEMMEL, J., DONGARRA, J., DU CROZ, J., GREENBAUM, A., HAMMARLING, S., MCKENNEY, A., OSTROUCHOV, S., AND SORENSEN, D. 1995 *LAPACK Users' Guide.* SIAM.

BUTLER, K. M. & FARRELL, B. F. 1992 Three-dimensional optimal perturbations in viscous shear flows. *Phys. Fluids A.* **4**, 8, 1637-1650.

CANUTO, C., HUSSAINI, M. Y., QUARTERONI, A., & ZANG, T. A. 1988 *Spectral Methods in Fluid Dynamics.* Springer.

DAILEY, R. L., DOYLE, J. C., STEIN, G., BANDA, S. S., & YEH, H. H. 1990 *Lecture Notes for the Workshop on $\mathcal{H}_\infty$ and μ Methods for Robust Control* Presented at 1990 American Control Conference, May 21-22, San Diego.

DOYLE, J. C., GLOVER, K., KHARGONEKAR, P. P., & FRANCIS, B. A. 1989 State-Space Solutions to Standard $\mathcal{H}_2$ and $\mathcal{H}_\infty$ Control Problems. *IEEE Trans. Auto. Control.* **34**, 8, 831-847.

GRACE, A., LAUB, A. J., LITTLE, J. N., & THOMPSON, C. M. 1992 *Control System Toolbox User's Guide.* The MathWorks, Inc.

JOSHI, S. S., SPEYER, J. L., & KIM, J. 1996 A systems theory approach to the feedback stabilization of infinitesimal and finite-amplitude disturbances in plane Poiseuille flow. Accepted for publication in *J. Fluid Mech.*

JOSLIN, R. D., GUNZBURGER, M. D., NICOLAIDES, R. A., ERLEBACHER, G., & HUSSAINI, M.Y. 1995 A self-contained, automated methodology for optimal flow control validated for transition delay *ICASE Report No 95-64*, NASA Langley Research Center, Hampton, VA.

KAILATH, T. 1980 *Linear Systems.* Prentice-Hall.

LAUB, A. J. 1991 Invariant subspace methods for the numerical solution of Riccati equations. In *The Riccati Equation* (ed. Bittaini, Laub, & Willems), 163-196. Springer.

LEWIS, F. L. 1995 *Optimal Control.* Wiley.

ORSZAG, S. A. 1971 Accurate solution of the Orr-Sommerfeld stability equation. *J. Fluid Mech.* **50**, 4, 689-703.

ORSZAG, S. A., & PATERA, A. T. 1983 Secondary instability of wall-bounded shear flows. *J. Fluid Mech.* **128**, 347-385.

ZHOU, K., DOYLE, J. C., & GLOVER, K. 1996 *Robust and Optimal Control.* Prentice-Hall.

NEXT
DOCUMENT

Simulation and modeling of the elliptic streamline flow

By G. A. Blaisdell[1] AND K. Shariff[2]

Direct numerical simulations are performed for the elliptic streamline flow, which is a homogeneous turbulent flow that combines the effects of solid body rotation and strain. Simulations are run over a range of parameters in order to determine the effect of changing rotation and strain separately. For early times the nonlinear cascade is suppressed, but then is re-established at later times. The growth rate of turbulent kinetic energy agrees at early times with the trends from linear theory, but at later times the flow seems to approach an asymptotic state that is independent of the ratio of mean flow rotation rate to strain rate. A comparison with standard Reynolds stress turbulence models is made. It is found that for strong rotation rates, the models predict decay of the turbulence, while the simulations show exponential growth. Close examination of the simulation results shows that they are affected by excessively low Reynolds numbers. Suggestions for reducing low Reynolds number effects in future simulations is given.

1. Introduction

1.1 Motivation

The elliptic streamline flow is an important flow for many reasons. This flow contains the effects of both rotation and strain and is therefore similar to the mean flow in a vortex strained in the plane perpendicular to its axis. Such flows provide insight into fundamental vortical interactions within turbulence, and the instability caused by the strain has been proposed as a universal mechanism for energy transfer from large scales to small scales (Pierrehumbert 1986).

A strained vortex also occurs in airplane wakes, in which each wingtip vortex induces a strain field on the other. The strain field can affect the stability of these vortices and thereby their turbulent structure downstream. The ability to understand and predict the turbulent structure of the vortices is important to the wake hazard problem, which is of major concern for the safety of commercial aircraft.

Another example of a flow with the combined effects of rotation and strain is the outer core of the earth's interior. The electrically conducting fluid in the outer portion of the earth's core rotates with the earth but is also strained by tidal forces. A large scale secondary flow results, which has been proposed as the cause of the

1 Purdue University
2 NASA Ames Research Center

magnetic field (Malkus & Berry 1988). Additional examples are flow in fluid-filled satellites and in rectangular cavities.

The elliptic streamline flow is also a good test case for turbulence models for rotating flows. It has an added complication beyond that of pure rotation, but it is still a basic flow. The additional strain rate is present in most practical engineering flows and, therefore, is a necessary effect for turbulence models to capture. As shown in Section 3, standard Reynolds stress models predict decay of the turbulent kinetic energy for cases with strong rotation, whereas the DNS shows exponential growth. Therefore, the elliptic streamline flow presents a challenging case for turbulence modelers.

1.2 Background

The elliptic streamline flow has been studied using Rapid Distortion Theory (RDT) by Cambon *et al.* (1985) and Cambon *et al.* (1994). Different approaches were used by Pierrehumbert (1986), Bayly (1986), and Waleffe (1990), who performed inviscid stability analyses. For circular streamlines (pure rotation) there are no unstable modes, while for elliptic streamlines a band of unstable modes exists in which the growth rate depends on the polar angle of the wavenumber vector. The band of unstable angles increases in width for increasing ellipticity of the streamlines. Also, the growth rate of the unstable modes is independent of the magnitude of the wavenumber vector. Therefore, arbitrarily small three-dimensional fluctuations can be created by an instability of a basic two-dimensional flow. Pierrehumbert suggested that this might be a mechanism for the cascade process in turbulent flows.

The effects of viscosity were studied by Landman & Saffman (1987) and are included in the RDT analyses of Cambon *et al.* The growth rate of the instabilities is modified by viscosity so that the growth rate is no longer independent of the magnitude of the wavenumber vector. Landman & Saffman found a high wavenumber cut-off of the instability. However, there is no low wavenumber cut-off, and arbitrarily large scales are unstable. This fact causes the turbulent eddies to eventually outgrow the computational domain in the DNS discussed below.

An interesting experiment corresponding to elliptic streamline flow was done by Malkus (1989). A tank with moving flexible walls was used to create a flow with elliptic streamlines. He observed a collapse phenomenon in which the two-dimensional flow suddenly breaks down into three-dimensional small scale motions. Waleffe (1990) studied the stability of the enclosed elliptic flow and suggested the collapse phenomenon is due to nonlinear interactions in which the mean flow is altered. It is not clear at this point how this confined flow is related to the homogeneous turbulent flow studied here.

Lundgren & Mansour (1996) investigated the stability of a vortex in a rectangular domain. This flow is very similar to the elliptic streamline flow and displays a similar instability. However, their flow has a mean velocity which decays in time, and their flow is inhomogeneous. These two factors introduce additional complicating effects and make gathering turbulence statistics difficult because of the low statistical sample that is available. The elliptic streamline flow and its instability is also related to the instability of a strained, finite-sized vortex with uniform vorticity

studied by Widnall *et al.* (1974) and others.

An experiment which was designed to correspond to the homogeneous elliptic streamline flow was performed by Benoit (1992). He investigated grid generated turbulence created by a rotating grid and then passed through a specially designed diffuser with elliptic cross-sections. Benoit also analyzed the flow using linear rapid distortion theory. In order to compare with his results, simulations at Reynolds numbers higher than those in the current study are needed. This point is discussed futher below.

There has been a considerable amount of work done on the stability of the elliptic streamline flow. However, the only numerical simulations that have been done are the preliminary simulations of Blaisdell & Shariff (1994). The current simulations are a continuation of that work. With the use of direct numerical simulation, the nonlinear development of the flow and the fully turbulent state can be examined.

1.3 Objectives

The objectives of this work are to investigate the elliptic streamline flow for the fully turbulent case and to provide statistics for comparison with turbulence models. One of the issues to be investigated is whether the linear instability modes grow to dominate the flow even in the presence of large initial disturbances. The effect of the governing parameters on the development of the flow is also to be studied. For the elliptic streamline flow the governing parameters are: (1) the ratio of the rotation rate to the strain rate, which gives the aspect ratio of the elliptic streamlines, (2) the ratio of a mean flow time scale, such as the rotation rate, to the turbulence time scale, and (3) the turbulent Reynolds number. Simulations are chosen to vary these parameters in a systematic way. However, it is found that the Reynolds numbers of these simulations is low enough that the development of the flow is significantly affected. Suggestions for overcoming this limitation in future simulations are discussed in Section 4.

Turbulence statistics, including full Reynolds stress budgets, have been calculated for each of the simulations. One objective was to do a detailed comparison with turbulence models. However, because of the low Reynolds numbers of the current simulations, a meaningful quantitative comparison cannot be done. Nonetheless a brief comparison of the turbulent kinetic energy growth is presented in Section 3.

2. Governing equations & numerical method

Consider homogeneous turbulence with the mean flow

$$U_i = U_{i,j} x_j, \quad U_{i,j} \equiv \begin{pmatrix} 0 & 0 & -\gamma - \epsilon \\ 0 & 0 & 0 \\ \gamma - \epsilon & 0 & 0 \end{pmatrix}. \tag{1}$$

which describes a one-parameter family of streamline patterns in the x-z plane (the other parameter sets the strength of the flow). The case $\gamma = 0$ corresponds to pure strain with two principal directions at $\pm 45°$ relative to the x axis while $0 < |\gamma| < |\epsilon|$ gives vortical strain dominated flows with hyperbolic streamlines, their asymptotes

being shallower or steeper than the pure strain case according as $(\epsilon-\gamma)/(\epsilon+\gamma) < 1$ or > 1. The limit $|\epsilon| = |\gamma|$ is pure shear. The case $\epsilon = 0$ corresponds to pure rotation while $0 < |\epsilon| < |\gamma|$ gives vortical rotation dominated flows with geometrically similar elliptic streamlines with aspect ratio $E \equiv \sqrt{(\gamma+\epsilon)/(\gamma-\epsilon)}$. This case is depicted in Fig. 1.

The code shear3, developed by Dr. R. S. Rogallo (of Los Altos Hills, Calif.) to run on the Intel parallel computers at NASA Ames for the case of pure shear and employing a subset of the techniques described in Rogallo (1981), was modified to treat the above cases and to run on the IBM SP2 using MPI for message passing. The xz plane was chosen as the plane of deformation to minimize disruption to the code. The program uses the second-order Runge-Kutta scheme to time-advance the Fourier transformed Navier-Stokes equation (notation will be explained momentarily):

$$\frac{d}{dt}(F\hat{u}_i) = F\left\{\Pi^{(2)}_{ij}U_{j,m}\hat{u}_m - i\Pi^{(1)}_{ij}k_m\widehat{u_j u_m}\right\} \tag{2}$$

Due to the use of coordinates that deform with the mean flow, the k_i in Eq. (2) represent time-dependent physical wavenumbers:

$$k_i = k'_j B_{ji}(t), \quad \dot{B}_{ij} = -B_{ik}U_{k,j}, \tag{3}$$

while hats denote the three-dimensional Fourier transform with respect to computational wavenumbers k'_i. Space discretization is implied by the restriction of k'_i to integers $-M/2 \le k'_i \le M/2$; homogeneity is realized when there is a sufficiently large range of small wavenumbers with energy tending to zero. The symbol $\Pi^{(n)}_{ij} \equiv \delta_{ij} - nk_ik_j/k^2$ with $n = 1$ is the projector applied to the Navier-Stokes equation to eliminate pressure; a slightly different projector, $\Pi^{(2)}_{ij}$, appears in the linear term due to an additional contribution from the time derivative term in deforming coordinates. The aliasing error concomitant with the pseudo-spectral evaluation of $\widehat{u_j u_m}$ is controlled (but not exactly eliminated) by a combination of phase shifting and spherical truncation in which modes with $k'^2 > 2(M/3)^2$ are discarded upon return to wavenumber space. The viscous integrating factor F, satisfying $(1/F)dF/dt = +\nu k^2(t)$, is obtained analytically. Since in the linearized limit exact time integration of (2) is not possible (or at least not trivial, Waleffe 1990), the present version of the program does not treat the rapid distortion limit exactly. Rather, the time step is chosen to be the more restrictive one obtained from the mean flow and the non-linear term. For pure shear the flow-field can be re-meshed to prevent extreme distortion of the computational domain. In the elliptic flow, however, a fluid element undergoes time-periodic shearing and straining, and rather than tackle the corresponding re-meshing problem, small enough ellipticities are considered so that the minimum interior angle of the element, $\theta_{min} = \tan^{-1}\left[2E/(E^2-1)\right]$, does not become too small (for the largest case of $E = 3$ considered, $\theta_{min} = 37°$).

In Blaisdell & Shariff (1994) the code was tested for: (i) The linear inviscid and viscous behavior of a single Fourier mode compared with the results of Landman &

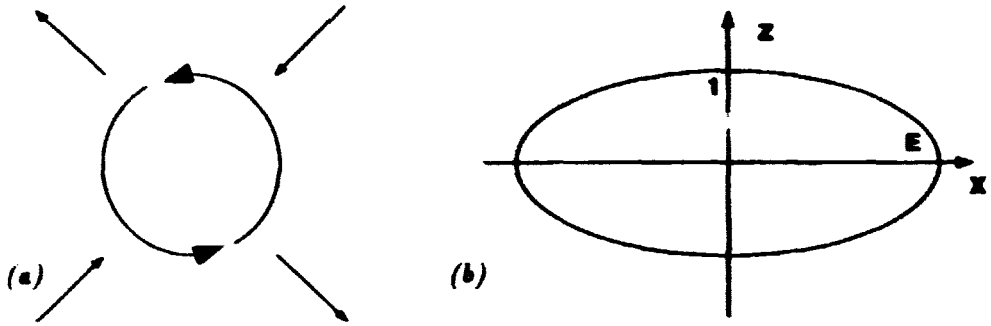

FIGURE 1. *(a)* Schematic view of combination of rotation and strain. *(b)* Elliptic streamline. (The direction of the arrows corresponds to $\gamma > 0$ and $\epsilon > 0$.)

Saffman (1987) (ii) Pure rotation (Mansour *et al.* 1991, $Ro = 0.247$, their Fig. 2(a)) (iii) Pure shear (Rogers *et al.* 1986, Case C128U).

3. Simulations and results

3.1 Initial conditions

The initial conditions for the simulations were obtained in the same way as those of Mansour *et al.* (1991). An initial energy spectrum was specified of the form

$$E(\kappa) = \kappa^4 \exp(-2(\kappa/\kappa_p)^2) \quad , \tag{4}$$

where κ_p is the location of the peak in the spectrum. For the runs described here κ_p was chosen to be either 24 or 48 depending on whether the number of grid points was nominally 128^3 or 256^3 respectively. The larger number of grid points and the larger κ_p means that those simulations have a larger computational domain size relative to the integral scales of the turbulence. The flow field was then evolved as decaying isotropic turbulence until it became fully developed as measured by the velocity derivative skewness obtaining a steady value near -0.5 and the turbulent kinetic energy displaying algebraic decay with a nearly constant decay rate. In practice it was found that by starting the simulations with a turbulent Reynolds number (see definition below) $Re_T = 823$ and allowing them to decay to $Re_T = 51$, the above conditions were met. This developed flow field was then used as initial conditions for the elliptic flow runs.

The simulations of Blaisdell & Shariff (1994) and those presented here do not match the Reynolds number of Mansour *et al.* We attempted to do so, but were confronted with the difficulty that, with the elliptic streamline flow, the large scales gain energy and quickly outgrow the computational domain. This problem does not occur for the pure rotation case where the turbulence simply decays. As a result, we found it necessary to change our initial conditions to make the computational domain larger relative to the initial integral scales of the turbulence. Because of the corresponding loss of resolution in the small scales, we reduced the Reynolds number.

The turbulent Reynolds number grows exponentially in the elliptic streamline flow and reaches values well over 1,000 in the current DNS. However, because this is not an equilibrium flow, the turbulent Reynolds number is not a good indicator of the ratio of length scales in the problem or the degree of nonlinearity. As is shown below, it is found that the current DNS are affected by the low Reynolds numbers of the simulations. This means that the DNS data cannot be used in a quantitative way to test high Reynolds number turbulence models. However, a qualitative comparison is made below with two standard Reynolds stress models, which shows the models fail to predict the correct behavior, especially at larger rotation rates. In Section 4, suggestions are made for changing the method of generating the initial conditions so that the initial turbulent Reynolds number will not be so low. Higher Reynolds number simulations will allow quantitative comparison with Reynolds stress models and will provide more useful information.

3.2 Parameter space & linear theory

The governing nondimensional parameters for the elliptic streamline flow are (1) the aspect ratio of the elliptic streamlines, E, which is related to the ratio of the mean strain rate to the mean rotation rate, (2) the ratio of the turbulent time scale to a mean flow time scale, which can be measured either in terms of the mean flow strain as $S_\epsilon^* = \epsilon k/\varepsilon$ or in terms of the mean flow rotation as $S_\gamma^* = \gamma k/\varepsilon$, where k is the turbulent kinetic energy and ε is its dissipation rate, and (3) the turbulent Reynolds number, $Re_T = q^4/(\varepsilon\nu) = 4k^2/(\varepsilon\nu)$. The parameters used in the current simulations are shown in Table 1. Simulations e1-e5 are elliptic streamline flows with aspect ratios varying from 1.1 to 3.0. Simulations s1 and s1a are shear flow simulations and, therefore, have a value $E = \infty$. Most of the simulations are done with the same initial nondimensional strain rate. This was done in order to examine the effect of varying the mean flow rotation rate. This can be seen in Fig. 2 which shows the parameter space in terms of S_ϵ^* and S_γ^*. The radial lines indicate a given aspect ratio, going from the 45° line for shear flow ($E = \infty$) to elliptic flows with $E = 3.0$, 2.0, 1.5, 1.25, and 1.1. Simulation e1 with $E = 1.1$ is off the scale of the plot. The circles give the initial values for each simulation and a given simulation is constrained to lie along one of the radial lines with a fixed aspect ratio, E. The values of S_ϵ^* and S_γ^* will change as the turbulence develops, and it is believed that asymptotic values of these quantities should be approached. Simulation e2a has the same aspect ratio as e2, but the value of nondimensional strain rate is changed so that the nondimensional rotation rate is the same as that of the corresponding shear flow simulation, s1. The two shear flow simulations, s1 and s1a, differ in the initial Reynolds number.

It is helpful in interpreting the results of the current simulations to examine the predictions of linear stability theory within the parameter space shown in Fig. 2. A linear stability code employing the method of Landman & Saffman (1987) was used to compute the maximum inviscid growth rate as a function of strain rate, ϵ, and rotation rate, γ. Fig. 3(a) shows a contour plot of the inviscid growth rate, σ. The nondimensional growth rate, σ/γ can be collapsed onto a single curve as shown by Landman & Saffman and given in Fig. 3(b). This curve corresponds to

Table 1. Initial condition and run parameters for the simulations.

Case	E	$S^*_{\gamma_0}$	$S^*_{\epsilon_0}$	Re_{T_C}	GRID	κ_p
e1	1.1	17.7527	1.68691	51	128 × 220 × 128	24
e2	1.25	7.68481	1.68691	51	256 × 440 × 256	48
e2a	1.25	1.68691	0.370297	51	128 × 220 × 128	24
e3	1.5	4.38597	1.68691	51	256 × 440 × 256	48
e4	2.0	2.81152	1.68691	51	256 × 440 × 256	48
e5	3.0	2.10864	1.68691	51	256 × 512 × 256	48
s1	∞	1.68691	1.68691	51	128 × 220 × 128	24
s1a	∞	1.68691	1.68691	102	192 × 330 × 192	24

a cross-section through the contour plot of Fig. 3(a) for a fixed rotation rate, γ, as indicated by the horizontal dotted line in Fig. 3(a). If the growth rate is nondimensionalized by the strain rate, one obtains the plot of σ/ϵ shown in Fig. 3(c). This curve correspond to a cross-section through the contour plot of Fig. 3(a) for fixed strain rate, ϵ, as indicated by the vertical dotted line. Bayly plotted the nondimensional growth rate as σ/Ω, where $\Omega = \sqrt{\gamma^2 - \epsilon^2}$ is the angular rotation rate for a fluid element as it traverses an elliptic streamline. This curve corresponds to a cross-section through the contour plot at a fixed Ω or through the nondimensional parameter space of Fig. 2 at a fixed Rossby number, $Ro = k/(\epsilon\Omega)$. Landman & Saffman point out that the plot of Bayly does not give a good indication of the behavior of the growth rate as one approaches pure shear, $\beta = 1$. The most complete picture, however, comes from the contour plot in Fig. 3(a) together with the cross-sections in Figs. 3(b) and (c). For cases with a fixed initial rotation rate, there is an aspect ratio for which the growth rate is a maximum (near $E = 3.0$). For cases with a fixed initial strain rate, the growth rate increases as the rotation rate increases. For cases with a fixed initial Rossby number, the growth rate decreases as the rotation rate increases. Therefore, the effect of rotation cannot be put into the simple statement that strong rotation suppresses the growth of turbulence, as is often assumed. In the sections that follow, the growth rate of the turbulence within the DNS will be examined and the trends will be compared to those seen from the linear theory.

3.3 Turbulence evolution

The elliptic streamline flow is linearly unstable for any non-zero strain rate, ϵ. From the linear theory the turbulent kinetic energy grows exponentially. Larger length scales are not affected by viscosity and have a larger growth rate. Therefore, eventually the flow becomes dominated by larger and larger length scales. When this happens the energy containing eddies outgrow the computational domain. They

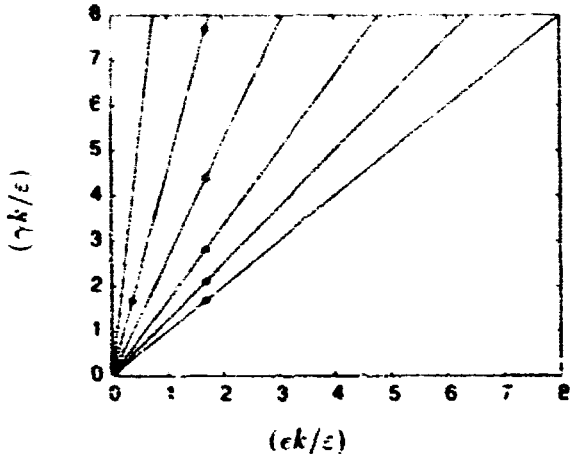

FIGURE 2. Parameter space based on the initial nondimensional strain rate and rotation rate. The 45° line corresponds to shear flow ($E = \infty$). The other radial lines are for $E = 3.0, 2.0, 1.5, 1.25$ and 1.1. The circles indicate the initial conditions for the current simulations.

become affected by the periodic boundary conditions and the statistics are no longer reliable.

Since the dominant effect of rotation on the turbulence is to suppress the nonlinear cascade, it is useful to have a measure of the nonlinear transfer of energy from large scales to small scales. Mansour *et al.* (1991) used a generalized skewness defined by

$$S = -\frac{6\sqrt{15}}{\tilde{\tau}} \frac{\int \kappa^2 T(\kappa)\, d\kappa}{\left(\int \kappa^2 E(\kappa)\, d\kappa\right)^{3/2}} \quad . \tag{5}$$

where κ is the magnitude of the wavenumber vector, $E(\kappa)$ is the three-dimensional energy spectrum, $T(\kappa)$ is the transfer spectrum, and the numerical prefactor is such that for isotropic turbulence S is approximately -0.5.

The evolution of the skewness S is shown in Fig. 4(a) for simulations which span the range of aspect ratios $E = 1.25$, 1.5, 2.0, and 3.0. As soon as the mean flow is turned on, the skewness begins to drop in magnitude, indicating that the nonlinear cascade is inhibited. The cases with lower aspect ratios (more dominated by rotation) have a skewness that comes closer to zero. So, as one would expect, stronger rotation leads to stronger suppression of the nonlinear processes. Interestingly enough the simulations show that the skewness recovers at later times as the turbulence grows. Also, it seems that the skewness approaches an asymptotic value that is the same for all aspect ratios, although the case with $E = 1.25$ could not be carried far enough in time to see if the skewness recovers fully.

The linear stability analysis of the elliptic streamline flow indicates that the turbulent kinetic energy grows exponentially. A nondimensional growth rate can be defined by

$$\frac{1}{\epsilon k}\frac{dk}{dt} \quad . \tag{6}$$

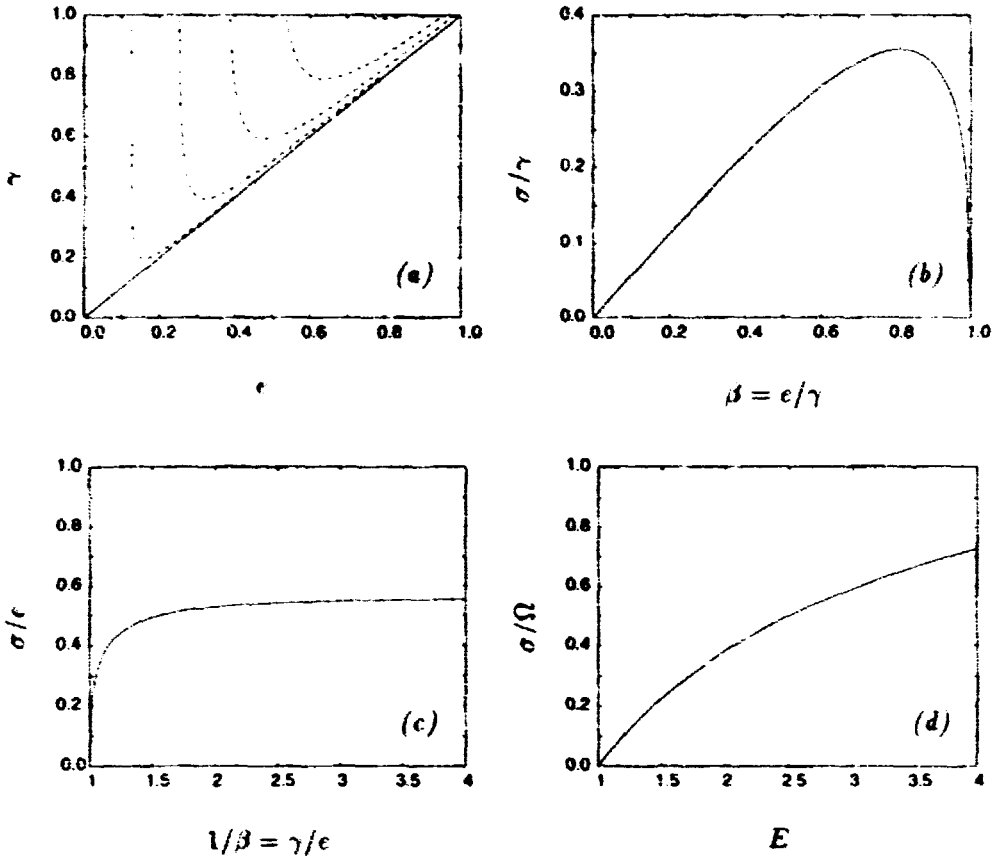

FIGURE 3. *(a)* Contours of inviscid growth rate σ. *(b)* Nondimensional growth rate for constant γ. *(c)* Nondimensional growth rate for constant ϵ. *(d)* Nondimensional growth rate for constant Ω.

This nondimensional growth rate is shown in Fig. 4(b) for the same series of simulations as above. After the flow develops for a while a roughly constant positive level is reached, which indicates that k is growing exponentially. The growth rate nondimensionalized by the strain rate, ϵ, is highest for the case with the lowest aspect ratio (strongest rotation), which is in agreement with the trend of the linear stability analysis shown in Fig. 3(c). However, at later times the simulations seem to change to a lower growth rate as nonlinear effects become more important. Without carrying the simulations further in time it is difficult to determine whether they approach a universal growth rate that is independent of aspect ratio.

One concern about the current simulations is that the initial Reynolds number is very low. In order to use the DNS results for comparisons with high Reynolds number formulations of turbulence models, the nondimensional turbulent statistics should be independent of Reynolds number. For the current simulations that is not the case. Figs. 5(a) and (b) show the skewness and the growth rate for the two shear

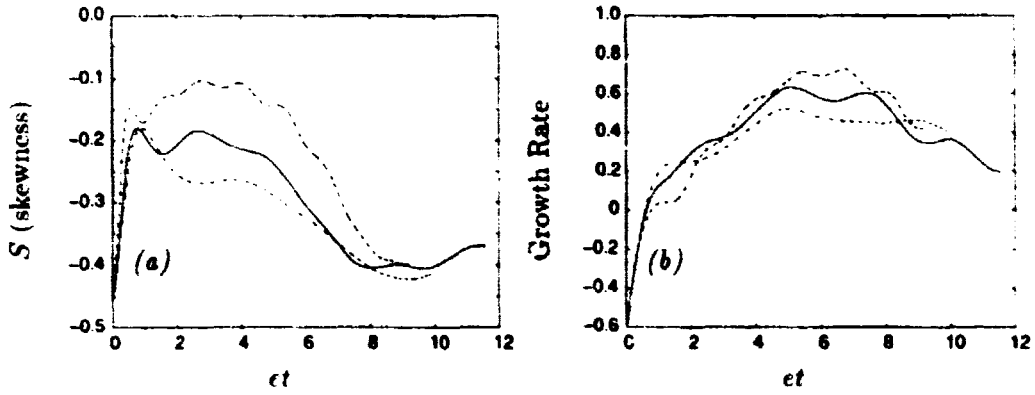

FIGURE 4. *(a)* Generalized skewness and *(b)* nondimensional growth rate of the turbulent kinetic energy for cases e2 (·····), e3 (- - - -), e4 (——), and e5 (— · —).

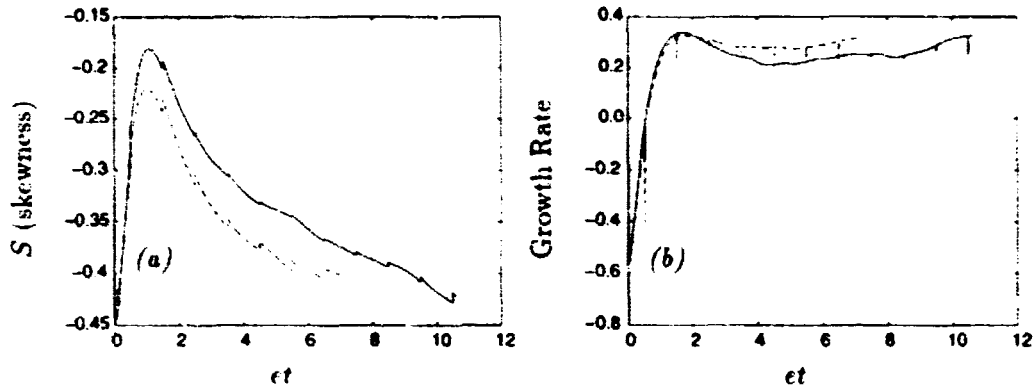

FIGURE 5. *(a)* Generalized skewness and *(b)* nondimensional growth rate of the turbulent kinetic energy for cases s1 (——), s1a (- - - -).

flow simulations s1 and s1a. Simulation s1 is similar to the elliptic streamline flow simulations that are described above. Simulation s1a has a higher initial turbulent Reynolds number, as shown in Table 1. The larger grid for case s1a is in order to ensure adequate resolution of the small scales. As shown in Fig. 5 there is a significant difference in the skewness and the growth rate for the two runs, which can be attributed to the differences in Reynolds number. The sudden jumps are an artifact of the periodic remeshing process used in the shear flow simulations (see Rogallo 1981). The low Reynolds numbers of the current simulations is caused by having a long period of isotropic decay before the elliptic flow runs are begun. Alternate methods that would allow the initial Reynolds number to be much higher are discussed in section 4.

Most of the simulations in this study have the same initial strain rate. This was done in order to focus on the effect of mean flow rotation. In order to make the study more complete, simulations were also done with a fixed initial mean rotation

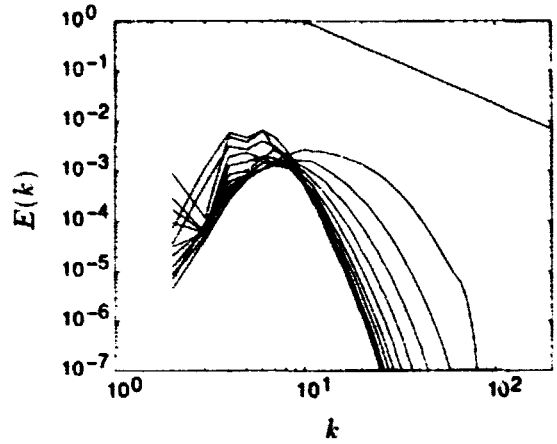

FIGURE 6. Development of the three-dimensional energy spectrum, $E(k)$, for case e2a.

rate, such as cases e2a and s1. However, cases with low aspect ratios and low mean rotation rates are difficult to do. The problem can be seen in Fig. 6, which shows the evolution of the three-dimensional energy spectrum for elliptic flow e2a. The energy in the small scales continually decays while energy in the large scales grows from the instability. The large scales quickly outgrow the computational box as indicated by the spectrum at low wavenumbers. It seems that it would be desirable to simply reduce the resolution of the small scales and increase the computational domain size. However, this cannot be done without compromising the resolution of the isotropic initial conditions. A simple analysis can be done to explain the behavior seen in Fig. 6. From the viscous analysis of Landman & Saffman, there is a high wavenumber cut-off beyond which the flow is stable. This wavenumber is given by a critical Ekman number, $E_\gamma(\beta) = 2\pi\nu\kappa_0^2/\gamma$, where κ_0 is the magnitude of the critical wavenumber. Using $Re_T = q^4/(\varepsilon\nu)$ and $S_\gamma^* = \gamma k/\varepsilon$, the definition of the critical Ekman number can be rearranged to give

$$\frac{\kappa_0}{\kappa_p} = \left(\frac{\varepsilon}{\kappa_p q^3}\right)\left[\frac{E_\gamma(\beta) Re_T S_\gamma^*}{\pi}\right]^{1/2}, \tag{7}$$

where κ_p is the peak in the instantaneous energy spectrum. Taking a value of $\varepsilon/(\kappa_p q^3) = 0.28$, $\beta = 0.22$, and $E_\gamma(\beta) = 0.6$ gives, $\kappa_0/\kappa_p = 1.1$. Therefore, for simulation e2a the viscous cut-off wavenumber is at about the peak in the energy spectrum from the decayed isotropic initial conditions, which seems to correspond roughly to what is observed in Fig. 6.

It is desirable to have a greater fraction of the wavenumbers used in the simulation in the unstable range. In order to perform good quality simulations one needs κ_0/κ_p to be large (preferably at least 2). Equation (7) shows that this is more difficult for simulations with lower nondimensional rotation rates, S_γ^*, and that to achieve this, simulations with higher Reynolds numbers are needed.

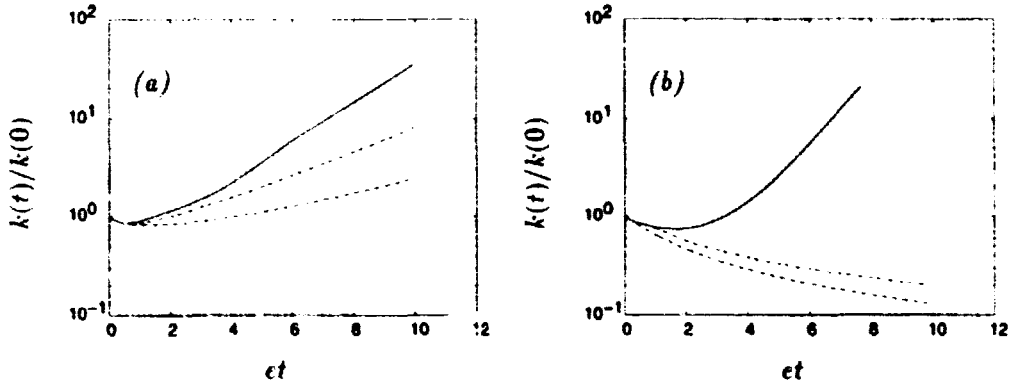

FIGURE 7. Nondimensional turbulent kinetic energy, k, from the DNS (——), using the LLR model (— · —), and using the SSG model (- - - -) for *(a)* case e5 with $E = 3.0$ and *(b)* case e2 with $E = 1.25$.

3.4 Comparison with turbulence models

A brief comparison is made between the DNS data for the elliptic streamline flow and two standard Reynolds stress models — the Launder, Reece and Rodi (1975) model (LRR) and the Speziale, Sarkar and Gatski (1991) model (SSG). It must, however, be borne in mind that the comparison being made is between low Reynolds number DNS data and high Reynolds number formulations of the turbulence models. Figs. 7(a) and (b) show the comparison for the nondimensional turbulent kinetic energy for cases e5 and e2 with $E = 3.0$ and 1.25 respectively. For the case with $E = 3.0$, which is not so dominated by strong rotation, the models predict exponential growth. However, the growth rate is substantially lower than that seen in the DNS. The LLR model gives a higher growth rate than the SSG model because the SSG model is sensitized to rotation and reduces the growth rate for strong rotation. Based on the growth rates seen at later times in Fig. 4(b), DNS at higher Reynolds numbers may give lower growth rates, which would be closer to those of the models.

In Fig. 7(b) the comparison is made for the case with $E = 1.25$, which is more rotation dominated. For this case both models predict decay while the DNS shows exponential growth. Here the models are seen to give the wrong qualitative behavior. Speziale *et al.* (1996) have pointed out the need for turbulence models to predict growth for flows that are linearly unstable. Clearly standard Reynolds stress models fail for strongly rotating flows, and there is a need for model improvement.

4. Conclusions and suggestions for future work

The study of the elliptic streamline flow begun by Blaisdell & Shariff (1994) has been continued by performing simulations over a range of parameters. The elliptic streamline flow is a homogeneous turbulent flow that combines solid body rotation and strain. It is an important flow for understanding the effects of rotation on engineering turbulent flows.

For short times the imposition of the mean flow suppresses the nonlinear cascade, but at later times nonlinearity is reestablished. As evidenced by the skewness, the growth rate of the turbulent kinetic energy, and other statistics, the turbulence seems to develop toward an asymptotic state that is independent of the ratio of mean rotation to mean strain

A comparison with standard Reynolds stress models shows that the models fail to give the correct qualitative behavior for large rotation rates. However, the current simulations have a very low initial turbulent Reynolds number and, therefore, meaningful quantitative comparisons with the models cannot be made.

Future simulations should be done at higher Reynolds numbers. One reason for the low Reynolds numbers of the current simulations is the method of generating initial conditions. The initial conditions for the elliptic flow simulations are taken from fully developed decaying isotropic turbulence. During the isotropic decay the Reynolds number falls to very low values. One approach to overcome this is to not have any isotropic decay period, similar to the shear flow simulations of Rogers *et al.* (1986). The mean flow would be turned on with randomly generated initial conditions. A disadvantage of this method is that turbulence models cannot be expected to follow the unphysical development at early time; however, comparisons can be made with turbulence models by starting the initial conditions for the model calculations using the DNS data at some time after the flow has developed. A second method to produce higher Reynolds number isotropic initial conditions is to artificially keep the turbulent Reynolds number fixed at a high value by changing the viscosity before allowing the turbulence to decay. This was done by Blaisdell *et al.* (1991) and produces developed isotropic turbulence at a relatively high Reynolds number. Both approaches are being pursued.

Acknowledgements

The authors thank Dr. R. S. Rogallo for use of his program. Also, discussions with Dr. A. A. Wray and Professors W. C. Reynolds and C. G. Speziale were very helpful.

REFERENCES

BAYLY, B. J. 1986 Three dimensional instability of elliptic flow. *Phys. Rev. Lett.* **57**, 2160-2171.

BENOIT, J.-P. 1992 Etude expérimentale et théorique d'une turbulence homogéne soumise à des effets couplés de rotation et de déformation plane. Ph.D. thesis, L'Ecole Central de Lyon, France.

BLAISDELL, G. A., MANSOUR, N. N. & REYNOLDS, W. C. 1991 Numerical simulation of compressible homogeneous turbulence. Thermosciences Division Report TF-50, Stanford University, Stanford, California.

CAMBON, C., BENOIT, J. P., SHAO, L. & JACQUIN, L. 1994 Stability analysis and large-eddy simulation of rotating turbulence with organized eddies. *J. Fluid Mech.* **278**, 175.

CAMBON, C., TEISSÈDRE, C. & JEANDEL, D. 1985 Etude d'effets couplés de déformation et de rotation sur une turbulence homogéne. *J. Méc. Théo. Appl.* **4**, 629.

LANDMAN, M. J. & SAFFMAN, P. G. 1987 The 3-D instability of strained vortices in a viscous fluid. *Phys. Fluids* **30**, 2339–2342.

LAUNDER, B. E., REECE, G. & RODI, W. 1975 Progress in the development of a Reynolds stress turbulence closure. *J. Fluid Mech.* **68**, 537.

LUNDGREN, T. S. & MANSOUR, N. N. 1996 Transition to turbulence in an elliptic vortex. *J. Fluid Mech.* **307**, 43–62.

MALKUS, W. V. R. 1989 An experimental study of global instabilities due to the tidal (elliptical) distortion of a rotating elastic cylinder. *Geophys. Astrophys. Fluid Dyn.* **48**, 123–134.

MALKUS, W. V. & BERRY, M. E. 1988 Order and disorder in planetary dynamos. *Summer Study Program in Geophysical Fluid Dynamics*, (eds. W. V. Malkus and M. E. Berry).

MANSOUR, N. N., CAMBON, C. & SPEZIALE, C. G. 1991 Single point modeling of initially isotropic turbulence under uniform rotation. Center for Turbulence Research. *Annual Research Briefs*, NASA Ames/Stanford Univ.

PIERREHUMBERT, R. T. 1986 Universal short-wave instability of two-dimensional eddies in an inviscid fluid. *Phys. Rev. Lett.* **57**, No. 17, 2157–2159.

ROGALLO, R. S. 1981 Numerical experiments in homogeneous turbulence. NASA Technical Memorandum 81315.

ROGERS, M. M., MOIN, P. & REYNOLDS, W. C. 1986 The structure and modeling of the hydrodynamic and passive scalar fields in homogeneous turbulent shear flow. Thermosciences Division Report TF-25. Stanford University, Stanford, California.

SPEZIALE, C. G., ABID, R. & BLAISDELL, G. A. 1996 On the consistency of Reynolds stress turbulence closures with hydrodynamic stability theory. *Physics Fluids.* **8**, 781–788.

SPEZIALE, C. G., SARKAR, S. & GATSKI T. B. Modeling the pressure-strain correlation of turbulence: An invariant dynamical systems approach J. Fluid Mech *227*. **245.**

WALEFFE, F. 1990 The three-dimensional instability of strained vortices. *Phys. Fluids A.* **2**, 76–80.

WIDNALL, S. E., BLISS, D. B., & TSAI, C.-Y. 1974 The instability of short waves on a vortex ring. *J. Fluid Mech.* **66**, 35–47.

NEXT
DOCUMENT

Drag reduction in turbulent MHD pipe flows

By P. Orlandi[1]

This is a preliminary study devoted to verifying whether or not direct simulations of turbulent MHD flows in liquid metals reproduce experimental observations of drag reduction. Two different cases have been simulated by a finite difference scheme which is second order accurate in space and time. In the first case, an external azimuthal magnetic field is imposed. In this case, the magnetic field acts on the mean axial velocity and complete laminarization of the flow at $Ha = 30$ has been achieved. In the second case, an axial magnetic field is imposed which affects only fluctuating velocities, and thus the action is less efficient. This second case is more practical, but comparison between numerical and experimental results is only qualitative.

1. Introduction

Magneto-Hydro-Dynamic (MHD) flows received much attention in the sixties and, after a period of loss of interest, there is a renewal of interest shown in this activity. Attempts, for example, have been recently done in laboratory experiments (Henoch & Stace 1995) to use MHD effects as an efficient way to reduce the drag of bluff bodies in sea water. The present study is devoted to showing that some of the experimental observations in liquid metals can be qualitatively described by a coarse direct simulation of the full system of Navier-Stokes equations and magnetic field equations without any low magnetic Reynolds number approximation. For liquid metals such as sodium or mercury, the Reynolds numbers are in a range affordable by direct simulations. Direct simulation can then be used as a design tool in practical applications. In liquid metals experiments, it is almost impossible to perform flow visualizations, and measurements of turbulent quantities are complex and difficult. Direct simulations provide these desired turbulent velocity profiles.

The previous direct simulations of MHD flows were, for the major part, devoted to isotropic turbulence (Kida *et al.* 1991) and, to my knowledge, there was only one devoted to LES of flows in the presence of solid boundaries. Shimomura (1991) considered the case of a magnetic field perpendicular to the wall and, in this case, the drag increased as observed in the experiment of Reed & Likoudis (1978). On the other hand, drag reduction occurs when the magnetic field is directed in the streamwise or spanwise directions. The realization in the laboratory of the second case is easy to observe for a plane channel with a reasonable aspect ratio, but the Hartmann boundary layers on the side walls can play a role. In a circular pipe

1 Università di Roma "La Sapienza" Dipartimento di Meccanica e Aeronautica, via Eudossiana 18 00184 Roma, Italy

one way to assign the external azimuthal magnetic field is by an electrical wire as thin as possible located at the center of the pipe; this set-up is difficult to realize and could influence the flow-field. This is why, for the case of spanwise external magnetic fields, there are a large number of experiments only for plane geometries, and some of these are listed in the review papers by Moffatt and Tsinober (1992) and by Tsinober (1990).

The realizations of an axial magnetic field inside a circular pipe is easier to set up, and two well documented experiments by Fraim & Heiser (1968) and by Krasil'nikov *et al.* (1973) are available. The friction coefficient reduction was measured at different Re and intensities of the externally applied magnetic field. The main difference between the cases of asymuthal and axial fields is that, in the case of an azimuthal field, the Lorenz force acts on the mean streamwise velocity profile, reducing the mean shear and thus the production of turbulent energy. In the presence of an axial field, the Lorenz force acts on the fluctuating components, and thus is less effective.

In both cases, without the use of superconducting materials, the efficiency, that is, the ratio between the input power and the power saved by the skin friction reduction, is very low. Thus, this approach is useful only in applications for which efficiency is not important, but it is important to reach a drag-free state. This, for example, occurs in nuclear reactors employing liquid sodium as cooling system and in some stainless steel production stages.

Dealing with liquid metals, the low magnetic Prandtl number approximation is valid. In this case, the current density can be calculated by solving one elliptic equation for the electrical potential instead of solving the full systems of Maxwell equations. This approximation was used by Shimomura (1991) and Tsinober (personal communication) in a pipe with an azimuthal external magnetic field. I made an attempt to follow this direction, but encountered numerical difficulties. Thus, I decided to solve the full system of Maxwell equations, which are straightforward to add to a code in which the Navier-Stokes equations are solved. The full solution can be used to test the solutions with the simplified equation.

2. Physical and numerical model

The dimensionless Navier-Stokes equations when a conducting fluid is subjected to a magnetic field are

$$\frac{D\mathbf{U}}{Dt} = -\nabla p + \frac{1}{Re}\nabla^2\mathbf{U} + \frac{Ha^2}{Re^2 P_m}\nabla \times \mathbf{B} \times \mathbf{B},$$

where in the Lorenz force the relationship between the current density, $\mathbf{J}$, and the magnetic field, $\mathbf{B}$, $\mathbf{J} = \nabla \times \mathbf{B}$ was used. $\mathbf{B}$ is calculated by

$$\frac{D\mathbf{B}}{Dt} = \frac{1}{Re P_m}\nabla^2\mathbf{B} + (\mathbf{B}\cdot\nabla)\mathbf{U}.$$

The dimensionless equations have been obtained by using the pipe radius R as reference length, the laminar Poiseuille velocity U_P as velocity scale, and the magnitude of the externally applied magnetic field B_0. Together with the fluid properties,

ν the kinematic viscosity, μ the magnetic permeability, and σ the electrical conductivity, the dimensionless numbers are: $Re = U_b D/\nu = U_P R/\nu$ is the Reynolds number, $P_m = \nu\mu\sigma$ is the magnetic Prandtl number, and $Ha = B_0 R\sqrt{\sigma/\rho\nu}$ is the Hartmann number.

These equations can be solved once the appropriate boundary conditions are assigned. This paper deals with flows inside a circular pipe, hence the usual no-slip conditions are assumed on the wall. Being interested only in the fully developed statistical steady state, periodicity is assumed in the streamwise direction. The components of the mean velocity $\mathbf{U}$ are $U_r = U_\theta = 0$ and $U_x(r) \neq 0$; if we assume the condition that the external magnetic field is only azimuthal, the mean magnetic field is $B_\theta = B_0 r$. On the other hand, if there is only an axial field, it must be $B_x = B_0$. By these boundary conditions, in the B_θ case, the result is that on the pipe wall there is a strong current density. In the B_x case the current density is low.

From a physical point of view it is interesting to compare the action of the Lorenz for the two cases, and the low Reynolds number approximation facilitates this analysis. With this approximation, the equations of the magnetic field are replaced by the equation for the potential of the electric field Φ which is related to the current density by $J = -\nabla\Phi + \mathbf{U} \times \mathbf{B}$. Φ can be calculated by the equation

$$\nabla^2\Phi = \nabla \cdot \mathbf{U} \times \mathbf{B},$$

which is obtained by imposing $\nabla \cdot \mathbf{J} = 0$. The components of the Lorenz force for $B_\theta = B_0 r$ are

$$\frac{\partial q_r}{\partial t} \approx \frac{Ha^2}{Re}\left[-\frac{r\partial\Phi}{\partial x} - q_r B_\theta\right]B_\theta$$

$$\frac{\partial q_x}{\partial t} \approx \frac{Ha^2}{Re}\left[-\frac{\partial\Phi}{\partial r} - q_x B_\theta\right]B_\theta$$

and for $B_x = B_0$

$$\frac{\partial q_r}{\partial t} \approx \frac{Ha^2}{Re}\left[-\frac{r\partial\Phi}{\partial\theta} - q_r B_x\right]B_x$$

$$\frac{\partial q_\theta}{\partial t} \approx \frac{Ha^2}{Re}\left[-\frac{r\partial\Phi}{\partial r} - q_\theta B_x\right]B_x.$$

The result is that in the first case the external magnetic field decreases the mean axial velocity, U_x, and thus the reduction of turbulence is more effective since the mean shear is reduced. In the second case the magnetic field acts only on the fluctuating components.

An attempt has been made to solve this simplified set of equations, but the results were not satisfactory. An initial explanation is that, to maintain a constant flow rate, the pressure gradient has to account for the part of the Lorenz force proportional to B_θ^2, and since this term at high Ha is greater than the friction losses, the evaluation of the skin friction is not accurate. Dealing with the full

system of equations, the contribution of Lorenz force to the mean pressure gradient is zero.

The second order staggered mesh finite difference scheme in space and time developed by Verzicco & Orlandi (1996) that has been tested for several laminar flows, and for rotating and non-rotating turbulent pipes (Orlandi & Fatica 1996), was adapted to solve the magnetic equations. To deal with the axis of symmetry, the quantities $h_r = rb_r, h_\theta = rb_\theta, h_z = b_z$ have been used, as was done for the velocity components ($q_r = rv_r, q_\theta = rv_\theta, q_z = v_z$). The B and U components are located at the center of the face of the cell. The fractional step method used for the velocity field was used for the magnetic field.

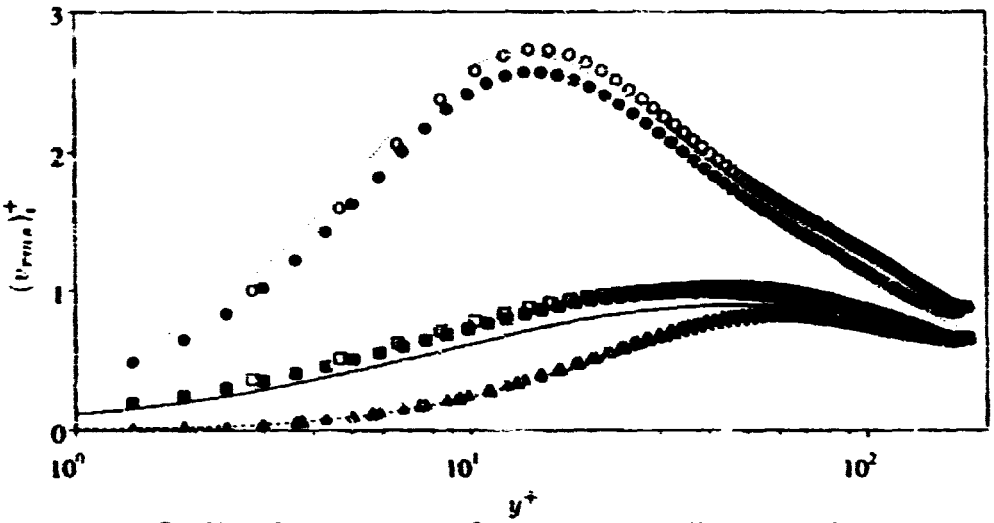

FIGURE 1. Profiles of rms vorticity fluctuations in wall units, a) lines, present $65 \times 65 \times 65$, b) closed symbols present $129 \times 97 \times 129$ c) open symbols Eggels *et al.* $257 \times 129 \times 129$ (——, ■, □, v'_θ), (- - - -, ▲, △, v'_r), (· · · · ·, ●, ○, v'_z).

3. Results

Without the magnetic field, the turbulence intensities are higher; therefore, the validation of the grid adequacy has been performed for $Ha = 0$. The simulation with the magnetic field requires more memory and longer CPU time because of three more parabolic equations. This study is limited to the investigation of whether or not direct simulations reproduce the drag reduction observed in the experiments. With this in mind,the strategy for the choice of the grid has been that the grid is kept as small as possible such as to give satisfactory results for the second order statistics. Fig. 1 shows that a grid with $65 \times 65 \times 65$ mesh points gives normal stresses profiles in wall units in good agreement with those by more refined simulations ($129 \times 97 \times 129$) and with that by Eggels *et al.* (1994) with a more refined grid in r. A coarse simulation does not resolve the velocity gradients, and this affects the *rms* profiles in a different manner. From previous simulations (Orlandi & Fatica 1996), at $Ha = 0$ it has been observed that insufficient resolution in θ and x produces a

reduction in the level of v_r' and v_θ' while that in r affects v_z'. This explains why the present coarse $v_{r,rms}$ profile near the wall agrees with that by Eggels *et al.* (1994), which was obtained by a uniform grid in r. 97 equidistant points in r located only 7 points within $y^+ = 15$, while the present nonuniform grid located 18 points in the same distance. The differences are not very pronounced, thus this resolution is satisfactory for a preliminary understanding of MHD drag reduction.

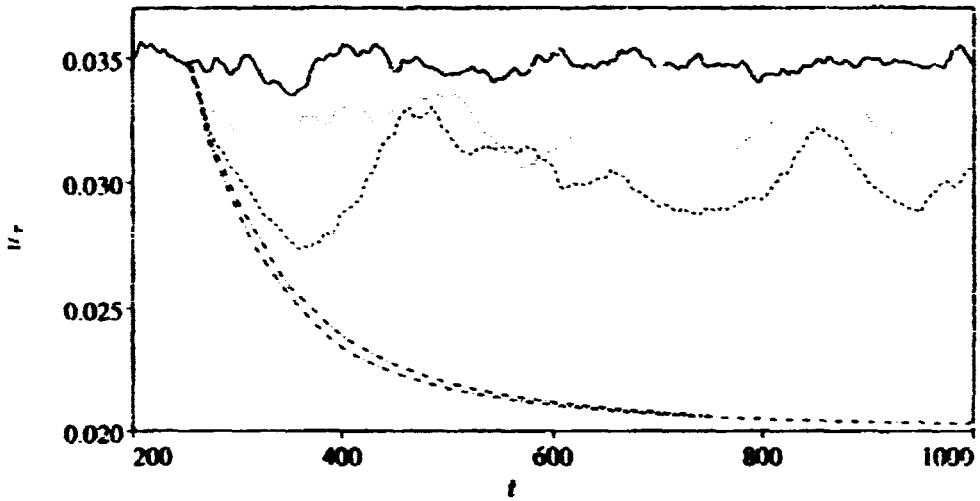

FIGURE 2. Time evolution of u_τ for external B_θ (—— $Ha = 0$), (····· $Ha = 20$), (- - - $Ha = 28$), (—·— $Ha = 30$), (——— $Ha = 32$).

The simulations of an external azimuthal magnetic field have been performed for $Ha = 20, 28, 30$, and 32, starting from the field at $t = 250$ of $Ha = 0$ and advancing for 750 dimensionless time units. The statistics were computed from 50 fields 10 time units apart. The evolution within the first 250 time units was discarded since in this period the flow adjusts to the abrupt effects of the magnetic field. The u_τ time evolution in Fig. 2 shows that this transitory period is long enough even for the high Ha number. Fig. 2 furthermore shows that the magnetic field reduces the high frequency oscillations, and that for high Hartmann numbers ($Ha \geq 30$) the flow becomes laminar. In the experiment by Branover *et al.* (1966), in a plane channel with an aspect ratio $b/a = 0.067$, the Hartman layers on the vertical wall do not play a substantial role. Thus the results could be considered for comparison with the present simulations. However also in absence of a magnetic field, the pipe and the two-dimensional channel differ, as for example shown by Durst *et al.* (1995), thus differences should be expected in the presence of the magnetic field. In the experiment $\lambda = C_{fH_a}/C_{f0}$, that is, the ratio between the C_f with and without magnetic field depends on the Reynolds number. At $Re = U_b D/\nu = 7600$ for $Ha = 20$ and 28, λ is respectively equal to 0.82 and 0.62. In the pipe it was found to be 0.86 and 0.77, and at approximately $Ha = 30$ a laminar state was achieved. Recall that, at $Re_\tau = 186$ in the channel, the corresponding Reynolds number based on full width and centerline velocity is $Re = U_b 2\delta/\nu = 5600$; at this Reynolds

number the experiments of Branover *et al.* (1966) show a laminar state, and the present simulations differ more from the experiments.

The same initial conditions were used to solve the case of an axial magnetic field. Fig. 3 shows that u_τ does not change considerably going from $Ha = 20$ to 60. The experiment by Fraim & Heiser for $Re = 4900$ at $Ha/Re = 0.122$ gives for the friction factor $\lambda = 0.0305$, a value smaller than 0.035 found in the present simulation. The experimental and the numerical simulations produce a value of 0.385 for $Ha = 0$. Attempts were done to perform simulations at higher Hartmann numbers to investigate whether the numerical simulation in this case also reproduces a laminar state. The numerical simulation after the initial u_τ drop showed an increase of drag, associated with larger turbulent intensities near the center, and the calculation diverged. Different initial conditions such as the field for $Ha = 60$ at $t = 1000$ have also been tried without any success.

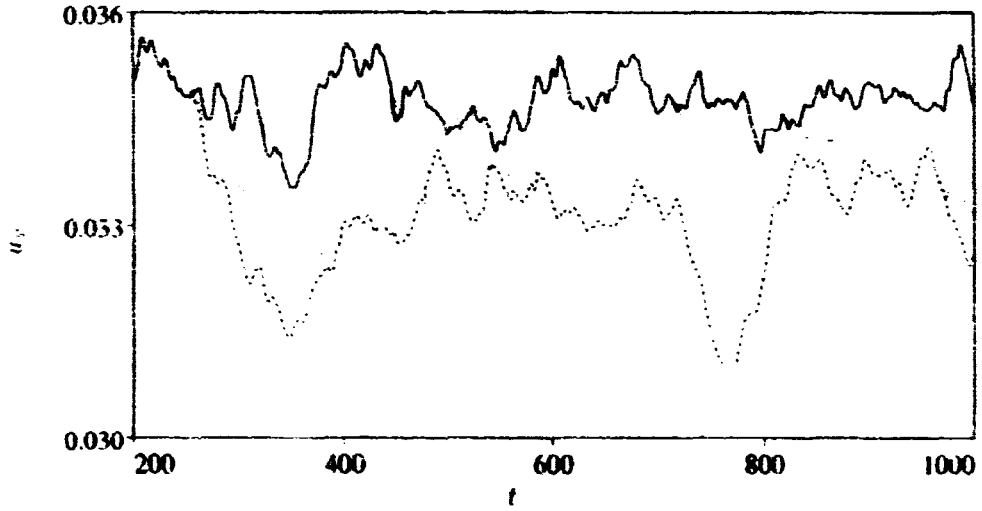

FIGURE 3. Time evolution of u_τ for external B_z (—— $Ha = 0$), (····· $Ha = 20$), (- - - - $Ha = 60$).

Before discussing the velocity and *rms* velocity profiles, it is interesting to understand why in these conditions the efficiency is very low. The efficiency is defined as the ratio between the energy saved by skin friction reduction and the input energy necessary to generate the magnetic field. It is $\epsilon = (1. - \lambda)ReR_\tau^2 Pm^2/Ha^2$. Since for liquid metals the magnetic Prandtl number is $O(10^{-7})$, it is clear why the efficiency is very low.

In spite of these difficulties it is interesting to make a comparison between the two cases, $Ha = 28$ and $Ha = 60$. Recall that, in presence of B_θ, the Lorenz force effects the mean velocity. Fig. 4 shows that the velocity profile no longer has the *log* law and that the profile is getting close to a laminar profile. On the contrary, the case with B_z has a well defined *log* law shifted upwards, reminiscent of other flows with drag reduction.

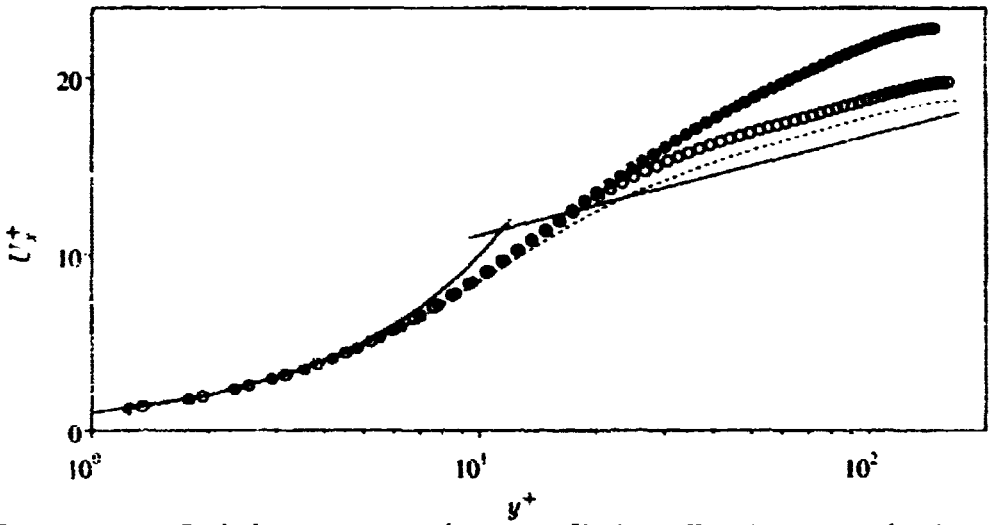

FIGURE 4. Radial streamwise velocity profile in wall units (—— *log* law), (····· $Ha = 0$), (• $Ha = 28$, B_θ), (○ $Ha = 60$, B_x).

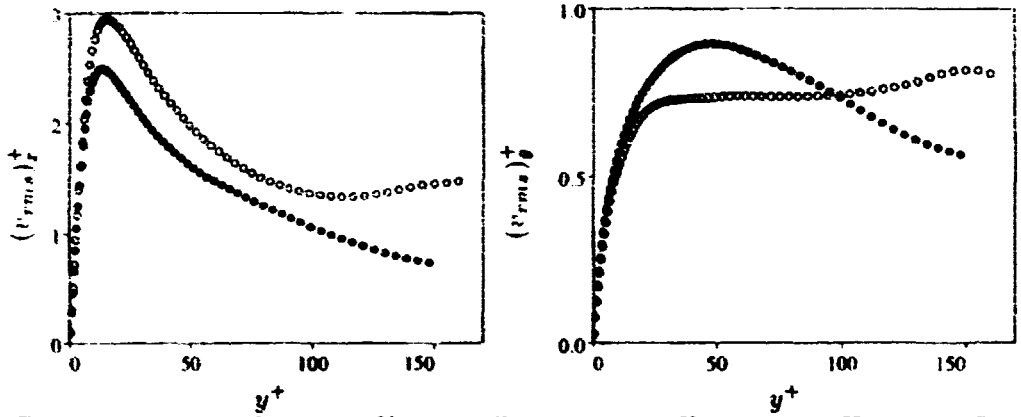

FIGURE 5. *rms* velocity profiles in wall units (····· $Ha = 0$), (• $Ha = 28$, B_θ), (○ $Ha = 60$, B_x).

The fields from direct simulations were used to explain through the profiles and the spectra of the normal turbulent stresses that the effects of the magnetic field are different in the two cases. The profiles of v_x' and v_r' in Figs. 5a-b show that B_θ reduces both the streamwise and the azimuthal fluctuation everywhere B_x has a more complex effect In fact, while the axial stress increases everywhere, v_θ' is reduced in the buffer region and increases at the center. For B_θ the drag reduction is associated with a reduction of turbulent intensity. On the other hand, for B_x the reduction is associated with modifications of the vortical structures. One-dimensional azimuthal energy spectra detect the size of the energy containing eddies, which near the wall are those responsible for the wall friction. These spectra are shown for the axial and azimuthal components at $y^+ \approx 10$, the location of high turbulence production.

In discussing the spectra in Figs. 6a-b, keep in mind contour plots of fluctuating velocity even if these plots are not presented. The spectra show that B_θ reduces the energy level at the small scales and there is a transfer of energy to the large scales. The spectrum for the B_r case shows that the containing energy scale of the v_r' components are larger than those without magnetic field. These then are located at a greater distance from the wall, and thus the friction decreases. For the azimuthal stresses, B_r produces a similar transfer at the large scales, but in this case the energy level is also reduced at each wave number.

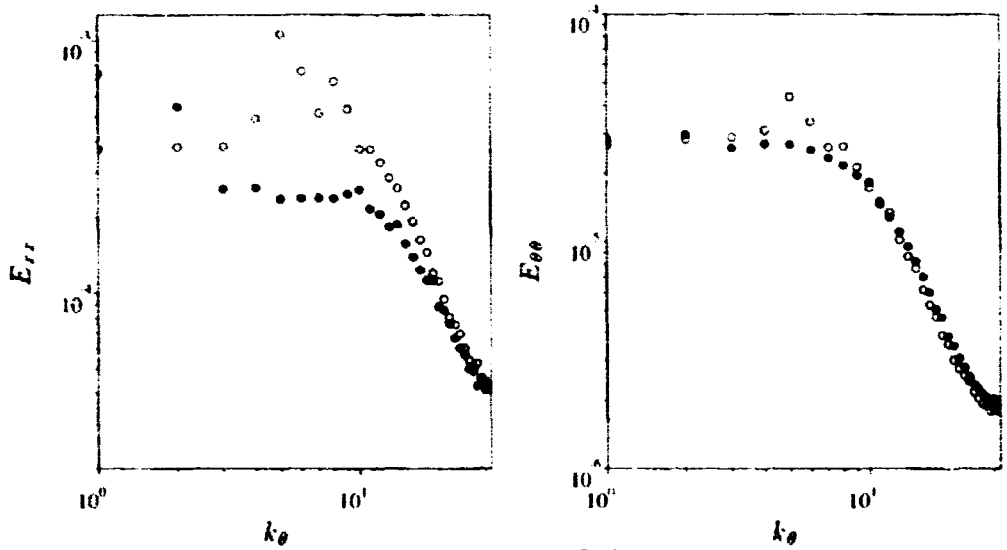

FIGURE 6. One-dimensional energy spectra: Left: azimuthal, Right: axial directions. (····· $Ha = 0$), (• $Ha = 28$, B_θ), (○ $Ha = 60$, B_r).

3. Conclusions

The present study has shown that the numerical simulation of MHD flows for liquid metal is feasible and that they can qualitatively reproduce experimental observations. It has been shown that for these fluids the drag reduction is inefficient: that is, that a large amount of electrical power must be furnished to achieve the desired goal. The reduction of the turbulent levels could be of great interest in several applications where the energy saving is not important. These direct simulations, moreover, have great interest *per se* in the study of turbulence physics when the turbulence is subjected to external forces. There are, in fact, similarities between MHD turbulence and turbulence subjected to background rotation as was claimed by Tsinober (1990). In both cases a drag reduction is achieved, but the mechanism is different. In a previous study (Orlandi 1995), it was found that background rotation breaks the symmetry of right- and left-handed vortical structures by increasing the helicity density near the wall. Thus the vortical structures have a greater degree of order leading to a reduction of production and dissipation near the wall. In the case of MHD flows the helicity density was null across the pipe

as for $Ha = 0$, and so the decrease of production and dissipation are due to the reduction of turbulence intensities. The effect is greater at the smaller scales. Thus, under the MHD effects, the small scale structures near the wall disappear and the large scales remain, producing less intense bursting events. However, the amount of disorder near the wall for MHD flows remains unchanged with respect to that of a non-rotating pipe.

It should be stressed that while these preliminary coarse direct simulations have reproduced the differences between the effects of an azimuthal and an axial magnetic field, the quantitative comparison between experimental and numeric results was poor. This needs to be explained and it requires a much longer time than that available during the summer program. All the mandatory grid resolution checks should be performed.

Acknowledgments

The author is sincerely grateful to the stimulating discussions with Prof. H. Choi during the summer school and to the private communication by Prof. A. Tsinober. The research was partially supported by MURST grants.

REFERENCES

BRANOVER, G. G., GEL'FAT, YU., M., & TSINOBER, A., 1966 Turbulent magnetohydrodynamic flows in prismatic and cylindrical ducts. *Magnetohydrodynamics.* **2,** 3-21.

DURST, F., JOVANOVIC', J. & SENDER, J. 1995 LDA measurements in the near-wall region of a turbulent pipe flow. *J. Fluid Mech.* **295,** 305-335.

KIDA, S., YANASE, S., & MIZUSHIMA, J. 1991 Statistical properties of MHD turbulence and turbulent dynamo. *Phys. Fluids A.* **3,** 457-465.

EGGELS, J. G. M., UNGER, F., WEISS, M. H., WESTERWEEL, J., ADRIAN, R. J., FRIEDRICH, R. & NIEUWSTADT, F. T. M. 1994 Fully developed turbulent pipe flow: a comparison between direct numerical simulation and experiment. *J. Fluid Mech.* **268,** 175-209.

FRAIM, F. W., & HEISER, W. H. 1968 The effect of a strong longitudinal magnetic field on the flow of mercury in a circular tube. *J. Fluid Mech.* **33,** 397-413.

HENOCH, C. & STACE, J. 1995 Experimental investigation of a salt water turbulent boundary layer modified by an apllied streamwise magnetohydrodynamic body force. *Phys. Fluids A.* **7,** 1371-1383.

KRASIL'NIKOV, E., YU. LUSHCHICK, V. G., NIKOLAENKO, V. S. & PANEVIN, I. G. 1970 Experimental study of the flow of an electrically conducting liquid in a circular tube in an axial magnetic field. *Fluid Dynamics.* **6,** 317-320.

MOFFATT, H. K. & TSINOBER, A. 1992 Helicity in laminar and turbulent flow. *Annu. Rev. Fluid. Mech.* **24,** 281-312.

ORLANDI, P. 1995 Helicity fluctuations and turbulent energy production in rotating and non-rotating pipes. *Annual Research Brief of CTR*, Center for Turbulence Research, NASA Ames/Stanford Univ., 198-208.

ORLANDI, P. & FATICA, M. 1996 Direct simulations of a turbulent pipe rotating along the axis. In the review process for *J. Fluid Mech.*

REED, C. B. & LIKOUDIS, P. S. 1978 The effect of a transverse magnetic field on shear turbulence. *J. Fluid Mech.* **89,** 147-171.

SHIMOMURA, Y. 1991 Large eddy simulation of magnetohydrodynamic turbulent channel flows under a uniform magnetic field. *Phys. Fluids A.* **3,** 3098-3106.

TSINOBER, A. 1990 MHD flow drag reduction. *Viscous drag reduction in boundary layers* Edited by D. M. Bushnell & J. N. Hefner Progress in Astronautics and Aeronautics. **123,** 327-349.

TSINOBER, A., 1990 Turbulent Drag Reduction Versus Structure of Turbulence. *Structure of Turbulence and Drag Reduction.* Ed. A. Gyr. Berlin: Springer Verlag. 313-340.

VERZICCO, R. & ORLANDI, P. 1996 A finite difference scheme for direct simulation in cylindrical coordinates. *J. Comp. Phys.* **123,** 402-414.